



Final Report

Aerodynamic Analysis and Design of Cable-Supported Bridges by Wind-Tunnel Test

By Assoc. Prof. Dr. Virote Boonyapinyo

January 2010





รายงานวิจัยฉบับสมบูรณ์

โครงการ การวิเคราะห์และออกแบบอากาศพลศาสตร์ ของสะพานขึง / แขวน โดยเคเบิล ด้วยการทดสอบในอุโมงค์ลม

โดย รศ. ดร. วิโรจน์ บุญญภิญโญ

มกราคม 2553

รายงานวิจัยฉบับสมบูรณ์

โครงการ
การวิเคราะห์และออกแบบอากาศพลศาสตร์
ของสะพานขึง / แขวน โดยเคเบิล
ด้วยการทดสอบในอุโมงค์ลม

รศ. ดร. วิโรจน์ บุญญูภิญโญ คณะวิศวกรรมศาสตร์ มหาวิทยาลัยธรรมศาสตร์

สนับสนุนโดยสำนักงานคณะกรรมการการอุดมศึกษา และสำนักงานกองทุนสนับสนุนการวิจัย

(ความเห็นในรายงานนี้เป็นของผู้วิจัย สกอ. และ สกว. ไม่จำเป็นต้องเห็นด้วยเสมอไป)

ACKNOWLEDGEMENTS

I would like to express my sincere gratitude to my formerly graduated students, department of civil engineering, Thammasat University, for their excellent assistants in doing this research and wind tunnel tests: Dr. Tharach Janesupasaeree, Mr. Worapoj Thammasungkheeti, and Mr. Pichet Klaharn.

I would also like to express my sincere acknowledge to Assoc. Prof. Dr. Pennung Warnitchai of Asian Institute of Technology, and Assoc. Prof. Dr. Nakhorn Poovarodom of Thammasat University for their good suggestions during my research work.

In addition, I would like to greatly acknowledge the Thailand Research Fund (TRF) and the Higher Education Commission under grant number RMU 4980012 for financial support this research, and Faculty of Engineering of Thammasat University for their supports in wind tunnel laboratory. Finally, I would like to thank the Department of Rural Road and the Public Works Department, Ministry of Interior, for information of the Industrial Ring Road Bridge project in this research.

บทคัดย่อ

รหัสโครงการ: RMU4980012

ชื่อโครงการ: การวิเคราะห์และออกแบบอากาศพลศาสตร์ของสะพานขึง / แขวน โดยเคเบิล ด้วย

การทดสอบในอุโมงค์ลม

ชื่อนักวิจัย : รศ. ดร. วิโรจน์ บุญญภิญโญ คณะวิศวกรรมศาสตร์ มหาวิทยาลัยธรรมศาสตร์

E-mail Address: bvirote@engr.tu.ac.th

ระยะเวลาโครงการ: กรกฎาคม 2549 – มกราคม 2553

งานวิจัยนี้ประกอบด้วยการเสนอวิธีการระบุค่าและการทดสอบเพื่อระบุค่าตัวแปรด้านอากาศพลศาสตร์ ที่สำคัญคือค่า Flutter derivatives และ ค่าสัมประสิทธิ์แรงสมสถิตของหน้าตัดสะพาน ค่าตัวแปรดังกล่าวเป็นตัว แปรหลักในการออกแบบสะพานช่วงยาว เช่น สะพานขึ้งและสะพานแขวน ภายใต้แรงลม ตลอดจนการหาค่า ความเร็วลมวิกฤติที่ทำให้สะพานเกิดการสูญเสียเสถียรภาพทางด้าน Flutter การระบุค่าตัวแปรเหล่านี้สามารถ กระทำใต้โดยการทดสอบในอุโมงค์ลม การศึกษานี้ได้เสนอวิธีการระบุค่าตัวแปร Flutter derivatives โดยวิธี ปริภูมิย่อยแบบเฟ้นสุ่ม (Stochastic subspace identification) จากข้อมูลการสั่นไหวของแบบจำลองของสะพาน ในอุโมงค์ลมภายใต้สภาพลมแบบราบเรียบและแปรปรวน จากการทดสอบทั้งแบบการสั่นแบบอิสระและการสั่น แบบสุ่ม ข้อดีของวิธีที่เสนอคือ การพิจารณาให้แรงลมที่มากระทำเป็นข้อมูลเข้า แทนที่จะเป็นสัญญาณรบกวน (Noise) งานวิจัยนี้ได้เสนอวิธีการที่เรียกว่า Data-driven stochastic subspace identification (SSI-DATA) ใน การระบุค่าตัวแปร และทำการเปรียบเทียบกับวิธีล่าสุดที่ได้รับความนิยมคือ Covariance-driven stochastic subspace identification (SSI-COV)

การศึกษาได้ประยุกต์ใช้สะพานขึ้งวงแหวนอุตสาหกรรมที่มีช่วงกลางสะพานยาว 398 เมตร โดยวิธี ทดสอบแบบต่างๆภายใต้สภาพลมแบบราบเรียบและแปรปรวน ผลการศึกษาพบว่าวิธี SSI-DATA ที่เสนอ ให้ ค่าที่ถูกต้องกว่าวิธี SSI-COV และวิธีนี้ยังใช้ได้กับการทดสอบทั้งแบบการสั่นแบบอิสระและการสั่นแบบสุ่ม นอกจากนี้ยังสามารถทำการทดสอบหาการสูญเสียเสถียรภาพแบบต่างๆและขนาดของการสั่นใหวของสะพานที่ ความเร็วลมต่างๆในการทดสอบครั้งเดียวกัน

ผลการศึกษาพบว่า ก) ภายใต้ความเร็วลมแบบราบเรียบสะพานจะเกิดการสูญเสียเสถียรภาพทางด้าน Flutter ที่ความเร็วลม 118 เมตรต่อวินาที ข) เกิดปรากฏการณ์ Vortex shedding ด้านการบิดที่ความเร็วลม 41 เมตรต่อวินาที ค) ผลของความแปรปรวนของลมทำให้สะพานมีเสถียรภาพที่ดีขึ้นโดยลดปรากฏการณ์ Vortex shedding และเพิ่มความเร็วลมที่ทำให้สะพานเกิดการสูญเสียเสถียรภาพ แต่จะเพิ่มการสั่นไหวของ สะพานเมื่อเปรียบเทียบกับสภาพลมแบบราบเรียบ และ ง) การปรับแต่งหน้าตัดเดิมโดยใช้ทั้ง Soffit plates และ Fairings ทำให้หน้าตัดมีประสิทธิภาพทางอากาศพลศาสตร์มากที่สุด โดยช่วยลดการตอบสนองแบบ Vortex shedding และเพิ่มความเร็วลมวิกฤติได้อย่างมาก ดังนั้นการออกแบบหน้าตัดให้เพรียวลมจึงเป็นสิ่งที่สำคัญ สำหรับการออกแบบสะพานช่วงยาวต้านทานแรงลม

คำหลัก: Flutter derivative, สะพานขึ้ง, การระบุค่าโดย Stochastic subspace, อุโมงค์ลม, การปรับ แต่งหน้าตัดทางอากาศพลศาสตร์

ABSTRACT

Project Code: RMU4980012

Project Title: Aerodynamic Analysis and Design of Cable-Supported Bridges by Wind-

Tunnel Test

Investigator: Assoc. Prof. Dr. Virote Boonyapinyo, Faculty of Engineering, Thammasat

University

E-mail Address: bvirote@engr.tu.ac.th

Project Period: July 2006 – January 2010

This study proposes the system identification technique and the experimental method for extracting the aerodynamic parameters of bridge decks. Flutter derivatives and aerostatic force coefficients are the essential aerodynamic parameters in the design of long-span cable supported bridges and the estimations of the flutter-instability critical wind velocity. These parameters can be experimentally estimated from wind tunnel test results. In this study, a theoretical model based on the stochastic subspace identification was used to extract the flutter derivatives of bridge deck sectional models from the two-degree-of-freedom free decay and buffeting responses. An advantage of the stochastic subspace identification technique is that it considers the buffeting forces and the responses as inputs instead of as noises as typically assumed in previous researches. The data-driven stochastic subspace identification technique (SSI-DATA) was proposed to directly extract the flutter derivatives of bridge deck sections model from their random vibration responses under wind flows. The results were then compared to those from the previous up-to-date covariance-driven stochastic subspace identification (SSI-COV).

Wind tunnel tests of a two-edge girder blunt type of Industrial-Ring-Road cable-stayed bridge (IRR) with 398 m center span length were conducted under both smooth and turbulence flows. The results from numerical simulation and wind tunnel tests show that applying the SSI-DATA yields better results than those of the SSI-COV. Moreover, the root-mean-square responses of a bridge deck can be obtained simultaneously from the same test without requiring separated tests as in case of the free decay method.

The results of study can be summarized as follows. a) the blunt type IRR Bridge section is susceptible to flutter instability at high wind speed of 118 m/s; b) the torsional vortex-shedding response was also observed at the full scale velocity of 41 m/s; c) compared with the smooth flow, the turbulence flow delays the onset of the flutter instability and reduces the vortex-shedding response; however, it raises the amplitude of the bridge responses progressively over the speed range; d) the combined fairing and soffit plate modified section is the most aerodynamic shape; this modified section can suppress the vortex shedding significantly and greatly increase the flutter velocity. Therefore, the aerodynamically-stable bridge section is the essential parameter for design of long-span cable-supported bridges under wind load.

Keywords: Flutter derivatives, cable-stayed bridge, stochastic subspace identification, wind tunnel, aerodynamic appendages

TABLE OF CONTENTS

		Page
	NOWLEDGEMENTS	
ABST	TRACT (IN THAI)	ii
	TRACT	
TABL	LE OF CONTENTS	iv
	PTER 1 INTRODUCTION	
	General Review and Problem Statements	
1.2	Objectives	4
1.3	Scope of Study	5
CITAT		0
	PTER 2 LITERATURE REVIEW	
	Free Vibration Method Output Only Model Identification Method	
	Output-Only Modal Identification Method	
	Stochastic Method A gradynamia A mandagas	
2.4	Aerodynamic Appendages	14
СНАІ	PTER 3 THEORETICAL BACKGROUND FOR WIND EFFECTS	
	ON LONG-SPAN CABLE-SUPPORTED BRIDGE	16
3.1	Design Concepts of a Cable-stayed Bridge	
	Static Behavior	
	Dynamic Behavior	
	Aerodynamic Instabilities	
	3.4.1 Vortex Shedding	18
	3.4.2 Galloping	
	3.4.3 Torsional Divergence	
	3.4.4 Flutter	24
	3.4.5 Flutter Derivatives at Vortex Lock-in	27
	3.4.6 Effects of Turbulence on Bridge Flutter Derivatives	28
3.5	Section Model Tests to Determine Aerodynamic Derivatives	29
	3.5.1 Test Arrangements for Free Vibration Responses	29
	3.5.2 Choice of Structural/Geometric Parameters for Section Tests	31
	3.5.3 General Equations of Motions	31
	3.5.4 Equations of Motions for SDOF Responses	33
	3.5.5 System Identification of 1-DOF Responses	34
	3.5.6 Equations of Motions for 2-DOF Responses	35
	3.5.7 System Identification of 2-DOF Responses	36
	3.5.7.1 Direct Curve Fit to 2-DOF Equations of Motion	37

		3.5.7.2 Covariance Block Hankel Matrix Method	40
3.6	Meth	odology for Section Model Tests in Wind Tunnel	41
	3.6.1	Description	41
	3.6.2	Model Simulations_	41
	3.6.3	Turbulent Flow Simulations in Wind Tunnel	43
		3.6.3.1 Turbulence Intensity	
		3.6.3.2 Integral Scale of Turbulence	
СНАР	TER	4 SYSTEM IDENTIFICATION TECHNIQUES FOR	
		FLUTTER DERIVATIVES IDENTIFICATION OF	
		BRIDGE DECK_	47
4.1	Introd	duction	47
4.2		nuous Time-State Space Method	
		A State Space Method of a Vibrating Structures	
	4.2.2	Modal Parameters and Model Reduction	49
4.3	Discr	ete Time-State Space Method	50
	4.3.1	About Sampling	50
		Modal Parameters and Model Reduction	
4.4		astic State Space Method	
	4.4.1	The Stochastic Components	53
		Properties of Stochastic System	
4.5	Stoch	astic Subspace System Identification	56
	4.5.1	Data Types	56
		4.5.1.1 Time Data	56
		4.5.1.2 Covariance Estimates	56
		4.5.1.3 Spectrum Estimates	56
	4.5.2	Covariance-Driven-Stochastic-Subspace Identification (SSI-COV)_	61
		Data-Driven-Stochastic-Subspace Identification (SSI-DATA)	
	4.5.4	Covariance-Driven VS Data-Driven Subspace	73
	4.5.5	Postprocessing	
		4.5.5.1 Spectrum Analysis	
		4.5.5.2 Modal Responses and Prediction Errors	75
4.6	Flutte	er Derivatives Identification	76
		Theoretical Formulation of Covariance-Driven SSI	
		Theoretical Formulation of Data-Driven SSI	
4.7		ication of the Method by Numerical Tests	
		Free Decay Responses Data	
	4.7.2	Simulated Responses Including the Motion-induced Force	95
		5 INDUSTRIAL RING ROAD BRIDGE	_102
5.1	Desci	ription of Bridge	_102

	5.1.1 Location_	_102
	5.1.2 Dimensioning Details	102
5.2	-	103
	5.2.1 General	_103
	5.2.2 Industrial Ring Road Bridge Section Model	_105
СНЛІ	PTER 6 METHODOLOGY AND WIND TUNNEL TESTS	
CHAI	MEHTOD METODOLOGI AND WIND TORNEL TESTS	115
6.1	Flow Conditions_	115
0.1	6.1.1 Smooth Flow	
		117
6.2	Test Procedure	
	Experimental Configuration_	
	-	125
		126
6.4	Determination of Stiffness, Mass and Mass Moment of Inertia	127
6.5	Flutter Derivatives Identification	128
6.6	Determination of Aerodynamic Force Coefficients	_130
6.7	Modified Sections by Aerodynamic Appendages	_132
CHAI	PTER 7 EXPERIMENTAL RESULTS	_134
7.1	Introduction	_134
7.2	Thin Flat Plate	_134
	7.2.1 Flutter Derivatives: Smooth Flow	_
	7.2.2 Aerodynamic Force Coefficients: Smooth Flow	
7.3	Industrial Ring Road Bridge Deck	
	7.3.1 Flutter Derivatives of IRR Bridge Model: Smooth Flow	
	7.3.1.1 Comparisons of Flutter Derivatives between the SSI	
	DATA and SSI-COV Method from the Free Decay Tes	
		_161
	7.3.1.2 Comparisons of Flutter Derivatives between the SSI	
	DATA and SSI-COV Method from the Buffeting Test	
	7.3.1.3 Comparisons of Flutter Derivatives between Free Decay	
	and Buffeting Test under Smooth Flow	
	7.3.1.1 Comparisons of Flutter Derivatives with the Previous Method	s _169
	7.3.2 Flutter Derivatives of IRR Bridge Model: Effects of Turbulence	_ _172
	7.3.3 Vortex Responses and Stability Limits of the IRR Bridge	177
	7.3.4 Aerodynamic Force Coefficients of the IRR Bridge	182
	7.3.4.1 Smooth Flow	_182
	7.3.4.2 Effects of Turbulence	19/

7.4	Modified Sections of Industrial Ring Road Bridge Deck by Aerodynamic		
	Appendages	186	
	7.4.1 Flutter Derivatives: Smooth Flow		
	7.4.2 Structural Dynamic Responses and Stability Limits		
	7.4.3 Aerodynamic Force Coefficients	193	
CHAI	PTER 8 CONCLUSIONS AND RECOMMENDATIONS	195	
	Conclusions for Flutter Derivatives	195	
	8.1.1 System Identification Method		
	8.1.2 Effect of Experimental Techniques: SDOF and 2-DOF	196	
	8.1.3 Effect of Deck Shape	197	
	8.1.4 Effect of Flow Condition: Smooth and Turbulence Flow	197	
8.2	Conclusions for Buffeting	198	
	8.2.1 Static Force Coefficients		
	8.2.2 Buffeting Responses, Vortex Shedding and Flutter Instability	199	
8.3	Recommendations and Suggestions for Future Works	200	
REFE	RENCES	202	
APPE	NDIXES	208	
A.	A SCHEMATIC DIAGRAM OF TU-AIT WIND TUNNEL_	209	
B.	WIND TUNNEL AND EXPERIMENTAL APPARATUS	210	
	B.1 The TU-AIT Wind Tunnel	210	
	B.2 Wind-Speed and Wind-Turbulence Measurements		
C	OUTPUT OF PROJECT		
D	MANUSCRIPT OF PROJECT	219	

CHAPTER 1

INTRODUCTION

1.1 General Review and Problem Statement

Long-span cable-supported bridges are highly susceptible to wind excitations because of their inherent flexibility and low structural damping. Wind loads play an important role in the design of these structures. A wind-induced aerodynamic force can be divided into two parts: a buffeting force that depends on the turbulence of the incoming flow, and an aeroelastic force that originates from the interactions between the airflow and the bridge motion. The motion-dependent forces feed back into the dynamics of the bridge as aerodynamic damping and stiffness; the effect is termed 'aeroelasticity' and is commonly described via 'flutter derivatives'. The problems of aerodynamic stability including vortex-induced vibrations, galloping, flutter, and buffeting, may have serious effects on the safety and the serviceability of the bridges. A brief description of each of these phenomena is as follows. A more comprehensive treatment is given in Simiu and Scanlan (1996).

Flutter instability describes an exponentially growing response of a bridge deck where one or more vibration modes participate at a particular critical wind velocity resulting in a failure due to the overstress of the main structural system.

Buffeting describes a random response of a bridge to the fluctuating incoming cross wind. This also includes the response of a bridge to an additional turbulence caused in the flow because of its bluff shape, usually referred to as the *signature turbulence*. (Sarkar 1993, Singh 1997)

Vortex-induced response occurs due to the synchronization of the frequency of Kármán-type vertices being shed from the bridge deck to one of its natural frequencies of vibration. Moderate-amplitude oscillation results for a range of shedding frequencies around the natural frequency of vibration. This phenomenon is more popularly known as "lock-in". The motion, however, is self-limiting in amplitude.

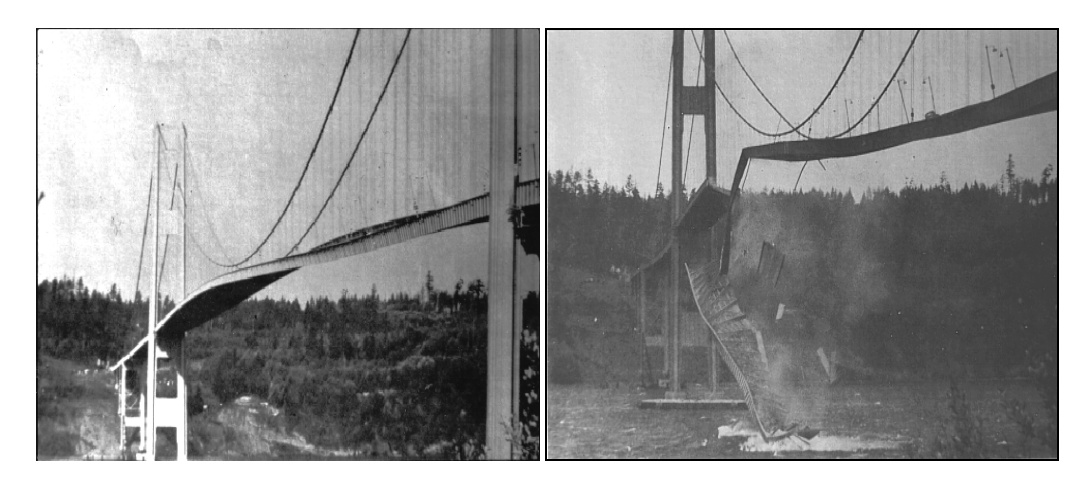


Fig. 1.1 Failure of Tacoma Narrow Bridge under wind flow

Among these, flutter is the most serious wind-induced vibration of bridges and may destroy the bridges due to the diverging motions in either single or torsion-bending coupled mode. Notorious examples of the flutter phenomenon are the failures of the Brighton Chain Pier Bridge in 1836 and the original Tacoma Narrow Bridge in 1940 (Fig. 1.1).

Unlike flutter, buffeting and the vortex-induced responses do not tend to cause catastrophic failures but are nevertheless important from design serviceability considerations. In order to reasonably predict the flutter critical wind velocity and buffeting response of the bridge, the flutter derivatives shall be determined in first place. The flutter derivatives depend primarily upon the wind conditions, the cross-sectional shape and the dynamic characteristics of the bridges. Nevertheless, no theoretical values exist for these derivatives for various bridge shapes except only for a simple thin plate section. A major research tool in these studies is, therefore, a wind tunnel test, in which a geometrically and aerodynamically representative scale model of a length of a bridge deck is built, mounted, and then tested in a wind tunnel. The flutter derivatives are non-dimensional functions of the wind speed, the geometry of bridge, and the frequency of vibrations; therefore they can be applied directly to the full-scale bridge in a piecewise manner.

The experimental methods used for determining flutter derivatives can be grouped into two types, i.e. forced (Chen and Yu 2002) and free vibration methods (Scanlan 1971, Poulsen et al. 1992, Sarkar et al. 1994, Gu et al., 2000). Having less emphasis on elaborate equipments required, and the amount of both time and work involved; the free vibration method seems to be more tractable than the forced method. In the determination of flutter derivatives by the free vibration method, the system identification method is the most important part required to extract these parameters from the response output of the section model. The free vibration method depends on the system identification techniques and can be classified into two types, i.e. the free decay and the buffeting tests. In the free decay test method, the bridge deck is given initial vertical and torsional displacements. The flutter derivatives are based on the transient (i.e. free decay) behavior that occurs when the bridge deck is released. The buffeting test, on the other hand, uses only the steady random responses (i.e. buffeting responses) of bridge deck under wind flow without any initial displacement given to the model. Compared with the free decay method, the buffeting test is simpler in the test methodology, is more cost effective, and is more closely related to the real bridge behaviors under wind flow, but with a disadvantage that the outputs appear randomlike. This makes the parameters extraction more difficult and a more advanced system identification technique is required.

In most of the previous studies, flutter derivatives were estimated by the deterministic system identification techniques that can be applied to the free decay method only. Examples of previous deterministic system identification techniques that were applied to the free decay method included the Scanlan's method (1971), the Poulsen's method (1992), the Modified Ibrahim Time Domain method (MITD) (Sarkar et al. 1994), and the Unified Least Square method (ULS) (Gu *et al.*, 2000). In these system identification techniques, the buffeting forces and their responses are regarded as external noises which then require many iterations in the identification process to obtain appropriate results. It also confronted with difficulties at high wind

speeds where the initial free decay is drowned by buffeting responses. Besides, at high reduced wind speed, the vertical bending motion of the structure will decay rapidly due to the effect of the positive vertical aerodynamic damping, and thus the length of decay time history available for system identifications will decrease. This causes more difficulties to the deterministic system identification techniques (Gu and Qin, 2004). In case of turbulence flow, the presence of the turbulence in the flow is equivalent to a more noisy-input signal to the deterministic system identification. This made the extraction process more complicated and most likely reduced the accuracy of the flutter derivatives identified (Sarkar, *et al.*, 1994). In addition, due to the test technique, the free decay method is impractical to determine flutter derivatives of real bridges in the field.

On the other hand, the buffeting test uses random responses data of bridge motion from wind turbulence only. This mechanism is more closely related to a real bridge under a wind flow and is applicable to real prototype bridges. The method costs less and is simpler than the free decay since no operator interrupts in exciting the model. However, as wind is the only excited source, it results in low signal-to-noise ratio, especially at low velocity, and therefore a very effective system identification technique is required. None of the aforementioned system identification techniques is applicable to the buffeting responses tests.

System identification techniques can be divided into two groups, i.e. deterministic and stochastic. If the stochastic system identification technique (Juang and Pappa 1985, Overchee 1991, Peeters 1999) is employed to estimate the flutter derivatives of a bridge deck from their steady random responses under the action of turbulent wind, the above-mentioned shortcomings of the deterministic system identification technique can be overcome. The reason is that the random aerodynamic loads are regarded as inputs rather than as noises, which are more coincident with the fact. Therefore, the signal-to-noise ratio is not affected by the wind speed, and the flutter derivatives at high reduced wind speeds are more readily available. These aspects give the stochastic system identification methods an advantage over the deterministic system identification.

Many stochastic system identification methods have been developed during the past decades, among which the stochastic subspace identification (SSI in short) (Overchee 1996, Peeters 2001) has proven to be a method that is very appropriate for civil engineering. The merit points of SSI are: (1) the assumptions of inputs are congruent with practical wind-induced aerodynamic forces, i.e. stationary and independent on the outputs; (2) identified modes are given in frequency stabilization diagram, from which the operator can easily distinguish structural modes from the computational ones; (3) since the maximum order of the model is changeable for the operator, a relatively large model order will give an exit for noise, which in some cases can dramatically improve the quality of the identified modal parameters; (4) mode shapes are simultaneously available with the poles, without requiring a second step to identify them.

There are two kinds of SSI methods, one is data-driven (SSI-DATA), and the other is covariance-driven (SSI-COV). The similarity of the covariance- and the data-driven SSI methods is that they both are aimed to cancel out the (uncorrelated) noise

using a stochastic realization. In the SSI-COV algorithm, the raw time histories are converted to the covariances of the Toeplitz matrix. The implementation of SSI-COV consists of estimating the covariances, computing the singular value decomposition (SVD) of the Toeplitz matrix, truncate the SVD to the model order n, estimating the observability and the controllability matrices by splitting the SVD into two parts, and finally estimating the system matrix(A,C). The modal parameters are found from A and C.

As opposed to SSI-COV, the data-driven stochastic subspace identification (SSI-DATA) avoids the computation of covariances between the outputs; since the error and noises may be squared up from the covariance estimation (Golub 1989). It is replaced by projecting the row space of the future outputs into the row space of the past outputs. This projection is computed in favor from the numerically robust square root algorithm, i.e. *QR* factorization. Theoretically, the numerical behavior of SSI-DATA should then be better than that of SSI-COV.

In this study, the data-driven stochastic subspace identification method is used to estimate the flutter derivatives from random responses (buffeting) under the action of smooth and turbulent wind. Tests are also carried out with the free decay method (single and two-degree-of-freedom) in order to examine the robustness of the present technique that the results are not affected by test methods used. To validate the applicability of the present technique, numerical simulations were performed. Then sectional-model tests of a quasi-streamlined thin plate model, which is the only section that theoretical flutter derivatives exist, were performed under smooth flow. Encouraged by the success in the evaluation process, the flutter derivatives of a real bridge were determined. The two-edge-girder type blunt section model of Industrial-Ring-Road Bridge (IRR in short), a cable-supported bridge with a main span of 398 m in Samutprakan province, Thailand, was tested both in the smooth and the turbulence flows. Tests were conducted in TU-AIT Boundary Layer Wind Tunnel in Thammasat University, the longest and the largest wind tunnel in Thailand.

1.2 Objectives

The main experimental parameters needed for examining whether a bridge is flutter-prone below a certain mean velocity are the flutter derivatives. The flutter derivatives associated with at least two degrees of freedom (vertical and torsional) needed to be determined rather reliably. Moreover, for the estimation of buffeting response of bridge decks, the static force coefficients should also be known.

Up to the present, all cable-stayed bridges in Thailand, such as the Rama IX Bridge, the RamaVIII Bridge, and the two Industrial Ring Road Bridges, were designed and conducted in wind tunnel test by oversea consultants. Therefore, there is a real need to increase the number of researchers in this field in order to minimize the oversea consultant dependency and the associated design cost. Since the TU-AIT boundary layer wind tunnel was jointly constructed under an academic collaboration between Thammasat University (TU) and the Asian Institute of Technology (AIT), a number of advance research of wind resistant design of long span bridges in Thailand have been significantly increased.

The present study concentrates on two major thrusts: First, the various state-of-the-art experimental techniques for accurate determinations of the parameters mentioned above (flutter derivatives and static coefficients) from section-model tests in the wind tunnel; Second, and the more important contribution of this study, was the system identification technique for extracting the flutter derivatives from the output response of the section model. Therefore, the objectives of the study are as follows:

- To propose a new system identification method, that overcomes the shortcomings of the previous deterministic system identification techniques those are commonly used, to identify flutter derivatives from a dynamic wind tunnel model test both in smooth and turbulent flows. Results from the application of the present system identification method to various experimental techniques are then compared.
- To identify aerostatic force coefficients, C_L , C_D , C_M , of bridge decks from wind tunnel test in both smooth and turbulent wind.
- To estimate some major aerodynamic phenomena (vortex shredding, flutter instability) of the bridge decks based on test results.
- To study main effects of two different aerodynamic shapes (e.g. streamlined and bluff section) upon aerodynamic behavior of bridge decks.
- To study effects of flow conditions (smooth and turbulence) on the aerodynamic phenomena and aerodynamic parameters of the bridge deck.
- To investigate the effectiveness of aerodynamic appendages on the responses of bridge deck, vortex shedding and flutter phenomenon

1.3 Scope of Study

The scope of the study can be summarized as follows.

- 1. The most advanced stochastic subspace identification technique was theoretically formulated to identify flutter derivatives of bridge decks under wind flows. The new proposed data-driven stochastic subspace identification (SSI-DATA) was used to extract flutter derivatives and results were compared with those from the popular covariance-driven stochastic subspace identification (SSI-COV).
- 2. The computer software of both SSI algorithms were developed to identify flutter derivatives of bridge decks from the response outputs of the section model from wind tunnel tests.
- 3. To validate the applicability of the present method to various experimental techniques (i.e. the free decay and the buffeting tests), numerical simulations of various signal outputs were adopted. Then, the present stochastic subspace

identification was applied to identify the modal parameter and system matrices from the simulated responses, and results were compared with the pre-set values.

- 4. In order to validate the present system identification technique and the experimental set-up, wind tunnel tests of a section model of a streamlined thin plate model were performed to extract flutter derivatives from various test techniques under smooth flows, i.e. the single-degree-of-freedom free decay method, the coupled-degree-of-freedom free decay and buffeting test methods. The results are then compared with the theoretical values.
- 5. Wind tunnel tests of the section model of the blunt type Industrial Ring Road Bridge (IRR) were conducted to extract flutter derivatives under smooth and turbulence flows. The results from the present method will be compared with those from the previous research in case of smooth flow.
- 6. The static aerodynamic force coefficients (C_D, C_L, C_M) of both the streamlined thin plate under smooth flow and the blunt type IRR Bridge under smooth and turbulent flow were determined from static test set-up. Effects of wind angle of attacks were also examined.
- 7. Identify the critical flutter wind speed and flutter derivatives of aerodynamic appendages modified sections, including fairings, soffit plates and combination of those two sections and compare their responses in smooth flow.

The study mainly focused on the Industrial Ring Road cable—stayed bridge. One of the two cable-stayed bridges (South Bridge) with the main span length of 398 m, was selected to perform in this study. This bridge is an example of bluff type cross section which exhibits difference aerodynamic mechanism compared to a thin plate model. Fig. 1.3 shows the general view of the deck cross section.

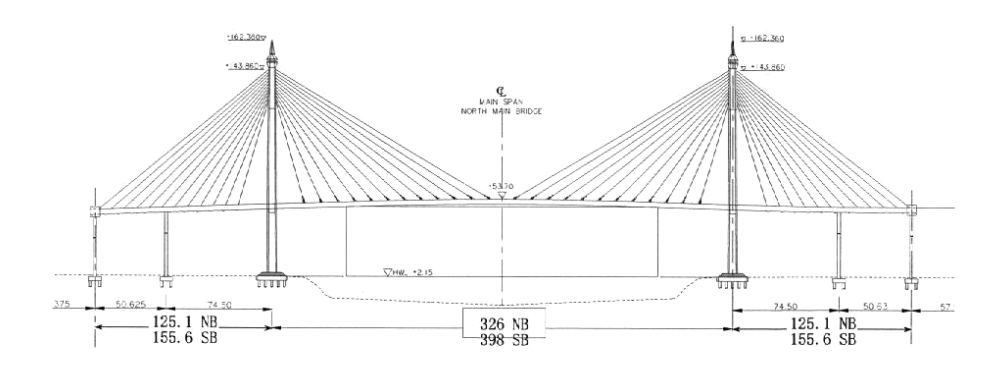






Fig. 1.2 General arrangement of the IRR cable-stayed bridges

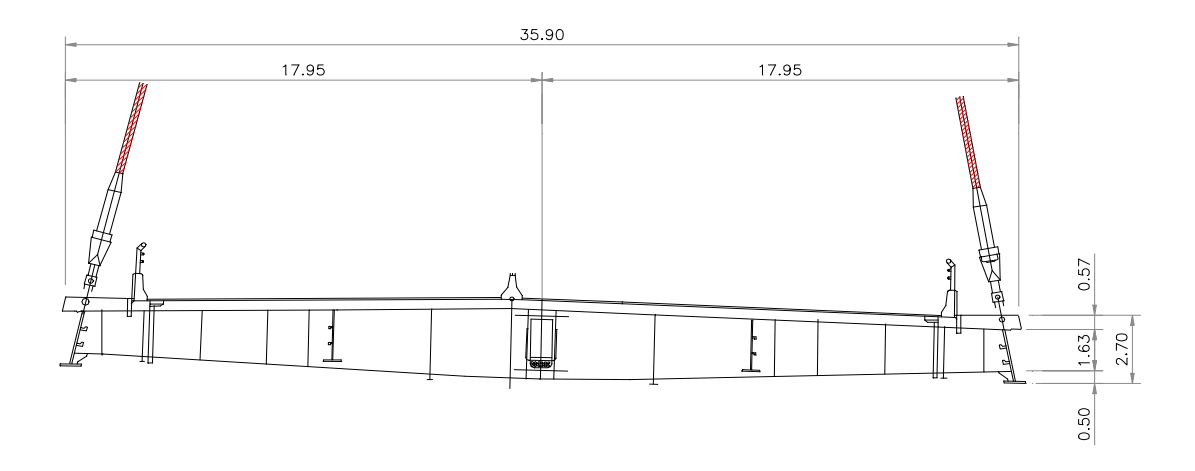


Fig. 1.3 Typical cross section of Industrial Ring Road bridges (unit in meter)

CHAPTER 2

LITERATURE REVIEW

The discipline of aeroelasticity refers to the study of phenomenon wherein aerodynamic forces and structural motions interact significantly. Flutter is an aeroelastic self-excited oscillation of a structural system. The frequency-domain approach has been widely used for estimating flutter speed of structures. The frequency-domain method uses flutter derivatives, which may be experimentally obtained from wind tunnel testing of section model. System identification technique is the crucial mean for the identification of bridge deck flutter derivatives and can be classified into two groups; i.e. deterministic and stochastic ones.

In most of the previous studies, flutter derivatives were estimated by deterministic system identification techniques. Deterministic system identification techniques involved in flutter derivative estimations can be group under two types, i.e. forced vibration method (Chen and Yu 2002) and free vibration method (Scanlan and Tomko 1970; Gu et al. 2000; Gu et al. 2001; Sarkar 1994; Scanlan and Lin 1978). The forced vibration method is somewhat expensive since they involve sizeable equipment and considerable time and work. Moreover, the forced vibration method is different from their kinetic characteristics in the natural wind.

2.1 Free Vibration Method

In the 1970s, R.H. Scanlan proposed a semi-experimental and semi-analytical approach for critical flutter wind speed and another approach for buffeting response (Scan lan et al. 1971; Scanlan and Gade 1977).

These two approaches are presently widely used. Flutter derivatives of bridge decks are parameters in these approaches essential for the flutter and buffeting analysis of long-span bridges. In the original technique, to extract the flutter derivatives in Scanlan's method (Scanlan et al.; 1971), a spring-suspended sectional model was tested and the free decay vibration signals were used. A great advantage of the free vibration technique is its simplicity, requiring no expensive and complicated driving machine. But Scanlan's method need three groups of test. Torsional and vertical bending motions have to be constrained, respectively, to obtain the so-called direct derivatives. Furthermore, to obtain cross derivatives, the vertical and torsion motions of the model must have the same frequency at all wind velocities. In view of this situation, many efforts have been made to simplify the identification procedure. ARMA model was used by M. Shinozuka et al. (1982) to try to identify the flutter derivatives. But the results seemed unsatisfactory for high noise.

H. Yamada et al. (1992) introduced the extended EKF method into the identification procedure of these derivatives based on the coupled vibration time histories. In this method, the time histories of the displacement and velocity as well as the information of the initial condition are simultaneously required.

Poulsen et al. (1992) used a method which combines control theory and system identification techniques to extract flutter derivatives from section model tests for the Great Belt East Bridge.

In 1994, P.P. Sarkar and R.H. Scanlan developed Modified Ibrahim Time-domain (MITD) method to extract all the direct and cross derivatives from the coupled free vibration data of 2-DOF model (Sarkar et al. 1994). This method requires selection of the time shifts N1 and N2. Sarkar and Scanlan have found a way to select these two time shifts close to optimal values.

Imai et al. (1989). have been reviewed other system identification (SID) methods that can be applied to problems in structural dynamics; least squares (LS), instrumental variable (IV), maximum likelihood (ML), and extended Kalman filtering (EKF).

Hsia (1976) described different least squares algorithms for system parameter identification. Extended Kalman filtering techniques were used by Yamada and Ichikawa (1992), Diana et al. (1995), Iwamoto and Fujino (1995) and Jones et al. (1995).

Jakobsen and Hjorth-Hansen (1995) and Brownjohn and Jakobsen (2001) have used covariance block Hankel matrix (CBHM) method for parameter extraction of a two-DOF system. The CBHM method has also been extended to cater for three-DOF flutter derivatives. However the principles were illustrated for a two-DOF system and eight flutter derivatives were experimentally extracted.

Gu et al. (2000) and Zhu et al. (2002) have used an identification method based on unifying least squares (ULS) theory to extract flutter derivatives of a two-DOF model. Though the ULS method could theoretically identify all 18 flutter derivatives using a three-DOF section model, only eight flutter derivatives were extracted due to lack of a more inclusive experimental set-up to accommodate the three-DOF section model. In this method, a unified error function which is linearly composed of two errors component of vertical bending and torsional motions is defined as the objective function to optimize the flutter derivatives. Nevertheless, if distinct difference exists in quantity between the two error components, unsatisfactory identification precision may occur. In order to improve the precision, the modified least-square method for adding weights to error components was proposed subsequently (Ding, et. al., 2001), In addition, the weighting ensemble least-square method was developed to extract eight flutter derivatives of bridge decks (Li, et al. 2003). In this method, several vibration records at the same wind speed are regarded as an ensemble. simultaneously fitted to identify the mode parameters by nonlinear least square method in the sense of minimizing the total error function.

The Iterative Least Square approach (ILS) was presented to identify all 18 flutter derivatives for a streamlined bridge deck and an airfoil section model (Chowdhury and Sarkar 2004). In the identification process, the time histories of the displacement, velocity as well as accelerations are simultaneously required.

The above least-square methods commonly apply alternate iteration technique to obtain solutions, and the same lengths of the vertical bending and torsional vibration

histories are necessary. Nevertheless, the solution precision of these alternate iteration techniques are closely relevant with and sensitive to the initial selected values of modal parameters, and the solution may not be converged sometimes.

Chen *et al.* (2006) have used empirical mode decomposition (EMD) method developed by Huang *et al.* (1989) to filter and reduce the noises from the free decay signal and the filtered signal were used to extract flutter derivatives based on unifyingleast square method.

Generally, the free vibration method seems to be more tractable than forced vibration testing. However, at high reduced wind speeds, the vertical bending motion of the structure will decay rapidly due to the effect of positive vertical bending aerodynamic damping, and thus the length of time history available for system identifications will decrease, which therefore add more difficulties to the system identification. Furthermore, the free vibration method regards the buffeting forces and the responses as external noises, and it is therefore confronted with great difficulties at higher wind speeds (Sarkar 1992).

In summary most of the above-mentioned methods are subsections of so-called output-only system identification (as input such as wind load are not exactly known and available parameters are output responses only). In a civil engineering context, the civil structures (e.g. bridges, towers) are the systems; that is excited by a not measurable input force and that only output measurements (e.g. accelerations) are available. Then some output-only identification methods are reviewed in next section.

2.2 Output-Only Modal Identification Methods

The ambient excitation has commonly a multiple input nature and wide band frequency content, stimulating a significant number of modes of vibration. For simplicity, output-only modal identification methods assume the excitation input as a zero mean Gaussian white noise, which means that the real excitation can be interpreted as the output of a suitable filter excited with that white noise input. Modelling the behaviour of the filter-structure system, one may conclude that some additional computational poles, without structural physical meaning, appear as consequence of the white noise assumption.

There are two main groups of output-only modal identification methods: nonparametric methods essentially developed in frequency domain and parametric methods in time domain.

The basic frequency domain method (Peak-Picking), though already applied some decades ago to the modal identification of buildings and bridges, was only conveniently systematized by Felber (1993) about twelve years ago. This approach, which leads in fact to estimates of operational mode shapes, is based on the construction of average normalized power spectral densities (ANPSDs) and ambient response transfer functions involving all the measurement points, and allowed the development of software for modal identification and visualization used at UBC and EMPA (13). The frequency domain approach was subsequently improved (Prevosto 1982) by performing a single value decomposition of the matrix of response spectra, so as to obtain power spectral densities of a set of SDOF systems. This method

(Frequency Domain Decomposition (FDD)) was better detailed and systematized by Brincker et al. (Brincker 2001), and subsequently enhanced (Brincker 2000) in order to extract modal damping factors estimates. In this last approach (EFDD) these estimates are obtained through inspection of the decay of auto-correlation functions, evaluated by performing the inverse Fourier transform of the SDOF systems' power spectral densities.

The time domain parametric methods involve the choice of an appropriate mathematical model to idealize the dynamic structural behavior (usually time discrete state space stochastic models, ARMAV or ARV models) and the identification of the values of the modal parameters so as that model fits as much as possible the experimental data, following some appropriate criterion. These methods can be directly applied to discrete response time series or, alternatively, to response correlation functions. The evaluation of these functions can be made based on their definition, using the FFT algorithm (Brincker 1982) or applying the Random Decrement method (RD) (Asmussen 1992). A peculiar aspect of output-only modal identification based on the fitting of response correlation functions is the possibility to use methods that stem from classical input-output identification methods, based on impulse response functions. Some of these methods are the Ibrahim Time Domain (ITD) (Ibrahim 1977), the Multiple Reference Ibrahim Time Domain (MRITD) (Fukuzono 1986), the Least-Squares Complex Exponential (LSCE) (Brown 1979), the Polyreference Complex Exponential (PRCE) (Vold 1982) or the Covariance-Driven Stochastic Subspace Identification (SSI-COV) (Peeters 2000). An alternative method that allows direct application to the response time series is the Data-Driven Stochastic Subspace Identification (SSI-DATA) (Overschee 1996). It's still worth noting that the Random Decrement technique, usually associated to the application of time domain methods like Ibrahim's, can be also the base for the application of frequency domain methods, like PP, FDD or EFDD, as it leads to free vibration responses, from which power spectral densities can be evaluated using the FFT algorithm (Rodrigues 2004), reducing noise effect (methods RD-PP, RD-FDD and RD-EFDD).

These methods, schematically represented in Fig. 2.1, have been recently systematized, applied and compared by Rodrigues (Rodrigues 2004). Fig. 2.1 also indicates the five different types of numerical techniques employed in their development (FFT, SVD, LS, EVD and QR).

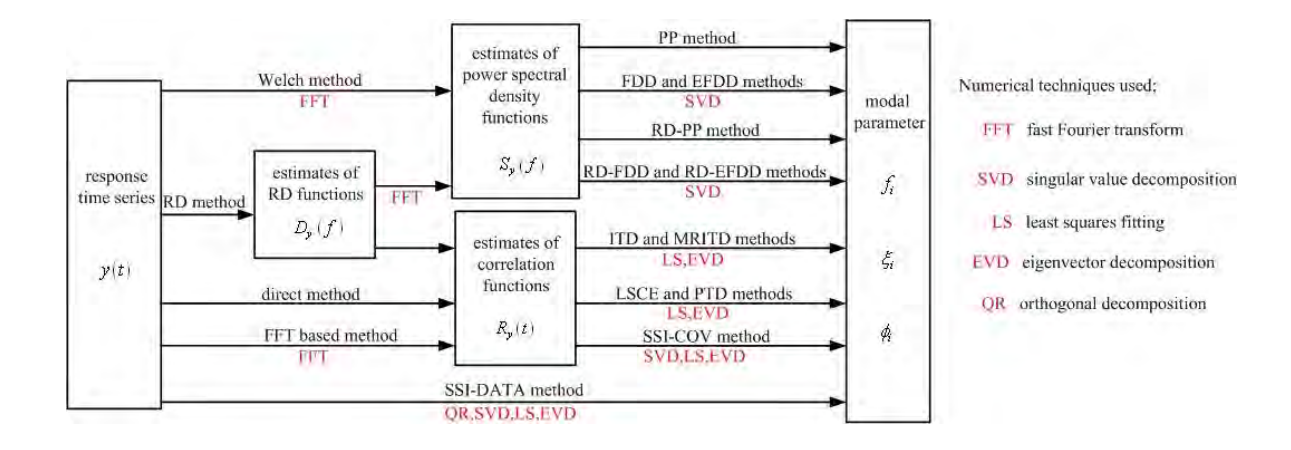


Fig. 2.1 Summary of output-only system identifications scheming apply to modal parameters estimation

2.3 Stochastic Methods

None of the aforementioned methods can simultaneously extract aerodynamic admittances and flutter derivatives, or other important aeroelastic parameters in flutter and buffeting analysis of long-span cable-supported bridges. If the stochastic system identification techniques are employed to extract flutter derivatives and aerodynamic admittances, then the above-mentioned shortcomings of the force measurement methods and the transient motivation system identification technique may be overcome. The stochastic system identification techniques (Juang and Pappa 1985; Overschee 1991; Peeters 1999) directly extract the required dynamic parameters from the steady random responses of the bridge section model subjected to turbulent wind. For this kind of identification methods, the random aerodynamic loads are regarded as input rather than noise, which are more coincident with the fact, so the signal-to-noise ratio is not affected by wind speed, and the flutter derivatives at high reduced wind speeds can thus be available. These aspects give the stochastic system identification methods an advantage over the deterministic methods in estimating the flutter derivatives and aerodynamic admittances of bridge decks. Moreover, flutter derivatives and aerodynamic admittances can be simultaneously obtained with the same random response data.

Many stochastic system identification methods have been developed during the past decades, among which the stochastic subspace identification (SSI in short) technique (Overschee 1991; Peeters 1999; Gu and Qin 2004) has proven to be a method very appropriate for civil engineering. The merit points of SSI are: (1) the assumptions of inputs are congruent with practical wind-induced aerodynamic forces, i.e. stationary and independent on the outputs; (2) identified modes are given in frequency stabilization diagram, from which the operator can easily distinguish structural modes from the computational ones; (3) since the maximum order of the model is changeable for the operator, a relatively large model order will give an exit

for noise, which in some cases can dramatically improve the quality of the identified modal parameters; (4) mode shapes are simultaneously available with the poles, without requiring a second step to identify them. There are two kinds of SSI methods, one is data-driven, and the other is covariance-driven.

2.4 Aerodynamic Appendages

The investigation in aerodynamic appendages had been considered for a long time and many studies are used in an effort to suppress the oscillation in real structures. Bronx-Whitestone Bridge which had to use poor aerodynamic I-girder to keep construction in tight schedule, the stiffening systems including fairings are installed along bridge deck. Another illustration is Deer Isle Bridge, which is stated below. Some investigations had been reviewed as listed:

Wardlaw R. L. and Goettler L. L. (1968) had purposed the experimental study of the effects of aerodynamic appendages. They measured the amplitude of oscillation of Long's Creek Bridge before and after installing aerodynamic appendages, which consisted of the soffit plates and various types of fairings, under the wind velocity of 8 to 18 m/s in wind tunnel test. The results of this study showed that the bridge responses via the vibration amplitude approached 11 cm of original section under 16 m/s wind speed. In the other hand, with fairings installed, the amplitude was decreased more and more following the fairings length. Since 3.0m fairings installed, the structure responded with amplitude less than 1 cm. The Long's Creek Bridge is a representative of satisfactory performance of the triangular fairing on bridge aerodynamic instability. Many said that Long's Creek Bridge is a representative of satisfactory performance of the triangular fairing on bridge aerodynamic instability.

The investigation of effects on geometry modification on aerodynamics of cable-stayed bridge deck had been carried out by Bienkiewicz in 1987. A 1:140 scale of Weirton-Steubenville cable-stayed bridge model was a case study which its original section behaved an unstable oscillation in torsional direction, including high vortex-induced response. The wind tunnel tests were carried out in smooth flow for four sections including original section, partially streamlined, enclosed lower cavity and fully streamlined section. Streamlining of deck resulted in improved aerodynamic performance, with an increase in the critical flutter wind speed for torsional flutter and decrease in vortex response.

Houston D. R. and Bosch H. R. had published the effects of fairings and of turbulence on the flutter derivatives of a notably unstable bridge deck in 1988. This study aimed to identify the flutter derivatives of Isle-Sedgwick Bridge by sectional model test in wind tunnel. Its deck had a same plate girder profile as the Tacoma Narrows Bridge, which was subsequently shown to have such poor aerodynamic characteristics. Like the Tacoma Narrows Bridge, the Deer Isle Bridge was built during the depression and has a relatively light and flexible stiffening structure. Almost immediately after its construction, the Deer Isle Bridge experienced large wind-induced oscillations. Therefore, the fairing-modified section was tested for comparison. The result of the torsional aerodynamic stability represented via flutter coefficient A_2^* as a function of wind speed whose positive values indicate unstable

conditions. It is clear that the fairing modification produces a more stable section. Furthermore, the fairing coverage effects are also carried out where the section with 100% covered with fairing introduced the most stable section.

Nagao F. et al. had investigated the effects of triangular edge fairing on bridge box girder aerodynamic stabilities in 1993. Various angles of triangular fairings were mounted to different type of bridge deck sections. The results showed that fairing which the upper slope angle is 0° showed only a little increase in onset flutter velocities. Generally speaking, the modification of flow properties along the upper deck is effective in preventing the flutter. In addition, fairing effects on flutter increased with the slenderness ratio of cross section. Moreover, the results show that an inner angle of 60° fairing gave the most effects of flutter onset velocity. This type of fairing can furthermore execute almost vortex shedding. Nonetheless, this study was carried out in the uniform flow and due to no flutter derivatives were indentified from this study; hence the effects of turbulence on the aerodynamic instability for bridge deck and flutter derivatives should be clarified in the next place.

Fang F. et al. had investigated on the aerodynamic instability of a suspension bridge with a hexagonal cross-section in 2007. Measurements of the dynamic responses of a sectional bridge model in the cross-wind and torsional directions were firstly carried out in wind tunnel. Three sections were mounted and tested for a comparison including bluff rectangular 180° side angle section, 90°, 60°, and 30° side angle sections. Among the hexagonal decks studied, it was found that one with 30° side angle leads to the greatest critical flutter speed. Beside wind tunnel model tests, the method of computational fluid dynamics (CFD) had also been used to examine the aerodynamic performance of the sections where the results of numerical predictions agreed well with those from the experiments.

From the investigations reviewed above, geometry modifications of cable-stayed bridges are suggested to mount on a considered section due to their efficiency in reducing static and dynamic responses. Fairings, soffit plates and combined sections are consequently first-rated. Most of previous studies had focused on the effects of geometry modifications on critical flutter velocities, where flutter derivatives were not widely judged due to lack of motivation on the simplicities and stabilities of extracted values. This thesis additionally carries out static responses, an overall response of bridge deck and all eight flutter derivatives which are affected by deck shape modifications as well.

CHAPTER 3

THEORETICAL BACKGROUND FOR WIND EFFECTS ON LONG-SPAN CABLE-SUPPORTED BRIDGES

In the design of long-span cable stayed bridges or suspended bridges, the wind effects are of primary concern. The failure of the Tacoma Narrows suspension bridge in 1940 is an example of wind effects on structures. Therefore to understand the response of long span suspension bridges under wind excitation, the basic wind phenomena needs to be clearly understood. Hence this chapter focuses on and reviews a number of topics connected with the effect of the wind on long-span cable stayed bridges. The aerodynamic effects of wind on the bridges are primarily vortex shedding, galloping, torsional-divergence, flutter and buffeting.

3.1 Design Concept of a Cable Stayed Bridges

The criteria for the design of long span cable stayed bridges are concerned with the static and dynamic responses of the bridge under wind loading. A basic knowledge of the wind forces are required to understand wind effects on these structures. The Aerodynamic design involves experimental results of aerodynamic coefficients and flutter derivatives. The wind velocity may cause the aerodynamic instability of bridge deck, which does not exceed the predicted critical velocity in order to avoid failure of the structures. The frequencies other than the fundamental one should be considered in design. There are static and dynamic behaviors that should be considered for design of bridges (ASCE 1987; Walther 1999).

3.2 Static Behavior

Wind flow exerts on the bridge deck and alters the pressure between sides of the body. The results of this phenomenon are aerodynamic forces that can be expressed by static wind load. Usually the fist consideration is the static phenomena that are not critical for the design of bridges. The static loads are lift force, drag force, and moment.

Lift force
$$L = \frac{1}{2} \rho U^2 B C_L$$
 (3.1)

Drag force
$$D = \frac{1}{2} \rho U^2 B C_D$$
 (3.2)

Moment
$$M = \frac{1}{2} \rho U^2 B^2 C_M$$
 (3.3)

where U is mean velocity of wind flow; B is characteristic dimension; C_L, C_D, C_M are lift, drag and moment coefficients, respectively. These coefficients are defined from experimental results using wind tunnel model test.

3.3 Dynamic Behavior

The methods of analysis of cable-stayed bridge are not only limited to consideration with static loads but also dynamic loads. Therefore, the dynamic analysis of cable-stayed bridge is concerned with their aerodynamic behavior. Dynamic studies include the determinations of the natural modes and modal frequencies, mode shapes under aerodynamic forces.

Under the wind loads, which are considered as forces varying with time, the cable-stayed bridge will oscillate. The oscillation excited by wind usually occurs in one of the following types of displacements:

- Vertical bending of the cable-stayed bridge in which the deck moves up and down.
- Torsion of the cable-stayed bridge in which the deck twists above a spanwise axis.
- Coupled motion of cable-stayed bridge in vertical bending and in torsion.

For the fist type, vertical bending oscillation is assumed as single-degree-of freedom (SDOF). Therefore, the equation of motion of SDOF can be written as

$$m\ddot{h} + c_h \dot{h} + k_h h = L_h \tag{3.4}$$

Where L_h is the lift force, m is the body mass, k_h is the stiffness coefficient and c_h is the damping coefficient.

Similar to the first type, the torsional oscillation also is considered as SDOF, the equation of motion of SDOF can be written as

$$I\alpha + c_{\alpha}\alpha + k_{\alpha}\alpha = M_{\alpha}$$
 (3.5)

Where M_{α} is aerodynamic moment, I is moment of inertia, k_{α} is the stiffness coefficient and c_{α} is the coefficient of damping.

The third type of motion is two DOFs, therefore the equations of motion are coupled as follow:

$$m\ddot{h} + c_h \dot{h} + k_h h = L_h \tag{3.6}$$

$$I \overset{\cdot}{\alpha} + c_{\alpha} \overset{\cdot}{\alpha} + k_{\alpha} \alpha = M_{\alpha} \tag{3.7}$$

where m, I, L_h and M_{α} represents mass, moment of inertia, lift and moment respectively; c and k represents damping and stiffness coefficients with the subscripts h and α meaning vertical and rotation displacements, respectively.

3.4 Aerodynamic Instability

Aeroelasticity is the discipline concerned with the study of the aerodynamic forces and structural motions interact significantly. When a structure is subjected to wind flow, it may vibrate or suddenly deflect in the airflow. This structural motion results in a change in the flow pattern around the structure. If the modification of wind pattern around the structure by aerodynamic forces, effects of which is increasing rather than decreasing the vibration of the structure, then the aeroelastic instability occurs. The aeroelastic phenomena that are considered in wind engineering are vortex shedding, torsional divergence, galloping, flutter and buffeting.

3.4.1 Vortex Shedding

When a body is subjected to wind flow, the separation of flow occurs around the body. Vortices are formed at points where the wind flow separates from the surface of a structure. They may break away at regular intervals causing a periodic variation of force on the structure. Excitation due to periodic formation of vortices in the wind flow in the wake of structure is primary depend on details of the shape of cross-section. If the structure is rigid and the incident flow steady, the vortex formation would be very precisely periodic at a frequency proportional with the wind velocity. With a flexible structure as cable-stayed bridge, the effect of motion of the structure is to modify the vortex frequency. This change is produced by movement of the structure, which may cause aerodynamic forces (lift, drag, moment) tending to increase the motion.

When the natural frequency f of structure differs significantly from vortex frequency called Strouhal frequency, the structure oscillates rather small. The Strouhal frequency f_s is defined as:

$$f_s = \frac{SU}{D} \tag{3.8}$$

where S is Strouhal number, D is typical cross flow dimension, f_s is frequency of vortex shedding, U is oncoming flow velocity.

When the vortex-induced and the natural frequencies coincide, the resonance will occur. This phenomenon is called lock-in. During lock-in condition, the structural member oscillates with increased amplitude but rarely exceeding half of the across wind dimension of the body (Simiu and Scanlan, 1996). The lock-in condition is illustrated in Fig. 2.1.

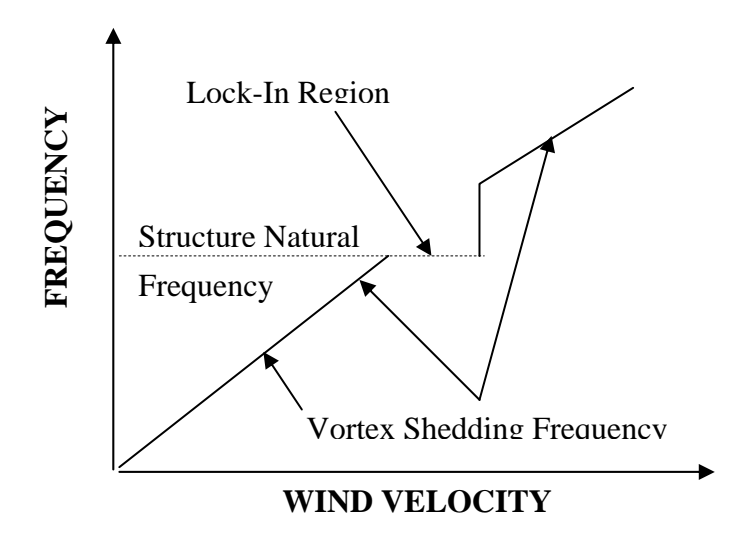


Fig. 3.1: Evolution of vortex-shedding frequency with wind velocity over elastic structure.

In the Fig. 3.1, the frequency of vortex-shedding at lock-in remains equal to natural frequency while wind velocities increases. The nature and extent of the vortex shedding phenomenon for different ranges of Reynolds number for a cylinder are shown in Fig3.2. The vortex-shedding phenomenon is describable in terms of a nondimensional number R_e , which is defined as;

$$R_e = \frac{\rho UD}{\mu} = \frac{UD}{\nu} \tag{3.9}$$

where U is characteristic velocity, D is characteristic body dimension, μ is dynamic viscosity of fluid, ρ is fluid density, ν is kinematics viscosity.

From Fig. 3.2, as illustrated by Simiu and Scanlan (1996), it is seen that for a very low Reynolds number, the flow remains the same. For higher Reynolds numbers, the flow starts to separate around the edges of the obstruction and vortices are generated in the immediate wake of the obstruction. Thereafter further increase in the Reynolds number causes the creation of cyclically alternating vortices and they are carried over with the flow downstream. From there on, the inertial effects become dominant over the viscous effects and turbulence sets in, resulting in shear of the flow. So this reasonably illustrates the vortices phenomenon starting from a smooth and low speed flow to a turbulent and high-speed flow.

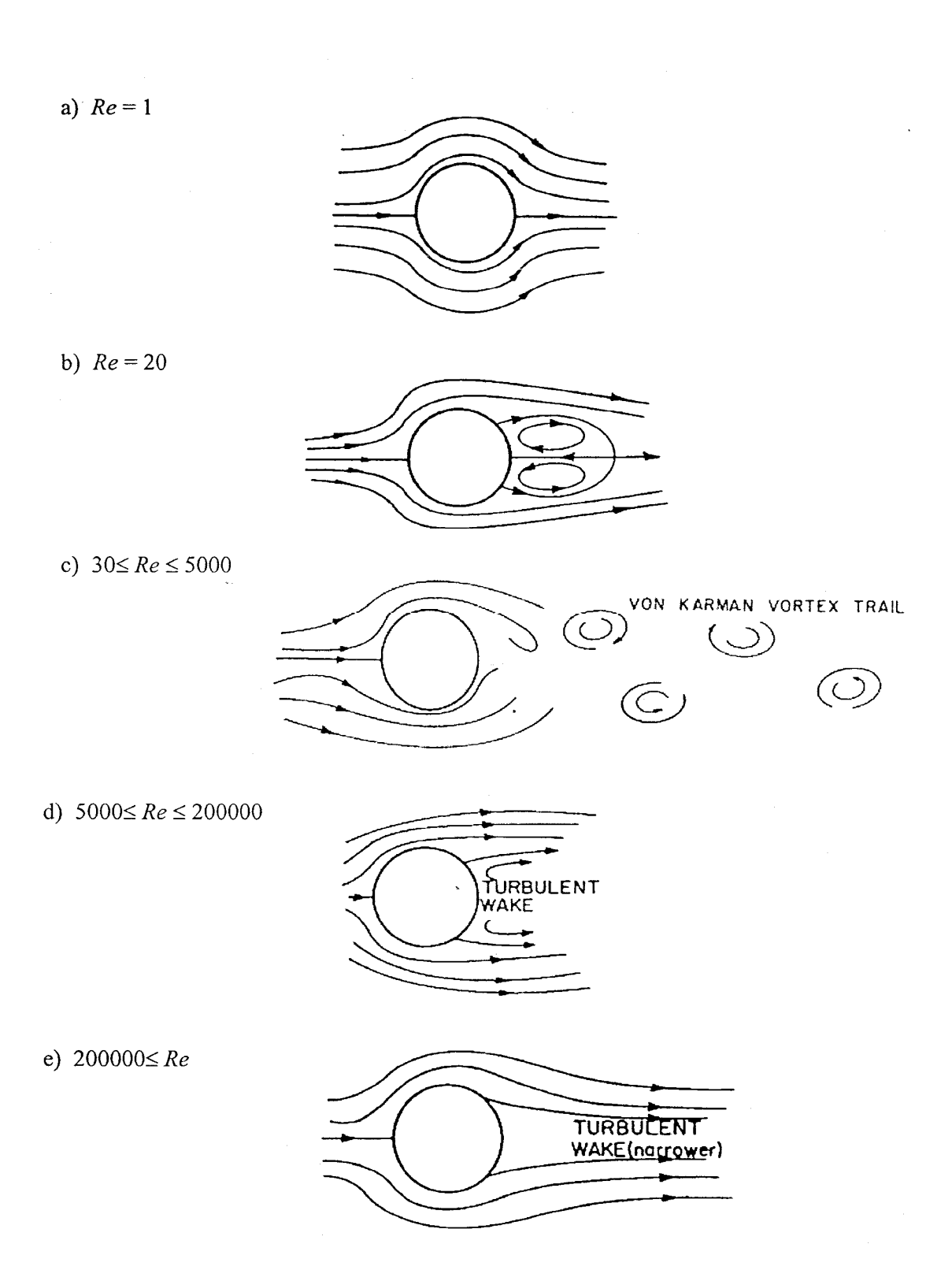


Fig. 3.2 Effects of Reynolds number

For wind engineering, the Reynolds number is in range from 10^4 to 10^5 then the inertial effects become dominant over the viscous effects. The periodic shedding of

vortices alternatively from the upper and lower surfaces of the bridge deck causes periodic fluctuation of aerodynamic forces on the structure. For this reason, the pressures on the upper and lower surfaces are unbalanced periodically that can cause transverse and torsional oscillation of the bridge deck that may lead to bridge deck instability. If this instability causes excessive deformations then it may lead to destruction of the bridge. It is the most serious problem for long-span bridges because of slenderness of structure.

3.4.2 Galloping

According Simiu and Scanlan, (1996), galloping is instability typical of slender structures having special cross sectional shape such as, for example, rectangular or D-section. Under certain conditions, these structures can exhibit large amplitude oscillations in the direction normal to the flow at frequency much lower than those vortex-shedding from the same direction. It is in this sense that galloping may be considered a low-frequency phenomenon.

The across wind galloping in a bridge causes a crosswise vibration in the body. As the section vibrates crosswise in a steady wind velocity U. By the relative reasons, when the velocity changes and the angle of attack α is also changed. Due to the change in α , the flow now is not symmetric, so that the pressure at top and bottom of section does not equal, that results lift force along y direction. This force accelerates the incipient motion of the body with the velocity y and has the destabilizing effects. The action of structure is against this motion by restoring force (Fig 3.3). Thus the body will oscillate in the y direction. And the equation of motion can be written as follow:

$$m \ddot{y} + c \dot{y} + ky = F(t)$$
 (3.10)

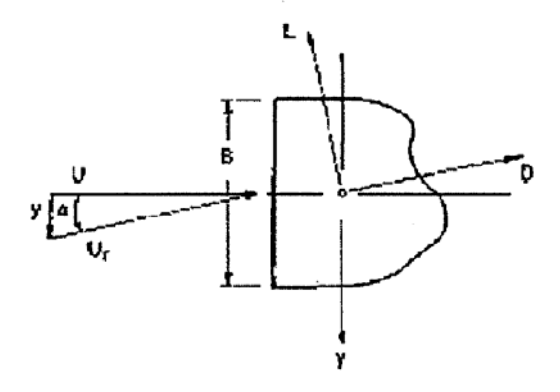


Fig. 3.3 Effective angle of attack on an oscillating bluff object

Analytical formulation of galloping

Drag force

$$D(\alpha) = \frac{1}{2} \rho U_r^2 B C_D(\alpha) \tag{3.11}$$

Lift force

$$L(\alpha) = \frac{1}{2} \rho U_r^2 B C_L(\alpha)$$
 (3.12)

Denote that the aerodynamic force $F_y(\alpha)$ is sum of projected of lift and drag forces on y-axis

$$F_{\nu}(\alpha) = -D(\alpha)\sin\alpha - L(\alpha)\cos\alpha \tag{3.13}$$

and

$$F(\alpha) = \frac{1}{2} \rho U_r^2 B C_{Fy}(\alpha)$$
 (3.14)

where
$$U = U_r \cos \alpha$$
 and $\alpha = \arctan^{-1} \frac{y}{U}$ (3.15)

Let consider the case $y \ll U \rightarrow \alpha \cong \frac{y}{U}$

Then
$$C_{Fy}(\alpha) = -\frac{U_r^2}{U^2} [C_D(\alpha) \sin \alpha + C_L(\alpha) \cos \alpha] = \frac{U_r^2}{U_r^2 (\cos \alpha)^2} [C_D(\alpha) \sin \alpha + C_L(\alpha) \cos \alpha]$$

$$\dots \dots (3.16)$$

$$C_{Fy}(\alpha) = -\frac{1}{\cos \alpha} \left[C_D(\alpha) \tan \alpha + C_L(\alpha) \right] = -\left[D_L(\alpha) + D_D(\alpha) \tan \alpha \right] \sec \alpha \qquad \dots (3.17)$$

U - wind velocity

 U_r - relative wind velocity with respect to moving body y velocity across-wind

 \dot{y} - velocity across wind

B - dimension of the section

L - lift force

D - drag fore

If the prism is sprung and the equation of motion is given as

$$m(y+2\zeta\omega_1y+\omega_1^2y) = -\frac{1}{2}\rho U^2 B \left[\frac{dC_L(\alpha)}{d\alpha} + C_D(\alpha)\right]_0 \frac{y}{U}$$
(3.18)

The total damping ratio

$$\zeta_T = 2\zeta m\omega_1 \dot{y} + \frac{1}{2}\rho UB \left[\frac{dC_L(\alpha)}{d\alpha} + C_D(\alpha) \right]_0$$
 (3.19)

The system is stable is $\zeta_T > 0$ it means that the energy of motion is dissipated. If the system is unstable when $\zeta_T < 0$, i.e. the lift force acts in the same sense at the motion and tend to increase amplitude of the oscillation. Due to $2\zeta m\omega$ is mechanic damping then always positive. The second term of the equation is aerodynamic damping that may be negative. If $\zeta_T < 0$ then

$$\left[\frac{dD_L(\alpha)}{d\alpha} + C_D(\alpha)\right]_0 < 0 \tag{3.20}$$

The galloping occur when ratio B/h is in range 0.75 to 3.0, where B is section width and h is section height, galloping may occur. At B/h \geq 3.0, the separated flow reattaches to the down stream of section. Therefore galloping is vanished (Ito and Nakamura 1982). For this reason, galloping only relates to pylon instability in cable-stayed bridge.

3.4.3 Torsional Divergence

Torsional divergence is an instance of a static response of a structure. Torsional divergence was at first associated with aircraft wings due to their susceptibility to twisting off at excessive air speeds. When the wind flow comes, drag, lift, and moment are produced on the structure. This moment induces a twist on the structure and causes the angle of incidence α to increase. The increasing of α is results of higher torsional moment and flexible structure. This phenomenon can be considered as the wind velocity increases. If the structure does not have sufficient torsional stiffness to resist this increasing moment, the structure becomes unstable and will be twisted to failure. The phenomenon depends upon structural flexibility and the manner in which the aerodynamic moments develop with twist. In most cases the critical divergence velocities are extremely high, well beyond the range of velocities normally considered in design (Simiu and Scanlan, 1996).

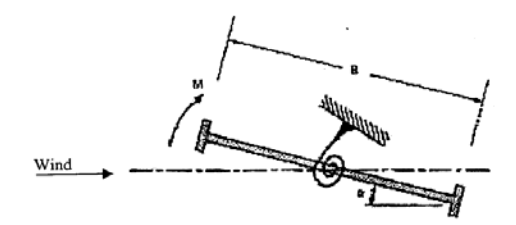


Fig. 3.4 Bridge deck under wind flow

The aerodynamic moment per unit span is given by

$$M_{\alpha} = \frac{1}{2} \rho U^2 B^2 C_M(\alpha) \tag{3.21}$$

where ρ is air density, U is the mean wind velocity, B is the deck width; α is the angle of twist and C_M is the aerodynamic moment coefficient about the twisting axis. At zero angle of attack the value of this moment is

$$M_{\alpha}(0) = \frac{1}{2}\rho U^2 B^2 C_{M0}$$
 where $C_{M0} = C_M(0)$ (3.22)

For a small change in α away from $\alpha = 0$, M_{α} is approximated as given by

$$M_{\alpha} = \frac{1}{2}PU^{2}B^{2} \left[C_{M0} + \left(\frac{dC_{M0}}{d\alpha} \right)_{\alpha=0} \alpha \right]$$
 (3.23)

Now equating the aerodynamic moment to the structural resisting moment gives

$$\frac{1}{2}\rho U^2 B^2 \left[C_{M0} + \left(\frac{dC_{M0}}{d\alpha} \right)_{\alpha=0} \alpha \right] = k_{\alpha} \alpha \tag{3.24}$$

$$\frac{1}{2}\rho U^{2}B^{2}\left[C_{M0} + C'_{M0}\alpha\right] = k_{\alpha}\alpha\tag{3.25}$$

where
$$C_{M0}' = \frac{dC_{M=0}}{d\alpha} | \alpha = 0$$
 (3.26)

Denote $\lambda = \frac{1}{2} \rho U^2 B^2$

Equation then becomes

$$(k\alpha - \lambda C_{M=0}) \alpha = \lambda C_{M0} \tag{3.27}$$

or

$$\alpha = \frac{\lambda C_{M0}}{(k_{\alpha} - \lambda C_{M=0})} \tag{3.28}$$

Divergence occurs when α approaches infinity

$$\lambda = \frac{k_{\alpha}}{C_{M=0}} \tag{3.29}$$

Thus the critical divergence velocity is given as

$$U_{cr} = \sqrt{\frac{2k_{\alpha}}{\rho B^2 C_{M0}}} \tag{3.30}$$

3.4.4 Flutter

The most dangerous dynamic instabilities of structure under wind effects are aeroelastic flutter. Flutter is an aeroelastic instability typical of structures such as airfoil or bridge deck that may oscillate in both translation and torsional displacements. This phenomenon can be explained as that the periodic shedding of vortices alternatively from the upper and lower surfaces of the bridge deck causes

periodic fluctuation of aerodynamic forces on the structure. Therefore, the pressures on the upper and lower surfaces are unbalanced periodically that can cause vertical and torsional oscillation of the bridge deck. This is the most serious problem for long-span bridges and is a very serious concern in the design of cable-stayed bridges. The failure of the Tacoma's narrows bridge was due to the flutter. The term flutter has been variously used to describe different types of wind-induced behavior. The most common type of flutter in design of the long-span bridge is classical flutter (Simiu and Scanlan, 1996).

Classical flutter applied to suspended span bridge decks. It implies an aeroelastic phenomenon in which two degrees of freedom of a structure, rotation and vertical translation, couple together in flow driven, unstable oscillation.

Flutter analysis is commonly based on the assumption of linear elastic system behavior. It is justified because the oscillations of the structures are usually harmonic. The governing equations of motion for translation and rotation of a bridge deck subjected to wind flow (Fig. 3.5) are given in Eqs. (3.6) and (3.7) repeated here as

$$m\ddot{h} + C_h \dot{h} + k_h h = L_h \tag{3.6}$$

$$I\overset{\cdot}{\alpha} + C_{\alpha}\overset{\cdot}{\alpha} + k_{\alpha}\alpha = M_{\alpha} \tag{3.7}$$

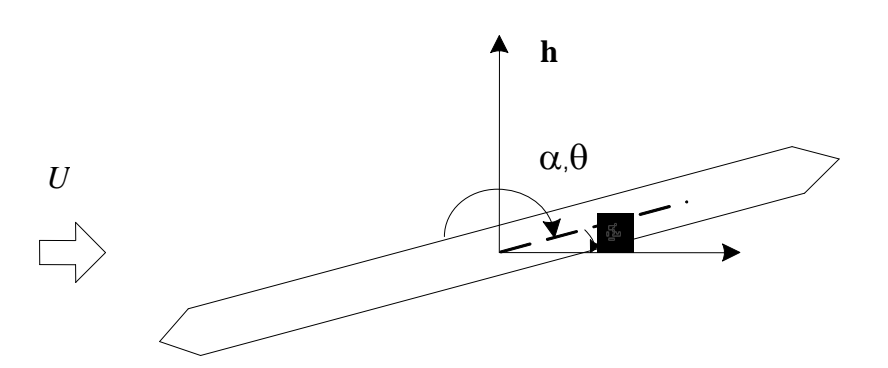


Fig. 3.5 Definitions of wind and deflections

where m, I, h, α , L_h and M_{α} represents mass, moment of inertia, heave, pitch, lift and moment respectively, c and k represents damping and stiffness coefficients with the subscripts h and α meaning heave and rotation respectively.

$$L_{h} = \frac{1}{2} \rho U^{2} B \left[K H_{1}^{*} \frac{\dot{h}}{U} + K H_{2}^{*} \frac{B \dot{\alpha}}{U} + K^{2} H_{3}^{*} \alpha + K^{2} H_{4}^{*} \frac{h}{B} \right]$$
(3.31)

$$M_{\alpha} = \frac{1}{2} \rho U^{2} B^{2} \left[K A_{1}^{*} \frac{\dot{h}}{U} + K A_{2}^{*} \frac{B \dot{\alpha}}{U} + K^{2} A_{3}^{*} \alpha + K^{2} A_{4}^{*} \frac{h}{B} \right]$$
(3.32)

In the classical theoretical case (Theodorsen 1934, Dyrbye 1996) of steady sinusoidal oscillation of and airfoil these coefficients is given as

in which F(k) + iG(k) = C(k) is the Theodorsen circulation function defined by Bessel function and k is based on the half chord, i.e. k = K/2. F(k) and G(k) are given by

$$F(k) = \frac{J_1(J_1 + Y_0) + Y_1(Y_1 - J_0)}{(J_1 + Y_0)^2 + (Y_1 - J_0)^2}$$
$$G(k) = \frac{J_1J_0 + Y_1Y_0}{(J_1 + Y_0)^2 + (Y_1 - J_0)^2}$$

where J_i, Y_i are Bessel functions of the first and second kind, respectively of order i.

If the coefficients, H_i^* and A_i^* are non dimensional function of the reduced frequency K then the equation hold not only for sinusoidal oscillation but for general motions of the form:

$$h = h_0 e^{\lambda t} \sin \omega t \tag{3.34}$$

$$\alpha = \alpha_0 e^{\lambda t} \sin(\omega t - \theta) \tag{3.35}$$

Where h_0 , α_0 is initial amplitudes, θ -relative phase, λ is the rate of decay or buildup of the oscillation (linear regime)

Lasen and Walther (1998) proposed that

$$L_{h} = \frac{1}{2} \rho U^{2} B \left[K H_{1}^{*} \frac{\dot{h}}{U} + K H_{2}^{*} \frac{B \dot{\alpha}}{U} + K^{2} H_{3}^{*} \alpha + K^{2} H_{4}^{*} \frac{h}{B} \right]$$
(3.36)

$$M_{\alpha} = \frac{1}{2} \rho U^{2} B \left[K A_{1}^{*} \frac{\dot{h}}{U} + K A_{2}^{*} \frac{B \dot{\alpha}}{U} + K^{2} A_{3}^{*} \alpha + K^{2} A_{4} \frac{h}{B} \right]$$
(3.37)

where $K = \frac{B\omega}{U}$ is reduced frequency coefficient, H_i^* , A_i^* are flutter derivatives, U is wind velocity, B is deck width of bridge.= $h_0 \exp(i\omega t)$, $\alpha = \alpha_0 \exp(i\omega t)$

Assuming that the motion are harmonic in time $h = h_0 \exp(i\omega t)$, $\alpha = \alpha_0 \exp(i\omega t)$. Under these assumptions, the above equation can be arranged in non-dimensional form to yield.

$$C_{L}e^{i(\omega t - \varphi)} = 2K^{2} \left[(iH_{1}^{*} + H_{4}^{*}) \frac{h}{B} + (iH_{2}^{*} + H_{3}^{*}) \alpha \right] e^{i\omega t}$$
 (3.38)

$$C_{M}e^{i(\omega t - \varphi)} = 2K^{2} \left[(iA_{1}^{*} + A_{4}^{*}) \frac{h}{B} + (iA_{2}^{*} + A_{3}^{*}) \alpha \right] e^{i\omega t}$$
 (3.39)

Dividing the above equations by $e^{i\omega t}$, substituting $e^{(-i\varphi)}$ by $(\cos\varphi-i\sin\varphi)$ Then the aerodynamic derivatives can be defined

$$H_{1}^{*} = \frac{-C_{L}\sin(\phi)}{2(2\pi)^{2}} \frac{B}{h} \left(\frac{U}{fB}\right)^{2} \qquad H_{4}^{*} = \frac{C_{L}\cos(\phi)}{2(2\pi)^{2}} \frac{B}{h} \left(\frac{U}{fB}\right)^{2}$$
(3.40)

$$A_{1}^{*} = \frac{-C_{M} \sin(\phi)}{2(2\pi)^{2}} \frac{B}{h} \left(\frac{U}{fB}\right)^{2} \qquad A_{4}^{*} = \frac{C_{M} \cos(\phi)}{2(2\pi)^{2}} \frac{B}{h} \left(\frac{U}{fB}\right)^{2}$$
(3.41)

$$H_{2}^{*} = \frac{-C_{L}\sin(\phi)}{2\alpha(2\pi)^{2}} \left(\frac{U}{fB}\right)^{2} \qquad H_{3}^{*} = \frac{C_{L}\sin(\phi)}{2\alpha(2\pi)^{2}} \left(\frac{U}{fB}\right)^{2}$$
(3.42)

$$A_{2}^{*} = \frac{-C_{M} \sin(\phi)}{2\alpha (2\pi)^{2}} \left(\frac{U}{fB}\right)^{2} \qquad A_{3}^{*} = \frac{C_{M} \sin(\phi)}{2\alpha (2\pi)^{2}} \left(\frac{U}{fB}\right)^{2}$$
(3.43)

3.4.5 Flutter Derivatives at Vortex Lock-in

As vortex-induced vibration are presented above, the most critical dynamic instability of body is when the natural frequency of oscillation differs a little from the Strouhal frequency ($f \cong f_s$). Then flutter derivatives are determined from experiment, but not always at lock-in. From the failure of Tacoma Narrow bridge, which was collapsed under rather low velocity in vortex shedding stage, state by (Billan and Scanlan 1991). Therefore the flutter derivatives will be considered at lock in and the equation of motion is given the same but $\omega = \omega_h$ and $\omega = \omega_a$

$$m\ddot{h} + c_h \dot{h} + k_h h = L_h \tag{3.44}$$

$$I\ddot{\alpha} + c_{\alpha}\dot{\alpha} + k\alpha = M_{\alpha} \tag{3.45}$$

$$m(\ddot{h} + 2\zeta_h \omega \dot{h} + \omega^2 h) = L_h \tag{3.46}$$

$$I(\alpha + 2\zeta_b \omega \alpha + \omega^2 \alpha) = M_{\alpha}$$
 (3.47)

where

$$L_{h} = \frac{1}{2} \rho U^{2} B \left[K H_{1}^{*} \frac{\dot{h}}{U} + K H_{2}^{*} \frac{B \dot{\alpha}}{U} + K^{2} H_{3}^{*} \alpha + K^{2} H_{4}^{*} \frac{h}{B} \right]$$
(3.48)

$$M_{\alpha} = \frac{1}{2} \rho U^{2} B \left[K A_{1}^{*} \frac{\dot{h}}{U} + K A_{2}^{*} \frac{B \dot{\alpha}}{U} + K^{2} A_{3}^{*} \alpha + K^{2} A_{4} \frac{h}{B} \right]$$
(3.49)

3.4.6 Effect of Turbulence on Bridge Flutter Derivatives

Buffeting is defined as the unsteady loading of a structure by velocity fluctuations in the incoming flow and not self-induced. Buffeting vibration is the vibration produced by turbulence. The buffeting is caused by turbulence in the airflow and can produce significant vertical and torsional motions of a bridge even at low speeds. This buffeting induced motion results in a gradual transition to large amplitude torsional oscillations, which could lead to the failure of a bridge. The natural wind is random process then the wind velocity is varied randomly with time. And the wind velocity and be expressed as $U = \overline{U} + u(t)$, where \overline{U} - mean velocity and u(t) - velocity fluctuation. Buffeting is defined as unsteady loading of a structure by fluctuation in oncoming flow (Scanlan and Lin 1978) .Then L_h and M_α becomes.

$$L_{h} = \frac{1}{2} \rho \overline{U}^{2} B \left[K H_{1}^{*} \frac{\dot{h}}{U} + K H_{2}^{*} \frac{B \dot{\alpha}}{U} + K^{2} H_{3}^{*} \alpha \right] + L(t)$$
 (3.50)

$$M_{\alpha} = \frac{1}{2} \rho \overline{U}^{2} B^{2} \left[KA_{1}^{*} \frac{\dot{h}}{\overline{U}} + KA_{2}^{*} \frac{B \dot{\alpha}}{\overline{U}} + K^{2} A_{3}^{*} \alpha \right] + M(t)$$
 (3.51)

where L(t) and M(t) are respectively buffeting lift and buffeting moment.

$$\frac{L_{t}}{\frac{1}{2}\rho \overline{U^{2}}} = C_{L}(\alpha_{0}) \left[1 + 2\frac{u(x,t)}{\overline{U}} \right] + \left[\frac{dC_{L}}{d\alpha} \Big|_{\alpha=0} + \frac{A}{B}C_{D}(\alpha_{0}) \right] \frac{w(x,t)}{\overline{U}}$$
(3.52)

$$\frac{M_{t}}{\frac{1}{2}\rho\overline{U^{2}}} = \left[C_{M}(\alpha_{0}) + C_{C}(\alpha_{0})\frac{Ar}{B^{2}}\right] + \left[1 + 2\frac{u(x.t)}{\overline{U}}\right] + \frac{dC_{L}}{D\alpha}\Big|_{\alpha=0}\frac{w(x.t)}{\overline{U}}$$
(3.53)

where B is deck width, A is across wind area, r is distance of the deck mass to the effective rotation axis; u(t), w(t) are fluctuation velocities along wind and vertical respectively.

3.5 Section Model Tests to Determine Aerodynamic Derivatives

Various methods (Jakobsen 1995) are used to extract the flutter derivatives from wind tunnel tests on geometrically and aerodynamically representative models of short sections of the deck. While it is possible to identify the forces from the difference of inertial and excitation forces on a structure forced to vibrate at a single frequency (Falco et al. 1992), or potentially from pressure taps on the section (Holmes 1995) it is usually experimentally simpler to obtain and analyses free vibration response records (Scanlan and Sabzevari 1969). The free vibration may be in response to a transient deflection (step relaxation) or to buffeting caused by the airflow turbulence. Having less emphasis on elaborate equipment and more on the signal processing and data reduction techniques, these procedures are more applicable to full-scale data.

The flutter derivatives are usually identified through the effect they have on the free decay vibration characteristics of the model section. A typical wind tunnel test involves suspending a rigid section model from a set of springs so that it can oscillate vertically and in torsion (about a transverse axis) as flutter traditionally involves only these two degrees of freedom. The section can be considered as a rigid body, having (in still air) a pair of uncoupled rigid-body vibration modes each with corresponding natural frequency and damping ratio.

When set in motion in airflow, changes in the frequency and damping of the two vibration modes and interaction effects between them are identified and flutter derivatives are obtained. If the model is restrained to move in pure torsion the effect of the wind will typically be to increase the damping ratio and reduce the natural frequency of the oscillation, and each effect is described by one derivative. From the study of damping and stiffness effects in pure vertical or torsional motion the four so-called 'direct derivatives' can be obtained for the two degrees of freedom (DOF). When motional restraints are removed the aerodynamic cross-coupling effects between the DOF inherent in the recorded response can be used to identify all the flutter derivatives including the additional set of four 'cross-derivatives' linking the DOF. A different approach is to estimate all flutter derivatives 'simultaneously' from the response data of a model moving freely in both vertical and torsional direction, due to buffeting loading or an initial excitation or deflection (Jakobsen and Hansen 1995; Sarkar et al. 1992; Iwamoto and Fujino 1995).

3.5.1 Test Arrangement for Free Vibration Response

Fig. 3.6 shows a schematic arrangement of a bridge section model in a wind tunnel with horizontal incident wind having mean speed U. The deck has chord B, mass m and moment of inertia I about the geometric centreline. Accidental or deliberate mass eccentricity is described by a mass $m_{\rm e}$ at radius $r_{\rm e}$ leading to total inertia $I_{\rm T}$ and total mass $m_{\rm T}$. The section is attached to a rigid test frame at each corner by linear springs with stiffness k arranged at distance e upstream or downstream of the geometric centreline. The contributions of spring mass to total mass and inertia are

accounted for by adding one-third of their mass at their point of attachment. Vertical and torsional displacements and their time derivatives at mid-chord are, respectively, denoted $h, \dot{h}, \ddot{h}, \theta, \dot{\theta}, \ddot{\theta}$ and can be recovered from measurement and subsequent signal processing of acceleration records \ddot{y}_1, \ddot{y}_2 from the leading and trailing edges of the section. It is also possible to obtain motion records via optical displacement transducers or load cells.

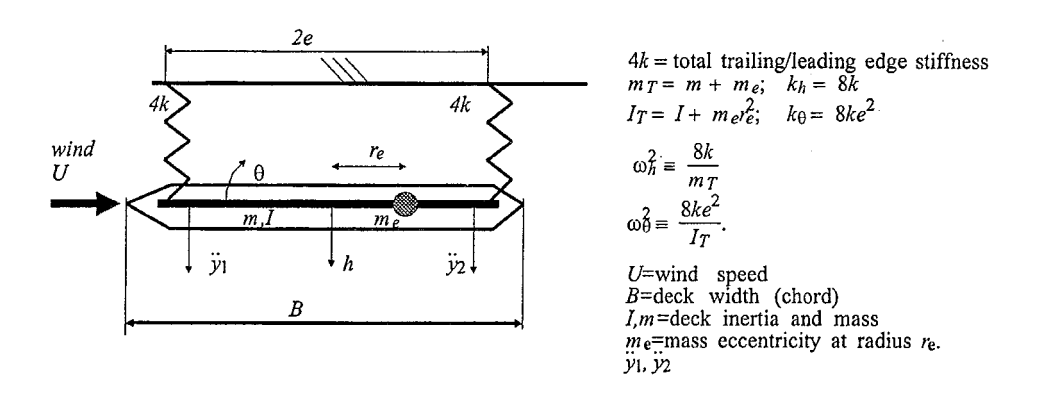


Fig. 3.6 Arrangement and conventions for section model

In still air without aerodynamic influence and zero (resultant) mass eccentricity the natural frequencies of the deck for rigid body vibration are in theory obtained as

$$f_{\theta} = \left(1/2\pi\right)\sqrt{k_{\theta}/I_{T}}$$

and

$$f_{h} = \left(1/2\pi\right)\sqrt{k_{h}/m_{T}}$$

where $k_{\theta} = 8ke^2$ and $k_h = 8k$

In practice the test rig and model do not present exact rigid body modes and there may be a degree of torsion or bending present in the model. These effects can be minimized by good construction but may have to be accounted for if measured motion parameters are not representative of the whole section.

In particular test rig flexibility at the connections with the model will lead to apparent spring rates different from nominal values of k. The exact effective values can be identified via the still-air natural vertical natural frequency given the known mass of the deck. Likewise the effective torsional inertia would be obtained from the torsional natural frequency once k is known.

Note that the above convention is not unique; a popular convention used in aeronautics is obtained by simple rotation about the wind axis.

3.5.2 Choice of Structural/Geometric Parameters for Section Test

For a wind tunnel with maximum wind speed \hat{U} the values of k and e are chosen to obtain a range of non-dimensional wind speeds U/fB consistent with prototype values of f and design wind speed. For example, if the prototype has vertical mode frequency 0.2 Hz, a chord of 40 m and a design wind speed of 60 m/s, a model with chord 0.6 m used in a wind tunnel with top speed of 22.5 m/s should have a maximum vertical mode frequency f_h set via $(U/f_h B)_{prototype}$ =7.5= $(\hat{U}/f_h B)_{model}$ i.e. f_h =5 Hz, with similar factors applying to f_θ . To provide stability against torsional divergence and for other practical considerations it is better that $f_\theta > f_h$.

The model mass depends on B and the recommended range (Hansen 1992) of 3–8 for the ratio of chord to span, to minimize the effect of deck flexibility in rigid body modes. For best detailing in a limited tunnel width the lower limit may be approached, although the end effects at extremities of the section then become more significant. Appropriate materials are used to achieve geometric accuracy with adequate stiffness to prevent occurrence of the low frequency deformation modes in the model. Given the resulting model mass the spring rate k can be chosen to achieve f_h , f_{θ} .

Additional considerations for the test rig and suspension arrangement are that a good linear range of spring deflection should be allowed and that the ratio of f_{θ} to f_h should be adjustable in a wide range either side of unity to suit the requirements of different identification techniques.

The set of eight vertical springs offers no restraint against small lateral or longitudinal deflections nor against rotation about a vertical axis and mechanical arrangements are used to restrain or restrict these. For example, drag wires can installed to resist but not entirely constrain these motions. Practical issues relating to constraints and geometric effects of the springs are well documented by Hjorth-Hansen (1992). In case it is desirable to provide restraint against rotation, a set of four additional drag wires may be connected to a rigid vertical bar attached to the section. Likewise, vertical motion may be restrained by anchoring a pair of roller bearings (to allow free rotation about a centroidal cross-wind axis). The drag wires do not offer complete restraint but they increase the stiffness of the restrained DOF to the extent that it cannot contribute significantly to the aerodynamic effects.

3.5.3 General Equations of Motion

For identification of all eight derivatives involving only vertical and torsional motion, the equations of motion for a 2DOF section with length L and width B, in air flow with density ρ and speed U according to the conventions of Fig. 3.5, are

$$m_{T}\ddot{h} + c_{h}\dot{h} + k_{h}h + m_{e}r_{e}\ddot{\theta} = \frac{\rho U^{2}BL}{2} \left[h_{1}\frac{\dot{h}}{U} + h_{2}\frac{B\dot{\theta}}{U} + h_{4}\frac{h}{B} + h_{3}\theta \right] + L_{buf}$$
 (3.54)

$$I_{T}\ddot{\theta} + c_{\theta}\dot{\theta} + k_{\theta}\theta + m_{e}r_{e}\ddot{h} = \frac{\rho U^{2}BL}{2} \left[a_{1}\frac{B\dot{h}}{U} + a_{2}\frac{B^{2}\dot{\theta}}{U} + a_{4}h + a_{3}B\theta \right] + M_{buf}$$
(3.55)

On the left-hand side the mechanical damping coefficients are c_h , c_θ for each DOF. The right-hand sides are aerodynamic lift and moment forces $L_{\rm ae}$, $M_{\rm ae}$ which evidently depend on non-dimensional coefficients or flutter derivatives. The 'direct derivatives' h_1 , h_4 , a_2 , a_3 represent effects within a single DOF response while 'cross-derivatives' h_2 , h_3 , a_1 , a_4 represent coupling between the DOF. Buffeting lift and moment forces are denoted $L_{\rm buf}$, $M_{\rm buf}$, respectively.

An alternative form for aerodynamic lift and drag forces uses flutter derivatives which are frequency dependent coefficients:

$$L_{ae} = \rho U^{2}BL \left[KH_{1}^{*}(K) \frac{\dot{h}}{U} + KH_{2}^{*}(K) \frac{B\dot{\theta}}{U} + K^{2}H_{3}^{*}(K)\theta + K^{2}H_{4}^{*}(K) \frac{h}{B} \right]$$
(3.56)

$$M_{ae} = \rho U^{2} B^{2} L \left[K A_{1}^{*} (K) \frac{\dot{h}}{U} + K A_{2}^{*} (K) \frac{B \dot{\theta}}{U} + K^{2} A_{3}^{*} (K) \theta + K^{2} A_{4}^{*} (K) \frac{h}{B} \right]$$
(3.57)

Note that there are different forms of (3.54) and (3.56) using for example the half-chord B/2 as reference instead of B and using $\rho U^2BL/2$ instead of ρU^2BL . Some alternate forms are presented by Zasso (1996).

Simple algebraic relations such as $h_1=2KH_1^*(K)$ link the A_i^*, H_i^* in (3.56) and (3.57) to the a_i, h_i in (3.54) and (3.55) where $K=B\omega/U=2\pi\,fB/U$ is the reduced frequency. In (3.54), (3.55), (3.56) and (3.57), the effect of p-derivatives i.e. those relating to lateral (drag) motion, are not considered since this type of motion is restrained. A few treatments (Singh et al. 1996 and Jain et al. 1996) relating to ultralong span suspension bridges where interactions with lateral motion are believed to be important are beginning to use the full formulation. Also at least one identification method for the full set of 18 derivatives for 3DOF has been presented (Singh 1994).

However, cases of classical vertical/torsional flutter are still practically covered using only the vertical and torsional DOF hence the principles are illustrated for 2DOF systems. Whereas both the A_i^*, H_i^* and a_i, h_i are functions of wind speed the form of (3.54) and (3.55) is used here with the convention of Fig. 3.6, as it delays a decision about which frequency to use in K.

3.5.4 Equations of Motion for SDOF Response

Eqs. (3.54) and (3.55) are examined in single degree of freedom (SDOF) and 2DOFs form for parameter identification. Considering SDOF vibration with zero resultant mass eccentricity, Eqs. (3.54) and (3.55) simplify to

$$m_{T}\ddot{h} + c_{h}\dot{h} + k_{h}h = \frac{\rho U^{2}BL}{2} \left[h_{1}\frac{\dot{h}}{U} + h_{4}\frac{h}{B} \right] + L_{buf}$$
 (3.58)

$$I_{T}\ddot{\theta} + c_{\theta}\dot{\theta} + k_{\theta}\theta = \frac{\rho U^{2}BL}{2} \left[a_{2}\frac{B^{2}\dot{\theta}}{U} + a_{3}B\theta \right] + M_{buf}$$
 (3.59)

having solution for free vibration (transient) decay from an initial deflections h_0, θ_0 , respectively

$$h(t) = h_0 e^{\lambda t} \cos(\omega t + \phi)$$
 (3.60)

$$\theta(t) = \theta_0 e^{\lambda t} \cos(\omega t + \phi) \tag{3.61}$$

For still-air vertical response, $-\lambda = \xi_h \omega_h$ and $\omega = \omega_h \sqrt{1 - \xi^2}$ where $\xi_h = c_h / 2m_T \omega_h$ $\omega_h = \sqrt{k_h / m_T}$

For still-air torsional response, $-\lambda = \xi_{\theta} \omega_{\theta}$ and $\omega = \omega_{\theta} \sqrt{1 - \xi^2}$ where. $\xi_{\theta} = c_{\theta} / 2I_{T} \omega_{\theta}$, $\omega_{\theta} = \sqrt{k_{\theta} / I_{T}}$

For response to random excitation such as by turbulent buffeting the auto-spectrum of vertical response is

$$S_{hh}(\omega) = \frac{S_{ll}}{k_h^2 \left[\left(1 - \left(\omega / \omega_{h'} \right)^2 \right)^2 + \left(2\xi_{h'} \omega / \omega_{h'} \right)^2 \right]}$$
(3.62)

where S_{ll} is the spectrum of lift forces. The factor S_{ll}/k_h^2 depends on static aerodynamic coefficients but is taken as constant around the model frequencies and ω_{h^+} , ξ_{h^-} are natural frequency and damping ratios assumed to be aerodynamically modified. A similar result is obtained for torsion response.

3.5.5 System Identification from 1DOF Response

In a wind stream with velocity U and vertical response given by Eq. (3.60) the direct vertical derivatives h_1 , h_4 are found from the shifts in λ , ω , given by

$$-\lambda = \xi_h \omega_h - \frac{\rho U B L h_1}{4 m_T} \text{ and } \omega^2 = \frac{k_h}{m_T} - \frac{\rho U^2 L h_4}{2 m_T}$$
 (3.63)

Similarly the direct torsional derivatives a_2 , a_3 are identified from the shifts in natural frequency and damping ratio from the still-air values:

$$-\lambda = \xi_{\theta} \omega_{\theta} - \frac{\rho U B^{3} L a_{2}}{4 I_{T}} \text{ and } \omega^{2} = \frac{k_{\theta}}{I_{T}} - \frac{\rho U^{2} B^{2} L a_{3}}{2 I_{T}}$$
(3.64)

Hence the identification of h_1 , h_4 , a_2 , a_3 is thus relatively straightforward, almost trivial. To obtain vertical direct derivatives the torsional DOF is restrained and the model is pulled down and released in a steady wind. This method is termed 'step relaxation'. If an acceleration response data acquisition system is used it can be triggered by the sudden large acceleration. Standard curve fitting tools can be used to obtain the best fit of Eq. (3.60) to the response signal. From a practical point of view this process is very simple, and it is possible to use the second derivative of Eq. (3.60) with acceleration data directly. Extraction of torsional direct derivatives uses an analogous process.

The free decay method is simple and accurate provided there is a clear decay signal. In the case where the wind speed is very large and the damping coefficient similarly large the useable portion of the trace may be very short and may have a poor signal to noise ratio, the noise being response to buffeting. It is also practically difficult to set a trigger threshold large enough to avoid triggering on buffeting and small enough to be mechanically achievable.

For low wind speeds the slight discrepancy which can be observed between the monitored and fitted curves is a result of the mechanical damping of the model being non-linear, i.e. amplitude dependent. A linear fit is however assumed to be satisfactory, according to the linearised equations of motion (3.54) and (3.55) and errors due to mechanical non-linearity as well as amplitude-dependent aerodynamic damping can be minimised by starting from a standard amplitude. For the decay with high wind speed the fit is also not exact, but for different reasons. At higher wind speeds, even for flows with very low turbulence the response is driven by the turbulence as it decays. Hence the 'better' part of the data with high 'signal' to noise ratio is rather short and also probably displays non-linear damping.

At the stage where buffeting response dominates, it is simpler to use the buffeting response data and find the values of ω_h , ξ_h to obtain the best fit of Eq. (3.62) to the auto-power spectrum obtained from the data. Satisfactory identification of ω_h , ξ_h using this method is subject to a number of conditions (Brownjohn 1994) such as stationary of input, flatness of input spectrum, adequate averaging to reduce

variance errors, and using sufficient spectral resolution with respect to the width of the peak in the spectrum. Since the wind speed and turbulence spectrum are well controlled in a wind tunnel and the damping is high it is only necessary to record a few minutes of response data, which would (by scaling of frequencies from prototype to model) represent much longer full-scale time series. These data are divided into n records of length T and the minimum value of n is found to obtain a 'confident' fit and the same is repeated for torsional direct derivatives. Given good estimates of $\omega_{h'}, \xi_{h'}, \omega_{\theta'}, \xi_{\theta'}$, the direct derivatives are obtained from

$$h_1 = 4m_T \left(\omega_h \xi_h - \omega_{h'} \xi_{h'} \right) / \rho UBL$$
 $h_4 = 2m_T \left(\omega_h^2 - \omega_{h'}^2 \right) / \rho U^2 L$ (3.65a)

$$a_2 = 4I_T \left(\omega_{\theta} \xi_{\theta} - \omega_{\theta'} \xi_{\theta'} \right) / \rho U B^3 L$$
 $a_3 = 2I_T \left(\omega_{\theta}^2 - \omega_{\theta'}^2 \right) / \rho U^2 B^2 L$ (3.65b)

As an alternative to frequency domain analysis of the random response, random decrement signature and auto-correlation function could also be used to obtain the single mode impulse response function. The auto- and cross-correlation functions are the starting point for the 2DOF time domain identification method discussed next

3.5.6 Equations of Motion for 2DOF Response

The equations of motion (3.54) and (3.55) may be rewritten in matrix form as

$$M\ddot{z} + C_{str}\dot{z} + K_{str}z = C_{ae}\dot{z} + K_{ae}z + p(t)$$
(3.66)

in which

$$\mathbf{M} = \begin{bmatrix} m_T & m_e r_e \\ m_e r_e & I_T \end{bmatrix}$$
 represents the mass with mechanical coupling.

$$\mathbf{C}_{\mathrm{str}} = \begin{bmatrix} 2\xi_h \omega_h m_T & 0 \\ 0 & 2\xi_\theta \omega_\theta I_T \end{bmatrix} \quad \text{represents mechanical damping}$$

$$\mathbf{K}_{\text{str}} = \begin{bmatrix} m_T \omega_h^2 & 0 \\ 0 & I_T \omega_\theta^2 \end{bmatrix}$$
 represents mechanical stiffness

$$C_{ae} = P \begin{bmatrix} h_1/U & h_2B/U \\ a_1B/U & a_2B^2/U \end{bmatrix}$$
 represents aerodynamic damping and

$$\mathbf{K}_{ae} = P \begin{bmatrix} h_4 / B & h_3 \\ a_4 & a_3 B \end{bmatrix}$$
 represents aerodynamic stiffness, with $P = \frac{1}{2} \rho U^2 B L$

Vectors of measurable response and of buffeting load are

$$z = \begin{bmatrix} h \\ \theta \end{bmatrix}, \quad p = \begin{bmatrix} L_{buf} \\ M_{buf} \end{bmatrix} = \begin{bmatrix} g_h \\ g_a \end{bmatrix} u(t)$$

The buffeting input is represented by a common (wind dependent) forcing function u(t) and two gain factors g_h , g_a which depend on mean wind speed, section shapes and static aerodynamic coefficients and it is implied that the lift force and moment due to buffeting are coherent.

Eq. (3.66) can be transformed to 'state space' form:

$$\mathbf{x} = \mathbf{A}\mathbf{x} + \mathbf{B}u, \qquad (3.67a)$$

$$\mathbf{y} = \mathbf{C}\mathbf{x} + \mathbf{D}u, \qquad (3.67b)$$

where

$$A = \begin{bmatrix} M^{-1}(C_{ae} - C_{str}) & M^{-1}(K_{ae} - K_{str}) \\ I & 0 \end{bmatrix}, \quad x = \begin{bmatrix} \dot{z} \\ z \end{bmatrix}$$

and

$$\mathbf{B} = \begin{bmatrix} \mathbf{M}^{-1} [g_h \ g_a]' \\ \mathbf{0} \end{bmatrix}$$

For the case of free vibration response to a transient, **B** and **D** are null matrices, otherwise they connect with the common forcing function u(t). **C** depends on which response parameter is observed. Initial conditions are given as $x_0 = [\dot{h}_0 \,\dot{\theta}_0 \,h_0 \,\theta_0]$. For the case of response where u(t) is approximately described as a Gaussian white noise process, such as excitation by turbulence in the air stream, the initial conditions are taken as zero.

3.5.7 System Identification from 2DOF Response

Three methods are used for identifying the system matrix **A**. The first method uses time domain free decay records, the second uses either free vibration decay or random response (from turbulent buffeting and the third, in frequency domain, uses turbulent buffeting response.

3.5.7.1. Direct Curve Fit to 2DOF Equations of Motion

Poulsen's method

This represents the first application of system identification and control theory techniques to the problem of extracting aerodynamic derivatives from bridge-section model tests. The method is used to apply with free decay signals (step response) of section model under wind flow.

The mathematical model is given by following coupled differential equations proposed by Scanlan (1971, 1977):

$$\ddot{h} + \mu_0 \dot{h} + \beta_0 h = H_1 \dot{h} + H_2 \dot{\alpha} + H_3 \alpha + H_4 h \tag{3.68}$$

$$\ddot{\alpha} + \sigma_0 \dot{\alpha} + \gamma_0 \alpha = A_1 \dot{h} + A_2 \dot{\alpha} + A_3 \alpha + A_4 h \tag{3.69}$$

These equations represent a general linearized form for self-excited forces under the assumption of small sinusoidal vertical (h) and torsional (α) motions with negligible horizontal motion effects.

The structural modal parameters ($\mu_0, \beta_0, \sigma_0, \gamma_0$) are presented in the following from:

$$\beta_0 = \omega_h^2$$

$$\mu_0 = 2\zeta\omega_h$$

$$\gamma_0 = \omega_\alpha^2$$

$$\sigma_0 = 2\zeta\omega_\alpha$$
(3.70)

It is a basic assumption that the aerodynamic parameters are zero under zero wind conditions so μ_0 , β_0 , σ_0 , γ_0 describe the test rig. In the common formulation of Eqs. 2.1 and 2.2 (Scanlan, 1977) the derivatives H_4^* and A_4^* are omitted as it is expected that the vertical position of the deck (h) has no effect on the torsional frequency, torsional damping or vertical stiffness. However, Eq (3.68) already contains the term β_0 h on the left-hand side, so he maintains H_4^* term that does not change his solution technique. Consequently, only the A_4^* parameter was omitted in his study.

For wind velocities greater than zero, the motion of the bridge is then given by:

$$\ddot{h} + (\mu_0 - H_1)\dot{h} + (\beta_0 - H_4)h - H_2\dot{\alpha} - H_3\alpha = 0$$
(3.71)

$$\ddot{\alpha} + (\sigma_0 - A_2)\dot{\alpha} + (\gamma_0 - A_3)\alpha - A_1\dot{h} - A_4h = 0$$
(3.72)

The wind effect is a shift in frequencies and damping terms - and a coupling between the two directions of motions. The analysis is consequently divided into two sub-problems, namely system identification and parameter determination.

The system identification problem is to estimate from the data, the parameters μ , β , ρ , σ , γ , and δ in the following equations:

$$\ddot{h} + \mu \dot{h} + \beta_0 h + \rho \dot{\alpha} - \kappa \alpha = 0 \tag{3.73}$$

$$\ddot{\alpha} + \sigma \dot{\alpha} + \gamma \alpha + \delta \dot{h} = 0 \tag{3.74}$$

The estimation procedure is performed for each value of the wind velocity for which tests are conducted including zero wind conditions.

The parameter determination problem involves two parts. The first is simple to compute the aerodynamic derivatives for a specific test by comparing the estimates obtained in the system identification analysis with the estimates obtained with zero wind conditions:

$$A_{1} = -\delta,$$
 $A_{2} = \sigma_{0} - \sigma,$
 $A_{3} = \gamma_{0} - \gamma,$
 $H_{1} = \mu_{0} - \mu,$
 $H_{2} = -\rho,$
 $H_{3} = -\kappa,$
 $H_{4} = \beta_{0} - \beta$
(3.75)

The second part of the parameter determination problem is to ensure that the parameters are extracted for similar amplitudes of vibration since some of the parameters may be amplitude dependent and to use statistical procedures to extract reliable estimates for the parameters.

System identification

The system identification starts with assumed model structure and Eqs. (2.6) and (2.7) are converted to continuous state space equations:

$$\dot{x}(t) = Ax(t)
y(t) = Cx(t) + e(t)$$
(3.76)

or

$$\dot{x}(t) = \begin{bmatrix} 0 & 1 & 0 & 0 \\ -\beta & -\mu & -\kappa & -\rho \\ 0 & 0 & 0 & 1 \\ 0 & -\delta & -\gamma & -\sigma \end{bmatrix} x(t)$$

$$y(t) = \begin{pmatrix} h(t) \\ \alpha(t) \end{pmatrix} = \begin{bmatrix} \frac{1}{0} & \frac{0}{0} & \frac{0}{1} & \frac{0}{0} \\ 0 & 0 & 1 & 0 \end{bmatrix} x(t)$$
(3.77)

where $\dot{x}(t) = (h(t), \dot{h}(t), \alpha(t), \dot{\alpha}(t))$ and $x(0) = x_0$ is the initial state(operator excitation). The disturbances from wind flow is regarded as noise in the output equation, e(t). The system matrix, **A**, is dependent on the parameters in the θ -vector.

$$\theta = (\beta, \mu, \gamma, \sigma, \delta, \kappa, \rho)$$

which is to be estimated. Since the data sampled are discrete in time, then the model is formulated in discrete time as:

$$x_{k+1} = A_d x_k$$

$$y_k = C x_k + e_k$$
(3.78)

where $A_d = \exp(A\Delta t)$ and e_k is noise in the output equation assumed to be zero-mean stochastic variable.

The solution to (3.77) or (3.78) depends on the parameters in θ . The method consists in adjusting the elements in θ until the solution to Eq. 3.77 matches the measurements, i.e. to minimize the loss function:

$$J_{N} = \frac{1}{2} \sum_{i=1}^{N} |\hat{y}_{i} - y_{i}|$$
 (3.79)

Here \hat{y}_i is a vector containing the actual measurements of heave and pitch and y_i is the solution to (2.10) or (2.14). The method requires iterations by using Newton-Raphson technique in searching the parameters in θ which minimize the loss function. The validity of the results of the method is naturally dependent on the assumption that the model structure is correct. The model is suitable for free decay signals which have good signal to noise ratio. However, if the system is poorly excited (e.g. primarily excited by the wind as in case of buffeting responses) then the loss function becomes less sensitive to change in specific (combinations of) parameters and results in large variance of estimate value. The results of method apply to identify seven flutter derivatives $(H_1^* - H_4^*)$ and A_1^* to A_3^* for Great Belt Bridge section model under smooth wind are reported (Poulsen *et.al.* 1992).

For the case of free vibration due to an initial deflection, MATLAB system identification routines such as 'PEM' (Ljung 1995) are also used to identify the values of $\bf A$ and $\bf x_0$ for which the time histories generated using Eq. (3.67) give the best match to the observed data. The quality of the fit is judged both visually in terms of overlays of fitted and measured data as well as by error norm values. Software 'PEM' was written around this technique based on software developed at Politecnico di Milano (Brownjohn and Jakobsen, 2001).

3.5.7.2 Covariance block Hankel matrix method: CBHM

When free vibration is due to turbulence, two more methods described here are available. In the first of these, the covariance block Hankel matrix (CBHM) method (Jakobsen and Hansen, 1995), it is shown that the state matrices can be recovered from the cross-covariance estimates obtained from the two motion signals such as acceleration or displacement. The program uses MATLAB elementary functions. The cross-covariance functions are known to be the same for both transient and buffeting response so the method can also be used for transient response signals.

The solution to Eq. (3.67a) is

$$x(t) = e^{At}x_0 + \int_0^t e^{A(t-\tau)}Bu(\tau) d\tau$$
 (3.80)

where eigenvalues of A are.

$$\lambda_{\rm A} = -\xi\omega \pm i\omega\sqrt{1-\xi^2}$$

A discrete time version of Eq. (3.67) representing sampled data is

$$\mathbf{x}(i+1) = \mathbf{F}\mathbf{x}(i) + \mathbf{G}u(i) \tag{3.81}$$

where

$$F = e^{A\Delta t}$$
 and $G = \int_{0}^{\Delta t} e^{A\Delta t} d\tau B$

The identification method computes, from at least N_p response data points sampled at intervals of Δt , a sequence of covariance matrices which (for no signal noise and a state variable covariance matrix C_{xx}) depend on the system matrices as defined in Eq. (3.67) as follows:

$$C_{yy}(k) = \begin{bmatrix} C_{hh}(k) & C_{h\theta}(k) \\ C_{\theta h}(k) & C_{\theta \theta}(k) \end{bmatrix} = CF^{k}C_{xx}C^{T}, \quad k = 1... \ 2l - 1, \ 2l \square \quad N_{p}$$
 (3.82)

By taking the sequence $C_{yy}(k)$ as blocks of a Hankel matrix with dimension $2l \times 2l$, the CBHM method (Jakobsen, 1995) finds a suitable decomposition of the $C_{yy}(k)$ to yield **F**, hence **A**. This technique is implemented in software CBHM developed at Norwegian Institute of Technology.

The heart of the algorithm is essentially the same as the eigensystem realisation algorithm (ERA) (Juang and Pappa, 1985) and shares its advantages of simplicity and efficiency.

3.6. Methodology for Section Model Test in Wind tunnel

3.6.1 Description

The section model consists of a typical rigid section model of the deck of cable-stayed bridge, of which scaled geometric and elastic behavior are simulated to the prototype. This section is supported by four equal coil springs (Fig. 3.5), in order that the vertical and torsional motions of the full-scale bridge are simulated by vertical and pitching motions of the model.

3.6.2 Model Simulation

The Law of similitude of which govern the scaling model are determined by laws of mechanics with particular regard to the specific characteristics of those forces involved in the mechanism under investigation. These forces include elastic force, inertia forces of the air and the structure, viscosity force and damping force. The relationships between them are represented in the five dimensionless parameters given in Table 3.1 in order to ensure similarity of the model to prototype.

Parameter	Symbol	Physical meaning	
1. Elasticity	$\frac{E}{ ho U^2}$	Elastic force of the structure Inertia force of the air	
2. Inertia (Density ratio)	$\frac{\rho_s}{ ho}$	Inertia force of the structure Inertia force of the air	
3. Gravitational (Froude number)	$\frac{U^2}{gB}$	Inertia force of the air Gravitational force on the structure	
4. Viscosity (Reynolds number)	$\frac{UB}{V}$	Inertia force of the air Viscous force of the air	
5. Structural Damping (Logarithm Decrement)	$\delta_{\scriptscriptstyle s}$	Dissipated energy per cycle Total energy of oscillation	

Table 3.1 Similarity requirements

The notations in Table 3.1 are defined as that E is young's modulus of material; U is characteristic speed; B is characteristic dimension of body; ν is kinematic viscosity; ρ, ρ_s are density of air and structure, respectively, g is gravitational acceleration and δ_s is logarithm decrement.

For a study of aerodynamic instability to be properly conducted, it is necessary that the model be appropriately scaled. Typically model-to-prototype scale ratios include

- λ_L (geometric length scale)
- λ_o (density scale)
- λ_v (velocity scale)
- λ_f (frequency scale)

As in most model tests, the first scale to be considered is geometric length scale. This value is usually in the range of 1/100 to 1/25 to ensure that all significant structural details can be reproduced adequately. Since testing is performed in natural air and within Earth's gravity field, both the air density ratio λ_{ρ} and gravity ratio λ_{g} are equal to unity.

Then length scale λ_L is determined as follow:

$$\lambda_{L} = \frac{\left[B\right]_{m}}{\left[B\right]_{p}} \tag{3.83}$$

where B is deck width, the subscripts m and p denote the model and prototype, respectively.

The modeling of the mass of the structure is determined by the requirement that the inertia force of the structure and those of the flow be scaled consistently. Similarity of inertia forces is achieved by maintaining a constant ratio of the bulk density of the structure to the air density. An equation to express density scaling is

$$\left[\frac{\rho_s}{\rho}\right]_m = \left[\frac{\rho_s}{\rho}\right]_p \tag{3.84}$$

where ρ_s and ρ are structural density and air density, respectively.

The modeling of the λ_m - mass scale, λ_I - mass moment of inertia become, for mass scale

$$\lambda_{m} = \frac{\left[m\right]_{m}}{\left[m\right]_{p}} = \frac{\left[\rho\right]_{m}}{\left[\rho\right]_{p}} \frac{\left[B\right]_{m}^{3}}{\left[B\right]_{p}^{3}} = \lambda_{L}^{3}$$
(3.85)

and for mass moment of inertia scaling

$$\lambda_{I} = \frac{\left[I\right]_{m}}{\left[I\right]_{p}} = \frac{\left[\rho\right]_{m}}{\left[\rho\right]_{p}} \frac{\left[B\right]_{m}^{5}}{\left[B\right]_{p}^{5}} = \lambda_{L}^{5}$$
(3.86)

In Table 3.1, the velocity scale λ_v can be computed by either equivalence of Froude number or Reynolds number. It is not possible to satisfy both the Froude number and Reynolds number simultaneously. In practice the selection between them is based on information as to which type of forces is dominated in the phenomenon under investigation. For bridge deck, the flow separation is caused by sharp edge; lift,

drag and moment coefficients are relatively insensitive to Reynolds number. Then the velocity scale λ_v is calculated according to equivalence of Froude number.

$$\left[\frac{gB}{U^2}\right]_m = \left[\frac{gB}{U^2}\right]_p \tag{3.87}$$

hence,

$$\lambda_{V} = \frac{\left[U\right]_{m}}{\left[U\right]_{p}} = \sqrt{\frac{\left[B\right]_{m}}{\left[B\right]_{p}}} = \sqrt{\lambda}$$
(3.88)

When the resistance to deformation is dominated the result of the action of elastic forces and essentially independent of gravity effects or self-weight, consistent scaling of stiffness and flow-induced forces is achieved by maintaining elasticity in model and in full scale.

$$\left[\frac{E}{\rho U^2}\right]_m = \left[\frac{E}{\rho U^2}\right]_p \tag{3.89}$$

This is equivalent to the reduced velocity

$$\left[\frac{U}{f_n B}\right]_m = \left[\frac{U}{f_n B}\right]_n \tag{3.90}$$

Hence, the scale of the oscillation frequency, λ_v becomes

$$\lambda_f = \frac{\left[f_n\right]_m}{\left[f_n\right]_p} = \sqrt{\frac{\left[B\right]_p}{\left[B\right]_m}} = \frac{1}{\sqrt{\lambda}}$$
(3.91)

where f_n is the frequency.

Similarity of damping forces is maintain by requiring that δ , the logarithm decrement for a particular mode of vibration, in the model is the same as that in full scale, i.e. $\lambda_{\delta}=1$

The section model is rigidly constructed and scaled elastic behavior is simulated. The vertical and torsional frequencies ω_h and ω_α are defined by adjusted spring.

3.6.3 Turbulent Flow Simulation in Wind Tunnel

To achieve similarity between the model and prototype, It is desirable to reproduce at the requisite scale the characteristics of the atmospheric flows expected to affect the structure of concern. In case of section model testing of bridge, to simulate

the turbulence flows in natural wind, the variation of turbulence intensities and integral scale as well as spectra of along wind and vertical direction are the main factors concerned.

3.6.3.1 Turbulence Intensity

The simplest descriptor of atmospheric turbulence is the turbulence intensity. Let

u(z) denote the velocity fluctuations parallel to the direction of the mean speed in a turbulent flow passing a point with elevation z. The longitudinal turbulence intensity is defined as

$$I(z) = \frac{\sqrt{u^2(z)}}{U(z)}$$

where U(z) = mean wind speed at elevation z and $\sqrt{u^2(z)}$ = root mean square value of u. Vertical and lateral turbulence intensities are similarly defined.

The longitudinal fluctuations can be written as

$$\overline{u^2} = \beta u_*^2$$

where u_* = friction velocity. It is commonly assumed that β does not vary with height. Values of β suggested by Simiu et al. (1978) on the basis of a large number of measurements are listed in Table 5.2

Table 3.2. Values of β corresponding to various roughness lengths

<i>Z</i> 0	0.005	0.07	0.30	1.00	2.50
β	6.5	6.0	5.25	4.85	4.00

For example, if z = 30 m, $z_0 = 0.07$ m, and U(30) = 20 m/s, it follows that turbulence intensity is I(30) = 0.162 (Simiu and Scanlan, 1996).

3.6.3.2 Integrals Scale of Turbulence

The velocity fluctuations in a flow passing a point may be considered to be caused by a superposition of conceptual eddies transported by the mean wind. Each eddy is viewed as causing at that point a periodic fluctuation with circular frequency $\omega = 2\pi n$, where n is the frequency. By analogy with the case of the traveling wave, we define the eddy wavelength as $\lambda = U/n$, where U = wind speed, and the eddy wave number, $K = 2\pi/\lambda$. The wave length is a measure of eddy size.

Integral scales of turbulence are measures of the average size of the turbulent eddy of the flow. There are altogether nine integral scales of turbulence, corresponding to the three dimensions of the eddies associated with the longitudinal,

transverse, and vertical components of the fluctuating velocity, u, v, and w. For example, L_u^x, L_u^y and L_u^z are respectively, measures of the average longitudinal, transverse, and vertical size of the eddies associated with the longitudinal velocity fluctuations (x is the direction of the mean wind U and of the longitudinal fluctuation u)

Mathematically L_u^x can be defined as

$$L_u^x = \frac{U}{u^2} \int_0^\infty R_u(\tau) \, d\tau$$

where $R_u(\tau)$ is the autocovariance function of the fluctuation $u(x_1,t)$.

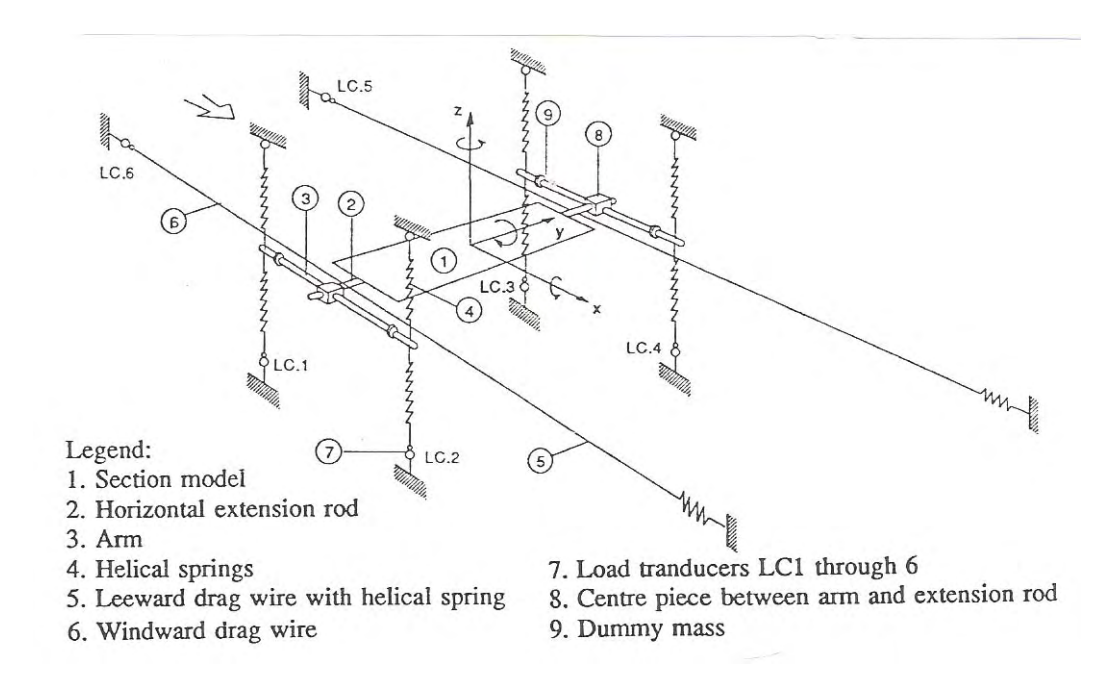


Fig. 3.7. Section model test setup





Fig. 3.8. The TU-AIT wind tunnel at Thammasat University



Fig. 3.9 Suspension device of the model in the dynamic system

CHAPTER 4

SYSTEM IDENTIFICATION TECHNIQUES FOR FLUTTER DERIVATIVES IDENTIFICATION OF BRIDGE DECK

4.1 INTRODUCTION

This chapter deals with propose system identification techniques using for extracting flutter derivatives of bridge deck. In a civil engineering context, structures such as bridges and towers are the *systems*; the estimation of the modal parameters is the particular type of *identification* and *stochastic* means that the structure is excited by an immeasurable input force and that only output measurements (e.g. accelerations) are available. In these methods the deterministic knowledge of the input is replaced by the assumption that the input is a realization of a stochastic process (white noise).

System identification starts by adopting a certain model that is believed to represent the system. Next, values are assigned to the parameters of the model as to match the measurements. Section 4.2 starts with continuous state-space model for a vibrating structure, and then converted to discrete time state space model to match real world measurements in section 4.3. Concept of stochastic process is applied to state space model in section 4.4. Section 4.5 contains the main theorem for stochastic subspace identification. This method can be divided according to the type of data that they require: raw time data or covariances. We start with covariance-driven methods (SSI-COV) to end with time-domain data-driven methods (SSI-DATA). This presentation order corresponds to the historical application of stochastic system identification methods. Application of both SSI methods to extract flutter derivatives of bridge deck are explained in section 4.6 together with implementation of developed computer program. Finally, numerical tests are performed to confirm applicability of proposed methods.

4.2 Continuous –Time State Space model

4.2.1 A State-Space Model of a Vibrating Structure

The state equation

The dynamic behaviour of a discrete mechanical system consisting of n masses connected through springs and dampers is described by following matrix differential equation:

$$M\ddot{q}(t) + C\dot{q}(t) + Kq(t) = f(t) = Bu(t)$$
 (4.1)

By casting the second order equation of motion (4.1) in first order form (2.12), an equation similar to the *state equation* from control theory is obtained. This equation usually has a normalized term in $\dot{x}(t)$ to yield the :

$$\dot{x}(t) = A_c x(t) + B_c u(t) \tag{4.2}$$

where $A_c \in R^{nxn}$ and $B_c \in R^{nxm}$ are defined as:

$$A_c = \begin{pmatrix} 0 & I \\ -M^{-1}K & -M^{-1}C \end{pmatrix} \tag{4.3}$$

The subindex 'c' denotes continuous time. In next section, the discrete-time equivalents of these matrices will be introduced. Using the modal decomposition, A_c is rewritten as:

$$A_c = \Psi \Lambda_c \Psi^{-1} \tag{4.4}$$

which is in fact a standard eigenvalue problem $(A_c \Psi = \Psi \Lambda_c)$. This shows that Λ_c contains the eigenvalues and Ψ the eigenvectors of A_c

The observation equation

In a practical vibration experiment, not all n **DOF**s of the structure are measured, but only a subset. If it is assumed that measurements are taken at l locations and that the sensors can be either accelerometers, velocity or displacements transducers (to keep it general) the observation equation is:

$$y(t) = C_{a}\ddot{q}(t) + C_{y}\dot{q}(t) + C_{d}q(t)$$
 (4.5)

where $y(t) \in R^l$ are the outputs; $C_a, C_v, C_d \in R^{lxn/2}$ are the output location matrices for acceleration, velocity and displacement, respectively. These matrices consist of a lot of zeros and a few ones and are in fact just selecting the measured **DOF**s out of the **FE** model **DOF**s to store them as the elements of the output vector y(t). In reality it can happen that, for instance, both accelerations and velocities are simultaneously measured. Using Eq. (4.1) to eliminate $\ddot{q}(t)$ and with the definition of the state vector, Eq. (4.5) can be transformed into

$$y(t) = C_c x(t) + D_c u(t)$$
(4.6)

where $C_c \in \mathbb{R}^{l \times n}$ is the output matrix and $D_c \in \mathbb{R}^{l \times m}$ is the direct transmission matrix. They are related to the **FE** model matrices as:

$$C_c = (C_d - C_a M^{-1} K \quad C_v - C_a M^{-1} C_2), \quad D_c = C_a M^{-1} B$$
 (4.7)

In many publications this direct transmission matrix D_c is omitted for some reason. However the modeling of a vibration experiment where accelerometers are used (and these are the most widely used sensors) requires a direct transmission term. If $C_a = 0$ (i.e. displacements and/or velocities are measured), there is no direct transmission.

The state-space model

The classical continuous-time state-space model is found by combining Eqs. (4.2) and (4.6):

$$\dot{x}(t) = A_c x(t) + B_c u(t)$$

$$y(t) = C_c x(t) + D_c u(t)$$
(4.8)

The order of the state-space model n is defined as the dimension of the state vector. The equations of motion are now written in state-space form and can be used to compute the response y(t) of the structure to a given input u(t). The state vector x(t) contains the displacements and the velocities of all **DOF**s.

A new state vector can be defined such that:

$$x(t) = Tz(t) (4.9)$$

where $T \in C^{n \times n}$ is a non-singular complex square matrix. This is called a *similarity* transformation. Substitution of this coordinate transformation into Eq. (4.9) yields:

$$\dot{z}(t) = T^{-1}A_cTz(t) + T^{-1}B_cu(t)$$

$$y(t) = C_cTz(t) + D_cu(t)$$
(4.10)

It is important to see that the transformed matrices $(T^{-1}A_cT, T^{-1}B_c, C_cT, D_c)$ describe the same input-output relationship as the original matrices. However, unlike x(t) the new state vector z(t) has not the meaning of physical displacements and velocities.

4.2.2 Modal Parameters and Model Reduction

Relation to classical modal analysis

A special similarity transformation is the transformation to (complex) modal states $x_m(t) \in \mathbb{C}^n$:

$$x(t) = \Psi x_m(t)$$

The modal state-space model is obtained by substituting T by Ψ in Eq. (4.10) and inserting the modal decomposition of A_c (4.4):

$$\dot{x}_m(t) = \Lambda_c x_m(t) + L_c^T u(t)$$

$$y(t) = V_c x_m(t) + D_c u(t)$$
(4.11)

where $L_c^T = \Psi^{-1}B_c$, V_c are modal input and modal output matrix respectively and the following definitions have been introduced:

$$L_c^T = \Psi^{-1}B_c$$

$$V_c = C_c\Psi$$
(4.12)

The eigenvalue matrix has the following structure:

$$\Lambda_c = egin{pmatrix} \Lambda & 0 \ 0 & \Lambda^* \end{pmatrix}, \quad \Lambda = egin{bmatrix} & & & & \ & - \xi_i \omega_i + j \sqrt{1 - \xi_i^2} \, \omega_i & \ & & \ & & \ & & \ & \end{pmatrix}$$

and the eigenvector matrix can be written in case of general viscous damping as:

$$\Psi = \begin{pmatrix} \Theta & \Theta^* \\ \Theta \Lambda & \Theta^* \Lambda^* \end{pmatrix} \tag{4.13}$$

4.3 Discrete-Time State-Space Models

4.3.1 About Sampling

Up to now all equations were expressed in continuous time, whereas in reality, measurements are taken at discrete time instants. In order to fit models to measurements (i.e. system identification), these models need to be converted to discrete time. Another reason for looking at discrete models is that they are needed for performing simulations. If it would be possible to find an analytical solution for the response of a structure to a given input, this analytical expression could be evaluated at any time instant t, without the need to convert the model to discrete time. However in most cases there is no analytical solution and one has to rely upon a numerical solution method to simulate the response of a structure. For instance, time integration schemes with a possible adaptive time step could be used. The approach that is useful for this thesis starts by choosing a certain fixed sampling period(s). The continuoustime equations are discretized and solved at all discrete time instants k (-), where t=kt, $k \in \mathbb{N}$. Typical for the sampling of a continuous time equation is that a certain behaviour of the time-dependent variables between two samples has to be assumed. A Zero-Order Hold (ZOH) assumption for instance, means that the input is piecewise

constant over the sampling period. Under this assumption, the continuous-time state-space model (4.8) is converted to the *discrete-time state-space model*:

$$x_{k+1} = Ax_k + Bu_k$$

$$y_k = Cx_k + Du_k$$
(4.14)

where $x_k = x(k\Delta t) = (q_k^T \dot{q}_k^T)$ is the discrete-time state vector containing the sampled displacements and velocities; u_k , y_k are the sampled input and output; A is the discrete state matrix; B is the discrete input matrix; C is the discrete output matrix; D is the direct transmission matrix. They are related to their continuous-time counterparts (4.8) as:

$$A = e^{A_c \Delta t}, B = \int_0^{\Delta t} e^{A_c \Delta t} \delta \tau B_c = (A - I) A_c^{-1} B_c$$

$$C = C_c, D = D_c$$

$$(4.15)$$

These relations are classical and are, for instance, derived in (Juan, 1994). The second equality for B is only valid if A_c is invertible. The matrices C_c and D_c are not influenced by **ZOH**-sampling.

4.3.2 Modal Parameters and Model Reduction

The eigenvalue decomposition of the discrete state matrix A is found by inserting the eigenvalue decomposition of the continuous state matrix A_c into Equation (4.15)

$$A = e^{A_c \Delta t} = e^{\Psi \Lambda_c \Psi^{-1} \Delta t} = \Psi \Lambda_d \Psi^{-1} = \Psi \begin{bmatrix} \\ \\ \\ \\ \end{bmatrix} \mu_i$$
 (4.16)

The third equality can be proven by the series expansion of the exponential function by the McLaurin series expansion, $e^M = \sum_{k=0}^{\infty} \frac{1}{k!} M^k$; the two last equalities define the notation of the discrete eigenvalue matrix. So, the discrete eigenvectors are equal to the continuous ones and the discrete eigenvalues, denoted as μ_i are related to the continuous eigenvalues as:

$$\mu_i = e^{\lambda \Delta t} \iff \lambda_i = rac{\ln\left(\mu_i
ight)}{\Delta t}$$

Similar to definition (4.12), the discrete modal participation matrix and the observed mode shapes are written as:

$$L^{T} = \Psi^{-1}B$$

$$V = C\Psi$$
(4.17)

The discrete modal participation factors are different from the continuous ones due to the different B-matrix. The observed mode shapes, on the contrary, are the same in discrete as in continuous time. In the acceleration-only case, the modal decomposition of D is found as follows:

$$D = D_c = V_c \Lambda_c^{-1} L_c^T = V(\Lambda_d - I) L^T = \sum_{i=1}^n \frac{1}{\mu_i - 1} \{v_i\} \langle l_i^T \rangle$$

The notation for the columns and rows of a matrix has been introduced before. The discrete-time model reduction is similar to the continuous one. This reduction can be formally proven by putting the next states (that have to eliminated) equal to the current states. This is the discrete-time equivalent of setting the derivative of the continuous states to zero.

4.4 Stochastic State Space Models

Stochastic subspace identification algorithms compute state space models from given output data. Fig. 4.1 states the stochastic (subspace) identification problem.

Stochastic identification problem:

Given: measurements of the output $y_k \in R^l$ generated by the unknown stochastic system of order n

$$x_{k+1} = Ax_k + w_k$$
$$y_k = Cx_k + v_k$$

with w_k and v_k zero mean, white vector sequences with covariance matrix:

$$E\begin{bmatrix} \begin{pmatrix} w_p \\ v_p \end{pmatrix} \begin{pmatrix} w_q^T & v_q^T \end{pmatrix} \end{bmatrix} = \begin{pmatrix} Q & S \\ S^T & R \end{pmatrix} \delta_{pq}$$

Determine:

- The order *n* of the unknown system
- The system matrices $A \in R^{n \times n}$, $C \in R^{l \times n}$ up to within a similarity transformation and $Q \in R^{n \times n}$, $S \in R^{n \times l}$, $R \in R^{l \times l}$ so that the second order statistics of the output of the model *and* of the given output are equal.

Fig. 4.1 The stochastic subspace identification problem

4.4.1 The Stochastic Components

This section describes the final step towards the experimental world: noise is added. Up to now it was assumed that the system was only driven by a deterministic input u_k . However, the deterministic models are not able to exactly describe real measurement data. Stochastic components have to be included in the models and following *discrete-time*

combined deterministic-stochastic state-space model is obtained:

$$x_{k+1} = Ax_k + Bu_k + w_k y_k = Cx_k + Du_k + v_k$$
 (4.18)

where $w_k \in \mathbb{R}^n$ is the process noise due to disturbances and modelling inaccuracies; $v_k \in \mathbb{R}^l$ is the measurement noise due to sensor inaccuracy. They are both unmeasurable vector signals assumed to be zero mean, white and with covariance matrices:

$$E\begin{bmatrix} \begin{pmatrix} w_p \\ v_p \end{pmatrix} \begin{pmatrix} w_q^T & v_q^T \end{pmatrix} \end{bmatrix} = \begin{pmatrix} Q & S \\ S^T & R \end{pmatrix} \delta_{pq}$$
 (4.19)

where **E** is the expected value operator; δ_{pq} is the Kronecker delta (if p=q then, $\delta_{pq}=1$, otherwise $\delta_{pq}=0$); p, q are two arbitrary time instants.

However, the primary case of interest for this thesis is a purely stochastic system. In a civil engineering context, the only vibration information that is available is the responses of a structure excited by some immeasurable inputs. Due to the lack of input information it is not possible (from a system identification point of view) to distinguish between the terms in u_k and the noise terms w_k , v_k in Eq. (4.18). The discrete-time stochastic state-space model reads:

$$x_{k+1} = Ax_k + w_k y_k = Cx_k + v_k$$
 (4.20)

The input is now implicitly modeled by the noise terms. However the white noise assumptions of these terms can not be omitted: it is necessary for the proofs of the system identification methods of next chapter. The consequence is that if this white noise assumption is violated, for instance if the input contains additional to white noise also some dominant frequency components, these frequency components cannot be separated from the eigenfrequencies of the system and they will appear as (spurious) poles of the state matrix $\bf A$.

4.4.2 Properties of Stochastic Systems

In this section, we summarize the main properties of stochastic processes of linear time invariant system, including the non-uniqueness of the state space description. Some important properties of stochastic systems are briefly resumed. They are well-known and can, for instance, be found in Overchee and Peeters (1996).

It is assumed that the stochastic process is *stationary*: noise terms have zero mean and their covariance matrices are given by:

$$E[x_{i}] = 0, E[x_{i}x_{i}^{T}] = \Sigma$$
 (4.21)

where the state covariance matrix Σ is independent of the time k. This implies that A is a stable matrix (all of its poles are strictly inside the unit circle). There are many representations of stochastic state space models. All of the representations are equivalent, in the sense that the second order statistics of the output generated by the models is the same, i.e. the covariance sequence of the output is identical. There are many stochastic model; the *forward model*, the *backward model*, the *forward innovation model*. In this thesis, we introduce only the *forward model*, and the *forward innovation model*.

Forward model

First we will develop some (well known) structural relations for linear time invariant stochastic processes. Since w_k , v_k are zero mean white noise vector sequences, and independent of the actual state, x_k , we have:

$$E[x_k w_k^T] = 0$$
, $E[x_k v_k^T] = 0$ (4.22)

Then we find the Lyapunov equation for the state covariance matrix Σ

$$\Sigma = E[x_{k+1} x_{k+1}^{T}]$$

$$= E[(Ax_{k} + w_{k})(Ax_{k} + w_{k})^{T}]$$

$$= AE[x_{k} x_{k}^{T}]A^{T} + E[w_{k} w_{k}^{T}]$$

$$= A\Sigma A^{T} + Q$$
(4.23)

The output covariance matrices $\Lambda_i \in \mathbb{R}^{l \times l}$ are defined as:

$$\Lambda_i = \mathrm{E}[y_{i+i} \, y_i^T] \tag{4.24}$$

where *i* is an arbitrary time lag. We find for Λ_0 :

$$\Lambda_{0} = E[y_{k} \ y_{k}^{T}]
= E[(Cx_{k} + v_{k})(Cx_{k} + v_{k})^{T}]
= CE[x_{k} \ x_{k}^{T}]C^{T} + E[v_{k} \ v_{k}^{T}]
= C\Sigma C^{T} + R$$
(4.25)

Defining the "next state - output" covariance matrix $G \in \mathbb{R}^{n \times l}$ as:

$$G = E[x_{k+1} \ y_k^T]$$

$$= E[(Ax_k + w_k)(Cx_k + v_k)^T]$$

$$= AE[x_k \ x_k^T]C^T + E[w_k \ v_k^T]$$

$$= A\Sigma C^T + S$$
(4.26)

Similarly, for other time lag i (i = 1,2,...) covariances, we get:

$$\Lambda_i = CA^{i-1}G$$

$$\Lambda_{-i} = G^T(A^{i-1})^T C^T$$
(4.27)

The last observation, indicates that the output covariances can be considered as Markov parameters of the deterministic linear time invariant system A, G, C, Λ_0 . The factorization of output covariance matrices into state-space matrices is similar to the factorization property of impulse responses. For stochastic systems, the matrices (A,G,C,Λ_0) play the role of the deterministic system matrices (A,B,C,D). This is an important observation that will play a major role in the derivation of stochastic subspace identification algorithms. This equation alone nearly constitutes the solution to the identification problem: the output covariance sequence can be estimated from the measurement data; so if we would be able to decompose the estimated output covariance sequence according to (4.27), the state-space matrices are found. This idea will be translated into output-only covariance-driven methods (SSI-COV).

The Forward innovation model

An alternative model for stochastic systems of Equations (4.20) that is more suitable for some applications is the so-called *forward innovation model*. It is obtained by applying the *steady-state Kalman filter*¹ to the stochastic state-space model (4.20):

$$z_{k+1} = Az_k + Ke_k$$

$$y_k = Cz_k + e_k$$
(4.28)

¹ The Kalman filter is standard in control theory.

The elements of the sequence e_k are called innovations, hence the name of the model. It is a white noise vector sequence, with covariance matrix:

$$E[e_n e_a^T] = \Lambda_e \delta_{na} \tag{4.29}$$

The computation of the forward innovation model (A, K, C, Λ_e) from the stochastic state space model (A, G, C, Λ_0) starts by finding the positive definite solution P of the discrete Riccati equation²:

$$P = APA^{T} + (G - APC^{T})(\Lambda_{0} - CPC^{T})^{-1}(G - APC^{T})^{T}$$
(4.30)

The matrix $P \in R^{n \times n}$ is the forward state covariance matrix $P = E[z_k z_k^T]$. The Kalman gain is then computed as:

$$K = (G - APC^{T})(\Lambda_{0} - CPC^{T})^{-1}$$
(4.31)

and the covariance matrix of the innovations equals:

$$\Lambda_e = \Lambda_0 - CPC^T \tag{4.32}$$

4.5 Stochastic Subspace System Identification

In previous sections, several models and main properties of stochastic system were presented. In this section stochastic system identification methods are discussed and compared. Starting with the primary data types that are required by the identification methods: time data or covariance sequences, next covariance-driven methods are presented and then data-driven methods. Finally, two methods are compared.

4.5.1 Data Types

In principle (output) data y_k is available as discrete samples of the time signal. This section deals with the transformation of time data to covariances or spectra. Also some notations are introduced.

4.5.1.1 Time Data

Since there is no external inputs for purely stochastic system, it is useful in the development of some of the identification methods to gather the output measurements

² An implementation to find the solution of this equation can, for instance, be found in Control system Toolbox of Matlab.

(l outputs) in a block Hankel³ matrix with 2i block rows and j columns. For the statistical proves of the methods, it is assumed that $j \to \infty$. The Hankel matrix $H \in \square^{2lixj}$ can be divided into a past (Y_p) and a future part (Y_f) . For convenience, we define the shorthand notation Y_p , Y_p^+ and Y_f , Y_f^- :

$$H = \frac{1}{\sqrt{j}} \begin{pmatrix} y_{0} & y_{1} & \cdots & y_{j-1} \\ y_{1} & y_{2} & \cdots & y_{j} \\ \vdots & \vdots & \ddots & \vdots \\ \frac{y_{i-1}}{y_{i}} & y_{i} & \cdots & y_{i+j-2} \\ y_{i+1} & y_{i+2} & \cdots & y_{i+j} \\ \vdots & \vdots & \ddots & \vdots \\ y_{2i-1} & y_{2i} & \cdots & y_{2i+j-2} \end{pmatrix} = \begin{pmatrix} Y_{0|i-1} \\ Y_{i|2i-1} \end{pmatrix} = \begin{pmatrix} Y_{p} \\ Y_{f} \end{pmatrix} \stackrel{\updownarrow}{\downarrow} \frac{li}{li} = \frac{"past"}{"future"}$$

$$(4.33)$$

Note that the output data is scaled by a factor $1/\sqrt{j}$. The subscripts of $Y_{i|2i-1} \in \Box^{lixj}$ are the subscripts of the first and last element in the first column of the block Hankel matrix. The subscripts p and f stand for past and future. The matrices Y_p and Y_f are defined by splitting H in two parts of i block rows. Another division is obtained by adding one block row to the past outputs and omitting the first block row of the future outputs.

$$H = \frac{1}{\sqrt{j}} \begin{pmatrix} y_{0} & y_{1} & \cdots & y_{j-1} \\ \cdots & \cdots & \cdots & \cdots \\ y_{i-1} & y_{i} & \cdots & y_{i+j-2} \\ y_{i} & y_{i+1} & \cdots & y_{i+j-1} \\ y_{i+1} & y_{i+2} & \cdots & y_{i+j+1} \\ \cdots & \cdots & \cdots & \cdots \\ y_{2i-1} & y_{2i} & \cdots & y_{2i+j-2} \end{pmatrix} = \begin{pmatrix} Y_{0|i} \\ Y_{i+1|2i-1} \end{pmatrix} = \begin{pmatrix} Y_{p}^{+} \\ Y_{f}^{-} \end{pmatrix} \frac{1}{\sqrt{j}} \frac{l(i+1)}{l(i-1)}$$

$$(4.34)$$

4.5.1.2 Covariance Estimates

Output covariances are defined in Equation (4.24) as:

$$\Lambda_{i} = E[y_{k+i} \ y_{k}^{T}] = \lim_{j \to \infty} \frac{1}{j} \sum_{k=0}^{j-1} y_{k+i} \ y_{k}^{T}$$

³ A Hankel matrix is a matrix that is constant along its anti-diagonal.

The second equality follows from the ergodicity⁴ assumption. Then, the output covariances are gathered in a block Toeplitz⁵ matrix $T_{||i} \in \square^{lixli}$ that can be computed from the data block Hankel matrix $(Y_p \text{ and } Y_f)$. Indeed, for $j \to \infty$ and assuming ergodicity, we have:

$$T_{1|i} = \begin{bmatrix} \Lambda_i & \Lambda_{i-1} & \cdots & \Lambda_1 \\ \Lambda_{i+1} & \Lambda_i & \cdots & \Lambda_2 \\ \vdots & \vdots & \vdots & \vdots \\ \Lambda_{2i-1} & \Lambda_{2i-2} & \cdots & \Lambda_i \end{bmatrix}$$
(4.35)

Then one can infer from the definition of covariance matrix that $T_{1|i}$ can be expressed as the product of two block Hankel matrices Y_f and Y_p

$$T_{\parallel i} = Y_{\rm f} Y_{\rm p}^{\rm T} \tag{4.36}$$

Of course, in reality a finite number j of data is available and a covariance estimate $\hat{\Lambda}_i$ is simply obtained by dropping the limit:

$$\hat{\Lambda}_{i} = \frac{1}{j} \sum_{k=0}^{j-1} y_{k+i} y_{k}^{T}$$
 (4.37)

Instead of computing the covariance estimate by multiplication and summation of time samples, a high-speed implementation of the convolution in Eq. (4.37) is possible by applying the **FFT** to the time signals, cross-multiplying the Fourier transforms and applying the inverse **FFT** to the cross-products. The inverse **FFT** results in a *periodic* covariance function estimate. The bias error due to this *circular convolution* is avoided by zero-padding the original signals (Bendat and Piersol, 1993). A disadvantage of using covariances as primary data in identification is that it squares up the data. This may affect the numerical accuracy (Golub and Van Loan 1989).

4.5.1.3 Spectrum Estimates

Another useful data format is the spectrum of the outputs $S_y \in \Box^{lxl}$., In discrete-time, the spectrum of a stationary stochastic process is defined as the double

⁴ Ergodicity means that the expected value of a time sample of a stationary stochastic process (i.e. the average over an infinite number of processes) can be replaced by the average over one infinitely long record of the process.

⁵ A Toeplitz matrix is a matrix that is constant along its diagonal.

sided *z*-transform of its covariance sequence. Therefore the discrete-time output spectrum equals:

$$S_{y}(z) = \sum_{k=-\infty}^{k=\infty} \Lambda_{k} z^{-k}$$
 (4.38)

where Λ_k is the output covariance at time lag k, defined in Eq. (4.24). By substituting z according to (Juang and Pappa 1994):

$$z = e^{j\omega\Delta t} \tag{4.39}$$

Then, the Fourier transform in discrete-time is obtained

$$S_{y}(e^{j\omega\Delta t}) = \sum_{k=-\infty}^{\infty} \Lambda_{k} e^{-j\omega k\Delta t}$$
 (4.40)

In case of a stationary process, the following property holds:

$$\Lambda_{-k} = \Lambda_k^T \tag{4.41}$$

and the spectrum (4.38) can be written as:

$$S_{y}(z) = S_{y}^{+}(z) + (S_{y}^{+}(z^{-1}))^{T}$$

where S_{v}^{+} is defined as:

$$S_{y}^{+}(z) = \frac{\Lambda_{0}}{2} + \sum_{k=1}^{\infty} \Lambda_{k} z^{-k}$$
 (4.42)

The important factorization property of the output covariances was given in Eq. (4.27):

$$\Lambda_k = CA^{k-1}G$$

If A is a stable matrix⁶, we have the following series expansion:

$$(zI - A)^{-1} = \sum_{k=1}^{\infty} A^k z^{-k}$$

This series is found after inserting the factorization property (4.27) into (4.42). Consequently, following closed-form expression is found for the spectrum (4.48):

⁶ A is a stable matrix if all of its poles are strictly inside the unit circle

$$S_{v}(e^{j\omega\Delta t}) = C(zI - A)^{-1}G + \Lambda_{0} + G^{T}(z^{-1}I - A^{T})^{-1}C^{T}$$
(4.43)

In Eq. 4.48 the numbers of covariances go to infinite time lag. Again, only a finite number of data is available: the covariances are estimated as in (4.37) and cannot be computed up to infinite time lag. There is a whole literature on estimating spectra from data (Bendat and Piersol, 1993). Two popular non-parametric spectrum estimates are the *weighted averaged periodogram* (also known as *modified Welch's periodogram*) and the *weighted correlogram*. Weighting means that the signal is weighted by one of the classical windows (Bartlett, Hamming, Hanning) to reduce leakage.

<u>Welch's method</u> starts with computing the **D**iscrete Fourier Transform (**DFT**) of the weighted output signal:

$$Y(e^{j\omega\Delta t}) = \sum_{k=0}^{j-1} w_k y_k e^{-j\omega k\Delta t}$$
(4.44)

where w_k denotes the window function in this context. If j is a power of 2, the **DFT** can be efficiently computed at the discrete frequencies

$$\omega = \frac{l}{j} \frac{2\pi}{\Delta t}, \ l = 0, ..., j-1$$

by using the **FFT**. An unbiased estimate of the spectrum is the weighted periodogram, i.e. the **DFT** of (4.44) times its complex conjugate transpose and scaled by the squared norm of the window:

$$\hat{S}_{y}(e^{j\omega\Delta t}) = \frac{1}{\sum_{k=0}^{j-1} |w_{k}^{2}|} Y(e^{j\omega\Delta t}) Y^{T}(e^{-j\omega\Delta t})$$

$$(4.45)$$

The variance of the estimate is reduced by splitting the signal in segments, computing the weighted periodograms of all segments and taking the average. The spectrum estimate in (4.45) yields a rank-one matrix (a column vector multiplied by a row vector). Segment averaging increases the rank of the estimate because several rank-one estimates are added.

The weighted correlogram method starts by computing the covariance estimates as in (4.40). The weighted correlogram is defined as the **DFT** of the weighted covariance estimates:

$$\hat{S}_{y}(e^{j\omega\Delta t}) = \sum_{k=-L}^{L} w_{k} \hat{\Lambda}_{k} e^{-j\omega k\Delta t}$$
(4.46)

where *L* is the maximum number of time lags.

These two algorithms are normally basic of many measurement hardware such as frequency analysers which deliver spectra instead of the original time data. Also as they are easily implemented in MATLAB, it is the common procedure in methods of non-parametric frequency-domain identification. However, they have to be considered as estimates and not as true spectra. Limitations and drawbacks of the **DFT** related to modal analysis are discussed in Mitchell (1986) and Pandit (1991). Advantages of frequency-domain identification are discussed in Schoukens (1991) and also recapitulated in McKelvey (1995) and Ljung (1999). Evidently, the frequency-domain advantages related to the use of a periodic input signal are not carrying over to the output-only case.

4.5.2 Covariance-Driven-Stochastic-Subspace Identification (SSI-COV)

Up to present, stochastic subspace theory are formulated, in this section time-domain covariance-driven method (SSI-COV) are presented. Most output-only system identification methods developed in the past utilize covariance matrix as important feature such as *Covariance Block Hankel Method*, CBHM, (Brownjohn and Jakobsen, 2001), the *instrumental variable* method, IV, (Peeters, 2000). An important feature is that a covariance matrix can be factorized into the system matrices, as point out in Eq. (4.27). Although some method such as *instrumental variable* used covariances in formulating main algorithm, it does not use the factorization property. The IV method use the ARMA model to "fit" measured data y_k The SSI-COV, on the contrary, is completely based on the factorization property. It is a so-called subspace method.

The SSI-COV method is addressing the so-called *stochastic realization problem*, i.e. the problem of identifying a stochastic state-space model from output-only data. Stochastic realization is closely related to deterministic (input-output) realization that goes back to Ho and Kalman (Ho and Kalman, 1966) and was extended with the **SVD** to treat noisy data in Zeiger (1974) and Kung (1978). The so-called Eigensystem Realization Algorithm (ERA), developed by Juang (Juang and Pappa 1985, 1994), is a modal analysis application of these deterministic realization algorithms. The stochastic (output-only) realization problem is solved in Akaike (1974), Aoki (1987), and Arun (1990). Application of stochastic realization to modal parameter estimation was reported by Benveniste and Fuchs (1985). They also proved that their algorithm is robust against non-stationary inputs (e.g. a white noise sequence with time-varying covariance).

The **SSI-COV** method identifies a stochastic state-space model from outputonly data. The stochastic state-space model, introduced in Subsection 4.4.3.1, has the following form:

$$x_{k+1} = Ax_k + w_k y_k = Cx_k + v_k$$
 (4.20)

where w_k and v_k are vector signals assumed to be zero mean, white and with covariance matrices:

$$E\begin{bmatrix} \begin{pmatrix} w_p \\ v_p \end{pmatrix} \begin{pmatrix} w_q^T & v_q^T \end{pmatrix} \end{bmatrix} = \begin{pmatrix} Q & S \\ S^T & R \end{pmatrix} \delta_{pq}$$
 (4.19)

Stochastic realization theory

In classical modal (input-output) analysis, the impulse response matrices h_k are rectangular matrices having l rows (i.e. the number of outputs) and m columns (i.e. the number of inputs). In output-only cases, the impulse responses are substituted by output covariances and the inputs by the (reference) outputs (see also Jame (1995), Hermans (1999)). The algorithm starts with gathering the output covariances in a block Toeplitz matrix $T_{1|i}$.

$$T_{1|i} = \begin{bmatrix} \Lambda_i & \Lambda_{i-1} & \cdots & \Lambda_1 \\ \Lambda_{i+1} & \Lambda_i & \cdots & \Lambda_2 \\ \vdots & \vdots & \vdots & \vdots \\ \Lambda_{2i-1} & \Lambda_{2i-2} & \cdots & \Lambda_i \end{bmatrix}$$

Applying the factorization property (4.20) to $T_{1|i}$ yields:

$$T_{\parallel i} = \begin{pmatrix} C \\ CA \\ ... \\ CA^{i-1} \end{pmatrix} (A^{i-1}G ... AG G) \updownarrow n = O_{\hat{i}}\Gamma_{\hat{i}}$$

$$\leftrightarrow n$$

$$(4.47)$$

where the definitions of the *extended* (i>n) observability matrix $O_i \in \square^{li\times n}$ and the reversed extended stochastic controllability matrix $\Gamma_i \in \square^{n\times li}$ are obvious from (4.47). For li>n, and if the system is observable and controllable, the rank of the $li\times li$ Toeplitz matrix equals n, since it is the product of a matrix with n columns and a matrix with n rows. The **SVD** is a numerically reliable tool to estimate the rank of a matrix. The application of the **SVD** to the block Toeplitz matrix yields:

$$T_{1|i} = USV^{T} = (U_{1} \ U_{2}) \begin{pmatrix} S_{1} & 0 \\ 0 & 0 \end{pmatrix} \begin{pmatrix} V_{1}^{T} \\ V_{2}^{T} \end{pmatrix} = U_{1}S_{1}V_{1}^{T}$$
(4.48)

where $U \in \square^{lixli}$ and $V \in \square^{lixli}$ are orthonormal matrices $(U^T U = U U^T = I_{li}, V^T V = V V^T = I_{li})$ and $S \in (\square^+)^{lixli}$ is a diagonal matrix containing the positive

singular values in descending order. The rank of a matrix is found as the number of non-zero singular values. In the last equality of (4.48), the zero singular values and corresponding singular vectors are omitted: $U_1 \in \square^{lixn}$, $S_1 \in (\square_0^+)^{nxn}$, $V_1 \in \square^{lixn}$. By comparing (4.47) to (4.48), the matrices O_i and Γ_i can be computed by splitting the **SVD** in two parts:

$$O_{i} = U_{1}S_{1}^{1/2}T$$

$$\Gamma_{i} = T^{-1}S_{1}^{1/2}V_{1}^{T}$$
(4.49)

where $T \in \square^{n \times n}$ is a non-singular matrix. It is easy to see that this matrix T can be considered as a similarity transformation that is applied to the identified state-space model. In other words, whatever the choice of T may be, similarity equivalent state-space models will result and we can simply set: T=I. The solution of the identification problem is now straightforward. From the definitions of the extended observability matrix O_i and the reversed extended stochastic controllability matrix Γ_i , we know that C equals the first l rows of O_i and G equals the last l columns of Γ_i ; or written in MATLAB notation:

$$C = O_i(1:l,:)$$

$$G = \Gamma_i(:, l(i-1)+1:li)$$
(4.50)

Zeiger (1974) proposed method to compute the state transition matrix A from the decomposition property of a shifted block Toeplitz matrix:

$$T_{2|i+1} = O_i A \Gamma_i \tag{4.51}$$

where the shifted matrix $T_{2|i+1}$ has a similar structure as (4.45), but is composed of covariances Λ_k from lag 2 to 2*i*. Matrix *A* is found by introducing (4.59) in (4.61) and solving for *A*:

$$A = O_i^{\dagger} T_{2|i+1} (\Gamma_i)^{\dagger} = S_1^{-1/2} U_1^T T_{2|i+1} V_1 S_1^{-1/2}$$
(4.52)

where $(\Box)^{\dagger}$ denotes the Moore-Penrose pseudo-inverse of a matrix.

At this point the identification problem is theoretically solved: the system order n is found as the number of non-zero singular values in (4.48) and the system matrices A,G,C, Λ_0 can be computed as in Eq.s (4.50) and (4.52). The fourth system matrix Λ_0 is simply the zero-lag output covariance matrix. The two matrices A,C are sufficient to compute the modal parameters. As discussed in Subsection 4.4.2, the discrete poles Λ_d and the observed mode shapes V are computed as (see also (4.16), (4.17)):

$$A = \Psi \Lambda_d \Psi^{-1}$$

$$V = C \Psi$$
(4.53)

Implementation and stabilization

In reality the number of measurements is not infinite and the output covariances have to be estimated (4.37). Since these output covariances form the basis of the realization method (4.47), it is evident that the identified system matrices also have to be considered as estimates: $\hat{A}, \hat{G}, \hat{C}, \hat{\Lambda}_0$.

Another remark is that in theory the system order n can be determined by inspecting the number of non-zero singular values of $T_{\parallel i}$ (4.58). In practice however, the estimated covariance Toeplitz matrix $\hat{T}_{\parallel i}$ is affected by "noise" leading to singular values that are all different from zero. As typical noise sources we have:

- Modelling inaccuracies. It is possible that the true system that generated the data cannot be modeled exactly as a stochastic state-space model. An attempt to model this system by a state-space model introduces an error in these cases.
- Measurement noise: introduced by the sensors and the electronics of the measurement hardware.
- Computational noise due to the finite precision of any computer. The finite number of data. The covariances have to be estimated, so that the factorization property (4.27) does not hold exactly. As a consequence the rank of the covariance Toeplitz matrix will not be exactly *n*; see Eq. (4.47).

In practice, the order can be determined by looking at a "gap" between two successive singular values. The singular value where the maximal gap occurs yields the model order. This criterion should however not be applied too dogmatically. For large, real structures there is generally no clear gap.

To obtain a good model for modal analysis applications, it is probably a better idea to construct a stabilization diagram, by identifying a whole set of models with different order. In case of the **SSI-COV** method, an efficient construction of the stabilization diagram is achieved by computing the **SVD** of the covariance Toeplitz matrix (4.48) only once. The number of block rows and columns i of $T_{\parallel i}$ should be such that li > n max, the maximum model order. Models of different order are then obtained by including a different number of singular values and vectors in the computation of O_i and Γ_i (4.49), from which the system matrices and the modal parameters are deduced as described in previous subsection.

4.5.3 Data-driven Stochastic Subspace Identification (SSI-DATA)

While most of output-only system identification main algorithms are based on formulation of spectra and covariances. The main advantage of data-driven algorithms is that they do not require any further preprocessing in order to obtain spectra or covariances. One disadvantage of using covariances as primary data in identification of system matrices is that it squares up the data. This may affect the numerical accuracy (Golub and Van Loan, 1989). The data-driven methods identify models directly from the time signals. One classical method is *prediction error method* **PEM** (Ljung, 1999) that identifies **AR**(**MA**) models from time data. This method identifies the parameters of a model by minimizing the so-called prediction error⁷. The straightforward application of **PEM** to estimate an **ARMA** model from data results in a highly nonlinear optimization problem with related problems as: convergence not being guaranteed, local minima, sensitivity to initial values and a high computational load (Peeteers, 1999).

Recently a lot of research effort in the system identification community was spent to subspace identification as evidenced by Overschee and De Moor (1996) and Ljung (1999). Subspace methods, originating from electrical engineering field, identify state-space models from (input and) output data by applying robust numerical techniques such as QR factorization, SVD and least squares. As opposed to SSI-COV, the DATA driven Stochastic Subspace Identification method (SSI-DATA) avoid the computation of covariances between the outputs. It is replaced by projecting the row space of future outputs into the row space of past outputs. In fact, the notions covariances and projections are closely related in aiming that: they both are aimed to cancel out the (uncorrelated) noise. The first SSI-DATA algorithms can be found in (Overchee 1991, 1993). A general overview of data-driven subspace identification (both deterministic and stochastic) is provided in Van Overschee and De Moor (1996). Although somewhat more involved as compared to previous methods, it is also possible with SSI-DATA to reduce the dimensions of the matrices by introducing the idea of the reference sensors. This is demonstrated in (Peeteers 1996).

Since the pioneering papers by Akaike (1975), canonical correlations (which were first introduced by Jordan (1975) in linear algebra and then by Hotelling (1936) in the statistical community) have been used as a mathematical tool in the stochastic realization problem. Overchee (1996) have shown how the approach by Akaike (1975) and others (e.g. Akaike 1990, Larimore 1983, Larimore 1990) boils down to applying canonical correlation analysis to two matrices that are (implicitly assumed to be) double infinite (i.e. have an infinite number of rows and columns). In his work, careful analysis reveals the nature of this double infinity and manages to reduce the canonical correlation approach to a semi infinite matrix problem, i.e. only the number of columns needs to be very large while the number of block rows remains sufficiently small. This observation is extremely relevant with respect to (for instance) the use of updating techniques.

_

⁷ Prediction errors are the part of the output data that cannot be predicted from past data.

In order to find the state space model, Overchee derive a finite dimensional vector sequence which, in the case of double infinite block Hankel matrices, would be a valid state sequence of the stochastic model. This sequence would correspond to the outputs of an infinite number of steady state Kalman filters with an infinite number of output measurements as inputs. For the semi infinite matrix problem, the sequence corresponds to the output of an infinite number of *nonsteady* state Kalman filters that have only used a finite number of output data as input. These state sequences are obtained directly from the output data, without any need for the state space model. The state space model is then derived from these sequences by solving a least squares problem.

In this thesis, we use main algorithm proposed by Overchee (1996) in identification of state matrix (A,G,C,K) as positive real sequence is guaranteed. Indeed, for an identified covariance sequence to be physically meaningful, it should be a positive real sequence. Almost all subspace algorithms presented in the literature (Akaike 1975, Aoki 1987, Akaike 90) do not guarantee this property, which implies that the spectral factor of the identified covariance sequence does not exist. With this algorithm it computes a slightly asymptotically biased solution (the bias decreases when the number of block rows increases), but the positive realness of the solution is guaranteed (if the identified system matrix $\bf A$ is stable).

Kalman filter states

In the derivation of the data-driven stochastic subspace identification algorithms for stochastic system identification, the Kalman filter plays a crucial role. In subsection 4.4.3.2, it was indicated how the forward innovation model (4.28) can be obtained by applying the steady state Kalman filter to the stochastic state-space model (4.28). In this section, the *nonsteady state Kalman filter* is introduced. The Kalman filter is described in many books. A nice derivation can be found in Appendix B of Juang (1994). The aim of the Kalman filter is to produce an *optimal prediction for the state vector* x_k by making use of *observations of the outputs* up to *time k-1* and the *available system matrices* together with the known *noise covariances*. These optimal predictions are denoted by a hat: \hat{x}_{k+1} . When the initial state estimate $\hat{x}_0 = 0$, the initial covariance of the state estimate $P_0 = E[\hat{x}_0 \ \hat{x}_0^T] = 0$ and the output measurements $y_0,..., y_{k-1}$ are given, the non-steady-state Kalman filter state estimates \hat{x}_k are obtained by the following recursive formulas (see Eqs. (4.30) and (4.31)):

$$\hat{x}_{k} = A\hat{x}_{k-1} + K_{k-1}(y_{k-1} - C\hat{x}_{k-1})
K_{k-1} = (G - AP_{k-1}C^{T})(\Lambda_{0} - CP_{k-1}C^{T})^{-1}
P_{k} = AP_{k-1}C^{T} + (G - AP_{k-1}C^{T})(\Lambda_{0} - CP_{k-1}C^{T})^{-1}(G - AP_{k-1}C^{T})^{T}$$
(4.54)

expressing the Kalman state estimate, the Kalman filter gain matrix and the Kalman state covariance matrix. The Kalman filter state sequence $\hat{X}_i \in \Box^{nxj}$ is defined as:

$$\hat{X}_i = (\hat{x}_i \ \hat{x}_{i+1} \ \dots \ \hat{x}_{i+j-1}) \tag{4.55}$$

The correct interpretation of the $(q+1)^{\text{th}}$ column of this matrix is that this state \hat{x}_{i+q} is estimated according to Eq. (4.64) by using only i previous outputs: y_q , ..., y_{i+q-1} . By consequence, two consecutive elements of \hat{X}_i cannot be considered as consecutive iterations of Eq. (4.64). More details can be found in Overchee (1996). Important to note is that a closed-form expression exists for this Kalman filter state sequence and that it is this sequence that will be recovered by the **SSI-DATA** algorithm (see further).

Data-Driven Stochastic Subspace Identification Theory

The **SSI-DATA** algorithm starts by projecting the row space of the future outputs into the row space of the past. The idea behind this projection is that it retains all the information in the past that is useful to predict the future.

Orthogonal projections

 $\Pi_{\rm \it B}$ denotes the operator that projects the row space of a matrix onto the row space of the matrix B

$$\Pi_B = B^T . (BB^T)^{\dagger} . B$$

where $(\Box)^{\dagger}$ denotes the Moore-Penrose pseudo-inverse of a matrix. \Box . A/B is shorthand for the projection of the row space of the matrix A on the row space of the matrix B:

$$A/\mathbf{B} = A.B^{T}.(BB^{T})^{\dagger}.B$$

The projection operator can be interpreted in the ambient j dimensional space as indicated in Fig. 4.2 (where j=2). The QR decomposition is the natural numerical tool for this orthogonal projection as will be shown in section of implementation. Note that in the notation A/B, the matrix B is printed bold face, which indicates that the result of the operation A/B lies in the row space of B.

Similarly, by projecting the row space of the future outputs into the row space of the past outputs, the notation and definition of this projection is:

$$\Pi_{i} = Y_{f} / Y_{p} = Y_{f} . Y_{p}^{T} . (Y_{p} Y_{p}^{T})^{\dagger} . Y_{p}$$
(4.56)

The matrices $Y_f, Y_p \in \square^{lixj}$ are partitions matrices of the output data block Hankel matrix, as indicated in (4.33).

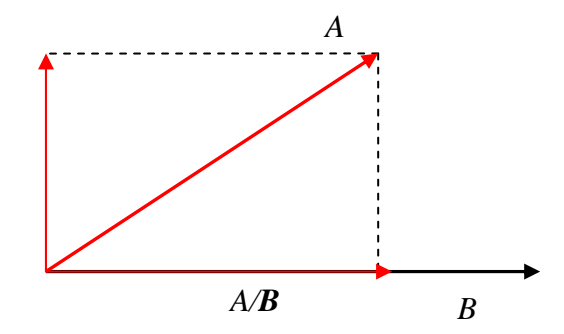


Fig. 4.2 Interpretation of the orthogonal projection A/B in the j-dimensional space (j=2).

Note that the expression of Eq. (4.56) is only the definition of Π_i ; it does not indicate how the projection is computed. From the definition (4.56), it is shown that projections and covariances are related. The matrix product $Y_f.Y_p^T$ is in fact block Toeplitz matrices containing covariances between outputs; (see Eq. 4.46).

The mian theorem of stochastic subspace identification (Overchee, 1996) states that the projection Π_i can be factorized as the product of the extended observability matrix $O_i(4.57)$ and the Kalman filter state sequence \hat{X}_i (4.65):

$$\Pi_{i} = O_{\hat{i}} \hat{X}_{\hat{i}} = \begin{pmatrix} C \\ CA \\ \dots \\ CA^{i-1} \end{pmatrix} (\hat{x}_{i} \ \hat{x}_{i+1} \ \dots \ \hat{x}_{i+j-1}) \updownarrow n$$

$$(4.57)$$

The prove of this theorem can be found in (Overchee, 1996) and graphical illustration is shown in Fig. 4.3.

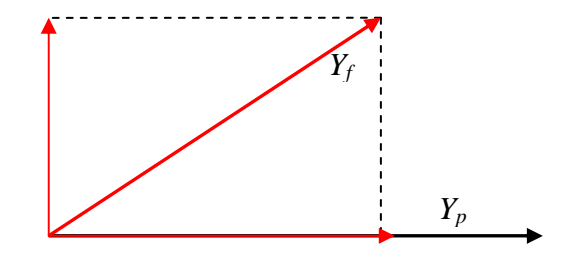
Since the projection matrix is the product of a matrix with n columns and a matrix with n rows (4.57), its rank equals n (if li > n). The **SVD** is a numerically reliable tool to estimate the rank of a matrix. After omitting the zero singular values and corresponding singular vectors, the application of the **SVD** to the projection matrix yields:

$$\Pi_i = U_1 S_1 V_1^T \tag{4.58}$$

where $U_1 \in \square^{lixn}$, $S_1 \in (\square_0^+)^{nxn}$, $V_1 \in \square^{lixn}$. The extended observability matrix and the Kalman filter state sequence are obtained by splitting the **SVD** in two parts:

$$O_i = U_1 S_1^{1/2} T$$

 $\hat{X}_i = O_i^{\dagger} \Pi_i$ (4.59)



 $\operatorname{rank}(Y_f/Y_p) = n$ $\operatorname{row space}(Y_f/Y_p) = \operatorname{row space} \hat{X}_i$ $\operatorname{column space}(Y_f/Y_p) = \operatorname{column space} O_i$

Fig. 4.3 Projection of the future outputs on the past determines the forward state sequence \hat{X}_i

Up to now, the system order n (as the number of non-zero singular values in Eq. (4.58)), the observability matrix O_i and the state sequence \hat{X}_i are determined. However, the identification problem is to recover the system matrices A,G,C,Λ . Through a similar reasoning and proof of Eq. (4.57), it can be shown that the following holds:

$$\Pi_{i-1} = Y_f^{-} / Y_p^{+} = O_{i-1} \hat{X}_{i+1}$$
 (4.60)

This new projection can be easily defined by shifting the separation between past and future outputs in the Hankel matrix one block row down. It is also easy to check that O_{i-1} is simply obtained after deleting the last 1 rows of O_i :

$$O_{i-1} = O_i(1:l(i-1))$$

Now the state sequence \hat{X}_{i+1} can be calculated from:

$$\hat{X}_{i+1} = O_{i-1}^{\dagger} \Pi_{i-1}$$

At this moment the Kalman state sequences \hat{X}_i , \hat{X}_{i+1} are calculated using only the output data. The system matrices can now be recovered from following overdetermined set of linear equations, obtained by stacking the state-space models for time instants i to i+j-1

$$\begin{pmatrix} \hat{X}_{i+1} \\ Y_{i|i} \end{pmatrix} = \begin{pmatrix} A \\ C \end{pmatrix} \hat{X}_i + \begin{pmatrix} W_i \\ V_i \end{pmatrix}$$
(4.61)

where $Y_{i|i} \in \Box^{lxj}$ is a Hankel matrix with only one block row. This set of equations can be easily solved for A,C. Intuitively, since the Kalman filter residuals $W_i \in \Box^{nxj}$, $V_i \in \Box^{lxj}$ (the innovations) are uncorrelated with \hat{X}_i , it seems natural to solve this set of equations in a least squares sense (since the least squares residuals are orthogonal and thus uncorrelated with the regressors \hat{X}_i). In Overschee and Moor (1993), it is shown that the least squares solution indeed computes an asymptotically unbiased estimate of A and C as:

$$\begin{pmatrix} A \\ C \end{pmatrix} = \begin{pmatrix} \hat{X}_{i+1} \\ Y_{i|i} \end{pmatrix} \hat{X}_{i}^{\dagger} \tag{4.62}$$

The noise covariances Q, R and S are recovered as the covariances of the least-squares residuals:

$$\begin{pmatrix} Q & S \\ S^T & R \end{pmatrix} = \begin{pmatrix} W_i \\ V_i \end{pmatrix} (W_i^T & V_i^T)$$
(4.63)

From the (Subsection 4.4.3.2), it is easy to see how the matrices A,C,Q,R,S can be transformed to A,G,C, Λ_0 . First the Lyapunov equation is solved for Σ :

$$\Sigma = A\Sigma C^T + Q$$

after which G and Λ_0 can be computed as:

$$\Lambda_0 = C\Sigma C^T + R$$

$$G = A\Sigma C^T + S$$
(4.64)

At this point the identification problem is theoretically solved: based on the outputs, the system order n and the system matrices A,G,C, Λ_0 are found.

The matrices A, C are sufficient to compute the modal parameters. As discussed in Subsection 2.4.2, the discrete poles Λ_d and the observed mode shapes V are computed as (see also Eqs. (4.16), (4.17), (4.53)):

$$A = \Psi \Lambda_d \Psi^{-1}$$
$$V = C \Psi$$

Positive realness

The computation of Q,R,S according to (4.73) only leads to asymptotically unbiased estimates if the number of block rows in the Hankel matrices goes to infinity: $i \to \infty$. So in practice, since $i \neq \infty$, a bias will be introduced on Q,R,S (and thus also on G, Λ_0). The modal parameters are only determined from A, C, then if only modal parameters are required, they are not suffering from this bias on G, Λ_0 .

Other algorithms exist that compute asymptotically unbiased estimates. Unfortunately these algorithms do not guarantee the *positive realness* of the identified covariance sequence. More details on positive realness can be found in Overcheee (1996). Important for the following of this thesis is that only positive real sequences have a corresponding spectrum matrix that is positive definite for all frequencies ω . If a matrix is positive definite, then all its diagonal entries are positive (Golub and Vanloan 1989). Peeters (2000), has shown that model identified with the SSI-COV method does not guarantee the positive realness of the identified covariance sequence. Then, an identified power spectrum becomes negative at certain frequencies (which has of course no physical meaning). A power spectrum is a diagonal entry of the spectrum matrix and therefore this matrix cannot be positive definite.

Also important is that only *positive real sequences* can be converted to a forward innovation state-space model. Such a model is sometimes useful, as we will see further. The conversion starts by solving the Riccati equation for P (see also Subsection 4.4.3.2 for forward innovation model):

$$P = APA^{T} + (G - APC^{T})(\Lambda_{0} - CPC^{T})^{-1}(G - APC^{T})^{T}$$
(4.30)

The matrix $P \in \mathbb{R}^{n \times n}$ is the forward state covariance matrix $P = E[z_k z_k^T]$. the covariance matrix of the innovations equals:

$$\Lambda_e = \Lambda_0 - CPC^T \tag{4.32}$$

And finally The Kalman gain is then computed as:

$$K = (G - APC^{T}) \Lambda_{e}^{-1}$$

= $(G - APC^{T}) (\Lambda_{0} - CPC^{T})^{-1}$ (4.31)

Implementation

Really implementation of data-driven subspace algorithms in general is the QR factorization of data Hankel matrices. Such a factorization applied to the output Hankel matrix of Eq. (4.33), (4.34) reads:

-

⁸ Asymptotic means that the number of data (theoretically) goes to infinity: $j \to \infty$.

$$H = \left(\frac{Y_p}{Y_f}\right) = \left(\frac{Y_p^+}{Y_f^-}\right) = RQ^T \tag{4.65}$$

where $Q \in \Box^{jxj}$ is an orthonormal matrix: $Q^TQ = QQ^T = I_j$ and $R \in \Box^{2lixj}$ is a lower triangular matrix. Since 2li < j, it is possible to omit the zeros in R and the corresponding rows in Q:

$$H = \begin{pmatrix} Y_{p} \\ \overline{Y}_{f} \end{pmatrix} = \begin{pmatrix} Y_{p}^{+} \\ \overline{Y}_{f}^{-} \end{pmatrix} = \begin{pmatrix} Y_{p} \\ \overline{Y}_{|i|} \\ \overline{Y}_{f}^{-} \end{pmatrix} = RQ^{T}$$

$$li \quad l \quad l(i-1) \quad j \to \infty$$

$$\leftrightarrow \quad \leftrightarrow \quad \leftrightarrow \quad \leftrightarrow$$

$$li \quad R_{11} \quad 0 \quad 0 \\ R_{21} \quad R_{22} \quad 0 \\ li \quad R_{31} \quad R_{32} \quad R_{33} \end{pmatrix} \begin{pmatrix} Q_{1}^{T} \\ Q_{2}^{T} \\ Q_{3}^{T} \end{pmatrix} li$$

$$li \quad l \quad l \quad li$$

$$Q_{1}^{T} \quad li$$

$$Q_{2}^{T} \quad li$$

$$Q_{3}^{T} \quad li$$

The division in block rows and columns is made such that the submatrices in (4.65) can all be expressed in terms of the R and Q submatrices. It is easy to show that the QR factorization yields following very simple expressions for the projections of future row spaces into past row spaces:

$$\Pi_{i} = \begin{pmatrix} R_{21} \\ R_{31} \end{pmatrix} Q_{1}^{T}, \quad \Pi_{i-1} = \begin{pmatrix} R_{31} & R_{32} \end{pmatrix} \begin{pmatrix} Q_{1}^{T} \\ Q_{2}^{T} \end{pmatrix} = \begin{pmatrix} Y_{p}^{+} \\ Y_{f}^{-} \end{pmatrix}$$
(4.67)

Also $Y_{i|i} \in \Box^{lxj}$, the output sequence that is present in the least-squares equations in A, C(4.62) is easily written in terms of the OR factors:

$$Y_{i|i} = \begin{pmatrix} R_{21} & R_{22} \end{pmatrix} \begin{pmatrix} Q_1^T \\ Q_2^T \end{pmatrix}$$

$$(4.68)$$

Since $\hat{X}_i = O_i^{\dagger}\Pi_i$ and $\hat{X}_{i+1} = O_{i-1}^{\dagger}\Pi_{i-1}$, all right-hand-side quantities of the least-squares Eq. (4.62) can be expressed in terms of the QR factors. Because of their orthonormality, the Q factors cancel out in this equation. So in this first step (4.65) the Q matrix should not be calculated. The MATLAB function qr (MatLab 1996), for instance, allows for the computation of the R factor only. Since typically $(2li) \ll j$, an important data reduction is obtained by replacing the $2li \times j$ data Hankel matrix by its R factor of dimension $2li \times 2li$.

Evidently, due to the finite data length, the identified state-space model is only an estimate of the true underlying state-space model that generated the data. This is denoted as \hat{A} , \hat{G} , \hat{C} , $\hat{\Lambda}_0$ for a covariance model and as \hat{A} , \hat{G} , \hat{C} , $\hat{\Lambda}_e$ for a forward innovation on model. The matrices \hat{A} , \hat{C} , are asymptotically unbiased estimates, but as stated before, a small bias introduced on the estimates of the other matrices (unless the number of block rows in the Hankel matrices goes to infinity: $i \to \infty$). In practice however, the (small) bias which is a function of the convergence of the nonsteady state Kalman filter, is a prize worth paying for the more guaranteed positive realness of the resulting covariance sequence.

The same remark as in the SSI-COV method concerning the determination of the model order n applies here. Due to noise (modelling inaccuracies, measurement noise and computational noise) none of the singular values in Eq. (4.58) are exactly zero and the order can only be determined by looking at a "gap" between two successive singular values. The singular value where the maximal gap occurs yields the model order. However in many practical cases (included in this thesis), no gap is visible. As previously, the problem of order determination is better solved by constructing a stabilization diagram. The number of block rows i of H should be such that $li > n_{\max}$, the maximum model order. Models of different order are then obtained by including a different number of singular values and vectors in the computation of O_i and \hat{X}_i (4.59), from which the system matrices and modal parameters are deduced as described previously.

In practice, amplitudes of singular values depend on amplitude of output signals. In case of very low signal to noise outputs, no gap is clearly visible. Several variants of stochastic subspace identification exist (see next Subsection). They differ in the weighing of the Π factor before application of the SVD. One of these variants that used in this thesis is so called Canonical Variate Analysis (CVA), in which the singular values can be interpreted as the cosines of the principal angles between two subspaces: the row space of the future outputs Y_f and the row space of the past outputs Y_p .

4.5.4 Covariance-Driven VS. Data-Driven Subspace

This section points out some of the similarities and differences between the **SSI-COV** (Subsection 4.5.2) and the **SSI-DATA** method (Subsection 4.5.3). First are the similarities. Both methods are based on stochastic (output-only) state space model (linear time invariant system loaded with white noise sequence with number of output and number of blolck . $j, i \to \infty$). In the **SSI-COV** algorithm the raw time histories y, consisting of l channels of j data points, are converted to the covariances of the Toeplitz matrix $T_{\parallel i} = Y_p Y_f^T$. In the **SSI-DATA** algorithm a similar reduction is obtained, but by projecting the row space of the future outputs into the row space of the past outputs $\Pi_i = Y_f / Y_p$. This projection is computed from the QR factorization of the data Hankel matrix. A more significant data reduction is obtained because only a

part of the R factor is needed in the sequel of the algorithm. Both methods then proceed with an **SVD**. The decomposition of $T_{i|i}$ reveals the order of the system, the column space of O_i and the row space of Γ_i . Similarly the decomposition of Π_i reveals the order of the system, the column space of O_i and the row space of \hat{X}_i .

Several variants of stochastic subspace identification exist. They differ in the weighting of the data matrices ($T_{\parallel i}$ for SSI-COV and Π_i for SSI-DATA) before the application of the SVD. The weighting determines the state-space basis in which the identified model will be identified. More details can be found in Arun (1990) and Overchee (1996). One of these variants is so-called Canonical Variate Analysis (CVA), in which the singular values can be interpreted as the cosines of the principal angles between two subspaces: the row space of the future outputs Y_f and the row space of the past outputs Y_p . In the SSI-DATA implementation of CVA, the weighting of the projection matrix before the application of the SVD goes as follows (Overchee, 1996):

$$(Y_f Y_f^T)^{-1/2} \Pi_i$$

Also the other subspace variants exists for implementations of both **SSI-COV** and **SSI-DATA**: principal component **PC** (Aoki 1987, Arun and Kung 1990), Unweighted principal component **UPC** (Arun and Kung, 1990). While, these methods give asymptotically unbiased system matrix, however positive real covariances are not guaranteed.

There are also differences between the covariance-driven and data-driven approaches. As indicated in Subsection 4.5.1.2, the covariance Toeplitz matrix computed by multiplying and sum up the time history outputs *y*, required more time consuming than SSI-DATA. However, this is not the significant for this thesis. Also, SSI-COV can be computed in a very fast way by using the FFT algorithm.

In favour of the data-driven method is that it is implemented as a numerically robust square root (QR) algorithm: the output data is not squared up as in the covariance-driven algorithm. More advantages of the data-driven method become clear in next section, where some postprocessing tools for the identified state-space model are presented: an analytical expression for the spectrum matrix and the separation of the total response in modal contributions.

4.5.5 Postprocessing

This section deals with some useful postprocessing tools that come after the identification of a parametric model. In the present context, once such a model is available, it can be analytically converted to other presentation forms. Modal analysis, a first type of postprocessing, was in fact already discussed in previous subsection. The state-space matrices identified with SSI-COV or SSI-DATA allow us to compute the modal parameters, as formulated in (4.63). Once the modal parameters computed,

the stiffness and damping matrices can be determined from pseudo inverse method (see next section) Other postprocessing tools such as spectrum analysis and modal responses are subsequently treated. First, response spectrum that are crucial tool for determining aerodynamic admittance, then modal responses that can only be applied to models that are identified with the SSI-DATA method.

4.5.5.1 Spectrum analysis

The covariance-driven and data-driven system identification methods use *time-domain* data to identify a model. It is however theoretically converted to *frequency-domain* model, hereto; the identified models are converted to a spectrum model. In previous section, a closed-form expression for the spectrum of a discrete-time stochastic state space model was derived:

$$S_{y}(e^{j\omega\Delta t}) = C(zI - A)^{-1}G + \Lambda_{0} + G^{T}(z^{-1}I - A^{T})^{-1}C^{T}|_{z=e^{j\omega\Delta t}}$$
(4.69)

By introducing the eigenvalue decomposition of A ($A = \Psi \Lambda_d \Psi^{-1}$), following "modal" spectrum is obtained:

$$S_{y}(e^{j\omega\Delta t}) = V(zI - \Lambda_{d})^{-1}G_{m} + \Lambda_{0} + G_{m}^{T}(z^{-1}I - \Lambda_{d})^{-1}V^{T}|_{z=e^{j\omega\Delta t}}$$
(4.70)

4.5.5.2 Modal response and prediction errors

This subsection presents a technique to split the total measured response in modal responses. A modal response is defined as the response of a single **DOF** system, having the same eigenfrequency and damping ratio as the considered mode, to the same force as applied to the full system. The technique assumes that the identified model is written in forward innovation form Eq. (4.28) (see Subsection 4.4.3.2):

$$z_{k+1} = Az_k + Ke_k$$
$$y_k = Cz_k + e_k$$

where $K \in \square^{nxl}$ is the Kalman gain and e_k is the white noise innovation sequence covariance matrix $E[e_p e_q^T] = \Lambda_e \delta_{pq}$ This model can be written in the modal basis:

$$z_{m,k+1} = \Lambda_d z_{m,k} + K_m e_k y_k = V z_{m,k} + e_k$$
 (4.71)

where $\Psi^{-1}z_k = z_{m,k}$ and $\Psi^{-1}K = K_m$. Because Λ_d is a diagonal matrix, each element of the modal state vector $z_{m,k}$ represents the contribution of a single mode. By eliminating the innovations e_k in the first equation and re-arranging the second, following state-space model is obtained:

$$z_{m,k+1} = (\Lambda_d - K_m V) z_{m,k} + K_m y_k$$

$$e_k = -V z_{m,k} + y_k$$
(4.72)

This modal state-space model $(\Lambda_d - K_m V, K_m, -V, I)$ can be simulated once all state-space matrices are known from the identification and the measured output y_k serves as input in the simulation. The results from the simulation are the modal state sequence $z_{m,k}$ and the innovation sequence e_k . The innovations can be interpreted as one-step-ahead prediction errors (Ljung, 1999). The one-step-ahead predicted output is defined as:

$$\hat{y}_k = V z_{m,k} \tag{4.73}$$

The prediction errors are the differences between the true output and the predicted output: $e_k = y_k - \hat{y}_k$. Because each element of the modal state vector $z^{(i)}_{m,k}$ represents the contribution of a single mode, the predicted output can be split in modal responses as:

$$\hat{y}_k = \sum_{i=1}^n \hat{y}_{i_k} = \sum_{i=1}^n \{v_i\} z^{(i)}_{m,k}$$
(4.74)

where \hat{y}_{i_k} is the (complex) response of the i^{th} mode. By combining the responses of a complex conjugated pair, a real output is obtained.

The modal response approach of this section can only be applied to models that are identified with the **SSI-DATA** method. In order to obtain the forward innovation model, the full *G* matrix is needed and not only as obtained with the **SSI-COV** method. Another more important problem, which could not be overcome by considering all sensors as references, is that the implementation of **SSI-COV** does not guarantee the positive realness of the identified covariance sequence. One of the consequences is that it is not always possible to obtain a forward innovation model (Peeters 2000, Overchee 1996).

4.6 Flutter Derivatives Identification

4.6.1 Theoretical Formulation of Covariance-Driven SSI

The dynamic behavior of a bridge deck with two degrees-of-freedom (DOF in short), i.e. h (bending) and α (torsion), in turbulent flow can be described by the following differential equations (Scanlan 1977)

$$m\left[\ddot{h}(t) + 2\xi_h \omega_h \dot{h}(t) + \omega_h^2 h(t)\right] = L_{se}(t) + L_b(t)$$
(4.75)

$$I\left[\ddot{\alpha}(t) + 2\xi_{\alpha}\omega_{\alpha}\dot{\alpha}(t) + \omega_{h}^{2}\alpha(t)\right] = M_{se}(t) + M_{b}(t)$$

where m and I are the mass and mass moment of inertia of the deck per unit span, respectively; ω_i is the natural frequency; ξ_i is the modal damping ratio ($i=h,\alpha$); $L_{\rm se}$ and $M_{\rm se}$ are the self-excited lift and moment, respectively; while $L_{\rm b}$ and $M_{\rm b}$ are the aerodynamic lift and moment. The self-excited lift and moment are given as follows (Simiu and Scanlan 1996)

$$L_{ae} = \rho U^{2}BL \left[KH_{1}^{*}(K) \frac{\dot{h}}{U} + KH_{2}^{*}(K) \frac{B\dot{\theta}}{U} + K^{2}H_{3}^{*}(K)\theta + K^{2}H_{4}^{*}(K) \frac{h}{B} \right]$$

$$M_{ae} = \rho U^{2}B^{2}L \left[KA_{1}^{*}(K) \frac{\dot{h}}{U} + KA_{2}^{*}(K) \frac{B\dot{\theta}}{U} + K^{2}A_{3}^{*}(K)\theta + K^{2}A_{4}^{*}(K) \frac{h}{B} \right]$$

$$(4.76)$$

where ρ is air mass density; B is the width of the bridge deck; U is the mean wind speed at the bridge deck level; $k_i = \omega_i B/U$ is the reduced frequency $(i = h, \alpha)$; and H_i^* and A_i^* (i=1,2,3) are the so-called flutter derivatives, which can be regarded as the implicit functions of the deck's modal parameters. The aerodynamic lift and moment can be defined as (Scanlan 1977)

$$L_{b}(t) = \frac{1}{2} \rho U^{2} B \left[2C_{L} \frac{u(t)}{U} \chi_{L}(t) + (C'_{L} + C_{D}) \frac{w(t)}{U} \chi_{L}(t) \right]$$

$$M_{b}(t) = \frac{1}{2} \rho U^{2} B^{2} \left[2C_{M} \frac{u(t)}{U} \chi_{M}(t) + (C'_{M}) \frac{w(t)}{U} \chi_{M}(t) \right]$$
(4.77)

where C_L , C_D and C_M are the steady aerodynamic force coefficients; C'_L and C'_M are the derivatives of C_L and C_M with respect to attack angles, respectively; u(t) and w(t) are the longitudinal and vertical fluctuations of wind speed, respectively; χ_L and χ_M are the lift and moment aerodynamic admittances of the bridge deck.

By moving L_{se} and M_{se} to the left side, and merging the congeners into column vectors or matrices, Eq. (4.75) can be rewritten as follows

$$[M]{\ddot{y}(t)} + [C^e]{\dot{y}(t)} + [K^e]{y(t)} = {f(t)}$$

$$(4.78)$$

where $\{y(t)\}=\{h(t) \ \alpha(t)\}^{T}$ is the generalized buffeting response; $\{f(t)\}=\{L_b(t) \ M_b(t)\}^{T}$ is the generalized aerodynamic force; [M] is the mass matrix; $[C^e]$ is the gross damping matrix, i.e. the sum of the mechanical and aerodynamic damping matrices; and $[K^e]$ is the gross stiffness matrix.

The fluctuations of wind speed u(t) and w(t) in Eq. (4.77) are random functions of time, so the identification of flutter derivatives and aerodynamic admittances of bridge decks can be simplified as a typical inverse problem in the theory of random vibration, and thus can be solved by stochastic system identification techniques.

Let

$$\begin{bmatrix} A_c \end{bmatrix} = \begin{bmatrix} \mathbf{O} & \mathbf{I} \\ -M^{-1}K^e & -M^{-1}C^e \end{bmatrix}$$

$$\begin{bmatrix} C_c \end{bmatrix} = \begin{bmatrix} \mathbf{I} & \mathbf{O} \end{bmatrix}$$
(4.79)

and

$$\{x\} = \begin{cases} y \\ \dot{y} \end{cases} \tag{4.80}$$

then Eq. (4.78) is transformed into the following stochastic state equations

$${\dot{x}} = [A_c] {x} + {w} {y} = [C_c] {x} + {v}$$
 (4.81)

The discrete form of Eq. (4.81) can be written as

where $[A_c]_{4\times4}$, $[C_c]_{2\times4}$ and $\{x\}$ are known as state matrix, output shape matrix and state vector, respectively; $\{w_k\}$ and $\{v_k\}$ are the input and output noise sequences, respectively. Subscript $*_k$ denotes the value of * at time $k\Delta t$, where Δt means the sampling interval. O and I are the zero and identity matrices, respectively.

It is common to assume that $\{x_k\}$, $\{w_k\}$ and $\{v_k\}$ in Eq. (4.82) are mutually independent and hence

$$E\left[x_{k} w_{k}^{\mathrm{T}}\right] = O \qquad E\left[x_{k} w_{k}^{\mathrm{T}}\right] = O$$
 (4.83)

Defining

$$\Sigma = E[x_k x_k^{\mathrm{T}}] \qquad Q = E[w_k w_k^{\mathrm{T}}]$$

$$\Lambda_i = E[y_{k+i} y_k^{\mathrm{T}}] \qquad R = E[v_k v_k^{\mathrm{T}}]$$

$$G = E[x_{k+i} y_k^{\mathrm{T}}] \qquad S = E[w_k v_k^{\mathrm{T}}]$$

$$(4.84)$$

then we get the following Lyapunov equations for the state and output covariance matrices

$$\Sigma = A\Sigma A^{T} + Q$$

$$\Lambda_{0} = C\Sigma C^{T} + R$$

$$G = A\Sigma C^{T} + S$$
(4.85)

From (4.82) and (4.83), it can be deduced

$$\Lambda_{1} = E \left[\left\{ y_{k+1} \right\} \left\{ y_{k} \right\}^{T} \right] \\
= E \left[\left(C \left\{ x_{k+1} \right\} + \left\{ v_{k+1} \right\} \right) \left\{ y_{k} \right\}^{T} \right] \\
= E \left[C \left\{ x_{k+1} \right\} \left\{ y_{k} \right\}^{T} \right] \\
= CG \tag{4.86}$$

$$\Lambda_{2} = E \Big[\{ y_{k+2} \} \{ y_{k} \}^{\mathsf{T}} \Big] = E \Big[(C \{ x_{k+2} \} + \{ v_{k+2} \}) \{ y_{k} \}^{\mathsf{T}} \Big] \\
= E \Big[C \{ x_{k+2} \} \{ y_{k} \}^{\mathsf{T}} \Big] \\
= CE \Big[\{ x_{k+2} \} \{ y_{k} \}^{\mathsf{T}} \Big] \\
= CE \Big[(A \{ x_{k+1} \} + \{ w_{k} \}) \{ y_{k} \}^{\mathsf{T}} \Big] \\
= CE \Big[A \{ x_{k+1} \} \{ y_{k} \}^{\mathsf{T}} \Big] \\
= CAE \Big[\{ x_{k+1} \} \{ y_{k} \}^{\mathsf{T}} \Big] \\
= CA^{2-1}G \tag{4.87}$$

and

$$\Lambda_i = CA^{i-1}G \tag{4.88}$$

Defining a block Toeplitz $T_{1|i}$ as

$$T_{1|i} = \begin{bmatrix} \Lambda_i & \Lambda_{i-1} & \cdots & \Lambda_1 \\ \Lambda_{i+1} & \Lambda_i & \cdots & \Lambda_2 \\ \vdots & \vdots & \vdots & \vdots \\ \Lambda_{2i-1} & \Lambda_{2i-2} & \cdots & \Lambda_i \end{bmatrix}$$
(4.89)

then one can infer from the definition of covariance matrix that $T_{1|i}$ can be expressed as the product of two block Hankel matrices $Y_{\rm f}$ and $Y_{\rm p}$

$$T_{\mathrm{I}|_{i}} = Y_{\mathrm{f}} Y_{\mathrm{p}}^{\mathrm{T}} \tag{4.90}$$

where Y_f and Y_p are composed of the 'future' and 'past' measurements, respectively.

$$Y_{f} = \frac{1}{\sqrt{j}} \begin{bmatrix} y_{i} & y_{i+1} & \cdots & y_{i+j-1} \\ y_{i+1} & y_{i+2} & \cdots & y_{i+j} \\ \vdots & \vdots & \vdots & \vdots \\ y_{2i-1} & y_{2i} & \cdots & y_{2i+j-2} \end{bmatrix} \qquad Y_{p} = \frac{1}{\sqrt{j}} \begin{bmatrix} y_{0} & y_{1} & \cdots & y_{j-1} \\ y_{1} & y_{2} & \cdots & y_{j} \\ \vdots & \vdots & \vdots & \vdots \\ y_{i-1} & y_{i} & \cdots & y_{i+j-2} \end{bmatrix}$$
(4.91)

In a manner similar to the classical eigensystem realization algorithm (ERA in short) (Juang and Pappa, 1985), one can find

$$A = o_i^{\dagger} T_{2|i} \varsigma_i = S_N^{-1/2} U^{\mathsf{T}} T_{2|i} V S_N^{-1/2}$$
(4.92)

where N is model order, i.e. the maximum number of modes to be computed. U, S and V are matrices derived from the singular value decomposition (SVD in short) of matrix $T_{1|i}$

$$T_{1|i} = USV^{\mathrm{T}} \tag{4.93}$$

Thus, the modal parameters can be determined by solving the eigenvalue problem of state matrix A. By now, the theoretical formulation of covariance-driven SSI has been achieved. According to (4.90), (4.91) and (4.92), a different combination of i, j and N will give a different state matrix, and thus a different pair of modal parameters. Therefore, modal parameters should be derived from a series of combinations, rather than a single combination. In the process of identification, N or i should be given in series for certain j to get the frequency stability chart.

Once the modal parameters are identified, the gross damping matrix C^e and the gross stiffness matrix K^e in Eq. (4.4) can be readily determined by the pseudo-inverse method.

Let

$$\overline{C}^{e} = M^{-1}C^{e} \qquad \overline{K}^{e} = M^{-1}K^{e}
\overline{C} = M^{-1}C^{0} \qquad \overline{K} = M^{-1}K^{0}$$
(4.94)

where C^0 and K^0 are the 'inherent' damping and stiffness matrices, respectively. Thus, the flutter derivatives can be extracted from the following equations

$$H_{1}^{*}(k_{h}) = -\frac{2m}{\rho B^{2} \omega_{h}} (\overline{C}_{11}^{e} - \overline{C}_{11}), \quad A_{1}^{*}(k_{h}) = -\frac{2I}{\rho B^{3} \omega_{h}} (\overline{C}_{21}^{e} - \overline{C}_{21})$$

$$H_{2}^{*}(k_{\alpha}) = -\frac{2m}{\rho B^{3} \omega_{\alpha}} (\overline{C}_{12}^{e} - \overline{C}_{12}), \quad A_{2}^{*}(k_{\alpha}) = -\frac{2I}{\rho B^{4} \omega_{\alpha}} (\overline{C}_{22}^{e} - \overline{C}_{22})$$

$$H_{3}^{*}(k_{\alpha}) = -\frac{2m}{\rho B^{3} \omega_{\alpha}^{2}} (\overline{K}_{12}^{e} - \overline{K}_{12}), \quad A_{3}^{*}(k_{\alpha}) = -\frac{2I}{\rho B^{4} \omega_{\alpha}^{2}} (\overline{K}_{22}^{e} - \overline{K}_{22})$$

$$H_{4}^{*}(k_{h}) = -\frac{2m}{\rho B^{3} \omega_{h}^{2}} (\overline{K}_{11}^{e} - \overline{K}_{11}), \quad A_{4}^{*}(k_{h}) = -\frac{2I}{\rho B^{4} \omega_{h}^{2}} (\overline{K}_{21}^{e} - \overline{K}_{21})$$

$$(4.95)$$

The pseudo-inverse method is here briefly described. It can be readily concluded from (4.88) and (4.89) that state matrix A will be different for different i, j and N. Therefore, it is impossible to directly determine matrix K^e and matrix C^e from the state matrix, i.e. Eq. (4.79). In this study, an alternative technique is utilized to estimate the gross stiffness and damping matrices.

Firstly, the modal parameters of the system are determined by solving the eigenvalue problem of state matrix A

$$A = \Psi \Lambda \Psi^{-1}$$

$$\Phi = C \Psi$$
(4.96)

where Ψ is the complex eigenvector matrix, Φ is the mode shape matrix, and Λ is a diagonal matrix composed of the complex poles of the system. Different combination of i, j and N are employed to derive the modal parameters statistically. For more details, see Refs. (Sarkar, 1994 and Jaung and Pappa, 1985).

Secondly, the gross damping matrix C^e and the gross stiffness matrix K^e in Eq. (4.78) are estimated from the modal parameters by the pseudo-inverse method

$$\begin{bmatrix} K^e & C^e \end{bmatrix} = -M \left[\Phi \Lambda^2 \Phi^* (\Lambda^*)^2 \right] \begin{bmatrix} \Phi & \Phi^* \\ \Phi \Lambda & \Phi^* \Lambda^* \end{bmatrix}^+$$
(4.97)

where the superscript * denotes the complex conjugate.

4.6.2 Theoretical formulation of data-driven SSI

Theoretical formulation of data-driven SSI applied to flutter derivatives identification of bridge decks is similar to previous covariance-driven SSI, (see Eqs. 4.75-4.78). However in identification process, SSI-DATA start with defying output block Hankel matrix:

$$H = \frac{1}{\sqrt{j}} \begin{pmatrix} y_{0} & y_{1} & \dots & y_{j-1} \\ y_{1} & y_{2} & \dots & y_{j} \\ \dots & \dots & \dots & \dots \\ \frac{y_{i-1} & y_{i} & \dots & y_{i+j-2}}{y_{i} & y_{i+1} & \dots & y_{i+j-1}} \\ y_{i+1} & y_{i+2} & \dots & y_{i+j} \\ \dots & \dots & \dots & \dots \\ y_{2i-1} & y_{2i} & \dots & y_{2i+j-2} \end{pmatrix} = \begin{pmatrix} Y_{0|i-1} \\ Y_{i|2i-1} \end{pmatrix} = \begin{pmatrix} Y_{p} \\ Y_{f} \end{pmatrix} \stackrel{\uparrow}{\downarrow} li = \frac{"past"}{"future"}$$
(4.33)

Then applying QR factorization to data Hankel Matrices. Such a factorization reads:

$$H = \left(\frac{Y_p}{Y_f}\right) = \left(\frac{Y_p^+}{Y_f^-}\right) = RQ^T \tag{4.65}$$

where $Q \in \Box^{jxj}$ is an orthonormal matrix: $Q^TQ = QQ^T = I_j$ and $R \in \Box^{2lixj}$ is a lower triangular matrix. Since 2li < j, it is possible to omit the zeros in R and the corresponding rows in Q:

$$H = \begin{pmatrix} \frac{Y_{p}}{Y_{f}} \end{pmatrix} = \begin{pmatrix} \frac{Y_{p}^{+}}{Y_{f}^{-}} \end{pmatrix} = \begin{pmatrix} \frac{Y_{p}}{Y_{|i|}} \\ \frac{Y_{p}}{Y_{f}^{-}} \end{pmatrix} = RQ^{T}$$

$$= \lim_{l \to \infty} \begin{pmatrix} R_{11} & 0 & 0 \\ R_{21} & R_{22} & 0 \\ li & R_{31} & R_{32} & R_{33} \end{pmatrix} \begin{pmatrix} Q_{1}^{T} \\ Q_{2}^{T} \\ Q_{3}^{T} \end{pmatrix} li$$

$$(4.66)$$

One can infer from previous subsection that:

$$\Pi_{i} = \begin{pmatrix} R_{21} \\ R_{31} \end{pmatrix} Q_{1}^{T}, \quad \Pi_{i-1} = \begin{pmatrix} R_{31} & R_{32} \end{pmatrix} \begin{pmatrix} Q_{1}^{T} \\ Q_{2}^{T} \end{pmatrix} = \begin{pmatrix} Y_{p}^{+} \\ Y_{f}^{-} \end{pmatrix}$$
(4.67)

where $Y_{i|i} \in \Box^{lxj}$, the output sequence that is present in the least-squares equations in A, C (4.62) is easily written in terms of the RQ factors:

$$Y_{i|i} = \begin{pmatrix} R_{21} & R_{22} \end{pmatrix} \begin{pmatrix} Q_1^T \\ Q_2^T \end{pmatrix}$$

$$(4.68)$$

In a manner similar to the SSI-COV, SVD is applied to the projection matrix yields:

$$\Pi_i = U_1 S_1 V_1^T$$

The extended observability matrix and the Kalman filter state sequence are obtained by splitting the **SVD** in two parts:

$$O_i = U_1 S_1^{1/2} T$$

 $\hat{X}_i = O_i^{\dagger} \Pi_i$ (4.59)

where the similarity transform matrix T = I. The extended observability matrix O_{i-1} is simply obtained after deleting the last 1 rows of O_i :

$$O_{i-1} = O_i(1:l(i-1))$$

Now the state sequence \hat{X}_{i+1} can be calculated from:

$$\hat{X}_{i+1} = O_{i-1}^{\dagger} \Pi_{i-1}$$

Now, the system matrices A, C can be determined simultaneousely by solving the sets of equations in a least square sense:

$$\begin{pmatrix} A \\ C \end{pmatrix} = \begin{pmatrix} \hat{X}_{i+1} \\ Y_{i|i} \end{pmatrix} \hat{X}_{i}^{\dagger}$$

Thus, the modal parameters can be determined by solving the eigenvalue problem of state matrix A. By now, the theoretical formulation of data-driven SSI has been achieved. The remaining parameters can be determined in similar manner to SSI-COV method.

Implementation

Both algorithms for SSI-COV and SSI-DATA are implemented in MATLAB named *ssi_cov* and *ssi_data*. These functions are executed by typing their names. For instance (for SSI-COV) method:

Applies the covariance-driven stochastic subspace identification. The program will promptly for recorded motion file (in.txt) as input.



The measured data shall be arranged in columns with each columns corresponding to each recorded data step for each channel. For instance:

200	
-2.54E-12	6.63E-12
-4.33E-11	1.21E-10
-3.78E-10	1.08E-09
-2.25E-09	6.43E-09
-1.02E-08	2.86E-08
-3.79E-08	1.03E-07
-1.19E-07	3.10E-07
-3.27E-07	8.16E-07
-8.02E-07	1.91E-06
-1.79E-06	4.08E-06
-3.66E-06	8.02E-06
-6.98E-06	1.47E-05
-1.25E-05	2.54E-05
-2.13E-05	4.16E-05
-3.44E-05	6.51E-05
-5.35E-05	9.78E-05
-8.00E-05	0.0001419
-0.00011577	0.0001993
-0.00016254	0.00027188
-0.00022208	0.00036117
-0.00029601	0.00046822
-0.00038571	0.00059343

The first row contains sampling frequency of signal.

Preprocessing

Preprocessing is the data treatment before system identification and it highly influences the identification result. Following possibilities are implemented:

Decimate: the data is low-pass filtered and resampled at a lower rate. The identification can concentrate on a limited frequency band.

Detrend: the best straight line fit is removed from the data. This removes the DCcomponent that can badly influence the identification results.

Preprocessing output

The effect of a preprocessing procedure can be seen immediately, both in time and frequency domain. The recorded signal is shown in time-history as shown in Fig. 4.4

The frequency domain representation of the signals is also available for preliminary check of signal before starting system identification process. The frequency domain representation is determined by *average periodogram* (Welch's method) where the variance of estimated spectrum is reduced by splitting the signal in 10 segements, computing the weighted periodograms of all segments and taking the average.

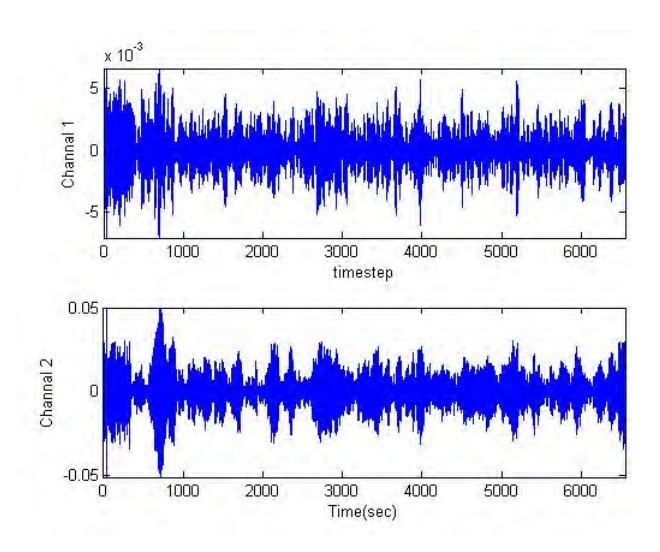


Fig.4.4 Preprocessing with time history representation of signals

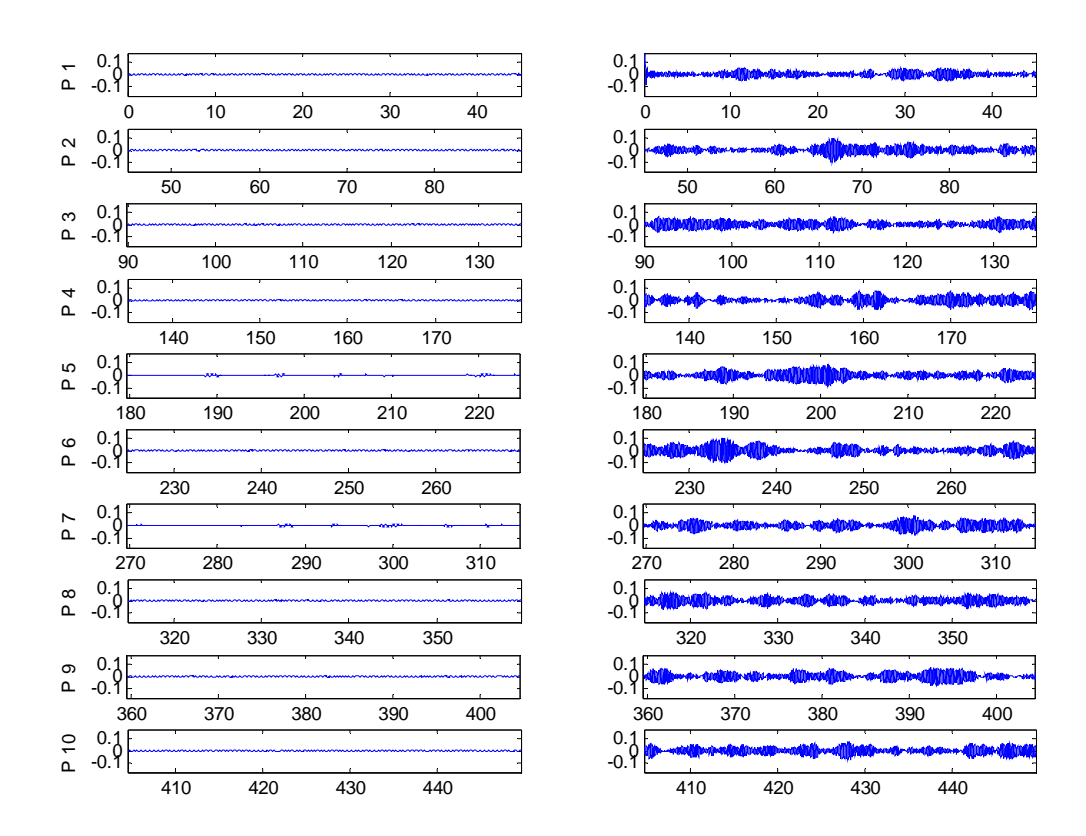
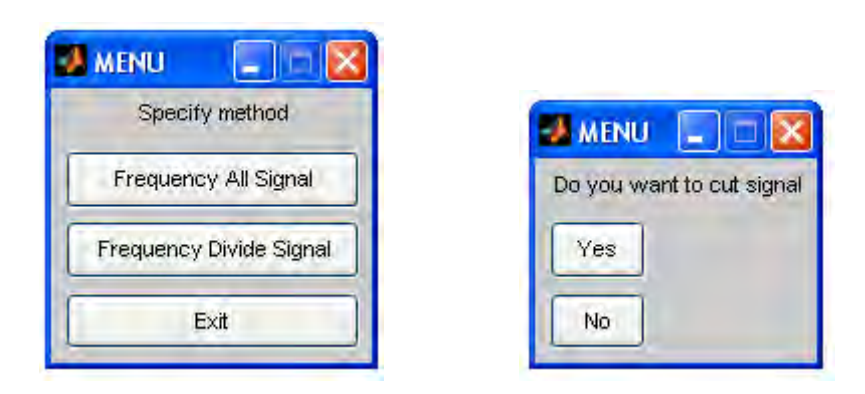


Fig. 4.5 Divided signals in (10) segments for averaged spectrum.



The user has options such as: frequency all signal sections, individual section, delete (cut) some of segments from averaging and even number of spectral estimate.



Based on number of choices from user's selection, response spectrums for each channel are plotted. Fig. 4.6 shows example of spectrum plot for vertical (channel 1) motion and torsional motion (channel 2) of IRR bridge section model and thin flat plate under smooth wind.

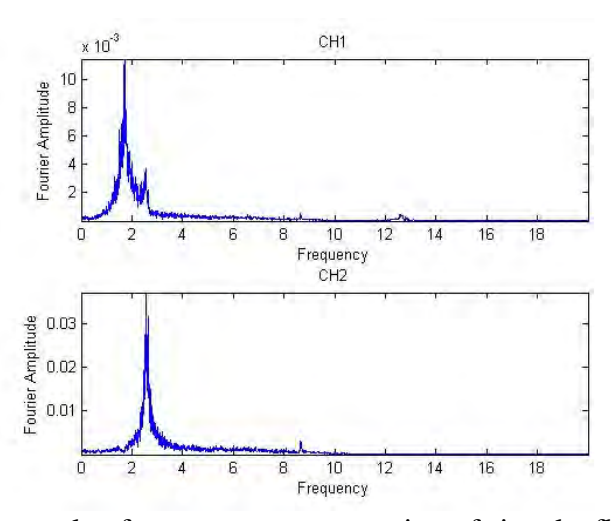


Fig.4.6a Example of spectrum representation of signals: flatplate model

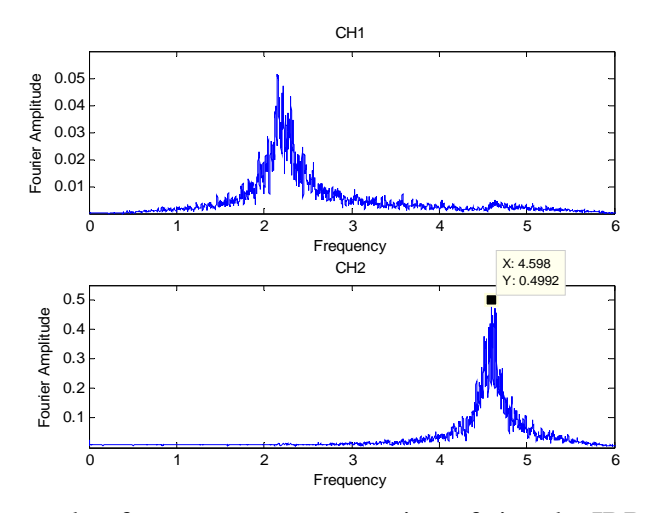


Fig.4.6b Example of spectrum representation of signals: IRR bridge model

System identification

First, the user has to specify some input-parameters of the algorithm: The numbers of block rows i (which determine the maximum number of orders that can be calculated), maximum number of order and the model order range. The numbers of block row i and model order are depend on user's choice. It is practically experience that it is better to over-specify the model order and to eliminate spurious numerical poles afterwards. The poles corresponding to a certain model order are compared to the poles of a one-order-lower model. If the eigenfrequency, the damping ratio and the related mode shape differences are within preset limits, the pole is labeled as a stable one and the system matrix is determined. In this thesis, the preset limits are 1% for eigenfrequencies, 5% for damping ratio. However depend on the quality of data at high wind speed 10% for damping ratio are set.

The number of block i has also effects the value of system matrix. As stated before in theoretical formulation these value are in asymptotically converged. Fig. 4.7 shows example of analyzing that each elements in system matrix are converged at number of block equal to 100. Fig. 4.8 shows that the number of block that modal parameters (frequency and damping ratio in this Fig.) are stable also depended on sampling rate.

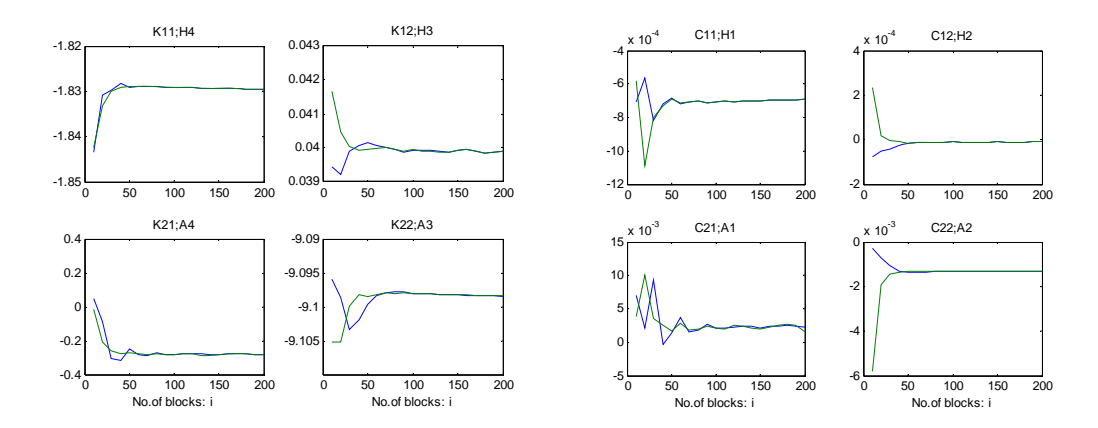


Fig. 4.7 Illustration of the asymptotically property of system matrix.

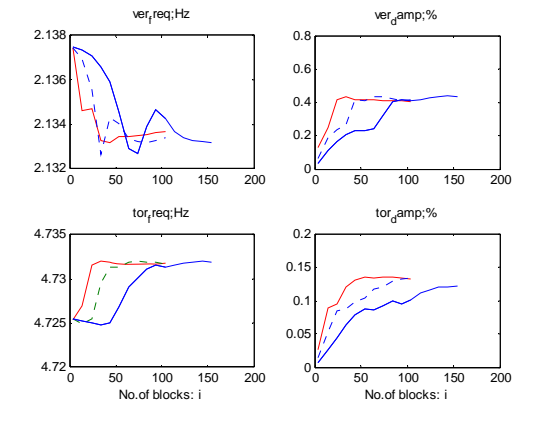


Fig. 4.8 Illustration of the asymptotically property of modal properties (...fs = 25 Hz, ---fs = 50 Hz and solid line for fs = 100 Hz)

After some computations, a stabilization diagram is constructed (Fig. 4.9). The diagram is represented together with the averaged of the response spectrum for visual reference. Singular values of the covariance Toeplitz matrix are also plotted on a log scale with the model order (Fig. 4.10).

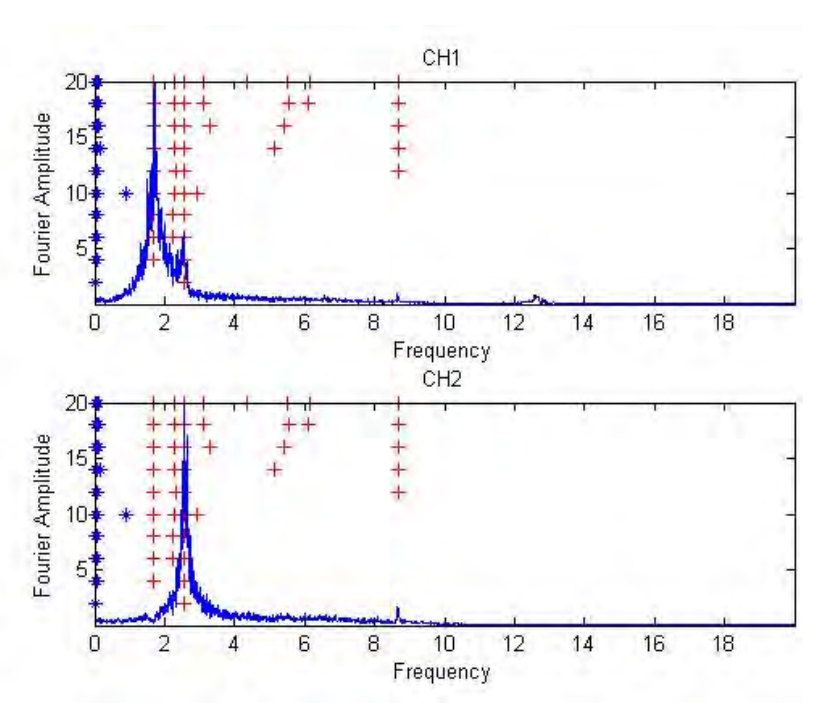


Fig. 4.9 Stabilization diagram obtained with the SSI-COV method (the model order are ranging from 2 to 20).

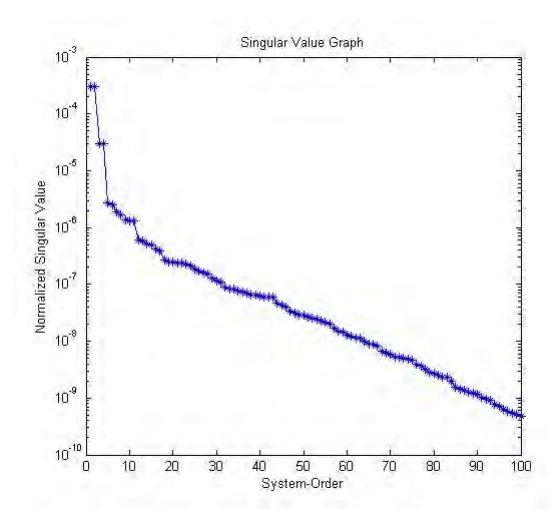


Fig. 4.10 Singular values of the covariance Toeplitz matrix.

Finally, the program reports the corresponding eigenfrequency, damping ratio for each pole and system matrix for combination of poles in each order. Outputs are arranged in rows in the following format:

- Number of blocks ,*i*,: the number of block rows, *i*, used in system identification.
- Order *n*: The order of the system where system identification are calculated.
- Frequencies of each poles, Eigenfrequencies of each pole are arranged in ascending order.
- Damping ratio for each poles
 Damping ratio corresponding to each modal (eigenfrequency) report in previous line.
- TEXT: "0" line This line with "0" text is intentionally for easy visualization without any meaning.
- Mode shape value
 Mode shape values for each channel are report for each mode in columnvise.
- Text: "SYSTEM MATRIX"
 The system matrix reported is in following format:

$$\begin{bmatrix} 0 & I \\ -M^{-1}K^e & -M^{-1}C^e \end{bmatrix}_{2lx2l}$$

where l = number of outputs. Fig.4.11 shows example of output report where l=2 (vertical and torsional motion)

The second method is SSI-DATA method which can be executed by typing function name in MATLAB command line as:

The preprocessing, preprocessing output and system identification output are analogous to SSI-COV method except that principle angles between the row space of future outputs and the row space of past reference outputs are plotted with the model order, n, instead of singular values.

Fig. 4.11 Example of output from both the SSI-DATA and SSI-COV methods

4.7 Verification of the Method by Numerical Tests

Before the method are applying to analyze both the free decay and the buffeting response time histories recorded in the wind tunnel, simulated data have been tested first in order to validate and check the performance of the method.

4.7.1 Free Decay Response Data

The preliminary tests included two synthetic but well controlled cases: two uncoupled degrees of freedom, excited first in transient motion (free decay) and then by a white noise loading process.

Free decay response time-series were obtained by direct calculation of displacement values for j = 4096 discrete time stations, with 'sampling' interval $\Delta t = 0.02$ s (fs = 50Hz.). Structural modal parameters used in this simulation were chosen as representative for the practical section model setup used in the aeroelastic tests. In this thesis, we selected the modal properties of section model based on test of Golden Gate Bridge by Jakobsen (1995). The modal matrices are given per unit length:

$$C_0 = \begin{bmatrix} 0.3616 & 0 \\ 0 & 0.0072 \end{bmatrix}, \quad K_0 = \begin{bmatrix} 397.0573 & 0 \\ 0 & 24.7315 \end{bmatrix}, M_0 = \begin{bmatrix} 2.6526 & 0 \\ 0 & 0.0189 \end{bmatrix}$$

i.e. $f_{ho}=1.9472~Hz$, $f_{\theta\theta}=5.7573~Hz$, $\delta_{ho}=0.035$, $\delta_{\theta\theta}=0.033$, where modal logarithmic decrements δ are representative for the range of small amplitudes. The damping ratio ξ were then multiplied in turn with 5, 10, 20 and 40, in order to cover values of total damping (structural + aerodynamic) which could be present in vibration of model section under wind flow. Values as high as $\xi=0.2$ could be expected for the vertical degree of freedom.

Free decay (transient) responses without noise corrupted

First, the preliminary numerical tests were tested with free vibration signals with initial displacement fixed at 15 mm and 0.08 radian for vertical and torsional motion, respectively, and with lowest and highest damping values. This was performed to check the applicability of the method to the free decay signal. The results are displayed in Table 4.1, in which values of preset eigenfrequencies and damping ratios are given together with the estimates based on both the SSI-COV and the SSI-DATA methods. Table 4.2 displayed pre-set and identified values of system matrices (K and C). The response signals for both damping ratios are shown in Fig. 4.12.

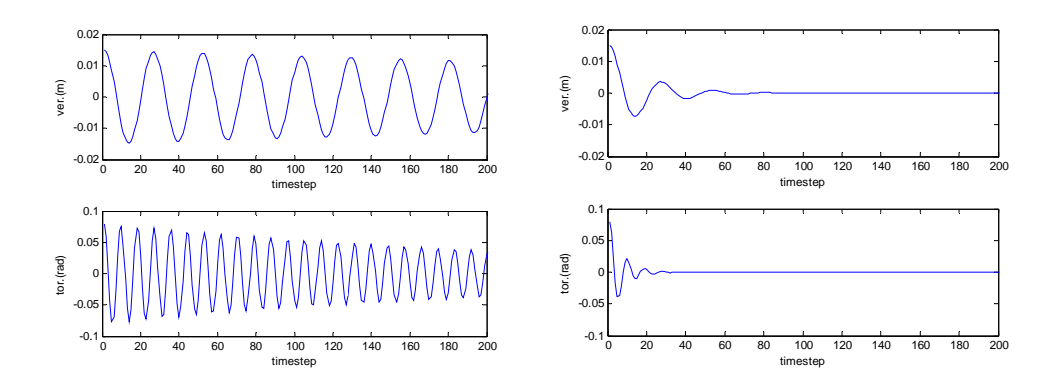


Fig. 4.12 Example of free decay responses simulated: a) $\xi_h = 0.0053$, $\xi_\theta = 0.0056$, b) $\xi_h = 0.2228$, $\xi_\theta = 0.2101$

Table 4.1a Preset and identified values of frequencies, damping ratios and system matrices for free decay response without noise, $j\Delta t = 4096 \text{ x} 0.02 \text{ s} = 81.92$ s. $\xi_h = 0.0053$, $\xi_\theta = 0.0056$

			SSI -	COV		SSI -DATA					
Preset		Ider	ntify	Erro	or(%)	Identify		Erro	or(%)		
fp	ξp	fp	ξp	error f errorξp		fp	ξp	error f	errorξp		
1.9472	0.0056	1.9472	0.0056	0.00%	0.00%	1.9472	0.0056	0.00%	0.00%		
5.7573	0.0053	5.7573	0.0053	0.00% 0.00%		5.7573	0.0053	0.00%	0.00%		

	proc	ot		SSI -C	OV		SSI -DATA				
	preset		recovered		error[%]		recov	vered	error[%]		
K	397.0573	0	397.056 0		0.00%		397.06	0	0.00%		
	0	24.73	0	24.73		0.00%	0	24.73		0.00%	
С	0.3616	0	0.3616	0	0.00%		0.3616	0	0.00%		
	0	0.0072	0	0.0072		0.00%	0	0.0072		0.00%	

Table 4.1b Preset and identified values of frequencies, damping ratios and system matrices for free decay response without noise, $j\Delta t = 4096 \text{ x} 0.02 \text{ s} = 81.92$ s. $\xi_h = 0.2232$, $\xi_\theta = 0.2112$

			SSI	-COV		SSI -DATA					
Preset		Ident	ify	Erro	Error(%)		ntify	Erro	r(%)		
fp	ξp	fp	ξp	error f error ξp		fp	ξp	error f	errorξp		
1.9472	0.2232	1.9462	0.224	-0.05%	0.36%	1.9469	0.2228	-0.02%	-0.18%		
5.7573	0.2112	5.7612	0.212	0.07%	0.38%	5.7565	0.2107	-0.01%	-0.24%		

	proso	\t		SSI -C	COV		SSI -DATA				
	preset		recovered		error[%]		recovered		error[%]		
K	397.0573	0	396.611	0.22	-0.11%		396.94	-0.04	-0.03%		
	0	24.73	-0.068	24.76		0.12%	-0.02	24.73		-0.02%	
C	14.464	0	14.47797	0.007	0.10%		14.4619	0.0002	-0.01%		
	0	0.288	0.002	0.289		0.35%	-0.0003	0.2880		0.01%	

Frequency and damping ratio estimates are practically identical to the preset values (less than 0.5% for the highest damping case). The system matrices are also excellent even for the short useful signal case with only a few cycles of vibration motion. However in case of highest damping with only short useful data, the estimate values of off-diagonal terms have small difference from zero-preset values where less scatter from SSI-DATA are noticed. The above estimates were obtained with number of block i=4 and order n=4.

Free decay (transient) responses with noise corrupted

In order to investigate the effect of measurement noise, free decay responses were modified by a white noise process with the standard deviation equal to 10% of the standard deviation of the original response. Structural data were taken as in the previous case; N and Δt were the same as the previous case except that noises were added to signals. Most of the previous works were tested with 5% -noise (see Jacobsen 1995). In this thesis, we decided to test with 10% noise corrupting as would represent the worsen case. Tests are performed in 20 sets; the preset and identified parameters are shown in Table.4.2. Identified frequencies were changed at lesser than 0.8% on both estimates by the SSI-COV and the SSI-DATA. Damping ratios were changed at most by 2% by both the SSI-COV and the SSI-DATA except in case of lowest damping case which are 5.4 %, respectively. The higher difference in estimates for the lowest damping case would result from assumption of noise added. In that case, the standard deviations of the original signals are higher than the other cases which resulting in higher standard deviation of noise added. The standard deviation from 20 tests for frequency estimates are less than 0.5% and 1.5% for the SSI-DATA and the SSI-COV method, respectively. The highest standard deviation of damping ratio estimates from the SSI-COV is 13.2% that seemed more scatter than those from SSI-DATA which is 5.7%.

The diagonal terms of system matrices (frequency and damping matrices) estimated by both methods are also identical to the preset values. Estimates of diagonal terms are distorted within 1% by both methods except only for case with the lowest damping case which values are 2.82% by the SSI-COV method. The values of off-diagonal terms which are distorted from the zero-preset value are also noted which terms related to H_3^* are highest.

Table 4.2a Preset and identified values of frequencies and damping ratios for free decay response with 10%-noise added, $j\Delta t = 4096 \text{ x} 0.02 \text{ s} = 81.92 \text{ s}$. $\xi_h = 0.2228$, $\xi_\theta = 0.2101$

				SSI-CO	V method		
Pre	eset	Ide	ntify	Erro	or(%)	standard (%)	deviation
fp	ξp	fp ξp		error fp	error ξp	fp	ξp
	0.0056	1.9496	0.0053	0.1%	-5.4%	0.2%	13.2%
	0.028	1.9509	0.0275	0.2%	-1.8%	0.2%	4.7%
1.9472	0.0557	1.9417	0.0556	-0.3%	-0.2%	0.2%	2.5%
	0.1114	1.9414	0.1093	-0.3%	-1.9%	0.5%	2.7%
	0.2228	1.9621	0.2276	0.8%	2.2%	1.3%	0.6%
	0.0053	5.7570	0.0052	0.0%	-1.9%	0.0%	1.9%
	0.0263	5.7560	0.0266	0.0%	1.1%	0.0%	0.8%
5.7573	0.0525	5.7581	0.0534	0.0%	1.7%	0.0%	0.6%
	0.105	5.7492	0.1042	-0.1%	-0.8%	0.1%	0.7%
	0.2101	5.7593	0.2107	0.0%	0.3%	1.3%	0.5%

				SSI-DA	ΓA method		
Pre	eset	ldei	ntify	Err	or(%)	standard ((%)	deviation
fp	ξp	fp ξp		error f	error ξp	fp	ξp
	0.0056	1.9460	0.0053	-0.1%	-5.4%	0.0%	5.7%
	0.028	1.9465	0.0285	0.0%	1.8%	0.1%	1.9%
1.9472	0.0557	1.9332	0.0570	-0.7%	2.3%	0.3%	1.9%
	0.1114	1.9472	0.1134	0.0%	1.8%	0.4%	1.3%
	0.2228	1.9453	0.2258	-0.1%	1.3%	0.2%	1.8%
	0.0053	5.7557	0.0053	0.0%	0.0%	0.0%	1.9%
	0.0263	5.7579	0.0264	0.0%	0.4%	0.0%	0.8%
5.7573	0.0525	5.7547	0.0530	0.0%	1.0%	0.1%	0.8%
	0.105	5.7519	0.1046	-0.1%	-0.4%	0.1%	0.6%
	0.2101	5.7719	0.2137	0.3%	1.7%	0.0%	0.7%

Table 4.2b Preset and identified values of system matrices for free decay response with 10%-noise added, $j\Delta t = 4096 \text{ x} 0.02 \text{ s} = 81.92 \text{ s}$. $\xi_h = 0.2228$, $\xi_\theta = 0.2101$

CASE		procet			SSI -C	OV			SSI -D	ATA	
ξp		preset	•	recov	ered	erro	r[%]	recov	ered	erro	r[%]
ver = 0.0056	K	397.0573 0	0 24.73	397.5447 0.0323	-0.0054 24.73	0.12%	0.00%	396.99 -0.01	-0.22 24.73	-0.02%	0.00%
tor = 0.0053	С	0.3616 0	0 0.0072	0.3514 -0.0009	0.0116 0.0072	-2.82%	0.57%	0.3594 -0.0038	0.0094 0.0073	-0.60%	1.30%
ver = 0.028	К	397.0573 0	0 24.73	397.2700 0.0000	0.1200 24.73	0.05%	0.00%	396.93 -0.02	0.23 24.73	-0.03%	0.00%
tor = 0.0263	O	1.808 0	0 0.036	1.8023 -0.0012	0.0013 0.0360	-0.32%	0.00%	1.8094 0.0006	-0.0006 0.0361	0.08%	0.40%
ver = 0.0557	K	397.0573 0	0 24.73	396.7300 -0.0700	-0.1700 24.74	-0.08%	0.04%	395.79 -0.03	0.49 24.74	-0.32%	0.04%
tor = 0.0525	С	3.616 0	0 0.072	3.6051 0.0029	-0.0034 0.0720	-0.30%	0.00%	3.6055 -0.0012	0.0073 0.0719	-0.29%	-0.15%
ver = 0.1114	K	397.0573 0	0 24.73	397.1800 0.0100	0.5900 24.74	0.03%	0.04%	397.16 0.02	0.33 24.75	0.02%	0.08%
tor = 0.105	С	7.232 0	0 0.144	7.2472 0.0012	-0.0074 0.1439	0.21%	-0.07%	7.2499 0.0052	-0.0001 0.1444	0.25%	0.25%
ver = 0.2228	K	397.0573 0	0 24.73	397.9101 -0.0098	1.9795 24.74	0.21%	0.04%	396.35 -0.11	0.83 24.74	-0.18%	0.03%
tor = 0.2101	С	14.464 0	0 0.288	14.5081 -0.0010	-0.0348 0.2886	0.30%	0.20%	14.5076 0.0052	0.0125 0.2896	0.30%	0.57%

4.7.2 Simulated response including the motion-induced forces

Next step in the simulation was a test with full effective stiffness and damping matrices (i.e. coupled degrees of freedom) and with lift and moment forces of the white noise type, as assumed in the SSI-method.

For the mean-wind speed equal to U=10.26~m/s, air density $\rho=1.18~kg/m^3$, and aerodynamic derivatives assumed according to the values reported for a similar bridge cross-section (see Jakobsen 1995), the effective stiffness and damping matrices, per unit length, were pre-set as:

$$C_e = \begin{bmatrix} 8.9308 & -0.0799 \\ 0.4345 & 0.0386 \end{bmatrix}, \quad K_e = \begin{bmatrix} 420.1002 & -59.1805 \\ 1.7552 & 19.6652 \end{bmatrix}, \quad M_0 = \begin{bmatrix} 2.6526 & 0 \\ 0 & 0.0189 \end{bmatrix}$$

The mass matrix was as in section 4.7.1. The response time-series were simulated with 10% turbulence intensity wind; then measurement white noises were superimposed on the simulated response.

Free decay (transient) response with noise corrupted

Preset and identified parameters are shown in Table 4.3, 4.4 and 4.5 for free decay responses to fix initial displacement with noise-free, 5% and 10% noise, respectively. Results are compared for those estimated by both SSI methods. Estimates of vertical frequency and damping by both methods are still excellence with precision within 1%. Estimates of the torsional frequency are still identical to the preset value while torsional damping are effected by noise added to less precision within 3% where estimated values from SSI-COV seemed to have more effected than SSI-DATA.

The stiffness and damping matrices estimated are also agree well with preset values with only few percent differences in noise-free case where most differences are in terms those related to A_4^* and . H_2^* . The noises added to the simulated signals are tentatively decreased the precision of these matrices. However, the precision of the diagonal terms still in good precision which are around 1% differences.

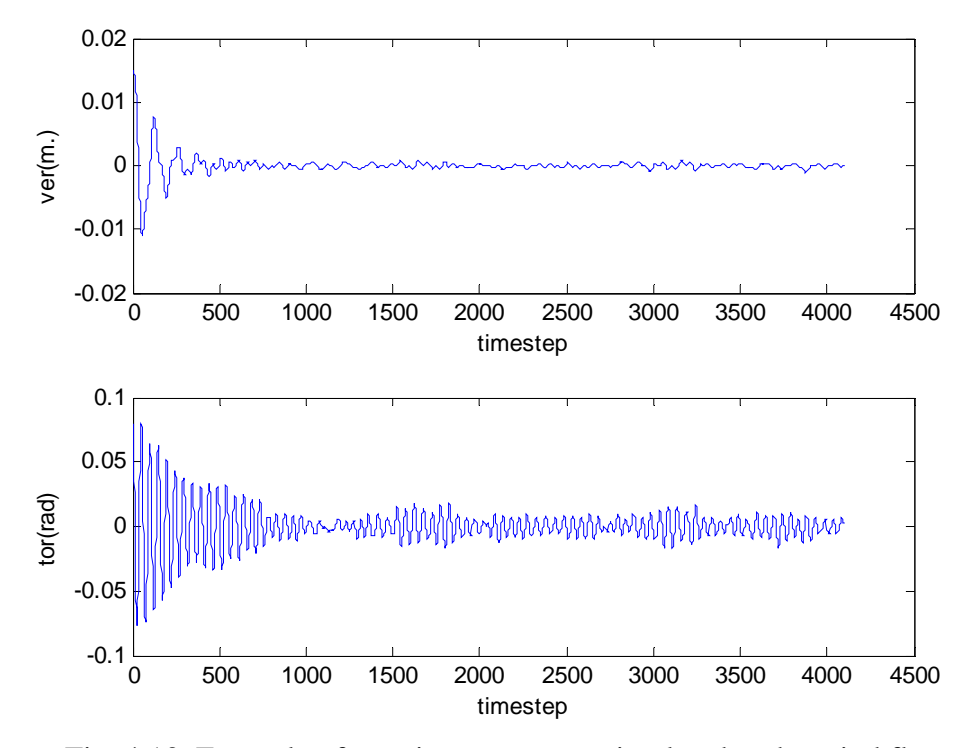


Fig. 4.13 Example of transient responses simulated under wind flow

Table 4.3 Preset and identified values of modal parameters and matrices for free decay response without noise added, $j\Delta t = 4096 \text{ x} 0.02 \text{ s} = 81.92 \text{ s}$.

			SSI -C	OV		SSI -DATA				
Pr	eset	Identi	fy	Error(%) Identify Error(9		r(%)				
fp	ξp	fp	ξp	error f errorξp		fp	ξp	error f	errorξp	
2.0157	0.1559	2.0152	0.1561	-0.04%	0.64%	2.0147	0.1552	-0.05%	-0.45%	
5.1332	0.0226	5.1351	0.0230 -0.04% -0.44%		-0.44%	5.1334	0.0229	0.00%	1.33%	

	pre	acat		SSI -	COV		SSI -DATA				
	preset		recovered		error[%]		recovered		error[%]		
K	420.1002	-59.1805	419.51	419.51 -59.15		-0.05%	419.99	-59.23	-0.03%	0.08%	
	1.7552	19.6652	1.83	19.65	4.26%	-0.08%	1.78	19.62	1.42%	-0.25%	
С	8.9308	-0.0799	8.9896	-0.0775	0.66%	-3.00%	8.8956	-0.0819	-0.39%	2.56%	
	0.4345	0.0386	0.4352	0.0385	0.16%	-0.26%	0.4363	0.0391	0.42%	1.24%	

Table 4.4 Preset and identified values of modal parameters and matrices for free decay response with 5% noise added, $j\Delta t = 4096 \text{ x} 0.02 \text{ s} = 81.92 \text{ s}$.

			SSI -	COV		SSI -DATA					
Pr	Preset		Identify		Error(%)		tify	Error(%)			
fp	ξp	fp	ξp	error f errorξp		fp	ξp	error f	errorξp		
2.0157	0.1559	2.0149	0.1569	-0.02%	0.13%	2.0142	0.1567	-0.07%	0.51%		
5.1332	0.0226	5.1312	0.0225	0.04%	1.77%	5.1295	0.0223	-0.07%	-1.33%		

	nro	sot		SSI -	COV		SSI -DATA				
	preset		recovered		error[%]		recovered		error[%]		
К	420.1002	-59.1805	2.0174	0.1564	-0.15%	0.02%	419.63	-59.09	-0.11%	-0.15%	
	1.7552	19.6652	5.1339	0.0232	7.11%	0.08%	1.71	19.64	-2.58%	-0.13%	
С	8.9308	-0.0799	8.9445	-0.0793	0.15%	-0.75%	8.9874	-0.0781	0.63%	-2.25%	
	0.4345	0.0386	0.4335	0.039	-0.23%	1.04%	0.4325	0.0381	-0.46%	-1.30%	

Table 4.5 Preset and identified values of modal parameters and matrices for free decay response with 10% noise added, $j\Delta t = 4096 \times 0.02 \text{ s} = 81.92 \text{ s}$.

			SSI -	COV		SSI -DATA				
Preset		Identify		Error(%)		Identify		Error(%)		
fp	ξp	fp	ξp	error f	errorξp	fp	ξp	error f	errorξp	
2.0157	0.1559	2.0149	0.1569	0.08%	0.32%	2.0131	0.1560	-0.13%	0.06%	
5.1332	0.0226	5.1312	0.0225	0.01%	2.65%	5.1327	0.0227	-0.01%	0.44%	

	preset		SSI -COV				SSI -DATA			
			recovered		error[%]		recovered		error[%]	
К	420.1002	-59.1805	421.15	-59	0.25%	-0.30%	418.51	-59.17	-0.38%	-0.02%
	1.7552	19.6652	1.64	19.67	-6.56%	0.02%	1.89	19.67	7.68%	0.02%
С	8.9308	-0.0799	8.9963	-0.0743	0.73%	-7.01%	8.9488	-0.0779	0.20%	-2.50%
	0.4345	0.0386	0.4302	0.0392	-0.99%	1.55%	0.4276	0.0386	-1.59%	0.00%

Buffet response

Finally, the response time-series were also simulated for the case of buffeting responses (without initial displacement) to check performance of both the SSI-COV and the SSI-DATA. The effective stiffness and damping matrices as well as Δt were taken as in the case of free decay; examples of response time-series are as shown in Fig. 4.14. Tests are performed for noise-free and 10%-noise added case. As predicted in theory, buffeting responses required longer recorded data to yield acceptable results. Tests with very short period of data as in transients response (N=4096) result in relatively large differences between preset and recovered values.

Buffet responses without noise corrupted

Table 4.6 displays estimated parameters by both the SSI-COV and SSI-DATA for N=20000 discrete time-stations in noise-free case. Several tests by varying simulated length were performed and the results show that parameters estimation are improved according to the time recorded until at N=20000 where estimated parameters are not much further improved beyond this point.

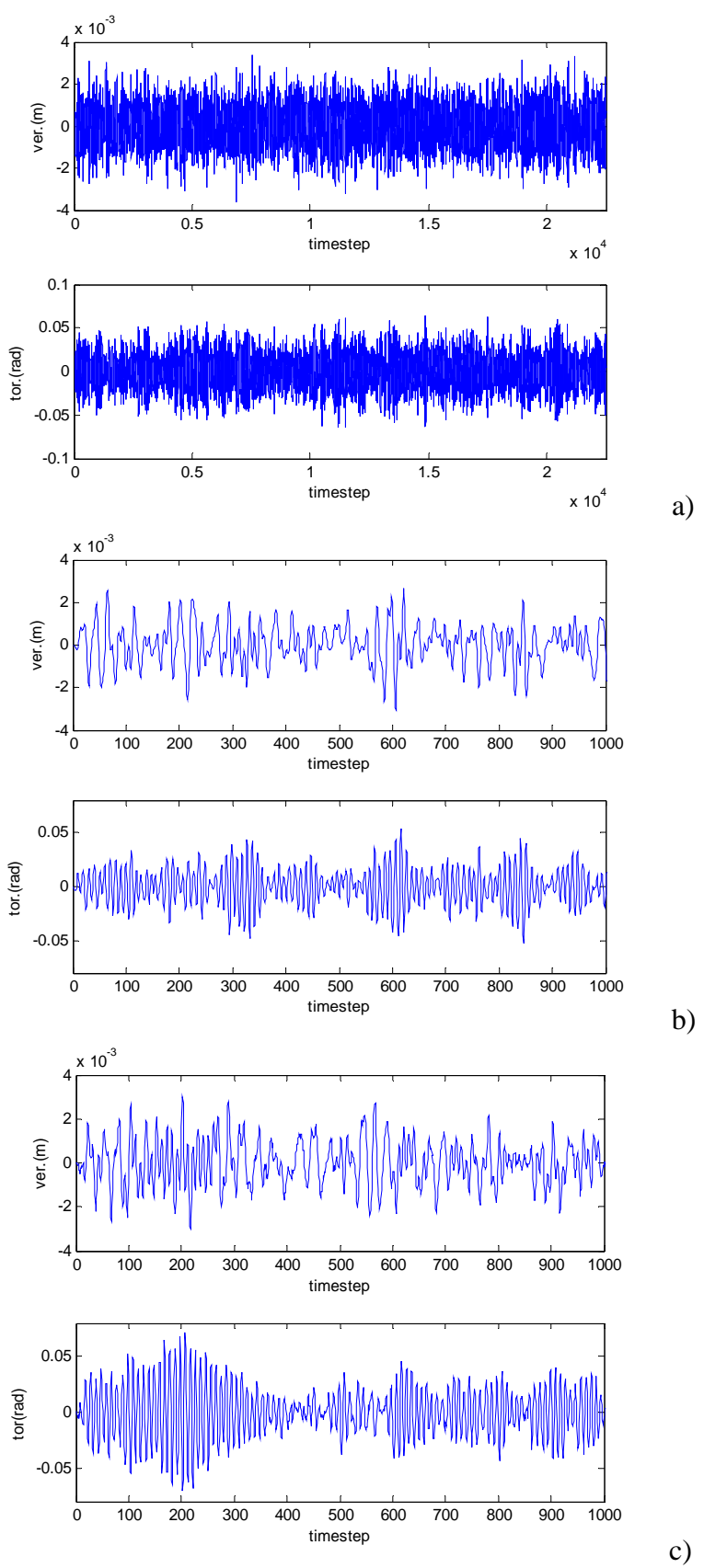


Fig. 4.14 Example of buffet responses simulated under wind flow; a) total response, b) part of response for noise-free case, c) part of response for 10%-noise added.

Table 4.6 Preset and identified values of modal parameters and matrices for buffeting response without noise, $j\Delta t = 20000 \text{ x} \cdot 0.02 \text{ s} = 400 \text{ s}$.

			SSI -	COV		SSI -DATA			
Preset		Ident	ify	Error(%)		Identify		Error(%)	
fp	ξp	fp	ξp	error f	errorξp	fp	ξp	error f	errorξp
2.0157	0.1559	2.0183	0.1585	0.13%	1.67%	2.0062	0.1562	-0.47%	0.19%
5.1332	0.0226	5.1326	0.023	-0.01%	0.44%	5.1336	0.0228	0.01%	0.88%

	preset		SSI -COV				SSI -DATA			
			recovered		error[%]		recovered		error[%]	
K	420.1002	-59.1801	421.54	-59.13	0.34%	-0.08%	420.62	-59.17	0.12%	-0.02%
	1.7552	19.6652	1.72	19.66	-2.01%	-0.03%	1.83	19.67	3.99%	0.03%
С	8.9308	-0.0799	9.156	-0.0745	2.52%	-6.76%	8.9972	-0.0774	0.74%	-3.12%
	0.4345	0.0386	0.431	0.0387	-0.81%	0.26%	0.4374	0.0390	0.66%	1.14%

Estimates of the frequencies and damping ratio by both methods agree well with preset values where precisions are within 0.5% and 2%, respectively. The diagonal terms in stiffness and damping matrices also agree well with preset values where differences almost in 1% except in case of C_{11} (related to vertical damping) estimated by the SSI-COV which is around 2.5%. The most differences in off-diagonal terms are K_{21} and C_{21} that relate to A_4 * and A_2 *, respectively.

Buffet responses with noise corrupted

Next, the measurement white noise were superimposed to the simulated responses under $\sim 10\%$ -turbulence wind flow. Sample of simulated signals with 10% noise added is shown in Fig. 4.13c. N and Δt are same as noise-free case except that 100 simulations are performed instead of 20 as in previous cases. Table 5.7 shows parameters estimated by both the SSI-DATA and the SSI-COV methods. Frequencies estimated from the SSI-DATA are practically identical to preset values with precision within 1% while damping estimatation are more affected by noise with precision within 4%. The frequencies precision estimated by the SSI-COV are more vulnerable to noise; the precision were reduced to within 3% in case of vertical. This effect is more pronounced in case of estimated damping ratio where large difference between preset and recovered values are seen especially in vertical mode as damping ratio is very high.

For stiffness and damping matrices estimation, the SSI-DATA shows more sustainable to noise added compared with the SSI-COV. For the SSI-DATA, the most differences between preset and estimated values are term relating to A_4 * and H_2 * as similar to those from noise-free case; maximum 5% for A_4 *-related term. In case of

the SSI-COV, not only term relating to A_4^* and H_2^* but also H_1^* were affected by noise added with relatively large differences from preset values.

These results show that the SSI-DATA are tentatively more sustainable to noise than the SSI-COV. The precision of estimated parameters are within few percents even when simulated signals were corrupted with large noise. Fig. 4.15 shows frequencies and damping ratio estimated by both SSI methods where more scatter are seen in vertical damping estimated by the SSI-COV.

Table 4.7 Preset and identified values of modal parameters and matrices for buffeting response with 10%-noise noise, $j\Delta t = 20000 \text{ x} \cdot 0.02 \text{ s} = 400 \text{ s}$.

			SSI -	COV		SSI -DATA				
Preset		Ide	ntify	Error(%)		Identify		Error(%)		
fp	ξp	fp	ξp	error f	errorξp	fp	ξp	error f	errorξp	
2.0157	0.1559	1.9557	0.133	-2.98%	-14.69%	2.0320	0.1597	0.81%	2.44%	
5.1332	0.0226	5.1392	0.021	0.12%	-5.31%	5.1292	0.0235	-0.08%	3.98%	

	preset		SSI -COV				SSI -DATA			
			recovered		error[%]		recovered		error[%]	
K	420.1002	-59.18	429.45	-58.95	2.23%	-0.38%	420.34	-59.20	0.06%	0.04%
	1.7552	19.6652	1.5591	19.66	-11.17%	-0.03%	1.86	19.67	5.74%	0.03%
С	8.9308	-0.0799	9.6940	-0.0576	8.55%	-27.86%	8.9964	-0.0782	0.73%	-2.16%
	0.4345	0.0386	0.4333	0.0388	-0.28%	0.50%	0.4392	0.0385	1.09%	-0.27%

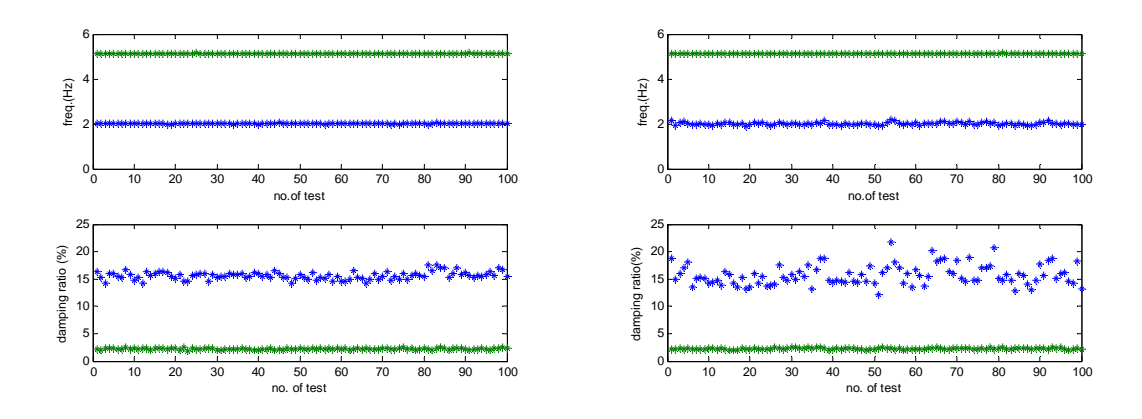


Fig. 4.15 Frequencies and damping ratio estimation results from 100 simulations: buffeting response with 10% noise added.

CHAPTER 5

INDUSTRIAL RING ROAD BRIDGE:

Prototype and Modeling

5.1 Description of the Bridge

5.1.1 Location

The Industrial Ring Road Bridges are part of the royally-initiated, the Industrial Ring Road Project, that aims to solve traffic problems within Bangkok and surrounding areas. The project comprises a new road and bridge network which links up the major industrial areas of Klong Toey Port, Pu Chao Saming Phrai Road in Samut Prakarn, Suksawad Road to the west and Rama III Road to the north. In future the system will link up to the southern ring road. The total length is around 25 kilometers (Fig.5.1). The outstanding and unique feature of the industrial Ring Road project is the two suspension bridges, one after another, crossing an oxbow in the Chao Phraya River. The bridges are designed with 173 meter tall diamond shaped pylons with double plane I-shape cable stays. The back spans of both bridges are of pre-stressed concrete while the main spans are steel/concrete composite deck structures. The main spans are 398 meters and 326 meters in length, for the South Bridge and the North Bridge (Fig. 5.2 and Fig. 5.3), respectively. The project is owned by the Department of Rural Roads, Ministry of Transport (formerly the Public Works Department, Minister of Interior) and funded by the Thai Government and loans from the Japan bank for International Cooperation (JBIC). Engineering is being undertaken by the Association of Consulting Engineers, a consortium of Asian Engineering Consultant Corp., Ltd., TEAM Consulting Engineering and Management Co., Ltd., Thai Engineering Consultant Co.,Ltd. Index International Group Co.,Ltd. and Jean Muller International.

5.1.2 Dimensioning Details

The North Bridge has a center span of 326 m and two side spans of 125.1 m each. To accommodate large vessels, navigation channel was required to be 220 m wide and 46.27 m high, necessitating the length of the center span of the bridge; which is designed as double-plane cable-stayed type. The deck is supported by two diamond shaped pylons, each 164 m in height (above sea level) which rest on bored pile foundations. These towers are constructed using reinforced concrete.

The South Bridge that used as prototype in this study has a center span of 398 m and two side spans of 155.6 m each. The navigation channel was 250 m wide and 50.50 m high. The deck is supported by two diamond shaped pylons, each 173 m

in height (above sea level) which rest on bored pile foundations. These towers are constructed using reinforced concrete as same as those of the North bridge.

The bridges are suspended from the pylons by three types of cable stay, with comprises of 61, 75 and 91 strands. Each strand itself composes of 7 cable quality strands with a HDPE sheath and wax coating. Fig. 5.2 and 5.3 gives an elevation of the bridges. The side spans of both bridges are of pre-stressed concrete while the main spans are concrete composite deck with I-shaped steel girders. The deck is supported by two cable planes. The deck was designed to accommodate 7-lane traffic with 35.9 m in width and the maximum height is 3.26 m. Fig. 5.4 shows the full scale dimensions of the deck of South Bridge. The tower details are as shown in Figs. 5.5. The mass and mass moment of inertia per unit length of the deck are 43000 kg/m and $4.11x10^9$ kg-m2/m, respectively.

There are three railings: one on each side of the deck and one at the center which will act as a traffic divide (three and four lanes on each side). The side railings are provided mainly as guard rails for the traffic. The railings are made of steel beams of circular cross section supported on steel columns placed on top of concrete barrier. Details are given in Fig. 5.6. The geometry described in this section and the dynamic characteristics mentioned in the following section are according to the initial design of the prototype-bridge (DMI, 1995).

5.2 Bridge Modeling

5.2.1 General

It is well established that careful bridge modeling plays an essential role in the wind resistant design of long-span bridges. Usually the design process begins with the selection of a deck configuration after fixing the dimensions of the deck width, span lengths, height of the tower and other bridge parameters. These are usually In order to verify whether the given governed by serviceability requirements. configuration of the deck is safe against flutter instability and exhibits acceptable levels of buffeting response, a section model and a full model of the bridge are often made. Sometimes, in addition to these models, a "taut-strip model" is also made. A description of the essential features of each of these models and their advantages and limitations may be found in Scanlan (1983), Hjorth-Hansen (1992), Davenport et al. (1992) and Irwin (1992). Since making a full model of the bridge is a time-consuming and expensive process, usually only a section model is made in the initial design stage. After appropriate modifications of the deck configuration are made, and deck design is finalized, a full model may be made and subjected to a properly scaled threedimensional turbulent flow for checking of the design. Making a section model is therefore usually the starting point for any wind-induced response analysis of flexible The next section will deal with the essential background needed to bridges. understand the section modeling technique and how the modeling features can possibly be improved so that the end result is a more accurate estimation of the prototype response.

Section Model

The primary purpose of this model is to establish that the proposed contour of the bridge deck has aerodynamically stable characteristics. Acceptance of a deck is based upon considerations of flutter stability and the impact of vortex-induced oscillations. Thus, a rapid check is first made on the preliminary design of the deck configuration. After establishing that the deck is aerodynamically acceptable, usually small modifications or any other added requirements are made to the deck for aesthetic reasons or other constraints that the bridge might need to satisfy. The section model also serves this intermediate design process by providing feedback as to whether or not these local changes render the deck aerodynamically unstable. The section model, in effect, is an analog simulator that reveals aerodynamic mechanisms affecting bridge stability and general response. After the final design of the deck is fixed, the section model serves as a means to investigate the static and dynamic forces expected on the prototype deck.

A section model represents a typical section of the bridge, including its proper degrees of freedom. It must duplicate faithfully, to scale, the local geometric forms and details of the prototype deck. In fact, it is in principle intended to represent the prototype *aerodynamically*, not simply geometrically. Two end plates are usually attached on each side of the section model parallel to the flow to reduce the end effects and enhance the two-dimensionality of the flow. The size of the end plates is usually decided based on the model dimensions. The model is then suspended from a set of springs configured so as to give the proper degrees of freedom, usually one (vertical or torsional) or at most two (vertical and torsional). With the increased importance of the sway motion in the context of very long cable-stayed bridges an additional along-wind or sway degree of freedom may be added. This requires an additional sway degree of freedom in experimental set up, however this is not usually the case.

The frequencies of oscillation of the model, determined by selecting the proper stiffness and spacing of the springs, should be decided very carefully and are chosen as discussed below. It is known from the principles of similitude (Simiu and Scanlan 1996) that the reduced velocities of the prototype $[U_r]_p$ and the model $[U_r]_m$ should match, which means

$$\left[U_{r}\right]_{m} = \left[\frac{U}{fB}\right]_{m} = \left[\frac{U}{fB}\right]_{m} = \left[U_{r}\right]_{p} \tag{5.1}$$

where f is the frequency (Hz). The non-dimensional flutter derivatives, the aerodynamic admittance functions and the normalized spectra of the buffeting forces are functions of the reduced velocity or reduced frequency (=fB/U). In some circumstances this may require that the ratios of all three frequencies (bending, torsion, sway) of the section model subjected to a coupled motion be close to unity, so that while estimating the flutter derivatives associated with different degrees of freedom, one can use anyone of the frequencies to calculate the reduced velocity.

For example, if the two frequencies are different for a two-degree-offreedom (vertical and torsional) model then an appropriate choice for calculating the reduced velocity would be to use the frequency associated with the vertical mode for the flutter derivatives $H_1^*, H_4^*, A_1^*, A_4^*$ and the frequency associated with the torsional mode for the flutter derivatives $H_2^*, H_3^*, A_2^*, A_3^*$. This implies that the range of flow velocities over which the model should be tested for a fixed range of reduced velocity will vary according to the associated oscillation frequency.

The purpose of the section model is to reliably duplicate the static or dynamic forces according to the velocity scaling and the geometric scaling. Since the static coefficients depend strongly on Reynolds Number - particularly in the lower range- it should be ensured that the scaled forces acting on the small details of the model are not too different from what they would be in the prototype. It can be shown that the prototype static force,

$$\left[F_{L,D}\right]_{p} = \left[F_{L,D}\right]_{m} \times \left[\frac{\lambda_{C_{L,D}}}{\lambda_{L}^{2}\lambda_{U}^{2}}\right]_{p} = \left[\frac{C_{L,D}^{m}}{\lambda_{L}^{2}\lambda_{U}^{2}}\right]$$

$$(5.2)$$

where

 $C_{L,D}$ are the static lift, drag coefficients, $F_{L,D}$ are the corresponding static forces, $\lambda_L = [B]_m / [B]_p$ is the geometric scale, $\lambda_U = [U]_m / [U]_p$ is the velocity scale and $\lambda_{C_{L,D}} = [C_{L,D}]_m / [C_{L,D}]_p$

where the subscripts p and m denote prototype and model, respectively. Thus, depending upon the Reynolds numbers holding in the field and in the wind tunnel, the $\lambda_{c_{L,D}}$ may be much different from unity (usually> 1). To overcome this difficulty, a cross section of modified shape and scaled area of its details relative to the prototype may be used. This procedure was used in the design of the railings of the IRR Bridge section model and is discussed in the next section.

5.2.2 Industrial Ring Road Bridge Section Model

A 1:90 geometrically scaled section model of the Industrial Ring Road Bridge (IRR Bridge) was constructed of wood. The width and the maximum depth of the model are 399 mm and 32 mm, respectively. The length of the section model was selected as 2260 mm to be compatible with the wind tunnel used (2.5 m width, Appendix B). All details were scaled down geometrically, with exception of some details such as edge parapets and railing. The walkway beneath the deck was not included in the model. A walkway with an open steel grid is judged to have negligible effect on the results as the walkway is behind the internal girders and the edge girder. Furthermore, it is partially covered by the flanges of the cross-girders.

The thickness of the deck slab, the internal girders and the edge girders were exaggerated in the model design as a pure geometrical scaling of these items would results in impractically the dimensions with too little stiffness. However, the

edge of the deck slab was modeled with correct thickness and the outer part of the bottom flange on the edge girders was also modeled correctly.

The inside was included in the exaggerated web thickness. For the internal girders the web thickness was given as same the bottom flange width. The cross girders were modeled with correct flange width and only slightly exaggerated web thickness. The dimensions of the model are shown in Fig.5.7

In order to simplify the production of the railings, the number of vertical posts were halved (two lumped into one) and the windward dimensions were doubled given the same wind area. The horizontal round elements in the railings were modeled to match the drag of the model item with that of the full-scale item such that

$$[C_D A]_n = [C_D A]_m \times FD / \lambda_L^2$$

where C_D is the drag force coefficient of the item and A is the projected area normal to wind, i.e. length x diameter. FD is a factor which indicates how well the drag forces match (it should be ideally equal to 1.0). In this process the two lower rail elements were lumped into one. Details of railings are outlined in next section.

All elements in the model were manufactured from wood, except the lower horizontal element in the railings and bottom plates of edge girders which were made from plastic wire mesh and aluminum.

In order to have sufficient vertical and torsional stiffness of the model a so-called"king-post" was installed. A king-post is a stiffening system composed of two posts and 16 gauges wires, see Figs. 5.8 and 5.9. As the king-post is symmetric from above and below the deck, and as it only consists of round members lift / vertical motion and moment / torsional motion are not influenced by the king-post.

The measured drag force coefficients are corrected for the increased drag caused by the king-post as described later in this study. The model cross section dimensions are shown in Fig. 5.7 and the section model is shown in Fig. 5.8 and 5.9. The design of the railings for the model needs further discussion.

Railing Design

It was difficult to make a geometrically scaled model of the railing because of the small dimensions involved: the smallest scaled dimension was 0.67 mm. Further, since the Reynolds number in the wind tunnel corresponding to this dimension was very small, the coefficient of drag would have changed significantly if a geometrically-faithful cross section of the railing had been used. The alternative was to use a replacement which was readily available and yet duplicated the aerodynamic and aeroelastic forces scaled according to the velocity and length scales only. It was decided to use a portion of a wire mesh for the railings. According to this, the numbers of vertical posts were halved (two lumped into one) and the windward dimensions were doubled given the same wind area. The horizontal round elements in the railings were modeled to match the drag of the model item with that of the full-scale item such that FD is closed to 1. The method for selecting a particular wire mesh size is demonstrated below:

$$[F_{D}]_{p} = [F_{D}]_{m} \times \left(\frac{U_{p}}{U_{m}}\right)^{2} \times \left(\frac{A_{p}}{A_{m}}\right)^{2} \times FD$$

$$\frac{1}{2} \rho U_{p}^{2} C_{D}^{p} A_{p} = \frac{1}{2} \rho U_{m}^{2} C_{D}^{m} A_{m}' \times \left(\frac{U_{p}}{U_{m}}\right)^{2} \times \left(\frac{A_{p}}{A_{m}}\right)^{2} \times FD$$

$$FD = \frac{\lambda_{L}^{2}}{\lambda_{C_{D}}} \times \frac{A_{p}}{A_{m}'}$$
(5.3)

where

 C_D^p and C_D^m are the static coefficients of drag as function of Reynolds number corresponding to prototype and model, respectively,

 U_p and U_m are the mean wind velocities acting on the prototype and model, respectively,

 A_n is the area of unit length of the prototype railing,

 A_m is the area according to geometric scale and A'_m is the area actually provided for the railing of unit length on the model, and

FD is a factor which indicates how well the drag forces match (it should be ideally equal to 1.0).

The wire meshes used to model these railings are shown in Fig. 5.7. The selection process for the wire mesh for railing is outlined below.

Design of Railing

The Reynolds Number for the prototype, $\Re e_p$, is $2.24 \times 10^4 < \Re e_p < 3.36 \times 10^6$ for a typical railing dimension of 168 mm and wind velocity ranging between 2 m/s and 30 m/s. For this range of $\Re e_p$ the static drag coefficient C_D^p is 1.20. The wire mesh selected has a wire diameter of 1.0 mm. If the velocity for the wind tunnel testing varies between 1 m/s to 10 m/s (typically) then the Reynolds number for the model $\Re e_m$ varies between 67 to 675. The drag coefficient for a circular cylinder C_D^m varies in the range 1.2 and 2.0 i.e., $1.0 < \lambda_{c_D} < 1.67$. Since $A_p = 0.703 \text{ m}^2$ per 2 m length of prototype railing, $A_m' = 58.37 \text{ mm}^2$ per 22.2 mm length of model railing and λ_L , = 1/90, then by using Eq. (5.3) it can be shown that FD varies between 0.89 and 1.48 where 1.48 corresponds to the highest velocity of the section-model tests. Thus, the values of FD and is close to one, as desired, especially at desired velocities.

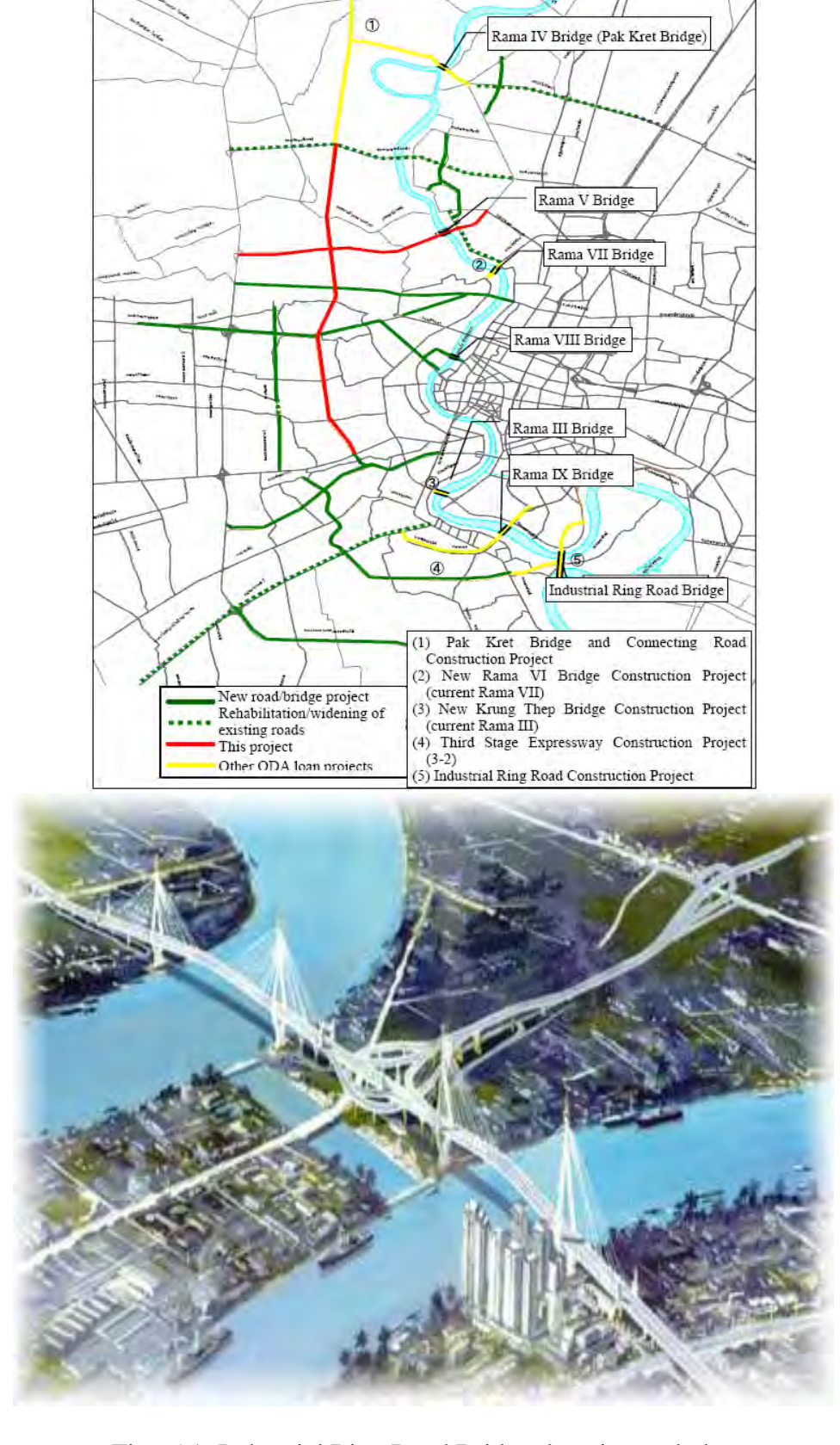
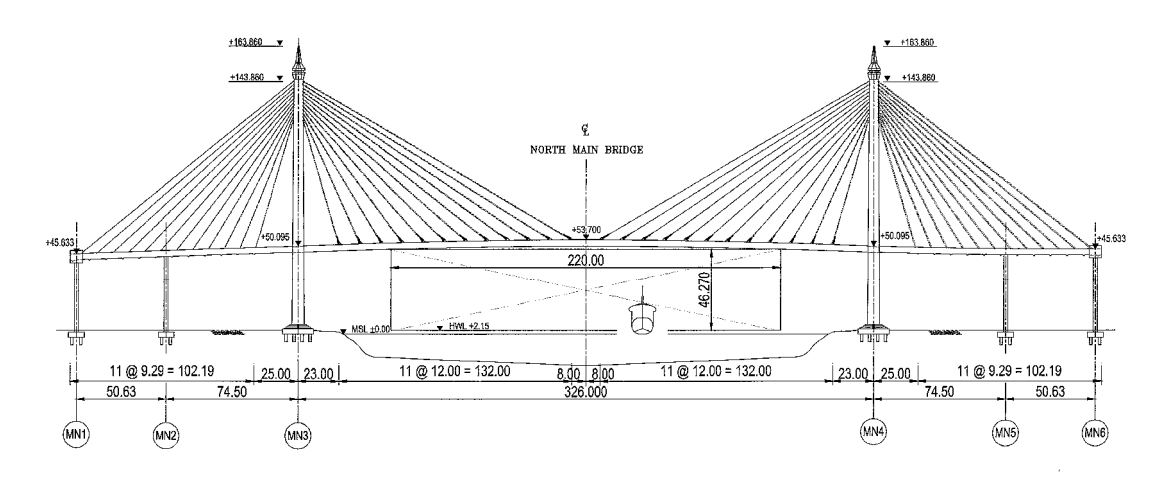


Fig. 5.1: Industrial Ring Road Bridge: location and plan



ELEVATION LAYOUT MN3 & MN4

Fig. 5.2 Industrial Ring Road Bridge: North Bridge Elevation

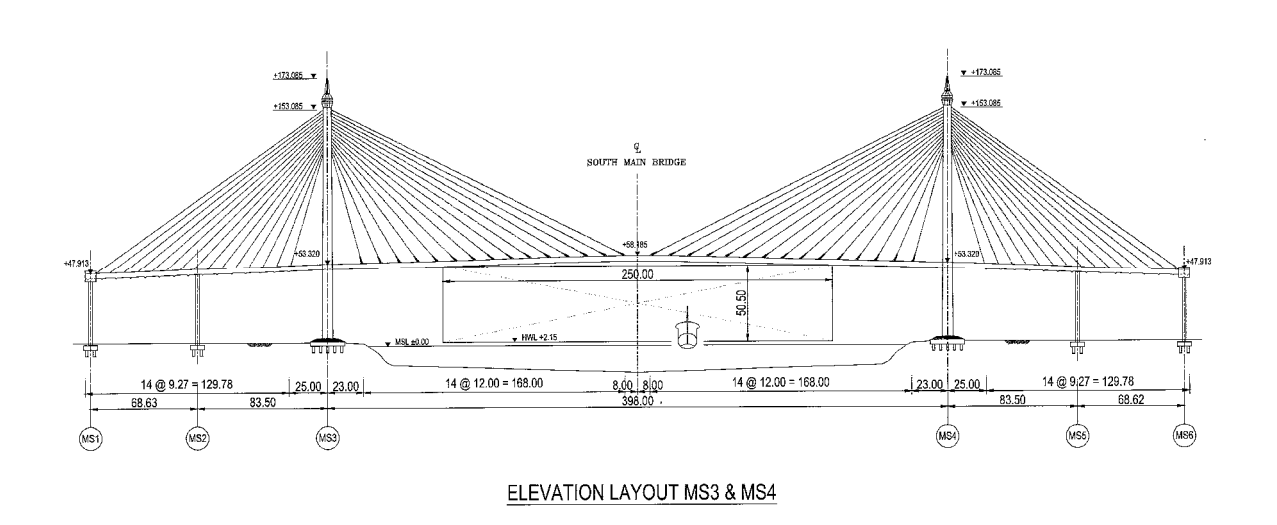


Fig. 5.3 Industrial Ring Road Bridge: South Bridge Elevation

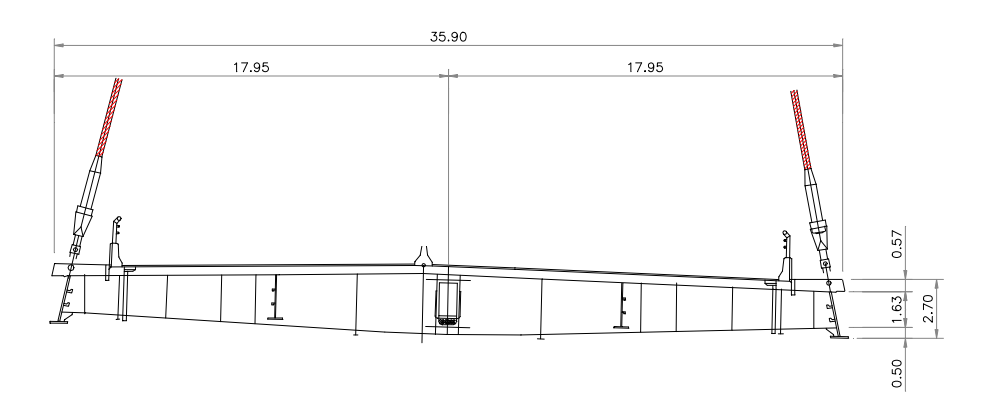


Fig. 5.4 Deck cross section of the South Bridge (unit in meter)

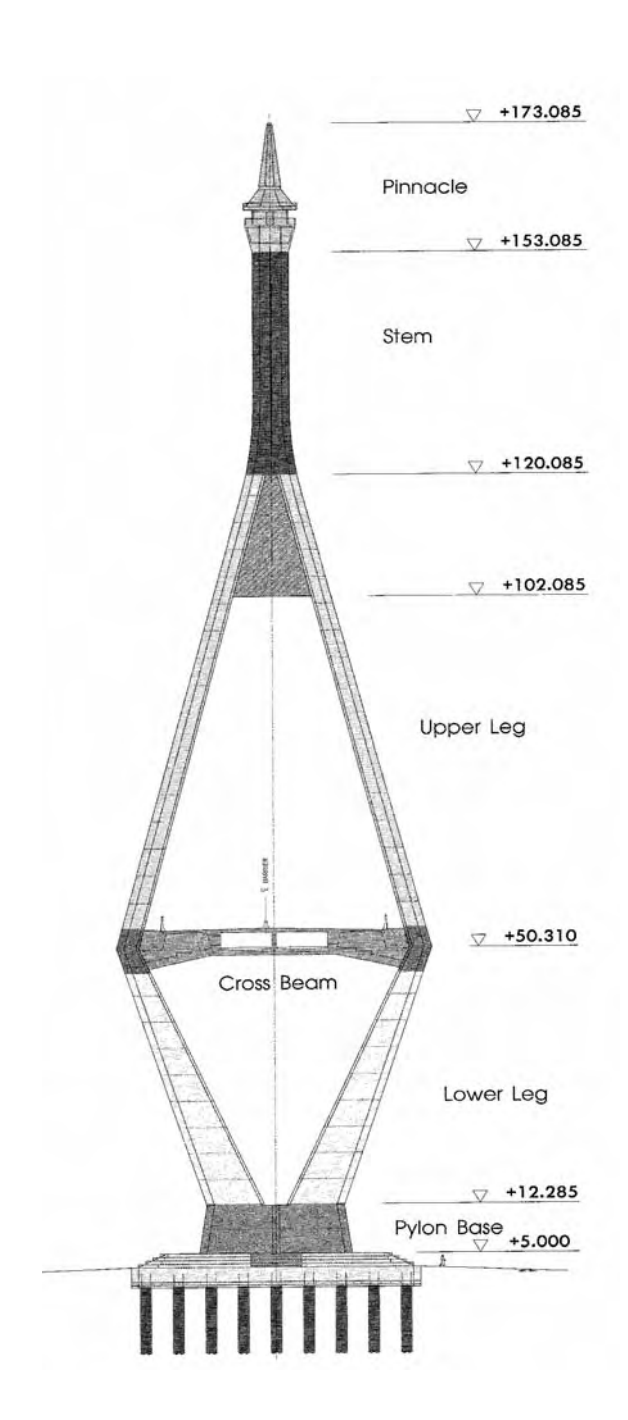


Fig. 5.5 Tower details of the South Bridge.

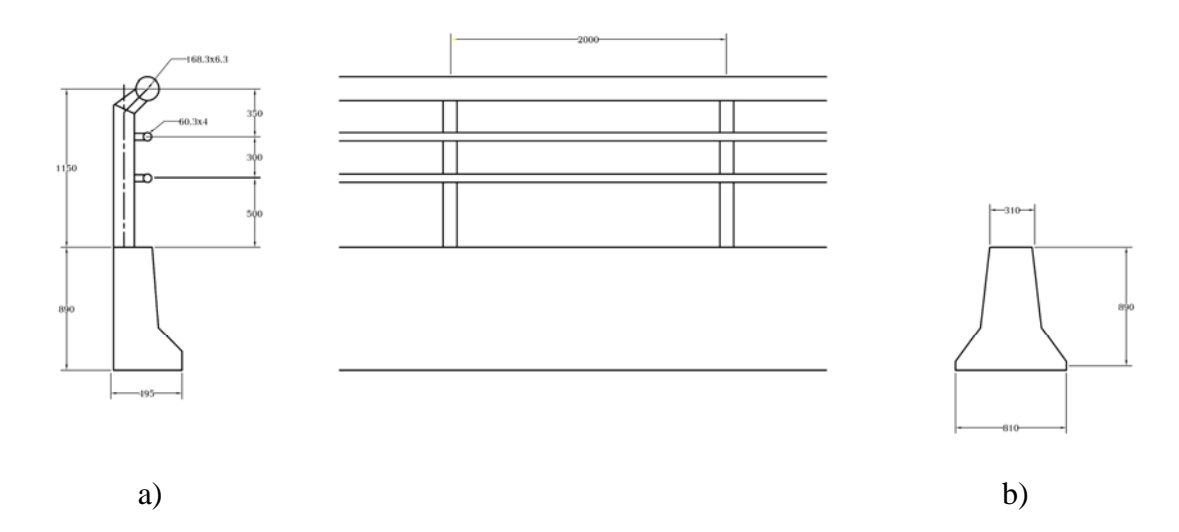
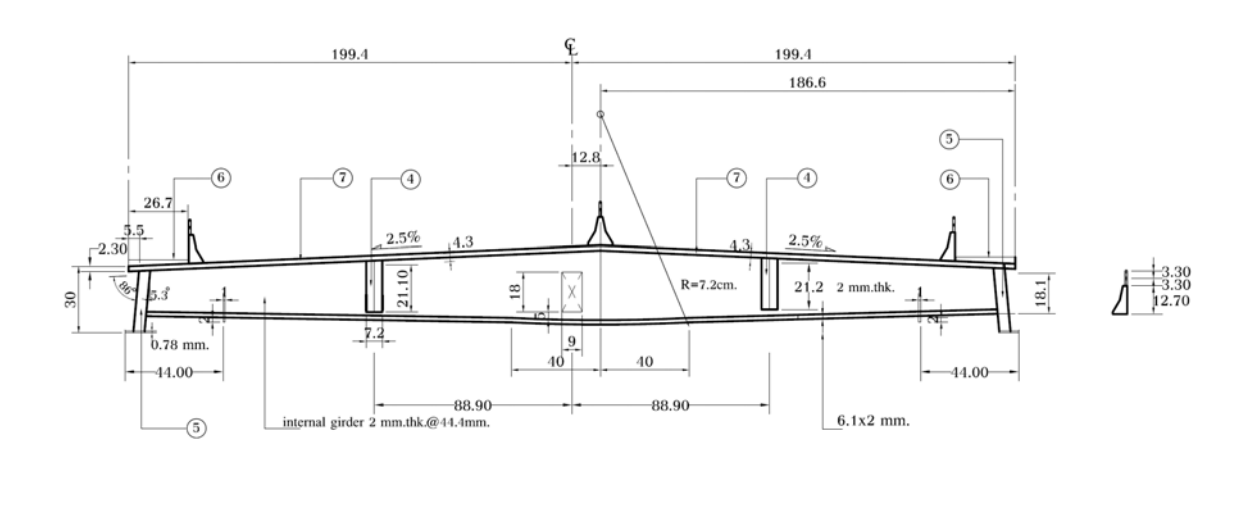


Fig. 5.6 Railing details of IRR-South Bridge : a) Side rail details b) center barrier



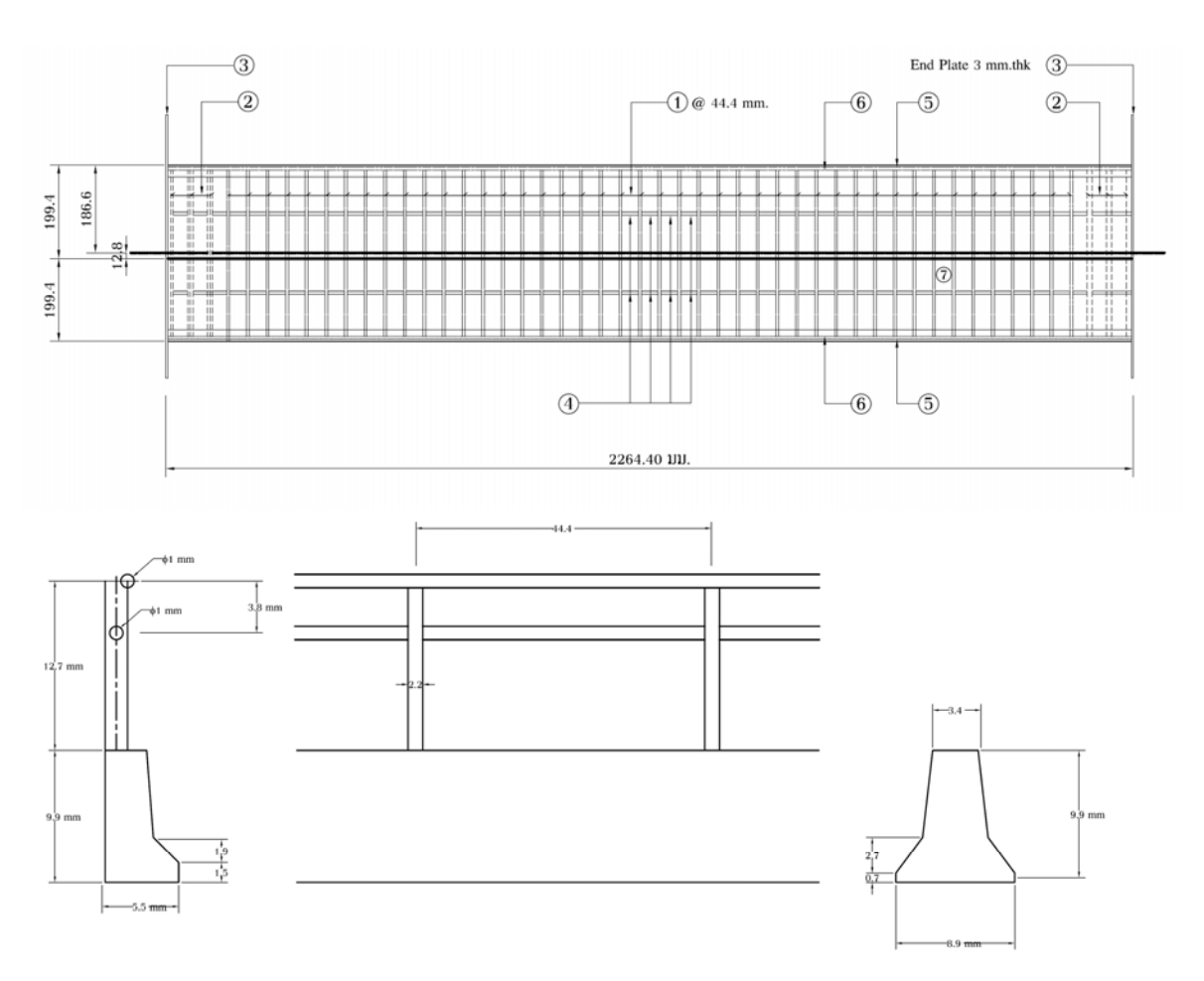


Fig. 5.7 Industrial Ring Road bridge: section model dimensions a) cross section, b) model dimensions c) rail dimensions



Fig. 5.8 The Industrial Ring Road Bridge: section model with king-post before the end plates installed. a) top of bridge b) bottom of bridge

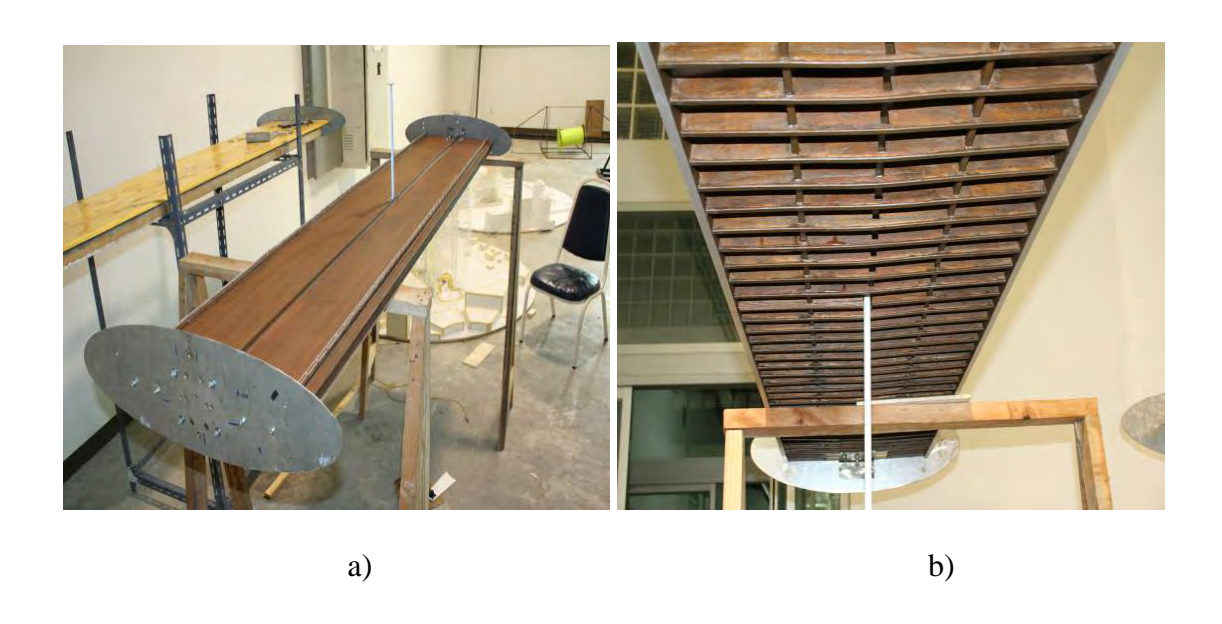


Fig. 5.9 The Industrial Ring Road Bridge after the end plates installed a) seen from above b) seen from below

CHAPTER 6

METHODOLOGY AND WIND TUNNEL TEST METHODS

The wind-tunnel experiments described in this chapter were conducted to extract the aeroelastic and aerodynamic parameters required for the analysis of the prototype bridge. All the flutter derivatives were found simultaneously from two-degree-of-freedom coupled-motion section-model tests using the system identification method described in the previous chapter. These tests were performed under both smooth and turbulence flows. Single-degree-of-freedom tests – vertical and torsional – were also performed to extract the direct flutter derivatives which were then compared with those found from coupled-motion tests. The static aerodynamic coefficients required to estimate the buffeting response were determined from fixed section-model tests under smooth and turbulent flows. In all the experiments performed under the turbulent flows the approximate two-dimensional turbulent flows were generated using grids and spires.

To evaluate the applicability of the present technique in flutter derivatives and aerodynamic coefficient estimation of bridge decks, wind tunnel tests of a quasi-streamlined thin plate model were first performed under smooth flow and results were then compared with the literature. Encouraged by the success in the thin plate model the flutter derivatives and the static aerodynamic coefficients of the IRR Bridge were estimated using the present technique.

6.1 Flow Conditions

The experiments were performed in the TU-AIT Wind Tunnel at Thammasat University. This tunnel is an open type wind tunnel with a cross-section of 2.50 m (width) x 2.50 m (height) and 22 m (length). A schematic diagram and additional details of the tunnel are given in Appendix A. The maximum wind speed is 20 m/s.

6.1.1 Smooth Flow

The section model was tested in smooth flow to determine the static load coefficients, the stability (flutter) limits, flutter derivatives and also to identify any potential vortex-shedding oscillations. The smooth flow was achieved with an empty wind tunnel. The turbulence intensities were measured with an x-wire hot-wire anemometer at the position of the section model which is approximately 4.0 m downstream from the wind-tunnel inlet. The turbulence intensities at the test section are of the order < 0.5 %. Figs. 6.1 and 6.2 show the mean wind speed and turbulence intensities across the tunnel section.

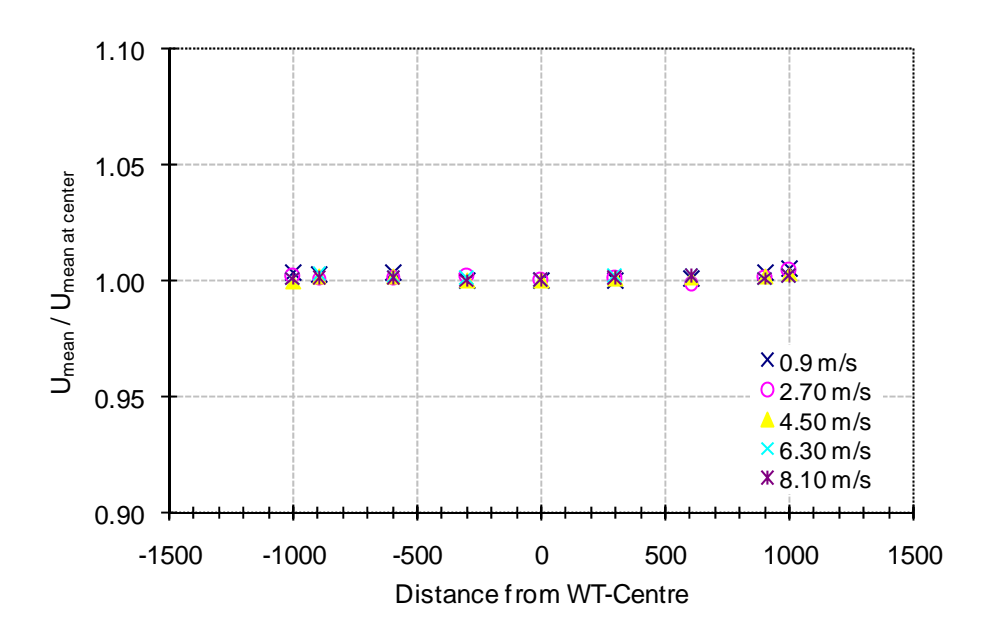


Fig. 6.1 Mean wind speed across the wind-tunnel section: smooth flow.

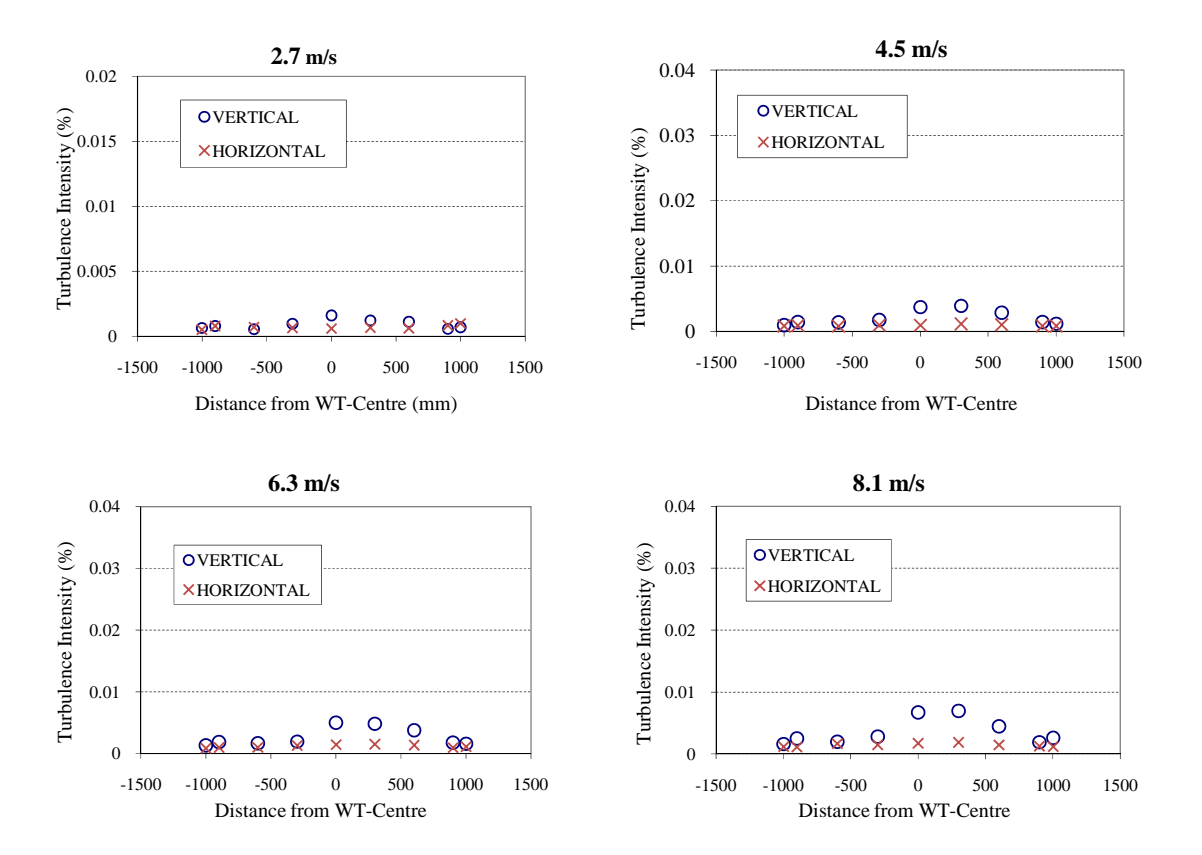


Fig. 6.2 Turbulence intensities across the wind-tunnel section: smooth flow.

6.1.2 Turbulence Flow

The IRR Bridge section model were also tested to determine the static load coefficients, the stability (flutter) limits, flutter derivatives and to identify any potential vortex-shedding oscillations in two turbulent flows. The lower turbulence intensity was achieved by installing three spires at the wind-tunnel inlet. The spires are triangular-shape with 1.8 m high, and the width is 0.35 m at the base. The position and dimensions of the spires are shown in Fig. 6.3. The horizontal velocity profile across the tunnel section of the mean wind speed and turbulence intensities were measured and shown in Figs. 6.4 and 6.5. The measured longitudinal and vertical turbulence intensities at the model deck level were 5.2% and 5.1%, respectively. In this study this turbulence referred to as "5%-turbulence".

The measured velocity spectrums have been fitted with both the Kaimal-and von Kármán-type spectra as (Strømmen 2006):

Kaimal spectra

For longitudinal component:

$$\frac{f S_u(f)}{\sigma_u^2} = \frac{6.8 \,\hat{f}}{\left(1 + 1.5 \cdot 6.8 \,\hat{f}\right)^{5/3}}$$

For vertical component:

$$\frac{f S_w(f)}{\sigma_w^2} = \frac{9.4 \,\hat{f}}{\left(1 + 1.5 \cdot 9.4 \,\hat{f}\right)^{5/3}}$$

Kármán spectra

For longitudinal component:

$$\frac{f S_u(f)}{\sigma_u^2} = \frac{4 \hat{f}}{\left(1 + 70.8 \hat{f}^2\right)^{5/6}}$$

For vertical component:

$$\frac{f S_w(f)}{\sigma_w^2} = \frac{4\hat{f} \left(1 + 755.2\hat{f}^2\right)}{\left(1 + 283.2\hat{f}^2\right)^{11/6}}$$

where $\hat{f} = f L_n / U$ and L_n is the integral length scale of the relevance turbulence component.

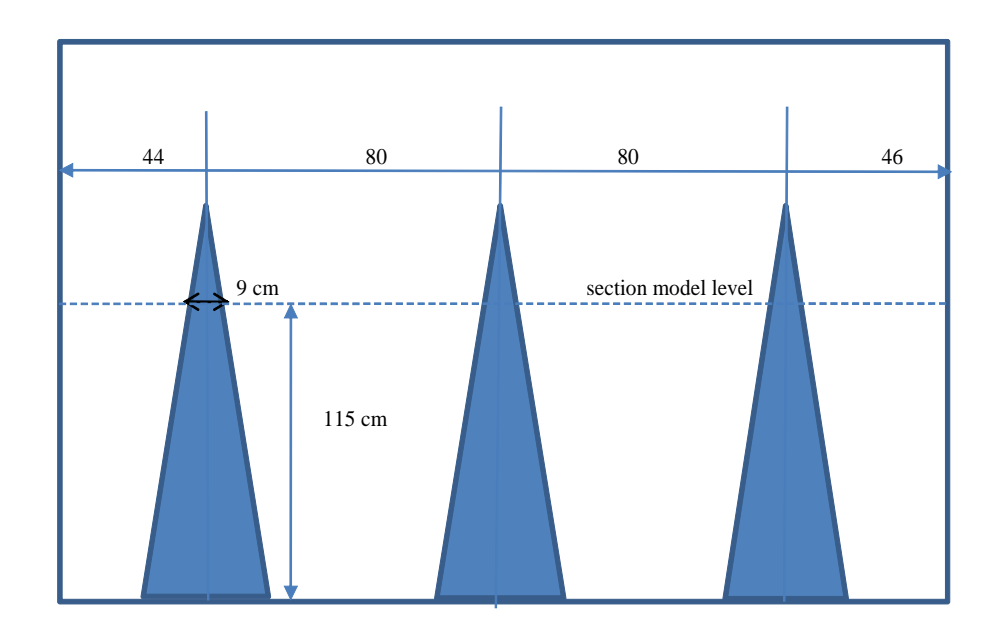


Fig 6.3 Spires in the wind tunnel. (dimension in centimeters).

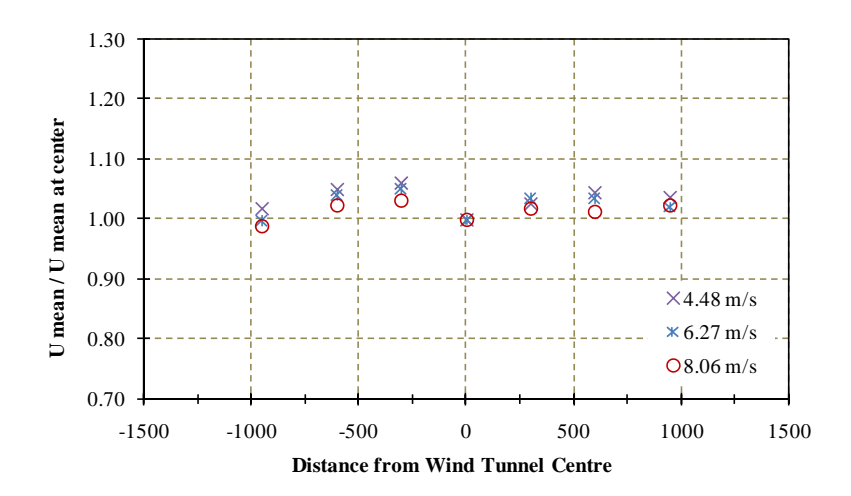
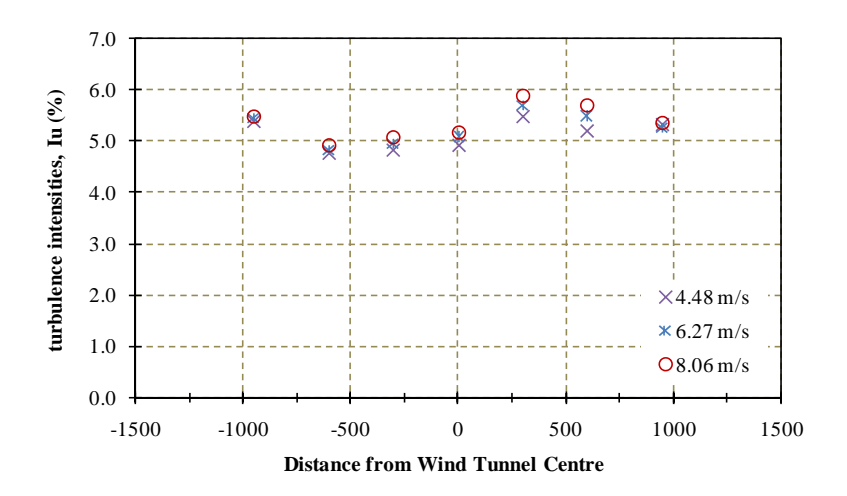
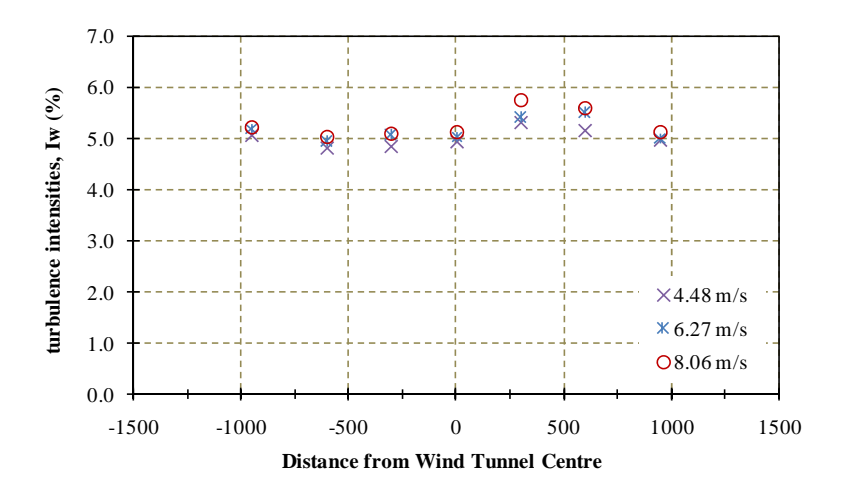


Fig 6.4 Horizontal mean wind speed profiles at the section model position: 5%-turbulence flow.



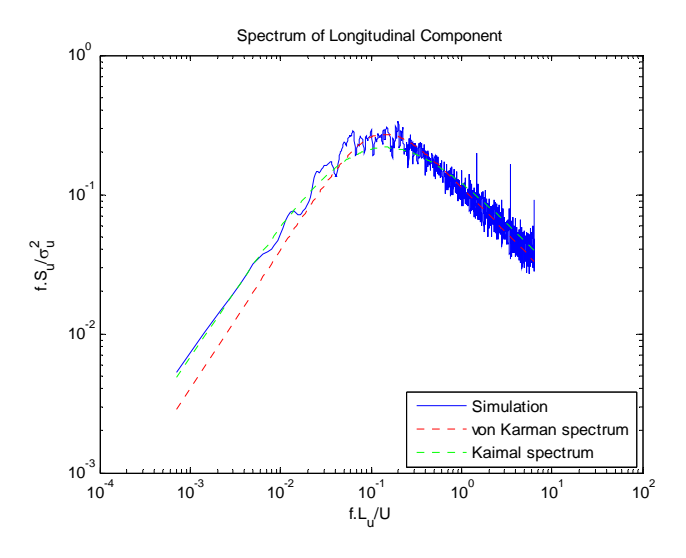
a) Longitudinal turbulence



b) Vertical turbulence

Fig 6.5 Turbulent flow intensities across the wind tunnel section at the section model position: 5%-turbulence flow.

Fig. 6.6 .shows the longitudinal and vertical measured spectra of the 5%-turbulence flow.



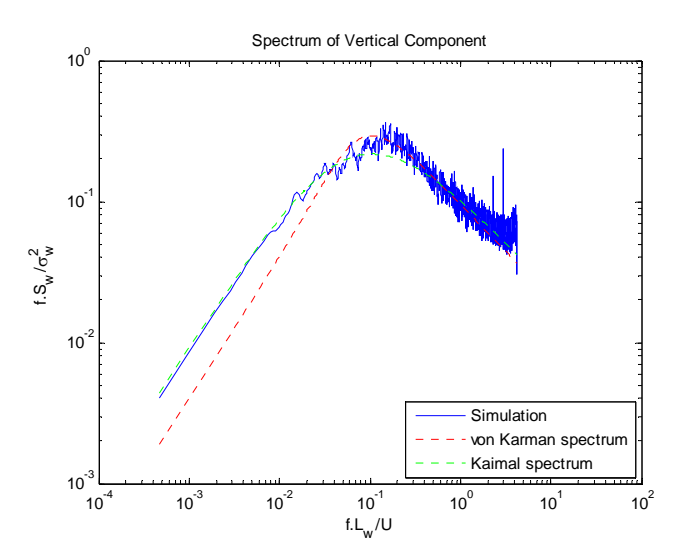


Fig 6.6 Normalized power spectra of the longitudinal and vertical velocity component: 5%-turbulence.

The higher turbulence was obtained by placing a grid at 0.5 m downstream of the spires. The grid is illustrated in Fig. 6.7. The mean wind speed and the turbulence intensities were measured prior to the tests. The results are shown in Figs 6.8 to 6.10. The measured longitudinal and vertical turbulence intensities at the model deck level were 7.9% and 7.0%, respectively. In this study, this turbulence referred to as "8%-turbulence". The measured velocity spectra have been fitted with both the Kaimal-and von Kármán-type spectra as (Strømmen, 2006) as shown in Figs. 6.9 and 6.10.

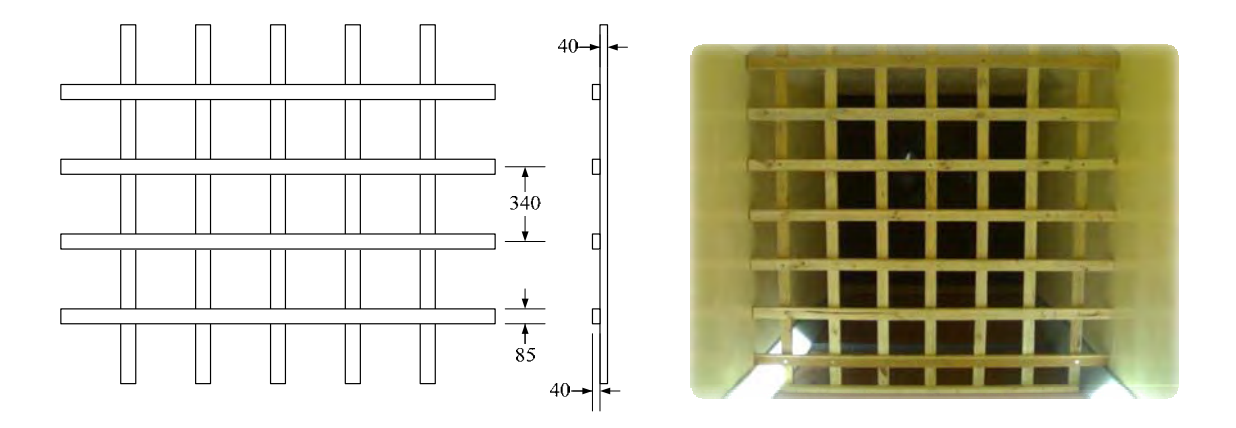


Fig 6.7 Schematic of the turbulence-generating grid: a) dimensions in mm. and b) after installation

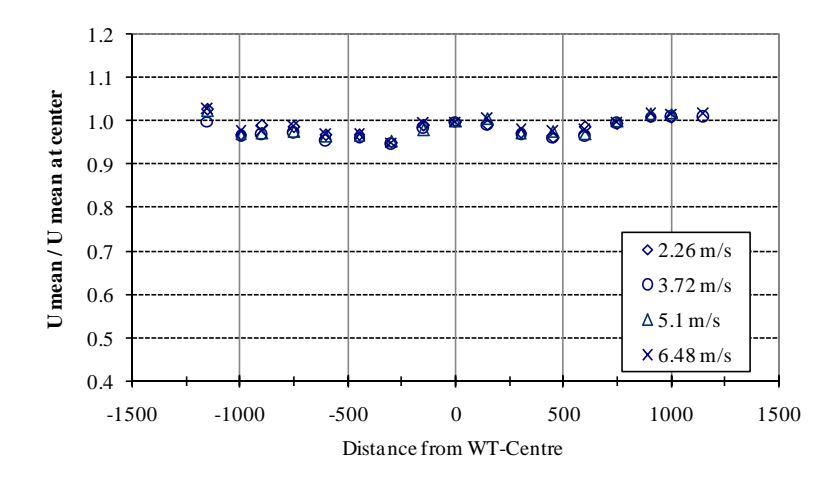
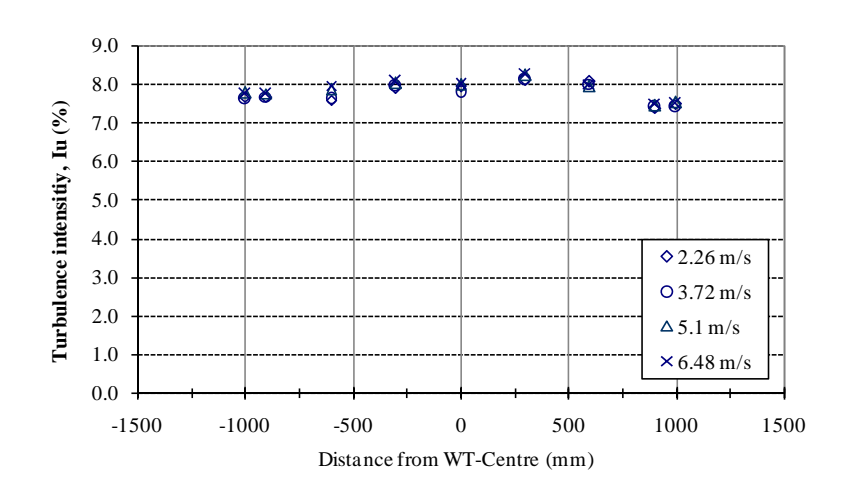
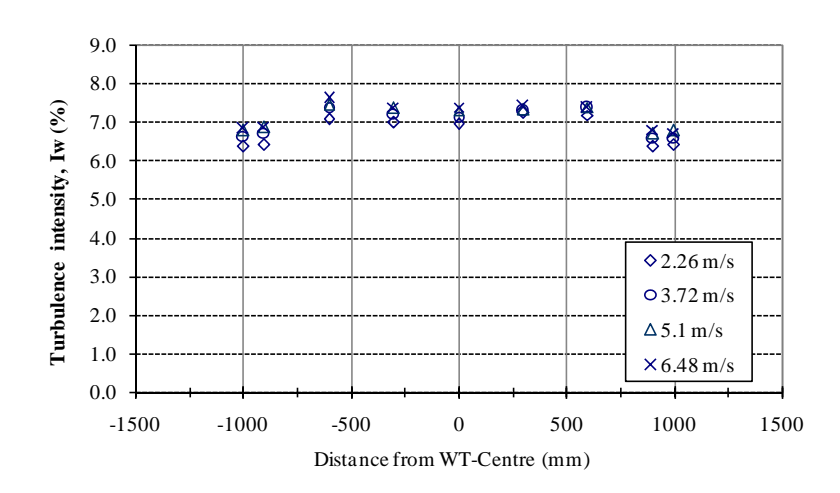


Fig 6.8 Horizontal mean wind speed profiles at the section model position: 8%-turbulence flow.

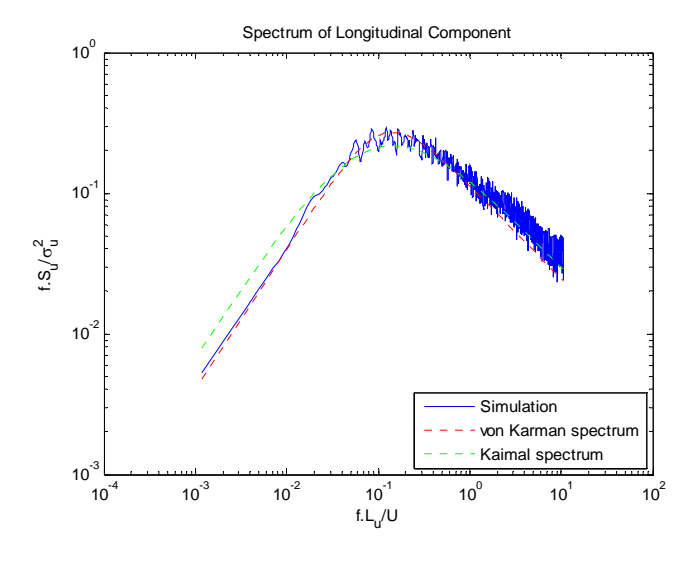


a) Longitudinal turbulence



b) Vertical turbulence

Fig 6.9 Turbulent flow intensities across the wind tunnel section at the section model position: 8%-turbulence flow.



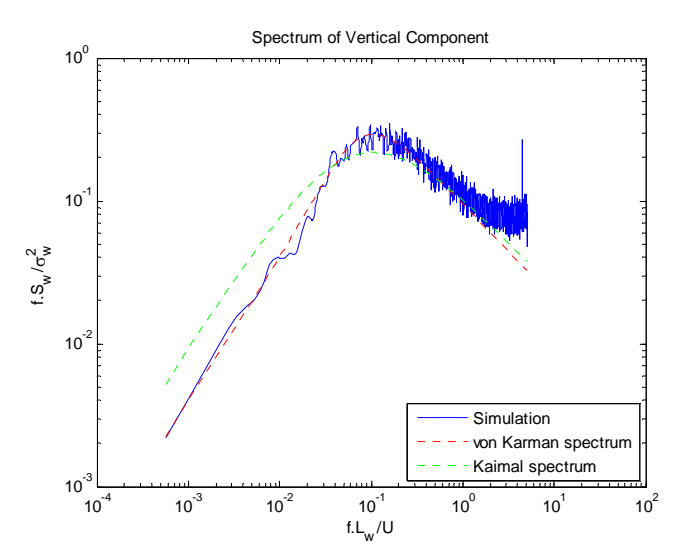


Fig 6.10 Normalized power spectrum of the longitudinal and vertical velocity component: 8%-turbulence.

6.2 Test Procedures

The streamlined thin flat plate which main parameters are shown in Table 6.1 were firstly tested under smooth flow. The width-to-height ratio is equal to 22.5. The experiments can be classified in the following categories:

(i) Single-degree-of-freedom vertical- or torsional-motion tests to extract the direct flutter derivatives under smooth flow.

- (ii) Coupled-motion two-degree-of-freedom vertical and torsional motion tests to extract both the direct- and cross-flutter derivatives under smooth flow by both initial (free decay) and without initial displacement (buffeting) methods.
- (iii) Fixed section-model tests under smooth flow to determine the static aerodynamic coefficients (C_D , C_L , C_M) with angles of attack vary from -12° to +12° in steps of 3°.

Tests i) and ii) were performed in the dynamic rig. Test iii) were performed in the static rig. The wind tunnel equipments and the test procedures are described in Appendix B.

Having success in verification of the streamlined thin flat plate model, the bridge model under study was of the IRR Bridge, details of which are given in chapter 5. The main parameters are shown in Table 6.2. The experiments were performed under smooth and two turbulence flows included

- (i) Coupled-motion two-degree-of-freedom vertical and torsional motion tests to simultaneously extract both the direct- and cross-flutter derivatives under smooth flow by both the free decay and the buffeting methods and only the buffeting method under two turbulence flows.
- (iii) Fixed section-model tests under both smooth and two turbulence flows with angles of attack vary from -12° to $+12^{\circ}$ in steps of 3° .

Table 6.1 Main parameters of the quasi-streamlined thin plate model

Parameter	Mark	Unit	Value
Length	l	m	2.30
Width	В	m	0.45
Height	H	m	0.02
Mass per unit length	M	kg/m	6.7391
Inertial moment of mass per unit length	J_m	$kg m^2 / m$	0.11832
Inertial radius	R	m	0.1325
First bending frequency	f_h , n_I	Hz	1.65
First torsional frequency	f_{α} , n_2	Hz	2.73
First torsion-bending frequency ratio	${\cal E}$		1.65

Parameter	Mark	Unit	Prototype	Value
Length	l	m	-	2.26
Width	B	m		0.399
Height	H	m		0.032
Mass per unit length	M	kg / m	43000	5.6801
Inertial moment of mass per unit length	J_m	$kg m^2 / m$	4.11x10 ⁹	0.17262
First bending frequency	f_h , n_I	Hz	0.376	2.13
First torsional frequency	f_{α} , n_2	Hz	0.850	4.73

Table 6.2 Main parameters of the IRR Bridge section model

6.3 Experimental Configuration

2.26

2.22

 ε

6.3.1 Static Tests

First torsion-bending frequency ratio

The section model was installed about its centre of rotation in the static rig inside the wind tunnel. The force gauges of the static rig were connected to a data-acquisition PC through amplifiers and filters. Samplings were performed at $200 \ Hz$ and the signals are filtered at $10 \ Hz$.

Two six-components force gauges (JR3 sensor, Model No. 45E15) were used. Each sensor was installed at both ends of section model and connected to External Electronic Box of JR3 sensor by a special cable provided. Overload Alarm & Power supply were also connected to External Electronic Box. Analog signals from External Electronic Box were then passed through analog amplifiers and filter, digitized by A/D converter and stored in PC by special software (LabView).

The force gauges were calibrated in order to establish the relation between the Volt signals read on the PC and the forces on model. Since the sensor is a six-component load cell, all six components in directions (+ve and -ve) (total of 12 calibrations) was individually calibrated to determine calibration matrix. This was performed with calibration apparatus designed to apply each component of forces (total 12) almost purely as shown in Fig. 6.1. The calibration was performed under 3 load (or moment) level. Once the calibration was finished, the calibration matrix is calculated using regression analysis.

After the model installation was completed, calibration of force gauges was again conducted to confirm accuracy of test-setup and the calibration matrix. This is because the JR3-sensor is very sensitive to tightening force. The drag forces were calibrated by pulling the model in the along-wind direction with known masses, using a string attached to the model centre and run over a pulley mounted at the corrected height for a horizontal pull. The lift forces were calibrated by hanging known masses to the model. The torsion forces were calibrated by applying known masses at fix distance from centre of the model. This set-up results in both torsion and vertical force readings. The applied moment is calculated as the applied masses times the distance (arm) from the center of rotation of the model to the point of load application.

The basic arrangement for the fixed section-model tests (static rig) consisted of the following:

- (i) Two force gauges (JR3 sensors) to which the section model could be fixed via hollow cylinder arms. These arms are made of aluminum with smooth surface.
- (ii) Data acquisition system consisted of External Electronic Box, Overload Alarm & Power supply, Analog amplifier and filters, A/D converter and PC.

The instrumentation and other equipments which were common to both suspended-model (dynamic rig) and fixed-model (static rig) tests are listed below.

- (i) A pitot tube connected to pressure sensors and data acquisition systems consisting of a personal computer and Analog to Digital Converter. The pitot tube was kept downstream of the model along the center line of the tunnel and was used to measure the mean wind velocity of the flow. Also the mean wind speed was recorded using "Hot-sphere" type wind anemometer.
- (ii) A multichannel data acquisition systems supported by a PC and data acquisition software.
- (iii) A set of grids and spires, one of which could be inserted upstream of the model to generate a two-dimensional turbulent flow.
 - (iv) A hot-wire anemometer to measure the turbulence intensities of the flow.

Full descriptions of the set-up and instrumentation are given in Appendix B.

6.3.2 Dynamic Tests

The section model was installed in the dynamic rig about the centre of rotation of the section. The basic set-up for the suspended-model tests consisted of the following:

(i) The section model, suspended from a set of four supports with upper and lower springs at each support, thus it can oscillate vertically and in torsion (about a transverse axis). Piano wires were used to arrest the motion of the model in the alongwind direction. The vertical length of the spring can be adjusted to set proper vertical frequency. The torsional frequency is set by adjusting spacing between the springs at

each end of the model. In case of single-degree-of-freedom tests, additional wires were used to arrest one of vertical or torsional motion and allow another motion.

(ii) An electromagnetic release system which could be operated from outside the tunnel to give an initial vertical or torsional (or both) displacements to the model.

The instrumentation which used in tests besides those common with static tests are listed below.

- (i) The laser displacement sensors were used in recording displacement time histories of the model. The laser displacement sensor consisted of sensor head and control block. The sensor head was attached on fix-frame at a distance from measured object. This distance is depended on type and model of sensor. Two laser used are KEYENCE LB300 with measured displacement range of \pm 100 mm and the resolution of 50 μ m. Each sensor was set up at equal distance from the center of rotation.
- (ii) Two acceleration transducers were used in recording acceleration time histories at the mid-section of the model. The acceleration sensor consisted of the acceleration transducer model AS-2GB, the PCD 300A sensor interface and control software. The transducer has almost constant frequency response (within $\pm 5\%$) up to 80 Hz.

Full descriptions of the set-up and instrumentation are given in Appendix B.

6.4 Determination of Stiffness, Mass and Mass Moment of Inertia

After the bridge section model was completely set in the dynamic support system with the piano wires limited the along wind motion. Then the mass and the mass moment of inertia have to be determined. It was necessary to determine the vertical and torsional stiffness, mass and mass moment of inertia of this system. If a mass m_i is added to the model along its centerline (so that the center of mass does not displace), the frequency of vertical oscillation (ω_{hi}) of the model assembly with the added mass m_i is given by

$$\omega_{hi}^2 = \frac{K_h}{m + m_i} \tag{6.1}$$

where K_h and m are the vertical stiffness and mass of the model assembly, respectively. Eqn. (6.1) can be rewritten in the form

$$\frac{1}{\omega_{hi}^2} = \frac{1}{K_h} m_i + \frac{m}{K_h} \tag{6.2}$$

By the linear least-squares method, m and K_h can be determined using different values of m_i and recording ω_{hi} . The vertical motion is then restrained at the center of mass and the above procedure is repeated to obtain torsional frequencies, $\omega_{\alpha i}$, corresponding to different added mass moment of inertias (I_i) to the assembly. The increment in mass moment of inertia of the assembly could be obtained by adding known weights at fixed distances from the model centerline. Using an equivalent form of Eqn. 6.2 the torsional stiffness (K_{α}) and mass inertia (I) of the model assembly can be found as

$$\frac{1}{\omega_{\alpha i}^2} = \frac{1}{K_{\alpha}} I_i + \frac{I}{K_{\alpha}} \tag{6.3}$$

6.5 Flutter Derivative Identification

In order to determine the flutter derivatives of bridge decks, the following procedure was followed:

The coupled motion test with initial displacement method (the free decay method)

- (i) The section model was given a fixed initial displacement both in heave and pitch responses for the coupled motion tests using the electromagnetic release system. The voltage outputs of the lasers (KEYENCE LB-300) and accelerometers were recorded simultaneously at zero wind speed (U =0) using the data acquisition system. The calibration factor of these instruments can then be used to determine heave and pitch responses from these voltage outputs. Typical acceleration time histories for a representative coupled motion at U = 0 are given in Figs. 7.5 and 7.19a for the thin plate and the IRR bridge section respectively.
- (ii) The approximate natural frequencies were ascertained using the spectrum analyzer (FFT) program. This was performed for preliminary checking of results before more advanced and detailed analysis, the SSI-DATA and the SSI-COV method, were used in flutter-derivative extraction.
- (iii) The mechanical stiffness and damping matrices of the two-degree-of-freedom system were then found from the free vibration time histories of h(t) and $\alpha(t)$ at U=0 using both the SSI-DATA and the SSI-COV methods. Since the values of these matrices in the wind-off condition was very important, this step was repeated several times to ensure consistency of results. An average of stiffness and damping matrices was obtained whenever the results varied slightly (maximum 10%) because of experimental errors.
- (iv) Steps (i) (iii) were repeated but for non-zero wind speed values. The only difference was that at a particular wind speed, the effective stiffness and damping matrices of the system were found instead of their purely mechanicals counterparts. Typical acceleration time histories of heave and pitch responses for thin plate are

plotted in Figs. 7.7. Fig 7.19 shows samples of acceleration time histories of the IRR Bridge section model at various wind speed.

(v) The effective (wind-on) stiffness and damping matrices for a two-degree-of-freedom system and the mechanical ones (wind-off) provides the necessary data to estimate all the flutter derivatives at a particular reduced velocity value. Both the modal frequencies (vertically and torsionally) were used to calculate two sets of flutter derivatives corresponding to the respective reduced velocities.

The coupled motion test without initial displacement method (the buffetting test)

(vi) The procedure is same as step (i) - (v) of initial displacement method except that no initial displacement was given to the model under wind flow.

The single degree of freedom test

(vii) All the above steps from (i)-(v) were repeated to obtain the direct flutter derivatives H_1^* and H_4^* by allowing only single-degree-of-freedom vertical motion ($\alpha = 0$) to the model, and A_2^* , A_3^* by allowing only torsional motion (h = 0) about the center of rotation of the model.

Turbulence flow tests

(vii) Steps (i) - (v) were repeated for grids generating turbulent flow conditions. Each grid configuration had a characteristic relationship between turbulence intensity and wind speed.

Data acquisition

For the streamlined thin plate model, in each of the above experiments the signal outputs from the sensors were:

- i. Sampled at 1000 Hz and 200 Hz, filtered at 10 Hz for the free decay and the buffeting test, respectively;
- ii. AC coupled, i.e., DC component removed;
- iii. Amplified, then
- iv. Re-sampled at 250 Hz and 50 Hz for the free decay and the buffeting test, respectively.

For the IRR bridge model, the signals were:

- v. Sampled at 1000 Hz and 200 Hz, filtered at 6 Hz for the free decay and the buffeting test, respectively;
- vi. AC coupled, i.e., DC component removed;
- vii. Amplified, then
- viii. Re-sampled at 250 Hz and 50 Hz for the free decay and the buffeting test, respectively.

6.6 Determination of Aerodynamic Force Coefficients

The aerodynamic force coefficients, which are the coefficients of lift (C_L) , moment (C_M) and drag (C_D) and their first derivatives with respect to angle of attack (α) at $\alpha=0$ as denoted by C'_L, C'_M, C'_D , were determined from the section-model test as described below:

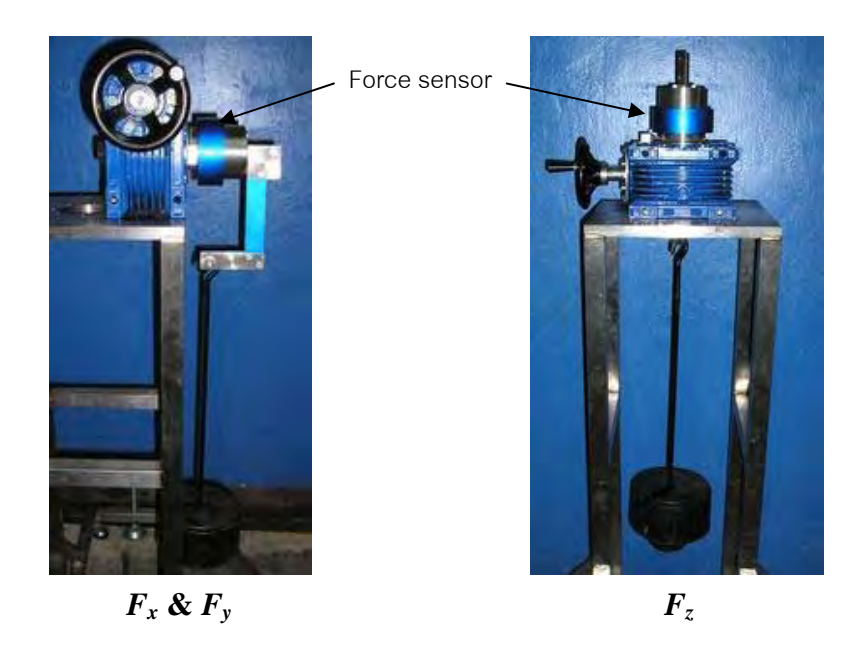
(i) The section model was fixed to the force gauges sensors at both ends with $\alpha=0$ and subjected to wind flow with three different wind velocities. At each of these velocities, the mean values of the voltage outputs of the lift, moment and drag channels from sensors were recorded. These voltage outputs at each wind speed were converted to mean forces values by multiplying the sensor's calibration matrix, which were found separately, with mean value of output voltages. Summing of mean forces at both ends yield the total forces act upon the model. The aerodynamic force coefficients were then found using the normalization:

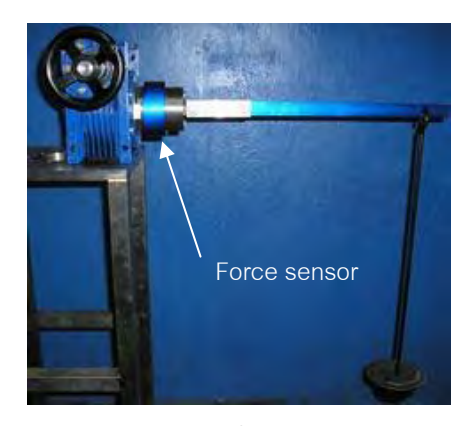
Lift coefficient
$$C_L = \frac{L}{0.5\rho U^2 B l}$$
 Drag coefficient
$$C_D = \frac{D}{0.5\rho U^2 B l}$$
 Moment coefficient
$$C_M = \frac{M}{0.5\rho U^2 B^2 l}$$
 (6.4)

where B and l are the deck width and length of the section model, respectively, L, D, M are total lift, drag and moment forces respectively.

The mean values of the force coefficients were obtained by averaging the values from three different wind speeds.

(ii) Step (i) was repeated with different values of α varying between -12° to +12° in steps of 3°. The angle α was measured by the scale provided with the force gauges supports at both sides. Each of the mean values of C_L , C_M and C_D was plotted with respect to the angle of attack α , and from the curves at $\alpha = 0$ the values of C_L' , C_M' , C_D' were obtained.





 $M_x & M_y$

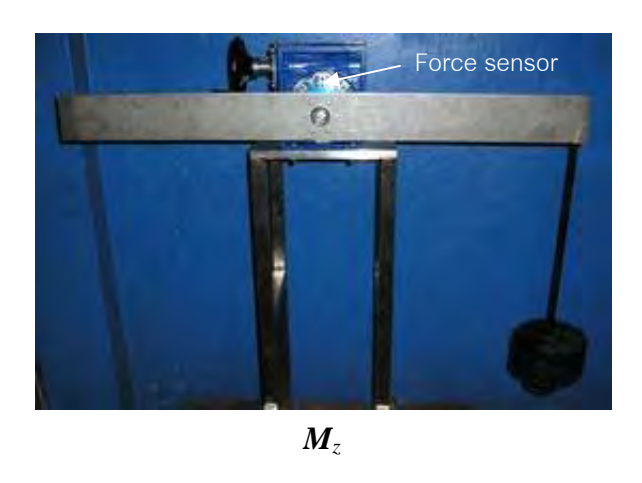


Fig. 6.11: Equipment setup for force sensor calibration.

6.7 Modified Sections by Aerodynamic Appendages

In this study, three types of aerodynamic appendages were mounted to the bridge sectional model, including fairings, soffit plate, and combination of those two types. Tests of those mentioned sections were performed statically and dynamically. Due to the literature appraisals, illustrated in section 2.2, the equilateral triangle fairings made from bagasse were mounted to a model, in both windward and leeward side. Fairing height is designed to fit the bridge model, 29.9 mm with the upper slope angle of 30°. The schematics of fairings and fairing-installed sections are respectively illustrated in figures 6.12 and 6.13 (a and b). Furthermore, soffit plates were fully mounted under the model with an intention to smoothen the wind attack to model's girders. Figure 6.13 (c and d) shows the bottom view of a model mounted with fairings and soffit plates.

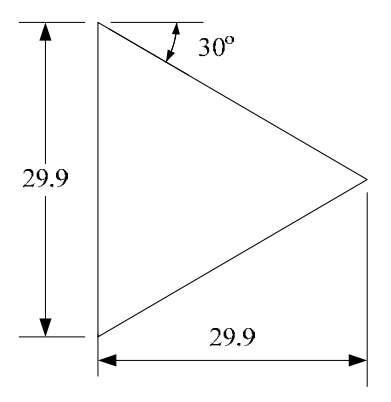


Fig. 6.12 Schematic of fairings (diameters in mm)



Fig. 6.13 Fairing-modified section; (a) side view of the section, (b) zoom-in at end plate, (c and d) combination of fairings and soffit plates section



Fig. 6.13 (Continued)

CHAPTER 7

EXPERIMENTAL RESULTS

7.1 Introduction

In this chapter the experimentally obtained results for the streamlined thin plate and a plate-girder type IRR Bridge section are presented and discussed. The thin plate was used to validate the reliability and applicability of the present system identification method in flutter derivatives estimation of bridge decks. Aerodynamic coefficients were also obtained by static tests. The thin plate model were conducted under smooth flow whereas the IRR Bridge model were conducted under smooth and turbulent flows.

The experimental arrangements and instrumentation, which were used in this study are presented in this chapter, are described in Chapter 6 and in Appendix B.

7.2 Thin Flat Plate

7.2.1 Flutter Derivatives: Smooth Flow

Three different sets of experiments were performed for the thin-plate-deck configuration under smooth flow for zero angle of attack:

- i. Single-degree-of-freedom tests (vertical and torsional motion); to identify direct flutter derivatives H_1^* , H_4^* , A_2^* and A_3^* ,
- ii. Coupled-motion tests in both vertical and torsional degrees of freedom simultaneously; with initial displacements (the free decay method); to identify eight flutter derivatives, and
- iii. Coupled-motion tests in both vertical and torsional degrees of freedom without initial displacements (the buffeting method).



Fig. 7.1(a) Thin flat plate model with king-post in wind tunnel

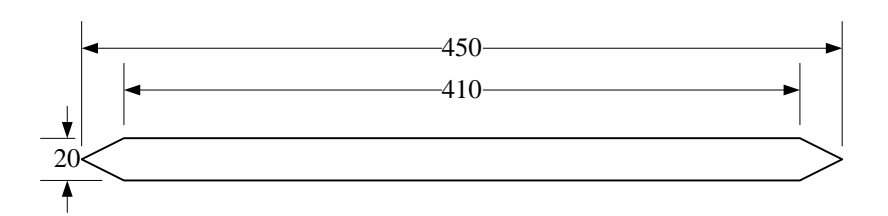


Fig. 7.1(b) Cross section of the thin plate model (unit in mm.)

In all cases piano wires were used to restrain the undesirable motions. The following experimental parameters were used for the coupled motion model tests: Mass = 15.50 kgs; mass moment of inertia about center of mass = 0.11832 kg m²; modal frequencies (U=0): $n_1=1.65$ Hz, $n_2=2.73$ Hz; modal damping (U=0): $\zeta_1=0.33\%$, $\zeta_2=0.28\%$ for vertical and torsional respectively; separation between springs (d) = 250 mm; length (span) of model = 2.30 m.; laser sensors were separated at 125 mm. Each acceleration transducers, installed at the mid-section of model, was placed at 62.5 mm apart from center of rotation. Determination of mass was performed method described in section 3.6.1. Determination of mass moment inertia was obtained by both methods describing in section 3.6.1 and 6.2 which results were agreed well.

In coupled-motion tests, two types of tests were conducted by fixed initial displacement (free decay) and without initial displacement (buffeting response tests). This was conducted to confirm applicability of the system identification method proposed to various types of tests.

As model was manufactured from wood and very long, in order to have sufficient vertical and torsional stiffness of the model a so-called "king-post" was installed. A king-post is a stiffening system composed of two posts and 8 gauged wires (see Fig.7.1). The king-post is symmetric from above and below the deck, and as it is only consists of rounded members, lift / vertical motion and moment / torsional motion are not influenced by the king-post. Fig. 7.1.b shows cross section of thin flat plate model in mm.

Single degree of freedom test

Single-degree-of-freedom tests (vertical and torsional) were performed first for 'smooth flow' with turbulence intensity *I* less than 0.05%. Test methods are similar to Scanlan's method (Scanlan and Tomko 1977). Detail procedures are described in subsection 6.5. It involves the measurement of the decay in amplitude with time of an initial displacement of the deck in heave and torsion-only case. To obtain vertical direct derivatives, the torsional motion is restrained and the model is pulled down and release; both 'in 'still air' and 'in wind' conditions. Extraction of torsional direct derivatives uses an analogous process. Fig. 7.2 shows experimental setups for each vertical and torsional motion restrained.

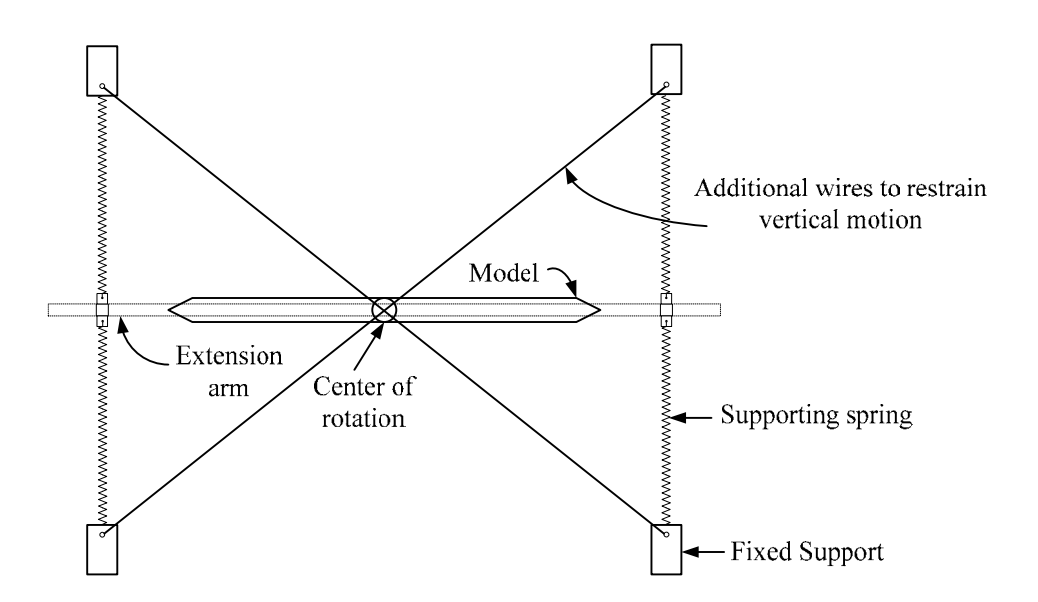


Fig. 7.2(a) Experimental setup for vertical motion restrained.

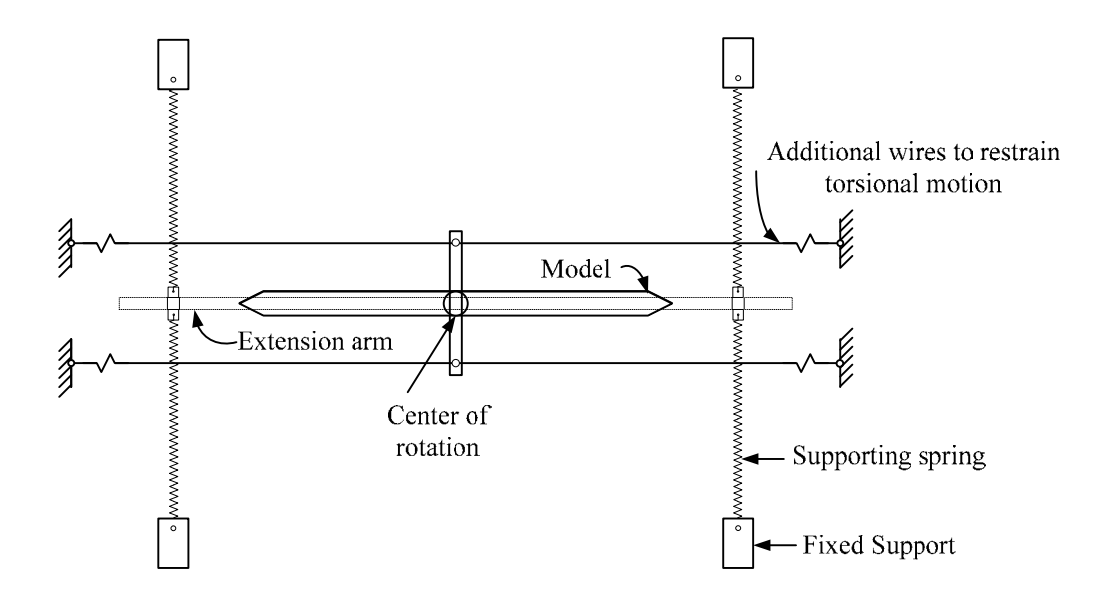


Fig. 7.2(b) Experimental setup for torsional motion restrained.

In order to ensure that model can vibrate only in torsion mode, the restraining cross wires are used where both ends are attached to fixed supports and connected to model at center of rotation (see Fig. 7.2a). Vertical SDOF tests were then done with restrained on torsional motion provided by an arrangement of drag wires attached to upper and lower ends of a vertical bar (Fig. 7.2b). Modal frequencies and damping ratios (U = 0) were slightly difference from 2DOF-coupled motion test due to effect of restraining wires as: $n_1 = 1.65$ Hz, $n_2 = 2.37$ Hz; modal damping (U = 0): $\zeta_1 = 0.41\%$, $\zeta_2 = 0.61\%$ for vertical and torsional respectively. Responses were sampling at 1000Hz in 60 sec-duration, low-pass filter at 10Hz and then re-sampling at 250 Hz. Only four direct flutter derivatives H_1^* , H_4^* , A_2^* and A_3^* were determined from vertical-motion-only (h) and torsion-motion-only (α)-SDOF tests (see subsection 3.6.5) as

$$H_{1}^{*} = \frac{2m}{\rho B^{2} \omega} (2\xi_{h} \omega_{h} - 2\xi_{h'} \omega_{h'}) \qquad H_{4}^{*} = \frac{2m}{\rho B^{3} \omega^{2}} (\omega_{h}^{2} - \omega_{h'}^{2})$$

$$A_{2}^{*} = \frac{2I}{\rho B^{4} \omega} (2\xi_{\alpha} \omega_{\alpha} - 2\xi_{\alpha'} \omega_{\alpha'}) \qquad A_{3}^{*} = \frac{2I}{\rho B^{4} \omega^{2}} (\omega_{\alpha}^{2} - \omega_{\alpha'}^{2})$$

where $\xi_{h,\alpha}$, $\omega_{h,\alpha}$ and $\xi_{h',\alpha'}$, $\omega_{h',\alpha'}$ are damping ratios and frequency of the record motion in still air and under wind conditions respectively, m, I are mass and mass moment of inertia per unit length, B is deck width.

Note that all flutter derivatives expressed above are expressing in form of Eqs. (3.31) and (3.32):

$$L_{h} = \frac{1}{2} \rho U^{2} B \left[K H_{1}^{*} \frac{\dot{h}}{U} + K H_{2}^{*} \frac{B \dot{\alpha}}{U} + K^{2} H_{3}^{*} \alpha + K^{2} H_{4}^{*} \frac{h}{B} \right]$$

$$(3.31)$$

$$M_{\alpha} = \frac{1}{2} \rho U^{2} B^{2} \left[K A_{1}^{*} \frac{\dot{h}}{U} + K A_{2}^{*} \frac{B \dot{\alpha}}{U} + K^{2} A_{3}^{*} \alpha + K^{2} A_{4}^{*} \frac{h}{B} \right]$$

$$(3.32)$$

The direct flutter derivatives H_I^* , H_4^* , extracted from vertical-motion-only tests are plotted in Fig. 7.3a against non-dimensional (reduced) wind speed U/nB, where n being the vertical mode eigenfrequency. The results also plotted with theoretical values from Theodorsen's theory. The H_I^* results show well agreement with theoretical values where H_4^* have a good trend corresponding to theoretical ones.

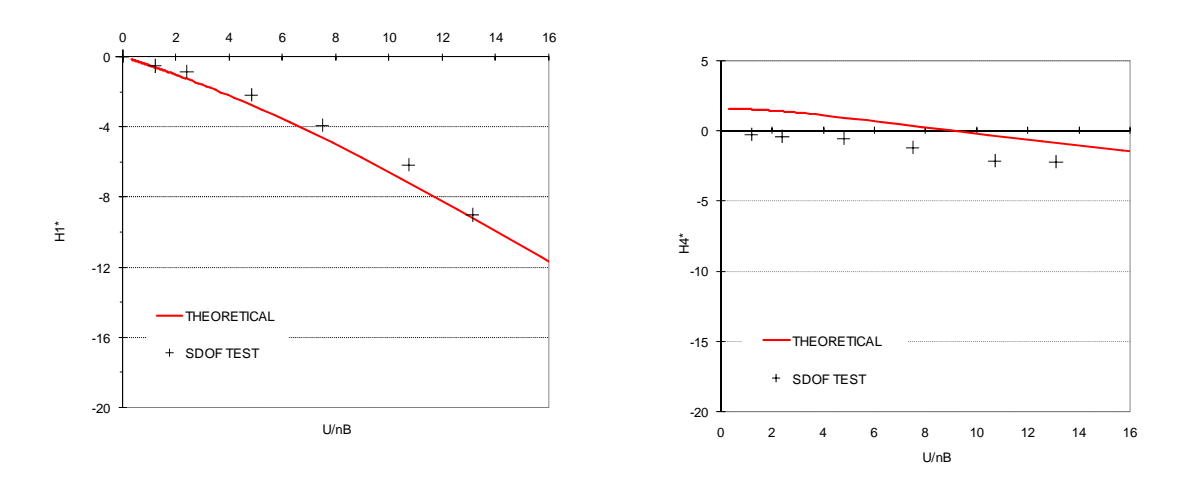


Fig.7.3a Direct Flutter derivatives (H_1^* , H_4^*) of the thin plate model singled motion tests with initial displacement (transience resp.) under smooth flow

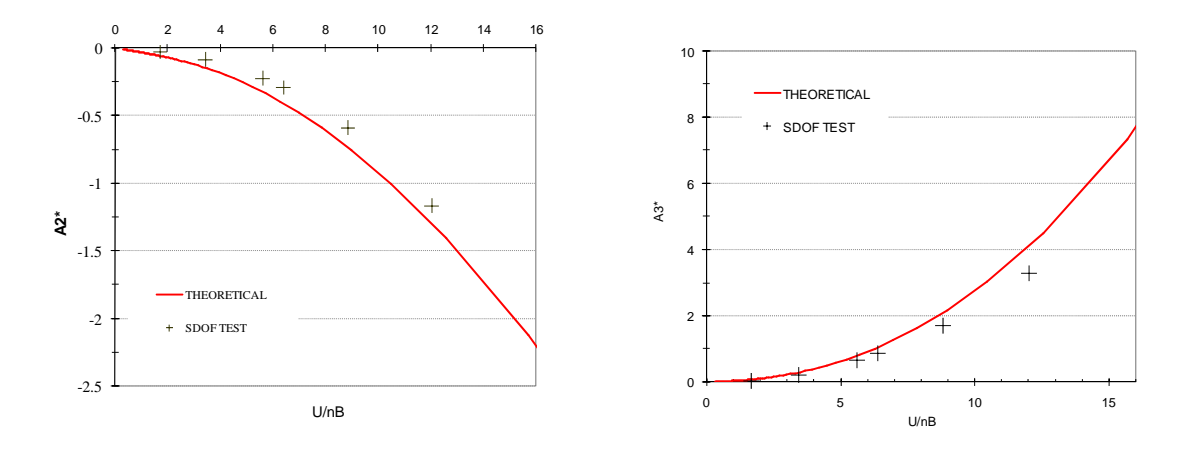


Fig.7.3b Direct Flutter derivatives (A_2^*, A_3^*) of the thin plate model singled motion tests with initial displacement (transience resp.) under smooth flow

Fig. 7.3b shows direct flutter derivatives A_2^* and A_3^* , extracted from torsional-motion-only tests against reduced wind speed where n being the torsional mode eigenfrequency. The results show that A_2^* and A_3^* are also in well agreement to the theoretical values.

The trends for H_1^* and A_2^* , which related to aerodynamic damping in vertical and tosional motion, respectively, are continuing increased (more negatively) and the trends are clear and strong. Hence there is no risk of SDOF instabilities; both stall (torsional) and galloping (vertical). The cross derivatives which would responsible for classical 2DOF flutter would be examined next in coupled motion tests.

<u>Coupled motion test with initial displacement method (free decay or transient response)</u>

In order to recover a full set of derivatives simultaneously, coupled (2DOF) tests were performed with no restrain on torsional or vertical motion. Transience response time-series were recorded for the model suspended in the dynamic rig by initial excitation both in heave and torsion simultaneously. Fig. 7.4 shows the supporting system of tests. The initial excitation is carefully controlled in order to have same level of excitation in each test. The acceleration response of the model was sampled at $1000 \ Hz$, low-pass filtering with nominal cut-off frequency of $10 \ Hz$ and then re-sampled at $250 \ Hz$. Time histories, approximately $60 \ \text{sec}$, of the decayed motion were recorded for the model scaled velocities varying from $0 \ \text{m/s}$ to $9 \ \text{m/s}$.



Fig. 7.4 Suspension device of the model

Fig. 7.5 shows example of free decay response at U=0 (still air). Fig. 7.6 plotted damping ratio with amplitude of vibrations, the damping ratios exhibit nonlinearities in ranges of small amplitudes as same as what reported in previous researches (Jakobsen 1995, Sarkar 1994) even in the case of electromagnetic dampers

were added. However, the damping ratios are practically accepted as damping vary from 0.33 to 0.45 and 0.24 to 0.30 for heave (vertical) and pitch (torsional) motion, respectively, in the range of amplitude tests. The inherent damping ratios were used by considering that adding special dampers such as electromagnetic dampers or silicone oil would increase damping to the system and results in very low amplitudes of motions. This would affect available range of wind speed for buffeting tests because wind is only a source of model exciting.

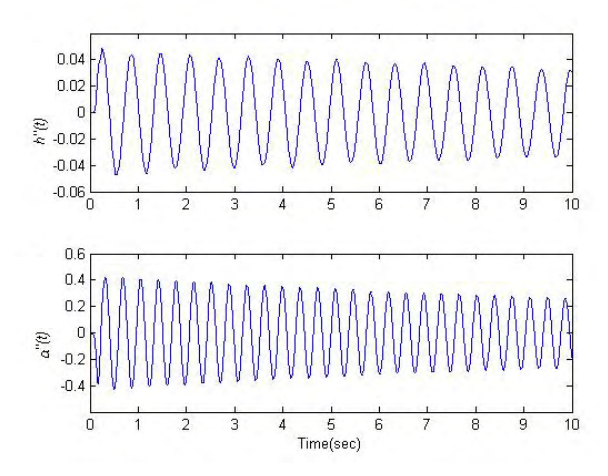


Fig. 7.5 The thin flat plate model under smooth flow: free decay acceleration time histories for heave and pitch motions at U = 0 m/s.

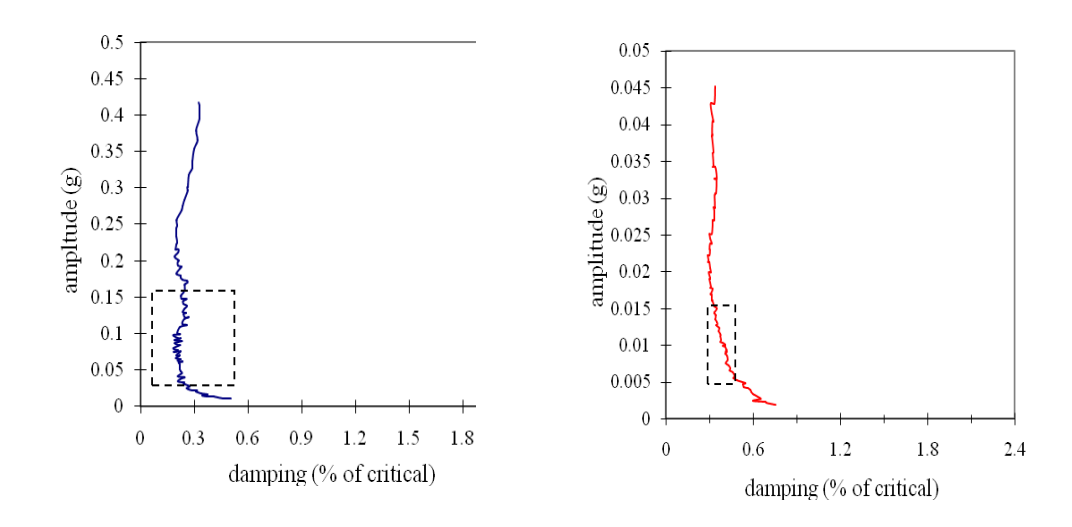


Fig. 7.6 Torsional (left) and vertical (right) damping ratio in still-air (zero wind speed)

Fig. 7.7 shows example of free decay response at some wind speed. Degrees of coupling are clearly seen as wind speed increased.

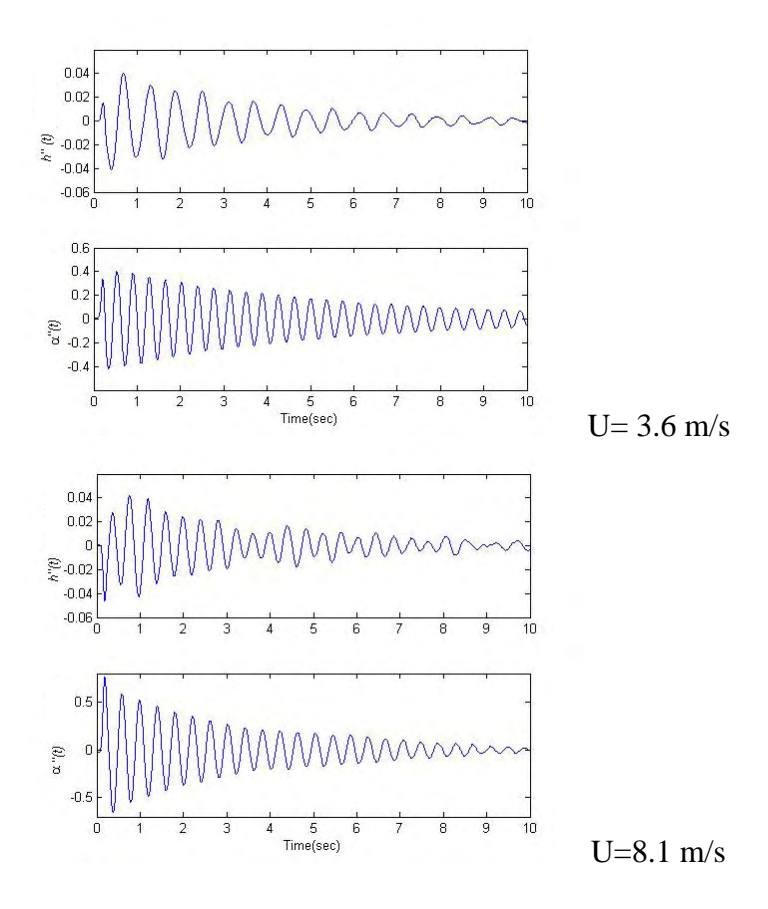


Fig. 7.7 The thin flat plate model under smooth flow: free decay acceleration time histories for heave and pitch motions at U = 3.6 m/s and 8.1 m/s

All derivatives were evaluated by system identification of the **A** matrix as described in chapter 4 by both the SSI-COV and the SSI-DATA method. The modal parameters can be determined by solving the eigenvalue problem of state matrix **A**. Once the modal parameters are identified, the mechanical damping matrix C^0 and the mechanical stiffness matrix C^0 can be readily determined in 'still-air' condition. The gross damping matrix C^0 and the gross stiffness matrix C^0 and the determined analogously under wind condition. Thus, the flutter derivatives can be extracted from the following equations:

$$\begin{split} H_{1}^{*}(k_{h}) &= -\frac{2m}{\rho B^{2}\omega_{h}}(\overline{C}_{11}^{e} - \overline{C}_{11}), \quad A_{1}^{*}(k_{h}) = -\frac{2I}{\rho B^{3}\omega_{h}}(\overline{C}_{21}^{e} - \overline{C}_{21}) \\ H_{2}^{*}(k_{\alpha}) &= -\frac{2m}{\rho B^{3}\omega_{\alpha}}(\overline{C}_{12}^{e} - \overline{C}_{12}), \quad A_{2}^{*}(k_{\alpha}) = -\frac{2I}{\rho B^{4}\omega_{\alpha}}(\overline{C}_{22}^{e} - \overline{C}_{22}) \\ H_{3}^{*}(k_{\alpha}) &= -\frac{2m}{\rho B^{3}\omega_{\alpha}^{2}}(\overline{K}_{12}^{e} - \overline{K}_{12}), \quad A_{3}^{*}(k_{\alpha}) = -\frac{2I}{\rho B^{4}\omega_{\alpha}^{2}}(\overline{K}_{22}^{e} - \overline{K}_{22}) \\ H_{4}^{*}(k_{h}) &= -\frac{2m}{\rho B^{3}\omega_{h}^{2}}(\overline{K}_{11}^{e} - \overline{K}_{11}), \quad A_{4}^{*}(k_{h}) = -\frac{2I}{\rho B^{4}\omega_{h}^{2}}(\overline{K}_{21}^{e} - \overline{K}_{21}) \end{split}$$

where m and I are mass and mass moment of inertia per unit length determined as in section 6.2. Fig. 7.7 shows examples of acceleration responses in wind flow at U=3.6 and 8.1 m/s. It is worth noting that the sign convention used in this study, where lift force and vertical movement are both positive upwards, gives H_2^* , H_3^* , A_I^* , A_4^* opposite signs to those by Simiu and Scanlan (1996).

All eight flutter derivatives H_i^* , $i=1,\ldots,4$ and A_i^* , $i=1,\ldots,4$, as obtained from the free decay coupled-motion tests for the thin plate deck, by both the SSI-COV and the SSI-DATA method are plotted in Figs. 7.8-7.9. These flutter derivatives also compared with those from theory. Unless otherwise noted, H_I^* , H_2^* , A_I^* , A_4^* associated with vertical motion were calculated using the frequency n_h (lower) and H_2^* , H_3^* , A_2^* , A_3^* associated with torsional motion were calculated using the frequency n_α (higher) at any wind speeds. The frequencies n_h and n_α are aerodynamically modified from their values at U=0 at any other wind speeds. This was done because in the corresponding single-degree-of-freedom motions, the natural frequencies of vibration for vertical and torsional motion were closed to n_h and n_α , respectively.

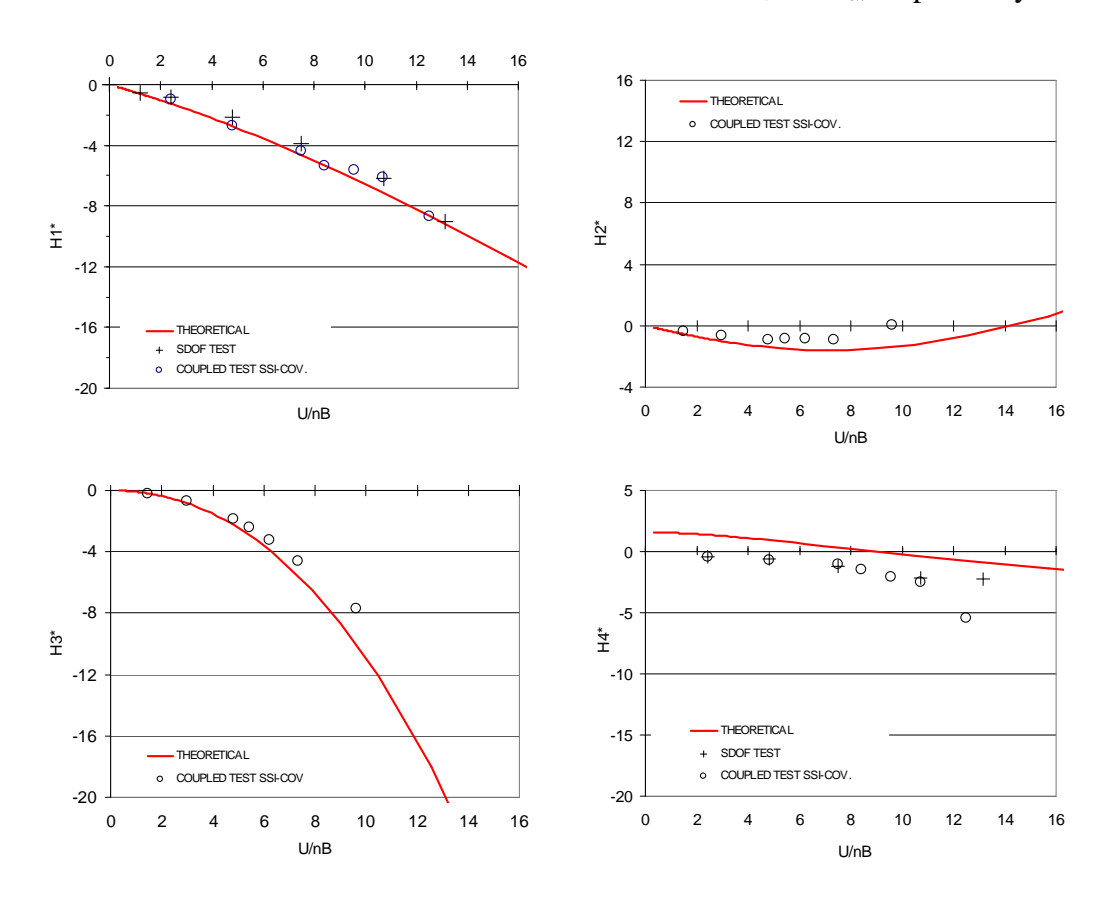


Fig. 7.8a Flutter derivatives $(H_1^*, H_2^*, H_3^*, H_4^*)$ of the thin plate model from the free decay coupled motion tests under smooth flow: SSI COV method

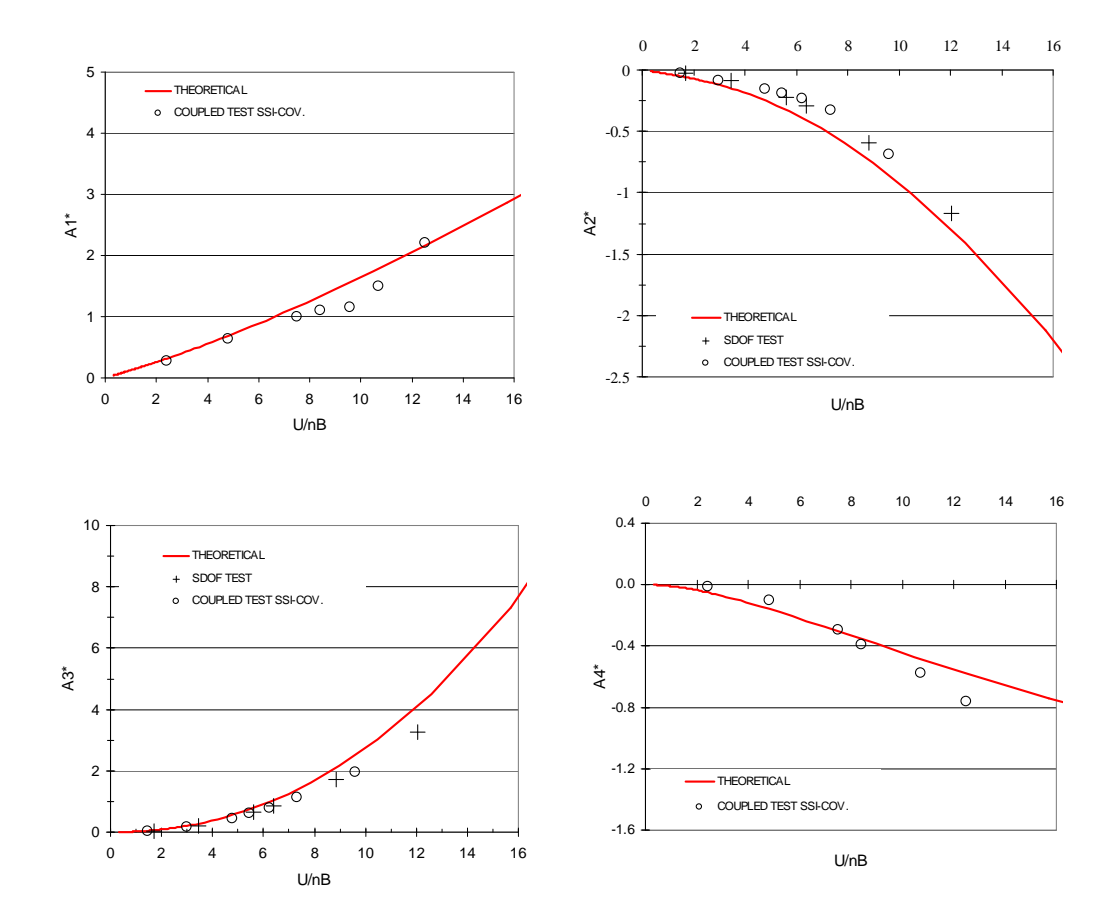


Fig. 7.8b Flutter derivatives $(A_1^*, A_2^*, A_3^*, A_4^*)$ of the thin plate model from the free decay coupled motion tests under smooth flow: SSI COV method

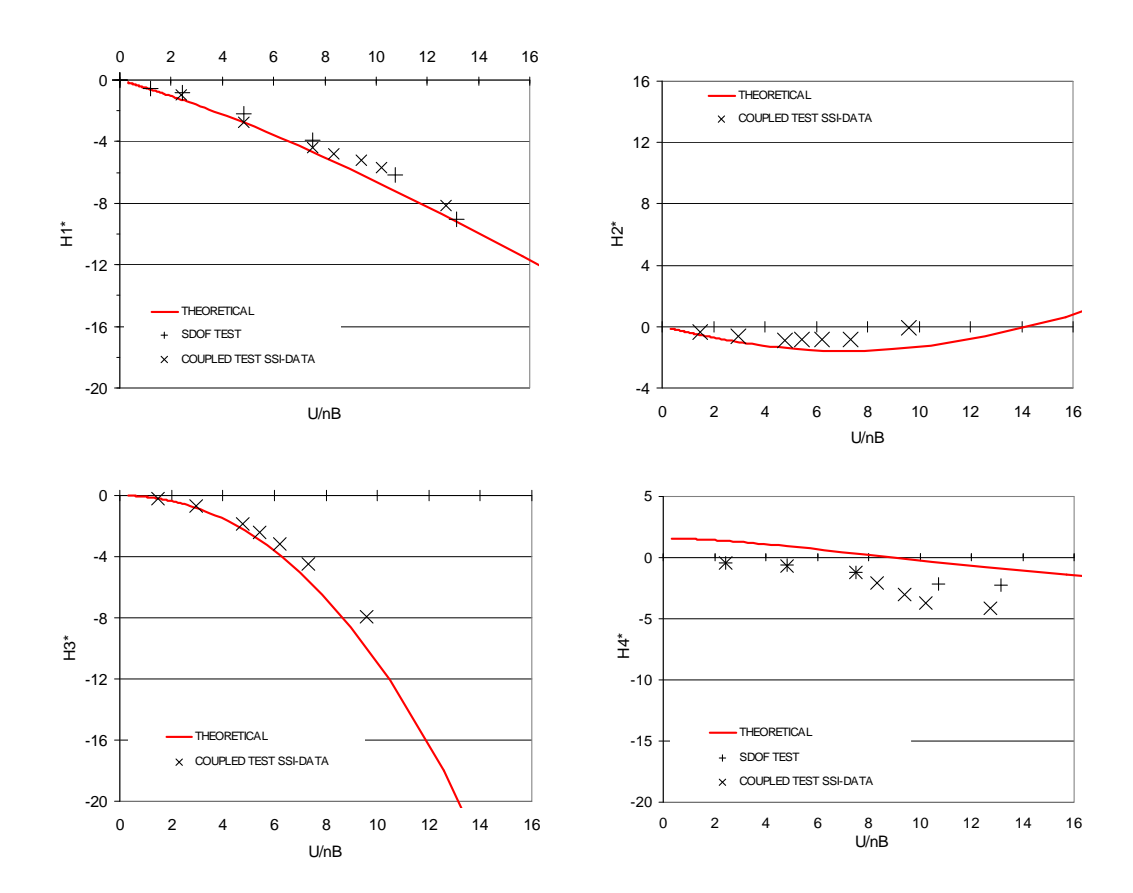


Fig. 7.9a Flutter derivatives $(H_1^*, H_2^*, H_3^*, H_4^*)$ of the thin plate model from the free decay coupled motion tests under smooth flow: SSI DATA method

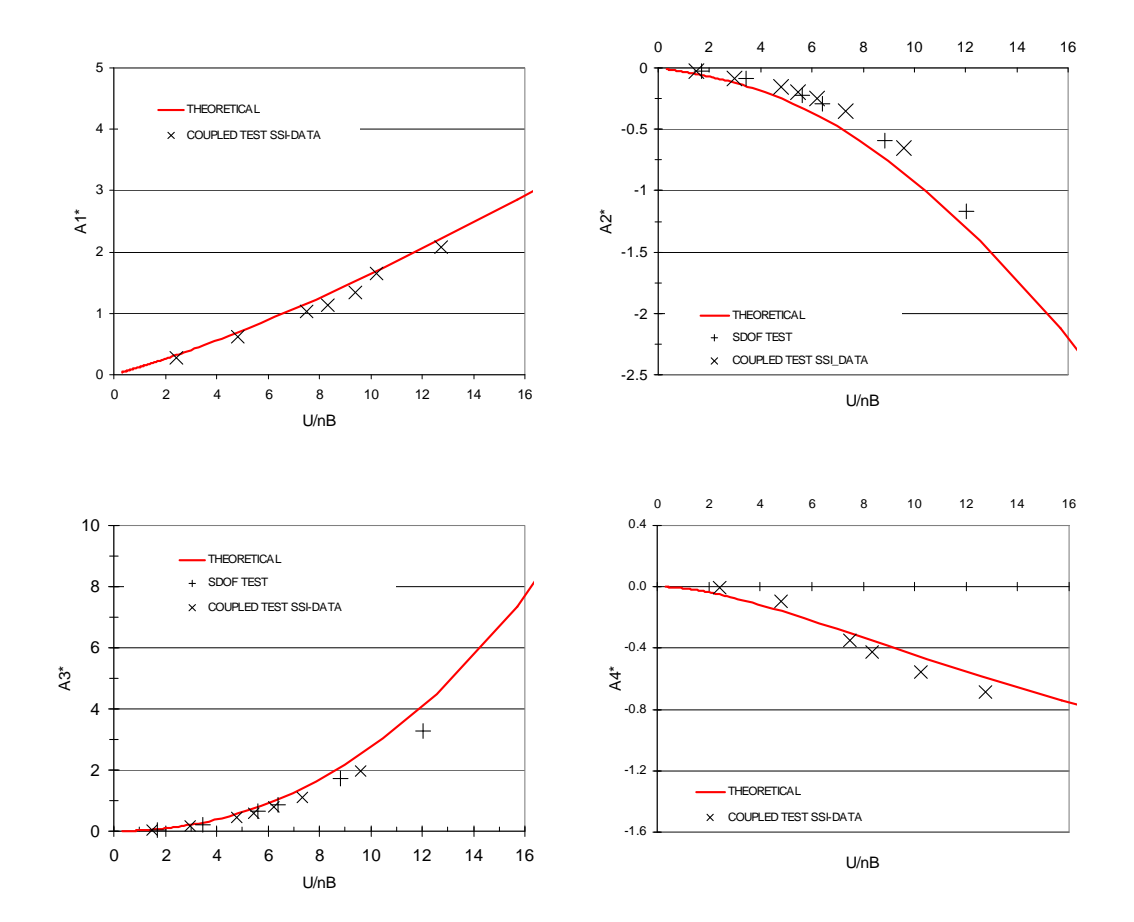


Fig. 7.9b Flutter derivatives $(A_1^*, A_2^*, A_3^*, A_4^*)$ of the thin plate model from the free decay coupled motion tests under smooth flow: SSI DATA method

Fig. 7.10 and 7.11 plotted all derivatives from the free decay coupled-motion tests extracted by the SSI-DATA and the SSI-COV method, compared with those from theory and the single-degree-of-freedom tests. The result shows that all derivatives extracted by both SSI methods from various tests are in very well agreement with the theoretical values.

The direct flutter derivatives H_1^* , H_4^* , A_2^* and A_3^* as found from single-degree-of-freedom tests compared with those from coupled-motion tests (Figs. 7.10 and 7.11) have near perfect match. This result shows that the direct-flutter derivatives are indeed not affected by the motion along the other degree of freedom, as predicted by theory i.e., those direct flutter derivatives associated with h motion are not affected by α motion, and vice versa.

All flutter derivatives of the thin plate – except H_4 *- from initial-coupled-motion tests by both SSI-methods are in well agreement with Theodorson's theoretical values. However, H_4 * extracted from SDOF and coupled motion tests are in good agreement and showing good agreement in trend with theoretical value. The factors made the extraction of H_4 * difficult are as follows. The change in the natural frequency due to the aeroelastic effect from which H_4 * were calculated was found to be very small.

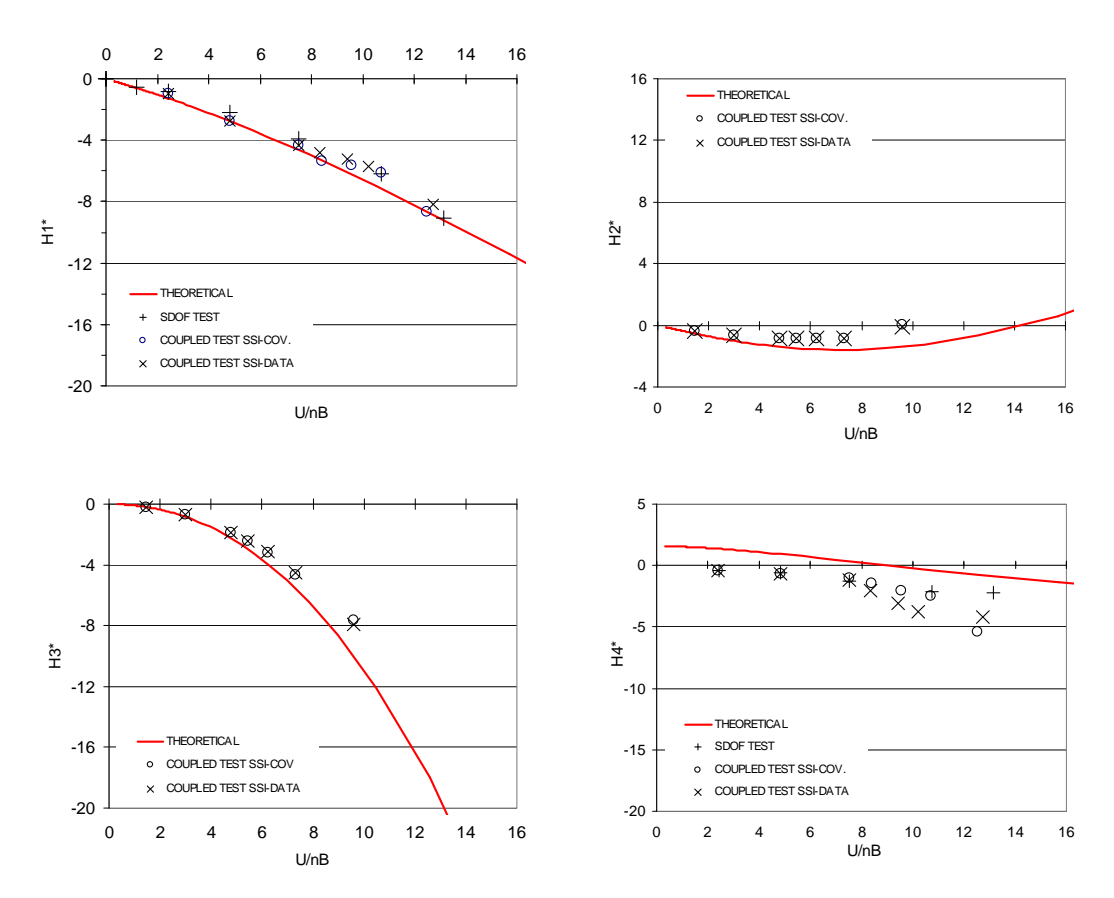


Fig. 7.10 Comparison of H_i^* for thin plate model from SDOF test and couple-degree-of-freedom tests with initial displacement for under smooth flow

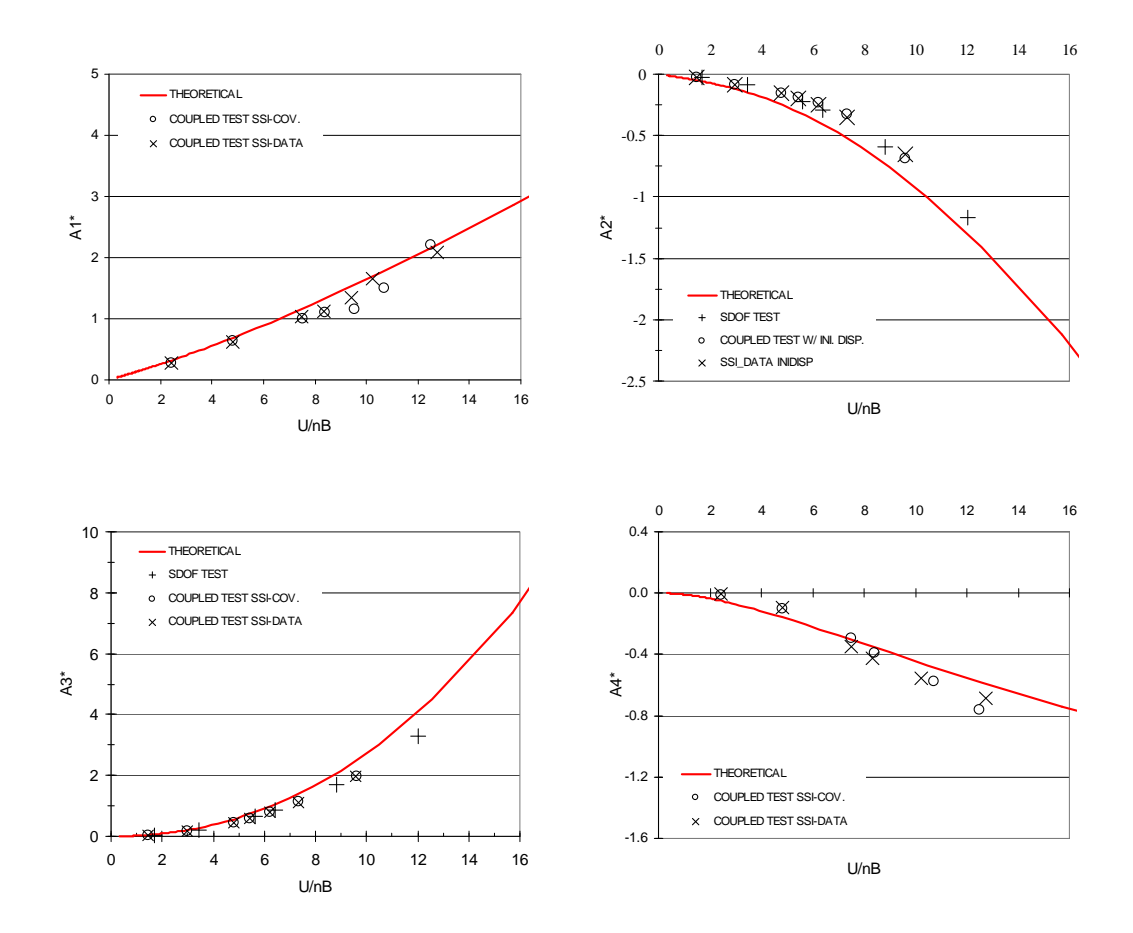


Fig. 7.11 Comparison of A_i^* for thin plate model from SDOF test and couple-degree-of-freedom tests with initial displacement for under smooth flow

<u>Coupled motion test without initial displacement method (buffeting or ambient response)</u>

The advantage of the buffeting test is that not only all flutter derivatives are simultaneously extracts, but also the aerodynamic admittance and root-mean-square responses can be determined at the same time. Besides, their mechanisms are closer to the real behavior of prototype bridges under wind flow. However, as wind is only the excited source and a relatively heavy model of the thin plate, the amplitudes of response are very low especially at the low wind speeds. Unlike the free decay responses where good signal to noise ratio are obtained, the signals at low wind speed are mostly in the same order with measurement noise. This makes the extraction of flutter derivatives of the thin plate model difficult or impractical in a very low wind speed range.

The experimental setup is same as coupled-free decay test except that no initial displacement has given to the model. Fig. 7.12 shows sample of buffet responses at U=5.6 m/s.

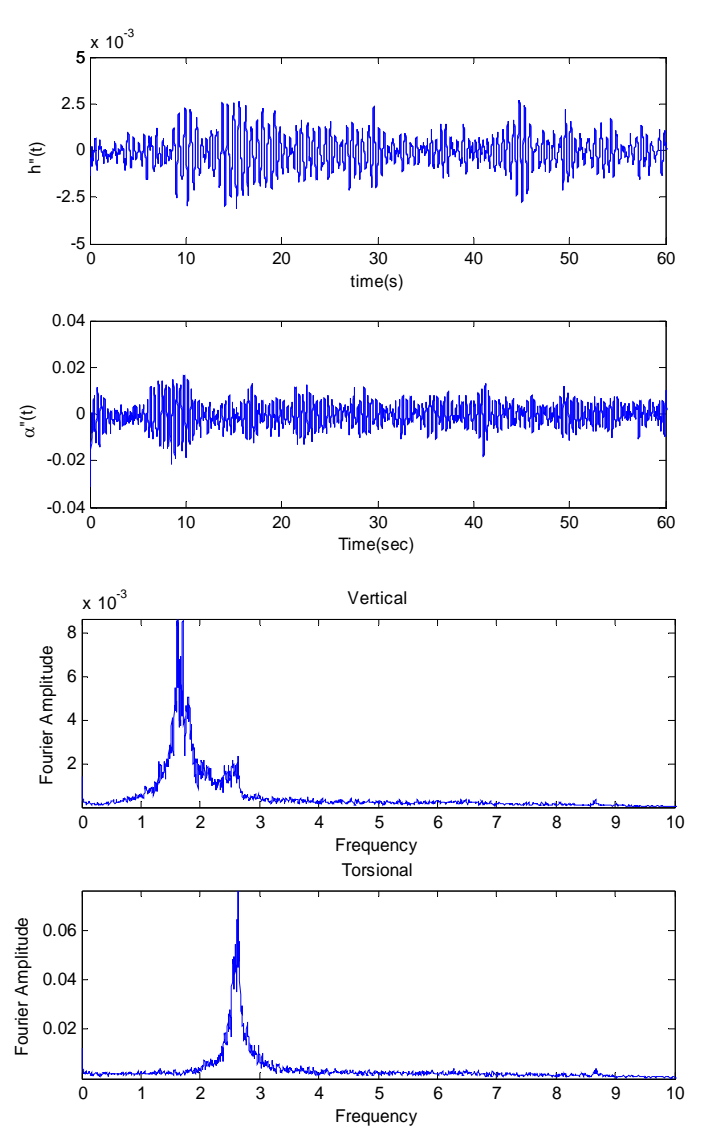


Fig. 7.12 Thin flat plate model under smooth flow: buffeting acceleration time histories and frequency spectrum for heave and pitch motions at U = 5.62 m/s

All derivatives were extracted by both the SSI-COV and the SSI-DATA methods in similar manner as in the free decay test. The sampling frequency was reduced to 200~Hz and recording time was 360~sec. The signals were low-pass at nominal frequency 10~Hz and then re-sampling at 50~Hz. The still-air free decay records were used in determining mechanical stiffness and damping matrices. Fig. 7.13~and~7.14~plotted~all~flutter~derivatives~extracted~by~the~SSI-COV~and~the~SSI-DATA~methods~together~with~those~from~the~SDOF~tests~and~theoretical~values.

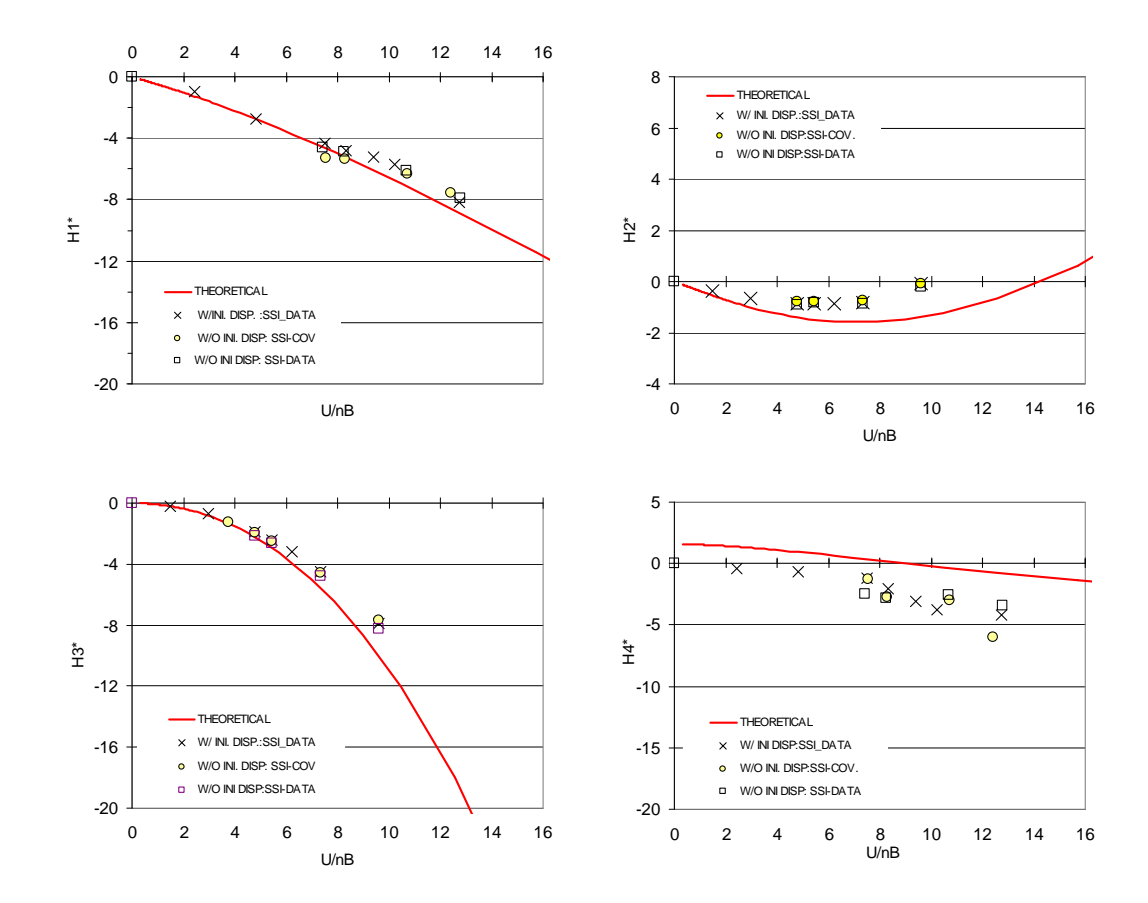


Fig. 7.13 Comparison of H_i^* for the thin plate model from couple-degree-of-freedom tests: from the free decay test by SSI DATA and from the buffeting test by the SSI –DATA and the SSI COV method under smooth flow

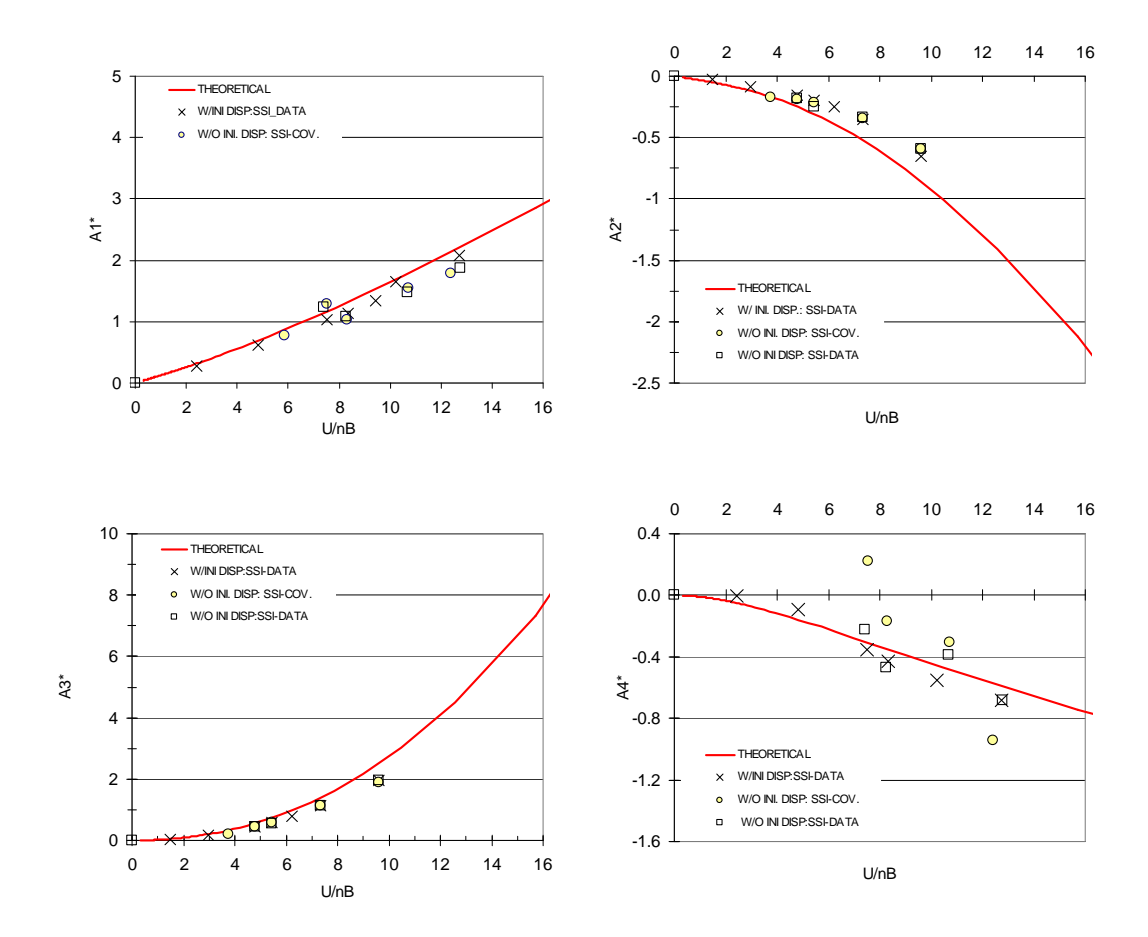


Fig. 7.14 Comparison of A_i^* for the thin flat plate model from couple-degree-of-freedom: from the free decay test by SSI DATA and from the buffeting test by the SSI –DATA and the SSI COV method under smooth flow

The six important flutter derivatives; $H_1^* \sim H_3^*$, $A_1^* \sim A_3^*$ found from buffeting responses by both the SSI-COV and the SSI-DATA match very well with both the theoretical and those from free decay responses. The results show very well agreement between two types of tests. This verifies the ability of the system identification methods (both the SSI-COV and the SSI-DATA) to apply with the free decay signal though it developed from stochastic model (white noise loading assumption). Nonetheless, at very low reduced velocities it difficult to extract the flutter derivatives by the buffeting response tests due to the relatively heavy of the thin plate model as well as the low energy from the wind to excite the model, then useful signal are almost embedded in noise. The H_4 *-derivatives by both the SSI-COV and the SSI-DATA are generally agreed in trend with theoretical value similar to free decay response tests. However, the A_4^* , in turn, found from the SSI-COV are more scatter without clearing trend compared to the SSI-DATA method. The effects of these derivatives are seemed to be less significant and negligible compared to the remaining. This was the reason where H_4^* and A_4^* were usually neglected in previous studies (Scanlan and Tomko 1971, Sarkar 1994, Jakobsen 1995, Gu 2000).

Summary of the thin plate test results

All eight flutter derivatives H_i^* , i=1,...,4 and A_i^* , i=1,...,4, as obtained from three type of experimental setups: the free decay-SDOF, the free decay- and the buffeting-coupled motion tests were identified and compared by two most up-to-date system identification methods: the SSI-COV and the SSI-DATA methods. The results show that free decay responses provided the best results as there are clearer signal to noise ratios. The difficulty in extraction of flutter derivatives at high wind speed due to short usable length of data, reported in the past, is improved by the SSI methods. In buffeting tests, less signal to noise ratios especially at low wind speed make extraction of flutter derivatives are more difficult and limit the range of wind speed test. This may be overcome by carefully select scale ratio and reducing model mass.

Generally, in the range of wind speed tests, the SSI-DATA method shows a good capability in extracting all flutter derivatives even in buffeting responses while the SSI-COV method shows similar performance in main derivatives except for very sensitive A_4 * in case of buffeting response.

Test results show that the thin flat plate model exhibits tentative of coupled flutter instability as predicted in theory where H_1^* and A_2^* are negative. The coupled terms H_3^* , A_1^* and A_3^* play the next important role in the coupled flutter phenomena of the section (Boonyapinyo et.al, 1999). This could be happened in synchronized responses between vertical and torsional motions at a frequency between the two eigenfrequencies in still air. A synchronized appearance of the two degrees of freedom is forced by the self-excited wind forces. Rotation is accompanied by a self- excited moment which corresponds to a reduction of the torsional stiffness (positive value of A_3^*). At the same time, vertical motion (i.e. vertical velocity; positive value of A_1^*) give rise to an additional moment, and this is absent in the case of restrained coupling. Regarding the vertical DOF, coupling is primarily felt through a lift caused by rotation (where the aeroelastic resultant force acts at some distance from shear center), this eccentric forcing which is become more dominant when wind speed increased up to the 'stability limit'. This is clearly seen by strongly increased in positive value of H_3^* . The original vertical motion (at the still-air eigenfrequency) is aerodynamically damped out by strong negative value of H_1 *.

7.2.2 Aerodynamic Force Coefficients: Smooth Flow

The static aerodynamic force coefficients of the thin flat plate were obtained under the smooth flow. The method used to obtain these static coefficients is described in Chapter 5. The experimental configuration is outlined in section 5.1.1. Fig. 7.15a shows experimental setup of thin flat plate model in wind tunnel. The results of the tests are presented in the form of drag, lift and moment coefficients. The section model was installed about its centre of rotation, then, the pitching moment is considered with respect this centre of rotation. The sign convention used in the presentation of the test results is shown in Figs. 7.15(e).



Fig. 7.15(a) Thin flat plate model with king-post in wind tunnel: static test setup



Fig. 7.15(b) Thin flat plate model with king-post in wind tunnel : static test setup with various wind angle of attack

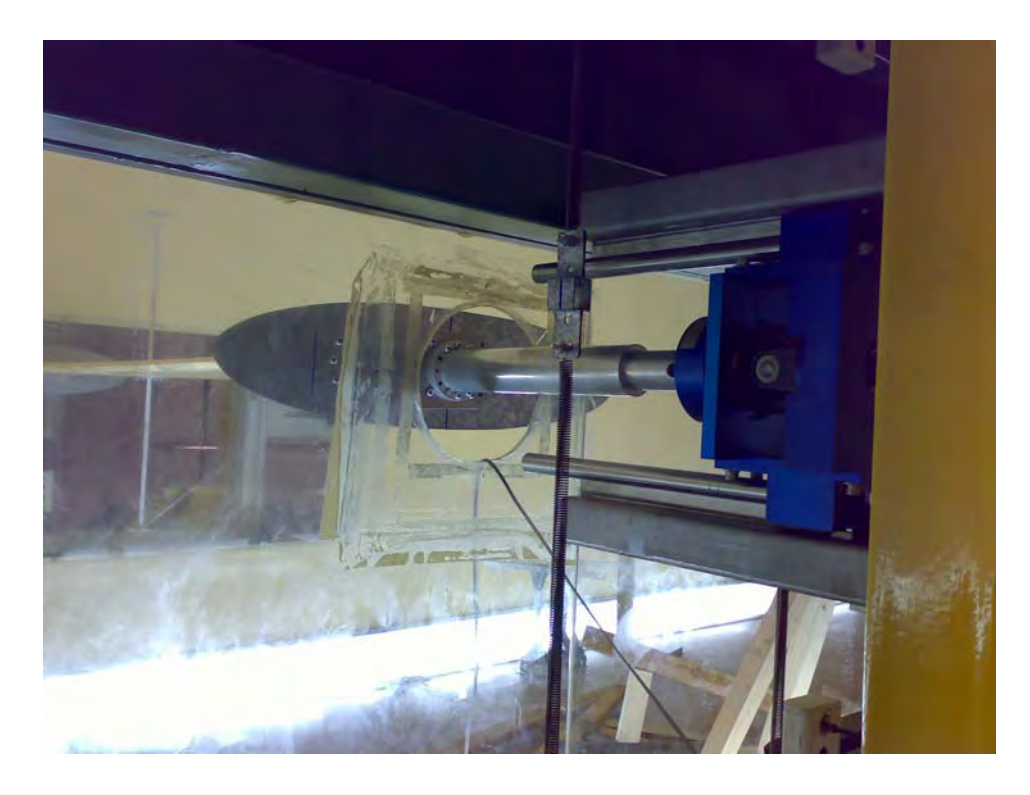


Fig. 7.15(c) Static force balance device of the model

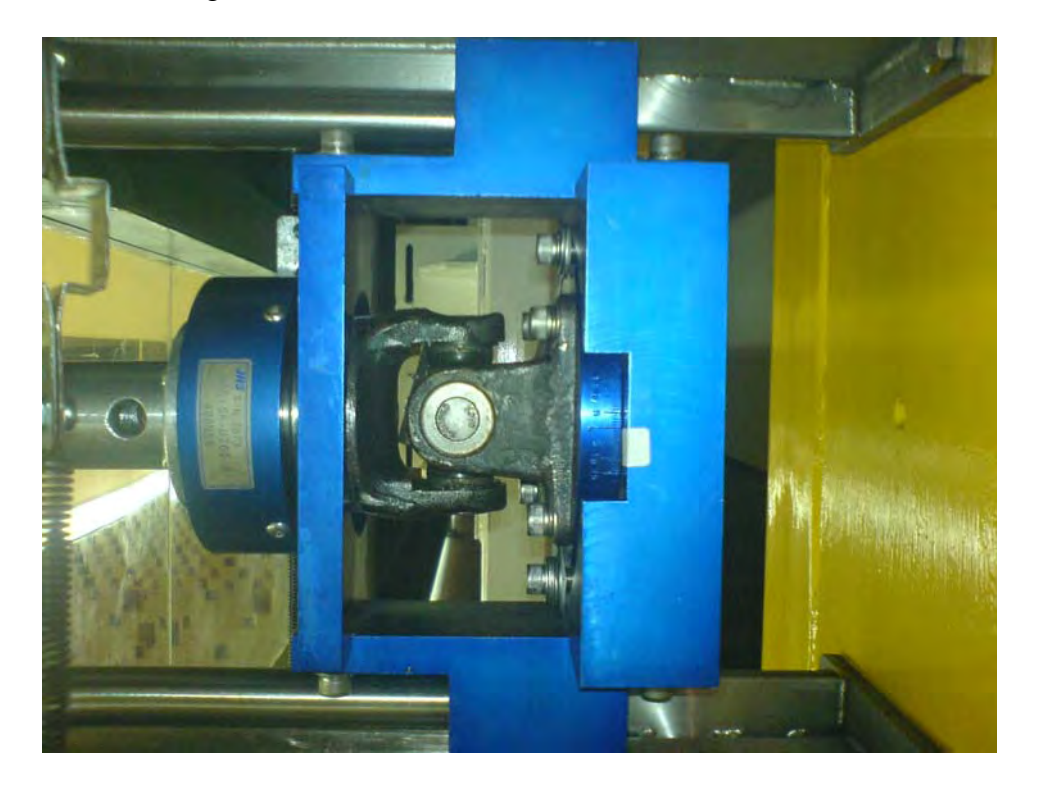


Fig. 7.15(d) Load cell supported by universal joint with angle-adjustable device.

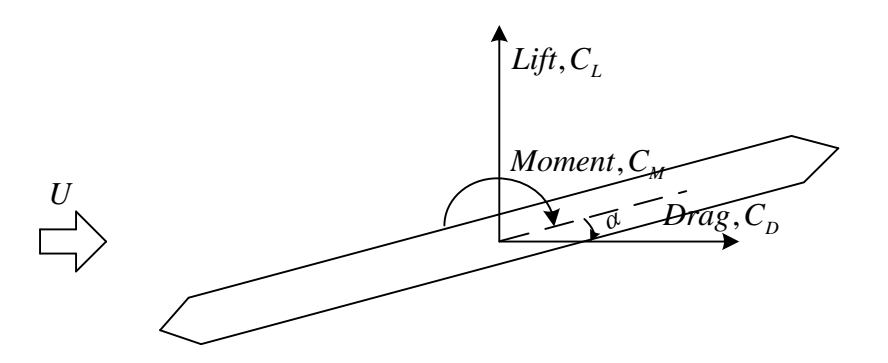


Fig. 7.15(e) Sign convention for static force coefficients

Two different sets of experiment were performed, model with and without king-post. In each set, static coefficients were determined in steps of 3° from -12° to +12°. In each angle of wind attack, model was subjected to three different wind velocities: U = 3.61, 5.65 and 8.14 m/s. At each of these velocities, the mean values of the voltage outputs of the lift, moment and drag channels from sensors were recorded. These voltage outputs at each of the wind speed values mentioned above were converted to mean force values using the calibration matrix, which were found separately, multiplied with mean value of voltage outputs. Summing of mean forces at both ends yield the total mean forces act upon the model. The aerodynamic force coefficients were then found using Eq. 6.4 as:

Lift coefficient	$C_L = \frac{L}{0.5 \rho U^2 B l}$
Drag coefficient	$C_D = \frac{D}{0.5\rho U^2 B l}$
Moment coefficient	$C_M = \frac{M}{0.5\rho U^2 B^2 l}$

where B and l are the deck width and length of the section model, respectively, L, D, M are total lift, drag and moment forces respectively

Table 7.1 lists the coefficients obtained from tests and Fig.7.16 shows aerodynamic coefficients obtained for various wind angles of attack. The mean value of the force coefficients are obtained by averaging the values measure at different wind speed. The mean values of the static tests are presented in Fig. 7.16, where the determined coefficients of both models - with and without king-post - are plotted versus wind angles of attack. Table 7.1 summarized the test results of the streamlined thin flat plate with various angles of attack. All presented drag coefficients have been corrected for the additional drag on the king-post. In an initial test, the drag on the section with king-post was measured. This was followed by a measurement without the king-post installed.

Table 7.1 Static load coefficients of the thin flat plate model: smooth flow

Coefficient	angle of attack [α, deg]									
	-12	-9	-5.5	-3	0	3	6	9	12	
With king-post										
C_{D}	0.204	0.141	0.048	0.040	0.040	0.039	0.062	0.141	0.209	
$\mathrm{C_L}$	-0.775	-0.744	-0.415	-0.189	0.062	0.318	0.581	0.837	0.876	
C_{M}	-0.069	-0.151	-0.116	-0.056	0.003	0.070	0.142	0.155	0.122	
Without king-post										
C_D	0.211	0.128	0.040	0.024	0.027	0.028	0.053	0.134	0.203	
$C_{ m L}$	-0.751	-0.729	-0.432	-0.178	0.053	0.318	0.561	0.836	0.861	
C_{M}	-0.084	-0.141	-0.118	-0.052	0.008	0.071	0.155	0.161	0.139	

The measured drag on the king-post matches very well the theoretical estimation. The Reynolds Number for the king-post, R_e , is $2.16 \times 10^3 < R_e < 4.86 \times 10^3$ for a typical diameter of 9 mm and wind velocity ranging between 3.61 m/s and 8.14 m/s. For this range of R_e the static drag coefficient (C_D) is 1.10. The drag force on kingpost is calculated based on this coefficient and then converted to equivalent drag coefficient based on the thin plate dimension for comparison. The equivalent drag coefficient equals 0.0126 compared to 0.0127 from test results. The measured lift and moment coefficients at various angles of attack are also plotted (Fig. 7.16) for both with and without kingpost models together with the theoretical values see e.g. Joukowski (1916) and Dyrbye and Hansen (1996). These theoretical values are valid for small angles of attack only. The sudden drop in pitching moment and lift force at an angle of attack of approximately 7° is due to flow separation occurring at angles of attack larger than approximately 7° . Flow separation has not been taken into account in the theoretical calculations presented. The results are shown that effects of kingpost are negligible for lift and pitching coefficients.

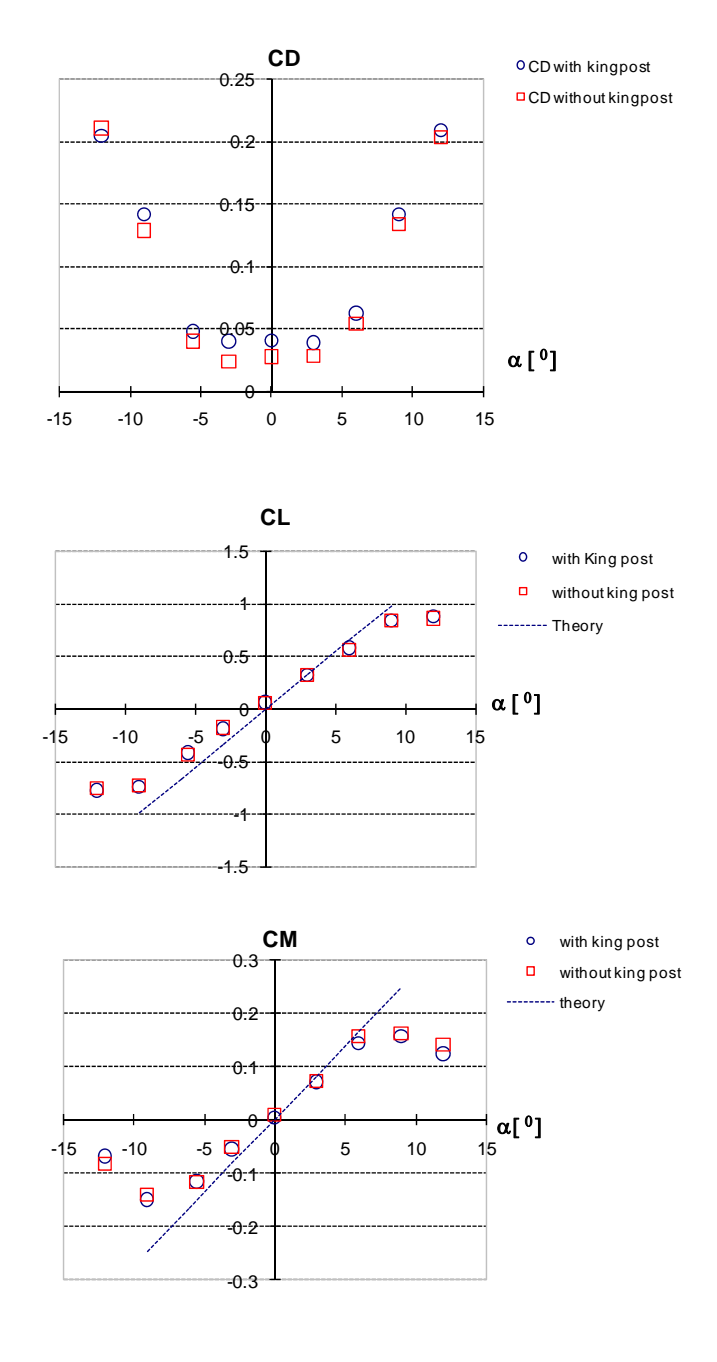


Fig. 7.16 Static load coefficients of the thin flat plate model: smooth flow

7.3 Industrial Ring Road Bridge Deck

Encouraged by the success in the thin plate model, the flutter derivatives of the IRR Bridge, a cable-supported bridge with a 2-edge girder, as shown in Fig. 5.4, were estimated by both the SSI-DATA and the SSI-COV techniques. The IRR Bridge has a main span of 398 m. The deck consists of a concrete deck slab and a web of steel girders. The deck is supported by two cable planes at the outside edge girders. A 2-edge-girder bridge section with A-shape pylons has a good cost performance, but at the same time the bridge cross-section is known to be aerodynamically unstable at high wind speed. Table 6.2 lists the main parameters of the prototype bridge and the section model. Tests were conducted under smooth and two levels of turbulence wind flows. The turbulent flow conditions were generated by grids and spires. The longitudinal and vertical turbulence intensities were both about 5% and 8%, respectively.

Using both SSI techniques, the flutter derivatives of the IRR Bridge were estimated for 2DOFs responses by both the free decay and the buffeting tests under smooth and two levels of turbulence flows. The results between two test methods were then compared.

Piano wires were used to restrain the undesirable lateral motions. The following experimental parameters were used for the coupled motion tests: Mass = 12.84 kgs; mass moment of inertia about center of mass = 0.17262-kg m²; modal frequencies (U=0): $n_h=2.13$ Hz, $n_\alpha=4.73$ Hz; modal damping (U=0): $\zeta_h=0.40\%$, $\zeta_\alpha=0.13\%$; separation between springs (d=380 mm; length (span) of model = 2.26 m.; laser sensors were separated at 380 mm. Each acceleration transducers, installed at the mid-section of model, was placed at 125 mm apart from center of rotation.

Determination of mass was performed by the method described in section 3.6.1. However, determination of the mass moment inertia describing in section 6.2 are somewhat difficult to apply as the top surface of bridge deck has 2.5%-slope. Then, the method described in section 3.6.1 was applied. First, the mass of model was obtained, and then the vertical stiffness can be determined. Having known separated distance of supported spring and torsional frequency of model from the free vibration test, the mass moment of inertia can be determined.

As model was manufactured from wood and very long, the geometrical scaling also results in thin dimensions with too little stiffness. The original model has local vertical bending mode around 9 Hz. In order to eliminate this local mode and having sufficient vertical and torsional stiffness of the model a so-called "king-post" was installed. A king-post is a stiffening system composed of two posts and 16 gauged wires as seen in Fig 7.17a. The model is supported by gauged wires at 4 points with equidistance. The king-post is symmetric from above and below the deck, and as it is only consists of rounded members lift / vertical motion and moment / torsional motion are not influenced by the king-post.



Fig. 7.17a The IRR Bridge section model with king-post in wind tunnel

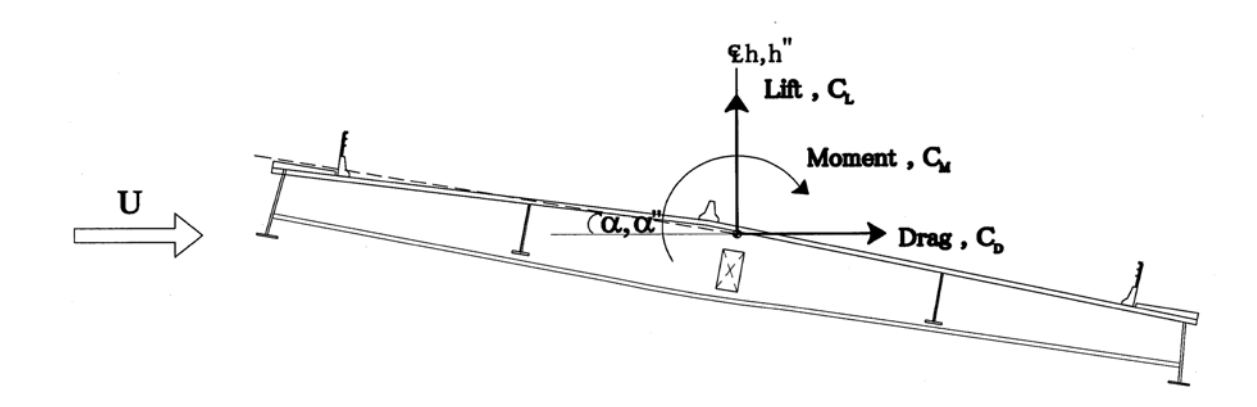


Fig. 7.17b Sign convention for IRR bridge section

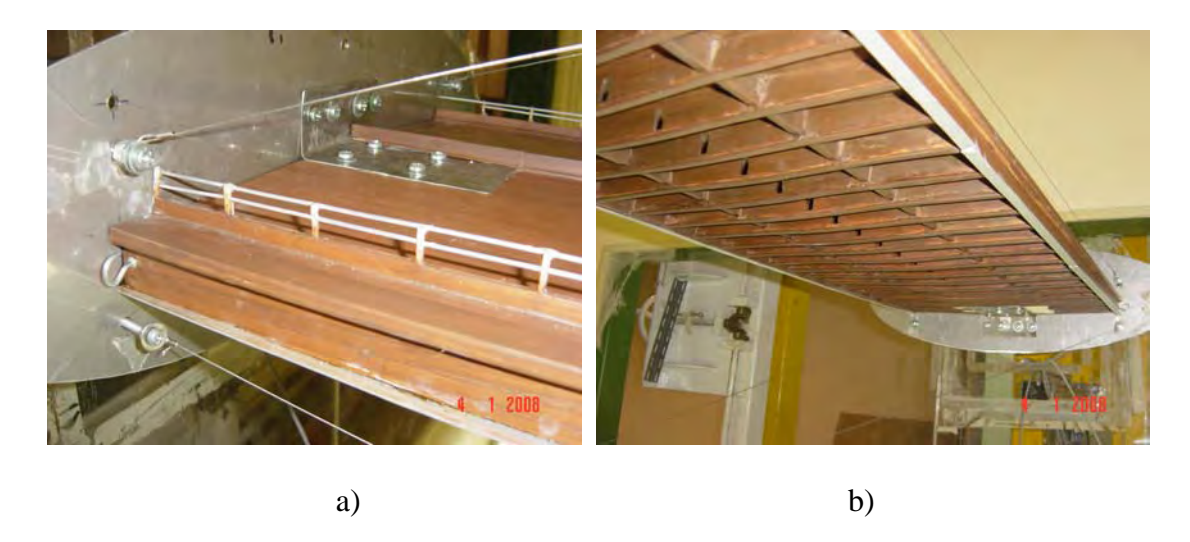


Fig. 7.18 The IRR Bridge section model details: a) model connection at end plate b) bottom view

Fig. 7.19 shows examples of free decay responses at various wind speeds. The amplitude dependence of the damping ratio was also checked. Fig. 7.20 plotted the damping ratios with the root mean square of response amplitude in 'still-air'. The damping ratios are considered to be practically acceptable as they are varying from 0.1-0.15\% and 0.33-0.40\% in range of responses in tests. The testing procedures are in similar as those in the thin flat plate case. The sampling frequencies were 1000 Hz and 200 Hz with the total time records equal to 60 s and 500 s for the free decay and the buffeting tests, respectively. The recorded data were then removed trend, resampled at 250 and 50 Hz, and then low pass filtered at 6 Hz by the 8-ordered butterworth filter. The low pass filter introduced no amplitude modification at $n_h =$ 2.13 Hz, while there was a 3% amplitude reduction at $n_{\alpha} = 4.73$ Hz. This filtered frequency was selected due to the reason that at high wind speed, there was presence of small amplitude of local torsional mode at 6.7 Hz. This mode was believed to be the local mode of the king post/thin deck slab system that could not be fully fixed at base due to the deck slab are thin and top-sloped. Many attempts have been made to eliminate this mode such as more guy wires added, nailing deck slab to cross girders and even increasing of the base plate thickness, but resulting only in lesser amplitude of this mode.

Carefully review of previous research found that such a low ratio of highest modal frequency to nominal cut-off frequency as 0.7 has been used as long as amplitude distortion are not much affects and the linear phase delay filter are used (Sakkar 1994, King 1995, Brownjohn and Jakobsen 1995). In order to check the effect of low pass filter used, a simple signal was simulated by combining two sinusoidal signals with the same frequencies of vertical and torsional mode, then this signal was pass through the 8-order low-pass filter with the cut-off frequency at 6 Hz. Fig. 7.21 compares the time-histories of the original and the filtered signals. The result shows that the filtered signal agreed well with the original signal with only the small distortion found at the end of signals.

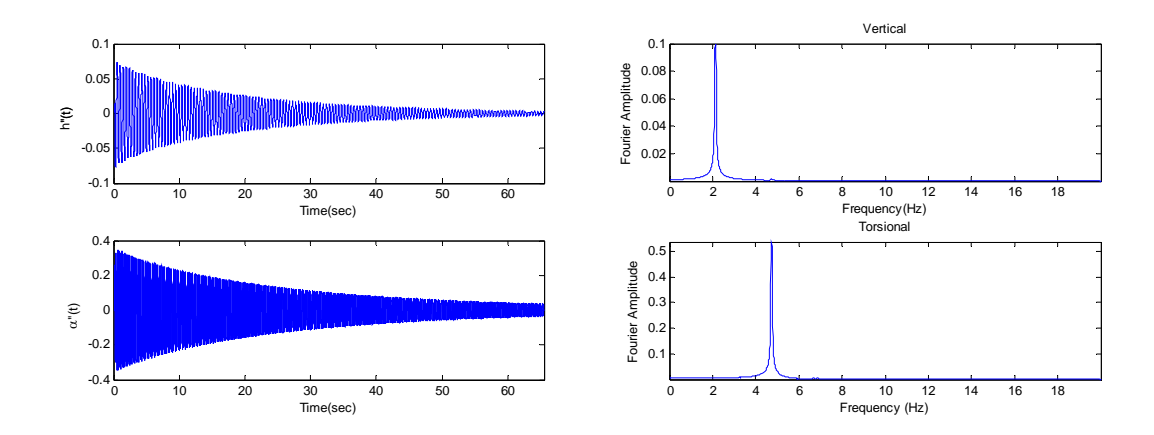


Fig. 7.19 The IRR bridge model : free decay acceleration time histories and frequency spectrum for h and α at U=0 m/s

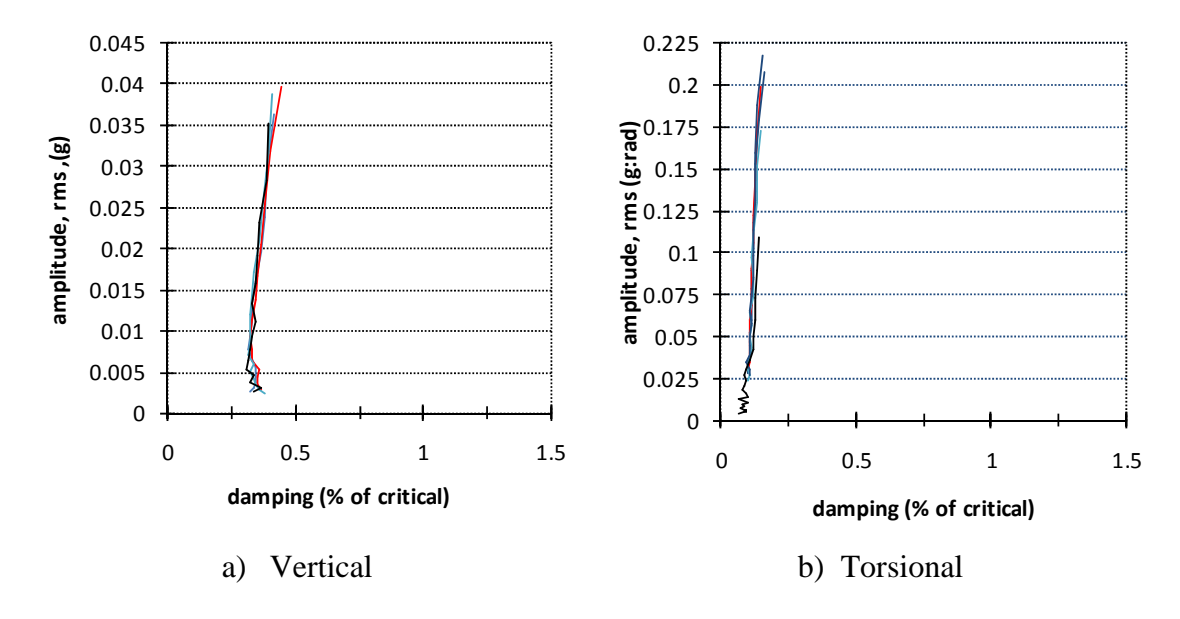


Fig.7.20 Damping ratio of the IRR Bridge model with amplitudes (rms in g)

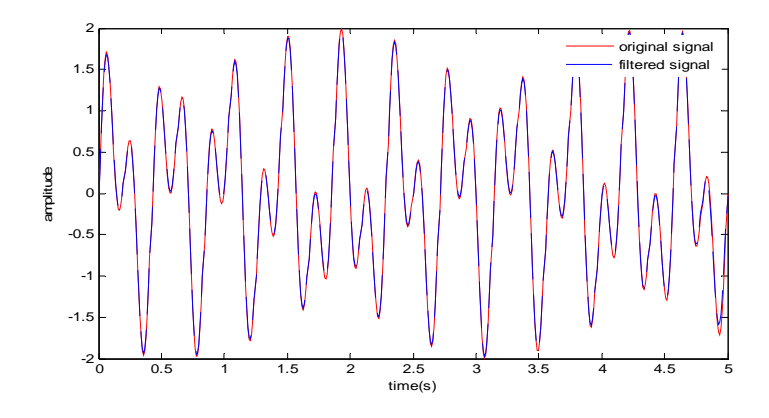


Fig.7.21 Example of low-pass filter effect to simulated signal.

7.3.1 Flutter Derivatives of the IRR Bridge Model: Smooth Flow

7.3.1.1 Comparisons of Flutter Derivatives between the SSI-DATA and the SSI-COV Method from the Free Decay Test Method.

Figs. 7.22a and 7.22b show samples of the typical test results from free decay responses of the bridge model at various wind speed. All eight flutter derivatives H_i^* , i = 1,...,4 and A_i^* , i = 1,...,4, identified by both the SSI-DATA and the SSI-COV from the free decay tests of the IRR bridge deck, are plotted and compared in Figs. 7.23 and 7.24. The notation used in case of the IRR Bridge model is in the form;

$$L_{h} = \rho U^{2} B \left[K H_{1}^{*} \frac{\dot{h}}{U} + K H_{2}^{*} \frac{B \dot{\alpha}}{U} + K^{2} H_{3}^{*} \alpha + K^{2} H_{4}^{*} \frac{h}{B} \right]$$
(3.31)

$$M_{\alpha} = \rho U^{2} B^{2} \left[K A_{1}^{*} \frac{\dot{h}}{U} + K A_{2}^{*} \frac{B \dot{\alpha}}{U} + K^{2} A_{3}^{*} \alpha + K^{2} A_{4}^{*} \frac{h}{B} \right]$$
(3.32)

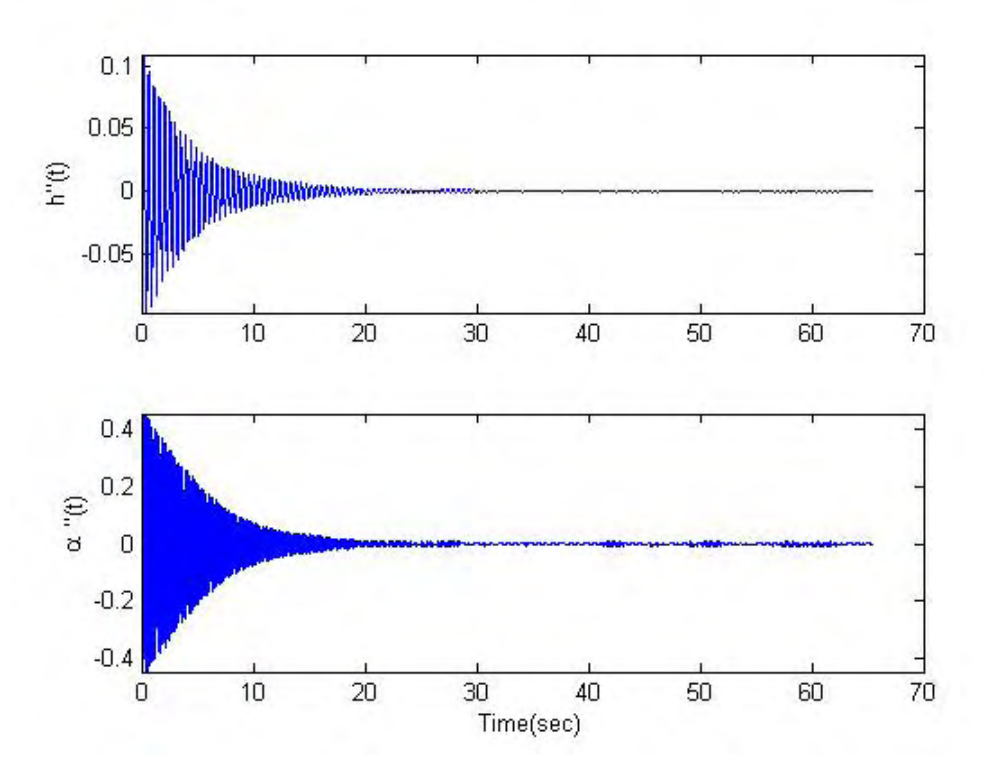


Fig. 7.22a The IRR Bridge model under smooth flow: free decay acceleration time histories h and α at U = 1.67 m/s

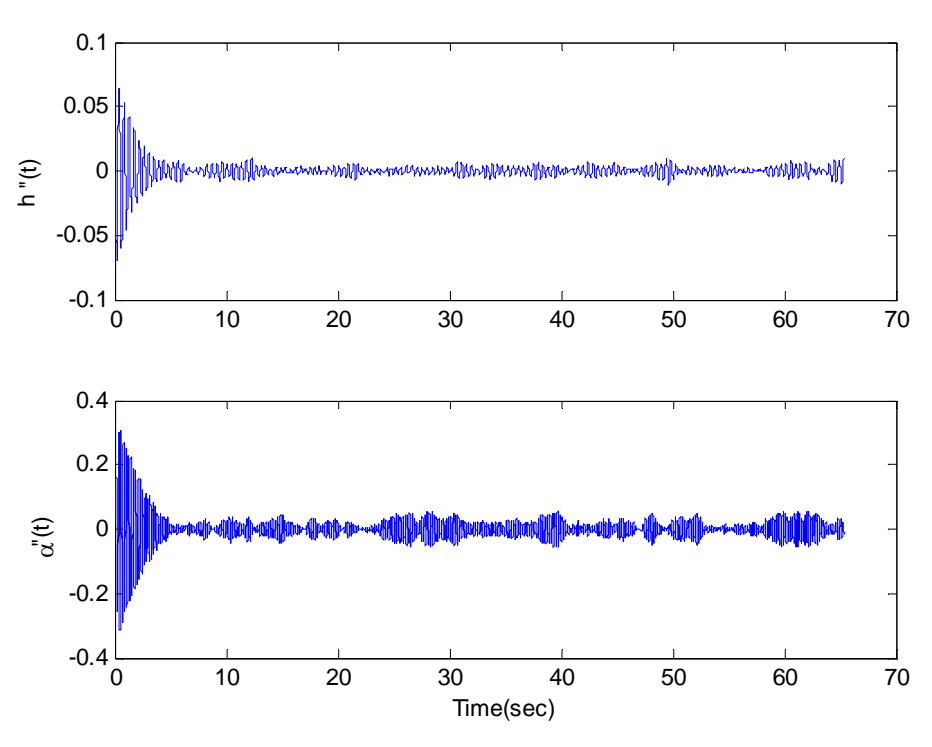


Fig. 7.22b The IRR Bridge model under smooth flow: acceleration time histories h and α at U = 6.20 m/s

This was done as the results will be compared later with the previous test (DMI 1995), the same notation was then used. This alternate form differs from the thin flat plate case where the definition of the flutter derivatives is 2 times higher.

From Figs. 7.23 and 7.24, it can be seen that the most important factor A_2^* extracted by both SSI methods match very well with each other. It is steadily increased (more negative) up to reduced velocity around 3, and then started to decreased. This sign reversal is the outstanding factor toward the SDOF-torsional instability (stall flutter) reported in the next section. The vertical aerodynamic damping term, H_1^* extracted by both methods remain negative in all reduced wind speed and match well to each other up to a certain wind speed where small difference can be seen. This is because at high wind speed, the vertical mode are rapidly damped out but the coupling of rotation motion by H_3^* were increased (as seen by the presence of torsion mode in vertical mode). The short useful length of recorded signal and the strongly presence of another mode made extraction of vertical damping more difficult. The frequency-related aerodynamic terms: H_4 *and A_3 * also match well between the two methods. However, the coupled aerodynamic terms (H_2^*, A_1^*, A_4^*) , in turn, found from the SSI-COV method are more scattered than those from the SSI-DATA method. The largest scatter among the extracted parameters are A_1 * and A_4 *.

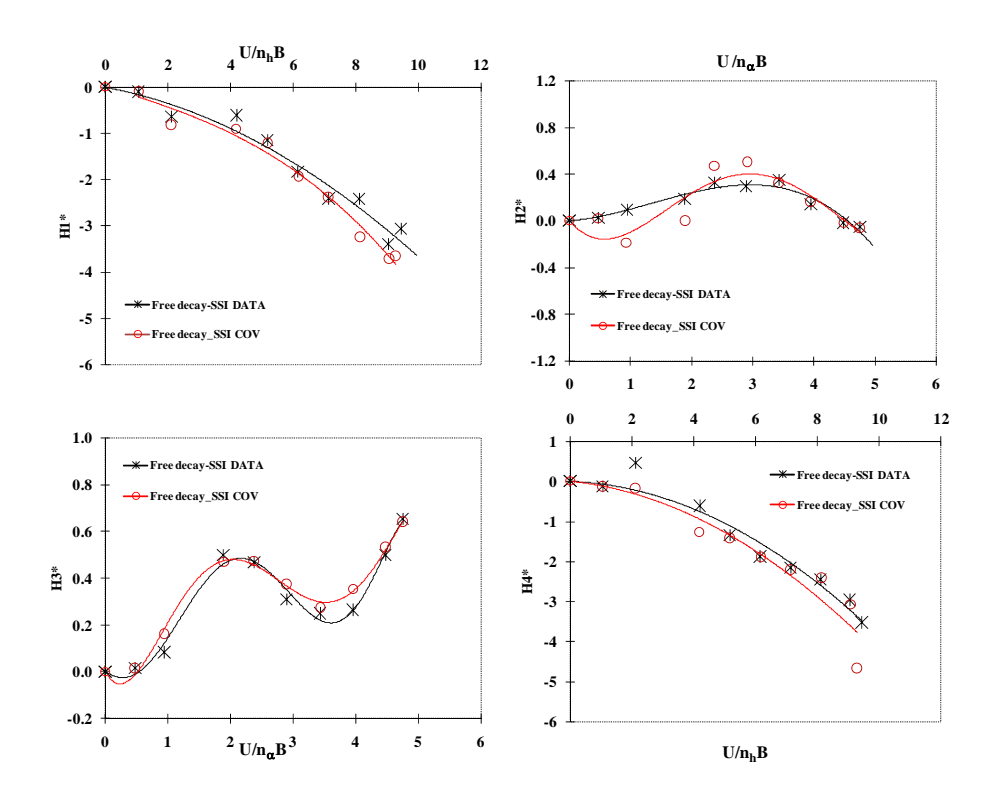


Fig. 7.23 Flutter derivatives $(H_1^*, H_2^*, H_3^*, H_4^*)$ of the IRR Bridge model from the free decay tests by the SSI-DATA and the SSI-COV under smooth flow

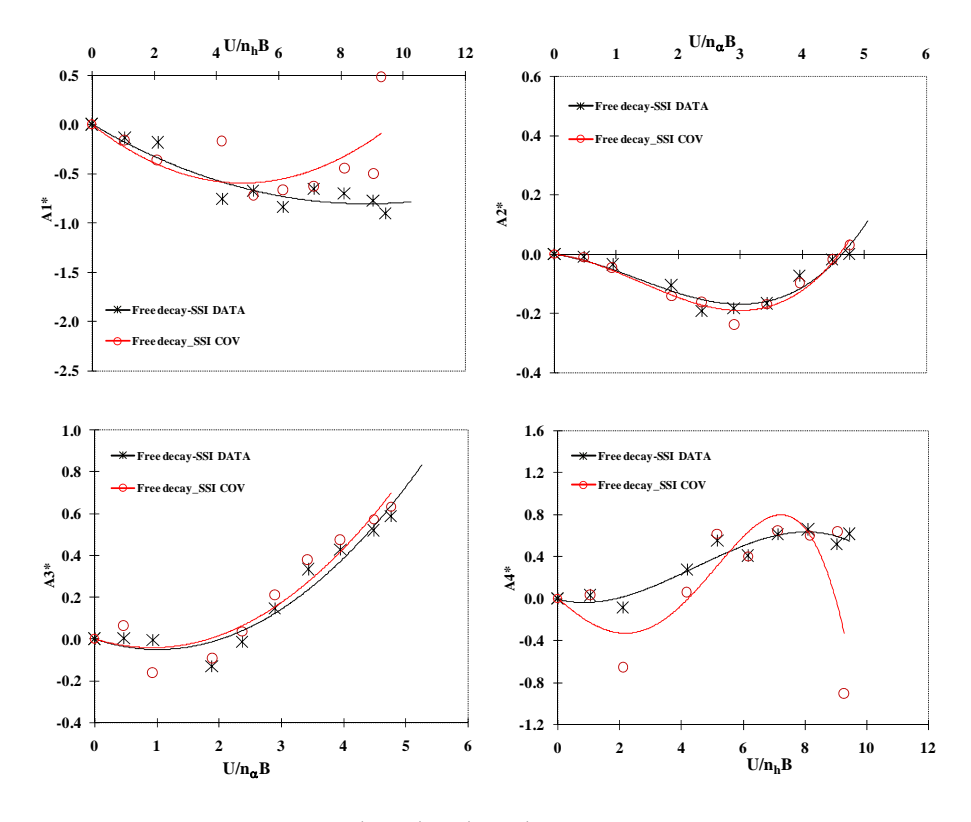


Fig. 7.24 Flutter derivatives $(A_1^*, A_2^*, A_3^*, A_4^*)$ of the IRR Bridge model from the free decay tests by the SSI-DATA and the SSI-COV under smooth flow.

7.3.1.2 Comparisons of Flutter Derivatives between the SSI-DATA and the SSI-COV Method from the Buffeting Test.

The buffeting response data were analyzed both by the SSI-COV and the SSI-DATA methods. The mass of the IRR Bridge model is approximately 25% lesser than the thin plate section. This makes possibility for extraction of flutter derivatives in lower wind speed range. Typical test results showing responses from the IRR Bridge model are in Fig. 7.25.

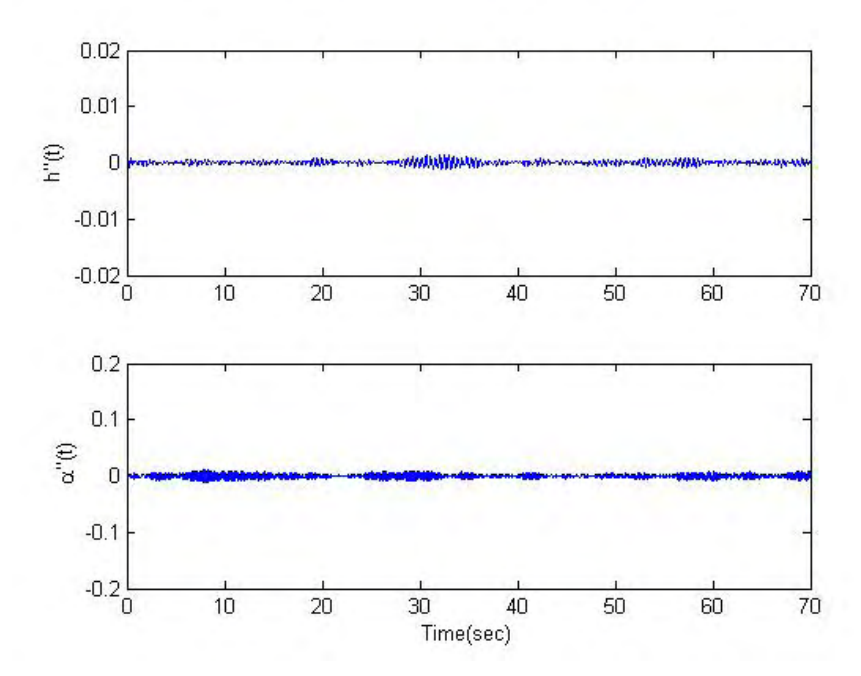


Fig. 7.25a Part of vertical (top) and torsional (bottom) buffeting acceleration responses of the IRR Bridge model at 1.72 m/s wind speed under smooth flow. (unit in g)

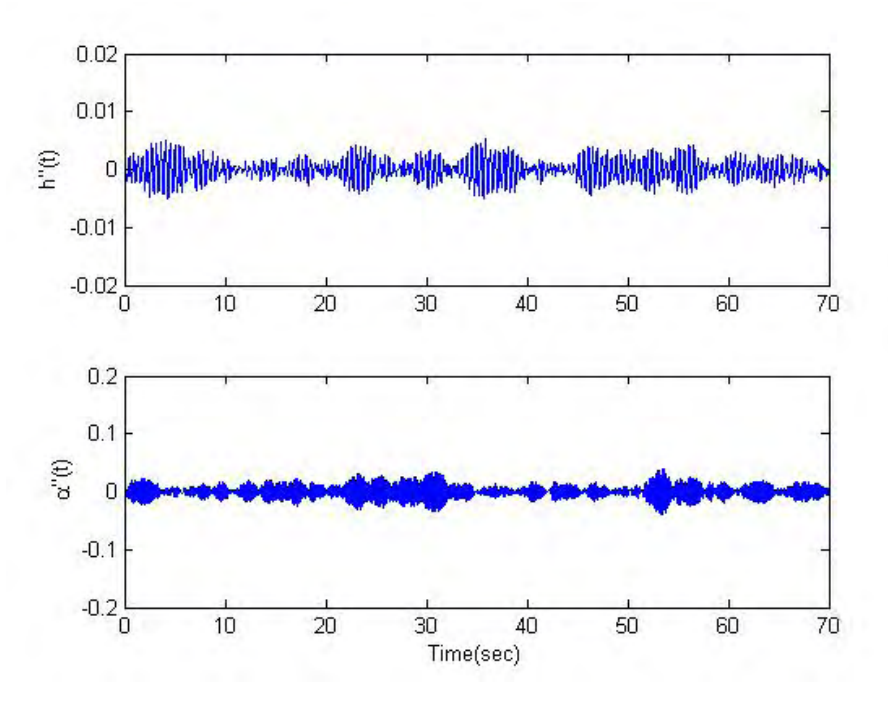


Fig. 7.25b Part of vertical (top) and torsional (bottom) buffeting acceleration responses of the IRR Bridge model at 3.95 m/s wind speed under smooth flow. (unit in g)

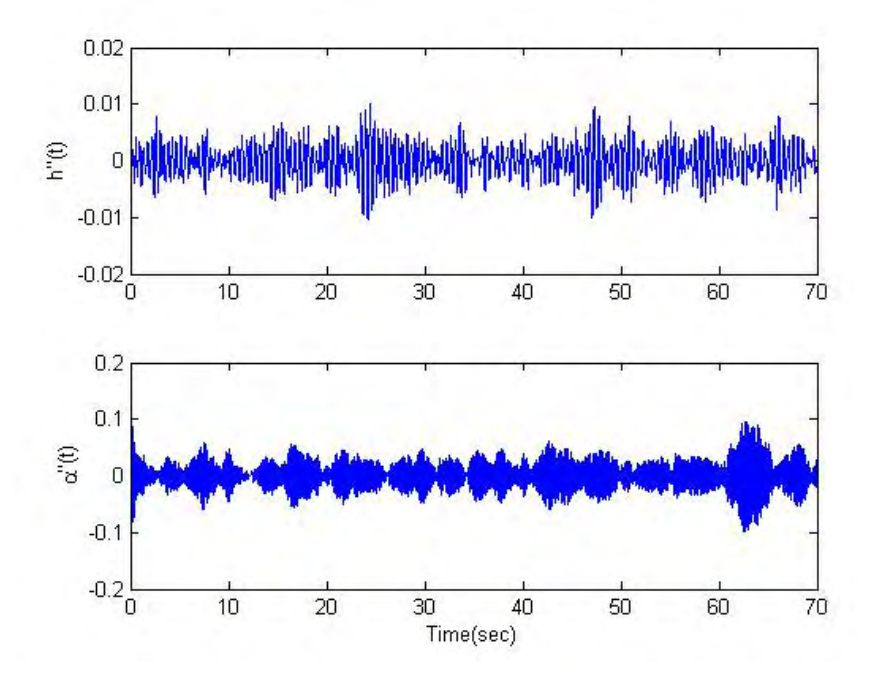


Fig. 7.25c Part of vertical (top) and torsional (bottom) buffeting acceleration responses of the IRR Bridge model at 5.32 m/s wind speed under smooth flow. (unit in g).

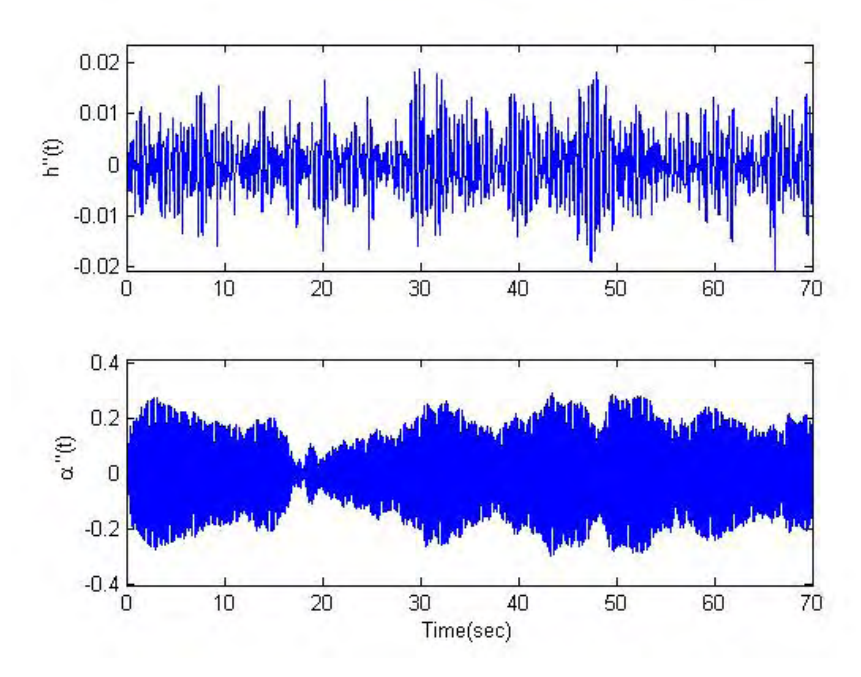


Fig. 7.25d Part of vertical (top) and torsional (bottom) buffeting acceleration responses of the IRR Bridge model at 6.88 m/s wind speed under smooth flow. (unit in g).

All eight flutter derivatives H_i^* , i = 1,, 4 and A_i^* , i = 1,, 4, as obtained by the SSI-COV and the SSI-DATA from the buffeting test, are plotted in Figs. 7.26-7.27. The torsional aerodynamic damping A_2^* and the vertical damping term H_1^* extracted by the two SSI methods match well to each other. The identified torsional aerodynamic stiffness term A_3^* are also almost identical by the two methods. The vertical aerodynamic stiffness H_4^* extracted by both methods also in good agreement with small scatter. The cross-coupling derivatives H_2^* and H_3^* also agree well except small difference of H_3^* at reduced wind speed around 2-3. On the other hand, the identified A_1^* term are somewhat different at high wind speeds. The largest difference is the most sensitive term A_4^* .

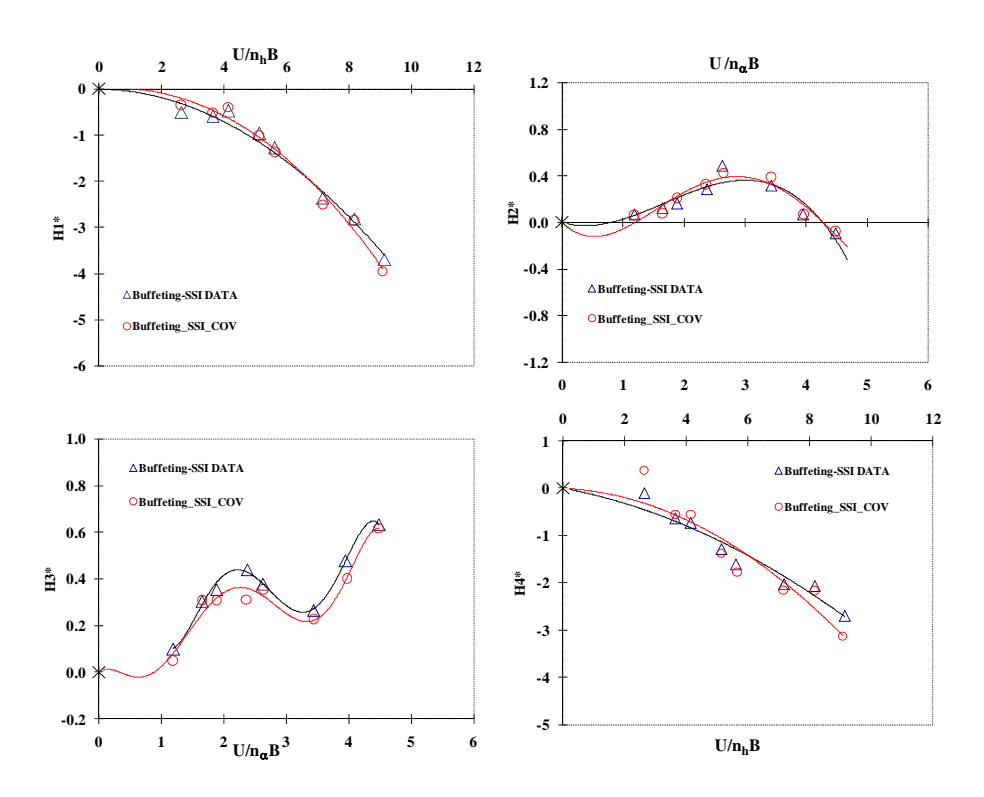


Fig. 7.26 Flutter derivatives $(H_1^*, H_2^*, H_3^*, H_4^*)$ of the IRR Bridge model from the buffeting test by the SSI-DATA and the SSI-COV under smooth flow.

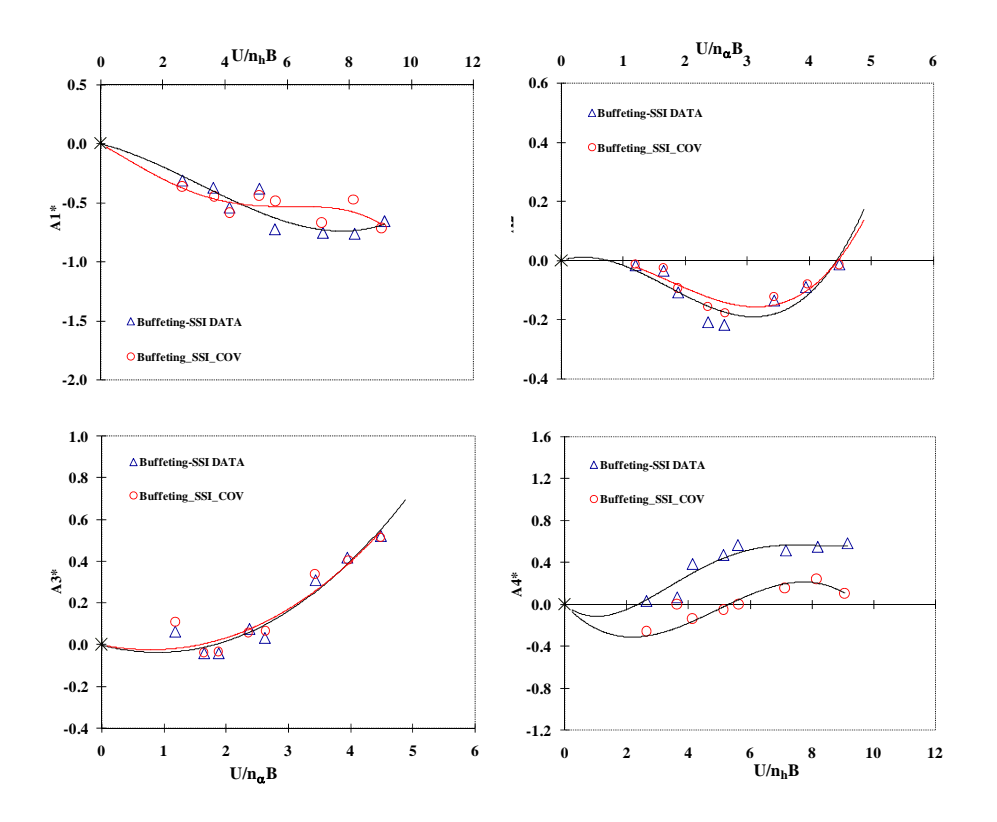


Fig. 7.27 Flutter derivatives $(A_1^*, A_2^*, A_3^*, A_4^*)$ of the IRR Bridge model from the buffeting test by the SSI-DATA and the SSI-COV under smooth flow.

7.3.1.3 Comparisons of Flutter Derivatives between the Free Decay and the Buffeting Tests under Smooth Flow.

All flutter derivatives found from the free decay (by the SSI DATA technique) and the buffeting tests (by the SSI DATA and the SSI–COV) are plotted and compared in Figs. 7.28 and 7.29. The results show that the flutter derivatives identified by the SSI-DATA from the buffeting test matched well with those from the free decay test. This result helped validate the reliability and applicability of the SSI-DATA technique to various experimental methods. This confirms the ability of the SSI-DATA to apply with the free decay signal though it developed from stochastic model (white noise loading assumption) as do the thin flat plate results. Besides, this result allowed focusing on applying the SSI-DATA technique to the buffeting test method.

On the other hand, there are more variations in the values of the A_1^* , A_4^* and H_2^* derivatives obtained by the SSI-COV between the free decay and the buffeting tests (see Figs. 7.24, 7.28 and 7.29).

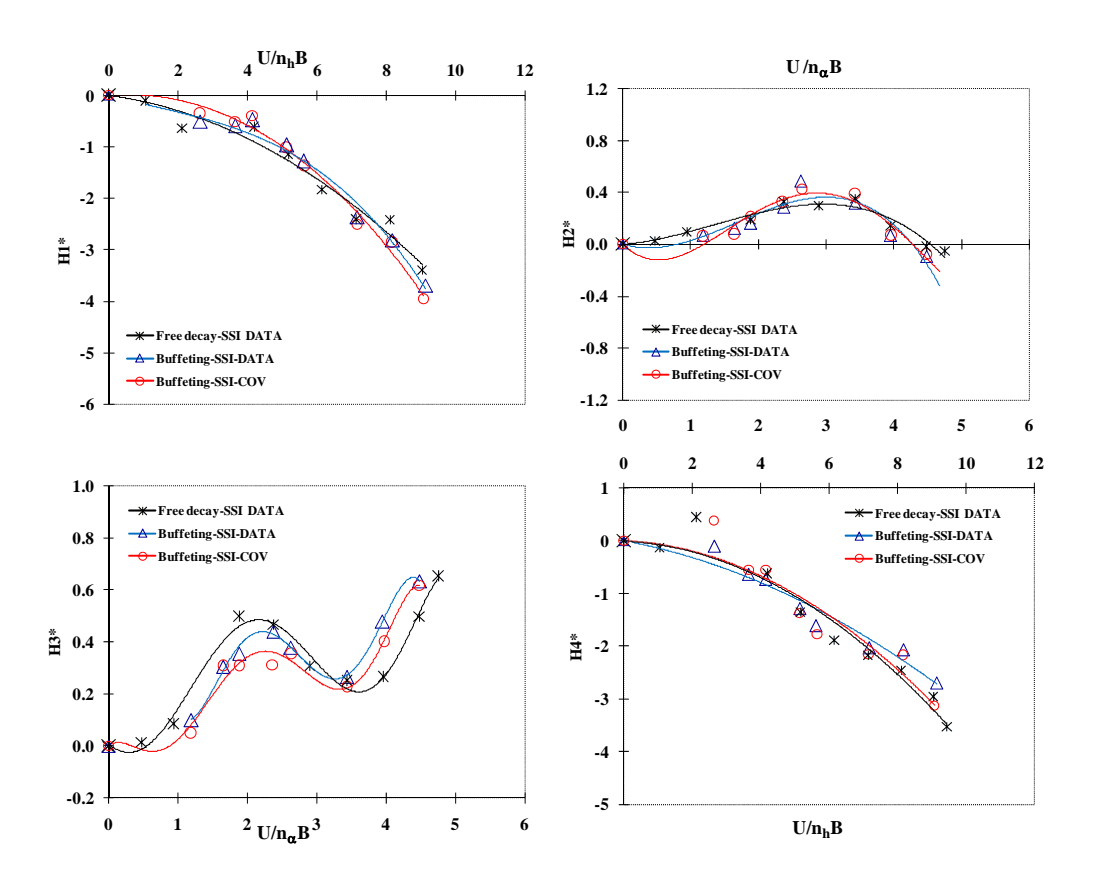


Fig.7.28 Comparison of H_i^* from couple-degree-of-freedom tests with initial displacement (SSI DATA) and without initial displacement (SSI-DATA, SSI-COV) under smooth flow

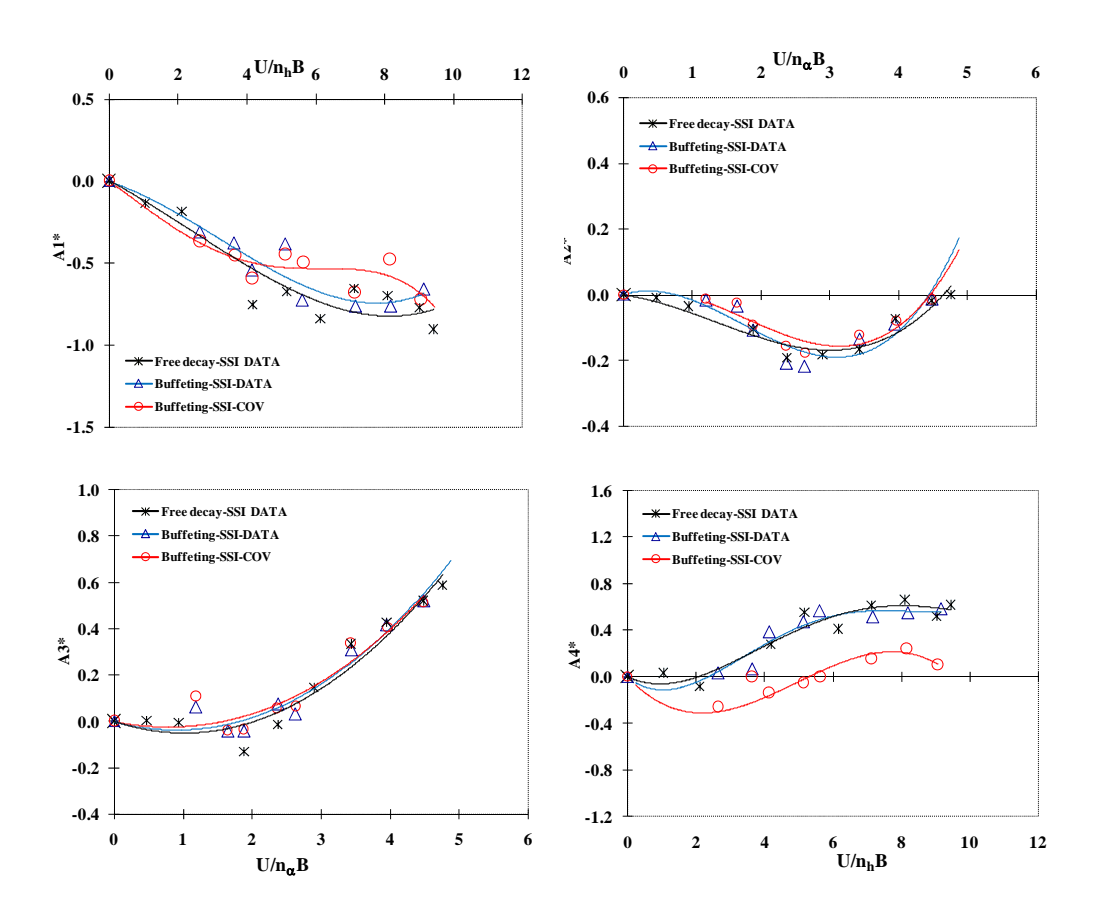


Fig.7.29 Comparison of A_i^* from couple-degree-of-freedom tests with initial displacement (SSI DATA) and without initial displacement (SSI-DATA, SSI-COV) under smooth flow

7.3.1.4 Comparisons of Flutter Derivatives with the Previous Method.

In order to validate the present system identification technique, the identified flutter derivatives were then compared with the previous work. The free decay test of the same bridge model had been previously carried out in smooth flow by DMI (1995) at the zero angle of attack. The system identification method used in extracting the flutter derivatives was based on that proposed by Poulsen and Damsgaard (1992). This method was briefly described in previous chapter. (see chapter 2) and identification process are iteration in nature to minimize the prediction error. The vertical and torsional frequencies of the model are 2.29 Hz and 5.18 Hz, respectively. The ratio of the torsional to vertical frequency is 2.26. Tests were performed with the inherent damping ratios that were found to vary from 0.2% at small amplitude to 0.3% of critical at higher amplitudes for heave (vertical) motion and range from 0.21% to 0.24% for pitch (torsional) motion.

Figs. 7.30 and 7.31 show the flutter derivatives of the IRR Bridge deck estimated by both SSI methods from the free decay tests as well as those by Poulsen's method. The derivatives obtained by Poulsen's method shown in Figs 7.30 and 7.31, have been fit by least square method, then the original extracted values were not known. All flutter derivatives – except H_1^* , H_4^* and A_4^* - from the SSI techniques

match well in trend with those from Poulsen's method (DMI 1995). The H_1^* and H_4^* coefficients are those related to the aeroelastic damping and frequency of vertical mode, respectively. From DMI's results, the aeroelastic damping increases with velocity at low reduced velocities up to the value around 6, and then decrease at higher velocities. This shall be resulted in the classical flutter (coupled mode instability). However, both buffeting responses from the present study and the DMI's tests show only flutter instability in the torsional mode (stall flutter), see Fig 7.44. The factor that made the difference in the extracted values of H_1^* and H_4^* is the system identification technique employed. For the system identification method proposed by Poulsen and Damsgaard (1992), it involves iterations in fitting the measurement of free decay time -histories of bridge deck in heave and torsion. This analysis procedure is complicated, requires good initial guess-values, and was found to work quite well for tests where the initial excitation produced a clearly defined initial condition where both heave and pitch responses decayed in a somewhat regular manner following the excitation. As reported by the authors of the method, according to the free decay method, the bridge model had to be excited initially in both modes to sufficient amplitudes to allow that the initial response to the excitation is well defined. This is usually not the case for tests at high velocities of bridge sections those exhibit strongly aeroelastic damping as the responses are damped very fast and meaning full signal are too short. In addition, the presence of torsional motion in vertical motion due to the effect of H_3^* made the identification more difficult. The factor that made the extraction of A_4 * difficult by the Poulsen's method is that this derivative is very sensitive. Besides, the A_4 * term was not included in the original works of the authors of the method.

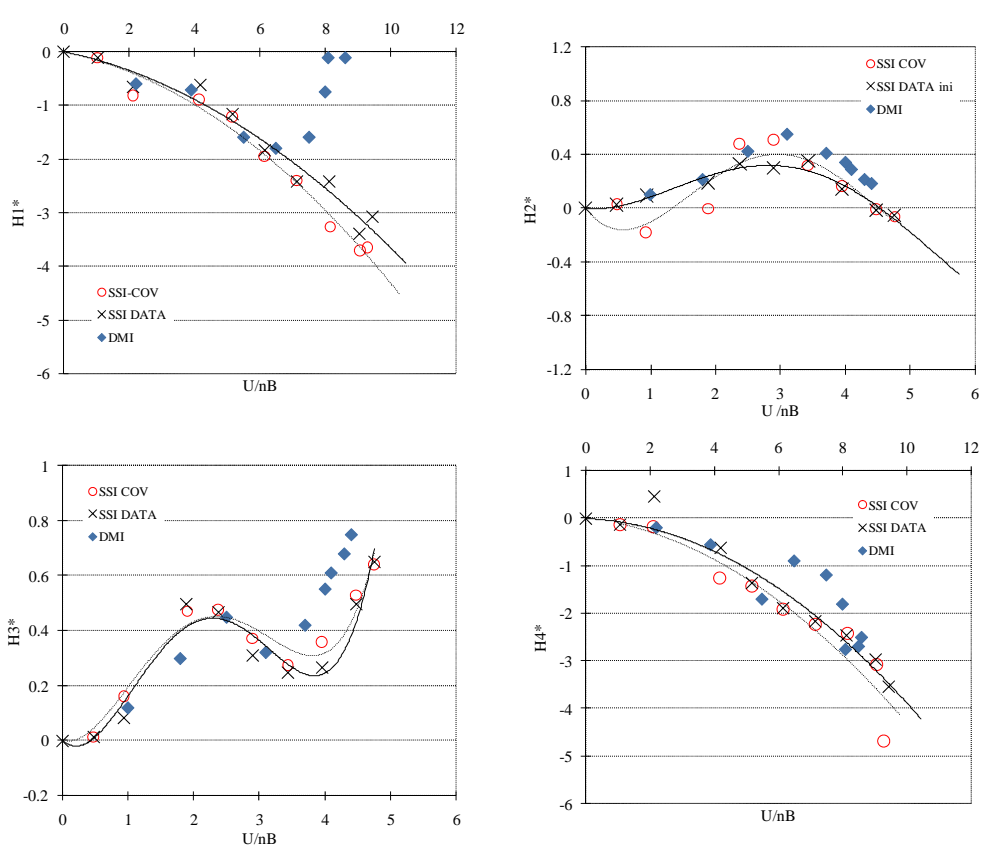


Fig.7.30. Comparison of H_i^* from the free decay test with difference system identification methods; SSI-DATA, SSI-COV and Poulsen's method.

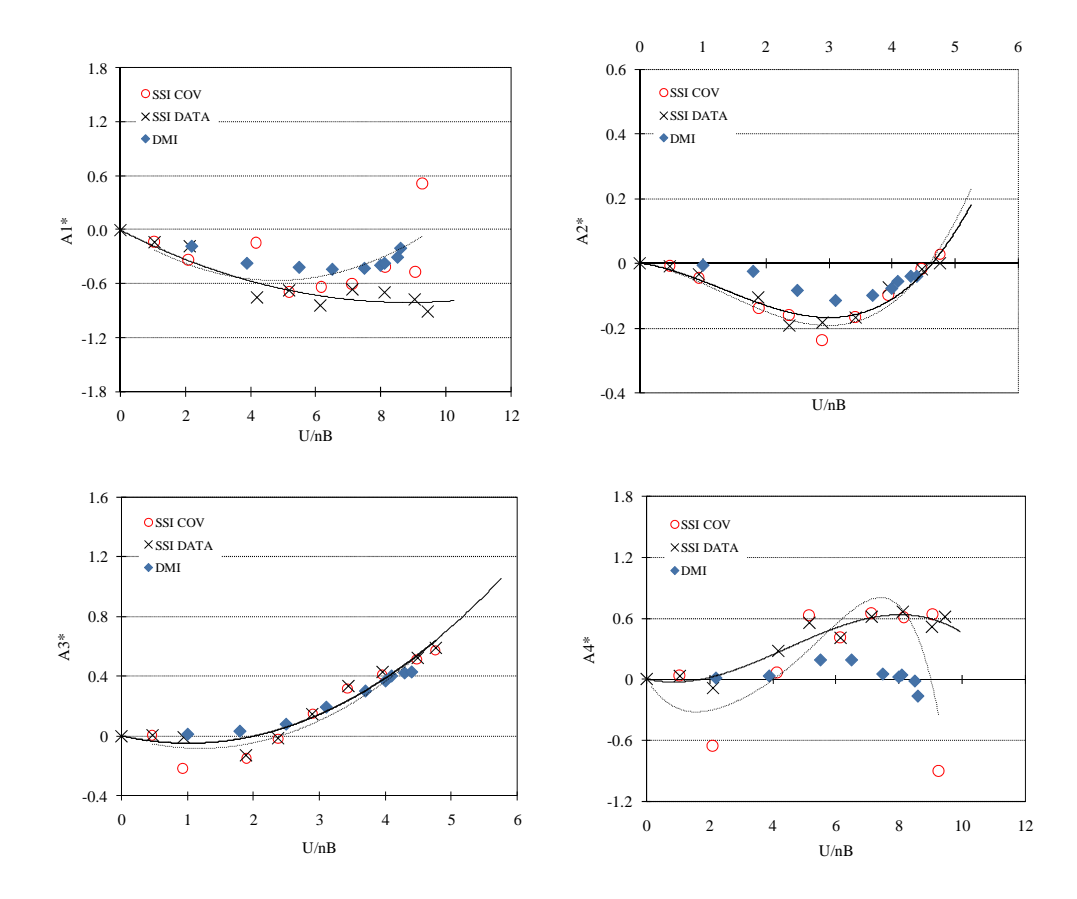


Fig.7.31 Comparison of A_i^* from from the free decay test with difference system identification methods; SSI-DATA, SSI-COV and Poulsen's method.

Summary of the test results of the IRR Bridge deck under smooth flow

Application of both the SSI-DATA and the SSI-COV to real bluff bridge section learned that both SSI methods have good capability in extracting derivatives from buffeting responses even they have less clear signal to noise ratio compared with free decay response. Generally, the flutter derivatives identified by the SSI-DATA match well with those from the free decay method. On the other hand, there are more variations in the values of the A_1^* , A_4^* and H_2^* derivatives obtained by the SSI-COV. There are also some difference for H_1^* from the free decay by two SSI methods and the Poulsen's method. This is the same as what reported in most previous research, where some difference exit. The factor that made extraction of H_1^* more difficult is that most of bridge sections shows that H_1^* remains negative in all various wind speed, resulting in very short useful length of recorded data in the free decay response. Besides, at high wind speed the trigger initial excitation was suddenly buried to buffeting response excited by wind. Therefore, it is clearly seen that the concept of stochastic response in SSI identification can dramatically improve the ability in extracting these parameters at high wind speed. Based on the identification algorithm, this identification process does not require cleared decay signals and factorization of signals are used instead of fitting the original signals. In case of Poulsen's method, as

original vertical mode are rapidly damped out and the strongly presence of another mode (coupling torsional mode) made the extraction of H_1^* difficult.

The methods will next be applied to analyze response of this bridge deck in turbulence wind flows.

7.3.2 Flutter Derivatives of the IRR Bridge Model: Effects of Turbulence



Fig. 7.32 The IRR Bridge model and grids to generate turbulent flow in wind tunnel.

Most of the prototype bridges are submerged in turbulent wind; therefore, detailed investigations of the effects of turbulence on the flutter derivatives are significant. Almost all the wind tunnel tests for flutter derivatives have been generally carried out in smooth flows. Although few researchers have studied the problem using wind tunnel tests, results and the identification methods were individually proposed (Scanlan and Lin 1978, Sarkar *et al.* 1994, Gu *et al.* 2000), and the results are still debatable and inconclusive. For streamlined section, tests showed little effect (Sarkar *et al.*, 1994), while tests on a rectangular box girder bridge showed galloping in smooth flow (Jakobsen and Hjort-Hansen 1998). For Π type section, Gu and Qin (2004) found that the effects of turbulence on the H_3^* and A_3^* seemed to be negligible; whereas the other four derivatives related to aerodynamic damping characteristics showed some deviations from those in smooth flow, especially at high reduced wind speed.

In order to examine the effects of turbulence to the identified flutter derivatives of the IRR Bridge deck, the buffeting test were performed. Tests were conducted under two levels of turbulence wind flows. The turbulent flow conditions were generated by two different obstacles i.e. spires and grids. Figs. 6.3 and 6.7 show the configuration of spires and grids, respectively. The longitudinal and vertical turbulence intensities were both about 5% and 8% for spires and grids, respectively.

Figs 6.6 and 6.10 show the wind-velocity power spectrum at various wind speed. The installation of bridge model is as shown in Fig. 7.32.

The buffeting responses from tests were sampled at the rates of $200 \, Hz$. The results were then removed trend, re-sampled at $50 \, Hz$, and low-pass filter as same as in the case of smooth flow. However, the total time records of buffeting responses were $500 \, sec \, (\sim 8 \, min.)$ instead of $360 \, sec$ as in the case of smooth flow.

Figs. 7.33 and 7.34 present the identified flutter derivatives of the bridge deck by the SSI-DATA method from buffeting responses under smooth flow and two turbulence wind flows with both the longitudinal and the vertical turbulence intensities of 5% and 8%, respectively. Generally, the flutter derivatives of the bridge in turbulent flows identified by the SSI-DATA are in agreement with those in smooth flow. From Figs. 7.33 and 7.34, it can be found that the influence of the flow type on H_4^* and A_3^* , i.e. flutter derivatives related to the direct aerodynamic stiffness, seems to be negligible. Though, the value of H_4^* obtained from the turbulence flow is somewhat less than that in the smooth flow case, it affected only the second decimal digit of the frequency value. The influence also has negligible effect on H_1^* and H_2^* i.e. direct and cross derivatives that are related to the vertical and the torsional aerodynamic dampings, respectively. On the other hand, the more important $A_1^* A_2^*$ and H_3^* , show rather noticeable deviations from those in the smooth flow, especially at high reduced wind speeds. The most important effect is that the reduced wind speed, which corresponds to the reversed sign of the torsional aerodynamic damping A_2^* , increased in the turbulent flow. It shows that turbulence tends to make bridges more aerodynamically stable by delaying the torsional flutter. The deviations of flutter derivatives may reveal the fact that for those bridges with bluff type sections similar to the IRR Bridge, the effects of turbulence can be significant. Hence, wind tunnel tests of such bridges for flutter derivative estimation should also be carried out in turbulent flows.

Figs. 7.35 and 7.36 present the identified flutter derivatives of the bridge deck by the SSI-COV method from buffeting responses under smooth flow and two turbulence wind flows. Figs. 7.37 and 7.38 compare the flutter derivatives extracted by the SSI-DATA and the SSI-COV methods under 8%-turbulence flow. Generally, the flutter derivatives obtained by the SSI-COV agree with those from the SSI-DATA. However, the coupled aerodynamic derivatives; A_I^* and A_4^* , extracted by the SSI-COV in turn seem to be difference from those obtained by the SSI-DATA.

Figs. 7.39 and 7.40 compare the A_I^* and A_4^* derivatives identified by the SSI-COV and the SSI-DATA under different flows. It can be seen that these two derivatives are more scattered than those obtained from the SSI-DATA. This result shows that, in the case of the 2-edge girder blunt type section, applying the SSI-DATA yields better results especially for the coupling derivatives.

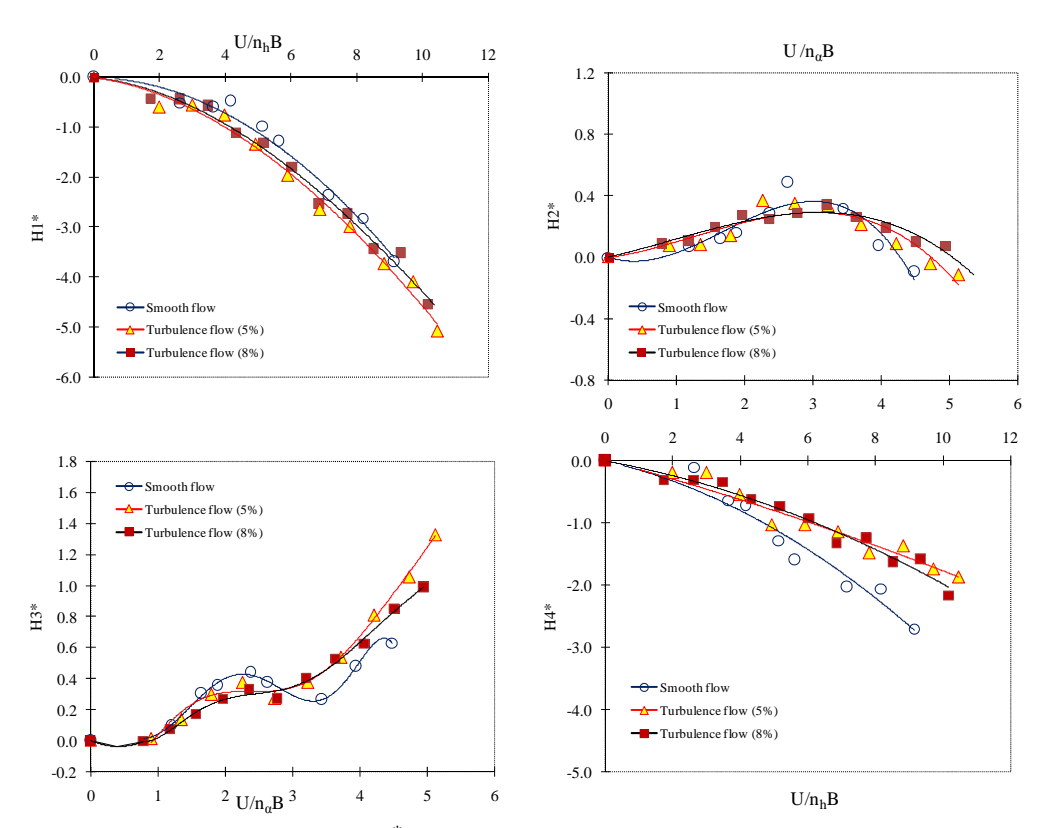


Fig. 7.33 Flutter derivatives (H_i^*) of the IRR Bridge model by the SSI-DATA from buffeting responses under smooth and turbulent flows.

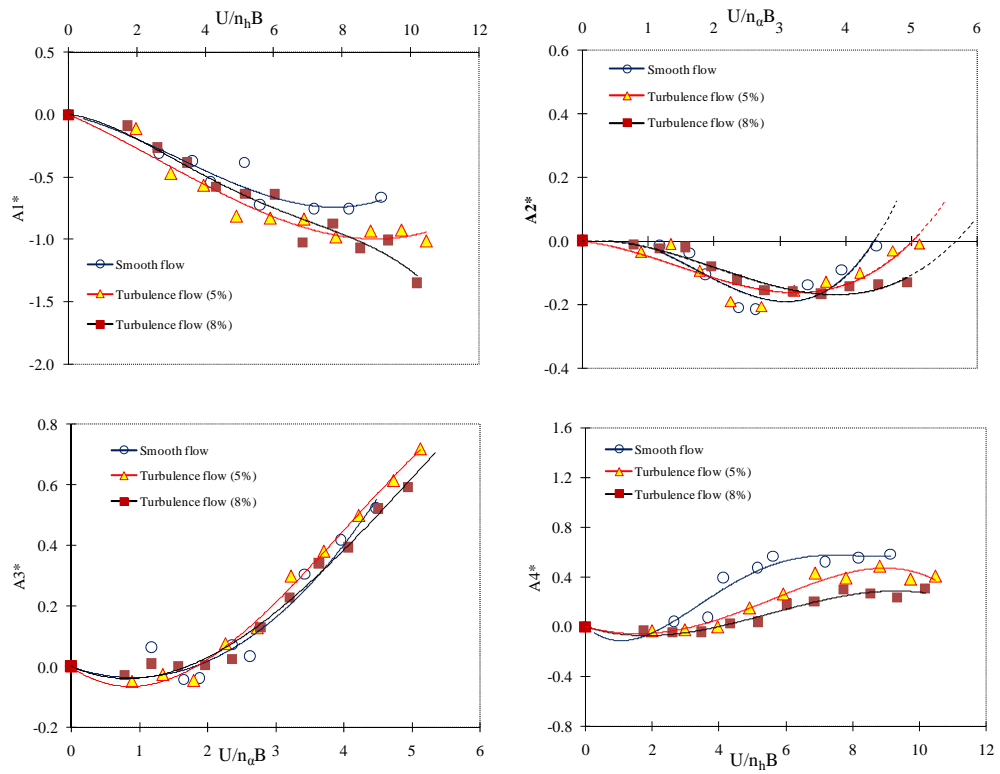


Fig. 7.34 Flutter derivatives (A_i^*) of the IRR Bridge model by the SSI-DATA from buffeting responses under smooth and turbulent flows.

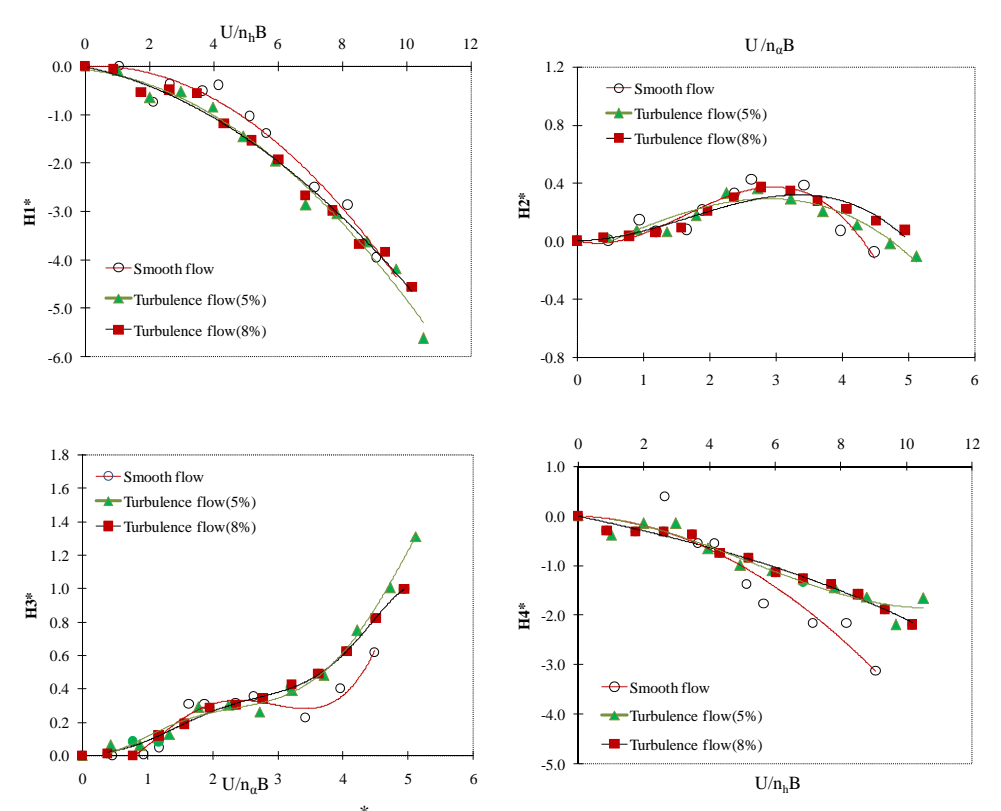


Fig. 7.35 Flutter derivatives (H_i^*) of the IRR Bridge model by the SSI-COV from buffeting responses under smooth and turbulent flows.

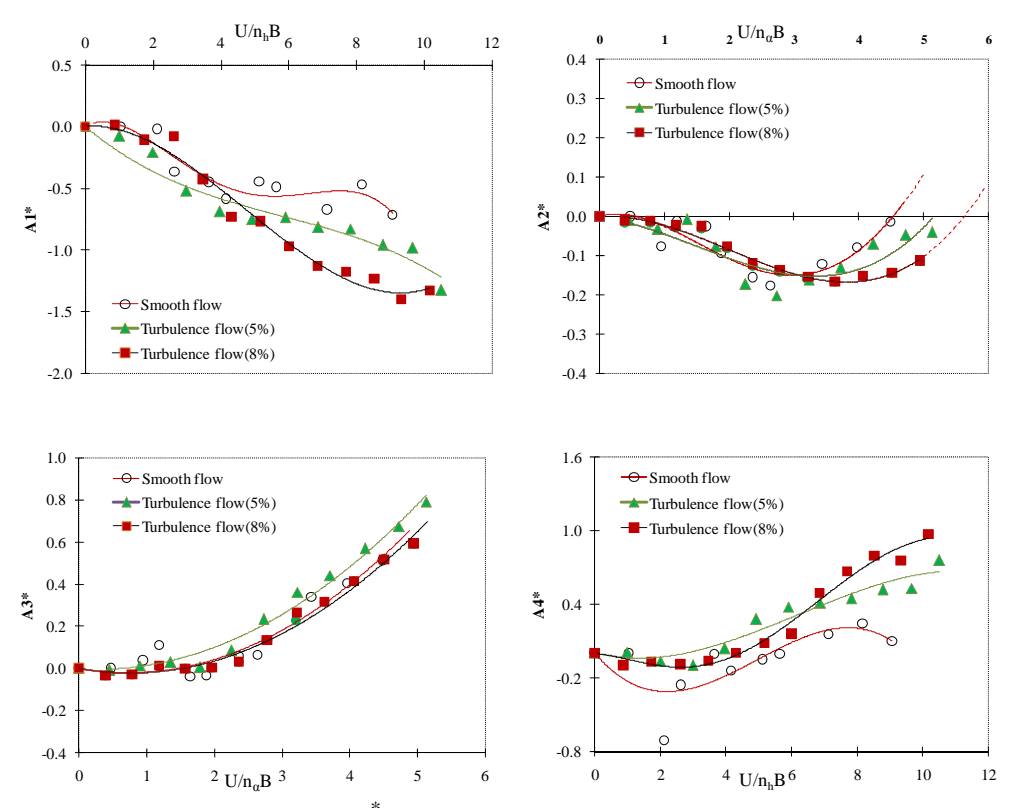


Fig. 7.36 Flutter derivatives (A_i^*) of the IRR Bridge model by the SSI-COV from buffeting responses under smooth and turbulent flows.

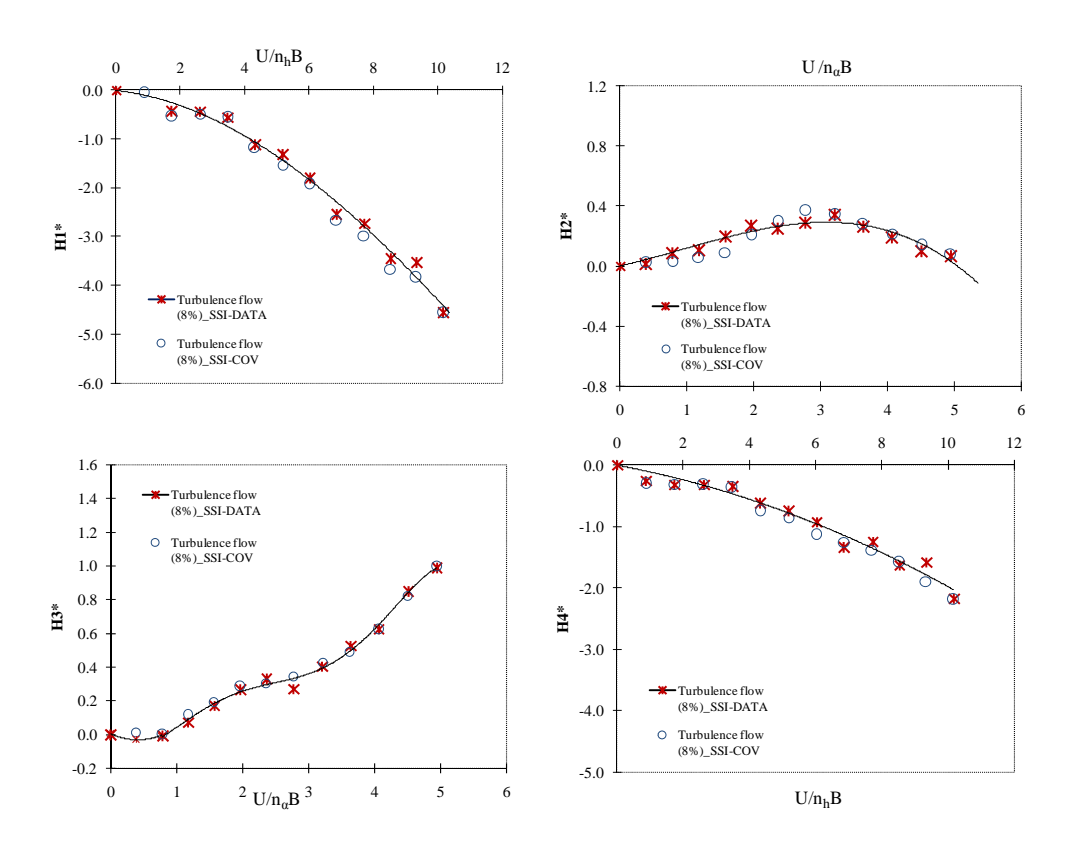


Fig.7.37 Comparisons of flutter derivatives (H_i^*) of the IRR Bridge model from the buffeting test by the SSI-DATA and the SSI-COV under 8%-turbulent flow.

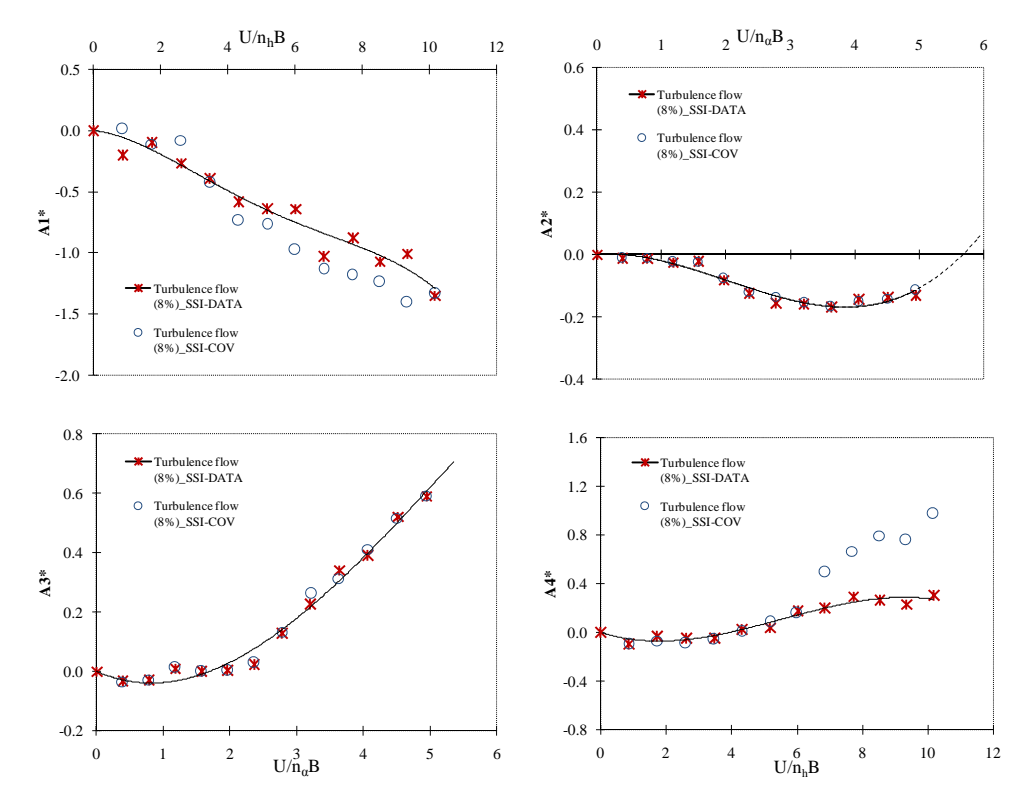


Fig.7.38 Comparisons flutter derivatives (A_i^*) of the IRR Bridge model from the buffeting test by the SSI-DATA and the SSI-COV under 8%-turbulent flow.

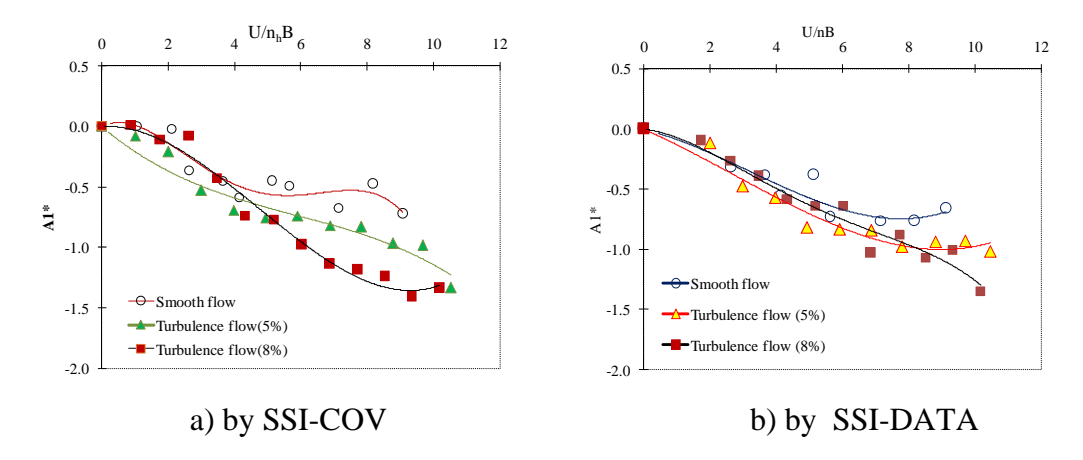


Fig. 7.39 Flutter derivatives (A_1^*) of the IRR Bridge model by the SSI-COV and the SSI-DATA methods from buffeting responses under smooth and turbulent flows.

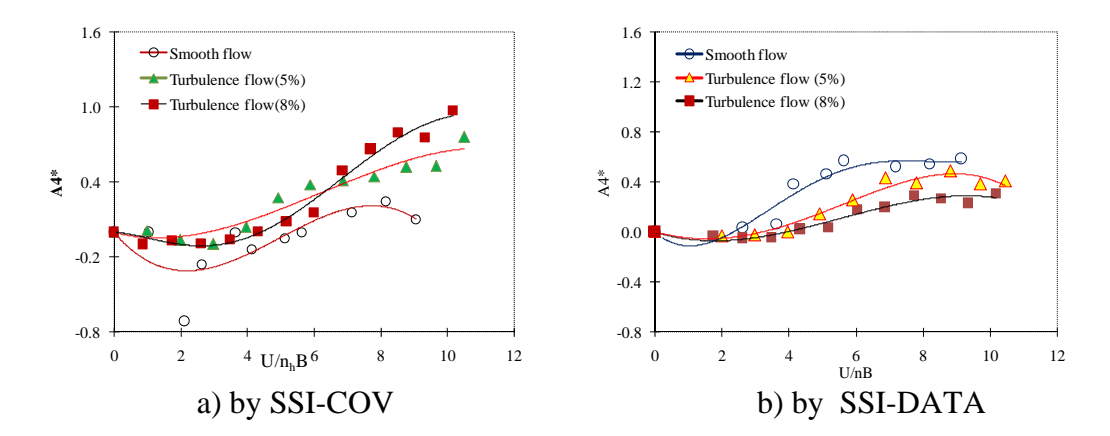


Fig. 7.40 Flutter derivatives (A_4^*) of the IRR Bridge model by the SSI-COV and the SSI-DATA methods from buffeting responses under smooth and turbulent flows.

7.3.3 Vortex Responses and Stability Limits of the IRR Bridge

The stability limit, i.e. the wind speed for onset of critical oscillations such as coupled flutter (classical) and torsional stability was determined in smooth flow for 0° angle of wind incidence. The stability limit was determined with rig inherent damping in order to have a more conservative determination of the stability limit and vortex shredding shall be seen.

Initially, the stability limit was determined roughly by increasing the wind speed and observing the behavior of the section. Subsequently, recordings were made of the response starting below the stability limit up to wind speed where the bridge deck exhibits clear unstable behavior.

The vortex response test was in a similar manner, where small increasing of wind speed around point that the bridge deck shows clearly strong vortex response. Figs. 7.41 and 7.42a show displacement response at slightly lower wind speed and at wind speed at vortex occurs, respectively. Fig 7.42b plotted frequency of each mode at vortex response. The strongly presence of torsional mode was noted. The velocity at vortex-shedding response was found at 2.58 m/s and the Strouhal number from the dynamic test was St = 0.065.

Fig. 7.43 plotted normalized-heave and pitch responses with reduced velocity. Heave response has been normalized with deck height (H) and the wind speed is presented as reduced velocity i.e. the wind speed is normalized with heave frequency, f_h and deck height. The pitch (torsional) response in deg. is plotted with reduced velocity where f_{α} is pitch frequency.

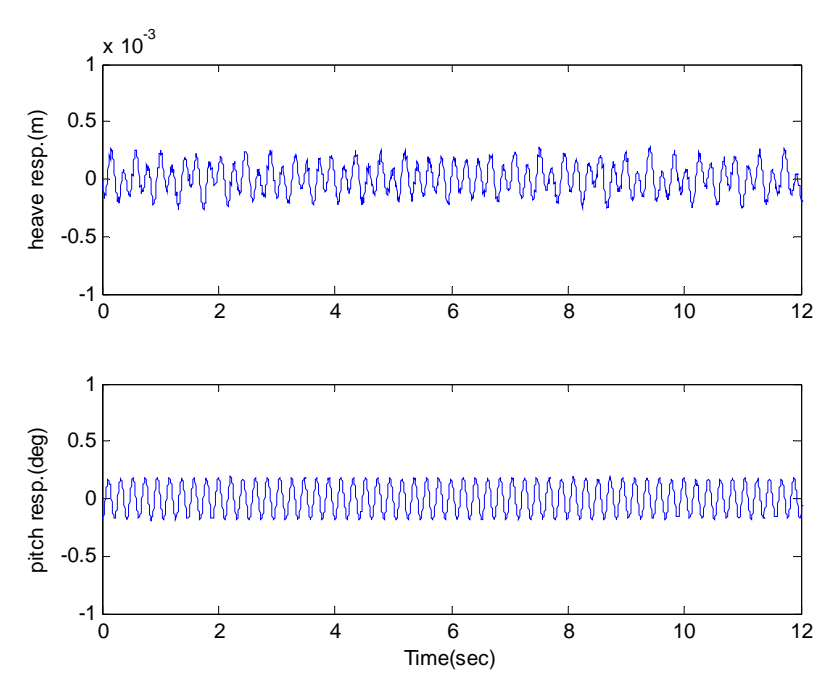


Fig. 7.41 The IRR bridge model under smooth flow: displacement time histories h and α at U = 2.37 m/s

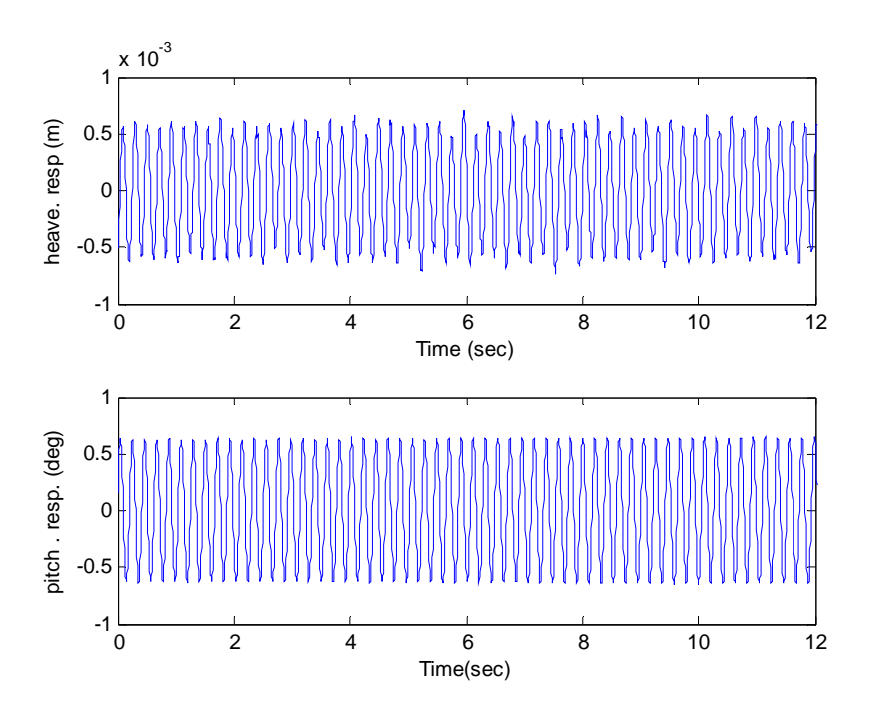


Fig. 7.42a The IRR bridge model under smooth flow: displacement time histories h and α at U = 2.58 m/s

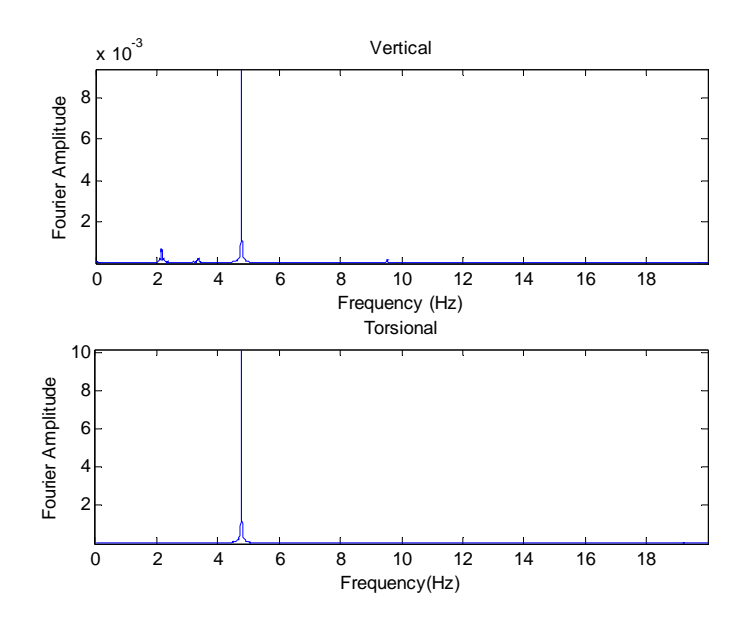
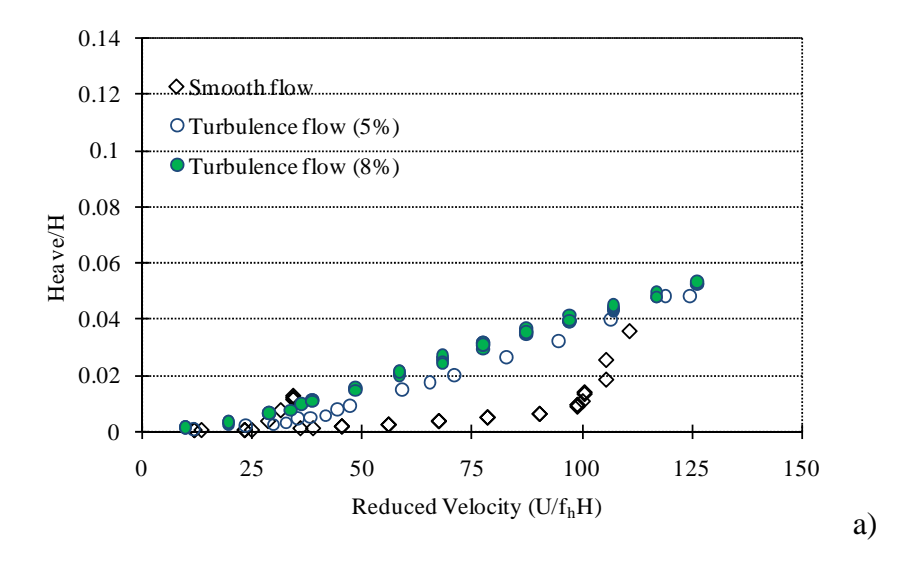


Fig.7.42b The IRR Bridge model frequency spectrum plot of h (vertical) and α (torsional) at U=2.58 m/s



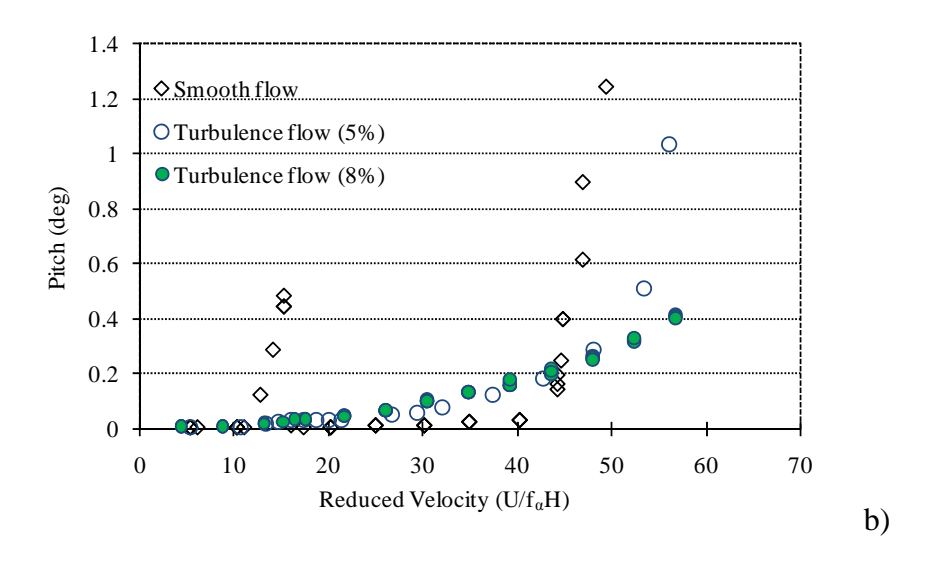


Fig. 7.43 The normalized heave (above) and pitch (below) responses of the IRR Bridge model under smooth and turbulent flows

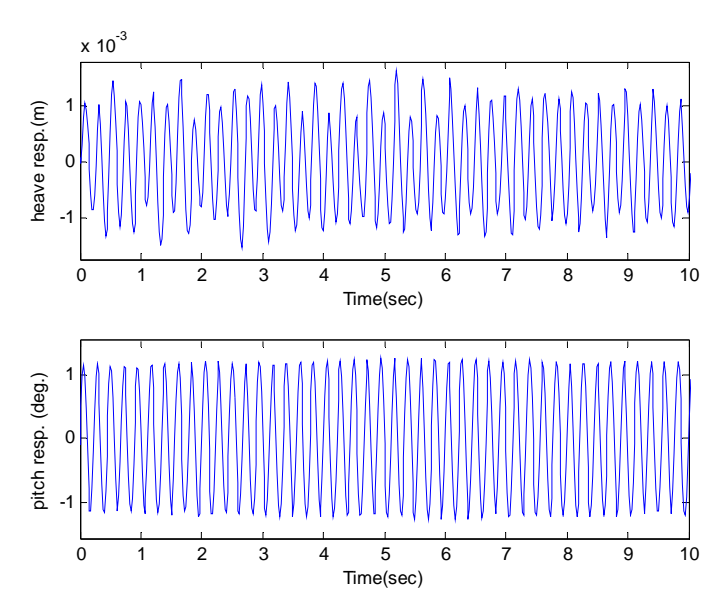


Fig. 7.44 Heave and pitch responses of the IRR Bridge model under smooth flow at flutter speed, U = 7.45 m/s.

Figs. 7.43 shows comparisons of the root-mean-square (RMS) torsional and vertical buffeting responses of the IRR Bridge model versus the reduced velocity between smooth and turbulence flows. Under smooth flow, the very abrupt transition with increasing velocity from the effectively zero torsional response amplitude to the clear instability occurs in the near neighborhood of the reduced velocity value (U/f_aH) of 45 (see Fig. 7.33b). From Fig. 7.44 it was found that the instability of the IRR Bridge model is the torsional flutter type. The stability limit has been defined as the mean wind speed at which this abrupt transition of torsional response was beginning. This is usually the case of actual response instead of the theoretical unstable limit that defined as a point where model exhibits an increasing in response with time. This stability limit velocity of the model was 7.45 m/s, which equivalent to 118 m/s in full The result agrees with that from DMI test results. The stability limit is considered relatively high compared to the design wind speed, and showing that the IRR Bridge section was safely design regarding the flutter instability. Fig. 7.44 plots the responses of the IRR Bridge model at the onset of the flutter instability. It is clearly seen from Fig. 7.45 that the abrupt change in the vertical response at high wind speed is the effect of the cross derivative H_3^* which causes the coupling of the highamplitude torsional responses on the vertical responses.

Compared with the smooth flow, the turbulence flow reduces the vortex-shedding response, because the turbulence tends to enhance the reattachment of flow and weaken the vortex shedding formulation. However, it raises the amplitude of the bridge responses progressively over the speed range. The turbulent flow results indicate that the torsional flutter is postponed to a slightly higher wind speed than that found in smooth flow in case of 5%-turbulence intensity. On the other hand, no clear and uniquely definable "flutter instability" was made evident by the experiment in case of 8%-turbulence intensity. It is worth noting however, that the largest amplitudes reach under this turbulence are probably additionally restrained by the nonlinear structural effects of test-setup.

7.3.4 Aerodynamic Force Coefficients of the IRR Bridge

The static aerodynamic force coefficients of the IRR Bridge were also obtained under different type of wind flow (see Fig. 7.45). The method used to obtain these static coefficients is described in Chapter 5 and similar to that the thin flat plate case. The experimental configuration is outlined in section 5.1.1. In each set, the static coefficients were determined in steps of wind angle of attack of 3° from -12° to +12°. In each angle of wind attack, model was subjected to three different wind velocities and average values are shown in Fig.7.47. The results of the tests are presented in the form of drag, lift and moment coefficients. The section model was installed about its centre of rotation, then, the pitching moment is considered with respect to this centre of rotation. The sign convention used in the presentation of the test results is as same as in the thin flat plate case (Figs. 7.15(b)).



Fig. 7.45 The static test set-up of the IRR Bridge model under turbulent flows in wind tunnel: a) with spires (at 3° angle of attack) b) with grids (at 0° angle of attack).

7.3.4.1 Smooth Flow

The force coefficients of the IRR Bridge section model measured in smooth flow are shown in Figs. 7.46. It shows that as the absolute value of wind attack angle increases; drag coefficient, C_D , (normalized with respect to a constant bridge width) increases due to the increase of front projected area. The absolute values of lift and torsional moment coefficients (C_L and C_M) also increase with wind angles of attack but in the range of small attack angles. The sudden drop in lift force and torsional moment at an angle of attack of approximately 3°, is due to flow separation occurring at angles of attack larger than this angle. Moreover, the model is subjected to a smaller torsional

moment at positive wind angle of attack, but a larger torsional moment at negative wind angle of attack.

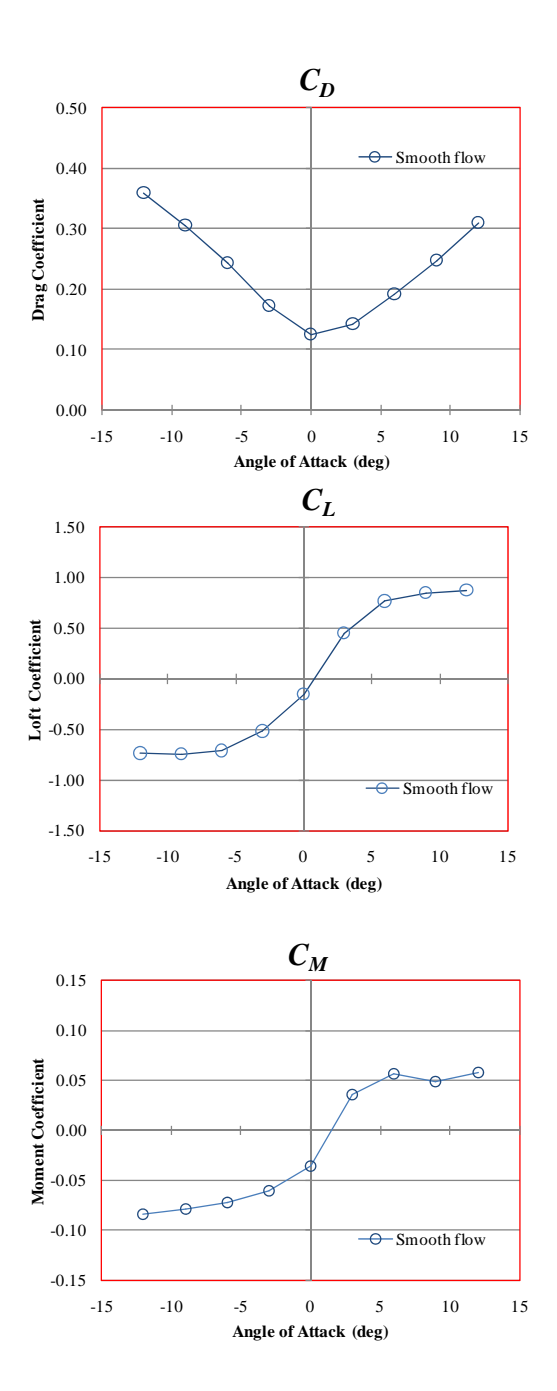


Fig. 7.46 The static force coefficients of the IRR Bridge model under smooth flow

7.3.4.1 Effect of Turbulence

The influence of the oncoming turbulence on the aerodynamic force coefficients are shown in Fig. 7.46. Two different level of turbulence flows were conducted, which values are 5% and 8%, respectively. In each set, static coefficients were determined in steps of 3 $^{\circ}$ from -12 $^{\circ}$ to +12 $^{\circ}$. In each angle of wind attack, model was subjected to three different wind velocities and average values are shown in Fig.7.47. The aerodynamic force coefficients were then determined using Eq. 6.4 as in case of the thin flat plate.

From Fig. 7.47, the drag coefficients of the IRR Bridge model under turbulent flow are slightly different from those in smooth flow. The absolute value of lift force coefficients under turbulent flow is slightly lower than those from smooth flow except at the highest angle of attack ($\pm 12^{\circ}$). On the other hand, the absolute values of moment coefficients under turbulent flow at high angle of attack are higher than those under smooth flow. The turbulence tends to enhance the reattachment of the flow by increasing the angle where the flow separation occurs from 3° to 6° for smooth and turbulence flow, respectively.

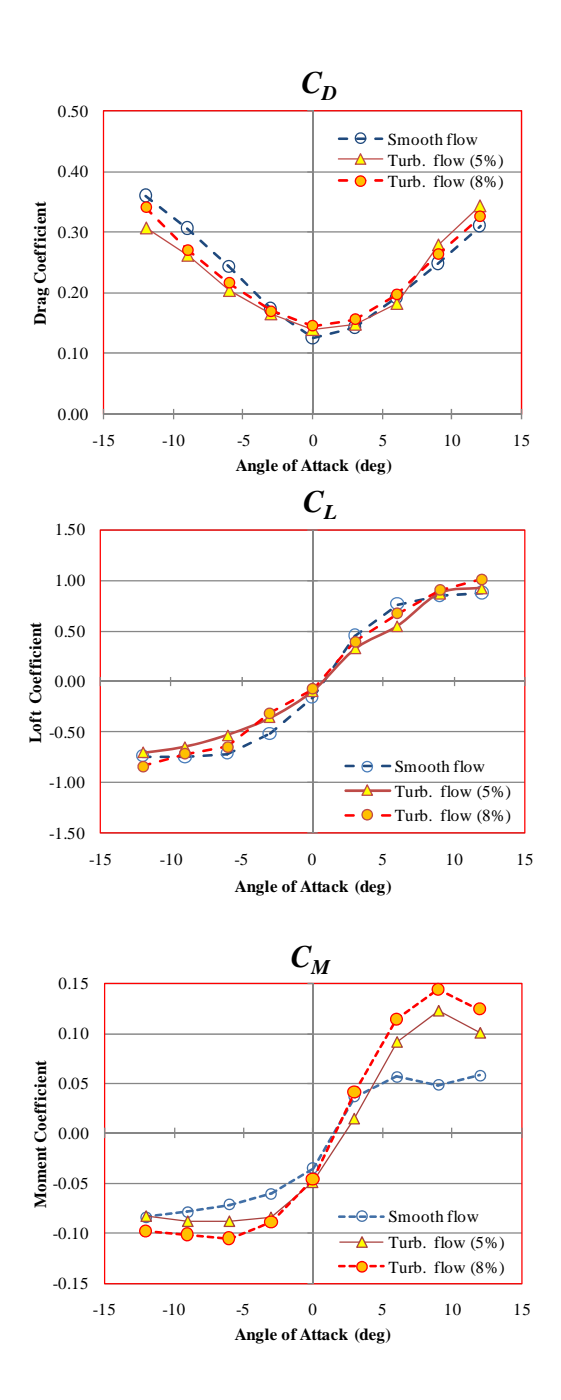


Fig.7.47 The static force coefficients of the IRR Bridge under smooth and turbulent flows

7.4 Modified Sections of Industrial Ring Road Bridge Deck by Aerodynamic Appendages

7.4.1 Flutter Derivatives: Smooth Flow

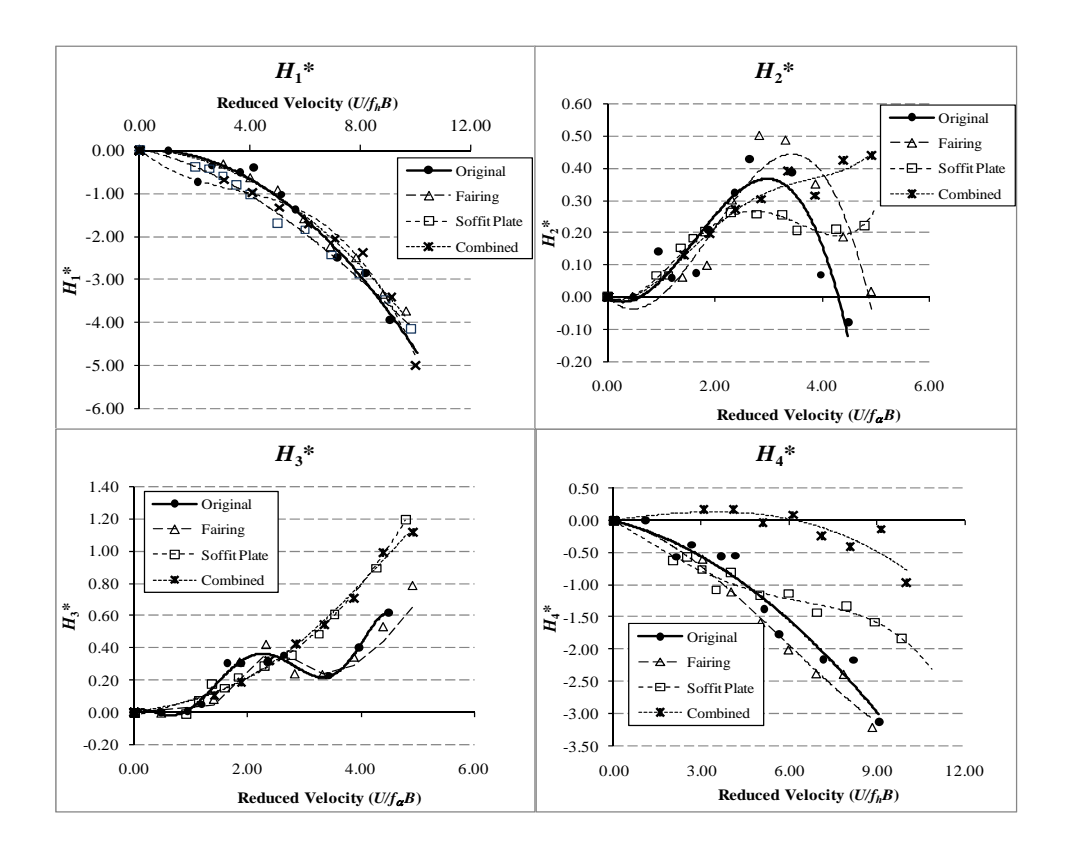


Fig.7.48 Comparisons of flutter derivatives (H_i^*) of the IRR Bridge model among original section and three modified sections.

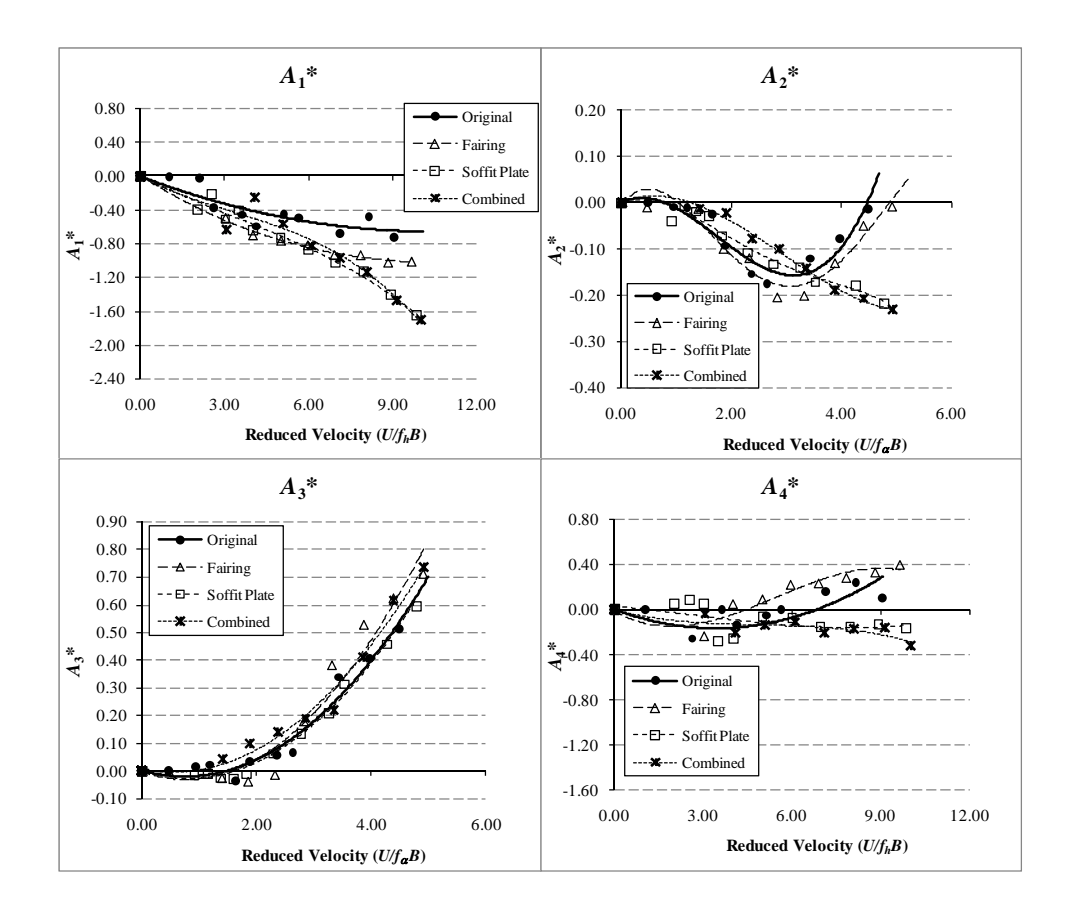


Fig.7.49 Comparisons of flutter derivatives (A_i^*) of the IRR Bridge model among original section and three modified sections.

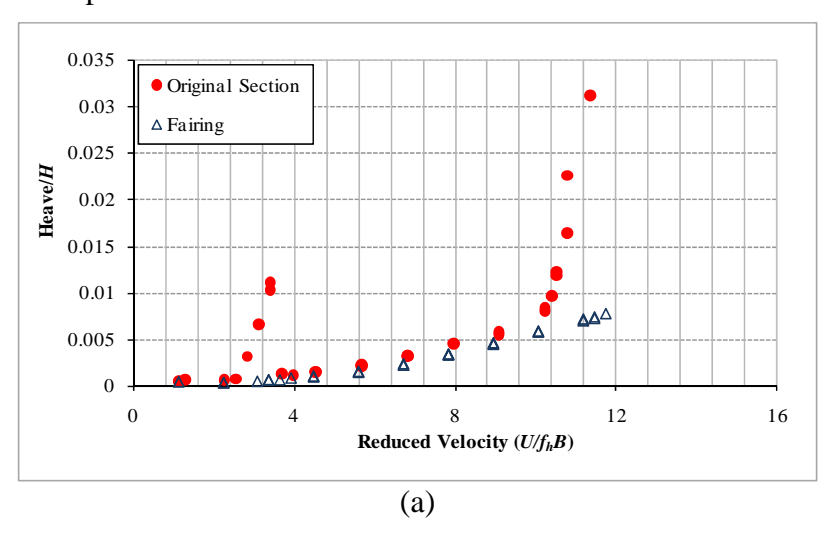
The results of flutter derivatives are presented in this section and their comparisons among four sections are presented as well. The aerodynamic derivatives were calculated for each wind speed as the average value of 10 tests at each velocity. Unless visual inspection of the results indicated some irregularities, the average values were carried forward in the analysis. For smooth flow condition, flutter derivatives of four sections are presented in figure 7.49. The most important terms are H_1^* and A_2^* which refer respectively on vertical and torsional damping of the section. Their positive values indicate unstable conditions. For vertical aerodynamic damping coefficient, H_1^* , the modification effects considered to be negligible, which all sections show in negative region. However, the section are influenced by the modifications in A_2^* which is most considerable in long-span bridges.

The original section and fairing modified section lead to a single torsional flutter at high wind velocity because A_2^* change from negative values to positive values. Flutter derivatives H_2^* term, cross derivatives to a torsional aerodynamic damping, are conversely agree well with A_2^* results. Fairing modified section shows a little improvement on the unstable behavior, delaying the unstable of bridge deck from reduced velocity of 4.5 to 5. Also, it was clearly found that soffit plate modified section, and combination of soffit plate and fairings modified sections produce more stable sections, whereas the classical flutter rather than the single torsional flutter will occur because of H_2^* and A_1^*

The results was found some dispersive in A_4 * and H_4 * terms between original section and modified ones, this coefficients are considered insignificant and usually neglected and in most of previous researches. Moreover, all modified sections show a little influence in A_1 * and A_3 *, which agree altogether well in trend. For H_3 * term, the fairings section agrees in trend with an original one, while soffit plates and combined sections are agree in trend to each other.

7.4.2 Structural Dynamic Responses and Stability Limits

The tests were carried on for aerodynamic appendage installed sections. Structural response of fairing-modified section, soffit plate-modified section, combined section and the comparisons between four sections are in ordered shown in figures 7.50, 7.51, 7.52 and 7.53. Similar to the original section, vortex shedding phenomenon and stability limit can be roughly identified from this test. The effects of fairing, soffit plates and combined section are then carried out.



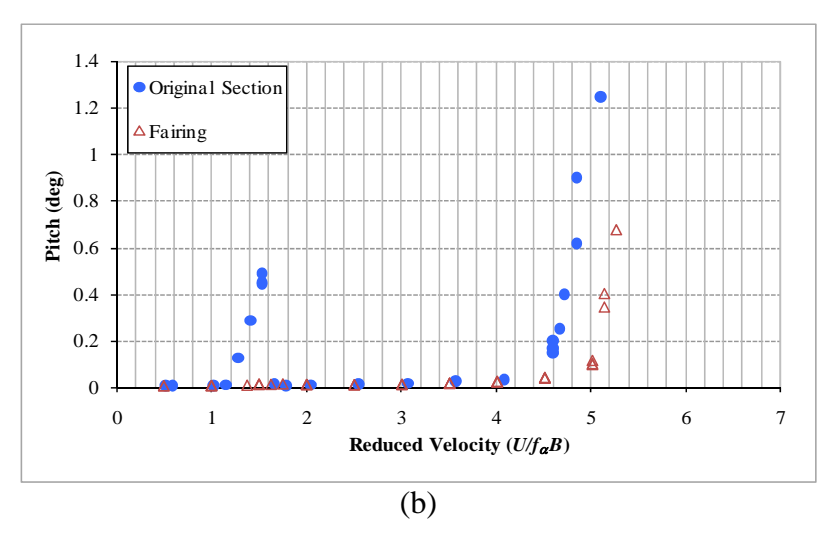
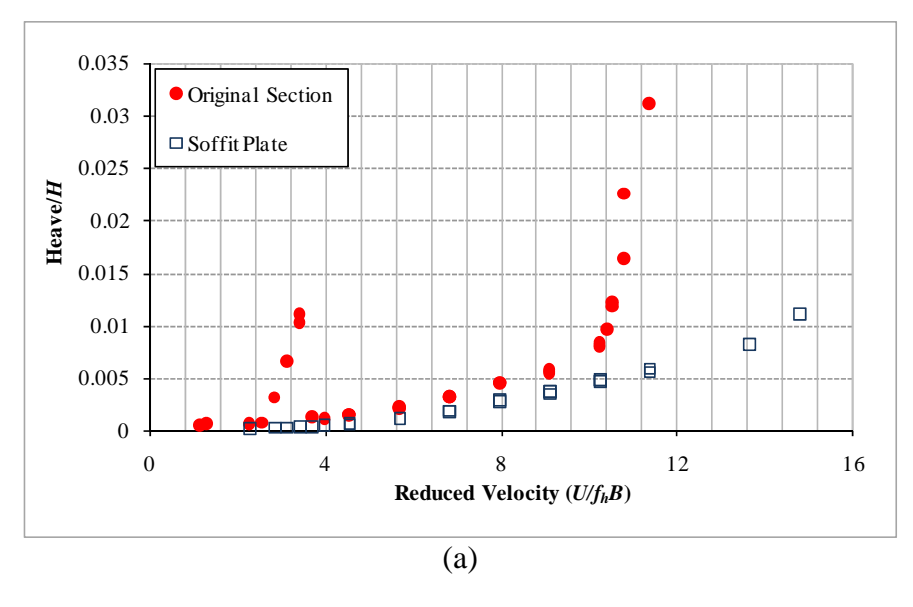


Fig.7.50 Comparisons of dynamic responses of IRR bridge deck with fairings; smooth flow (a) Heave responses and (b) Pitch responses



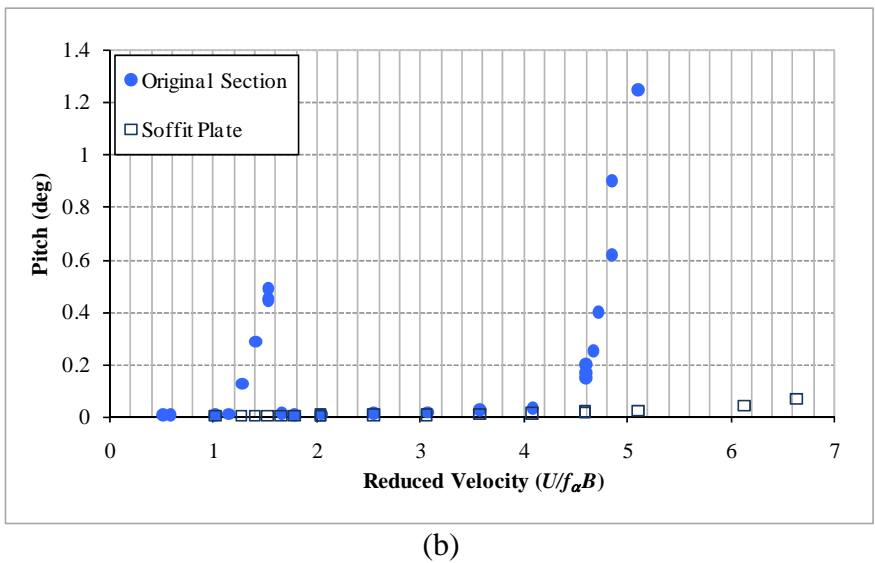
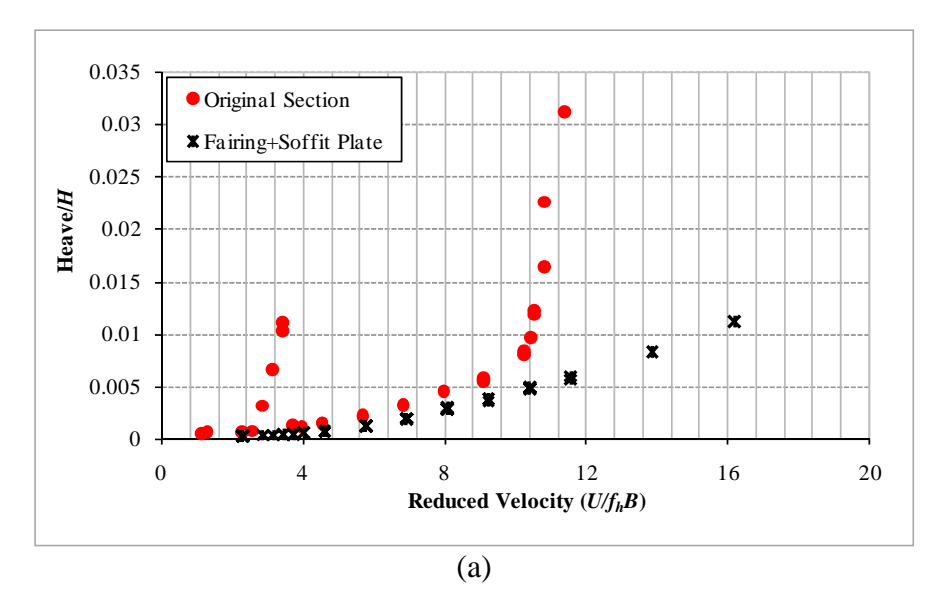


Fig. 7.51 Comparisons of dynamic responses of IRR bridge deck with soffit plates; smooth flow (a) Heave responses and (b) Pitch responses



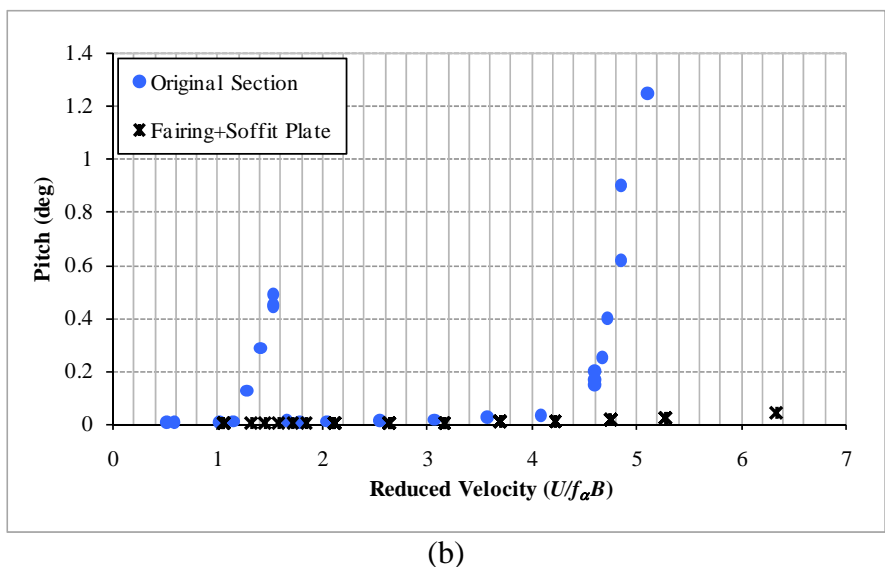
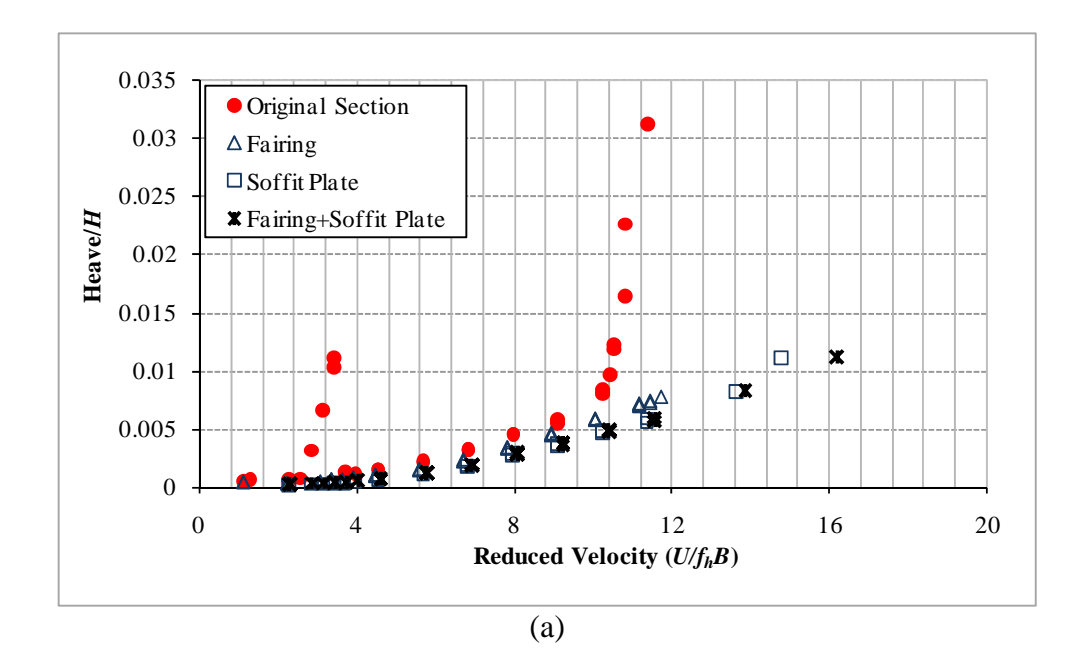


Fig. 7.52 Comparisons of dynamic responses of IRR bridge deck with combined section; smooth flow (a) Heave responses and (b) Pitch responses



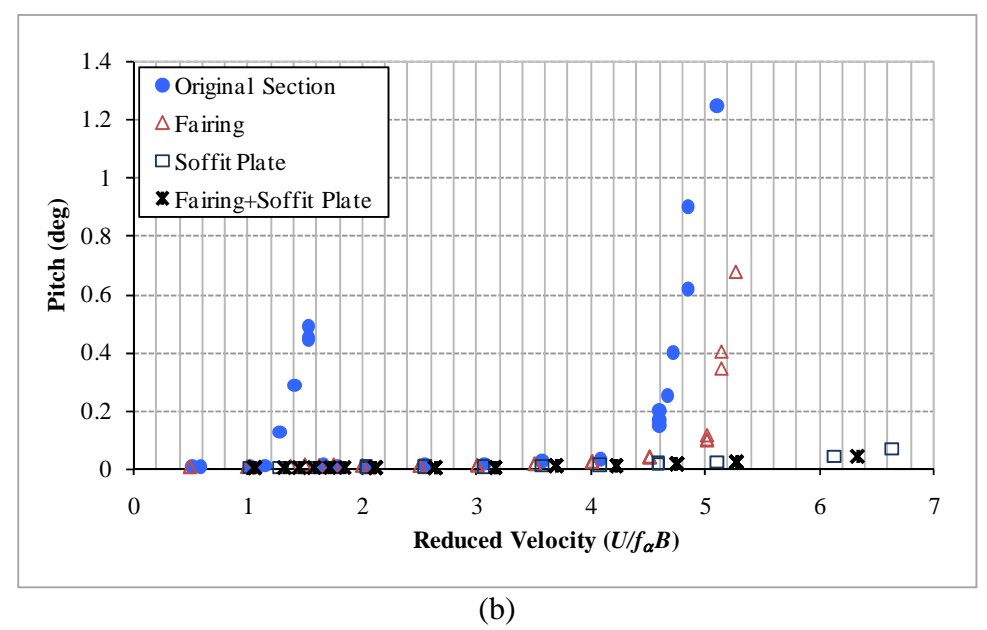


Fig. 7.53 Comparisons of dynamic responses of IRR bridge deck with various types of aerodynamic appendages mounted; smooth flow (a) Heave responses and (b) Pitch responses

The instability of the model was found not involved coupled motion between vertical and torsional degree-of-freedom, i.e. the observed instability is not classical flutter. A stability limit can be extended by all type of modifications. Since the frequency scale of this model can be identified from the ratio of model to the prototype frequency, which equals to 5.715, the velocity scale can be accordingly identified. 1:90 length scales regard 15.75 of velocity scale. For fairing mounted section, critical wind speed is 135 m/s, around 16% is extended from original section. For soffit plate and combined case, the flutter could not be found even in very high

wind speed. Hence, soffit plate and combined case are effective in delaying a torsional instability of bridge. For buffeting and vortex shedding response, three types of modifications can suppress the dynamic response of bridge significantly. That is, if we consider the effective of three modifications on buffeting response and structural stability, the results shall be: combine > soffit plate > fairing. Though combined case seem to be the most effective, but it still hold a numerous weight. The most suitable modification of bridge should be carried out in design and construction in boundary of architectural point of view and safety of passenger cars.

7.4.3 Aerodynamic Force Coefficients

The aerostatic experiment was then carried on for aerodynamic appendages mounted sections. The comparisons of static coefficients among original section and three modified sections are shown in figure 7.54

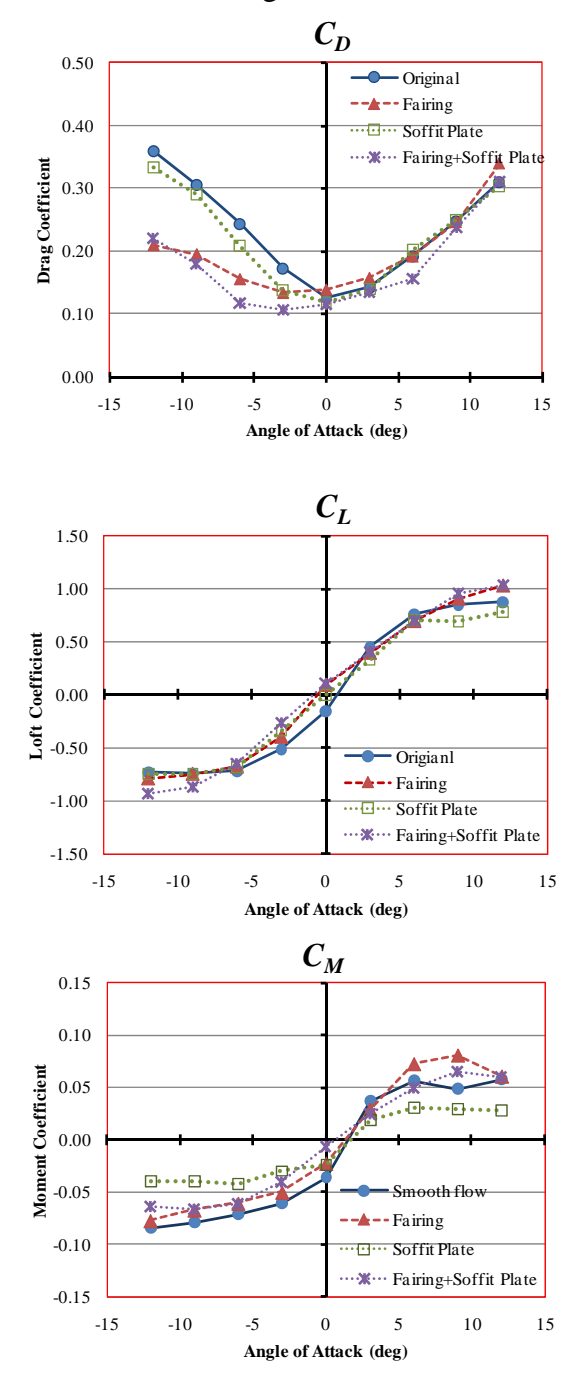


Fig. 7.54 Comparison of static coefficients of original section, fairing-modified section, soffit plate section and combined section; smooth flow

The study was found that, according to figure 7.54 (smooth flow condition), fairings can significantly reduce drag coefficient. A combined section seems to be the most effective one since the approaching wind can be more smoothly flew through a section than those through an original bluff section. For lift and moment coefficient, the modifications mounted to a model however represent a little improvement, except at zero angle of attack of moment coefficient which the modifications show a considerable improvement. Hence, it can be concluded that fairing can effectively reduce the drag coefficients.

CHAPTER 8

CONCLUSIONS AND RECOMMENDATIONS

The research work described herein consists principally of identification of aeroelastic and aerodynamic parameters of bridge decks. This work was pursued with the aim of improving the tools required for the identification of experimental parameters used for the wind-induced response prediction of long-span bridges.

8.1 Conclusions for Flutter Derivatives

8.1.1 System Identification Method

A theoretical model based on the stochastic subspace identification was used to extract the flutter derivatives of bridge deck sectional models from the two-degree-offreedom free decay and buffeting responses. An advantage of the stochastic subspace identification technique is that it considers the buffeting forces and the responses as inputs instead of as noises as typically assumed in previous research. The efficiency and simplicity of the stochastic subspace identification (SSI) lie in output-only measurements and its non-iterative nature in computations. For the first times, the data-driven stochastic system identification technique (SSI-DATA) was employed to directly extract the flutter derivatives of bridge deck sections model from their random vibration responses under wind flows and the results were then compared to those from the previous up-to-date covariance-driven-stochastic system identification (SSI-COV). Comparing with the SSI-COV, the SSI- DATA method avoids the computation of covariances between the outputs. It is replaced by projecting the row space of the future outputs into the row space of the past outputs. This projection is computed from the numerically robust square root algorithm, QR factorization instead of squared up the output data as in the SSI-COV algorithm. Moreover, this reduces both the dimensions of the matrices and the computation time considerably. The conclusions of the present study are as follows.

- 1) Numerical simulations of the bridge deck responses confirmed that the SSI-DATA technique can be used to estimate flutter derivatives from buffeting and free decay responses with reliable results. This shows the applicability of the SSI-DATA method with various test techniques, though it was developed from a stochastic model. Comparing with the SSI-COV, the identified modal parameter and system matrices from the SSI-DATA are more precise and less scattered.
- 2) For the thin plate model under smooth flow, wind tunnel tests showed that flutter derivatives identified by the SSI-DATA technique from both the free decay and the buffeting tests matched well with theoretical values. The flutter derivatives identified by the SSI-COV method from both tests also agreed with theoretical values, except in the case of A_4^* that was identified from buffeting responses.

- 3) When apply to the bluff section model of the IRR Bridge under smooth flow, the flutter derivatives estimated by the SSI-DATA from the buffeting test agreed with those obtained from the free decay test. This result allowed focusing on applying the SSI-DATA technique to the buffeting test method. On the other hand, there are more variations in the values of the A_1^* , A_4^* and H_2^* derivatives obtained by the SSI-COV. From the test results, the sign reversal of the A_2^* derivative was observed as the reduced wind speed reached the value of 4.5. This indicates that this bridge section is susceptible to flutter instability at high wind speed.
- 4) Under turbulence wind, the identified flutter derivatives by the SSI-DATA of a blunt section model of the IRR Bridge are generally in agreement with those in smooth flow. Though, there are small deviations from those in smooth flow at high reduced wind speeds. The most important effect is that the reduced wind speed, which corresponds to the reversed sign of the torsional aerodynamic damping A_2^* , increased in the turbulent flows. It shows that turbulence tends to make bridges more aerodynamically stable by delaying the torsional flutter. Comparing with the SSI-COV, the identified flutter derivatives from the SSI-DATA are more precise and less scattered, especially for the very sensitive A_1^* and A_4^* .

In summary, the numerical simulation tests showed that the precision of modal parameters and system matrices can be clearly improved by using the SSI-DATA technique when compared with those from the SSI-COV. From the results of wind tunnel tests, it was found that for a simple streamlined section, the flutter derivatives identified from both the SSI-DATA and the SSI-COV agreed well together. However, in the case of the 2-edge girder blunt type section, the SSI-DATA technique yields better results especially for the coupling derivatives. Applying the proposed SSI-DATA technique to the buffeting test yields a straightforward, cost effective, and reliable system identification process that can be used to identify flutter derivatives of various bridge decks. The method uses only output measurements. Instrument and extra efforts of input measurements are therefore not required as in case of the free decay and the force vibration tests. Moreover, the root-mean-square responses of bridge deck can be obtained simultaneously from the same test without requiring separated tests as in case of the free decay method.

8.1.2 Effect of Experimental Techniques: SDOF and 2-DOF

The direct-flutter derivatives of the thin plate model as found from the singledegree of freedom tests matched well with those found from the two-degree-offreedom coupled motion tests (i.e. the free decay and the buffeting tests) which clarified two points:

1) The direct-flutter derivatives are independent of other motions incidental to the principal degree of freedom with which they are associated. The result shows that the direct-flutter derivatives are indeed not affected by the motion along the other degree of freedom, as predicted by theory i.e., those flutter derivatives associated with h motion are not affected by α motion, and vice versa.

2) The present system identification method is well applicable to various experimental test methods.

8.1.3 Effect of Deck Shape

For the streamlined thin plate section under smooth flow, the values of the most important flutter derivatives H_1^* and A_2^* - related to aerodynamic damping in vertical and torsional mode, respectively- remained negative at all wind speed tests. In case of the blunt type IRR Bridge model the vertical aerodynamic damping, H_1^* , remained negative at all wind speed test. However, the torsional aerodynamic damping, A_2^* , remained negative at low reduced wind speed but showed the sign reversal at high reduced wind speed. The sign-reversal phenomenon is the outstanding factor toward the flutter instability of bridge decks. This result show that the relatively streamlined bridge section exhibits more aerodynamic stability than that of blunt type section. Then, the streamlined bridge sections seemed to be an obvious choice for the ultra-long span bridges.

Flutter derivatives of four sections are investigated. For vertical aerodynamic damping coefficient, H_1^* , the modification effects considered to be negligible, which all sections show in negative region. However, the section are influenced by the modifications in A_2^* which is most considerable in long-span bridges. Fairing modified section shows a little improvement on the unstable behavior, delaying the unstable of bridge deck from reduced velocity of 4.5 to 5. Also, it was clearly found that soffit plate modified section, and combination of soffit plate and fairings modified sections produce more stable sections, whereas the classical flutter rather than the single torsional flutter will occur because of H_2^* and A_1^* . In case of the blunt type bridge deck, modifying the cross-sectional geometry to be more streamlined design by aerodynamic appendages can significantly improve the aerodynamic stability of bridge.

8.1.4 Effect of Flow Conditions: Smooth and Turbulence Flow

The flutter derivatives of the IRR Bridge deck under smooth and turbulent flow were determined and then compared. The IRR Bridge is a 2-edge-girder bridge section with A-shape pylons. This bridge is an example of blunt type section that has a good cost performance, but at the same time the bridge cross-section is known to be aerodynamically unstable at high wind speed.

From the test results under smooth flow, the sign reversal of the A_2^* derivative was observed as the reduced wind speed reached the value of 4.5 (i.e. at velocity equals 118 m/s in full scale). This indicates that this bridge section is susceptible to flutter instability at high wind speed. The instability of the IRR Bridge was found to be torsional SDOF-type ("stall flutter"). Under turbulence wind, the identified flutter derivatives –except A_2^* - are generally in agreement with those in smooth flow. The most important and positive effect of the turbulence is that it tends to make the bridge more aerodynamically stable by delaying the sign reversal of the aerodynamic damping A_2^* . This may reveal that for those bridges with bluff type sections similar to

the IRR Bridge, the effects of turbulence can be significant. Hence, the wind tunnel tests of such bridges for flutter derivatives estimation should also be carried out in turbulent flow

It is important to note that the results presents in this study are based on the wind-tunnel investigations of only the IRR Bridge deck section under the conditions of the present experiments and the turbulence generated by grids and spires.

8.2 Conclusions for Buffeting

8.2.1 Static Force Coefficients

Buffeting is the random response of the bridge due to wind forces associated with the pressure fluctuations on the bridge deck caused by the turbulence of the wind flow over the section. This turbulence may be due to the gustiness in the incident natural wind, and may also contain contributions from the so-called signature or the self-induced turbulence. Wind flow over the bluff sections such as bridge decks generally causes separation of the flow at or near the leading edge of the section. This separated flow around the section is turbulent and causes forces of random nature on the section. The total buffeting forces on a section will depend on the level of the turbulence and the bridge deck section shape. For the estimation of buffeting forces and responses of bridge decks, the aerodynamic force coefficients are one of the important factors that should be experimentally determined.

The aerodynamic forces (static forces coefficient) on the rigidly mounted section model (static test set-up) of both a streamlined thin plate under smooth flow and a bluff (IRR) bridge deck section under smooth and turbulence flow were investigated. The conclusions are as follows.

- 1) For the streamlined thin plate model, generally, the static force coefficients agree with the theoretical values at the small angles of wind attack. The sudden drop of lift forces and pitching moment (torsion a) from theoretical values occur at wind angle of attack around 7°. The sudden drop in pitching moment and lift force is due to flow separation occurring at angles of attack larger than this angle. The flow separation has not been taken into account in the theoretical calculations. Then, the theoretical values for the thin plate model are valid for small angles of attack only and wind tunnel test is still an effective way in determining the aerodynamic force coefficient of bridge deck.
- 2) For the bluff type section of the IRR Bridge under smooth flow, the angle of attack where the flow separation occurs is reduced to 3° comparing to that of 7° in case of thin plate model. This smaller angle of wind separation is due to the sharp leading edge of bluff type section that generally causes the flow separation occurs more easily.

- 3) Under the turbulence flow, the static force coefficients of the IRR Bridge were moderately different from those determined under smooth flow. The turbulence tends to enhance the reattachment of the flow by increasing the angle where the flow separation occurs from 3° in case of smooth flow to that of 6° in case of turbulence flow, respectively.
- 4) Fairings can significantly reduce drag coefficient. A combined section seems to be the most effective one since the approaching wind can be more smoothly flew through a section than those through an original bluff section. For lift and moment coefficient, the modifications mounted to a model however represent a little improvement, except at zero angle of attack of moment coefficient which the modifications show a considerable improvement. Hence, it can be concluded that fairing can effectively reduce the drag coefficients.

8.2.2 Buffeting Responses, Vortex-Shedding and Flutter Instability

The effects of turbulence upon various aerodynamic phenomena based on a model study of the IRR Bridge were also studied. The model was tested under smooth and two levels of turbulence flows.

Under smooth flow, the torsional vortex-shedding response of the blunt type IRR Bridge was observed at velocity value of 2.58 m/s (i.e. the full scale velocity = 41m/s). The approximate Strouhal number from the dynamic test which was St = 0.065. The very abrupt transition with increasing velocity from the effectively zero torsional response amplitude to the clear instability occurs in the near neighborhood of the velocity value of 7.45 m/s. (i.e. the full scale velocity =118 m/s). This result indicates that the blunt type IRR Bridge section is susceptible to flutter instability at high wind speed.

For fairing mounted section, critical wind speed is 135 m/s, around 16% is extended from original section. For soffit plate and combined case, the flutter could not be found even in very high wind speed. Hence, soffit plate and combined case are effective in delaying a torsional instability of bridge. For buffeting and vortex shedding response, three types of modifications can suppress the dynamic response of bridge significantly. That is, if we consider the effective of three modifications on buffeting response and structural stability, the results shall be: combine > soffit plate > fairings. Though combined case seem to be the most effective, but it still hold a numerous weight. The most suitable modification of bridge should be carried out in design and construction in boundary of architectural point of view and safety of passenger cars.

Compared with the smooth flow, the turbulence flow reduces the vortex-shedding response, because the turbulence tends to enhance the reattachment of flow and weaken the vortex shedding formulation. However, it raises the amplitude of the bridge responses progressively over the speed range. The results from the turbulent flows indicate that the serious torsional oscillations (flutter instability) are postponed to a slightly higher wind speed than that found in smooth flow in case of 5%-

turbulence flow. However, no clear and uniquely definable "flutter instability" was made evident by the experiment in case of 8%-turbulent flow.

8.3 Recommendations and Suggestions for Future Works

From the study of this research, the following issues may be noted and investigated further to enhance a better understanding of the bridge aerodynamics:

- 1) In this study, in order to reveal the vortex shedding-response phenomena, the low-inherent damping of model was selected. This vortex-shedding amplitude is well-known as damping dependence, then tests may be carried out in the case of higher structural damping of real bridge.
- 2) The effect of incident turbulence on the aerodynamic parameters should be further examined for a wide range of bluff sections and different turbulent intensities. The results presented and suggestions made in this study are based on the wind-tunnel investigations of only two bridge deck sections under the conditions of the present experiments. The experimental set-up in this study is suitable only for a small range of amplitude responses and exhibit an amplitude dependence of the structural damping at high amplitude. It is probably the effects of additional restrain by the nonlinear structural effects of the test-setup. This limits the maximum reduced velocity that can be tested to identify flutter derivatives in this study, especially for high turbulence intensities where a large amplitude of the buffeting response occurs. In order to identify flutter derivatives of a bridge deck under high turbulence intensities, a new experimental set-up or an additional artificial damping such as electro-magnetic may be required.
- 3) From this study, it is found that there are some limitations for the identification of flutter derivatives from the buffeting test. For example, it becomes more difficult to extract the flutter derivatives from the buffeting responses in the situation when a relatively heavy model (i.e. the thin plate model in this study) is excited at a very low reduced wind velocity, i.e. low wind energy. The useful signal is in the same order as the measurement noises. In this case, using the SSI-DATA technique with the free decay method will yield more accurate results in this low wind speed range.
- 4) Theoretically, both the SSI-DATA and the SSI-COV can be applied to extract eighteen flutter derivatives. Then, they may be applied further to experimentally determine all the eighteen flutter derivatives for a wide range of bridge deck cross sections shapes to gain further insights into the complex phenomena of flutter and buffeting. However, a more extensive experimental set-up is required. Besides, this system identification technique may be applied further to identify flutter derivatives of real bridge decks in the field.

5) In this study, the effects of turbulence upon the aeroelastic and the aerodynamic phenomena of a blunt type bridge deck of IRR Bridge were investigated. The turbulence has positive effects when concerning bridge stability. It delays the onset of flutter and reduces the vortex-shedding response when compared with the smooth flow. On the other hand, the turbulence raises the amplitude of response progressively over the wind speed range and may causes problem to the serviceability of the bridge. Then, an improving of bridge stability as well as the reduction of bridge responses by the other methods such as the tuned mass damper (Malhortra 1987, Boonyapinyo *et.al.* 2001) are expected in future.

REFERENCES

Asmussen, J.C. (1997). Modal Analysis based on the Random Decrement Technique. Application to Civil Engineering Structures, Ph.D. Thesis, Univ. Alborg

Ayorinde, E.O., and Warburton, G.B. (1980), Minimizing Structural Vibrations with Absorbers, *J. of Earthquake Engineering and Structural Dynamics*, 8, pp. 219-236.

Bienkiewicz, B. (1987). Wind Tunnel Study of Effects on Geometry Modifications on Aerodynamics of Cable-stayed Bridge Deck. *Journal of Wind Engineering and Industrial Aerodynamics*, 26, pp. 325-339.

Billan K.Y and Scalan R.H. (1991), Resonance, Tacoma Narrow bridge failure, and under graduate physics textbooks. *Journal of Physics*, 59, No 2.

Boonyapinyo V., Miyata T. and Yamada H. (1999), Advanced Aerodynamic Analysis of Suspension Bridges by State-Space Approach. *Journal of Structural Engineering*, ASCE, 125(12), pp. 1357-1366.

Boonyapinyo, V., Phanichtripop, P. and Lukkunaprasit, P. (2001), Tuned Mass Dampers for Suppression of Buffeting and Flutter Response of Long-Span Suspension Bridges under Wind Load, *Proc. of 3rd World Conference on Structural Control*, Como Italy, pp.35-44

Brincker, R., Krenk, S., Kirkegaard, P.H. & Rytter, A. (1992), Identification of the Dynamical Properties from Correlation Function Estimates, Bygningsstatiske Meddelelser, Danish Society for Structural Science and Engineering, Vol.63,N.1, pp.1-38

Brincker, R., Zhang, L. & Andersen, P. (2000), Modal Identification from Ambient Responses using Frequency Domain Decomposition, *Proc.* 18th Int. *Modal Analysis Conference*, Kissimmee, USA.

Brincker, R., Ventura, C. & Andersen, P. (2001), Damping Estimation by Frequency Domain Decomposition, *Proc.* 19th Int. Modal Analysis Conference, San Antonio, USA.

Brown, D.L., Allemang, R.J., Zimmerman, R. & Mergeay, M. (1979) Parameter Estimation Techniques for Modal Analysis, *SAE Technical Paper Series*, N.790221

Brownjohn J.M.W. (1994), Estimation of Damping in Suspension Bridges, Buildings Struct. *Proc. Inst. Civil Eng.*, 104, pp. 401–415

Brownjohn J.M.W. and Jakobsen J.B. (2001), Strategies for Aeroelastic Parameter Identification from Bridge Deck Free Vibration Data. *J Wind Eng Ind Aerodyn*, 89, pp. 1113–1136.

Chen Z.Q. and Yu X.D. (2002), A New Method for Measuring Flutter Self-Excited Forces of Long-Span Bridges. *China Civil Engineering Journal*, 35, pp. 34–41.

Chen A.R., Xu F.Y. and Ma R.J. (2006), Identification of flutter derivatives of bridge decks using stochastic search technique., *Wind and Structures*, 9(6), pp.441-455.

Danish Maritime Institute (1995), Wind-Tunnel Study for the IRR Cable-Stayed Bridges, DMI 97034, Lyngby, Denmark.

Davenport A.G., King J.P.C. and Larose G. (1992), Taut strip model testing, *Aerodynamics of Large Bridges*, Balkema, Rotterdam.

Diana G., Cheli F. and Resta F. (1995), Time Domain Aeroelastic Force Identification on Bridge Decks. *Proce 9th Int Conf Wind Eng*, New Delhi, India, Wiley Eastern Ltd., pp. 938–949.

Ding, Q.S., Chen, A.R., and Xiang, H.F. (2001), Modified least-square method for identification of bridge deck aerodynamic derivatives. *J. of Tongji University*, 29(1),pp. 25-29.

Dryver, R. H., & Harold, R. B. (1996). Aerodynamic Design of Highway Structures. U.S. Department of Transportation, Federal Highway Administration, 59 (3).

Dyrbye C. and Hansen S.O., (1996), Wind loads on structures., John Wiley, New Jersey.

Falco M., Curami A. and Zasso A. (1992), Nonlinear Effects in Sectional Model Aeroelastic Parameter Identification. *J. Wind Eng. Ind. Aerodyn.*, 42, pp. 1321–1332.

Fang, F.-M., Li, Y.-C., Liang, T.-C., & Chen, C.-C. (2007). Investigation on the Aerodynamic Instability of a Suspension Bridge with a Hexagonal Cross-section. *Journal of the Chinese Institute of Engineers*, 30 (6), pp. 1009-1022.

Felber, A. (1993), Development of a Hybrid Bridge Evaluation System", Ph.D. Thesis, University of British Columbia (UBC), Vancouver, Canada,

Fukuzono, K. (1986), Investigation of Multiple-Reference Ibrahim Time Domain Modal Parameter Estimation Technique", M.Sc. Thesis, Univ. Cincinnati, USA

Gu M., Zhang R.X. and Xiang H.F. (2001), Parametric Study on Flutter Derivatives of Bridge Decks. *Engineering Structures*, 23, pp. 1607–1613.

Gu M. and Qin X.R. (2004), Direct Identification of Flutter Derivatives and Aerodynamic Admittances of Bridge Decks. *Engineering Structures*, 26, pp. 2161–2172.

Gu M., Zhang R.X. and Xiang H. (2000), Identification of Flutter Derivatives of Bridge Decks. *J Wind Eng Ind Aerodyn*, 84, pp. 151–162.

Hjorth-Hansen E. (1992), Section model tests, Aerodynamics of Large Bridges, Balkema, Rotterdam.

Holmes J.D. (1994) Methods of Fluctuating Pressure Measurements in Wind Engineering, *Davenport Sixtieth Anniversary: A State of Art in Wind Engineering, Ninth International Conference on Wind Engineering*, New Delhi, 1995, Wiley Eastern Limited, New Delhi.

Hsia T.C. (1976), On Least Squares Algorithms for System Parameter Identification. *IEEE Trans Autom Contr*, 21 (1), pp. 104–108.

Imai H., Yun C.B., Maruyama O. and Shinozuka M. (1989), Fundamentals of System Identification in Structural Dynamics. *Prob Eng Mech*, 4, pp. 162–173.

Irwin H.P.A.H. (1992), Full aeroelastic model test, Aerodynamics of Large Bridges, Balkema, Rotterdam

Iwamoto M. and Fujino Y. (1995), Identification of Flutter Derivatives of Bridge Deck from Free Vibration Data. *J Wind Eng Ind Aerodyn*, 54/55, pp. 55–63

Jain A., Jones N.P. and Scanlan R.H. (1996), Coupled Aeroelastic and Aerodynamic Response Analysis of Long Span Bridges. *J. Wind Eng. Ind. Aerodyn.*, 60, pp. 81–89.

Jakobsen J.B. and Hjorth-Hansen E. (1995), Determination of the Aerodynamic Derivatives by a System Identification Method. *J Wind Eng Ind Aerodyn*, 57, pp. 295–305.

Jakobsen J. B. (1995). Fluctuating Wind Load and Response of a Line-like Engineering Structure with Emphasis on Motion-Induced Wind Forces, NTH 1995:62, Department of Structural Engineering, Norwegian Institute of Technology, University of Trondheim, Norway.

Jones N.P., Shi T., Ellis J.H. and Scanlan R.H. (1995), System-Identification Procedure for System and Input Parameters in Ambient Vibration Surveys. *J Wind Eng Ind Aerodyn*, 54/55, pp. 91–99.

Juang J.N. and Pappa R.S. (1985), An Eigensystem Realization Algorithm for Modal Parameter Identification and Model Reduction. *Journal of Guidance, Control, and Dynamics*, 85, pp. 620–627.

Larsen A. (1992), Aerodynamic of Large bridges. *Proceeding of the fist international symposium on aerodynamic of large bridges*, 19-21 Feb 1992, AA Balkema Rotterdam/Copenhagen/Denmark.

Larsen A and Walther J.H. (1998), Discrete Vortex Simulation of Flow Around Five Generic Bridge Deck Sections. *Journal of Wind Engineering and Industrial Aerodynamics.*, 77 & 78, pp. 591-602.

Ljung L. (1995), System Identification Toolbox, For use with MATLAB, The Mathworks, USA.

Ljung L. (1999) System Identification: Theory for the User. 2nd Ed., Prentice Hall, Upper Saddle River, NJ, USA.

Li Q.S. (1995), Measuring Flutter Derivatives for Bridge Section Models in Water Channel. *J. Eng. Mech.*, *ASCE* 121 (1), pp. 102–116.

Li Y.L., Liao H.L., and Qiang S.Z. (2003), Weighting ensemble of least-square method for flutter derivatives of bridge decks. *J. Wind Eng. Ind. Aerodyn*, 91, pp. 713-721.

Malhortra, L., and Wieland, M. (1987), Tuned Mass Damper for Suppressing Wind Effects in a Cable-Stayed Bridges, *Proc. Int. Conf. on Cable-Stayed Bridges*, Bangkok.

McKelvey T. (1995), Identification of State-Space Models From Time and Frequency Data. PhD thesis, Department of Electrical Engineering, Linköping University, Sweden,

[ftp://ftp.control.isy.liu.se/pub/Reports/Ph.D.Thesis/PhD380.ps.Z].

Mitchell L.D. (1986), Signal processing and the Fast-Fourier-Transform (FFT) analyzer - a survey. *Modal Analysis: the International Journal of Analytical and Experimental Modal Analysis*, **1**(1), 24-36.

Nagao, F., Utsonomiya, H., Oryu, T., & Manabe, S. (1993). Aerodynamic Efficiency of Triangular Fairing on Box Girder Bridge. *Journal of Wind Engineering and Industrial Aerodynamics*, 49, pp. 565-574.

Overschee P.V. (1991), Subspace Algorithms for the Stochastic Identification Problem. *Proc.*, 30th Conference on Decision and Control, Brighton, England, pp. 1321–1326.

Overschee P.V. and Moor D.B. (1996), Subspace Identification for Linear System: Theory-Implementation-Applications. Kluwer Academic Publishers, The Netherlands.

Pandit S.M. (1991), Modal and Spectrum Analysis: Data Dependent Systems in State Space. John Wiley & Sons, New York, USA.

Peeters B. (1999), Reference-based Stochastic Subspace Identification for Out-put only Modal Analysis. *Mechanical Systems and Signal Processing*, 13 (6), pp. 855–878.

Prevosto, M. (1982), Algorithmes d'Identification des Caractéristiques Vibratoires de Structures Mécaniques Complexes, Ph.D. Thesis, Univ. de Rennes I, France.

Rodrigues, J., Brincker, R. and Anderson, P. (2004). Improvement of Frequency Domain Output-Only Modal Identification from the Apllication of the Random Decrement Technique. *Proc.* 22th *Int. Modal Analysis Conference*, Dearborn, USA.

Sarkar PP. (1992). New-identification Methods Applied to the Response of Flexible Bridges to Wind. PhD thesis. Baltimore, MD: The Johns Hopkins University.

Sarkar P.P., Jones N.P. and Scanlan R.H. (1992), System Identification for Estimation of Flutter Derivatives. *J Wind Eng Ind Aerodyn*, 41-44., pp. 1243–1254.

Sarkar P.P., Jones N., and Scanlan R.H. (1994), Identification of Aeroelastic Parameters of Flexible Bridges. *Journal of Engineering Mechanics*, ASCE ,120 (8), pp. 1718–1741.

Scanlan, R.H and Sabzevari (1969). Experimental Aerodynamic Coefficients in the Analytical of Suspension Bridge Flutter. *Journal of Mechanical Engineering Science*, ASCE, 11,(3).

Scanlan, R.H and Tomko J.J. (1971), Airfoil and Bridge Deck Flutter Derivatives. *Journal of The Engineering Mechanics Division*, ASCE, EM6, Proc.

Scanlan RH. (1977), Motion of Suspended Bridge Spans under Gusty Wind. *Journal of the Structural Division, ASCE* ,,103(9), pp.1867–83.

Scanlan R.H. (1978), Bridge flutter derivatives. *Journal of Engineering Mechanics*, *ASCE*, 104 (4), pp. 719–733.

Scanlan, R.H. and Lin W.H. (1978). Effects of Turbulence on Bridge Flutter Derivatives. *Journal of The Engineering Mechanics Division*, ASCE, 104, EM4.

Scanlan, R.H. (1987). Interpreting Aerodynamic Models of Cable Stayed Bridge. *Journal of the Engineering Mechanics, ASCE*, 113, No 4.

Schoukens J. and Pintelon R. (1991), Identification of Linear Systems: a Practical Guideline to Accurate Modelling. Pergamon Press, London, UK.

Simiu E. and Scanlan R.H. (1996), Wind effects on structures, 3rd Ed., John Wiley, New Jersey.

Singh L., Jones N.P., Scanlan R.H. and Lorendeaux O. (1996), Identification of Lateral Flutter Derivatives of Bridge Decks. *J. Wind Eng. Ind. Aerodyn*,.60, pp. 69–80.

Strømmen E., (2006), *Theory of Bridge Aerodynamics*, First edition, New York, Springer.

Tanaka H. (1992), Similitude and modelling in bridge aerodynamics, Aerodynamics of Large Bridges, Balkema, Rotterdam.

Vold, H., Kundrat, J., Rocklin, G.T. & Russel, R. (1982), A Multi-Input Modal Estimation Algorithm for Mini-Computers, SAE Technical Paper Series, N.820194

Walther R. (1999), Cable-Stayed Bridges. 2nd Ed., London, ThomasTelford.

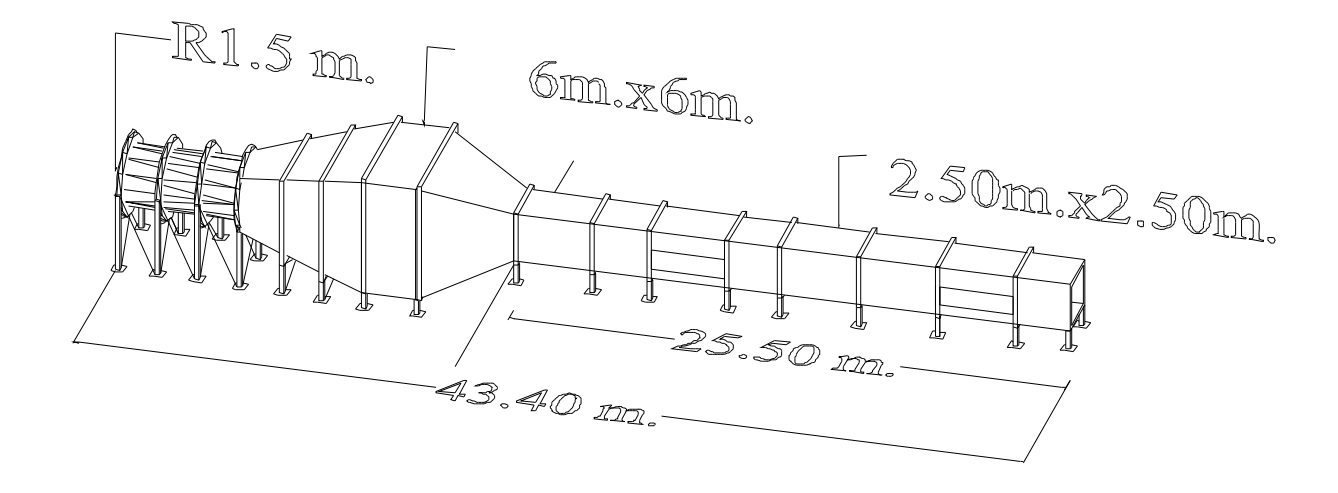
Wardlaw, R. L., & Goettler, L. L. (1968). A Wind Tunnel Study of Modifications to Improve the Aerodynamic Stability of Long's Creek Bridge. NAE, National Research Council, Ottawa, Canada.

Yamada H. and Ichikawa H. (1992), Measurement of aerodynamic parameters by extended Kalman filter algorithm. *J Wind Eng Ind Aerodyn*, 42 ,pp. 1255–1263.

Zhu L.D., Xu Y.L., Zhang F. and Xiang H.F. (2002), Tsing Ma bridge Deck under Skew Winds. Part II: Flutter derivatives. *J Wind Eng Ind Aerodyn*, 90., pp. 807–837.

Appendix

Appendix A Schematic diagram of TU-AIT Wind Tunnel



Appendix B

THE WIND TUNNEL AND THE EXPERIMENTAL APPARATUS

All the experiments were performed in the TU-AIT Wind tunnel at the Thammasat University. Brief descriptions with illustrations of the wind tunnel, measurement of the wind speed and wind turbulence, the force sensor system, the aeroelastic support systems and the data-acquisition software, are given in this appendix.

B.1 The TU-AIT Wind Tunnel

This wind tunnel is an opened-circuit tunnel capable of producing wind speed as high as 20 m/s with a very low level of turbulence over the testing length. A schematic of the wind tunnel is given in appendix A.

B.2 Wind-Speed and Wind-Turbulence Measurements

A pressure transducer (VaLidyne system, Model no.DP45-14) was used in conjunction with the pitot-static tube to measure the horizontal mean wind velocity (U) in smooth flow. Hot-sphere anemometer as shown in Fig. B1 was also used to measure the horizontal mean wind velocity. A hot-wire X-probe was used to measure the mean wind velocity, the horizontal (u) and the vertical (w) wind turbulences for two cases: (a) without a turbulence grid, and (b) with a turbulence grid.



Fig. B.1 Hot-sphere anemometer

The basic working principle of the pitot-static tube and hot-wire anemometer is described below.

Pitot-Static Tube

A pitot-static tube is an instrument that yields both the total and the static pressure heads. A standard pitot-static tube is shown in Fig. B.2. It was used to measure the mean wind speed for a smooth-flow case. The orifice at A yields the total head

 $(p_0 + 1/2\rho U^2)$, and the orifices at B yield the static pressure (p_0) . If the pressure differential (p) of pressures at A and B is measured using an electronic manometer, $1/2\rho U^2$ will be represented in terms of voltage output. This pressure differential (p) of pressures at A and B is measured using an electronic manometer, $1/2\rho U^2$ will be represented in terms of voltage output. This pressure differential (p) as displayed by the electronic manometer in Volts can be converted to actual pressure units

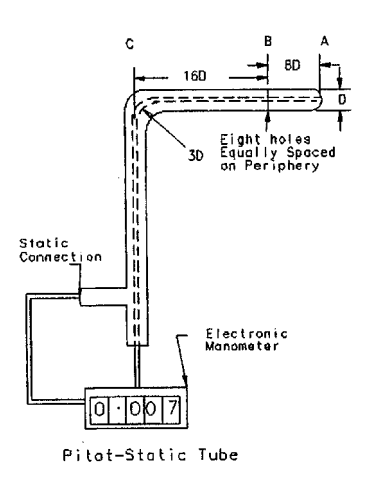


Fig. B.2 A standard pitot-static tube

$$p \text{ , mm H}_2O = 4.9515x \text{ Volts}$$

 $p \text{ (kg/m}^2) = 4.9515x \text{ Volts}$

Then,

$$U = \sqrt{\frac{2p}{\rho}}$$

where p is the air density at the temperature and pressure of the air flowing through the tunnel. The air density varies according to

$$\rho = \rho_0 \frac{P}{P_0} \frac{T_0}{T}$$

where $T=T^{\circ}(F)+459.6$ is the temperature in ${}^{\circ}R$. ρ_0, P_0, T_0 are the air density, pressure and temperature at sea level and ρ is the air density at any pressure (P) and temperature (T). $\rho_0=1.22557~{\rm kg/m^3}$, $P_0=101.32~{\rm kPa}$ and $T_0=59^{\circ}F$ (518.6°R). Voltage corrections are applied to manometer output p if there is a non-zero voltage output at zero wind velocity.

Hot-Sphere Anemometer

A hot-sphere anemometer (FlowMaster, Model 54N60) contains velocity sensor and a temperature compensator made of nickel wire coils-both are clad with metal. The electronics is operated from the front plate which incorporates keyboard and LCD-display. Connections for transducer and output signals are found on the back plate. It's range of application covers velocities from 0.1 m/s to 30 m/s and temperatures from -15 to 85°C, with compensation for pressure and humidity variations. Integration times shall be selected from 1-180 seconds in either continuous or single-period modes; calculation of mean velocity and temperature together with minimum and maximum values.

Hot-Wire Anemometer

Hot-wire anemometers have some special features which makes them a very common tool in any modern wind tunnel. These are:

- Small sensing element dimensions, hence high spatial resolution and little interference to flow
- Short response time due to small sensor mass.

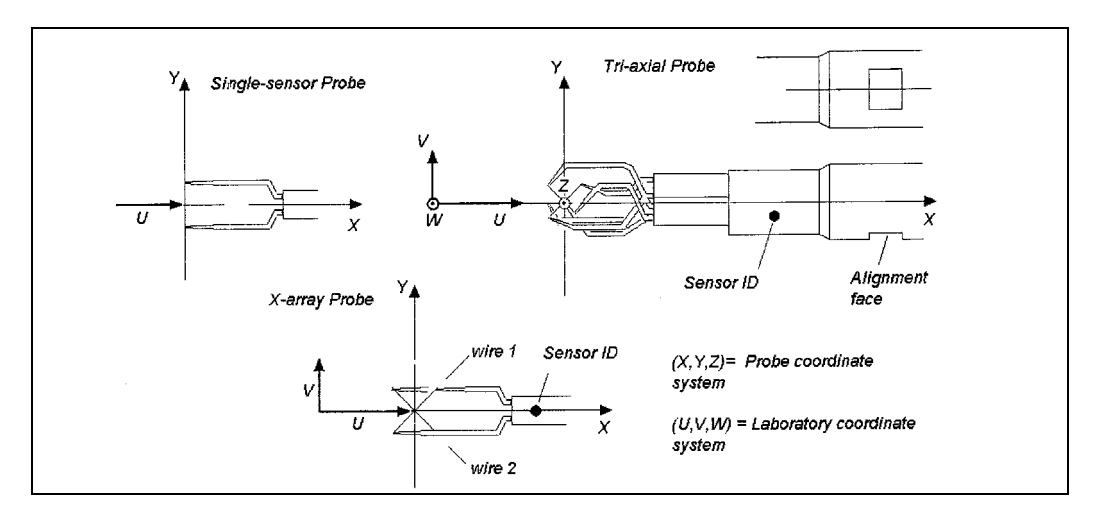


Fig. B.3 Probe array and orientation with respect to laboratory coordinate system

There are various types of hot-wire X-probes which are commercially available (see Fig. B.3). The selection of a particular probe is based upon: fluid medium, number of velocity components to be measured (1-, 2- or 3), expected velocity range, turbulence intensity and fluctuation frequency in the flow, etc.. Based upon the above selection criteria, a Dantec/DISA 55P51 type hot-wire X-probe was selected for the present experiment. DISA 55P51 is a dual-sensor X-array probe with the cylindrical sensors. It has two platinum plated tungsten wires (sensors) of diameter 5μ m of overall length 3 mm. The sensitive wire length is 1.25 mm; it is copper and gold plated at the ends to a diameter of approximately 30μ m. The mounting is a 6 mm diameter cylindrical probe. The probe connected to the constant temperature

anemometer (CTA) as shown in Fig. B3. The CTA anemometer works on the basis of convective heat transfer from a heated sensor to the surrounding fluid, the heat transfer being primarily related to the fluid velocity. The measuring equipment constitutes a measuring chain (see Fig. B.4). It consists typically of a probe with probe support and cabling, a CTA anemometer, a signal conditioner, an A/D converter, and a computer.

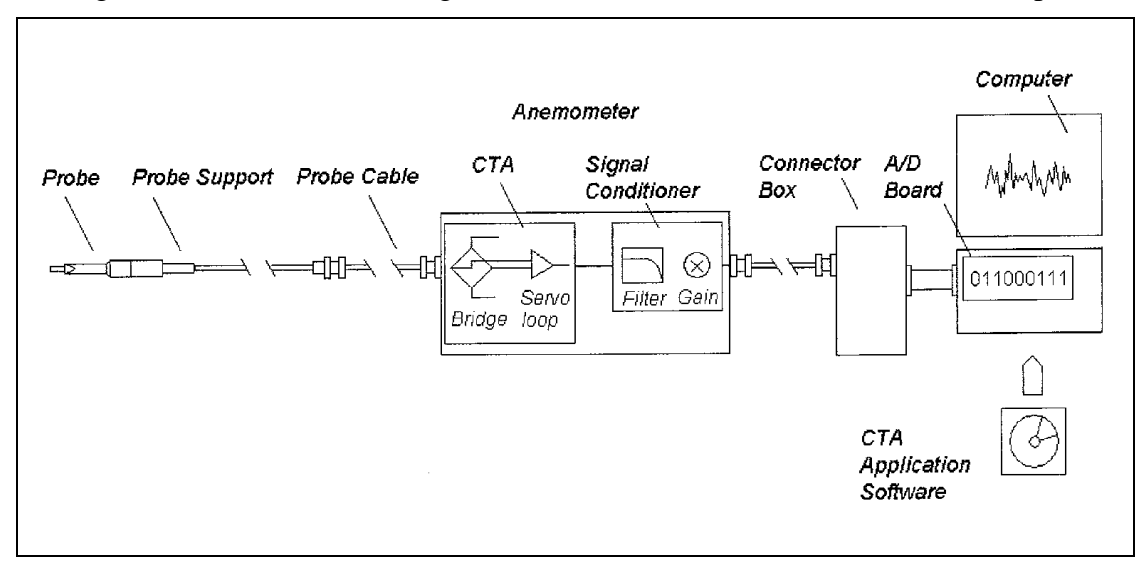


Fig. B.4 Typical CTA measuring chain

Calibration is required to establish a relation between CTA output and the flow velocity. It is performed by exposing the probe to a set of known velocities, U, and then record the voltage, E. A curve fit through points (E,U) represents the transfer function to be used when converting data records from voltages into velocities. Calibration may be carried out in wind tunnel with for example a pitot-static tube or hot sphere anemometer as the velocity reference. It is important to keep track of the temperature during calibration. If it varies from calibration to measurement, it may be necessary to correct the CTA data records for temperature variations.

Data Acquisition

The hardware used was a PC/AT computer system with 2GB of disk, 1 MB RAM, Pentium IV coprocessor and an enhanced color monitor. AT-MIO-16XE-50 A/D card was used for analog-to-digital conversion. The data-acquisition software used was *LabView*.

The Aeroelastic Support System (Dynamic Rig)

The dynamic rig and its components are illustrated in Fig. 3.7. The model section (1) forms an integral part of the test rig which is double symmetric with regard to the model span and cord, except for the drag wires (5,6) having different lengths.

The dominated flexibility of the rig is given by the set of helical springs in which the model section is suspended. Secondary flexibilities are given by the rig

arms and the model section itself and need to be considered when determining the modal stiffness of the rig. This is the purpose of setting acceleration transducers at mid-section of the model to detect local mode of model section. Model vibration frequencies are adjusted by varying the spring lengths / dimensions and the spring spacing.

Both the section model and the rig components are constructed with emphasis on keeping the mass low and stiffness high. Adjustment of model mass and mass moment inertia is done by adding masses (8,9) to the rig such that the scaling requirements are met within the given tolerances.

Some of the features of the aeroelastic support system are mentioned below.

- (i) The length of the extension springs can be adjusted, thereby changing the vertical stiffness (K_h) value.
- (ii) The distance between springs, d, can be adjusted, thereby adjusting the torsional stiffness (K_{α}) keeping K_h constant. The offset r_h between the elastic center and mass center can be adjusted in such a way that the amount of coupling between h and α motions can be varied.
- (iii) Movable weights on the bars fixed perpendicularly to the model axis can change the mass moment of inertia about the axis of rotation without changing the total weight.
- (iv) A release system exists to impose the desired initial conditions on the displacements.
- (v) For restraining the h motion and allowing only α motion, the cross wires fixed to the supporting frame and crossed the center of rotation of model are provided. For restraining the α motion and allowing only h motion, two pairs of horizontal drag wires are provided at distance a above and below the center of model.

Two laser displacement sensors consists of head and control box are used for h and α measurements. The sensor head is attached on frame at a distance from measured object, which depends on type of sensor. Two lasers sensors used for this experiment are LB300 with measured displacement range of \pm 100 mm and resolution of 50 μ m. Each sensor is placed at distance l from center of rotation, and then the vertical and torsional responses can be respectively calculated by

$$h = \frac{x_1 + x_2}{2} \qquad \qquad \alpha = \frac{x_1 - x_2}{2l}$$

where x_1, x_2 are the measurements of laser displacement sensor, respectively; 21 is the space between sensor 1 and sensor 2.

Two acceleration transducers consisted of acceleration transducer, PCD 300A sensor interface and control software are used (option) for acceleration in h and α directions at mid-section of model. Each sensor is placed at distance l from center of section, and then the vertical and torsional responses can be respectively calculated similar to the displacement responses whereas x_1, x_2 are the measurements of acceleration transducers.

APPENDIX C

OUTPUT OF PROJECT

C.1 Papers Published in International Journal

- 1. Janesupasaeree Tharach, and Boonyapinyo Virote (2010), "Determination of Flutter Derivatives of Bridge Deck b
- y Covariance-Driven Stochastic Subspace Identification", *Accepted for publication in International Journal of Structural Stability and Dynamics (IJSSD)*, World Scientific Publishing, Impact Factor = 0.537, 22 pp. (see accepted E-mail in page 217 and manuscript in Appendix D)
- 2. Boonyapinyo Virote, and Janesupasaeree Tharach (2010), "Data-Driven Stochastic Subspace Identification of Flutter Derivatives of Bridge Deck", *Submitted for possible publication in Journal of Wind Engineering and Industrial Aerodynamics*, ELSEVIER, Impact Factor = 0.752, 25 pp. (see corresponding E-mail in page 218 and manuscript in Appendix D)
- 3. Janesupasaeree Tharach, and Boonyapinyo Virote (2009), "Identification of Flutter Derivatives of Bridge Deck in Wind Tunnel Test by Stochastic Subspace Identification", *American Journal of Engineering and Applied Sciences*, Science Publications, Vol. 2, No. 2, pp. 304-316. (see reprint in Appendix D)

C.2 Papers Published in International Conferences

- 4. Boonyapinyo Virote, Janesupasaeree Tharach, and Thamasungkeeti Worapoj (2009), "Identification of Flutter Derivatives of Bridge Deck by Stochastic Subspace Method", *Proceeding in Seventh Asia-Pacific Conference on Wind Engineering*, Taipei, Taiwan, 8 pp. (see manuscript in Appendix D)
- 5. Boonyapinyo Virote (2009), "Wind Loading Standard for Building Design in Thailand and Country", *Proceeding in 5th International Workshop on Regional Harmonization of Wind Loading and Wind Environmental Specifications in Asia-Pacific Economies*, Taipei, Taiwan, 21 pp. (see manuscript in Appendix D)
- 6 Boonyapinyo Virote, Thamasungkeeti Worapoj, and Janesupasaeree Tharach (2009), "Identification of Flutter Derivatives of Bridge Deck in wind Tunnel by Stochastic Subspace Method", *Proceeding in International Symposium on Engineering, Energy and Environment*, Rayong, Thailand, 6 pp.

C.3 Papers Published in National Conferences

- 7. Boonyapinyo Virote, Janesupasaeree Tharach, and Thamasungkeeti Worapoj (2009), "Identification of Flutter Derivatives of IRR Cable-Stayed Bridge in Wind Tunnel", *Proc. of 14th National Convention on Civil Engineering*, Nakhon ratchasima, Thailand, 8 pp.
- 8. Janesupasaeree Tharach, Boonyapinyo Virote, and Poovarodom, Nakhorn (2008), "Identification of Flutter Derivatives of Bridge Deck in Wind Tunnel by Stochastic Subspace Method," *Proc. of 13th National Convention on Civil Engineering*, Paper No. STR 067, pp. (STR) 332-339, Pattaya, Thailand

C.4 การนำผลงานวิจัยไปใช้ประโยชน์

C.4.1 เชิงพาณิชย์

ปัจจุบันประเทศไทยมีสะพานขึ้งช่วงยาวจำนวน 5 สะพาน การพัฒนางานวิจัยนี้สามารถนำไปใช้ในการ
วิเคราะห์ การออกแบบและการประเมินสะพานช่วงยาว เช่น สะพานขึ้งและสะพานแขวน ภายใต้แรงลมได้
เป็นการลดการพึ่งพาบริษัทที่ปรึกษาของต่างประเทศได้เป็นอย่างมาก

C.4.2 เชิงวิชาการ

- 1. พัฒนาศูนย์เชี่ยวชาญเฉพาะทางด้านวิศวกรรมแรงลม อากาศพลศาสตร์ และพลศาสตร์ของโครงสร้าง ให้ เป็นศูนย์ชั้นนำของประเทศไทย
- ผลิตงานวิจัยพื้นฐานและประยุกต์ที่สามารถตอบสนองต่อการพัฒนาด้านวิศวกรรมแรงลม อากาศ
 พลศาสตร์ และพลศาสตร์ของโครงสร้าง และตีพิมพ์ในวารสารระดับนานาชาติ ซึ่งนำไปสู่การเพิ่มขีด
 ความสามารถในการแข่งขันของประเทศในระดับนานาชาติ
- 3. ผลิตบัณฑิตที่มีคุณภาพระดับปริญญาเอกจำนวน 1 คน และปริญญาโทจำนวน 3 คน ทางด้านวิศวกรรม แรงลม อากาศพลศาสตร์ และพลศาสตร์ของโครงสร้าง

C.4.3 อื่น ๆ

- 1. วิทยากร ในการสัมมนาเรื่อง ผลกระทบของลมที่มีต่อโครงสร้าง และการคำนวณแรงลมสำหรับออกแบบ อาคาร จัดโดยวิศวกรรมสถานแห่งประเทศไทย ในพระบรมราชูปถัมภ์ พ.ศ. 2545 ถึง ปัจจุบัน
- 2. วิทยากร ในการฝึกอบรม การคำนวณแรงถมและการตอบสนองของอาคาร จัดโดยกรมโยธาธิการและผัง เมือง กระทรวงมหาดไทย พ.ศ. 2551 ถึง ปัจจุบัน
- 3. อนุกรรมการผลกระทบจากแผ่นดินใหวและแรงลม วิศวกรรมสถานแห่งประเทศไทย ในพระบรม ราชูปถัมภ์ พ.ศ. 2539 ถึง ปัจจุบัน
- 4. เป็นตัวแทนของประเทศไทยในการนำเสนองานวิจัยด้านวิศวกรรมแรงลม ใน 1st 5th International Workshop on Regional Harmonization of Wind Loading and Wind Environmental Specifications in Asia-Pacific Economies พ.ศ. 2546 ถึง ปัจจุบัน

/ Newer 14 of 1742 Older +

You are currently using 4322 MB (58%) of your 7416 MB.

More actions

Back to Inbox Archive Report spam Delete Move to Labels

Last account activity: 1 hour ago on this computer. Details Faculty of Engineering, Thammasat University Mail view: standard | turn off chat | older version | basic HTML Learn more ©2010 Google - Terms of Service - Privacy Policy - Program Policies - Google Home Powered by Guigle

Print all

Collapse all

Forward all

Newer 6 of 1814 Older

Search Mail Search the Web

Compose Mail

Spam (16)

Chat

Virote Boonyapin

Nakhorn Poovarod... Pomtipa Kompinyo... Yosita Pleansom Sak Ruangprayoon Phanida Saikhwan Sangteain Pikuli Nantida Nilboot Naret Limsamphan... Phadungsak Ratan... Sunisa Smittakom

Wired Top Stones - Review: Science Trips Out on Music in 'The Heart Is a Drom Machine' - 11 hours ago-

Back to Inbox Archive Report spam Delete Move to Labels More actions

Submission Confirmation Lober X

From Ted Stathopoulos satatho@beee.concordia called thide details 11:06 PM (17 hours ago) Reply

bvirote@engr.tu.ac.th Tue, Mar 9, 2010 at 11:06 PM Tue, Mar 9, 2010 at 11:06 Submission Confirmation

Dear Assoc. Prof. Dr. Virote Boonyapinyo,

Your submission entitled "Data-Driven Stochastic Subspace Identification of Flutter Derivatives of Bridge Decks" has been received by Journal of Wind Engineering & Industrial Aerodynamics

You may check on the progress of your paper by logging on to the Elsevier Editorial System as an author. The URL

Your username is: bvirote@engr tu ac.th If you need to retrieve password details, please go to:

Your manuscript will be given a reference number once an Editor has been assigned.

Thank you for submitting your work to this journal.

Kind regards,

Elsevier Editorial System
Journal of Wind Engineering & Industrial Aerodynamics

Reply Forward Virote Boonyapinyo to tharach.j

show details 11:10 PM (17 hours ago)

Reply Forward

Back to Inbox Archive Report spam Delete Move to Labels

Newer 6 of 1814 Older

You are currently using 4502 MB (60%) of your 7425 MB.

More actions

Last account activity: 4 hours ago on this computer. Details Faculty of Engineering, Thammasat University Mail view: standard | turn off chat | older version | basic HTML Learn more ©2010 Google - Terms of Service - Privacy Policy - Program Policies - Google Home Powered by Google

APPENDIX D

MANUCRIPT OF PROJECT

Paper accepted for publication in International Journal of Structural Stability and Dynamics (IJSSD)

World Scientific Publishing

DETERMINATION OF FLUTTER DERIVATIVES OF BRIDGE DECKS BY COVARIANCE-DRIVEN STOCHASTIC SUBSPACE IDENTIFICATION

THARACH JANESUPASAEREE¹

Toyo-Thai Corporation Public Ltd., Sermmit Tower, Suhumvit 21,
Asoke Rd., North Klongtoey, Wattana, Bangkok, 10110, Thailand.
tharach.j@toyo-thai.com

VIROTE BOONYAPINYO²

Faculty of Engineering, Thammasat University, Rangsit Campus

Klong-Luang, Pathumthani, 12120, Thailand.

bvirote@engr.tu.ac.th

In this paper, the covariance-driven stochastic subspace identification technique (SSI-COV) was presented to extract the flutter derivatives of bridge decks from the buffeting test results. An advantage of this method is that it considers the buffeting forces and responses as inputs rather than as noises. Numerical simulations and wind tunnel tests of a streamlined thin plate model conducted under smooth flows by the free decay and the buffeting tests were used to validate the applicability of the SSI-COV method. Then the wind tunnel tests of a two-edge girder blunt type of Industrial-Ring-Road Bridge deck (IRR) were conducted under smooth and turbulence flows. The flutter derivatives of the thin plate model identified by the SSI-COV technique agree well with those obtained theoretically. The results obtained for the thin plate and the IRR Bridge deck validated the reliability and applicability of the SSI-COV technique to various wind tunnel tests and conditions of wind flows. The results also show that for blunt type of IRR Bridge deck, the turbulence wind will delay the onset of flutter, compared with the smooth wind.

Keywords: Flutter instability; flutter derivatives; covariance-driven stochastic subspace identification; wind tunnel test; bridge decks; turbulent flow

1. Introduction

Long-span cable-supported bridges are highly susceptible to wind excitations because of their inherent flexibility and low structural damping. Wind loads play an important role in the design of these structures. A wind-induced aerodynamic force can be divided into two parts: the buffeting force that depends on the turbulence of incoming flow, and the aeroelastic force that originates from the interaction between the airflow and bridge motion. The motion-dependent forces feed back into the dynamics of the bridge as aerodynamic damping and stiffness; the effect is termed 'aeroelasticity' and is commonly described via 'flutter derivatives'. The problems of aerodynamic stability including the vortex-induced vibration, galloping, flutter, and buffeting, may have serious effects on the safety and serviceability of bridges. Among these, flutter is the most serious wind-induced vibration for bridges and may destroy a bridge due to diverging motions either in single or torsion-bending coupled mode. Notorious examples of flutter failures are the collapse of the Brighton Chain Pier Bridge in 1836 and the original Tacoma Narrow Bridge in 1940. The buffeting response, on the other hand, may affect serviceability and fatigue strength of a bridge. Flutter derivatives are essential parameters and shall be determined at first place in order to estimate the flutter-instability critical wind velocity and the responses of long-span cable supported bridges. Analysis can be performed in the frequency¹ or the time domain². More detail may be found in Yang et al.¹, Boonyapinyo et al.² and Michaltsos et al.³. The flutter derivatives depend primarily upon the conditions of wind, cross-sectional shape and dynamic characteristics of the bridge. Nevertheless, no theoretical formulas exist for these derivatives for various bridge shapes except for a simple thin plate section. A major research tool in these studies is, therefore, a wind tunnel test, in which a geometrically and aerodynamically representative scale model of a segment of the bridge deck is mounted in a wind tunnel. The flutter derivatives are non-dimensional functions of wind speed, geometry and frequency of vibrations; therefore they can be applied directly to full-scale bridge in a piecewise manner.

The experimental methods used to determine the flutter derivatives can be grouped under two types, i.e., the forced 4 and free vibration methods. 5-8 Having less emphasis on elaborate equipment, time and effort, the free vibration method seems to be more tractable than the forced method. In determining flutter derivatives by the free vibration method, system identification techniques are required to extract these parameters from the response measured for the section model. The free vibration method depends on the system identification techniques used and can be classified into two types, i.e., the free decay and buffeting tests. In the free decay method, the bridge deck is given an initial vertical and torsional displacement. The flutter derivatives are calculated from transient (i.e. free decay) response that occurs when the bridge deck is released. The buffeting test, on the other hand, uses only the steady random responses (i.e. buffeting responses) of the bridge deck under the wind flow with no initial displacement given to the model. Compared with the free decay method, the buffeting test is simpler in the test methodology, more cost effective, and more closely related to real bridge behaviors under the wind flow, except that the output responses appear random-like. This makes the parameters extraction more difficult and a more advanced system identification is required.

In most of the previous studies, flutter derivatives were estimated by deterministic system identification techniques that can be applied to the free decay method only. Examples of previous deterministic system identification techniques that were applied to the free decay method include Scanlan's method,⁵ Poulsen's method,⁶ Modified Ibrahim Time Domain method (MITD),⁷ and Unified Least Square method (ULS).⁸ In these system identification techniques, the buffeting forces and their responses are regarded as external noises, and the identification process requires many iterations. ^{6,7,8} It also confronted with difficulties at high wind speeds where the initial free decay is drowned by the buffeting response.⁶⁻⁸ Moreover, at high reduced wind speed, the vertical bending motion of the structure decays rapidly due to the effect of positive vertical aerodynamic damping, and thus the length of decaying time history available for system identification decreases. This causes more difficulties to the deterministic system identification techniques. ^{7,8} In case of turbulence flows, the presence of turbulence in the flow is equivalent to a more noisy-input signal to the deterministic system identification. This made the extraction process more complicated and most likely reduced the accuracy of the flutter derivatives identified.^{6,7} In addition, due to the restraint of the test technique itself, the free decay method can hardly be applied to determining the flutter derivatives of real bridges in field.

On the other hand, the buffeting test uses the random responses data of a bridge under the wind turbulence only. This mechanism is more closely related to the real behavior of the bridge under wind flows and is applicable to real prototype bridges. The buffeting method costs less and is simpler than the free decay method, since no artificial interruptions are required in exciting the model. However, as wind is the only excited source, the signal-to-noise ratio is generally low, especially at low velocity, and therefore a very effective system identification is required. None of the aforementioned system identification techniques is applicable to the buffeting response tests.

System identification techniques can be divided into two groups, i.e. deterministic and stochastic. If the stochastic system identification technique ⁹⁻¹² is employed to estimate the flutter derivatives of a bridge deck from their steady random responses under the action of a turbulent wind, the above-mentioned shortcomings of the deterministic system identification technique can be overcome. The reason is that the random aerodynamic loads are regarded as inputs rather than noises, which are closer to the fact. Therefore, the signal-to-noise ratio is not affected by the wind speed, and the flutter derivatives at high reduced wind speeds are more likely to be available. As such, the stochastic system identification methods is more advantageous than the deterministic system identification methods.

Many stochastic system identification methods have been developed during the past decades, among which the stochastic subspace identification (SSI in short)^{10, 11} has proven to be a method that is appropriate for civil engineering. The merits of SSI include: (1) the assumptions of inputs are congruent with practical wind-induced aerodynamic forces, i.e. stationary and independent of the outputs; (2) identified modes are given in frequency stabilization diagram, from which the operator can easily distinguish structural modes from the computational ones; (3) since the maximum order of the model can be adjusted by the operator, a relatively large model order will give an exit for noise, which in some cases can dramatically improve the quality of the identified modal parameters; and (4) mode shapes are simultaneously available with the poles, without requiring a second step to identify them.

There are two kinds of SSI methods, one is data-driven (SSI-DATA), and the other is covariance-driven (SSI-COV). Theoretically, the SSI is developed and applicable to the random responses under the turbulent wind only. In the first application, Gu and Qin¹² have applied the SSI-COV method to determine flutter derivatives of a bridge deck from random responses under the turbulent wind. The results were then compared with those from the smooth wind by the deterministic system identification technique (ULS)⁸ with the free decay method. However, the effect of turbulence found may raise questions regarding difference in test methods and system identifications used, perhaps because of the reliability of different techniques. Answers to such questions are sought as part of this study.

In this paper, the covariance-driven stochastic subspace identification method is used to estimate the flutter derivatives from random responses (buffeting) under the action of smooth and turbulent winds. Tests are also carried out with the free decay method (single and two-degree-of-freedom) in order to examine the robustness of the present technique, i.e., to see if the results are not affected by test methods used. To validate the applicability of the present technique, numerical simulations are performed first, followed by sectional-model tests of a quasi-streamlined thin plate model, which is the only section for which theoretical flutter derivatives exist, under smooth flows. Encouraged by the success in the evaluation process, the flutter derivatives of a real bridge are determined. The two-edge-girder type blunt section model of the Industrial-Ring-Road Bridge (IRR in short), a cable-supported bridge with a main span of 398 m in Samutprakan province, Thailand, was tested both in smooth and turbulence flows. Tests were conducted in the TU-AIT Boundary Layer Wind Tunnel in Thammasat University, the longest and largest wind tunnel in Thailand.

2. Theoretical Formulation of Covariance-Driven SSI

2.1 Flutter and buffeting forces

The dynamic behavior of a bridge deck with two degrees-of-freedom (DOF in short), i.e. h (bending) and α (torsion), in turbulent flow can be described by the following differential equations: 12,13

$$m\left[\ddot{h}(t) + 2\xi_{h}\omega_{h}\dot{h}(t) + \omega_{h}^{2}h(t)\right] = L_{se}(t) + L_{b}(t)$$

$$I\left[\ddot{\alpha}(t) + 2\xi_{\alpha}\omega_{\alpha}\dot{\alpha}(t) + \omega_{\alpha}^{2}\alpha(t)\right] = M_{se}(t) + M_{b}(t)$$
(1)

where m and I are the mass and mass moment of inertia of the deck per unit span, respectively; ω_i is the natural circular frequency; ξ_i is the modal damping ratio $(i=h,\alpha)$; L_{se} and M_{se} are the self-excited lift and moment, respectively; while L_b and M_b are the aerodynamic lift and moment. The self-excited lift and moment are given as follows:

$$L_{se} = \frac{1}{2} \rho U^2 B \left[K_h H_1^* (K_h) \frac{\dot{h}}{U} + K_\alpha H_2^* (K_\alpha) \frac{B \dot{\alpha}}{U} + K_\alpha^2 H_3^* (K_\alpha) \alpha + K_h^2 H_4^* (K_h) \frac{h}{B} \right]$$
(2.a)

$$M_{se} = \frac{1}{2} \rho U^2 B^2 \left[K_h A_1^* (K_h) \frac{\dot{h}}{U} + K_\alpha A_2^* (K_\alpha) \frac{B \dot{\alpha}}{U} + K_\alpha^2 A_3^* (K_\alpha) \alpha + K_h^2 A_4^* (K_h) \frac{h}{B} \right]$$
(2.b)

where ρ is the air mass density; B is the width of the bridge deck; U is the mean wind speed at the bridge deck level; $K_i = \omega_i B/U$ is the reduced frequency $(i=h,\alpha)$; and H_i^* and A_i^* (i=1,2,3,4) are the so-called flutter derivatives, which can be regarded as the implicit functions of the deck's modal parameters. The alternate form of self-excited forces is as given in Eq. (2) but without the factor 1/2, (see Ref. 3).

The aerodynamic lift and moment can be defined as ¹³

$$L_{b}(t) = \frac{1}{2} \rho U^{2} B \left[2C_{L} \frac{u(t)}{U} \chi_{L}(t) + (C'_{L} + C_{D}) \frac{w(t)}{U} \chi_{L}(t) \right]$$

$$M_{b}(t) = \frac{1}{2} \rho U^{2} B^{2} \left[2C_{M} \frac{u(t)}{U} \chi_{M}(t) + (C'_{M}) \frac{w(t)}{U} \chi_{M}(t) \right]$$
(3)

where C_L , C_D and C_M are the steady aerodynamic force coefficients; C'_L and C'_M are the derivatives of C_L and C_M with respect to the attack angle, respectively; u(t) and w(t) are the longitudinal and vertical fluctuations of wind speed, respectively; χ_L and χ_M are the lift and moment aerodynamic admittances of the bridge deck.

By moving L_{se} and M_{se} to the left side, and merging the congeners into column vectors or matrices, Eq. (1) can be rewritten as follows:

$$[M]\{\ddot{y}(t)\} + [C^e]\{\dot{y}(t)\} + [K^e]\{y(t)\} = \{f(t)\}$$
(4)

where $\{y(t)\} = \{h(t) \ \alpha(t)\}^{T}$ is the generalized buffeting response; $\{f(t)\} = \{L_b(t) \ M_b(t)\}^{T}$ is the generalized aerodynamic force; [M] is the mass matrix; $[C^e]$ is the gross damping matrix, i.e. the sum of the mechanical and aerodynamic damping matrices; and $[K^e]$ is the gross stiffness matrix.

2.2 Stochastic state space models

The fluctuations of wind speed u(t) and w(t) in Eq. (3) are random functions of time, so the identification of flutter derivatives for the bridge deck can be simplified as a typical inverse problem in the theory of random vibration, and thus solved by the stochastic system identification techniques. Let

$$\begin{bmatrix} A_c \end{bmatrix} = \begin{bmatrix} O & I \\ -M^{-1}K^e & -M^{-1}C^e \end{bmatrix}$$

$$\begin{bmatrix} C_c \end{bmatrix} = \begin{bmatrix} I & O \end{bmatrix}$$
(5)

and

$$\{x\} = \begin{cases} y\\ \dot{y} \end{cases} \tag{6}$$

then Eq. (4) is transformed into the following stochastic state equations

$${\dot{x}} = [A_c] {x} + {w}$$

$${y} = [C_c] {x} + {v}$$
(7)

The discrete form of Eq. (7) can be written as

$${\dot{x}_{k+1}} = [A] {x_k} + {w_k} {y_k} = [C] {x_k} + {v_k}$$
 (8)

where $[A_c]_{4\times4}$, $[C_c]_{2\times4}$ and $\{x\}$ are known as the state matrix, output shape matrix and state vector, respectively; $\{w_k\}$ and $\{v_k\}$ are the input and output noise sequences, respectively. The subscript in $(\bullet)_k$ denotes the value of (\bullet) at time $k\Delta t$, where Δt means the sampling interval. $\mathbf{0}$ and \mathbf{I} are the zero and identity matrices, respectively.

An assumption of the stochastic model is that $\{x_k\}$, $\{w_k\}$ and $\{v_k\}$ in Eq. (8) are mutually independent and hence

$$E[x_k w_k^{\mathrm{T}}] = \mathbf{0} \quad E[x_k v_k^{\mathrm{T}}] = \mathbf{0}$$

$$(9)$$

Defining the output covariance matrix of lag i, Λ_i , and the "next state-output" covariance matrix G as

$$\Sigma = E[x_k x_k^{\mathrm{T}}] \qquad Q = E[w_k w_k^{\mathrm{T}}]$$

$$\Lambda_i = E[y_{k+i} y_k^{\mathrm{T}}] \qquad R = E[v_k v_k^{\mathrm{T}}]$$

$$G = E[x_{k+i} y_k^{\mathrm{T}}] \qquad S = E[w_k v_k^{\mathrm{T}}] \qquad (10)$$

and combining Eqs. (9) and (10), we obtain the following Lyapunov equations for the state (Σ) and output covariance matrices

$$\Sigma = A\Sigma A^{T} + Q$$

$$\Lambda_{0} = C\Sigma C^{T} + R$$

$$G = A\Sigma C^{T} + S$$
(11)

From Eqs. (8) and (9), it can be deduced

$$\Lambda_{1} = E \left[\left\{ y_{k+1} \right\} \left\{ y_{k} \right\}^{T} \right]
= E \left[\left(C \left\{ x_{k+1} \right\} + \left\{ v_{k+1} \right\} \right) \left\{ y_{k} \right\}^{T} \right]
= E \left[C \left\{ x_{k+1} \right\} \left\{ y_{k} \right\}^{T} \right]
= CG$$
(12)

$$\Lambda_{2} = E[\{y_{k+2}\}\{y_{k}\}] = E[(C\{x_{k+2}\} + \{v_{k+2}\})\{y_{k}\}^{T}]
= E[C\{x_{k+2}\}\{y_{k}\}^{T}] = CE[\{x_{k+2}\}\{y_{k}\}^{T}]
= CE[(A\{x_{k+1}\} + \{w_{k}\})\{y_{k}\}^{T}]
= CE[A\{x_{k+1}\}\{y_{k}\}^{T}] = CAE[\{x_{k+1}\}\{y_{k}\}^{T}]
= CA^{2-1}G$$
(13)

and

$$\Lambda_i = CA^{i-1}G \tag{14}$$

2.3 Covariance-driven stochastic subspace identification

The main algorithm of SSI-COV proceeds with defining a covariance block Toeplitz $\ T_{1|i}$ as

$$T_{1|i} = \begin{bmatrix} \Lambda_i & \Lambda_{i-1} & \cdots & \Lambda_1 \\ \Lambda_{i+1} & \Lambda_i & \cdots & \Lambda_2 \\ \vdots & \vdots & \vdots & \vdots \\ \Lambda_{2i-1} & \Lambda_{2i-2} & \cdots & \Lambda_i \end{bmatrix}$$

$$(15)$$

One can infer from the definition of the covariance matrix that $T_{\parallel i}$ can be expressed as the product of two block Hankel matrices $Y_{\rm f}$ and $Y_{\rm p}$

$$T_{1|i} = Y_{\rm f} Y_{\rm p}^{\rm T} \tag{16}$$

where Y_f and Y_p are composed of the 'future' and 'past' measurements, respectively,

$$Y_{f} = \frac{1}{\sqrt{j}} \begin{bmatrix} y_{i} & y_{i+1} & \cdots & y_{i+j-1} \\ y_{i+1} & y_{i+2} & \cdots & y_{i+j} \\ \vdots & \vdots & \vdots & \vdots \\ y_{2i-1} & y_{2i} & \cdots & y_{2i+j-2} \end{bmatrix} \qquad Y_{p} = \frac{1}{\sqrt{j}} \begin{bmatrix} y_{0} & y_{1} & \cdots & y_{j-1} \\ y_{1} & y_{2} & \cdots & y_{j} \\ \vdots & \vdots & \vdots & \vdots \\ y_{i-1} & y_{i} & \cdots & y_{i+j-2} \end{bmatrix}$$
(17)

Next, applying the factorization property to $T_{i|i}$ by the singular value decomposition yields

$$T_{||i|} = USV^{T} = (U_{1} \ U_{2}) \begin{pmatrix} S_{1} & 0 \\ 0 & 0 \end{pmatrix} \begin{pmatrix} V_{1}^{T} \\ V_{2}^{T} \end{pmatrix} \approx U_{1}S_{1}V_{1}^{T}$$
(18)

where U, S and V are orthonormal matrices. S is a diagonal matrix containing positive singular values in descending order. The number of nonzero singular values indicates the rank of the Toeplitz matrix $T_{\parallel i}$. The reduced diagonal matrix S_1 is obtained by omitting the zero singular values from the matrix S. Matrices U_1 and U_1 are obtained by omitting the corresponding columns from the matrices U and U respectively. Now the identification of system matrices is almost achieved. In practice however, the estimated covariance Toeplitz matrix $T_{\parallel i}$ is affected by "noise" leading to singular values that are all different from zero. Actually, some of the singular values associated with the noise modals are small, or very small. Generally, the model order can be determined by looking at a "gap" between two successive singular values. The singular value where the maximal gap occurs yields the model order. To obtain a good model for modal analysis applications, a better idea is to construct a stabilization diagram, by identifying a whole set of models with different orders. Matrix $I_{\parallel i}$ is then obtained by factorizing a shifted Toeplitz matrix $I_{\parallel i+1}$ that has similar structure as of $I_{\parallel i}$, but consists of covariance from lag 2 to $I_{\parallel i}$ in a manner similar to the classical eigensystem realization algorithm (ERA in short), one can find

$$A = o_i^{\dagger} T_{2|i+1} \varsigma_i = S_N^{-1/2} U^T T_{2|i+1} V S_N^{-1/2}$$
(19)

where N is the model order, i.e. the maximum number of modes to be computed and $(\bullet)^+$ denotes the Moore-Penrose pseudo-inverse of a matrix. Thus, the modal parameters can be determined by solving the eigenvalue problem of the state matrix A. By now, the theoretical formulation of the covariance-driven SSI has been achieved.

According to Eqs. (16)-(19), a different combination of i, j and N will give a different state matrix, and thus a different pair of modal parameters. Therefore, modal parameters should be derived from a series of combinations, rather than a single combination. In the process of identification, N or i should be given in series for certain values of j in order to obtain a frequency stability chart. Solving the eigenvalue problem of the state matrix A by the pseudo-inverse method yields

$$A = \Psi \Lambda_d \Psi^{-1}$$

$$\Phi = C \Psi$$
(20)

where Ψ is the complex eigenvector matrix, Φ is the mode shape matrix, and Λ is a diagonal matrix composed of the complex poles of the system. Different combinations of i, j and N are employed to derive the modal parameters statistically. For more details, see Refs. 7 and 9.

Once the modal parameters are identified, the gross damping matrix C^e and the gross stiffness matrix K^e in Eq. (4) can be readily determined by the pseudo-inverse method

$$[K^e \ C^e] = -M[\Phi \Lambda^2 \ \Phi^* (\Lambda^*)^2] \begin{bmatrix} \Phi & \Phi^* \\ \Phi \Lambda & \Phi^* \Lambda^* \end{bmatrix}^{\dagger}$$
(21)

where the superscript * denotes the complex conjugate of the corresponding term. Let

$$\overline{C}^{e} = M^{-1}C^{e}, \ \overline{K}^{e} = M^{-1}K^{e}
\overline{C} = M^{-1}C^{0}, \ \overline{K} = M^{-1}K^{0}$$
(22)

where C^0 and K^0 are the 'inherent' damping and stiffness matrices, respectively. Thus, the flutter derivatives can be extracted from the following equations

$$\begin{split} H_{1}^{*}(k_{h}) &= -\frac{2m}{\rho B^{2}\omega_{h}}(\overline{C}_{11}^{e} - \overline{C}_{11}), \quad A_{1}^{*}(k_{h}) = -\frac{2I}{\rho B^{3}\omega_{h}}(\overline{C}_{21}^{e} - \overline{C}_{21}) \\ H_{2}^{*}(k_{\alpha}) &= -\frac{2m}{\rho B^{3}\omega_{\alpha}}(\overline{C}_{12}^{e} - \overline{C}_{12}), \quad A_{2}^{*}(k_{\alpha}) = -\frac{2I}{\rho B^{4}\omega_{\alpha}}(\overline{C}_{22}^{e} - \overline{C}_{22}) \\ H_{3}^{*}(k_{\alpha}) &= -\frac{2m}{\rho B^{3}\omega_{\alpha}^{2}}(\overline{K}_{12}^{e} - \overline{K}_{12}), \quad A_{3}^{*}(k_{\alpha}) = -\frac{2I}{\rho B^{4}\omega_{\alpha}^{2}}(\overline{K}_{22}^{e} - \overline{K}_{22}) \\ H_{4}^{*}(k_{h}) &= -\frac{2m}{\rho B^{3}\omega_{h}^{2}}(\overline{K}_{11}^{e} - \overline{K}_{11}), \quad A_{4}^{*}(k_{h}) = -\frac{2I}{\rho B^{4}\omega_{h}^{2}}(\overline{K}_{21}^{e} - \overline{K}_{21}) \end{split} \tag{23}$$

2.4 Constitution of Toeplitz matrices and selection of model order

A good knowledge of the model order (system order) is essential for modal analysis. First, the numbers of block rows i (which determine the maximum number of orders that can be calculated) have to be specified. The numbers of block row i in $T_{\parallel i}$ in Eq. (18) and model order

N in Eq. (19) are depend on user's choice. According to experience, it is better to over-specify the model order and then to eliminate spurious numerical poles afterwards. The operation was carried out with the help of MATLAB. In each number of block row i selected, for construction of stability diagram, the poles corresponding to a certain model order are compared with the poles of a one-order-lower model. If the frequencies and the damping ratios differences are within preset limits, the pole is labeled as a stable one and the model order is determined. The modal frequency (ω_i) and damping ratio (ζ_i) corresponding to each pole can be obtained by

$$\omega_i = \sqrt{a_i^2 + b_i^2} \quad , \quad \zeta_i = \frac{a_i}{\omega_i} \tag{24}$$

where a_i and b_i are real and imaginary parts of the continuous time poles λ_i defined as

$$\lambda_i = \frac{\ln(\mu_i)}{\Lambda t} = a_i + jb_i \tag{25}$$

where $j=\sqrt{-1}$ and μ_i is the discrete time poles (eigenvalue), corresponding to the *i*th mode of Λ . The preset limits are normally 1% for frequencies and 5% for damping ratios. However, depending on the quality of data, at high wind speed, a difference of 10% for damping ratio may be set⁴. A brief description follows:

- 1. For a selected number of time history data recorded, n, select the number of block row i. Accordingly, the maximum number of orders is specified. The output covariances were determined for lags k = 1, 2, i.
- 2. In each i, the Toeplitz matrix is formulated once as per Eq. (16). Models of different orders (N=2...i) were then obtained by including different numbers of singular values S_N in the computation of matrix A. Thus the modal parameters can be determined by

- solving the eigenvalue of the state matrix A. The poles corresponding to a certain model order are compared with the poles of a one-order-lower model and the stable poles and system order are then determined.
- 3. The frequencies and damping coefficients corresponding to the stable poles are reported as stable ones for selected value of *i*.
- 4. To assess if a suitable number of block rows is selected, steps 1-3 are repeated by varying *i*, and the model order, stable poles, modal frequencies and damping for each value of *i*. Theoretically, the number of block rows *i* is related to the precision level of the SSI method and generally shows asymptotic convergence.

Figure 1 shows a sample of the identified (stable) modal frequencies and damping coefficients of the two modes (vertical and torsion) as a function of i. The variability of the modal frequencies looks small but the modal damping coefficients are uncertain and illegitimate when a small number i is used. However, they do show asymptotic convergence after certain value of i. The number of block i, for which the modal parameters have converged, is also affected by the sampling frequency. From Fig. 1, the convergence starts at number of block rows $i = 2f_s$, where f_s is the sampling rate (Hz) which is usually taken as ten times that of the highest expected modal frequency or higher⁷.

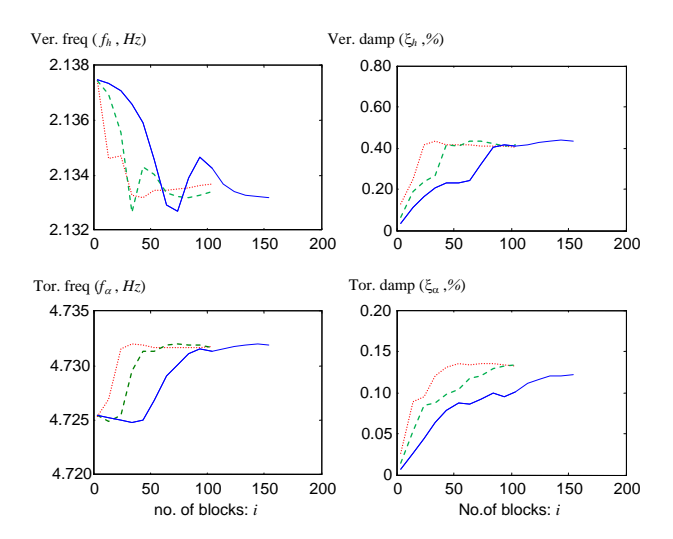


Fig. 1 Asymptotic convergence property of modal properties (...fs = 25 Hz, ---fs = 50 Hz and solid line for fs = 100 Hz)

2.5 Determination of System Matrices and Extraction of Flutter Derivatives

Once the model order and stable poles are identified as in Section 2.4, only the Ψ , Φ , and Λ matrices of the stable poles are used to obtain the K and C matrices in Eq. (21) in order to eliminate noises. The stable poles are regarded as the true modes whereas the spurious poles represent the effects of noises. The flutter derivatives are then estimated by using Eq. (23).

3. Numerical Simulation Test

In order to validate the applicability of the covariance-driven SSI technique in flutter derivatives estimation, the numerical tests are first carried out. The response signals of bridge decks from different wind-tunnel test methods were simulated. The numerical tests included two synthetic but well controlled cases: two uncoupled degrees of freedom and two coupled degrees of freedom (simulated response including the motion induced aeroelastic terms). Both cases are first excited in the transient (i.e. free decay) motion and then by a white noise loading process. Measurement noises are also added by a white noise process with a standard deviation equal to 10% of the standard deviation of the original responses, in order to investigate the effect of measurement noise.

3.1 Two uncoupled degrees of freedom: free decay

Time-history free decay responses were obtained by direct calculations of the displacement values for n=4096 discrete time stations, with a 'sampling' interval Δt =0.02s (fs= 50Hz). Structural modal properties used in this simulation were chosen from the previously tested sectional model of the Great Belt Bridge. ¹⁵ The modal matrices are given per unit length as:

$$C_0 = \begin{bmatrix} 0.3616 & 0 \\ 0 & 0.0072 \end{bmatrix}, \quad K_0 = \begin{bmatrix} 397.0573 & 0 \\ 0 & 24.7315 \end{bmatrix}, M_0 = \begin{bmatrix} 2.6526 & 0 \\ 0 & 0.0189 \end{bmatrix}$$

i.e. $f_{ho} = 1.9472~Hz$, $f_{\theta\theta} = 5.7573~Hz$, $\xi_{h0} = 0.0053$, $\xi_{\theta\theta} = 0.0056$, where damping ratios, ξ , are representatives for the range of small amplitudes. The damping ratios were then multiplied in turn by 5, 10, 20 and 40 to cover the total damping (structural + aerodynamic) effect which will be present in vibration of the model section under wind flows. Values as high as $\xi = 0.2$ can be expected for the vertical degree of freedom under the wind flow. The Liepmann approximation of Sear's function¹⁴ is further assumed to be the aerodynamic admittance of the model.

Table 1a Preset and identified values of frequencies and damping ratios for free decay responses, $n\Delta t = 4096 \times 0.02 \text{ s}$ = 81.92 s.

case	Mode	<u>Preset values</u>		Identify values		<u>Error(%)</u> .	
		$f_{ m p}$	$\xi_{ m p}$	$f_{ m p}$	$\xi_{ m p}$	$f_{ m p}$	$\xi_{ m p}$
<u>1.</u>	Vertical mode	1.9472	0.0056	1.9472	0.0056	0 %	0 %
	Torsional mode	5.7573	0.0053	5.7573	0.0053	0 %	0 %
<u>2.</u>	Vertical mode	1.9472	0.2228	1.9462	0.2236	-0.05%	0.36%
	Torsional mode	5.7573	0.2120	5.7612	0.2128	0.07%	0.38%
case1+10% noise	Vertical mode	1.9472	0.0056	1.9496	0.0053	-0.1%	-5.4%
	Torsional mode	5.7573	0.0053	5.7570	0.0052	0 %	-1.9%
case2+10% noise	Vertical mode	1.9472	0.2228	1.9621	0.2276	0.8%	2.2%
	Torsional mode	5.7573	0.2120	5.7593	0.2126	0 %	0.3%

Table 1b Preset and identified values of stiffness and damping matrices for free decay responses, $n\Delta t = 4096 \text{ x} \cdot 0.02 \text{ s}$ = 81.92 s

case	Preset stiffness matrix.		Preset damping matrix.		Recover stiffness matrix		Recover damping matrix	
	K_{II}	K_{22}	C_{II}	C_{22}	K_{II}	K_{22}	C_{II}	C_{22}
1	397.057	24.73	0.3616	0.0072	397.056	24.73	0.3616	0.0072
2	397.057	24.73	14.464	0.288	396.611	24.76	14.477	0.289
case1+10% noise	397.057	24.73	0.3616	0.0072	397.5447	24.73	0.3514	0.0072
Case2+10% noise	397.057	24.73	14.464	0.288	397.0573	24.73	14.5081	0.2886

Tables 1a and b show the identified values of modal parameters and system matrices for the lowest and highest preset damping ratios cases (case1 and case 2 respectively). As can be seen, the estimated frequency and damping ratio are practically identical to the preset values (less than 0.5% for the highest damping case). The system matrices are also good even for the short useful signal case with only a few cycles of vibration. For the case where 10%-measurement noises are added, the variations in identified frequencies are less than 0.8%. The variations in damping ratios are no more than 2%, except for the lowest damping case for which the variation is 5.4 %. The diagonal terms of the estimated system matrices (frequency and damping matrices) are also identical to the preset values. The estimates of diagonal terms are distorted within 1% except for the lowest damping case in which values are within 2.82%.

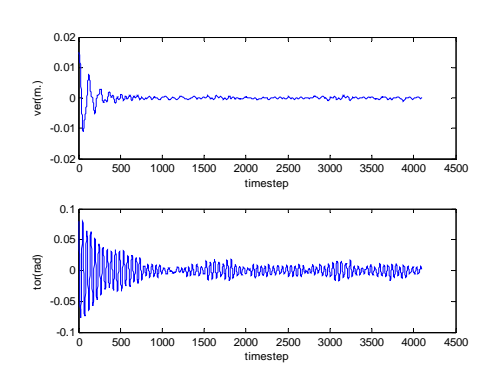
3.2 Two Coupled Degrees of Freedom: Free decay and Buffeting responses

The next step was a simulation test with full effective stiffness and damping matrices (i.e. coupled degrees of freedom) and with lift and moment forces of the white noise type, as assumed in the SSI-method. For the mean-wind speed of 10.26 m/s and the aerodynamic derivatives assumed to be those reported for a similar bridge cross-section, the effective structural matrices were pre-set as

$$C_{e} = \begin{bmatrix} 8.9308 & -0.0799 \\ 0.4345 & 0.0386 \end{bmatrix}, \quad K_{e} = \begin{bmatrix} 420.1002 & -59.1805 \\ 1.7552 & 19.6652 \end{bmatrix}, \quad M_{0} = \begin{bmatrix} 2.6526 & 0 \\ 0 & 0.0189 \end{bmatrix}$$

The time-history response were simulated for both free decay and buffeting responses under turbulence winds with 10% turbulence intensity; then measurement white noises were superimposed on the simulated response. The time-history free decay response were computed by constant acceleration method, for which some results are shown in Fig.2a. With the SSI-COV method applied to these responses data, we can obtain the effective structural matrices with the deviation from the pre-set ones (C and K) in percentage as

$$\Delta C_{\%} = \begin{bmatrix} 0.66 & -3.00 \\ 0.16 & -0.26 \end{bmatrix}, \quad \Delta K_{\%} = \begin{bmatrix} -0.14 & -0.05 \\ 4.26 & -0.08 \end{bmatrix}$$



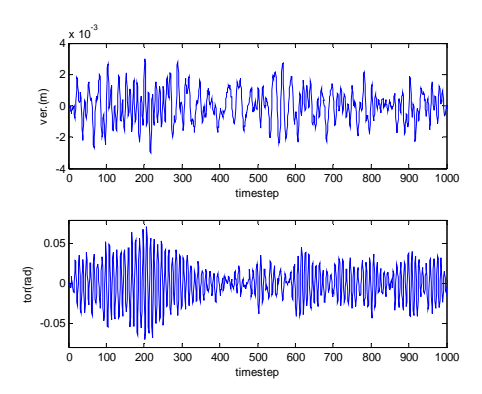


Fig.2a. Example of vertical (top) and torsional (bottom) free decay responses simulated under wind flow.(time step =0.02 sec.)

Fig.2b. Example of vertical (top) and torsional (bottom) buffeting responses simulated under wind flow. (time step =0.02 sec.)

Superimposing 10% measurement white noise on the simulated response made the structural matrices differ from those of the noise-free cases within 3%. The time-history response was also simulated for the case of buffeting responses where wind turbulence is the only exciting source. The effective stiffness and damping matrices were taken as in the case of transient response; examples of the time-history response are shown in Fig. 2b. The buffeting responses required longer data records (20,000 data points in the present study) as compared to that in the free decay case (4096 data points) to yield acceptable results. The computed frequencies and damping ratios agree well with preset values with precisions within 0.5% and 2%, respectively. The diagonal terms in the stiffness and damping matrices also agree well with preset values, showing a difference of less than 1%, except for the C_{11} (related to vertical damping) where the difference is around 2.5%. The largest differences in the off-diagonal terms are K_{21} and C_{21} , which are related to A_4^* and H_2^* , respectively. In the case with 10%-measurement noise added, the deviations of the reconstructed matrices from the pre-set ones, in percentage, are

$$\Delta C_{\%} = \begin{bmatrix} 8.55 & -27.86 \\ -0.28 & 0.5 \end{bmatrix}, \quad \Delta K_{\%} = \begin{bmatrix} 2.23 & -0.38 \\ -11.17 & -0.03 \end{bmatrix}$$

4. Wind Tunnel Tests

To evaluate further the applicability of the present method in estimating the flutter derivatives of bridge decks, wind tunnel tests of a quasi-streamlined thin plate model and a two-edge girder type blunt bridge section model were performed.

4.1 Outline of wind tunnel tests

The wind tunnel tests were performed in the TU-AIT wind tunnel in Thammasat University. The working section of the wind tunnel has a width of 2.5 m, a height of 2.5 m and a length of 25.5 m. The required turbulent flow was generated by grids, as shown in Fig. 3. A hot-sphere anemometer was applied to measuring the mean wind speed of the flow, and a hot-wire anemometer was used to measure the fluctuations of wind speed. The longitudinal and vertical turbulence intensities are both less than 0.05% for smooth flows and about 8% for turbulence flows. Typical normal spectral densities of the longitudinal and vertical fluctuation components of 8%-turbulence flow are presented in Fig. 5 and compared with both the Von Karman and Kaimal spectrum¹⁹.

The model was suspended by eight springs outside the wind tunnel (see Fig. 4). To simulate a bridge section model with 2DOFs, i.e. vertical bending and torsion, piano wires were used to prevent the motion of the model in the longitudinal direction, as can be seen from the schematic diagram of the top view of the test setup in Fig. 6. Two piezoelectric acceleration transducers were mounted at the mid length of the model to capture the acceleration signals. The responses of the models were captured by the acceleration transducers, and then the vertical and torsional responses can be respectively obtained by

$$h = \frac{x_1 + x_2}{2}$$
, $\alpha = \frac{x_1 - x_2}{l}$ (26)

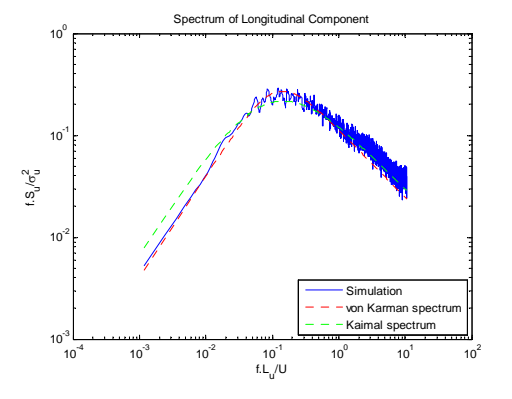
where x_1 and x_2 are the measurements of transducers 1 and 2, respectively; and l is the space between transducers.



Fig. 3. IRR bridge model and grids to generate turbulent flow in wind tunnel.



Fig. 4. Suspension device of the model.



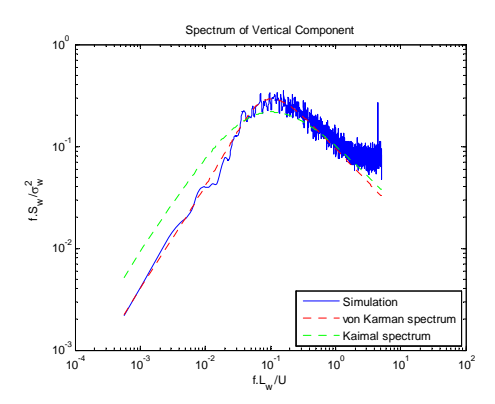


Fig 5 Normalized power spectrum of the longitudinal and vertical velocity component: 8%-turbulence flow.

4.2 CASE 1: Thin plate model under smooth flow

A quasi-streamlined thin plate with a width to height (thickness) ratio of about 22.5 (see Fig. 7) was first selected for the wind tunnel test. The Table 2 lists the main parameters of the model.

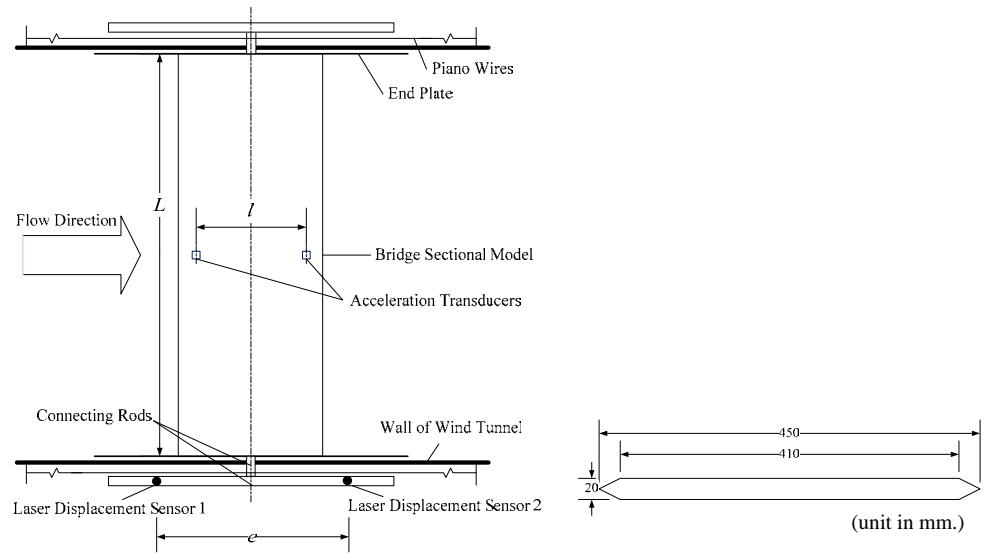


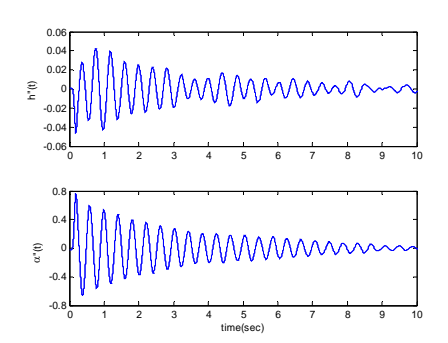
Fig. 6 Top view of the test setup.

Fig. 7 Cross-section of the thin plate.

The flutter derivatives of the thin plate were extracted using the SSI-COV technique from the results of three types of tests, namely, a) single-degree-of-freedom (SDOF) motion tests, 5 b) free decay coupled-motion test (2DOFs), and c) buffeting coupled-motion test (2DOFs). Typical test results showing the responses from the bridge model have been plotted in Figs. 8 and 9. The responses for the free decay and buffeting tests are sampled at the rates of $1000 \, Hz$ and $200 \, Hz$, respectively. The results are then removed mean and re-sampled at $250 \, Hz$ and $50 \, Hz$, respectively. The covariance-driven SSI technique is applied to identifying modal parameters from these data, and a pseudo-inverse method is applied to estimating the stiffness and damping matrices. The flutter derivatives are estimated by Eq. (23) and reported in the form of Eq. (2) but without the factor 1/2.

Table 2. Main parameters of the thin plate model

Parameter	Mark	Unit	Value
Length	L	m	2.30
Width	B	m	0.45
Height	H	m	0.02
Mass per unit length	M	kg/m	6.7391
Inertial moment of mass per unit length	I_m	kg m ² / m	0.1183
Inertial radius	R	m	0.1325
First bending frequency	f_h , n_h	Hz	1.65
First torsional frequency	f_{α} , n_{α}	Hz	2.73
First torsion-bending frequency ratio	ε		1.65



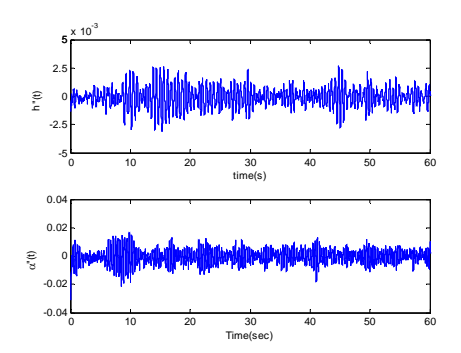


Fig. 8 Vertical (top) and torsional (bottom) free decay acceleration responses of the thin plate at 8.1 m/s wind speed under smooth flow.(unit in g)

Fig. 9 Vertical (top) and torsional (bottom) buffeting acceleration responses of the thin plate at 5.6 m/s wind speed under smooth flow.(unit in g)

4.2.1 Comparisons between SDOF and 2DOF-coupled-motion tests: free decay method

Figures 10 and 11 show the flutter derivatives of the thin plate computed by the SSI-COV technique using the aforementioned three test methods against Theodorsen's theoretical values. Unless otherwise noted, at any wind speed, the flutter derivatives associated with the vertical motion, i.e., H_1^* , H_4^* , H_4^* , and H_4^* , were calculated using the frequency H_4^* , were calculated using the derivatives associated with the torsional motion, i.e., H_2^* , H_3^* , H_3^* , and H_4^* , were calculated using the frequency H_4^* , where H_4^* is the first term of the fi

In Figs. 10 and 11, the direct flutter derivatives H_1^* and H_4^* as found from the SDOF vertical-motion tests and A_2^* and A_3^* as found from the SDOF torsional-motion tests were also plotted and compared with those from the coupled-motion tests. The near perfect match shows that the direct flutter derivatives are indeed not affected by the motion along the other degrees of freedom, as was predicted by the theory, namely, the flutter derivatives associated with the h motion are not affected by the α motion, and vice versa. It also demonstrates the reliability of both the coupled-motion tests and the system identification method (SSI-COV).

4.2.2 Comparisons of coupled-2DOF motion tests between the free decay and buffeting tests

The flutter derivatives obtained from both the free decay and buffeting tests for the coupled-2DOF cases were compared in Figs. 10 and 11. The results show good agreement between the two methods, which validates the reliability of the system identification method (SSI-COV) in application to both the free decay and buffeting tests, although it was developed from a stochastic model (i.e. white noise loading assumption). However, when a relatively heavy model is excited at a very low reduced wind velocity, i.e., with low wind energy, it becomes more difficult to extract the flutter derivatives from the buffeting responses.

The results also show that calculated flutter derivatives agree well with the theoretical ones. The six important flutter derivatives $H_1^* \sim H_3^*$ and $A_1^* \sim A_3^*$ identified by the SSI from different tests match well with theoretical ones. The H_4^* derivatives agree generally in trend with the theoretical ones. However, the A_4^* derivatives obtained from the buffeting responses are more scattered compared with those from the free decay responses. The impacts of the H_4^* and A_4^* derivatives, however, seem to be less significant when compared with those of the other derivatives. This explains the reason why H_4^* and A_4^* were usually neglected in previous studies. 5,6,8,13

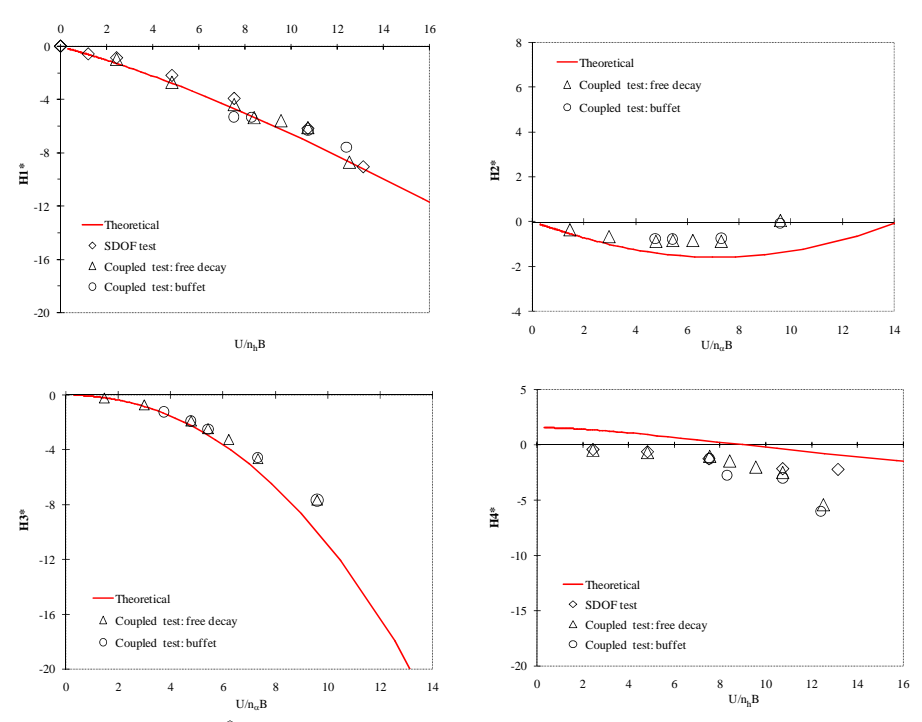


Fig. 10 Flutter derivatives (H_i^*) of the thin plate by SDOF test and coupled test by free decay and buffeting responses under smooth flow.

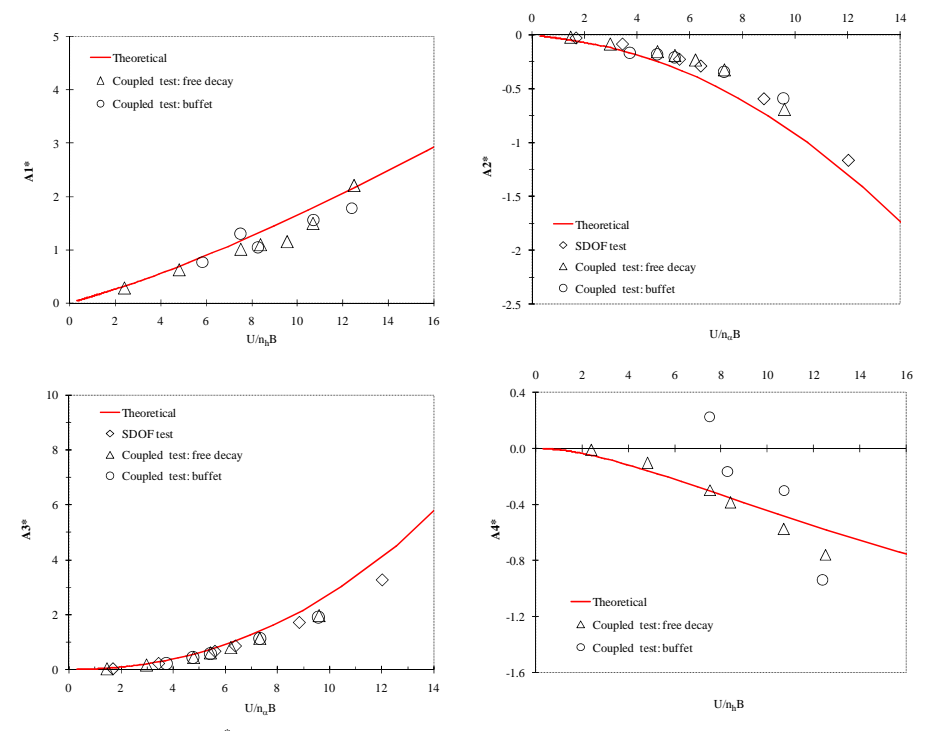


Fig. 11 Flutter derivatives (A_i^*) of the thin plate by SDOF test and coupled test by free decay and buffeting responses under smooth flow.

4.3 CASE 2: Section model of IRR Bridge

Encouraged by the success in the thin plate model testing, the flutter derivatives of the IRR Bridge, a cable-supported bridge with 2-edge girder, as shown in Fig. 12, were estimated by the SSI-COV technique. The IRR Bridge has a main span of 398 m. The deck consists of a concrete deck slab and a web of steel girders. The deck is supported by two cable planes at outside edge girders. A 2-edge-girder bridge section with A-shape pylons is known to be economically competitive, but also aerodynamically unstable at high wind speeds. Table 3 lists the main parameters of the prototype bridge and the section model. Tests were conducted under both the smooth and turbulence wind flows.

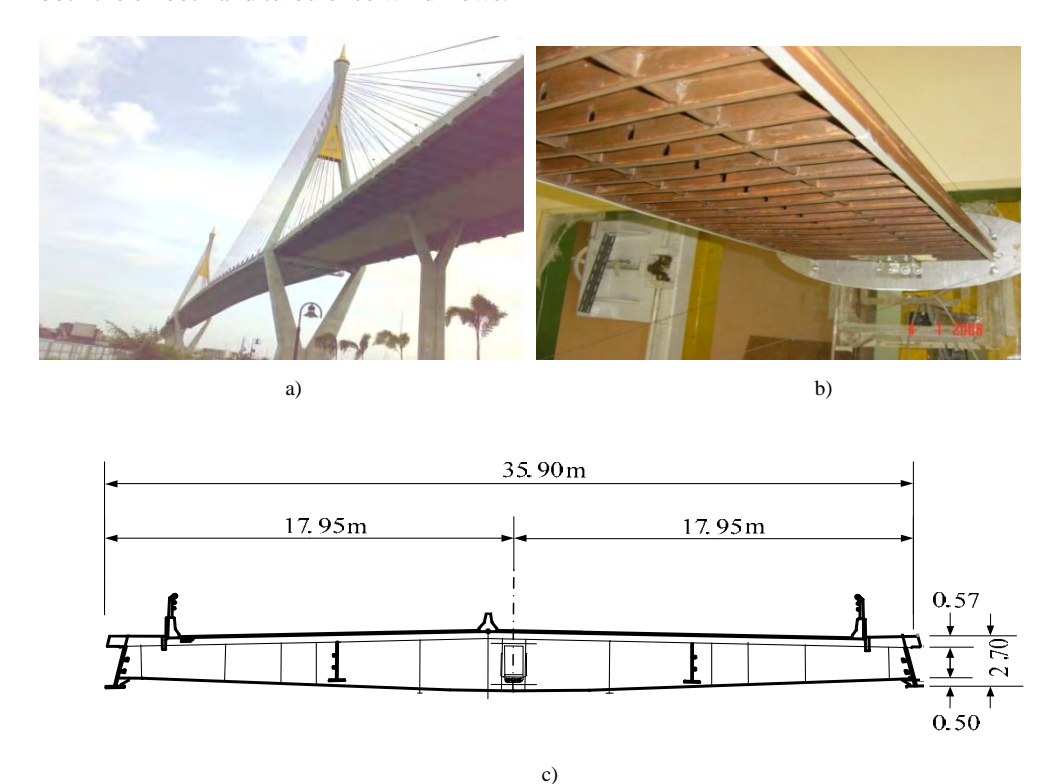


Fig.12. a) Three dimensional view of IRR Bridge, b) IRR bridge deck model in wind tunnel and c) Schematic cross-section of IRR Bridge.

Table 3. Main parameters of the IRR Bridge model

Parameter	Mark	Unit	Prototype	Model
Length	L	m	-	2.26
Width	B	m	35.9	0.399
Height	H	m	3.20	0.035
Mass per unit length	M	kg / m	43000	5.6801
Inertial moment of mass per unit length	I_m	$kg m^2 / m$	$4.11x10^9$	0.1726
First bending frequency	f_h , n_h	Hz	0.376	2.13
First torsional frequency	f_{α} , n_{α}	Hz	0.850	4.73
First torsion-bending-frequency ratio	ε		2.26	2.22

Using the SSI-COV technique, the flutter derivatives of the IRR Bridge were estimated for the 2DOF responses under the smooth flow by both the free decay and buffeting tests, and under the turbulence flow by the buffeting test only.

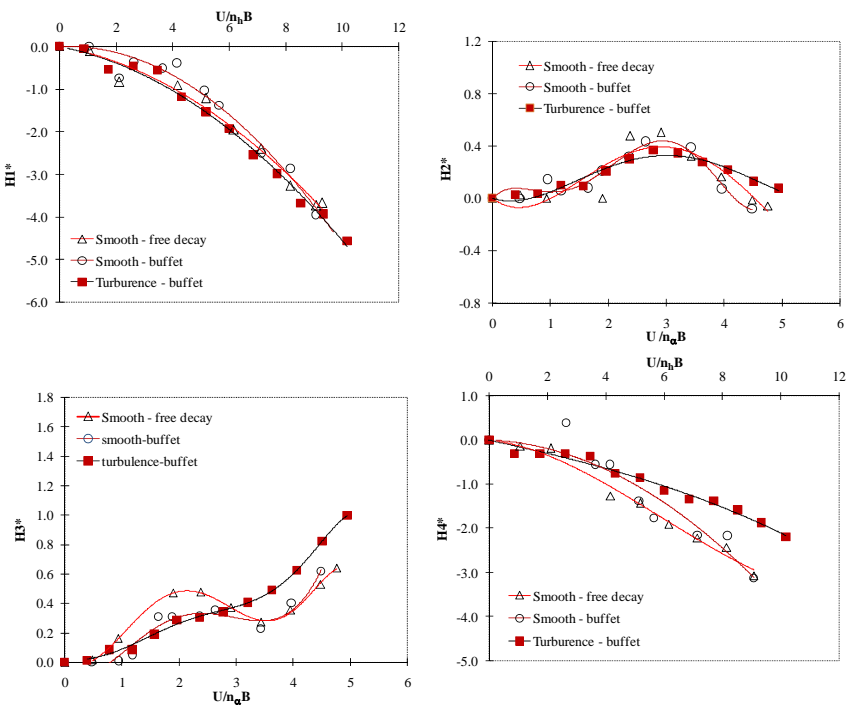


Fig. 13 Flutter derivatives (H_i^*) of the IRR Bridge by free decay and buffeting responses under smooth and turbulence flows.

4.3.1 Comparisons of test method: Smooth flow

Figures 13 and 14 present the identified flutter derivatives of the bridge deck from the free decay and buffeting tests under smooth flows, and from the buffeting tests under turbulent flows. The term "buffeting test under smooth flow", though not theoretically precise, is weakly implied by considering the existence of very small turbulence (<0.05%) in the smooth flow. The flutter derivatives were calculated using Eq. (23) and reported in the form of Eq. (2) but without the factor 1/2.

Generally, the flutter derivatives of the bridge identified by the SSI method from both the free decay and buffeting tests in smooth flow are in good agreement. The difference of A_4^* identified from both tests, seems to be negligible, as the effect of this derivative is usually considered to be less significant. For smooth flows, the most important derivative A_2^* has increased steadily (more negative) up to the reduced wind velocity around 3, and then started to decrease. This sign reversal is the primary factor toward the SDOF-torsional instability ("stall flutter") for bluff type sections.

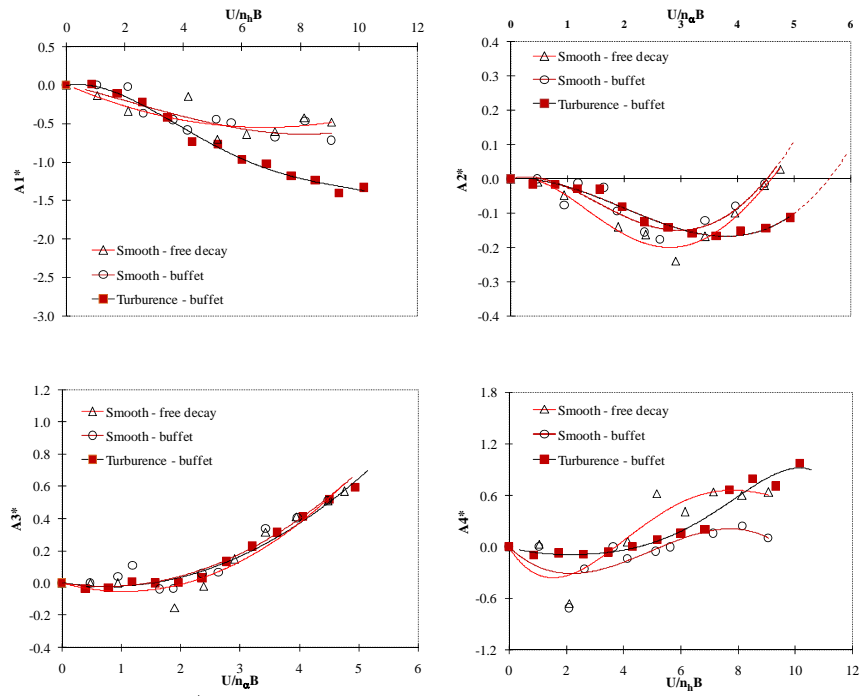


Fig. 14 Flutter derivatives (A_i^*) of the IRR Bridge by free decay and buffeting responses under smooth and turbulence flows.

In Figs. 15 and 16, the root-mean-square (RMS) torsional and vertical buffeting responses of the IRR bridge model were plotted against the reduced wind velocity. Under smooth flow, the sharp abrupt transition with increasing velocity from virtually zero torsional response to clear instability occurs in the neighborhood of reduced velocity of 4.5 (see Fig. 16). Figure 17 shows the responses of the IRR bridge model at the onset of flutter instability. As is evident from the response Fourier spectrum in Fig. 18, the IRR bridge model exhibits the SDOF-torsional instability. The abrupt change in the vertical response at high wind speed is due to the effect of cross derivatives H_2^* and H_3^* which causes the coupling of the torsional responses with the vertical responses in terms of damping and stiffness, respectively².

4.3.2 Effect of turbulence

Most of the real bridges are submerged in turbulent winds. Therefore, a detailed investigation of the effects of turbulence on the flutter derivatives is necessary. Almost all the wind tunnel tests for flutter derivatives have been carried out in smooth flow. Although some researchers have studied the problem using the wind tunnel tests, 7,17 in general, the results are still debatable and inconclusive. For instance, for streamlined sections, the wind tunnel tests showed little effect, 7,17 while the tests conducted on a rectangular box girder bridge showed galloping in smooth flow. 18

Figures 15 and 16 show the responses of the IRR Bridge model under the smooth and turbulence flows. The turbulence flow reduces the vortex-shedding response, compared with the smooth flow, but it raises the amplitude of bridge responses progressively over the speed range. However, no clear and uniquely definable "flutter instability" can be identified from the test results. From Figs. 13 and 14, it is found that the influence of flow types on H_4^* and A_3^* , i.e. flutter derivatives related to direct aerodynamic stiffness, is generally negligible. Though,

the value of H_4^* from the turbulence flow is somewhat less than that in the smooth flow case, it affects the frequency value only up to the second decimal digit. The flow type influence is also negligible for H_1^* and H_2^* , i.e., the direct and cross derivatives related to the vertical and torsional aerodynamic damping, respectively. On the other hand, the more important derivatives A_1^* A_2^* and H_3^* show rather noticeable deviations from those in smooth flow, especially at high reduced wind speeds. The most important effect is that the reduced wind speed corresponding to the reversed sign of the torsional aerodynamic damping A_2^* increased in the turbulent flow. This means that turbulence tends to make bridges aerodynamically more stable by delaying the torsional flutter.

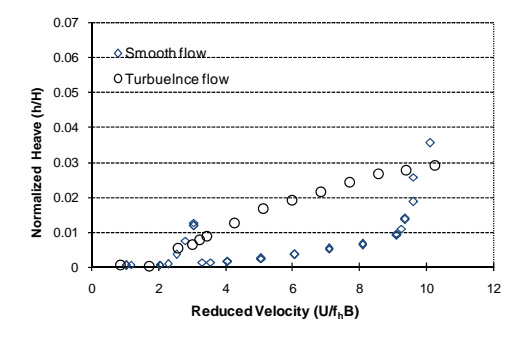
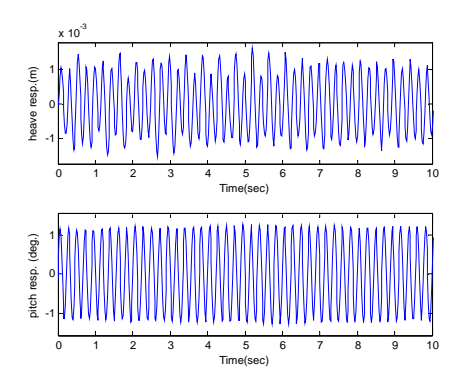


Fig. 15. Vertical RMS responses of IRR bridge model under smooth and turbulence flows.

Fig. 16. Torsional RMS responses of IRR bridge model under smooth and turbulence flows.



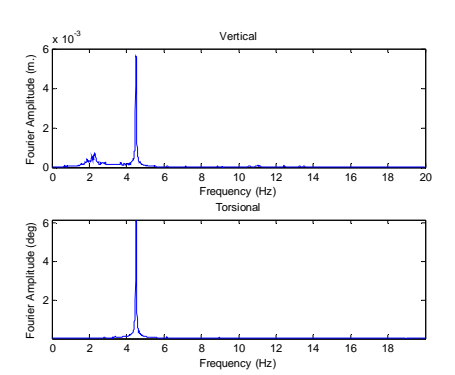


Fig. 17. Heave and pitch responses of IRR bridge model under smooth flow at flutter wind speed.

Fig. 18. Fourier spectrum of heave (vertical) and pitch (torsional) responses of IRR bridge model at flutter wind speed.

The deviations of flutter derivatives may reveal the fact that for those bridges with bluff type sections similar to the IRR Bridge, the effects of turbulence can be significant. Hence, the wind tunnel tests of such bridges for flutter derivative estimation should be carried out in turbulent flow as well.

5. Conclusions

A theoretical model based on the covariance-driven SSI technique was proposed to extract the flutter derivatives of bridge deck sectional models from two-degree-of-freedom free decay and buffeting responses under both the smooth and turbulent winds. An advantage of the adopted SSI-COV technique is that it considers the buffeting forces and responses as inputs, instead of as noises as typically assumed. The conclusions of this study are as follows:

- Numerical simulations of bridge deck responses confirmed that the SSI-COV technique can
 be used to estimate the flutter derivatives from the buffeting and free decay responses with
 reliable results. This shows the applicability of the SSI-COV method with various test
 techniques, though it was originally developed from a stochastic model.
- 2) For the thin plate model under smooth flow, wind tunnel tests showed that the flutter derivatives identified by the SSI technique from both the free decay and the buffeting tests match well with theoretical values. Although some variations exist in the values of the derivative A_4^* obtained from the buffeting test, this derivative is considered insignificant and has been neglected by most of the previous studies.
- 3) For the bluff section model of the IRR Bridge under smooth flow, the flutter derivatives estimated from the buffeting test agreed with those from the free decay test. This result allowed us to focus on applying the SSI-COV technique to the buffeting test method. Variations exist in the values of the A_4^* derivative as obtained from the two test methods, but they agree in trend. We also observed the sign reversal of the A_2^* derivative as the reduced wind speed reached the value of 4.5. This indicates that this bridge section is susceptible to flutter instability at high wind speeds.
- 4) The test result of the blunt section model of the IRR Bridge in turbulence wind revealed the most important and positive effect for the turbulence in that it tends to make the bridge aerodynamically more stable by delaying the sign reversal of the aerodynamic damping A₂*. The implication is that for bridges with bluff type sections similar to the IRR Bridge, the effect of turbulence is significant, and should be included in the wind tunnel tests for estimating the flutter derivatives.

Applying the proposed SSI-COV technique to the buffeting test yields a straightforward, cost effective, and reliable system identification process that can be adopted to identify the flutter derivatives for various bridge decks. This technique also has some limitations. For example, it becomes more difficult to extract the flutter derivatives from the buffeting responses for the case when a relatively heavy model is excited at a very low reduced wind velocity, i.e., with low wind energy. For this case, using the SSI-COV technique with the free decay test will yield more accurate results than those with the buffeting test.

Acknowledgements

The authors would like to greatly acknowledge the Thailand Research Fund (TRF) for the financial support under the grant number RMU 4980012. In addition, the authors are greatly thankful to Mr. Worapoj Thamasungkeeti, graduate students of Thammast University, for his assistance in the wind tunnel tests.

References

- 1. Y.B. Yang, S.V. Mac and C.H. Chen, Multi-Mode Coupled Buffeting Analysis of Cable-Stayed Bridges, *Int. J. Struct. Stability & Dyn.*, **1** (3) (2001), pp. 429-453.
- 2. V. Boonyapinyo, T. Miyata and H. Yamada, Advanced Aerodynamic Analysis of Suspension Bridges by State Space Approach, *J. Str. Eng.*, ASCE, **125**(12), 1357-1366.
- 3. G. T. Michaltsos, I. G. Rafttoyiannis and T. G. Konstantakopoulos, Dynamic Stability of Cable-Stayed Bridge Pylons, *Int. J. Struct. Stability & Dyn.*, **8** (4) (2008), pp. 627-643.
- 4. Z.Q. Chen and X.D. Yu, A New Method for Measuring Flutter Self-Excited Forces of Long-Span Bridges, *China Civil Engineering Journal*, **35** (2002), pp. 34–41.
- 5. R.H. Scanlan, Airfoil and Bridges Deck Flutter Derivatives, *J. of Eng. Mech*, ASCE, **97** (6) (1971), pp. 1717–1733.
- 6. N.K. Poulsen, A. Damsgaard, and T.A. Reinhold, Determination of Flutter Derivatives for the Great Belt Bridge, *J. Wind. Eng. Ind. Aerodyn.*, **57** (1992), pp. 295–305.
- 7. P.P. Sarkar, N. Jones, and R.H. Scanlan, Identification of Aeroelastic Parameters of Flexible Bridges, *J. of Eng. Mech.*, ASCE, **120** (8) 1994, pp.1718–1741.
- 8. M. Gu, R.X. Zhang and H. Xiang, Identification of Flutter Derivatives of Bridge Decks, *J Wind. Eng. Ind. Aerodyn.*, **84** (2000), pp.151–162.
- 9. J.N. Juang and R.S. Pappa, An Eigensystem Realization Algorithm for Modal Parameter Identification and Model Reduction, *Journal of Guidance, Control, and Dynamics*, **85** (1985), pp. 620–627.
- 10. P.V. Overschee, Subspace Algorithms for the Stochastic Identification Problem, *Proc.*, *30th Conference on Decision and Control*, Brighton, England (1991), pp. 1321–1326.
- 11. B. Peeters, Reference-based Stochastic Subspace Identification for Out-put only Modal Analysis, *Mechanical Systems and Signal Processing*, **13** (6) (1999), pp.855–878.
- 12. M. Gu and X.R Qin, Direct Identification of Flutter Derivatives and Aerodynamic Admittances of Bridge Decks, *Eng. Strucs*, **26** (2004), pp. 2161–2172.
- 13. R.H. Scanlan, Motion of Suspended Bridge Spans under Gusty Wind, *J. of Struc. Div.*, ASCE, **103**(9) (1977), pp.1867–83.
- 14. E. Simiu and R.H. Scanlan, *Wind effects on structures, 3rd Ed.*, John Wiley, New Jersey. (1996).
- 15. J.B. Jakobsen and E. Hjorth-Hansen, Determination of the Aerodynamic Derivatives by a System Identification Method, *J. Wind. Eng. Ind. Aerodyn.*, **57** (1995), pp.295–305.
- 16. C. Dyrbye and S.O. Hansen, Wind loads on structures, John Wiley, New Jersey (1996).
- 17. R.H. Scanlan, W.H. Lin, 1978. Effects of Turbulence on Bridge Flutter Derivatives, *J. of Eng. Mech*, ASCE, **104** (4): 719–733.
- 18. J.B. Jakobsen and E. Hjorth-Hansen, Aeroelasticic Effects on a Rectangular Box-Girder Bridge. *J. Wind. Eng. Ind. Aerodyn.*, **74-76** (1998), pp.819–827.
- 19. E. Strømmen, (2006), Theory of Bridge Aerodynamics, First edition, New York, Springer.

Paper submitted for possible publication in Journal of Wind Engineering and Industrial Aerodynamics

ELSEVIER

Data-Driven Stochastic Subspace Identification of Flutter Derivatives of Bridge Decks

Virote Boonyapinyo a*, Tharach Janesupasaeree b

Abstract: Most of the previous studies on flutter derivatives have used the deterministic system identification techniques, in which the buffeting forces and the responses are considered as noises. In this paper, one of the most advanced stochastic system identification, the data-driven stochastic subspace identification technique (SSI-DATA) was proposed to extract the flutter derivatives of bridge decks from the buffeting test results. An advantage of this method is that it considers the buffeting forces and the responses as inputs rather than as noises. Numerical simulations and wind tunnel tests of a streamlined thin plate model conducted under a smooth flow by the free decay and the buffeting tests were used to validate the applicability of the SSI-DATA method. The results were compared with those from the popular covariance-driven SSI method. Wind tunnel tests of a two-edge girder blunt type of Industrial-Ring-Road Bridge deck (IRR) were then conducted under both smooth and turbulence flows. The identified flutter derivatives of the thin plate model based on the SSI-DATA technique agree well with those obtained theoretically. The results from the thin plate and the IRR Bridge deck helped validate the reliability and applicability of the SSI-DATA technique to various experimental methods and wind flow conditions. The results for the two-edge girder blunt type section show that applying the SSI-DATA yields better results than those of the SSI-COV. The results also indicate that the turbulence tends to delay the onset of flutter compared with the smooth flow case.

Keywords: Flutter derivatives; data-driven stochastic subspace identification; wind tunnel test; bridge decks; turbulent flow

1. Introduction

Long-span cable-supported bridges are highly susceptible to wind excitations because of their inherent flexibility and low structural damping. Wind loads play an important role in the design of these structures. The actions of wind load are broadly divided into aerostatic and aerodynamic loads. Effects of aerostatic wind load are given by Boonyapinyo et al. (1994, 2006), among others. The wind-induced aerodynamic force can be divided into two parts: a buffeting force that depends on the turbulence of the incoming flow, and an aeroelastic force that originates from the interactions between the airflow and the bridge motion. The motion-dependent forces feed back into the dynamics of the bridge as aerodynamic damping and stiffness; the effect is termed 'aeroelasticity' and is commonly described via 'flutter derivatives'. The problems of aerodynamic stability including vortex-induced vibrations, galloping, flutter, and buffeting, may have serious effects on the safety and the serviceability of the bridges. Among these, flutter is the most serious wind-induced vibration of bridges and may destroy the bridges due to the diverging motions in either single or torsion-bending coupled mode. Notorious examples of the flutter phenomenon are the failures of the Brighton Chain Pier Bridge in 1836 and the original Tacoma Narrow Bridge in 1940. The flutter derivatives depend primarily upon the wind conditions, the cross-sectional shape and the dynamic characteristics of the bridges. Nevertheless, no theoretical values exist for these derivatives for various bridge shapes except only for a simple thin plate section. A major research tool in

1

^a Department of Civil Engineering, Thammasat University, Rangsit Campus, Pathumthani 12120, Thailand ^b Toyo-Thai Corporation Public Company Limited, 28th Serm-Mitr Tower, Bangkok 10110, Thailand

Corresponding author. Tel.: +66 2 5643001 ext. 3111 E-mail address: bvirote@engr.tu.ac.th (V. Boonyapinyo)

these studies is, therefore, a wind tunnel test, in which a geometrically and aerodynamically representative scale model of a length of a bridge deck is built, mounted, and then tested in a wind tunnel. The flutter derivatives are non-dimensional functions of the wind speed, the geometry of bridge, and the frequency of vibrations; therefore they can be applied directly to the full-scale bridge in a piecewise manner.

The experimental methods used for a determination of flutter derivatives can be grouped under two types, i.e. forced (Chen & Yu, 2002) and free vibration methods (Scanlan and Tomko, 1971; Poulsen et al., 1992; Sarkar et al., 1994; Gu et al., 2000). Having less emphasis on elaborate equipments required, time, and the amount of work involved; the free vibration method seems to be more tractable than the forced method. In the determination of flutter derivatives by the free vibration method, the system identification method is the most important part required to extract these parameters from the response output of the section model. The free vibration method depends on the system identification techniques and can be classified into two types, i.e. the free decay and the buffeting tests. In the free decay test method, the bridge deck is given initial vertical and torsional displacements. The flutter derivatives are based on the transient (i.e. free decay) behavior that occurs when the bridge deck is released. The buffeting test, on the other hand, uses only the steady random responses (i.e. buffeting responses) of bridge deck under wind flow without any initial displacement given to the model. Compared with the free decay method, the buffeting test is simpler in the test methodology, is more cost effective, and is more closely related to the real bridge behaviors under wind flow, but with a disadvantage that the outputs appear random-like. This makes the parameters extraction more difficult and a more advanced system identification technique is required.

In most of the previous studies, flutter derivatives were estimated by the deterministic system identification techniques that can be applied to the free decay method only. Examples of the previous deterministic system identification techniques that were applied to the free decay method included the Scanlan's method (Scanlan & Tomko, 1971), the Poulsen's method (Poulsen et al., 1992), the Modified Ibrahim Time Domain method (MITD) (Sarkar et al., 1994), the Unified Least Square method (ULS) (Gu et al., 2000), and the Iterative Least Square method (ILS) (Chowdhurry and Sarkar, 2003). In these system identification techniques, the buffeting forces and their responses are regarded as external noises. the identification process then requires many iterations. It also confronted with difficulties at high wind speeds where the initial free decay is drowned by buffeting responses. Besides, at high reduced wind speed, the vertical bending motion of the structure will decay rapidly due to the effect of the vertical aerodynamic damping, and thus the length of decaying time history available for system identifications will decrease. This causes more difficulties to the deterministic system identification techniques (Gu and Qin, 2004). In the case of turbulence flow, the presence of the turbulence in the flow is equivalent to a more noisy-input signal to the deterministic system identification. This made the extraction process more complicated and most likely reduced the accuracy of the flutter derivatives identified (Sarkar et al., 1994). In addition, due to the test technique, the free decay method is impractical to determine flutter derivatives of real bridges in the field.

On the other hand, the buffeting test uses random responses data of bridge motion from wind turbulence only. This mechanism is more closely related to a real bridge under wind flow and is applicable to real prototype bridges. The buffeting method costs less and is simpler than the free decay method since no operator interrupts in exciting the model. However, as wind is the only excited source, it results in low signal-to-noise ratio, especially at low velocity, and therefore a very effective system identification technique is required. None of the aforementioned system identification techniques is applicable to the buffeting responses tests. System identification techniques can be divided into two groups, i.e. deterministic and stochastic.

If the stochastic system identification technique (Juang and Pappa, 1985; Overschee, 1991; Peeters, 1999) is employed to estimate the flutter derivatives of a bridge deck from their steady random responses under the action of turbulent wind, the above-mentioned shortcomings of the deterministic system identification technique can be overcome. The reason is that the random aerodynamic loads are regarded as inputs rather than noises, which are more coincident with the fact. Therefore, the signal-to-noise ratio

is not affected by the wind speed, and the flutter derivatives at high reduced wind speeds are more readily available. These aspects give the stochastic system identification methods an advantage over the deterministic system identification.

Many stochastic system identification methods have been developed during the past decades, among which the stochastic subspace identification (SSI in short) (Overschee, 1991; Peeters, 1999) has proven to be a method that is very appropriate for civil engineering. The merit points of SSI are: (1) the assumptions of inputs are congruent with practical wind-induced aerodynamic forces, i.e. stationary and independent on the outputs; (2) identified modes are given in frequency stabilization diagram, from which the operator can easily distinguish structural modes from the computational ones; (3) since the maximum order of the model is changeable for the operator, a relatively large model order will give an exit for noise, which in some cases can dramatically improve the quality of the identified modal parameters; (4) mode shapes are simultaneously available with the poles, without requiring a second step to identify them. There are two kinds of SSI methods, one is data-driven, and the other is covariance-driven.

The similarity of the covariance- and the data-driven SSI methods is that they both are aimed to cancel out the (uncorrelated) noise using stochastic realization. In the SSI-COV algorithm, the raw time histories are converted to the covariances of the Toeplitz matrix. The implementation of SSI-COV consists of estimating the covariances, computing the singular value decomposition (SVD) of the Toeplitz matrix, truncate the SVD to the model order n, estimating the observability and the controllability matrices by splitting the SVD into two parts and finally estimating the system matrices (A, C). The modal parameters are then found from A and C. Gu and Qin (2004) applied the SSI-COV to extract six derivatives ($H_1^* \sim H_3^*$, $A_1^* \sim A_3^*$). Mishra et at. (2006) used the SSI-COV to extract 18 flutter derivatives from wind tunnel tests, but the identified flutter derivatives seem to be scattered.

As opposed to SSI-COV, the data-driven stochastic subspace identification (SSI-DATA) avoids the computation of covariances between the outputs; since the error and noises may be squared up from the covariance estimation (Golub and Van Loan, 1996). It is replaced by projecting the row space of the future outputs into the row space of the past outputs. This projection is computed in favor from the numerically robust square root algorithm, i.e. *QR* factorization. Theoretically, the numerical behavior of SSI-DATA should then be better than that of SSI-COV (Peeters and De Roeck, 2001). However, very few researchers, if any, have applied the SSI-DATA for identification of the flutter derivatives of bridge decks.

In this paper, the data-driven stochastic subspace identification method is proposed to estimate the flutter derivatives from random responses (buffeting) under the action of smooth and turbulent wind. Tests are also carried out with the free decay method (single and two-degree-of-freedom) in order to examine the robustness of the present technique that the results are not affected by test methods used. To validate the applicability of the present technique, numerical simulations were firstly performed. Then, sectional-model tests of a quasi-streamlined thin plate model, which is the only section that theoretical flutter derivatives exist, were performed under smooth flow. Encouraged by the success in the evaluation process, the flutter derivatives of a real bridge were determined. The two-edge-girder type blunt section model of Industrial-Ring-Road Bridge (IRR in short), a cable-supported bridge with a main span of 398 m in Samutprakan province of Thailand, was tested both in the smooth and the turbulence flows. Tests were conducted in TU-AIT Boundary Layer Wind Tunnel in Thammasat University, the longest and the largest wind tunnel in Thailand.

2. Theoretical formulation of data-driven stochastic subspace identification.

2.1 Flutter and buffeting forces

The dynamical behaviors of a bridge deck with two degrees-of-freedom (DOF in short), i.e. h (bending) and α (torsion), in turbulent flow can be described by the following differential equations (Scanlan, 1977)

$$m\left[\ddot{h}(t) + 2\xi_{h}\omega_{h}\dot{h}(t) + \omega_{h}^{2}h(t)\right] = L_{se}(t) + L_{b}(t)$$

$$I\left[\ddot{\alpha}(t) + 2\xi_{\alpha}\omega_{\alpha}\dot{\alpha}(t) + \omega_{\alpha}^{2}\alpha(t)\right] = M_{se}(t) + M_{b}(t)$$
(1)

where m and I are the mass and the mass moment of inertia of the deck per unit span, respectively; φ_i is the natural circular frequency; ξ_i is the modal damping ratio ($i=h,\alpha$); L_{se} and M_{se} are the self-excited lift and moment, respectively; while L_b and M_b are the aerodynamic lift and moment. The self-excited lift and moment are given as follows (Simiu and Scanlan, 1996).

$$L_{se} = \frac{1}{2} \rho U^{2} B \left[K_{h} H_{1}^{*}(K_{h}) \frac{\dot{h}}{U} + K_{\alpha} H_{2}^{*}(K_{\alpha}) \frac{B\dot{\alpha}}{U} + K_{\alpha}^{2} H_{3}^{*}(K_{\alpha}) \alpha + K_{h}^{2} H_{4}^{*}(K_{h}) \frac{h}{B} \right]$$

$$M_{se} = \frac{1}{2} \rho U^{2} B^{2} \left[K_{h} A_{1}^{*}(K_{h}) \frac{\dot{h}}{U} + K_{\alpha} A_{2}^{*}(K_{\alpha}) \frac{B\dot{\alpha}}{U} + K_{\alpha}^{2} A_{3}^{*}(K_{\alpha}) \alpha + K_{h}^{2} A_{4}^{*}(K_{h}) \frac{h}{B} \right]$$
(2)

where ρ is the air mass density; B is the width of the bridge deck; U is the mean wind speed at the bridge deck level; $K_i = \omega_i B/U$ is the reduced frequency $(i=h,\alpha)$; and H_i^* and A_i^* (i=1,2,3,4) are the so-called flutter derivatives, which can be regarded as the implicit functions of the deck's modal parameters. An alternate form of the self-excited forces is as in Eq. (2) but without the factor 1/2 (Poulsen et al., 1992).

The aerodynamic lift and moment can be defined as (Scanlan, 1977)

$$L_{b}(t) = \frac{1}{2} \rho U^{2} B \left[2C_{L} \frac{u(t)}{U} \chi_{L}(t) + (C'_{L} + C_{D}) \frac{w(t)}{U} \chi_{L}(t) \right],$$

$$M_{b}(t) = \frac{1}{2} \rho U^{2} B^{2} \left[2C_{M} \frac{u(t)}{U} \chi_{M}(t) + (C'_{M}) \frac{w(t)}{U} \chi_{M}(t) \right],$$
(3)

where C_L , C_D and C_M are the steady aerodynamic force coefficients; C'_L and C'_M are the derivatives of C_L and C_M with respect to the attack angles, respectively; u(t) and w(t) are the longitudinal and vertical fluctuations of the wind speed, respectively; χ_L and χ_M are the lift and moment aerodynamic admittances of the bridge deck.

By moving L_{se} and M_{se} to the left side, and merging the congeners into column vectors or matrices, Eq. (1) can be rewritten as follows

$$[M]\{\ddot{y}(t)\}+[C^e]\{\dot{y}(t)\}+[K^e]\{y(t)\}=\{f(t)\}$$
(4)

where $\{y(t)\} = \{h(t) \ \alpha(t)\}^{T}$ is the generalized buffeting response; $\{f(t)\} = \{L_b(t) \ M_b(t)\}^{T}$ is the generalized aerodynamic force; [M] is the mass matrix; $[C^e]$ is the gross damping matrix, i.e. the sum of the mechanical and the aerodynamic damping matrices; and $[K^e]$ is the gross stiffness matrix.

2.2 Stochastic state space models

The fluctuations of the wind speed u(t) and w(t) in Eq. (3) are random functions of time, so the identification of flutter derivatives of bridge decks can be simplified as a typical inverse problem in the theory of random vibration, and thus can be solved by the stochastic system identification techniques. Let

$$\begin{bmatrix} A_c \end{bmatrix} = \begin{bmatrix} O & I \\ -M^{-1}K^e & -M^{-1}C^e \end{bmatrix}$$

$$\begin{bmatrix} C_c \end{bmatrix} = \begin{bmatrix} I & O \end{bmatrix}$$
(5)

and

$$\{x\} = \begin{cases} y \\ \dot{y} \end{cases} \tag{6}$$

then Eq. (4) is transformed into the following stochastic state equations

$$\begin{aligned} & \{\dot{x}\} = [A_c] \{x\} + \{w\} \\ & \{y\} = [C_c] \{x\} + \{v\} \end{aligned}$$
 (7)

The discrete form of Eq. (7) can be written as

$$\{x_{k+1}\} = [A]\{x_k\} + \{w_k\}$$

$$\{y_k\} = [C]\{x_k\} + \{v_k\}$$
(8)

where $[A_c]_{4\times4}$, $[C_c]_{2\times4}$ and $\{x\}$ are known as state matrix, output shape matrix and state vector, respectively; $\{w_k\}$ and $\{v_k\}$ are the input and output noise sequences, respectively. Subscript *k denotes the value of * at time $k\Delta t$, where Δt means the sampling interval. 0 and I are the zero and identity matrices, respectively.

It is an assumption of the stochastic model that $\{x_k\}$, $\{w_k\}$ and $\{v_k\}$ in Eq. (8) are mutually independent and hence

$$E[x_k w_k^{\mathrm{T}}] = \mathbf{0} , E[x_k v_k^{\mathrm{T}}] = \mathbf{0}$$
 (9)

The output covariance matrix of lag i, Λ_i , and the "next state-output" covariance matrix G are defined as:

$$\Sigma = E[x_k x_k^{\mathrm{T}}] \qquad Q = E[w_k w_k^{\mathrm{T}}]$$

$$\Lambda_i = E[y_{k+i} y_k^{\mathrm{T}}] \qquad R = E[v_k v_k^{\mathrm{T}}]$$

$$G = E[x_{k+i} y_k^{\mathrm{T}}] \qquad S = E[w_k v_k^{\mathrm{T}}]$$

$$(10)$$

By combining Eqs. (9) and (10), we obtain the following Lyapunov equations for the state and output covariance matrices

$$\Sigma = A\Sigma A^{T} + Q$$

$$\Lambda_{0} = C\Sigma C^{T} + R$$

$$G = A\Sigma C^{T} + S$$
(11)

From (8) and (9), it can be deduced

$$\Lambda_{1} = E[\{y_{k+1}\}\{y_{k}\}] = CG$$

$$\Lambda_{i} = E[\{y_{k+i}\}\{y_{k}\}] = CA^{i-1}G$$
(12)

2.3 Data-driven stochastic subspace identification

The main algorithm of the data-driven stochastic subspace identification (SSI DATA) proceeds with projecting the row space of the future outputs, Y_f , into the row space of the past outputs, Y_p . This projection is noted and defined as (Overschee and Moor, 1996):

$$\Pi_{i} = Y_{f} / Y_{p} = Y_{f} . Y_{p}^{T} . (Y_{p} Y_{p}^{T})^{\dagger} . Y_{p}$$
(13)

where $(\bullet)^{\dagger}$ represents the pseudo-inverse of a matrix. The idea behind this projection is that it retains all the information in the past that is useful to predict the future. The matrices $Y_f, Y_p \in \mathbb{R}^{lixj}$ are partitions matrices of the output data block Hankel matrix, H, defined as:

$$H = \frac{1}{\sqrt{j}} \begin{pmatrix} y_0 & y_1 & \cdots & y_{j-1} \\ \cdots & \cdots & \cdots & \cdots \\ y_{i-1} & y_i & \cdots & y_{i+j-2} \\ y_i & y_{i+1} & \cdots & y_{i+j-1} \\ y_{i+2} & y_{i+3} & \cdots & y_{i+j+1} \\ \cdots & \cdots & \cdots & \cdots \\ y_{2i-1} & y_{2i} & \cdots & y_{2i+j-2} \end{pmatrix} = \begin{pmatrix} Y_{0|i} \\ Y_{i+1|2i-1} \end{pmatrix} = \begin{pmatrix} Y_p \\ Y_f \end{pmatrix} \updownarrow l(i)$$

$$(14)$$

where l is the number outputs. The main theorem of the stochastic subspace identification states that the projection Π_i can be factorized as the observability matrix O_i and the Kalman filter state sequence \hat{X}_i (Peeters and De Roeck, 2001):

$$\Pi_{i} = O_{\hat{i}} \hat{X}_{\hat{i}} = \begin{pmatrix} C \\ CA \\ \dots \\ CA^{i-1} \end{pmatrix} (\hat{x}_{i} \ \hat{x}_{i+1} \ \dots \ \hat{x}_{i+j-1}) \updownarrow n$$

$$\longleftrightarrow n$$
(15)

Both factors of Eq.(15), O_i and \hat{X}_i , are obtained by applying the singular value decomposition (SVD) to the projection matrix:

$$\Pi_{i} = USV^{T} = (U_{1} \ U_{2}) \begin{pmatrix} S_{1} & 0 \\ 0 & 0 \end{pmatrix} \begin{pmatrix} V_{1}^{T} \\ V_{2}^{T} \end{pmatrix} \approx U_{1}S_{1}V_{1}^{T}$$
(16)

Combining Eq. (15) and (16) gives:

$$O_i = U_1 S_1^{1/2} T$$
, $\hat{X}_i = O_i^{\dagger} \Pi_i$ (17)

where U, S and V are orthonormal matrices. S is a diagonal matrix containing positive singular values in descending order. The number of nonzero singular values indicates the rank of the matrix (the order of system). The reduced diagonal matrix S_1 is obtained by omitting the zero singular values from the matrix S. Matrices U_1 and V_1 are obtained by omitting the corresponding columns and rows from the matrices U and V respectively. Up to now we found the order of the system N (as the number of non-zero singular values in Eq.(16)), O_i and \hat{X}_i . In practice however, the effect of "noise" leads to singular values that are all different from zero. Actually, some of singular values associated with the noise modals are small, or very small. Generally, the model order can be determined by looking at a "gap" between two successive singular values. The singular value where the maximal gap occurs yields the model order. To obtain a good model for modal analysis applications, it is probably a better idea to construct a stabilization diagram (Peeters and De Roeck, 2001), by identifying a whole set of models with different order. If the separation between the past and future outputs is shifted one block row down in Eq.(14), another projection can be defined as:

$$\Pi_{i-1} = Y_f^{-} / Y_p^{+} = Y_{i+||2i-1|} / Y_{0|i} = O_{i-1} \hat{X}_{i+1}$$
(18)

where the last equation is similar to the main theorem (Eq.15). O_{i-1} is obtained after deleting the last l rows of O_i computed as in Eq. (17).

$$O_{i-1} = O_i(1:l(i-1)) (19)$$

Now the shifted state sequence \hat{X}_{i+1} can be calculated from:

$$\hat{X}_{i+1} = O_{i-1}^{\ \ \dagger} \Pi_{i-1} \tag{20}$$

At this moment the Kalman state sequences \hat{X}_i , \hat{X}_{i+1} are calculated using only the output data (Eqs. (17) and (20)). The system matrices can now be recovered from following the overdetermined set of linear equations. These can be obtained by extending Eq.(7).

$$\begin{pmatrix} \hat{X}_{i+1} \\ Y_{i|i} \end{pmatrix} = \begin{pmatrix} A \\ C \end{pmatrix} \hat{X}_i + \begin{pmatrix} W_i \\ V_i \end{pmatrix}$$
 (21)

where $Y_{i|i} \in \mathbb{R}^{l \times j}$ is a Hankel matrix with only one block row. Since the Kalman state sequences and the outputs are known and the Kalman filter residuals W_i , V_i are uncorrelated with \hat{X}_i , the set of equations can be solved for A, C in a least square sense:

$$\begin{pmatrix} A \\ C \end{pmatrix} = \begin{pmatrix} \hat{X}_{i+1} \\ Y_{i|i} \end{pmatrix} \hat{X}_{i}^{\dagger} \tag{22}$$

Now the realizations of the system matrices (A, C) are achieved. Thus, the modal parameters can be determined by solving the eigenvalue problem of the state matrix A.

$$A = \Psi \Lambda \Psi^{-1} \quad , \quad \Phi = C \Psi \tag{23}$$

where Ψ is the complex eigenvector matrix, Φ is the mode shape matrix, and Λ is a diagonal matrix composed of the complex poles of the system. According to Eqs. (16)-(23), a different combination of i, j and n will give a different state matrix, and thus a different pair of modal parameters. The order n are determined by inspecting the singular values in S and obtain $U_I = U_n$ and $S_I = S_n$. Therefore, modal parameters should be derived from a series of combinations, rather than a single combination. In the process of identification, n or i should be given in series for certain values of j in order to obtain a frequency stability chart.

Once the modal parameters are identified, the gross damping matrix C^e and the gross stiffness matrix K^e in Eq. (4) can be readily determined by the pseudo-inverse method

$$[K^e \ C^e] = -M[\Phi \Lambda^2 \ \Phi^* (\Lambda^*)^2] \begin{bmatrix} \Phi & \Phi^* \\ \Phi \Lambda & \Phi^* \Lambda^* \end{bmatrix}^{\dagger}$$
(24)

Let
$$\overline{C}^e = M^{-1}C^e, \quad \overline{K}^e = M^{-1}K^e$$

$$\overline{C} = M^{-1}C^0, \quad \overline{K} = M^{-1}K^0$$
(25)

where C^0 and K^0 are the 'inherent' damping and stiffness matrices, respectively. Thus, the flutter derivatives can be extracted from the following equations

$$H_{1}^{*}(k_{h}) = -\frac{2m}{\rho B^{2} \omega_{h}} (\overline{C}_{11}^{e} - \overline{C}_{11}), \quad A_{1}^{*}(k_{h}) = -\frac{2I}{\rho B^{3} \omega_{h}} (\overline{C}_{21}^{e} - \overline{C}_{21})$$

$$H_{2}^{*}(k_{\alpha}) = -\frac{2m}{\rho B^{3} \omega_{\alpha}} (\overline{C}_{12}^{e} - \overline{C}_{12}), \quad A_{2}^{*}(k_{\alpha}) = -\frac{2I}{\rho B^{4} \omega_{\alpha}} (\overline{C}_{22}^{e} - \overline{C}_{22})$$

$$H_{3}^{*}(k_{\alpha}) = -\frac{2m}{\rho B^{3} \omega_{\alpha}^{2}} (\overline{K}_{12}^{e} - \overline{K}_{12}), \quad A_{3}^{*}(k_{\alpha}) = -\frac{2I}{\rho B^{4} \omega_{\alpha}^{2}} (\overline{K}_{22}^{e} - \overline{K}_{22})$$

$$H_{4}^{*}(k_{h}) = -\frac{2m}{\rho B^{3} \omega_{h}^{2}} (\overline{K}_{11}^{e} - \overline{K}_{11}), \quad A_{4}^{*}(k_{h}) = -\frac{2I}{\rho B^{4} \omega_{h}^{2}} (\overline{K}_{21}^{e} - \overline{K}_{21})$$

$$(26)$$

2.4 Implementation issues

Very important in the implementation of the data-driven subspace algorithms in general is the *QR*-factorization of the data Hankel matrices. Such a factorization applied to the Hankel matrix of Eq. (14) yields:

$$H = \left(\frac{Y_p}{Y_f}\right) = \left(\frac{Y_p^+}{Y_f^-}\right) = RQ^T \tag{27}$$

where $Q \in \mathbb{R}^{j \times j}$ is an orthonormal matrix: $Q^T Q = Q Q^T = I_j$ and $R \in \mathbb{R}^{2li \times j}$ is a lower triangular matrix. Since 2li < j, it is possible to omit the zeros in R and the corresponding rows in Q^T :

$$li \qquad l \qquad l(i-1) \qquad j \to \infty$$

$$\leftrightarrow \qquad \leftrightarrow \qquad \leftrightarrow \qquad \leftrightarrow$$

$$= \begin{cases} li \\ R_{11} \qquad 0 \qquad 0 \\ R_{21} \qquad R_{22} \qquad 0 \\ R_{31} \qquad R_{32} \qquad R_{33} \end{cases} \begin{pmatrix} Q_1^T \\ Q_2^T \\ Q_3^T \\ l(i-1) \end{cases} \qquad (28)$$

The division in block rows and columns is made such that the submatrices in Eq. (14) can all be expressed in terms of the R and Q submatrices. It is easy to show that the QR factorization yields the following very simple expressions for the projections of the future row spaces into the past row spaces:

$$\Pi_{i} = \begin{pmatrix} R_{21} \\ R_{31} \end{pmatrix} Q_{1}^{T}, \quad \Pi_{i-1} = \begin{pmatrix} R_{31} & R_{32} \end{pmatrix} \begin{pmatrix} Q_{1}^{T} \\ Q_{2}^{T} \end{pmatrix} = \begin{pmatrix} Y_{p}^{+} \\ Y_{f}^{-} \end{pmatrix}$$
(29)

Also $Y_{i|i} \in \mathbb{R}^{l \times j}$, the output sequence that is present in the least-squares equations in A, C of Eq. (22), is easily written in terms of the RQ factors:

$$Y_{i|i} = \begin{pmatrix} R_{21} & R_{22} \end{pmatrix} \begin{pmatrix} Q_1^T \\ Q_2^T \end{pmatrix}$$
(30)

2.5 Constitution of projection matrices and selection of model order

Knowledge of a good model order (system order) is desired for modal analysis. First, the numbers of block rows i (which determine the maximum number of orders that can be calculated) have to be specified. The numbers of block row i in Π_i in Eq. (16) and model order n in Eq. (17) are depend on

user's choice. It is practically experience that it is better to over-specify the model order and to eliminate spurious numerical poles afterwards. The operation was carried out with the help of MATLAB. In each number of block row i selected, for construction of stability diagram, the poles corresponding to a certain model order are compared to the poles of a one-order-lower model. If the frequencies and the damping ratios differences are within preset limits, the pole is labeled as a stable one and the model order is determined. The modal frequency(ω_i) and damping ratio (ξ_i) corresponding to each pole can be obtained by

$$\omega_i = \sqrt{a_i^2 + b_i^2} \quad , \quad \xi_i = \frac{a_i}{\omega_i} \tag{31}$$

where a_i and b_i are real and imaginary parts of the continuous time poles, λ_i defined as

$$\lambda_i = \frac{\ln(\mu_i)}{\Lambda t} = a_i + jb_i \tag{32}$$

where $j=\sqrt{-1}$ and μ_i is the discrete time poles (eigenvalue), corresponding to the i th mode of Λ . The preset limits are normally 1% for frequencies and 5% for damping ratios. However depend on the quality of data, at high wind speed, 10% differences for damping ratio may be set (Sarkar et al., 1994). A brief description follows:

- 1. For a selected value of number of time history data recorded, N, select number of block row i, then maximum number of orders is specified. The projection matrix were determined for lags k = 1, 2, ..., i.
- 2. In each i, the projection matrix is formulated once as per Eq.(29). Models of different orders (n=2...i) were then obtained by including different number of singular values S_n in the computation of matrix A. Thus the modal parameters can be determined by solving eigenvalue of the state matrix A. The poles corresponding to a certain model order are compared to the poles of a one-order-lower model and the stable poles and system order are determined.
- 3. The frequencies and damping corresponding to the stable poles are reported as stable ones for selected value of *i*.
- 4. To asses if a suitable number of block rows is selected, step 1-3 are repeated with the varying of *i*, and the model order, stable poles, modal frequencies and damping for each *i* is reported. Theoretically, the number of block rows *i* is related to the precision of SSI method and generally shows asymptotic convergence.

Fig. 1 shows sample of the identified (stable) modal frequencies and damping coefficients of the two modes (vertical and torsion) as a function of i. The variability of the modal frequencies looks small but the modal damping coefficients are uncertain and illegitimate when a small number i is used. However, they show the asymptotic convergence after certain value of i. The number of block i, where the modal parameters are converged, is also affected by the sampling frequency. From Fig. 1, the convergent starts at number of block rows $i = 2f_s$, where f_s is sampling rate (Hz.) that usually taken as ten times higher of the highest expected modal frequency or higher (Sarkar et al., 1994).

2.6 Determination of System Matrices and Extraction of Flutter Derivatives

Once, the model order and the stable poles are identified from section 2.5, only the Ψ , Φ , and Λ matrices of the stable poles are used to obtain K and C matrices in Eq. (24) in order to eliminate noises.

The stable poles are regarded as true modes whereas the spurious poles are effects of noises. The flutter derivatives are then estimated by using Eq. (26).

3. Numerical simulation tests

In order to validate the applicability of the data-driven SSI technique in the flutter derivatives estimation of bridge decks, numerical simulations of signals from different test methods are first carried out. The numerical tests included two syntheses but well controlled cases: two uncoupled degrees of freedom and two coupled degrees of freedom (simulated response including the motion induced aeroelastic terms). Both cases are first excited in the transient (i.e. free decay) motion and then by a white noise loading process (buffeting). Measurement noises are also added by a white noise process with a standard deviation equal to 10% of the standard deviation of the original responses, in order to investigate the effect of the measurement noise. The parameters estimated by the SSI-DATA were also compared with those by the SSI-COV method.

3.1 Two uncoupled degrees of freedom; free decay

Free decay response time-series were obtained by direct calculations of the displacement values for N=4096 discrete time stations, with the 'sampling' interval $\Delta t = 0.02$ s (i.e. $f_s = 50$ Hz). Structural modal properties used in this simulation were chosen from the previously tested sectional model of the Great Belt Bridge (Jacobsen and Hjorth-Hansen, 1995). The modal matrices are given per unit length as:

$$C_0 = \begin{bmatrix} 0.3616 & 0 \\ 0 & 0.0072 \end{bmatrix}, \quad K_0 = \begin{bmatrix} 397.0573 & 0 \\ 0 & 24.7315 \end{bmatrix}, \quad M_0 = \begin{bmatrix} 2.6526 & 0 \\ 0 & 0.0189 \end{bmatrix}$$

i.e. $f_{h_0} = 1.9472\,\mathrm{Hz}$, $f_{\theta_0} = 5.7573\,\mathrm{Hz}$, $\xi_{h_0} = 0.0053$, $\xi_{\theta_0} = 0.0056$, where the damping ratios, ξ , are representatives for the range of small amplitudes. The damping ratios were then multiplied in turn with 5, 10, 20 and 40, in order to cover the values of the total damping (structural + aerodynamic) which could be presented in the vibration of the model section under wind flow. Values as high as $\xi = 0.2$ could be expected for the vertical degree of freedom under wind flow.

Frequencies and damping ratios that were estimated from the SSI-DATA and the SSI-COV are practically identical to the preset values (errors are less than 0.5% for the highest damping case). The system matrices are also excellent even for the short useful signal case with only a few cycles of vibration motion. In the case where 10%-measurement noise was added, the estimated parameters by both SSI methods were also in good agreements, though more distortion was found in the SSI-COV. The identified frequencies by the SSI-COV were changed at lesser than 0.8%. Damping ratios were changed at most by 2% except in the case of the lowest damping case which was 5.4%. The diagonal terms of the estimated system matrices (i.e. frequency and damping matrices) are also identical to the preset values. Estimates of the diagonal terms are distorted within 1% except only in the case with lowest damping case in which the values are within 2.82%. However, the standard deviations of the damping ratios from 20-simulation tests estimated by the SSI-COV are larger than that by the SSI-DATA which the values are 13.2% and 5.7%, respectively.

3.2 Simulated responses including the motion-induced forces

The next step in the simulation was a simulation test with full effective stiffness and damping matrices (i.e. coupled degrees of freedom) and with lift and moment forces of the white noise type, as assumed in the SSI-method. For the mean-wind speed of 10.26 m/s, and the aerodynamic derivatives assumed according to the values reported for a similar bridge cross-section (Jacobsen and Hjorth-Hansen, 1995), the effective structural matrices were pre-set at

$$C_e = \begin{bmatrix} 8.9308 & -0.0799 \\ 0.4345 & 0.0386 \end{bmatrix}, \quad K_e = \begin{bmatrix} 420.1002 & -59.1805 \\ 1.7552 & 19.6652 \end{bmatrix}, \quad M_0 = \begin{bmatrix} 2.6526 & 0 \\ 0 & 0.0189 \end{bmatrix}$$

The response time-series were simulated for both the free decay and the buffeting responses under turbulence wind with 10% turbulence intensity; then the measurement white noises were superimposed on the simulated response. The free decay response time-series were computed by the constant acceleration method and samples are as shown in Fig.2. The SSI-DATA and the SSI-COV methods, applied to these responses data, returned the modal parameters (i.e. frequency and damping ratio) that are practically identical to the preset values (error are less than 1%). Table 1 shows the deviation of identified system matrices from the pre-set values for the simulated free decay responses by both the SSI-COV and the SSI-DATA in case of with and without noise. The structural matrices identified by the SSI-DATA are agreed well with the preset values (see Table 1). Superimposing 10% measurement white noise on the simulated response results in insignificant changes to system matrices identified by the SSI-DATA. However, the effect of noises to the identified matrices is more pronounced in the case of the SSI-COV, especially in the coupling terms K_{21} , C_{12} .

The response time-series were also simulated for the case of the buffeting responses where wind turbulence is the only exciting source. The effective stiffness, K, and damping matrices, C, were taken as in the case of transients; examples of the response time-series are as shown in Fig. 3. Buffeting responses required longer data records (20,000 data points in the present study) as compared to those in the free decay case (4096 data points) in order to yield acceptable results. Tables 2 and 3 show the deviations of the identified modal parameters and system matrices from the pre-set values, respectively. In the noise-free case, estimates of the frequencies and damping ratios by both SSI methods agreed well with the preset values where precisions are within 0.5% and 1% for the SSI-DATA and 0.5% and 2% for the SSI-COV, respectively (see Table 2). Table 3 shows the deviation of the identified system matrices ([K], [C]) from the pre-set values by both the SSI-DATA and the SSI-COV methods. In the noise-free case, the system matrices identified by both SSI methods agreed well with the pre-set values. The most difference parameters are K_{21} (related to K_{21}) and K_{21} (related to K_{21}) identified by the SSI-COV which equal 3.99% and -6.76%, respectively.

In the case of 10%-measurement noise added, all parameters (frequencies, damping and system matrices) estimated by the SSI-DATA are still in good agreements with the pre-set values (see Table 2 and 3). On the other hand, these parameters that were estimated by the SSI-COV are more affected by noise. Fig. 4 shows frequencies and damping ratios estimated by both SSI methods from 100 simulations, where more scattered of estimated values from the SSI-COV are found, especially the vertical frequency and damping ratios. The differences of mean values for the vertical frequency and damping ratio from the pre-set value were 2.98% and 14.69%, respectively. Moreover, comparing with the SSI-DATA, the estimated system matrices by the SSI-COV are also more distorted by noise. The most deviated parameters are C_{21} , K_{21} and C_{11} which are related to H_2^* , A_4^* and H_1^* , respectively (see Table 3). It can be seen that the precision of the estimated parameters by the SSI-DATA are more reliable and more sustainable to noises as comparing to those from the SSI-COV.

4. Wind tunnel tests

To further evaluate the applicability of the data-driven stochastic subspace identification method in the flutter derivatives estimation of bridge decks, wind tunnel tests of a quasi-streamlined thin plate model and a two-edge girder type blunt bridge section model were performed.

4.1 Outline of wind tunnel tests

The wind tunnel tests were performed in the TU-AIT wind tunnel at Thammasat University. The working section of the wind tunnel has a width of 2.5 m, a height of 2.5 m and a length of 25.5 m. The required turbulent flow was generated by grids, as shown in Fig. 5. A hot-sphere and a hot-wire

anemometers were used to measure the mean wind speed of the flow and the fluctuations of the wind speed, respectively. The longitudinal and vertical turbulence intensities are both less than 0.05% in the case of smooth flow and both are about 5% and 8% in two levels of turbulence flows, respectively. The typical normal spectral densities of the longitudinal and vertical fluctuation components of 8%-turbulence flow are presented in Fig.7 and compared with both Von Karman and Kaimal spectrum (Strømmen, 2006).

The model was suspended by eight springs outside the wind tunnel (see Fig. 6). To simulate a bridge section model with 2DOFs, i.e. vertical bending and torsion, piano wires were used to prevent the motion of the model in longitudinal direction; this can be seen in Fig.8, i.e. the schematic diagram of the top view of the test setup. Two piezoelectric acceleration transducers were mounted at the mid-length of the model to capture the acceleration signals. The responses of the models were captured by the acceleration transducers, and then the vertical and torsional responses can be respectively obtained by

$$h = \frac{x_1 + x_2}{2}$$
, $\alpha = \frac{x_1 - x_2}{l}$ (33)

where x_1 and x_2 are the measurements of the acceleration transducers 1 and 2, respectively; l is the horizontal distance between transducers.

4.2 CASE 1: Thin plate model under smooth flow

A quasi-streamlined thin plate (see Fig. 9) was first selected for wind tunnel test under smooth flow. The width to height (thickness) ratio of the plate is about 22.5. Table 4 lists the main parameters of the model.

4.2.1 Comparisons of flutter derivatives between the free decay and the buffeting test methods under smooth flow

The extraction of flutter derivatives of the thin plate, using the SSI-DATA techniques, were performed on results from three types of tests, namely, a) single-degree-of-freedom (SDOF) motion tests (Scanlan and Tomko, 1971), b) free decay coupled-motion test (2DOFs), and c) buffeting coupled-motion test (2DOFs). The term "buffeting test under smooth flow", though not theoretically concise, is weakly implied by considering the existence of very small turbulence (<0.05%) in smooth flow. The flutter derivatives were also estimated using the SSI-COV techniques for comparing the results between the two SSI techniques. Typical test results showing responses from the thin plate model are in Figs. 10 and 11. The responses for the free decay and the buffeting tests were sampled at the rates of 1000 Hz and 200 Hz, respectively. The results were then removed trend and re-sampled at 250 Hz and 50 Hz, respectively. The data-driven and covariance-driven SSI techniques were applied to identify the modal parameters from these data, and a pseudo-inverse method was applied to estimate the stiffness and damping matrices. The flutter derivatives were estimated by Eq. (26) and reported in the form of Eq. (2).

Figs. 12 and 13 compare the flutter derivatives of the thin plate that were estimated by the SSI-DATA technique using the three test methods mentioned above and those identified by the SSI-COV method, as well as the Theodorsen's theoretical values (Dyrbye and Hansen, 1996). Unless otherwise noted, at any wind speed, the derivatives H_1^* , H_4^* , A_1^* , and A_4^* , which are associated with the vertical motion were calculated using the frequency n_h (lower). In addition, the derivatives H_2^* , H_3^* , A_2^* , and A_3^* which are associated with the torsional motion were calculated using the frequency n_α (higher).

The direct flutter derivatives H_1^* and H_4^* , as found from the single-degree-of-freedom vertical-motion tests, and A_2^* and A_3^* , as found from the single-degree-of-freedom torsional-motion tests, were also plotted and compared with those from the coupled-motion tests. The results are shown in Figs. 12 and 13. The near perfect match shows that the direct-flutter derivatives are indeed not affected by the

motion along the other degree of freedom, as predicted by theory i.e., those flutter derivatives associated with the h motion are not affected by the α motion, and vice versa.

All flutter derivatives of the thin plate – except H_4 *- from free decay-motion tests by both SSI-methods are in good agreements with Theodorsen's theoretical values. However, H_4 * extracted from the SDOF and the coupled motion tests are in good agreement and showing good agreement in trend with the theoretical value. The factor that made the extraction of H_4 * difficult is due to the very small change in the natural frequency from which H_4 * were calculated.

4.2.2 Comparisons of flutter derivatives between the SSI-DATA and the SSI-COV method.

From Figs. 12 and 13, the six important flutter derivatives; $H_1^* \sim H_3^*$, $A_1^* \sim A_3^*$ determined by the buffeting responses by both the SSI-COV and the SSI-DATA matched very well with both the theoretical values and those from the free decay responses. The results show very good agreements between the two types of tests. This verifies the ability of the system identification methods (both the SSI-COV and the SSI-DATA) to apply to the free decay signal though it was developed from a stochastic model (white noise loading assumption). Nonetheless, as the thin plate model is relatively heavy, it is difficult to accurately extract the flutter derivatives by the buffeting response tests at the very low reduced velocities due to the low energy from the wind that is available to excite the model. The useful signal is embedded in the noise. The H_4^* -derivatives by both the SSI-COV and the SSI-DATA are generally agreed in trend with the theoretical values similar to the free decay tests. However, the A_4^* , in turn, found from the SSI-COV are more scattered without an obvious trend as compared to that from the SSI-DATA.

4.3 CASE 2: Section model of the IRR Bridge

Encouraged by the success in the thin plate model, the flutter derivatives of the IRR Bridge, a cable-supported bridge with a 2-edge girder, as shown in Fig. 14, were estimated by the SSI-DATA technique. The IRR Bridge has a main span of 398 m. The deck consists of a concrete deck slab and a web of steel girders. The deck is supported by two cable planes at the outside edge girders. A 2-edge-girder bridge section with A-shape pylons has a good cost performance, but at the same time the bridge cross-section is known to be aerodynamically unstable at high wind speed. Table 5 lists the main parameters of the prototype bridge and the section model. Tests were conducted under smooth and two levels of turbulence wind flow. The turbulent flow conditions were generated by two different grids. The longitudinal and vertical turbulence intensities were both about 5% and 8%, respectively.

Using the SSI-DATA technique, the flutter derivatives of the IRR Bridge were estimated for 2DOFs responses under smooth flow by both the free decay and the buffeting tests, and under two levels of turbulence flow by the buffeting test only. The results were also compared with those from the SSI-COV in the case of the free decay responses under smooth flow.

4.3.1 Comparisons of flutter derivatives between the free decay and the buffeting test methods under smooth flow

Figs. 15 and 16 present the identified flutter derivatives of the bridge deck by the SSI-DATA method from both the free decay and the buffeting tests under smooth flow. The flutter derivatives were estimated by Eq. (26) and reported in the form of Eq. (2) but without the factor 1/2. The identified flutter derivatives were also compared with those by the SSI-COV from the free decay responses.

Generally, all flutter derivatives of the bridge in smooth flow identified by the SSI-DATA method from both the free decay and the buffeting tests are in good agreements. This verifies the ability of the SSI DATA system identification method under different type of tests. In smooth flow, the most important derivative A_2^* is steadily increased (more negative) up to the reduced wind velocity around 3, and then started to decrease. This sign reversal at reduced wind speed of 4.5 (Fig. 16) is the primary factor toward the SDOF-torsional instability ("stall flutter") for bluff type sections.

4.3.2 Comparisons of flutter derivatives between the SSI-DATA and the SSI-COV method.

From Figs. 15 and 16, they were shown that the flutter derivatives identified by the SSI-COV method are generally agreed in trend with those identified by the SSI-DATA method. However, the coupled aerodynamic derivatives; H_2^* , A_I^* , A_I^* , extracted by the SSI-COV in turn seem to be more scattered than those obtained from the SSI-DATA. The largest scatter among the extracted parameters were A_I^* and A_I^* .

4.3.3 Effects of turbulence flow on flutter derivatives and responses of bridge deck

Most of the prototype bridges are submerged in turbulent wind; therefore, detailed investigations of the effects of turbulence on the flutter derivatives are significant. Almost all the wind tunnel tests for flutter derivatives have been generally carried out in smooth flows. Although few researchers have studied the problem using wind tunnel tests (Sarkar et al. 1994; Gu et al., 2000; Scanlan & Lin, 1978), in general, the results are still debatable and inconclusive. For streamlined section, tests showed little effect (Sarkar et al., 1994), while tests on a rectangular box girder bridge showed galloping in smooth flow (Jacobsen & Hjorth-Hansen, 1998). For Π type section, Gu and Qin (2004) found that the effects of turbulence on the H_3^* and A_3^* seemed to be negligible; whereas the other four derivatives related to aerodynamic damping characteristics showed some deviations from those in smooth flow, especially at high reduced wind speed.

Figs. 17 and 18 present the identified flutter derivatives of the bridge deck by the SSI-DATA method from buffeting responses under smooth flow and two turbulence wind flows with both the longitudinal and the vertical turbulence intensities of 5% and 8%, respectively. Generally, the flutter derivatives of the bridge in turbulent flow identified by the SSI-DATA are in agreement with those in smooth flow. From Figs.17 and 18, it can be found that the influence of the flow type on H_4^* and A_3^* , i.e. flutter derivatives related to the direct aerodynamic stiffness, seems to be negligible. Though, the value of H_4^* obtained from the turbulence flow is somewhat less than that in the smooth flow case, it affected only the second decimal digit of the frequency value. The influence also has negligible effect on H_1^* and H_2^* i.e. direct and cross derivatives that are related to the vertical and the torsional aerodynamic dampings, respectively. On the other hand, the more important A_1^* A_2^* and H_3^* show rather noticeable deviations from those in the smooth flow, especially at high reduced wind speeds. The most important effect is that the reduced wind speed, which corresponds to the reversed sign of the torsional aerodynamic damping A_2^* , increased from 4.5 in the smooth flow to 5.1 in the 5% turbulent flow (Fig. 18). It shows that turbulence tends to make bridges more aerodynamically stable by delaying the torsional flutter. The deviations of flutter derivatives may reveal the fact that for those bridges with bluff type sections similar to the IRR Bridge, the effects of turbulence can be significant. Hence, the wind tunnel tests of such bridges for flutter derivative estimation should also be carried out in turbulent flows.

Figs. 19 and 20 show comparisons of the root-mean-square (RMS) torsional and vertical buffeting responses of the IRR bridge model versus the reduced velocity between smooth and turbulence flow. Under a smooth flow, the very abrupt transition with increasing velocity from the effectively zero torsional response amplitude to the clear instability occurs in the near neighborhood of the reduced velocity value of 4.5 (Figs. 16 and 20). The abrupt change in the vertical response at high wind speed is due to the effect of cross derivatives H_2^* and H_3^* which causes the coupling of the torsional responses with the vertical responses in terms of damping and stiffness, respectively (Boonyapinyo et al. 1999). Compared with the smooth flow, the turbulence flow reduces the vortex-shedding response, because the turbulence tends to enhance the reattachment of flow and weaken the vortex shedding formulation. However, it raises the amplitude of the bridge responses progressively over the speed range. No clear and uniquely definable "flutter instability" was made evident in the range of wind velocity test.

5. Conclusions

A theoretical model based on the data-driven SSI technique was proposed to extract the flutter derivatives of bridge deck sectional models from the two-degree-of-freedom free decay and buffeting responses. An advantage of the stochastic subspace identification technique is that it considers the buffeting forces and the responses as inputs instead of as noises as typically assumed. Therefore, the signal-to-noise ratio is not affected by the wind speed, and the flutter derivatives at high reduced wind speeds are more readily available. These aspects give the stochastic system identification methods an advantage over the deterministic system identification. Comparing with the SSI-COV, the SSI- DATA method avoids the computation of covariances between the outputs. It is replaced by projecting the row space of the future outputs into the row space of the past outputs. This projection is computed from the numerically robust square root algorithm, *QR* factorization instead of squaring up the output data as in the SSI-COV algorithm. Moreover, this reduces both the dimensions of the matrices and the computation time considerably. The conclusions of the present study are as follows.

- Numerical simulations of the bridge deck responses confirmed that the SSI-DATA technique can be used to estimate flutter derivatives from buffeting and free decay responses with reliable results. This shows the applicability of the SSI-DATA method with various test techniques, though it was developed from a stochastic model. Comparing with the SSI-COV, the identified modal parameter and system matrices from the SSI-DATA are more precise and less scattered.
- 2) For the thin plate model under smooth flow, wind tunnel tests showed that flutter derivatives identified by the SSI-DATA technique from both the free decay and the buffeting tests matched well with theoretical values. The flutter derivatives identified by the SSI-COV method from both tests also agreed with theoretical values, except in the case of A_4^* that was identified from buffeting responses
- 3) When applied to the bluff section model of the IRR Bridge under smooth flow, the flutter derivatives estimated by the SSI-DATA from the buffeting test agreed with those obtained from the free decay test. This result allowed focusing on applying the SSI-DATA technique to the buffeting test method. On the other hand, there are more variations in the values of the A_1^* , A_4^* and H_2^* derivatives obtained by the SSI-COV. The sign reversal of the A_2^* derivative is observed as the reduced wind speed reached the value of 4.5. This indicates that this bridge section is susceptible to the SDOF-torsional flutter instability at high wind speed.
- 4) Under turbulence wind, the identified flutter derivatives by the SSI-DATA of a blunt section model of the IRR Bridge revealed that the most important and positive effect of the turbulence is that it tends to make the bridge more aerodynamically stable by delaying the sign reversal of the aerodynamic damping A_2^* from 4.5 in the smooth flow to 5.1 in the 5% turbulent flow. This may help explain that for those bridges with bluff type sections similar to the IRR Bridge, the effects of turbulence can be significant. Hence, the wind tunnel tests of such bridges for flutter derivatives estimation should also be carried out in turbulent flow.

In summary, the numerical simulation tests showed that the precision of modal parameters and system matrices can be clearly improved by using the SSI-DATA technique, compared with the SSI-COV. From the results of wind tunnel tests, it was found that for a simple streamlined section, the flutter derivatives identified from both the SSI-DATA and the SSI-COV agreed well together. However, in the case of the 2-edge girder blunt type section, applying the SSI-DATA yields better results especially for the coupling derivatives. Applying the proposed SSI-DATA technique to the buffeting test yields a straightforward, cost effective, and reliable system identification process that can be used to identify flutter derivatives of various bridge decks.

Acknowledgements

The authors would like to greatly acknowledge the Thailand Research Fund (TRF) under grant number RMU 4980012 for financial supports. In addition, the authors are greatly thanked to Mr. Worapoj Thamasungkeeti, graduate student of Thammasat University, for his assistant in wind tunnel tests.

References

- Boonyapinyo V., Yamada H., and Miyata T. (1994), "Wind-Induced Nonlinear Lateral-Torsional Buckling of Cable-Stayed Bridges," *J. of Struct. Eng*, ASCE, 120(2), 486-506.
- Boonyapinyo V., Miyata T. and Yamada H. (1999), "Advanced Aerodynamic Analysis of Suspension Bridges by State-Space Approach," *J. of Struct. Eng*, ASCE, 125(12), 1357-1366.
- Boonyapinyo V., Lauhatanon Y., and Lukkunaprasit P. (2006), "Nonlinear Aerostatic Stability Analysis of Suspension Bridges," *Eng. Struct.*, ELSEVIER, 28(5), 793-803.
- Chen Z.Q., and Yu X.D. (2002), "A New Method for Measuring Flutter Self-Excited Forces of Long-Span Bridges", *China Civil Engineering Journal*, **35**, 34–41.
- Chowdhury A.G., and Sarkar P.P. (2003), "A new technique for identification of eighteen flutter derivatives using a three-degree-of-freedom section model", *Eng. Struct*, **25**, 1763–1772.
- Dyrbye C., and Hansen S.O. (1996), Wind loads on structures. John Wiley, NJ.
- Golub G.H., and Van Loan C.F. (1996), Matrix Computations. 3rd edition, John Hopkins Univ. Press, MD. USA
- Gu M., Zhang R.X., and Xiang H. (2000), "Identification of Flutter Derivatives of Bridge Decks", *J. Wind. Eng. Ind. Aerodyn.*, **84**, 151–162.
- Gu M., and Qin X.R. (2004), "Direct Identification of Flutter Derivatives and Aerodynamic Admittances of Bridge Decks", *Eng. Struct*, **26**, 2161–2172.
- Jakobsen J.B., and Hjorth-Hansen E. (1995), "Determination of the Aerodynamic Derivatives by a System Identification Method", *J. Wind. Eng. Ind. Aerodyn.*, **57**, 295–305.
- Jakobsen J.B., and Hjorth-Hansen E. (1998), "Aeroelasticic Effects on a Rectangular Box-Girder Bridge", *J. Wind. Eng. Ind. Aerodyn.*, **74-76**, 819–827.
- Juang J.N., and Pappa R.S. (1985), "An Eigensystem Realization Algorithm for Modal Parameter Identification and Model Reduction", *J. of Guidance, Control, and Dynamics*, **8**, 620–627.
- Mishra S.S., Kumar K., and Krishna P. (2006), "Identification of 18 flutter derivatives by covariance driven stochastic subspace method.", *Wind and Struct.*, **9**(2), 159-178.
- Overschee P.V. (1991), Subspace Algorithms for the Stochastic Identification Problem", *Proc.*, 30th Conference on Decision and Control, Brighton, England, 1321–1326.
- Overschee P.V., and Moor D.B., (1996), Subspace Identification for Linear System: Theory-Implementation-Applications. Kluwer Academic Publishers, The Netherlands.
- Peeters B. (1999), "Reference-based Stochastic Subspace Identification for Out-put only Modal Analysis", *Mechanical Systems and Signal Processing*, **13** (6), 855–878.
- Poulsen N.K., Damsgaard A., and Reinhold T.A. (1992). "Determination of Flutter Derivatives for the Great Belt Bridge", *J. Wind. Eng. Ind. Aerodyn.*, **57**, 295–305.
- Peeters B., and De Roeck (2001), "Stochastic System Identification for Operational Modal Analysis: A Review", *J. of Dyn. Sys. Meas. Contr.*, **123**, 659–666.
- Sarkar P.P., Jones N., and Scanlan R.H. (1994), "Identification of Aeroelastic Parameters of Flexible Bridges", *J. of Eng. Mech.*, ASCE, **120** (8), 1718–1741.
- Scanlan R.H., and Tomko J.J. (1971), "Airfoil and Bridges Deck Flutter Derivatives", *J. of Eng. Mech.*, ASCE, **97**(6), 1717–1733.

Scanlan R.H. (1977), "Motion of Suspended Bridge Spans under Gusty Wind", *J. of the Struct. Div.*, ASCE, **103**(9), 1867–83.

Scanlan R.H., and Lin W.H., 1978. "Effects of Turbulence on Bridge Flutter Derivatives", *J. of Eng. Mech.*, ASCE, **104** (4), 719–733.

Simiu E., and Scanlan R.H. (1996), Wind effects on structures, 3rd Ed., John Wiley, NJ.

Strømmen E. (2006), Theory of Bridge Aerodynamics, 1st edition, New York, Springer.

Table 1 Deviation of identified system matrices ($\Delta[K]$, $\Delta[C]$) (in %) from the pre-set values for the simulated free decay responses.

2000		SSI-	COV		SSI-DATA			
case	% error of [K]		% error of [C]		% error of [K]		% error of [C]	
1. without noise	-0.14%	-0.05%	0.66%	-3.00%	-0.03%	0.08%	-0.39%	2.56%
	4.26%	-0.08%	0.16%	-0.26%	1.42%	-0.25%	0.42%	1.24%
2 with 100/ noise	0.25%	-0.30%	0.73%	-7.01%	-0.38%	-0.02%	0.20%	-2.50%
2. with 10% noise	-6.56%	0.02%	-0.99%	1.55%	6.68%	0.02%	-1.59%	0.0%

Table 2 Deviation of identified modal parameters (frequencies, f_h , f_θ and damping ratio ξ_h , ξ_θ) (in %) from pre-set values for simulated buffeting responses.

	SSI-COV			SSI-DATA				
Parameters	$\Delta f_h(\%)$	$\Delta \xi_h(\%)$	$\Delta f_{\theta}(\%)$	$\Delta \xi_{\theta}(\%)$	$\Delta f_h(\%)$	$\Delta \xi_h(\%)$	$\Delta f_{\theta}(\%)$	$\Delta \xi_{\theta}(\%)$
Case 1) without noise	0.13%	1.67%	-0.01%	0.44%	-0.47%	0.19%	0.01%	0.88%
Case 2) with 10% noise	-2.98%	-14.69%	0.12%	-5.31%	0.81%	2.44%	-0.08%	-3.98%

Table 3 Deviation of identified system matrices ($\Delta[K]$, $\Delta[C]$) (in %) from pre-set values for simulated buffeting responses.

2002	SSI-COV				SSI-DATA			
case	% error of [K]		% error of [C]		% error of [K]		% error of [C]	
Case 1) without noise	0.34%	-0.08%	2.52%	-6.76%	0.12%	-0.02%	0.74%	-3.12%
	3.99%	-0.03%	-0.81%	0.26%	-2.01%	0.03%	0.66%	1.14%
Cons 2) with 100/ mains	2.23%	-0.38%	8.55%	-27.86%	0.06%	0.04%	0.73%	-2.16%
Case 2) with 10% noise	-11.17%	-0.03%	-0.28%	0.50%	5.74%	0.03%	1.09%	-0.27%

Table 4 Main parameters of the thin plate model

Parameter	Mark	Unit	Value
Length	L	m	2.30
Width	B	m	0.45
Height	H	m	0.02
Mass per unit length	M	kg/m	6.7391
Inertial moment of mass per unit length	I_m	kg m²/ m	0.1183
Inertial radius	R	m	0.1325
First bending freq.	f_h , n_h	Hz	1.65
First torsional freq.	f_{α} , n_{α}	Hz	2.73
First torsion-bending frequency ratio	${\cal E}$		1.65

Table 5 Main parameters of the IRR Bridge model

Parameter	Mark	Unit	Prototype	Model
Length	L	m	-	2.26
Width	B	m	35.9	0.399
Height	H	m	3.20	0.035
Mass per unit length	M	kg/m	43000	5.6801
Inertial moment of mass per unit length	I_m	$kg m^2 / m$	$4.11x10^9$	0.1726
First bending frequency	f_h , n_h	Hz	0.376	2.13
First torsional frequency	f_{α} , n_{α}	Hz	0.850	4.73
First torsion-bending-frequency ratio	ε		2.26	2.22

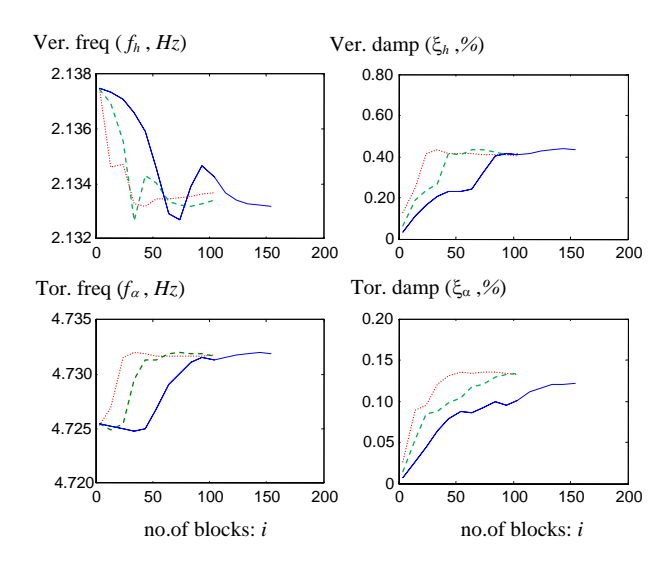


Fig. 1 Illustration of the asymptotically property of modal properties (... fs = 25 Hz, --- fs = 50 Hz and solid line for fs = 100 Hz)

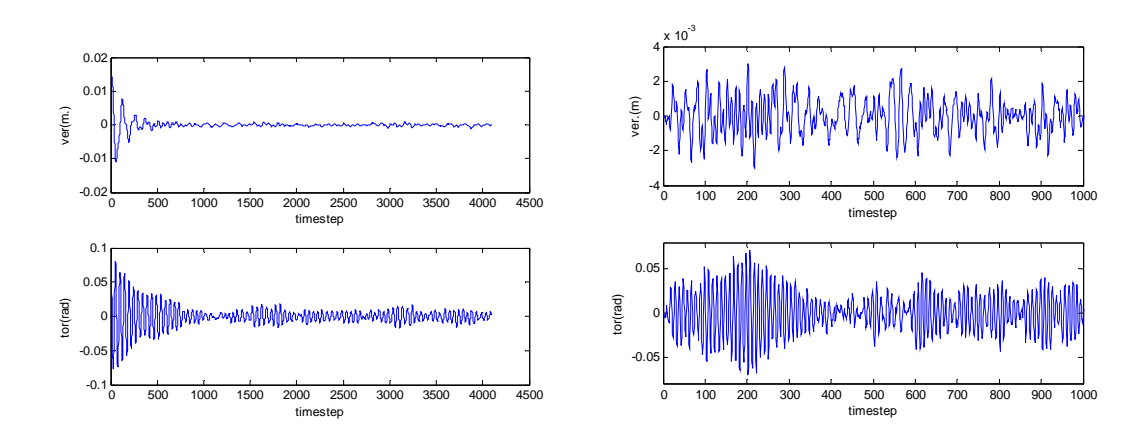


Fig.2 Example of vertical (top) and torsional (bottom) free decay responses simulated under wind flow.

Fig.3 Example of vertical (top) and torsional (bottom) buffeting responses simulated under wind flow.

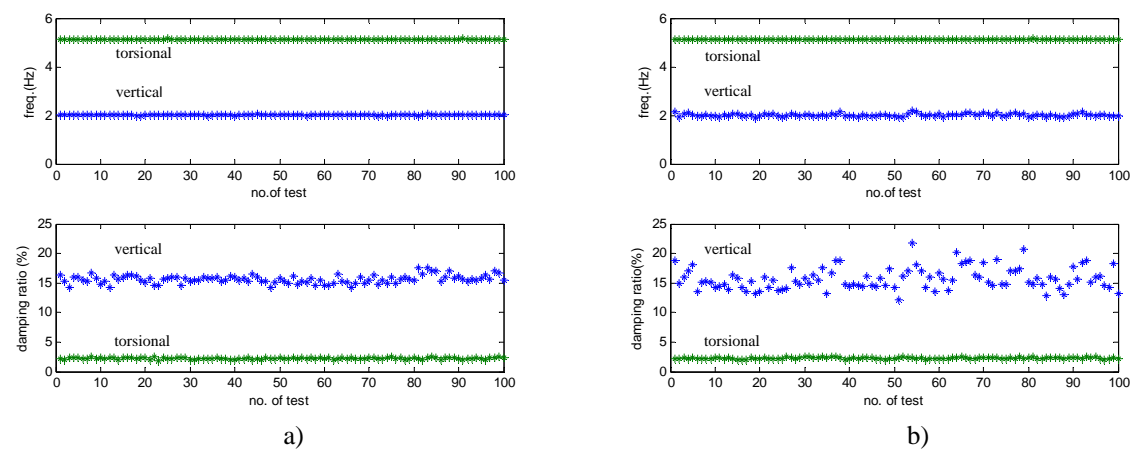


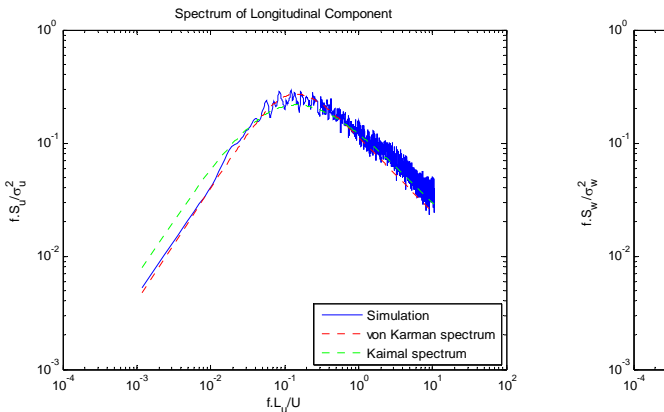
Fig. 4 Estimated frequencies and damping ratio from 100 buffeting response simulations with 10% noise added.; a) by SSI-DATA, b) by SSI-COV.



Fig. 5 IRR bridge model and grids to generate turbulent flow in wind tunnel.



Fig. 6 Suspension device of the model.



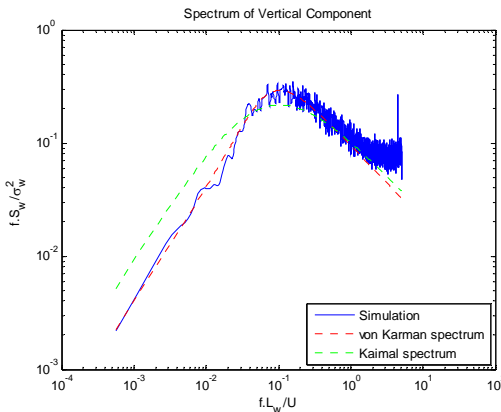


Fig. 7 Normalized power spectrum of the longitudinal and vertical velocity component: 8%-turbulence flow.

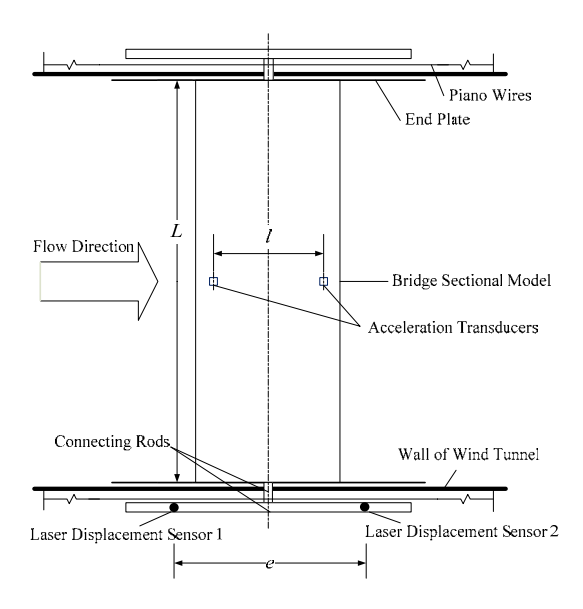


Fig. 8 Top view of the test setup.

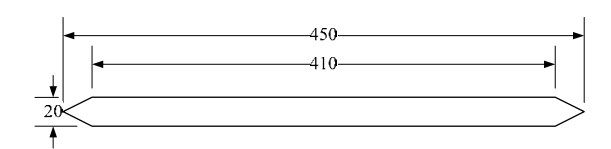


Fig. 9 Cross-section of the thin plate (Unit in mm).

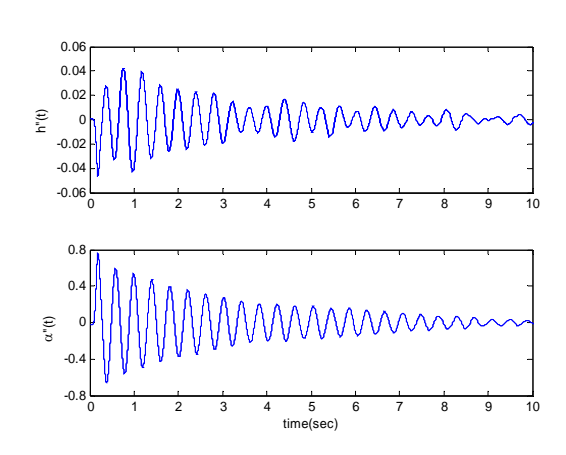


Fig.10 Vertical (top) and torsional (bottom) free decay acceleration responses of the thin plate at 8.1 m/s wind speed under smooth flow.(unit in g)

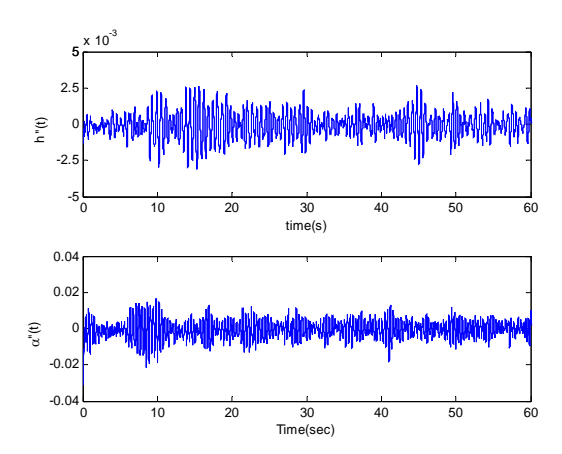


Fig.11 Part of vertical (top) and torsional (bottom) buffeting acceleration responses of the thin plate at 5.6 m/s wind speed under smooth flow. (unit in g)

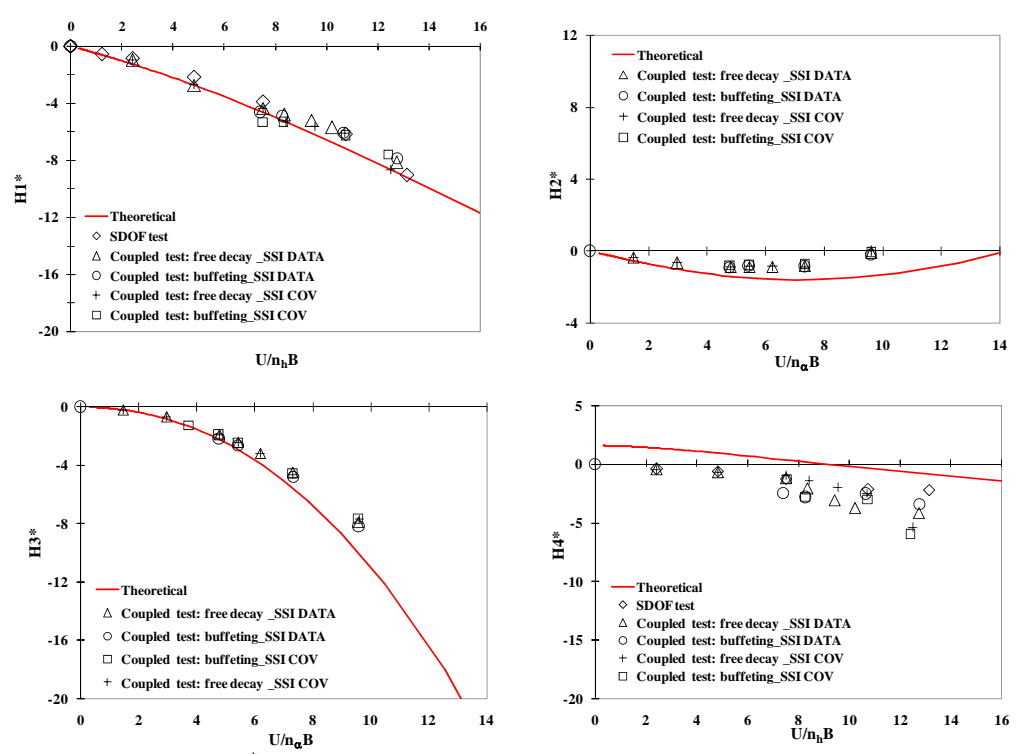


Fig. 12 Flutter derivatives (H_i^*) of the thin plate by SDOF test and coupled test by free decay and buffeting responses under smooth flow by both the SSI-DATA and the SSI-COV.

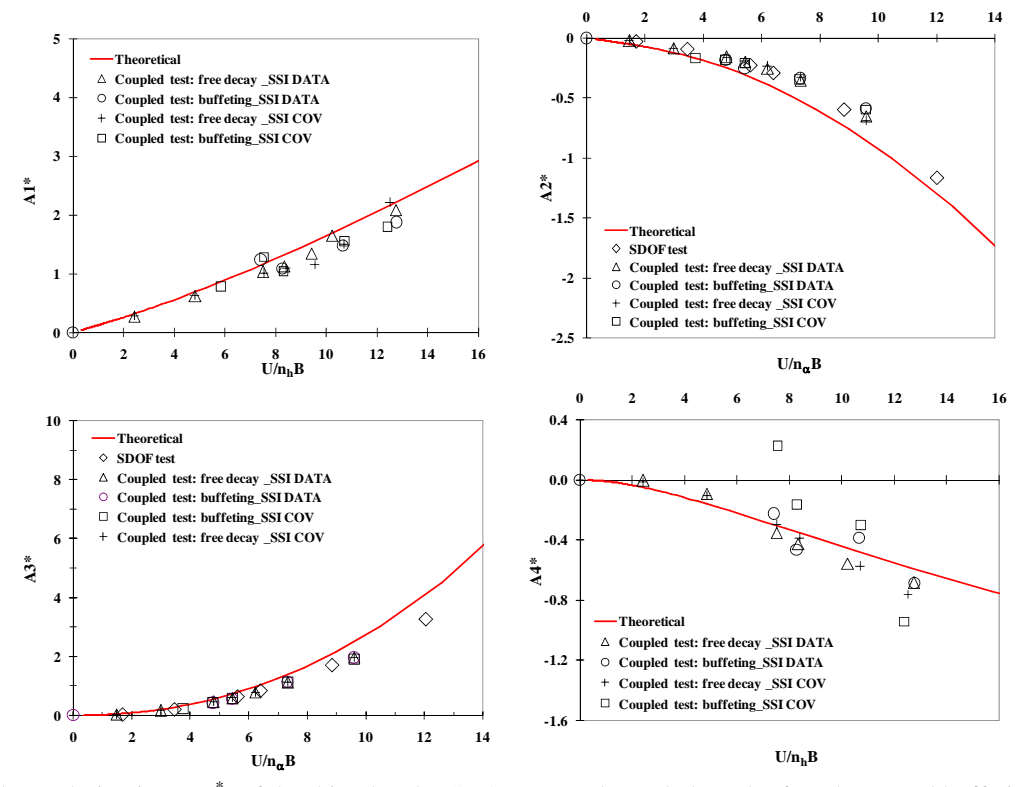


Fig. 13 Flutter derivatives (A_i^*) of the thin plate by SDOF test and coupled test by free decay and buffeting responses under smooth flow by both the SSI-DATA and the SSI-COV.

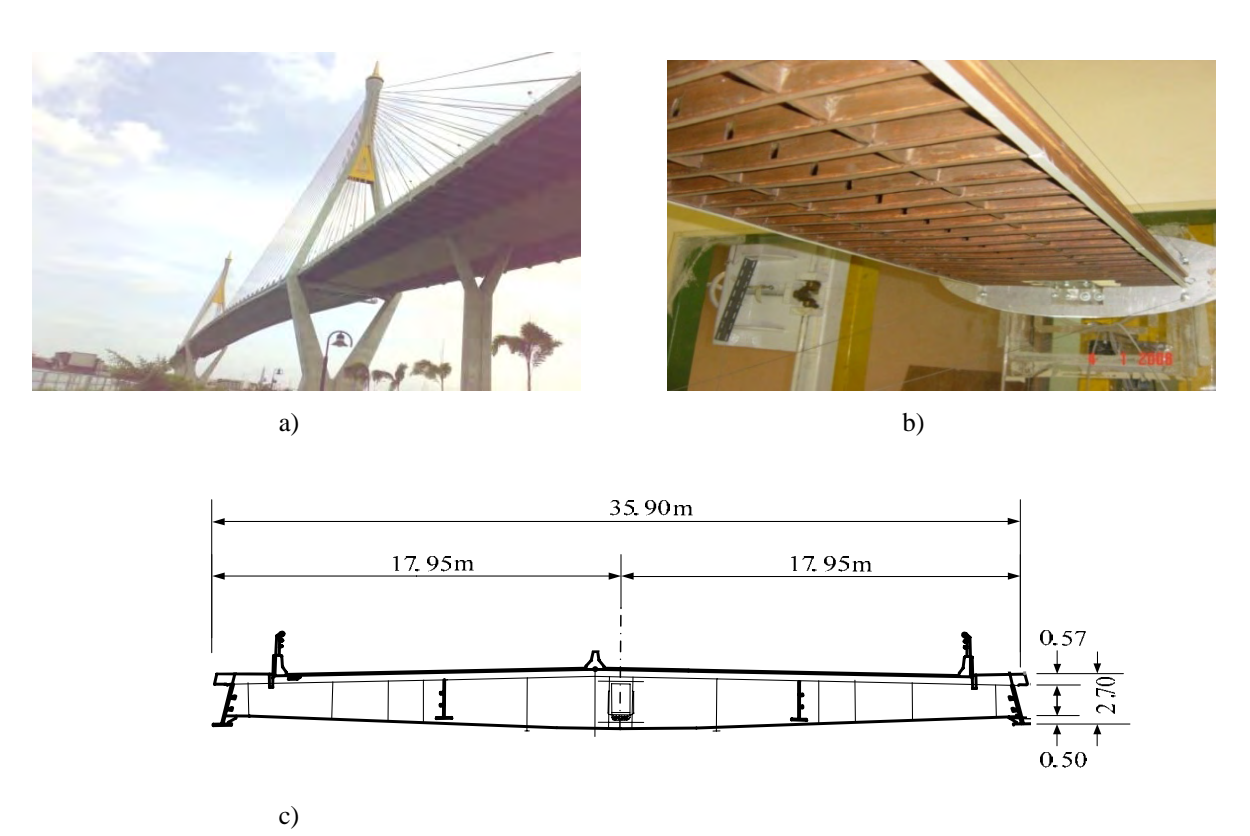


Fig. 14 a) Three dimensional view of IRR Bridge, b) IRR bridge deck model in wind tunnel and c) Schematic cross-section of IRR Bridge.

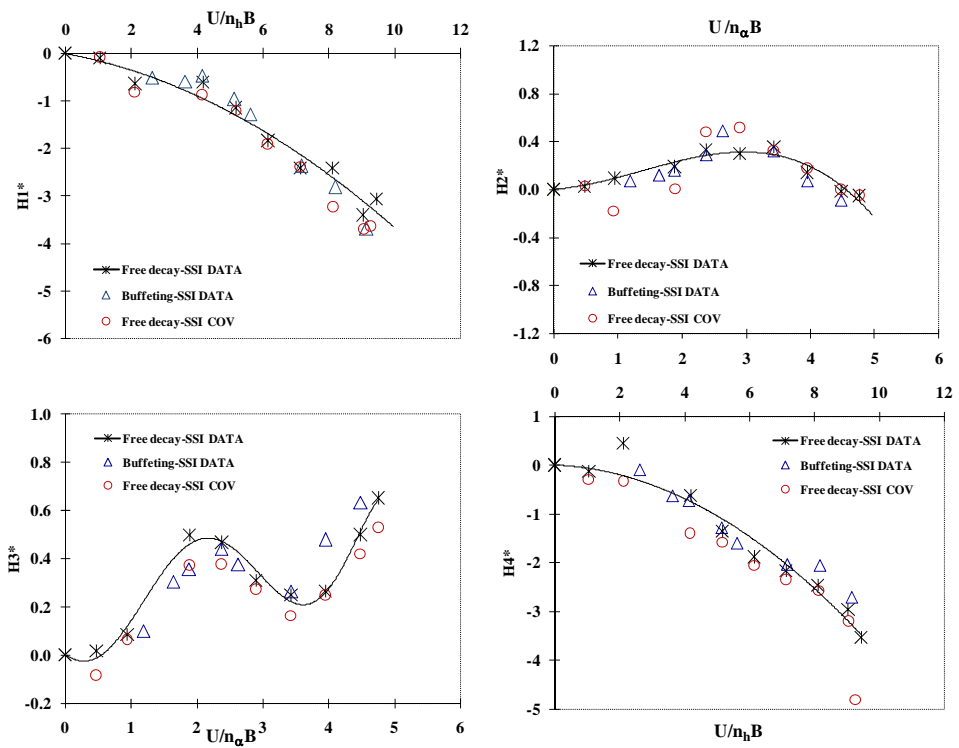


Fig. 15 Flutter derivatives (H_i^*) of the IRR Bridge model from coupled free decay test by the SSI-DATA and the SSI-COV and from buffeting test by the SSI-DATA under smooth flow.

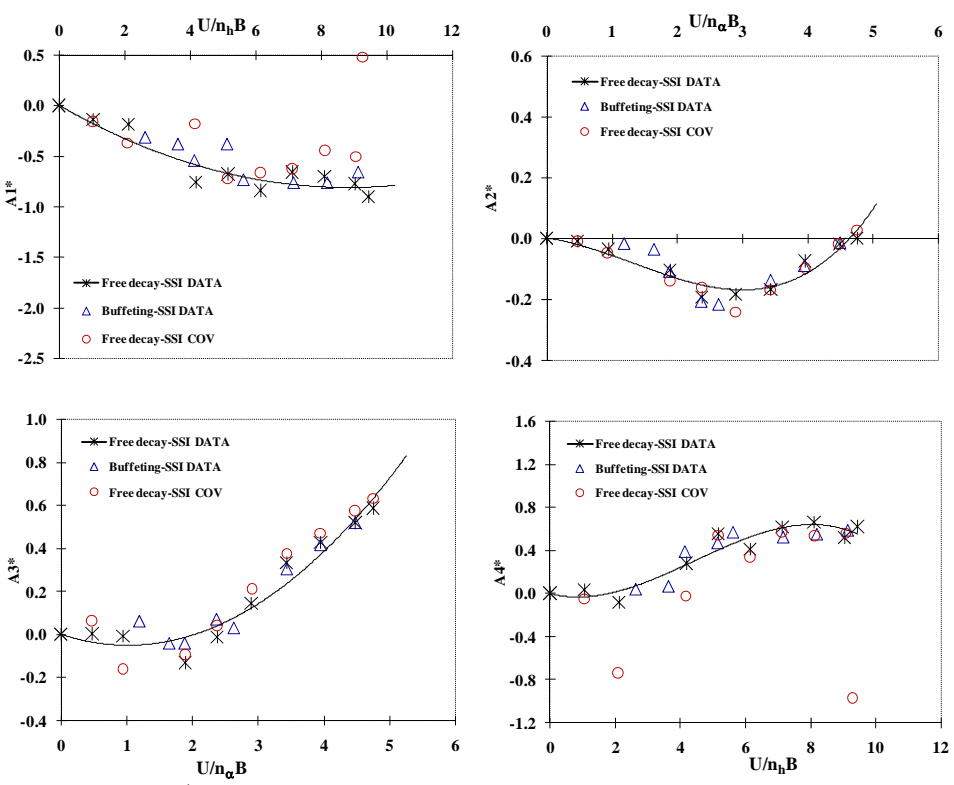


Fig. 16 Flutter derivatives (A_i^*) of the IRR Bridge model from coupled free decay test by the SSI-DATA and the SSI-COV and from buffeting test by the SSI-DATA under smooth flow.

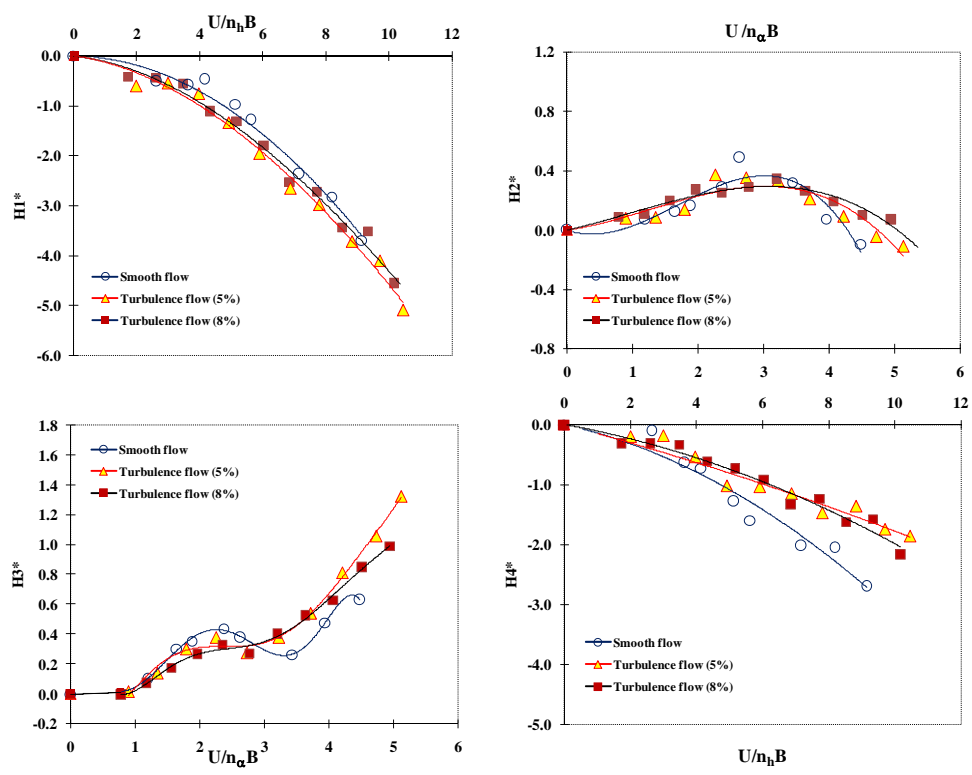


Fig. 17 Flutter derivatives (H_i^*) of the IRR Bridge model by SSI-DATA from buffeting responses under smooth and turbulent flows.

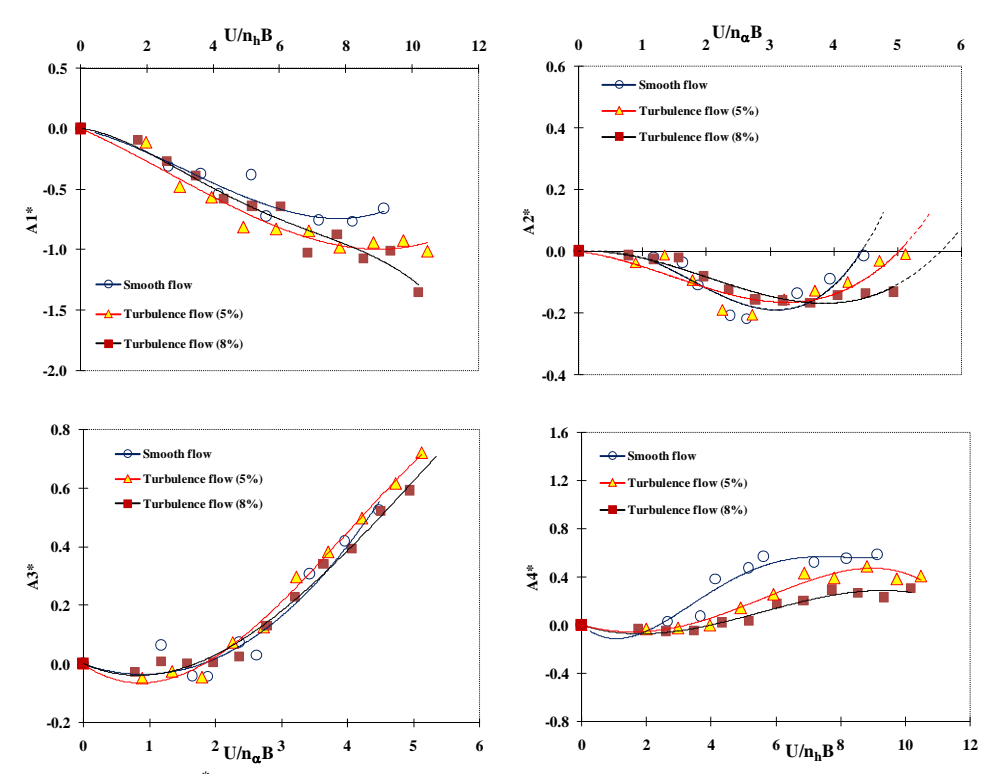


Fig. 18 Flutter derivatives (A_i^*) of the IRR Bridge model by SSI-DATA from buffeting responses under smooth and turbulent flows.

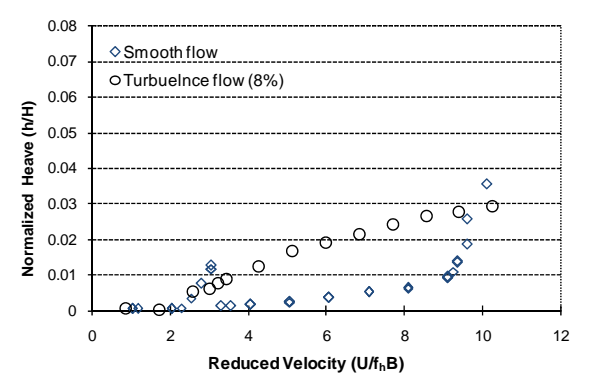


Fig.19 Vertical RMS responses of the IRR bridge model under smooth and turbulence flows.

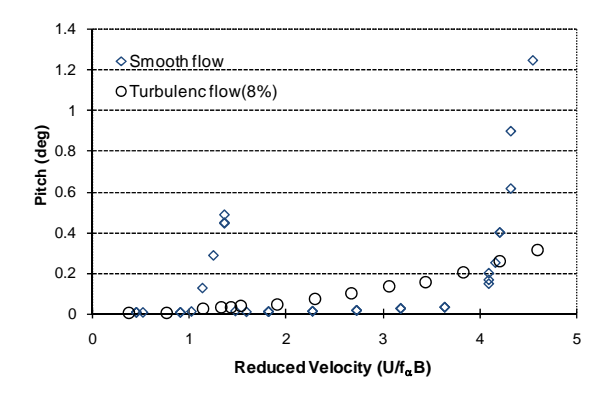


Fig.20 Torsional RMS responses of the IRR bridge model under smooth and turbulence flows.

Identification of Flutter Derivatives of Bridge Decks in Wind Tunnel Test by Stochastic Subspace Identification

T. Janesupasaeree and V. Boonyapinyo Faculty of Engineering, Thammasat University, Rangsit Campus, Pathumthani, 12120, Thailand

Abstract: Problem statement: Flutter derivatives are the essential parameters in the estimations of the flutter critical wind velocity and the responses of long-span cable supported bridges. These derivatives can be experimentally estimated from wind tunnel test results. Generally, wind tunnel test methods can be divided into free decay test and buffeting test. Compared with the free decay method, the buffeting test is simpler but its outputs appear random-like. This makes the flutter derivatives extraction from its outputs more difficult and then a more advanced system identification is required. Most of previous studies have used deterministic system identification techniques, in which buffeting forces and responses are considered as noises. These previous techniques were applicable only to the free decay method. They also confronted some difficulties in extracting flutter derivatives at high wind speeds and under turbulence flow cases where the buffeting responses dominate. Approach: In this study, the covariance-driven stochastic subspace identification technique (SSI-COV) was presented to extract the flutter derivatives of bridge decks from the buffeting test results. An advantage of this method is that it considers the buffeting forces and responses as inputs rather than as noises. Numerical simulations and wind tunnel tests of a streamlined thin plate model conducted under smooth flow by the free decay and the buffeting tests were used to validate the applicability of the SSI-COV method. Then, wind tunnel tests of a two-edge girder blunt type of Industrial-Ring-Road Bridge deck (IRR) were conducted under smooth and turbulence flow. Results: The identified flutter derivatives of the thin plate model by the SSI-COV technique agree well with those obtained theoretically. The results from the thin plate and the IRR Bridge deck validated the reliability and applicability of the SSI-COV experimental methods conditions various and of Conclusion/Recommendations: The SSI-COV was successfully employed to identify flutter derivatives of bridge decks with reliable results. It is a proven technique that can be readily applied to identify flutter derivatives of other bridge decks either by the free decay or the buffeting tests.

Key words: Flutter derivatives, covariance-driven stochastic subspace identification, wind tunnel test, bridge decks, turbulent flow

INTRODUCTION

Long-span cable-supported bridges are highly susceptible to wind excitation because of their inherent flexibility and low structural damping. Wind loads play an important role in the design of these structures. A wind-induced aerodynamic force can be divided into two parts: a buffeting force that depends on the turbulence of incoming flow and an aeroelastic force that originates in the interaction between the airflow and the bridge motion. The motion-dependent forces feed back into the dynamics of the bridge as aerodynamic damping and stiffness; the effect is termed 'aeroelasticity' and is commonly described via 'flutter

derivatives'. The problems of aerodynamic stability including vortex-induced vibrations, galloping, flutter and buffeting, may have serious effects on the safety and the serviceability of the bridges. Among these, flutter is the most serious wind-induced vibration of bridges and may destroy the bridges due to diverging motions either in single or torsion-bending coupled mode. Notorious examples by the flutter phenomenon are the failures of the Brighton Chain Pier Bridge in 1836 and the original Tacoma Narrow Bridge in 1940. The flutter derivatives depend primarily upon the conditions of wind, the cross-sectional shape and the dynamic characteristics of the bridges. Nevertheless, no theoretical values exist for these derivatives for various

bridge shapes except only for a simple thin plate section. A major research tool in these studies is, therefore, a wind tunnel test, in which a geometrically and aerodynamically representative scale model of a length of a bridge deck is mounted in a wind tunnel. The flutter derivatives are non-dimensional functions of wind speed, geometry and frequency of vibrations; therefore they can be applied directly to full-scale bridge in a piecewise manner.

The experimental method used for a determination of flutter derivatives can be grouped under two types, i.e. forced^[1] and free vibration methods^[2-5]. Having less emphasis on elaborate equipment, time and work; the free vibration method seems to be more tractable than the forced method. In the determination of flutter derivatives by free vibration method, the system identification method is the most important part required to extract these parameters from the response output of the section model. The free vibration method depends on system identification techniques and can be classified into two types, i.e. free decay and buffeting tests. In the free decay method, the bridge deck is given an initial vertical and torsional displacement. The flutter derivatives are based on the transient (i.e., free decay) behavior that occurs when the bridge deck is released. The buffeting test, on the other hand, uses only the steady random responses (i.e., buffeting responses) of bridge deck under wind flow without any initial displacement given to the model. Compared with the free decay method, the buffeting test is simpler in the test methodology, more cost effective and more closely related to real bridge behaviors under wind flow, but with a disadvantage that the outputs appear randomlike. This makes the parameters extraction more difficult and a more advanced system identification is required.

In most of the previous studies, flutter derivatives were estimated by deterministic system identification techniques that can be applied to the free decay method only. Examples of previous deterministic system identification that were applied to the free decay method included Scanlan's method^[2], Poulsen's method^[3], Modified Ibrahim method (MITD)^[4] and Unified Least Square method (ULS)^[5]. In these system identification techniques, the buffeting forces and their responses are regarded as external noises, the identification process then requires many iterations^[3-5]. It also confronted with difficulties at high wind speeds where the initial free decay is drowned by buffeting responses^[3-5]. Moreover, at high reduced wind speed, the vertical bending motion of the structure will decay rapidly due to the effect of the positive vertical aerodynamic damping and thus the length of decaying time history available for system identifications will decrease. This causes more difficulties to the deterministic system identification techniques^[4,5]. In case of turbulence flow, the presence of turbulence in the flow is equivalent to a more noisy-input signal to the deterministic system identification. This made the extraction process more complicated and most likely reduced the accuracy of the flutter derivatives identified^[3,4]. In addition, due to test technique, the free decay method is impractical to determine flutter derivatives of real bridges in field.

On the other hand, the buffeting test uses random responses data of bridge motion from wind turbulence only. This mechanism is more closely related to a real bridge under wind flow and is applicable to real prototype bridges. The method costs less and simpler than the free decay since no operator interrupts in exciting the model. However, as wind is the only excited source, it results in low signal-to-noise ratio, especially at low velocity and therefore a very effective system identification is required. None of the aforementioned system identification techniques is applicable to the buffeting responses tests. System identification techniques can be divided into two groups, i.e., deterministic and stochastic.

If the stochastic system identification technique [6-9] is employed to estimate the flutter derivatives of a bridge deck from their steady random responses under the action of turbulent wind, the above-mentioned shortcomings of the deterministic system identification technique can be overcome. The reason is that the random aerodynamic loads are regarded as inputs rather than noises, which are more coincident with the fact. Therefore, the signal-to-noise ratio is not affected by wind speed and the flutter derivatives at high reduced wind speeds are more readily available. These aspects give the stochastic system identification methods an advantage over the deterministic system identification.

Many stochastic system identification methods have been developed during the past decades, among which the Stochastic Subspace Identification (SSI in short)^[7,8] has proven to be a method that is very appropriate for civil engineering. The merit points of SSI are: (1) The assumptions of inputs are congruent with practical wind-induced aerodynamic forces, i.e. stationary and independent on the outputs; (2) Identified modes are given in frequency stabilization diagram, from which the operator can easily distinguish structural modes from the computational ones; (3) Since the maximum order of the model is changeable for the operator, a relatively large model order will give an exit for noise, which in some cases can dramatically improve the quality of the identified modal parameters;

(4) Mode shapes are simultaneously available with the poles, without requiring a second step to identify them. There are two kinds of SSI methods, one is data-driven and the other is covariance-driven.

In this study, the covariance-driven stochastic subspace identification method is used to estimate the flutter derivatives from random responses (buffeting) under the action of smooth and turbulent wind. Tests are also carried out with the free decay method (single and two-degree-of-freedom) in order to examine the robustness of the present technique that the results are not affected by test methods used. To validate the applicability of the present technique, first numerical simulations are performed then sectional-model tests of a quasi-streamlined thin plate model, which is the only section that theoretical flutter derivatives exist, are performed under smooth flow. Encouraged by the success in the evaluation process, the flutter derivatives of a real bridge are determined. The twoedge-girder type blunt section model of Industrial-Ring-Road Bridge (IRR in short), a cable-supported bridge with a main span of 398 m in Samutprakan province, Thailand, was tested both in smooth and turbulence flow. Tests were conducted in TU-AIT Boundary Layer Wind Tunnel in Thammasat University, the longest and the largest wind tunnel in Thailand.

MATERIALS AND METHODS

Theoretical formulation of covariance-driven SSI: The dynamic behavior of a bridge deck with two Degrees-Of-Freedom (DOF in short), i.e., h (bending) and α (torsion), in turbulent flow can be described by the following differential equations^[9,10]:

$$\begin{split} m \Big[\ddot{h}(t) + 2\xi_{h}\omega_{h}\dot{h}(t) + \omega_{h}^{2}h(t) \Big] &= L_{se}(t) + L_{b}(t) \\ I \Big[\ddot{\alpha}(t) + 2\xi_{\alpha}\omega_{\alpha}\dot{\alpha}(t) + \omega_{\alpha}^{2}\alpha(t) \Big] &= M_{w}(t) + M_{b}(t) \end{split} \tag{1}$$

Where:

m and I = The mass and mass moment of inertia of the deck per unit span, respectively

 ω_i = The natural circular frequency ξ_i = The modal damping ratio (i = h, α)

 $L_{se} \ and \ M_{se} = The \quad self-excited \quad lift \quad and \quad moment,$ respectively

 L_b and M_b = The aerodynamic lift and moment

The self-excited lift and moment are given as follows^[11]:

$$\begin{split} L_{se} = & \frac{1}{2} \rho U^{2} B \begin{bmatrix} K_{h} H_{1}^{*}(K_{h}) \frac{\dot{h}}{U} + K_{\alpha} H_{2}^{*}(K_{\alpha}) \frac{B \dot{\alpha}}{U} + K_{\alpha}^{2} H_{3}^{*}(K_{\alpha}) \alpha \\ + K_{h}^{2} H_{4}^{*}(K_{h}) \frac{\dot{h}}{B} \end{bmatrix} \\ M_{se} = & \frac{1}{2} \rho U^{2} B^{2} \begin{bmatrix} K_{h} A_{1}^{*}(K_{h}) \frac{\dot{h}}{U} + K_{\alpha} A_{2}^{*}(K_{\alpha}) \frac{B \dot{\alpha}}{U} + K_{\alpha}^{2} A_{3}^{*}(K_{\alpha}) \alpha \\ + K_{h}^{2} A_{4}^{*}(K_{h}) \frac{\dot{h}}{B} \end{bmatrix} \end{split}$$
(2)

Where:

ρ = Air mass density; B is the width of the bridge deck

U = The mean wind speed at the bridge deck level

 $k_i = \omega_i B/U$ = The reduced frequency (i = h, α)

 H_i^* and A_i^* = The so-called flutter derivatives,

(i = 1, 2, 3, 4) which can be regarded as the implicit functions of the deck's modal parameters

The alternate form of self-excited forces is as Eq. 2 but without the factor $1/2^{[3]}$.

The aerodynamic lift and moment can be defined as $^{[10]}$.

$$L_{b}(t) = -\rho U^{2}B \left[2C_{L} \frac{u(t)}{U} \chi_{L}(t) + (C_{L}^{'} + C_{D}) \frac{w(t)}{U} \chi_{L}(t) \right]$$

$$M_{b}(t) = -\rho U^{2}B \left[2C_{M} \frac{u(t)}{U} \chi_{M}(t) + (C_{M}^{'}) \frac{w(t)}{U} \chi_{M}(t) \right]$$
(3)

Where:

 C_L , C_D and C_M = The steady aerodynamic force coefficients

 C'_L and C'_M = The derivatives of C_L and C_M with respect to the attack angles, respectively

u(t) and w(t) = The longitudinal and vertical fluctuations of wind speed, respectively

 χ_L and χ_M = The lift and moment aerodynamic admittances of the bridge deck

By moving L_{se} and M_{se} to the left side and merging the congeners into column vectors or matrices, Eq. 1 can be rewritten as follows:

$$[M]{\ddot{y}(t)} + [C^{e}]{\dot{y}(t)} + [K^{e}]{y(t)} = {f(t)}$$
(4)

Where:

 $\{y(t)\} = \{h(t) \alpha(t)\}^{T}$ = The generalized buffeting response

 $\{f(t)\} = \{L_b(t)M_b(t)\}^T = The$ generalized aerodynamic force

[M] = The mass matrix

[C^e] = The gross damping matrix, i.e., the sum of the mechanical and aerodynamic damping matrices

[K^e] = The gross stiffness matrix

The fluctuations of wind speed u(t) and w(t) in Eq. 3 are random functions of time, so the identification of flutter derivatives of bridge decks can be simplified as a typical inverse problem in the theory of random vibration and thus can be solved by the stochastic system identification techniques. Let:

$$[A_c] = \begin{bmatrix} I & I \\ -M^{-1}K^c & -M^{-1}C^c \end{bmatrix}$$

$$[C_c] = [I \quad O]$$
(5)

and

$$\{x\} = \begin{cases} y \\ \dot{y} \end{cases} \tag{6}$$

then Eq. 4 is transformed into the following stochastic state equations:

$$\begin{aligned} {\dot{x}} &= [A_c] {x} + {w} \\ {y} &= [C_c] {x} + {v} \end{aligned} \tag{7}$$

The discrete form of Eq. 7 can be written as:

$${\dot{x}_{k+1}} = [A] {x_k} + {w_k}$$

$${y_k} = [C] {x_k} + {v_k}$$
(8)

where, $[A_c]_{4\times4}$, $[C_c]_{2\times4}$ and $\{x\}$ are known as state matrix, output shape matrix and state vector, respectively; $\{w_k\}$ and $\{v_k\}$ are the input and output noise sequences, respectively. Subscript *k denotes the value of * at time k Δt , where Δt means the sampling interval. O and I are the zero and identity matrices, respectively.

It is assumption of stochastic model that $\{x_k\}$, $\{w_k\}$ and $\{v_k\}$ in Eq. 8 are mutually independent and hence:

$$E(x_k w_k^T) = 0 \quad E[x_k v_k^T] = 0$$
 (9)

Defining:

$$\sum = E[x_k x_k^T] \qquad Q = E[x_k x_k^T]$$

$$\Lambda_i = E[y_{k+i} y_k^T] \qquad R = E[v_k v_k^T]$$

$$G = E[x_{k+i} y_k^T] \qquad S = E[w_k w_k^T]$$
(10)

and combining Eq. 9 and 10 we obtain the following Lyapunov equations for the state and output covariance matrices:

$$\sum = A \sum A^{T} + Q$$

$$\Lambda_{0} = C \sum C^{T} + R$$

$$G = A \sum C^{T} + S$$
(11)

From (8) and (9), it can be deduced:

$$\Lambda_{1} = E \Big[\{ y_{k+1} \} \{ y_{k} \}^{T} \Big]
= E \Big[(C \{ x_{k+1} \} + \{ v_{k+1} \}) \{ y_{k} \}^{T} \Big]
= E \Big[C \{ x_{k+1} \} \{ y_{k} \}^{T} \Big]
= CG$$
(12)

$$\begin{split} &\Lambda_{2} = E\Big[\{y_{k+2}\}\{y_{k}\}^{T}\Big] = E\Big[(C\{x_{k+2}\} + \{v_{k+2}\})\{y_{k}\}^{T}\Big] \\ &= E\Big[(C\{x_{k+2}\}\{y_{k}\}^{T}\Big] \\ &= CE\Big[\{x_{k+2}\}\{y_{k}\}^{T}\Big] \\ &= CE\Big[(A\{x_{k+1}\} + \{w_{k}\})\{y_{k}\}^{T}\Big] \\ &= CE\Big[A\{x_{k+1}\}\{y_{k}\}^{T}\Big] \\ &= CAE\Big[\{x_{k+1}\}\{y_{k}\}^{T}\Big] \\ &= CA^{2-1}G \end{split} \tag{13}$$

and

$$\Lambda_{i} = CA^{i-1}G \tag{14}$$

Defining a block Toeplitz $T_{1|i}$ as:

$$T_{l|i} = \begin{bmatrix} \Lambda_i & \Lambda_{i-1} & \cdots & \Lambda_1 \\ \Lambda_{i+1} & \Lambda_i & \cdots & \Lambda_2 \\ \vdots & \vdots & \vdots & \vdots \\ \Lambda_{2i-1} & \Lambda_{2i-2} & \cdots & \Lambda_i \end{bmatrix}$$
 (15)

one can infer from the definition of covariance matrix that $T_{1|i}$ can be expressed as the product of two block Hankel matrices Y_f and Y_p :

$$T_{1|i} = Y_f Y_p^T \tag{16}$$

where, Y_f and Y_p are composed of the 'future' and 'past' measurements, respectively:

$$Y_{f} = \frac{1}{\sqrt{j}} \begin{bmatrix} y_{i} & y_{i+1} & \cdots & y_{i+j-1} \\ y_{i+1} & y_{i+2} & \cdots & y_{i+j} \\ \vdots & \vdots & \vdots & \vdots \\ y_{2i-1} & y_{2i} & \cdots & y_{2i+j-2} \end{bmatrix} Y_{p} = \frac{1}{\sqrt{j}} \begin{bmatrix} y_{0} & y_{1} & \cdots & y_{j-1} \\ y_{1} & y_{2} & \cdots & y_{j} \\ \vdots & \vdots & \vdots & \vdots \\ y_{i-1} & y_{i} & \cdots & y_{i+j-2} \end{bmatrix}$$
(17)

Next, applying the factorization property to $T_{1\mid i}$ by the singular value decomposition yields:

$$T_{\parallel i} = USV^{T} = (U_{1} \ U_{2}) \begin{pmatrix} S_{1} & 0 \\ 0 & 0 \end{pmatrix} \begin{pmatrix} V_{1}^{T} \\ V_{2}^{T} \end{pmatrix} \approx U_{1}S_{1}V_{1}^{T}$$
(18)

Where:

 $U, S \text{ and } V = Orthonormal matrices}$

S = A diagonal matrix containing positive singular values in descending order

The number of nonzero singular values indicates the rank of the Toeplitz matrix. The reduced diagonal matrix S_1 is obtained by omitting the zero singular values from the matrix S. Matrices U_1 and V_1 are obtained by omitting the corresponding columns from the matrices U and V respectively. Now realizations of the system matrices are almost achieved. Matrix A is realized by using factorization of a shifted Toeplitz matrix $T_{2|i+1}$ that has similar structure as of $T_{1|i}$ but consists of covariance from lag 2-2i. In a manner similar to the classical Eigensystem Realization Algorithm (ERA in short), one can find:

$$A = O_i^+ T_{2i} \zeta_i = S_N^{-1/2} U^T T_{2i} V S_N^{-1/2}$$
(19)

where, N is model order, i.e., the maximum number of modes to be computed. Thus, the modal parameters can be determined by solving the eigenvalue problem of the state matrix A. By now, the theoretical formulation of covariance-driven SSI has been achieved.

According to Eq. 16-19, a different combination of i, j and N will give a different state matrix and thus a different pair of modal parameters. Therefore, modal parameters should be derived from a series of combinations, rather than a single combination. In the process of identification, N or i should be given in series for certain values of j in order to obtain a frequency stability chart. Solving the eigenvalue problem of the state matrix A by the pseudo-inverse method yields:

$$A = \Psi \Lambda_{d} \Psi^{-1}$$

$$\Phi = C \Psi$$
(20)

Where:

 Ψ = The complex eigenvector matrix

 Φ = The mode shape matrix

 $\Lambda = A$ diagonal matrix composed of the complex poles of the system

Different combinations of i, j and N are employed to derive the modal parameters statistically^[3,6].

Once the modal parameters are identified, the gross damping matrix C^e and the gross stiffness matrix K^e in Eq. 4 can be readily determined by the pseudo-inverse method:

$$[K^{e} C^{e}] = -M[\Phi \Lambda^{2} \Phi^{*} (\Lambda^{*})^{2}] \begin{bmatrix} \Phi & \Phi^{*} \\ \Phi \Lambda & \Phi^{*} \Lambda^{*} \end{bmatrix}^{\dagger}$$
(21)

where the superscript*denotes the complex conjugate of the corresponding term. Let:

$$\overline{C}^{e} = M^{-1}C^{e} \overline{K}^{e} = M^{-1}K^{e}$$

$$\overline{C} = M^{-1}C^{0} \overline{K} = M^{-1}K^{0}$$
(22)

where, C^0 and K^0 are the 'inherent' damping and stiffness matrices, respectively. Thus, the flutter derivatives can be extracted from the following equations:

$$\begin{split} &H_{1}^{*}(k_{_{h}})=-\frac{2m}{\rho B^{2}\omega_{_{h}}}(\overline{C}_{11}^{e}-\overline{C}_{11}), \quad A_{1}^{*}(k_{_{h}})=-\frac{2I}{\rho B^{3}\omega_{_{h}}}(\overline{C}_{21}^{e}-\overline{C}_{21})\\ &H_{2}^{*}(k_{_{\alpha}})=-\frac{2m}{\rho B^{3}\omega_{_{\alpha}}}(\overline{C}_{12}^{e}-\overline{C}_{12}), \quad A_{2}^{*}(k_{_{\alpha}})=-\frac{2I}{\rho B^{4}\omega_{_{\alpha}}}(\overline{C}_{22}^{e}-\overline{C}_{22})\\ &H_{3}^{*}(k_{_{\alpha}})=-\frac{2m}{\rho B^{3}\omega_{_{\alpha}}^{2}}(\overline{K}_{12}^{e}-\overline{K}_{12}), \quad A_{3}^{*}(k_{_{\alpha}})=-\frac{2I}{\rho B^{4}\omega_{_{\alpha}}^{2}}(\overline{K}_{22}^{e}-\overline{K}_{22})\\ &H_{4}^{*}(k_{_{h}})=-\frac{2m}{\rho B^{3}\omega_{_{h}}^{2}}(\overline{K}_{11}^{e}-\overline{K}_{11}), \quad A_{4}^{*}(k_{_{h}})=-\frac{2I}{\rho B^{4}\omega_{_{h}}^{2}}(\overline{K}_{21}^{e}-\overline{K}_{21}) \end{split}$$

Numerical simulation tests: In order to validate the applicability of the covariance-driven SSI technique in flutter derivatives estimation of bridge decks, numerical simulations of signals from different test methods are first carried out. The numerical tests included two syntheses but well controlled cases: two uncoupled degrees of freedom and two coupled degrees of freedom (simulated response including the motion induced aeroelastic terms). Both cases are first excited in the transient (i.e., free decay) motion and then by a white noise loading process. Measurement noises are also added by a white noise process with a standard deviation equal to 10% of the standard deviation of the original responses, in order to investigate the effect of measurement noise.

Two uncoupled degrees of freedom; free decay: Transient responses time-series were obtained by direct calculations of the displacement values for N = 4096 discrete time stations, with 'sampling' interval $\Delta t = 0.02$ sec (fs = 50 Hz). Structural modal properties used in this simulation were chosen from the previously tested sectional model of the Great Belt Bridge^[12]. The modal matrices are given per unit length as:

$$C_0 = \begin{bmatrix} 0.3616 & 0 \\ 0 & 0.0072 \end{bmatrix}, \quad K_0 = \begin{bmatrix} 397.0573 & 0 \\ 0 & 24.7315 \end{bmatrix}$$
$$M_0 = \begin{bmatrix} 2.6526 & 0 \\ 0 & 0.0189 \end{bmatrix}$$

i.e., $f_{ho} = 1.9472$ Hz, $f_{\theta0} = 5.7573$ Hz, $\xi_{h0} = 0.0053$, $\xi_{\theta0} = 0.0056$, where damping ratios, ξ , are representatives for the range of small amplitudes. The damping ratios were then multiplied in turn with 5, 10, 20 and 40, in order to cover the values of total damping (structural + aerodynamic) which could be presented in vibration of model section under wind flow. Values as high as $\xi = 0.2$ could be expected for the vertical degree of freedom under wind flow.

Frequency and damping ratio estimates are practically identical to the preset values (less than 0.5% for the highest damping case). The system matrices are also excellent even for the short useful signal case with only a few cycles of vibration motion. In the case where 10%-measurement noises were added, identified frequencies were changed at lesser than 0.8%. Damping ratios were changed at most by 2% except in the case of the lowest damping case which was 5.4%. The diagonal terms of the estimated system matrices (frequency and damping matrices) are also identical to the preset values. Estimates of diagonal terms are distorted within 1% except only for the case with lowest damping case in which values are within 2.82%.

Two coupled degrees of freedom; free decay and buffeting responses: The next step in the simulation was a simulation test with full effective stiffness and damping matrices (i.e., coupled degrees of freedom) and with lift and moment forces of the white noise type, as assumed in the SSI-method. For the mean-wind speed of 10.26 m sec⁻¹ and the aerodynamic derivatives assumed according to the values reported for a similar bridge cross-section^[12], the effective structural matrices were pre-set at:

$$C_{e} = \begin{bmatrix} 8.9308 & -0.0799 \\ 0.4345 & 0.0386 \end{bmatrix}, \quad K_{e} = \begin{bmatrix} 420.1002 & -59.1805 \\ 1.7552 & 19.6652 \end{bmatrix},$$

$$M_{0} = \begin{bmatrix} 2.6526 & 0 \\ 0 & 0.0189 \end{bmatrix}$$

The response time-series were simulated for both free decay and buffeting responses under turbulence wind with 10% turbulence intensity; then measurement white noises were superimposed on the simulated response. The free decay response time-series were computed by constant acceleration method and samples are as shown in Fig. 1. The SSI-COV method, applied

to these responses data, returned the effective structural matrices with the deviation from the pre-set ones (C and K) in percentage as:

$$\Delta C_{\%} = \begin{bmatrix} 0.66 & -3.00 \\ 0.16 & -0.26 \end{bmatrix}, \quad \Delta K_{\%} = \begin{bmatrix} -0.14 & -0.05 \\ 4.26 & -0.08 \end{bmatrix}$$

Superimposing 10% measurement white noise on the simulated response made the structural matrices differed from those of the noise-free cases within 3%. The response time-series were also simulated for the case of buffeting responses where wind turbulence is the only excited source. The effective stiffness and damping matrices were taken as in the case of transients; examples of response time-series are as shown in Fig. 2. Buffeting responses required longer data records (20,000 data points in the present study) as compared to that in the free decay case (4096 data points) to yield acceptable results. Estimates of the frequencies and damping ratios agree well with preset values where precisions are within 0.5 and 2%, respectively. The diagonal terms in stiffness and damping matrices also agree well with preset values where the differences are less than 1% except for the C₁₁ (related to vertical damping) where the difference is around 2.5%. The most differences in the off-diagonal terms are K_{21} and C_{21} which are related to A_4^* and H_2^* , respectively. In the case of 10%-measurement noise added, the deviation of the reconstructed matrices from the pre-set ones, in percentage, is:

$$\Delta C_{\%} = \begin{bmatrix} 8.55 & -27.86 \\ -0.28 & 0.5 \end{bmatrix}, \quad \Delta K_{\%} = \begin{bmatrix} 2.23 & -0.38 \\ -11.17 & -0.03 \end{bmatrix}$$

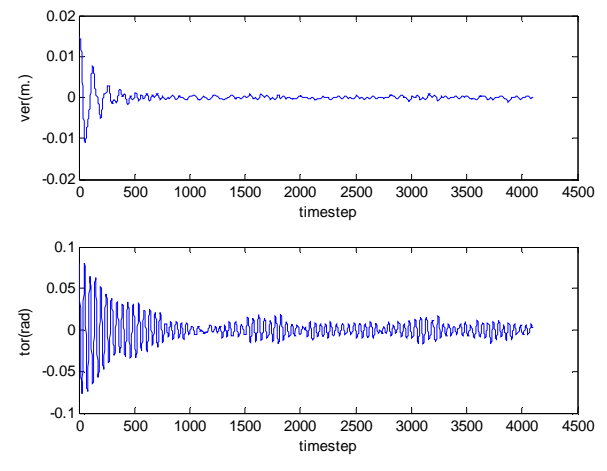


Fig. 1: Example of vertical (top) and torsional (bottom) transient responses simulated under wind flow

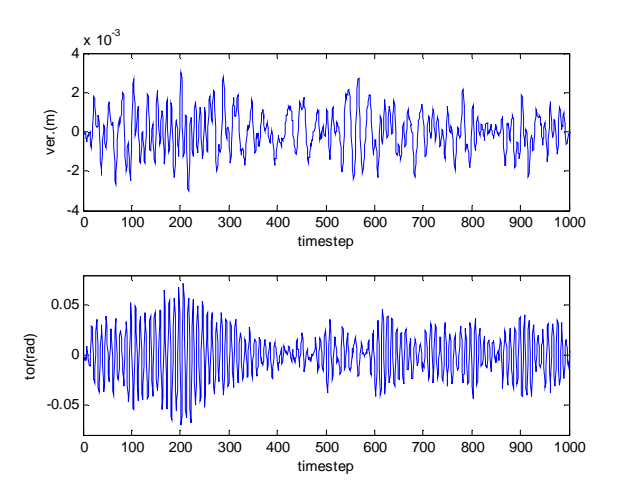


Fig. 2: Example of vertical (top) and torsional (bottom) buffeting responses simulated under wind flow



Fig. 3: IRR bridge model and grids to generate turbulent flow in wind tunnel

Wind tunnel tests: To evaluate further the applicability of the present method in flutter derivatives estimation of bridge decks, wind tunnel tests of a quasi-streamlined thin plate model and a two-edge girder type blunt bridge section model are performed.

Outlined of wind tunnel tests: The wind tunnel tests were performed in TU-AIT wind tunnel in Thammasat University. The working section of the wind tunnel has a width of 2.5 m, a height of 2.5 m and a length of 25.5 m. The required turbulent flow was generated by grids, as shown in Fig. 3. A hot-sphere anemometer was applied to measure the mean wind speed of the flow and a hot-wire anemometer was used to measure the fluctuations of wind speed. The longitudinal and vertical turbulence intensities are both less than 0.05% in case of smooth flow and about 8% in turbulence flow.



Fig. 4: Suspension device of the model

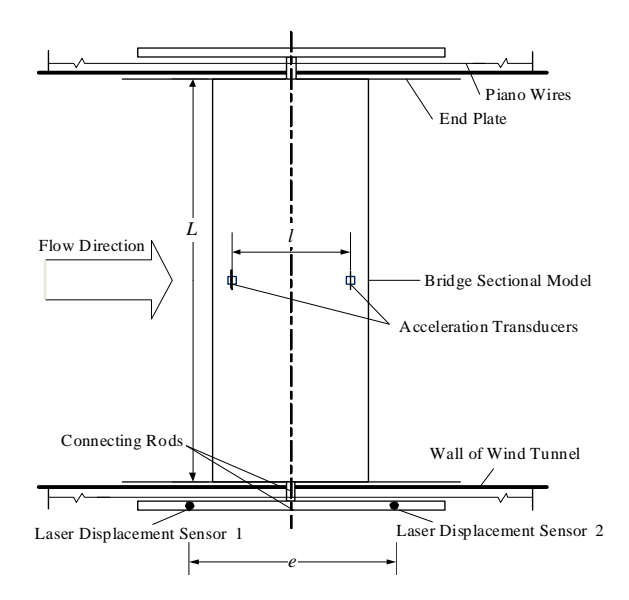


Fig. 5: Top view of the test setup

The model was suspended by eight springs outside the wind tunnel (Fig. 4). To simulate a bridge section model with 2DOFs, i.e. vertical bending and torsion, piano wires were used to prevent the motion of the model in longitudinal direction; this can be shown from Fig. 5, the schematic diagram of the top view of the test setup. Two piezoelectric acceleration transducers were mounted at the mid length of the model to capture the acceleration signals. The responses of the models were captured by the acceleration transducers and then the vertical and torsional responses can be respectively obtained by:

$$h = \frac{x_1 + x_2}{2}$$
, $\alpha = \frac{x_1 - x_2}{1}$ (24)

where, x_1 and x_2 are the measurements of transducers 1 and 2, respectively; 1 is the space between transducers.

RESULTS AND DISCUSSION

Case 1: Thin plate model under smooth flow: A quasi-streamlined thin plate (Fig. 6) was first selected for wind tunnel test. The width to height (thickness) ratio of the plate is about 22.5. Table 1 shows the main parameters of the model.

The extraction of flutter derivatives of the thin plate, using the SSI-COV technique, were performed on results from three types of tests, namely, (a) Single-Degree-Of-Freedom (SDOF) motion tests^[2], (b) free decay coupled-motion test (2DOFs) and (c) buffeting coupled-motion test (2DOFs). Typical test results showing responses from the bridge model are in Fig. 7 and 8. The responses for the free decay and the buffeting tests are sampled at the rates of 1000 and 200 Hz, respectively.

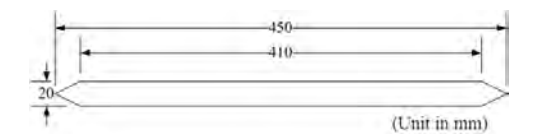


Fig. 6 Cross-section of the streamlined thin plate

Table 1: Main parameters of the thin plate model

Parameter	Mark	Unit	Value
Length	L	m	2.3000
Width	В	m	0.4500
Height	Н	m	0.0200
Mass per unit length	M	kg m ⁻¹	6.7391
Inertial moment of mass unit ⁻¹ length	I_{m}	$kg m^2 m^{-1}$	0.1183
Inertial radius	R	m	0.1325
First bending frequency	f_h, n_1	Hz	1.6500
First torsional frequency	f_{α} , n_2	Hz	2.7300
First torsion-bending frequency ratio	ε		1.6500

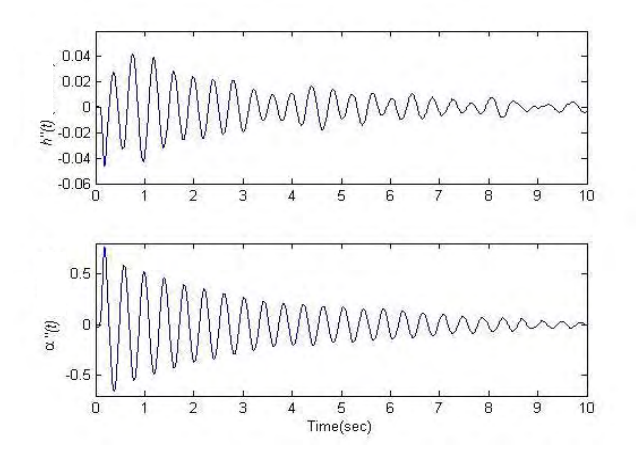


Fig. 7: Vertical (top) and torsional (bottom) free decay acceleration responses of the thin plate at 8.1 m sec⁻¹ wind speed under smooth flow. (Unit in g)

The results are then removed trend and re-sampled at 250 and 50 Hz, respectively. The covariance-driven SSI technique is applied to identify modal parameters from these data and a pseudo-inverse method is applied to estimate the stiffness and damping matrices. The flutter derivatives are estimated by Eq. 23 and reported in the form of Eq. 2 but without the factor 1/2.

Comparisons between SDOF and 2DOF-coupled-motion tests: free decay method: Figure 9 and 10 compare the flutter derivatives of the thin plate that are estimated by the SSI-COV technique using the above mentioned three test methods together with the Theodorsen's theoretical values^[13]. Unless otherwise noted, at any wind speed, H_1^* , H_4^* , A_1^* and A_4^* which are associated with the vertical motion were calculated using the frequency n_1 (lower). In addition, the derivatives H_2^* , H_3^* , A_2^* and A_3^* which are associated with the torsional motion were calculated using the frequency n_2 (higher).

The direct flutter derivatives H_1^* and H_4^* as found from the single-degree-of-freedom vertical-motion tests and A_2^* and A_3^* as found from the single-degree-of-freedom torsional-motion tests are also plotted and compared with those from the coupled-motion tests. The results are shown in Fig. 9 and 10. The near perfect match shows that the direct-flutter derivatives are indeed not affected by the motion along the other degree of freedom, as predicted by theory i.e., those flutter derivatives associated with h motion are not affected by α motion and vice versa. It also demonstrates the reliability of both the coupled-motion tests and the system identification method (SSI-COV).

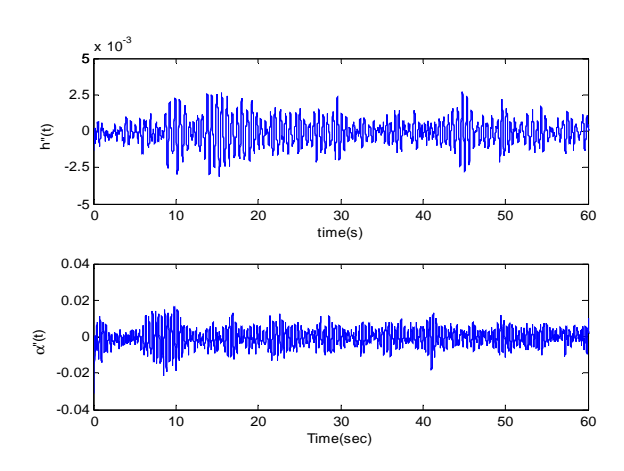


Fig. 8: Part of vertical (top) and torsional (bottom) buffeting acceleration responses of the thin plate at 5.6 m sec⁻¹ wind speed under smooth flow. (Unit in g)

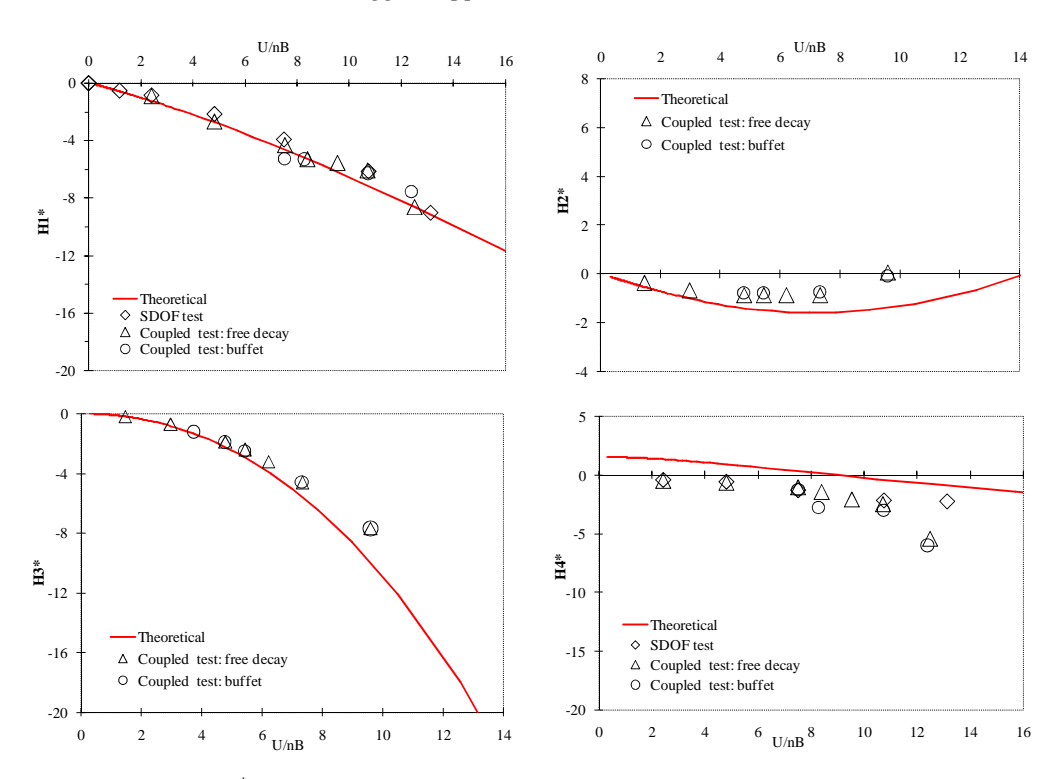


Fig. 9: Flutter derivatives (H_i^*) of the thin plate by SDOF test and coupled test by free decay and buffeting responses under smooth flow

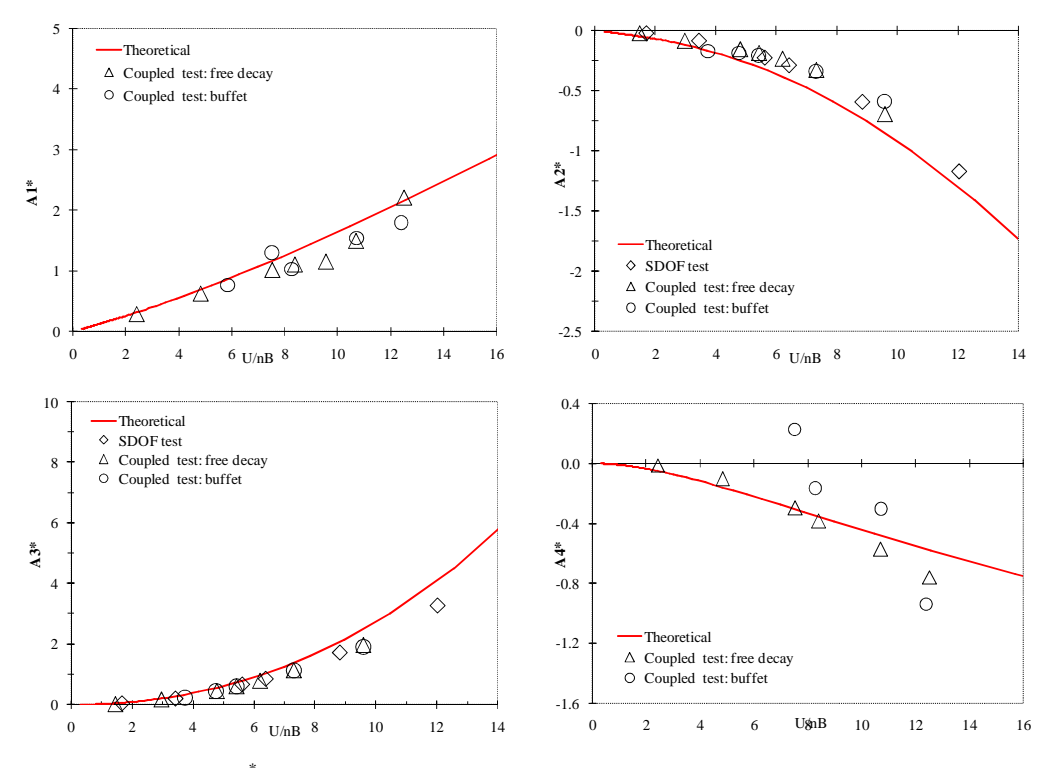


Fig. 10: Flutter derivatives (A_i^*) of the thin plate by SDOF test and coupled test by free decay and buffeting responses under smooth flow

Comparisons of coupled-2DOF motion tests between the free decay and the buffeting tests: The flutter derivatives found from both the free decay and the buffeting tests for the coupled-2DOF cases are compared in Fig. 9 and 10. The results show good agreement between the two methods. This validates the ability of the system identification method (SSI-COV) to apply with both the free decay and the buffeting tests although it was developed from a stochastic model (i.e., white noise loading assumption). However, when a relatively heavy model is excited at a very low reduced wind velocity, i.e., low wind energy, it becomes more difficult to extract the flutter derivatives from the buffeting responses.

The results also show that identified flutter derivatives agree well with the theoretical ones. The six important flutter derivatives $H_1^* \sim H_3^*$ and $A_1^* \sim A_3^*$ identified by SSI from different tests match well with theoretical values. The H_4^* derivatives are generally agreed in trend with theoretical values. However, the A_4^* , in turn, found from buffeting responses are more scattered compared to those from free decay responses. The impacts of the H_4^* and A_4^* derivatives, however, seem to be less significant when compared to those of other derivatives. This was the reason why H_4^* and A_4^* were usually neglected in previous studies $^{[2,3,5,10]}$.

Case 2: Section model of IRR Bridge: Encouraged by the success in the thin plate model, the flutter derivatives of IRR Bridge, a cable-supported bridge with 2-edge girder, as shown in Fig. 11, were estimated by the SSI-COV technique. The IRR Bridge has a main span of 398 m. The deck consists of a concrete deck slab and a web of steel girders. The deck is supported by two cable planes at outside edge girders. A 2-edge-girder bridge section with A-shape pylons has good cost performance, but at the same time the bridge cross-section is known to be aerodynamically unstable at high wind speed. Table 2 shows the main parameters of the prototype bridge and the section model. Tests were conducted under smooth and turbulence wind flow.

Using the SSI-COV technique, the flutter derivatives of the IRR Bridge were estimated for 2DOFs responses under smooth flow by both the free decay and the buffeting tests and under turbulence flow by the buffeting test only.

Comparisons of test method; Smooth flow: Figure 12 and 13 show the identified flutter derivatives of the bridge deck by free decay and buffeting responses under smooth flow and by buffeting responses under turbulent flow. The flutter derivatives are estimated by Eq. 23 and reported in the form of Eq. 2 but without the factor 1/2.

Table 2: Main parameters of the IRR Bridge model

Parameter	Mark	Unit	Prototype	Model
Length	L	m	-	2.2600
Width	В	m	35.9	0.3990
Height	H	m	3.20	0.0350
Mass per unit length	M	kg m ⁻¹	43000	5.6801
Inertial moment of	$I_{\rm m}$	$kg m^2 m^{-1}$	4.11×10^{9}	0.1726
mass unit-1 length				
First bending frequency	f_h, n_1	Hz	0.376	2.1300
First torsional frequency	f_{α} , n_2	Hz	0.850	4.7300
First torsion-bending-	ε		2.260	2.2200
frequency ratio				



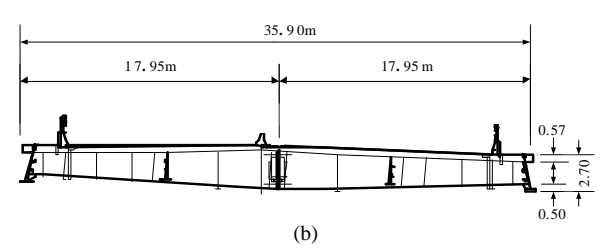




Fig. 11: (a): Three dimensional view of IRR Bridge; (b): Schematic cross-section of IRR Bridge; (c): IRR Bridge sectional model in wind tunnel

Generally, the flutter derivatives of the bridge in smooth flow identified by the SSI method from both the free decay and the buffeting tests are in good agreements.

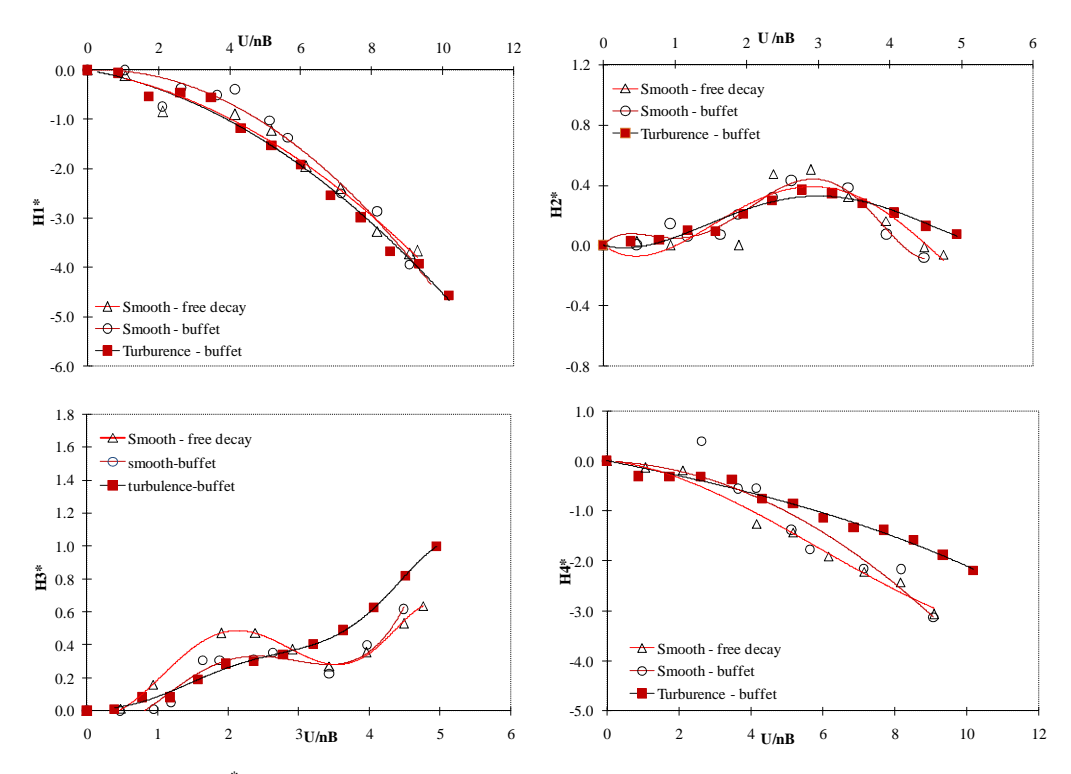


Fig. 12: Flutter derivatives (H_i^*) of the IRR Bridge by free decay and buffeting responses under smooth and turbulence flow

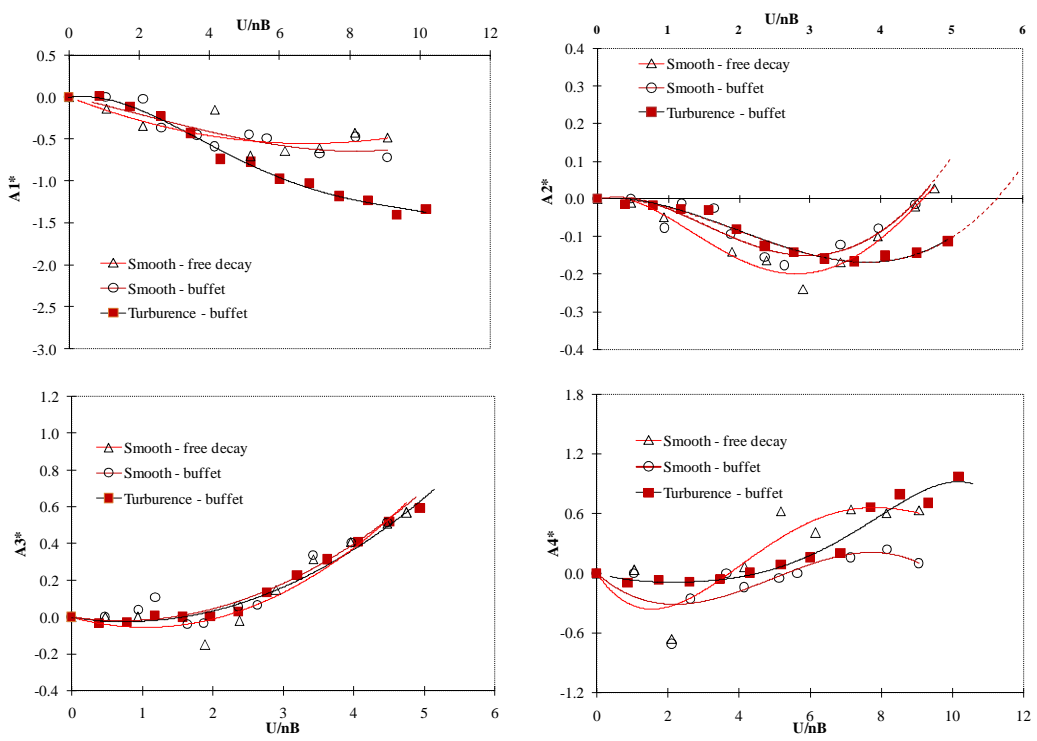


Fig. 13: Flutter derivatives (A_i^*) of the IRR Bridge by free decay and buffeting responses under smooth and turbulence flow

The difference of A_4^* identified from both tests, seems to be negligible as effect of this derivative is usually considered to be less significant. In smooth flow, the most important derivative A_2^* are steadily increased (more negative) up to the reduced wind velocity around 3 and then started to decrease. This sign reversal is the primary factor toward the SDOF-torsional instability ("stall flutter") for bluff type sections. The torsional flutter was found at the reduced wind speed around 4.7.

Effect of turbulence: Most of the prototype bridges are submerged in turbulent wind, therefore, detailed investigations of the effects of turbulence on the flutter derivatives is significant. Almost all the wind tunnel tests for flutter derivatives have been generally carried out in smooth flow. Although few researchers have studied the problem using wind tunnel tests, results and the identification methods were individually proposed^[4,14] and the results are still debatable and inconclusive. For streamlined section, tests showed little effect^[4,14], while tests on a rectangular box girder bridge showed galloping in smooth flow^[15].

From Fig. 12 and 13, it can be found that the influence of flow type on H_4^* and A_3^* , i.e., flutter derivatives related to direct aerodynamic stiffness, seems to be negligible. Though, the value of H₄* from turbulence flow is somewhat lesser than that in the smooth flow case, it affected only the second decimal digit of the frequency value. The influence also has negligible effect on H_1^* and H_2^* i.e., direct and cross derivatives related to vertical and torsional aerodynamic dampings, respectively. On the other hand, the more important A_1^* A_2^* and H_3^* , show rather noticeable deviations from those in smooth flow, especially at high reduced wind speeds. The most important effect is that the reduced wind speed corresponding to the reversed sign of the torsional aerodynamic damping A₂* increased in turbulent flow. It shows that turbulence tends to make bridges more aerodynamically stable by delaying torsional flutter. The deviations of flutter derivatives may reveal the fact that for those bridges with bluff type sections similar to IRR Bridge, the effects of turbulence can be significant. Hence, the wind tunnel tests of such bridges for flutter derivative estimation should be carried out in turbulent flow as well.

CONCLUSION

A theoretical model based on the covariance-driven SSI technique was proposed to extract the flutter derivatives of bridge deck sectional models from coupled two-degree-of-freedom system by free decay and buffeting responses. An advantage of the adopted SSI-COV technique is that it considers the buffeting forces and responses as inputs instead of as noises as typically assumed. The conclusions of this study are as follows:

- Numerical simulations of bridge deck responses confirmed that the SSI-COV technique can be used to estimate flutter derivatives from buffeting and free decay responses with reliable results. This shows the applicability of the SSI-COV method with various test techniques, though it was developed from a stochastic model
- For the thin plate model under smooth flow, wind tunnel tests showed that flutter derivatives identified by the SSI technique from both the free decay and the buffeting tests matched well with theoretical values. Although there are some variations in the values of A₄* obtained from the buffeting test, this derivative is considered as insignificant and is usually neglected in most of the previous studies
- When apply to the bluff section model of the IRR Bridge under smooth flow, the flutter derivatives estimated from the buffeting test agreed with those obtained from the free decay test. This result allowed focusing on applying the SSI-COV technique to the buffeting test method. There are variations in the values of the A₄* derivative as obtained from the two test methods but they agree in trend. We also observed the sign reversal of the A₂* derivative as the reduced wind speed reached the value of 4.7. This indicates that this bridge section is susceptible to flutter instability at high wind speed
- The test result of bluff section model of the IRR Bridge under turbulence wind revealed that the most important and positive effect of the turbulence is that it tends to make the bridge more aerodynamically stable by delaying the sign reversal of the aerodynamic damping A_2^* . This may help explain that for those bridges with bluff type sections similar to the IRR Bridge, the effects of turbulence can be significant. Hence, the wind tunnel tests of such bridges for flutter derivatives estimation should be carried out in turbulent flow as well

Applying the proposed SSI-COV technique to the buffeting test yields a straightforward, cost effective and reliable system identification process that can be used to identify flutter derivatives of various bridge decks. It, however, has some limitations. For example, it becomes more difficult to extract the flutter

derivatives from the buffeting responses in the situation when a relatively heavy model is excited at a very low reduced wind velocity, i.e., low wind energy. In this case, using the SSI-COV technique with the free decay method will yield more accurate results.

ACKNOWLEDGEMENT

The researchers would like to greatly acknowledge the Thailand Research Fund (TRF) under grant number RMU 4980012 for financial supports. In addition, the authors are greatly thanked to Mr. T. Worapoj, graduate students of Thammast University, for his assistant in wind tunnel tests.

REFERENCES

- Chen, Z.Q. and X.D. Yu, 2002. A new method for measuring flutter self-excited forces of long-span bridges. China Civil Eng. J., 35: 34-41. www.cces.net.cn/eng/
- Scanlan, R.H., 1971. Airfoil and bridges deck flutter derivatives. J. Eng. Mech. ASCE., 97: 1717-1733. http://cedb.asce.org/cgi/WWWdisplay.cgi?7100095
- Poulsen, N.K., A. Damsgaard and T.A. Reinhold, 1992. Determination of flutter derivatives for the great belt bridge. J. Wind Eng. Ind. Aerodyn., 41: 153-164. http://www2.imm.dtu.dk/pubdb/views/publication_ details.php?id=2609
- Sarkar, P.P., N. Jones and R.H. Scanlan, 1994. Identification of aeroelastic parameters of flexible bridges. J. Eng. Mech. ASCE., 120: 1718-1741. DOI: 10.1061/(ASCE)0733-9399(1994)120:8(1718))
- Gu, M., R.X. Zhang and H. Xiang, 2000. Identification of flutter derivatives of bridge decks. J Wind. Eng. Ind. Aerodyn., 84: 151-162. DOI: 10.1016/S0167-6105(99) 00051-3
- Juang, J.N. and R.S. Pappa, 1985. An eigensystem realization algorithm for modal parameter identification and model reduction. J. Guidance Control Dynam, 85: 620-627. http://www.aiaa.org/content.cfm?pageid=406&gTa ble=japaperimportPre97&gID=20031

- Overschee, P.V., 1991. Subspace algorithms for the stochastic identification problem. Proceeding of the 30th Conference on Decision and Control, Dec. 11-13, Brighton, England, pp. 1321-1326. DOI: 10.1109/CDC.1991.261604
- 8. Peeters, B., 1999. Reference-based stochastic subspace identification for out-put only modal analysis. Mech. Syst. Signal Process., 13: 855-878. DOI: 10.1006/mssp.1999.1249
- Gu, M. and X.R. Qin, 2004. Direct identification of flutter derivatives and aerodynamic admittances of bridge decks. Eng. Struct., 26: 2161-2172 http://cat.inist.fr/?aModele=afficheN&cpsidt=1631 5034
- Scanlan, R.H., 1977. Motion of suspended bridge spans under gusty wind. J. Struct. Divis. ASCE., 103: 1867-1883.
 - http://cedb.asce.org/cgi/WWWdisplay.cgi?5013222
- 11. Simiu, E. and R.H. Scanlan, 1996. Wind Effects on Structures. 3rd Edn., John Wiley, New Jersey. ISBN: 10: 0471121576, pp: 704.
- 12. Jakobsen, J.B. and E. Hjorth-Hansen, 1995. Determination of the aerodynamic derivatives by a system identification method. J. Wind. Eng. Ind. Aerodyn., 57: 295-305. http://cat.inist.fr/?aModele=afficheN&cpsidt=3648469
- 13. Dyrbye, C. and S.O. Hansen, 1996. Wind Loads on Structures. John Wiley, New Jersey. http://as.wiley.com/WileyCDA/
- ScanLan, R.H. and W.H. Lin, 1978. Effects of turbulence on bridge flutter derivatives. J. Eng. Mech. ASCE., 104: 719-733. http://cedb.asce.org/cgi/WWWdisplay.cgi?5013939
- Jakobsen, J.B. and E. Hjorth-Hansen, 1998.
 Aeroelasticic effects on a rectangular box-girder bridge. J. Wind. Eng. Ind. Aerodyn., 74-76: 819-827.
 DOI: 10.1016/S0167-6105(98)00074-9

Proceeding in Seventh Asia-Pacific Conference on Wind Engineering

Taipei, Taiwan, 2009



IDENTIFICATION OF FLUTTER DERIVATIVES OF BRIDGE DECKS BY STOCHASTIC SUBSPACE METHOD

Virote Boonyapinyo¹, Tharach Janesupasaeree² and Worapoj Thamasungkeeti³

¹ Associate Professor, Department of Civil Engineering, Thammasat University, Rangsit Campus, Pathumthani, Thailand 12120, bvirote@engr.tu.ac.th
² Toyo-Thai Corporation Public Company Limited, North Klongtoey, Wattana, Bangkok, Thailand, 10110, tharach.j@toyo-thai.com
³ Graduated Student, Department of Civil Engineering, Thammasat University, Rangsit Campus, Pathumthani, Thailand 12120, tworapoj@gmail.com

ABSTRACT

Flutter derivatives are the essential parameters in the estimations of the critical wind velocity for flutter-instability and the responses of long-span cable supported bridges. These derivatives can be experimentally estimated from wind tunnel tests results. Most of previous studies have used deterministic system identification techniques, in which buffeting forces and responses are considered as noises. In this paper, the covariance-driven stochastic subspace identification technique (SSI-COV) was presented to extract the flutter derivatives of bridge decks from the buffeting test results. An advantage of this method is that it considers the buffeting forces and responses as inputs rather than as noises. The Industrial Ring Road (IRR) cable-stayed bridge crossed Chao Phraya River with main span of 398m was applied for 1:90 scale sectional model test in TU-AIT wind tunnel test as the study case. Wind tunnel tests were performed for four section bridge models, i.e. original section, fairing-modified section, soffit plate modified section, and combination of those two modified section. The results found that the original section result in high vortex-shedding response and lead to a single torsional flutter at high wind velocity. The results also indicated that the combined fairing and soffit plate modified section is the most aerodynamic shape.

KEYWORDS: FLUTTER DERIVATIVES, STOCHASTIC SUBSPACE METHOD, CABLE-STAYED BRIDGE, AERODYNAMIC APPENDAGES

Introduction

Long-span cable supported bridges are highly susceptible to wind excitation because of their inherent flexibility and low structural damping. Wind loads play an important role in the design of these structures. In the most previous studies, flutter derivatives were estimated by deterministic system identification techniques that can be applied to the free decay method only. Examples of previous deterministic system identification that were applied to the free decay method included Scanlan's method [Scanlan (1971)], Modified Ibrahim method (MITD) [Sarkar *et al.* (1994)], and Unified Least Square method [Gu *et al.* (2000)]. In these system identification techniques, the buffeting forces and their responses are regarded as external noises, the identification process then requires many iteration [Sarkar *et al.* (1994) and Gu *et al.* (2000)]. Moreover, at high reduced wind speed, the vertical bending motion of the structure will decay rapidly due to the effect of the positive vertical aerodynamic damping, and thus the length of decaying time history available for system identification will decrease.

If the stochastic system identification technique [Overschee (1991), Peeters (1999) and Gu *et al.* (2004)] is employed to estimate the flutter derivatives of bridge deck from their steady random responses under the action of turbulent wind, the above-mentioned short coming of the deterministic system identification technique can be overcame. The reason is

that the random aerodynamic loads are regarded as inputs rather than noises, which are more coincident with the fact. Therefore, the signal-to-noise ratio is not affected by wind speed, and the flutter derivatives at high reduced wind speeds are more readily available. These aspects give the stochastic system identification methods an advantage over the deterministic system identification.

Vibration control of long-span bridges have been widely manufactured by aerodynamic appendages. The investigations of aerodynamic appendages have been considered in an effort to suppress the oscillation in the real bridges [Houston *et al.* (1988) and Sakai *et al.* (1993)]. Many tried to modify the deck shape neighborhood to ideal flat plate model. The illustrations, among others, are Bronx-Whitestone Bridge and Deer Isle Bridge [Bosch (1990)], which recognized as an achievement for fairing-modified section.

In this paper, the covariance-driven stochastic subspace identification technique (SSI-COV) was presented to extract the flutter derivatives from random responses (buffeting) under the action of smooth wind. The two-edge girder type blunt section model of Industrial Ring Road Bridge (IRR in short, Fig. 1), a cable stayed bridge with a main span of 398m, Thailand, was tested in smooth flow. Wind tunnel tests were performed for four section bridge models, i.e. original section, fairing-modified section, soffit plate modified section and combination of those two modified section. Tests were conducted in TU-AIT Boundary Layer Wind Tunnel in Thammasat University, the longest and the largest wind tunnel in Thailand.

Theoretical Formulation of Covariance-driven Stochastic Subspace Identification

Flutter and Buffeting Forces

The dynamic behavior of a bridge deck with two degrees-of-freedom (DOF in short), i.e. h (bending) and α (torsion), in turbulent flow can be described by the following differential equations [Scanlan (1971) and Gu *et al.* (2004)]



Figure 1: Three-dimensional view of IRR cable-stayed bridge

$$\begin{split} m \left[\ddot{h}(t) + 2\xi_{h} \omega_{h} \dot{h}(t) + \omega_{h}^{2} h(t) \right] &= L_{se}(t) + L_{b}(t) \\ I \left[\ddot{\alpha}(t) + 2\xi_{\alpha} \omega_{\alpha} \dot{\alpha}(t) + \omega_{\alpha}^{2} \alpha(t) \right] &= M_{se}(t) + M_{b}(t) \end{split} \tag{1}$$

where m and I are the mass and mass moment of inertia of the deck per unit span, respectively; ω_i is the natural circular frequency; ξ_i is the modal damping ratio $(i=h,\alpha)$; L_{se} and M_{se} are the self-excited lift and moment, respectively; while L_b and M_b are the aerodynamic lift and moment. The self-excited lift and moment are given as follows:

$$L_{se}(t) = \frac{1}{2} \rho U^{2} B \left[K_{h} H_{1}^{*}(K_{h}) \frac{\dot{h}}{U} + K_{\alpha} H_{2}^{*}(K_{\alpha}) \frac{B\dot{\alpha}}{U} + K_{\alpha}^{2} H_{3}^{*}(K_{\alpha}) \alpha + K_{h}^{2} H_{4}^{*}(K_{h}) \frac{h}{B} \right]$$

$$M_{se}(t) = \frac{1}{2} \rho U^{2} B^{2} \left[K_{h} A_{1}^{*}(K_{h}) \frac{\dot{h}}{U} + K_{\alpha} A_{2}^{*}(K_{\alpha}) \frac{B\dot{\alpha}}{U} + K_{\alpha}^{2} A_{3}^{*}(K_{\alpha}) \alpha + K_{h}^{2} A_{4}^{*}(K_{h}) \frac{h}{B} \right]$$

$$(2)$$

where ρ is air mass density; B is the width of the bridge deck; U is the mean wind speed at the bridge deck level; $k_i = \omega_i B/U$ is the reduced frequency $(i=h,\alpha)$; and H_i^* and A_i^* (i=1,2,3,4) are the so-called flutter derivatives, which can be regarded as the implicit functions of the deck's modal parameters. The alternate form of self-excited forces is as Eq. (2) but without the factor 1/2. The aerodynamic lift and moment can be defined as [Simiu & Scanlan (1996)]

$$L_{b}(t) = \frac{1}{2} \rho U^{2} B \left[2C_{L} \frac{u(t)}{U} \chi_{L}(t) + (C'_{L} + C_{D}) \frac{w(t)}{U} \chi_{L}(t) \right]$$

$$M_{b}(t) = \frac{1}{2} \rho U^{2} B^{2} \left[2C_{M} \frac{u(t)}{U} \chi_{M}(t) + (C'_{M}) \frac{w(t)}{U} \chi_{M}(t) \right]$$
(3)

where C_L , C_D and C_M are the steady aerodynamic force coefficients; C'_L and C'_M are the derivatives of C_L and C_M with respect to the attack angles, respectively; u(t) and w(t) are the longitudinal and vertical fluctuations of wind speed, respectively; χ_L and χ_M are the lift and moment aerodynamic admittances of the bridge deck. By moving L_{se} and M_{se} to the left side, and merging the congeners into column vectors or matrices, Eq. (1) can be rewritten as follows

$$[M]\{\ddot{y}(t)\} + [C^e]\{\dot{y}(t)\} + [K^e]\{y(t)\} = \{f(t)\}$$

$$\tag{4}$$

where $\{y(t)\} = \{h(t) \ \alpha(t)\}^T$ is the generalized buffeting response; $\{f(t)\} = \{L_b(t) \ M_b(t)\}^T$ is the generalized aerodynamic force; [M] is the mass matrix; $[C^e]$ is the gross damping matrix, i.e. the sum of the mechanical and aerodynamic damping matrices; and $[K^e]$ is the gross stiffness matrix.

Stochastic State Space Models

The fluctuations of wind speed u(t) and w(t) in Eq. (3) are random functions of time, so the identification of flutter derivatives of bridge decks can be simplified as a typical inverse problem in the theory of random vibration, and thus can be solved by the stochastic system identification techniques. Let

$$[A_c] = \begin{bmatrix} O & I \\ -M^{-1}K^e & -M^{-1}C^e \end{bmatrix}, [C_c] = [I \quad O] \text{ and } \{x\} = \begin{cases} y \\ \dot{y} \end{cases}$$
 (5)

Eq. (4) is then transformed into the following stochastic state equations in discrete form as

$$\{\dot{x}_{k+1}\} = [A]\{x_k\} + \{w_k\} \text{ and } \{y_k\} = [C]\{x_k\} + \{v_k\}$$
 (6)

where $[A]_{4\times4}$, $[C]_{2\times4}$ and $\{x\}$ are known as state matrix, output shape matrix and state vector, respectively; $\{w_k\}$ and $\{v_k\}$ are the input and output noise sequences, respectively. Subscript *k denotes the value of * at time $k\Delta t$, where Δt means the sampling interval. O and I are the zero and identity matrices, respectively. It is assumption of stochastic model that $\{x_k\}$, $\{w_k\}$ and $\{v_k\}$ are mutually independent and hence

$$E[x_{\nu}w_{\nu}^{\mathrm{T}}] = \mathbf{0} \quad E[x_{\nu}v_{\nu}^{\mathrm{T}}] = \mathbf{0} \tag{7}$$

Defining

$$\Sigma = E[x_k x_k^T] \quad Q = E[w_k w_k^T] \quad \Lambda_i = E[y_{k+1} y_k^T] \quad G = E[x_{k+1} y_k^T] \quad R = E[v_k v_k^T] \quad \text{and} \quad S = E[w_k v_k^T] \quad (8)$$

and combining Eqs. (7) and (8) we obtain the following Lyapunov equations for the state and output covariance matrices

$$\Sigma = A\Sigma A^{T} + Q \qquad \Lambda_{0} = C\Sigma C^{T} + R \quad \text{and} \quad G = A\Sigma C^{T} + S$$
 (9)

From (6) and (7), it can be deduced

$$\Lambda_i = CA^{i-1}G \tag{10}$$

Covariance-driven Stochastic State Space Identification

The main algorithm of SSI-COV proceeds with defining a covariance block Toeplitz

as
$$T_{1|i} = \begin{bmatrix} \Lambda_i & \Lambda_{i-1} & \cdots & \Lambda_1 \\ \Lambda_{i+1} & \Lambda_i & \cdots & \Lambda_2 \\ \vdots & \vdots & \vdots & \vdots \\ \Lambda_{2i-1} & \Lambda_{2i-2} & \cdots & \Lambda_i \end{bmatrix}$$
(11)

one can infer from the definition of covariance matrix that $T_{\parallel i}$ can be expressed as the product of two block Hankel matrices Y_f and Y_p as $T_{1|i} = Y_f Y_p^T$ where Y_f and Y_p are composed of the 'future' and 'past' measurements, respectively.

$$Y_{f} = \frac{1}{\sqrt{j}} \begin{bmatrix} y_{i} & y_{i+1} & \cdots & y_{i+j-1} \\ y_{i+1} & y_{i+2} & \cdots & y_{i+j} \\ \vdots & \vdots & \vdots & \vdots \\ y_{2i-1} & y_{2i} & \cdots & y_{2i+j-2} \end{bmatrix} \qquad Y_{p} = \frac{1}{\sqrt{j}} \begin{bmatrix} y_{0} & y_{1} & \cdots & y_{j-1} \\ y_{1} & y_{2} & \cdots & y_{j} \\ \vdots & \vdots & \vdots & \vdots \\ y_{i-1} & y_{i} & \cdots & y_{i+j-2} \end{bmatrix}$$
(12)

Next, applying the factorization property to $T_{\parallel i}$ by the singular value decomposition yields

$$T_{\parallel i} = USV^{T} = (U_{1} \ U_{2}) \begin{pmatrix} S_{1} & 0 \\ 0 & 0 \end{pmatrix} \begin{pmatrix} V_{1}^{T} \\ V_{2}^{T} \end{pmatrix} \approx U_{1} S_{1} V_{1}^{T}$$
(13)

where U, S and V are orthonormal matrices. S is a diagonal matrix containing positive singular values in descending order. The number of nonzero singular values indicates the rank of the Toeplitz matrix. The reduced diagonal matrix S_1 is obtained by omitting the zero singular values from the matrix S. Matrices U_1 and V_1 are obtained by omitting the corresponding columns from the matrices U and V respectively. Now realizations of the system matrices are almost achieved. Matrix A is realized by using factorization of a shifted Toeplitz matrix $T_{2|i+1}$ that has similar structure as of $T_{1|i}$ but consists of covariance from lag 2 to 2i. In a manner similar to the classical eigensystem realization algorithm (ERA in short), one can find

$$A = o_i^{\dagger} T_{2|i} \zeta_i = S_N^{-1/2} U^{\mathsf{T}} T_{2|i} V S_N^{-1/2}$$
(14)

where N is model order, i.e. the maximum number of modes to be computed. Thus, the modal parameters can be determined by solving the eigenvalue problem of the state matrix A. By now, the theoretical formulation of covariance-driven SSI has been achieved.

According to Equations (12)-(14), a different combination of i, j and N will give a different state matrix, and thus a different pair of modal parameters. Therefore, modal parameters should be derived from a series of combinations, rather than a single combination. In the process of identification, N or i should be given in series for certain values of j in order to obtain a frequency stability chart. Solving the eigenvalue problem of the state matrix A by the pseudo-inverse method yields

$$A = \Psi \Lambda_{\lambda} \Psi^{-1} \quad \text{and} \quad \Phi = C \Psi \tag{15}$$

where Ψ is the complex eigenvector matrix, Φ is the mode shape matrix, and Λ is a diagonal matrix composed of the complex poles of the system. Different combinations of i, j and N are employed to derive the modal parameters statistically.

Once the modal parameters are identified, the gross damping matrix C^e and the gross stiffness matrix K^e in Eq. (4) can be readily determined by the pseudo-inverse method

$$[K^e \ C^e] = -M[\Phi \Lambda^2 \ \Phi^* (\Lambda^*)^2] \begin{bmatrix} \Phi & \Phi^* \\ \Phi \Lambda & \Phi^* \Lambda^* \end{bmatrix}^{\dagger}$$
(16)

where the superscript * denotes the complex conjugate of the corresponding term. Let

$$\overline{C}^{e} = M^{-1}C^{e} \qquad \overline{C} = M^{-1}C^{0} \qquad \overline{K}^{e} = M^{-1}K^{e} \qquad \overline{K} = M^{-1}K^{0}$$
(17)

 $\overline{C}^e = M^{-1}C^e$ $\overline{C} = M^{-1}C^0$ $\overline{K}^e = M^{-1}K^e$ $\overline{K} = M^{-1}K^0$ (17) where C^0 and K^0 are the 'inherent' damping and stiffness matrices, respectively. Thus, the flutter derivatives can be extracted from the following equations

$$H_{1}^{*}(k_{h}) = -\frac{2m}{\rho B^{3} \overline{\varpi}_{h}} (\overline{C_{11}^{e}} - \overline{C_{11}^{0}}) \qquad H_{2}^{*}(k_{a}) = -\frac{2m}{\rho B^{3} \overline{\varpi}_{a}} (\overline{C_{12}^{e}} - \overline{C_{12}^{0}}) \qquad H_{3}^{*}(k_{a}) = -\frac{2m}{\rho B^{3} \overline{\varpi}_{a}^{2}} (\overline{K_{12}^{e}} - \overline{K_{12}^{0}}) \qquad H_{4}^{*}(k_{h}) = -\frac{2m}{\rho B^{3} \overline{\varpi}_{h}^{2}} (\overline{K_{11}^{e}} - \overline{K_{11}^{0}}) \qquad H_{4}^{*}(k_{h}) = -\frac{2m}{\rho B^{3} \overline{\varpi}_{h}^{2}} (\overline{K_{12}^{e}} - \overline{K_{12}^{0}}) \qquad A_{1}^{*}(k_{h}) = -\frac{2I}{\rho B^{4} \overline{\varpi}_{h}^{2}} (\overline{C_{21}^{e}} - \overline{C_{21}^{0}}) \qquad A_{2}^{*}(k_{a}) = -\frac{2I}{\rho B^{4} \overline{\varpi}_{h}^{2}} (\overline{K_{22}^{e}} - \overline{K_{22}^{0}}) \qquad A_{3}^{*}(k_{a}) = -\frac{2I}{\rho B^{4} \overline{\varpi}_{h}^{2}} (\overline{K_{21}^{e}} - \overline{K_{21}^{0}}) \qquad A_{4}^{*}(k_{a}) = -\frac{2I}{\rho B^{4} \overline{\varpi}_{h}^{2}} (\overline{K_{21}^{e}} - \overline{K_{21}^{0}}) \qquad A_{4}^{*}(k_{a}) = -\frac{2I}{\rho B^{4} \overline{\varpi}_{h}^{2}} (\overline{K_{21}^{e}} - \overline{K_{21}^{0}}) \qquad A_{4}^{*}(k_{a}) = -\frac{2I}{\rho B^{4} \overline{\varpi}_{h}^{2}} (\overline{K_{21}^{e}} - \overline{K_{21}^{0}}) \qquad A_{4}^{*}(k_{a}) = -\frac{2I}{\rho B^{4} \overline{\varpi}_{h}^{2}} (\overline{K_{21}^{e}} - \overline{K_{21}^{0}}) \qquad A_{4}^{*}(k_{a}) = -\frac{2I}{\rho B^{4} \overline{\varpi}_{h}^{2}} (\overline{K_{21}^{e}} - \overline{K_{21}^{0}}) \qquad A_{4}^{*}(k_{a}) = -\frac{2I}{\rho B^{4} \overline{\varpi}_{h}^{2}} (\overline{K_{21}^{e}} - \overline{K_{21}^{0}}) \qquad A_{4}^{*}(k_{a}) = -\frac{2I}{\rho B^{4} \overline{\varpi}_{h}^{2}} (\overline{K_{21}^{e}} - \overline{K_{21}^{0}}) \qquad A_{4}^{*}(k_{a}) = -\frac{2I}{\rho B^{4} \overline{\varpi}_{h}^{2}} (\overline{K_{21}^{e}} - \overline{K_{21}^{0}}) \qquad A_{4}^{*}(k_{a}) = -\frac{2I}{\rho B^{4} \overline{\varpi}_{h}^{2}} (\overline{K_{21}^{e}} - \overline{K_{21}^{0}}) \qquad A_{4}^{*}(k_{a}) = -\frac{2I}{\rho B^{4} \overline{\varpi}_{h}^{2}} (\overline{K_{21}^{e}} - \overline{K_{21}^{0}}) \qquad A_{4}^{*}(k_{a}) = -\frac{2I}{\rho B^{4} \overline{\varpi}_{h}^{2}} (\overline{K_{21}^{e}} - \overline{K_{21}^{0}}) \qquad A_{4}^{*}(k_{a}) = -\frac{2I}{\rho B^{4} \overline{\varpi}_{h}^{2}} (\overline{K_{21}^{e}} - \overline{K_{21}^{0}}) \qquad A_{4}^{*}(k_{a}) = -\frac{2I}{\rho B^{4} \overline{\varpi}_{h}^{2}} (\overline{K_{21}^{e}} - \overline{K_{21}^{0}}) \qquad A_{4}^{*}(k_{a}) = -\frac{2I}{\rho B^{4} \overline{\varpi}_{h}^{2}} (\overline{K_{21}^{e}} - \overline{K_{21}^{0}}) \qquad A_{4}^{*}(k_{a}) = -\frac{2I}{\rho B^{4} \overline{\varpi}_{h}^{2}} (\overline{K_{21}^{e}} - \overline{K_{21}^{0}}) \qquad A_{4}^{*}(k_{a}) = -\frac{2I}{\rho B^{4} \overline{\varpi}_{h}^{2}} (\overline{K_{21}^{e}} - \overline{K_{21}^{0}}) \qquad A_{4}^{*}(k_{a}) = -\frac{2I}{\rho B^{4} \overline{\varpi}_{h}^{2}} (\overline{K_{21}^{e}} - \overline{K_{21}^{0}}) \qquad A_$$

Outline of Wind Tunnel Tests

The wind tunnel tests were performed in TU-AIT wind tunnel in Thammasat University. The working section of the wind tunnel has a width of 2.5 m, a height of 2.5 m and a length of 25.5 m. A hot-sphere anemometer was applied to measure the mean wind speed of the flow, and a hot-wire anemometer was used for a measurement of wind fluctuations. The longitudinal and vertical turbulence intensities are both less than 0.05%. All main parameters of IRR bridge model and prototype are shown in Table 1.

The sectional bridge model of IRR cable-stayed bridge in wind tunnel is shown in Fig. 2. To simulate a bridge section model with 2DOFs, i.e. vertical bending and torsion, piano wires were used to prevent the motion of the model in longitudinal direction. Two piezoelectric acceleration transducers are located at mid-span of a model, placed on both sides by an equal distance from the center of rotation, to capture the acceleration signals.

Besides, two laser displacement sensors were mounted on both two sides of dynamic arms for displacement acquisitions. The responses of the models were captured by the sensors, and then the vertical and torsional responses can be respectively obtained by $h = (x_1+x_2)/2$ and $\alpha = (x_1-x_2)/l$, whereas x_1 and x_2 are the measurements of sensors 1 and 2, respectively and l represents the space between transducers.

To increase the aerodynamic stability of IRR cable-stayed bridge, wind tunnel tests were performed for original section bridge model (Fig. 2) and three types of aerodynamic appendages, i.e., fairing-modified section, soffit plate modified section, and combination of those two modified section (Fig. 3). Fairing height of 29.9 mm is designed to fit the bridge model with the upper and lower slope angles of 30°. The equilateral triangle fairings made from hard paper were mounted to a model, in both windward and leeward side. Soffit plates were mounted under the model with an intention to smoothen the wind attack to model's girders.

Table 1 Main parameters of the IRR Bridge

Parameter	Notation	Unit	Prototype	Model
Length	L	m	-	2.26
Width	B	m	35.9	0.399
Height	H	m	3.20	0.035
Mass per unit length	M	kg/m	43000	5.6801
Inertial moment of mass per unit length	I_m	$kg m^2 / m$	$4.11x10^9$	0.1726
First bending frequency	f_h	Hz	0.376	2.13
First torsional frequency	f_{lpha}	Hz	0.850	4.73
First torsion-bending-frequency ratio	${\cal E}$		2.26	2.22

Results of Wind Tunnel Test

Flutter Derivatives

The aerodynamic derivatives were calculated for each wind speed as the average value of 10 tests at each velocity. Flutter derivatives of four sections are presented and compared in Fig. 4. The most important terms are H_1^* and A_2^* which refer respectively on vertical and torsional damping of the section. Their positive values indicate unstable conditions. For vertical aerodynamic damping coefficient, H_1^* , the modification effects considered to be negligible, which all sections show in negative region. However, the section are influenced by the modifications in A_2^* which is most considerable in long-span bridges.



Figure 2: Original section of IRR bridge in wind tunnel

Figure 3: Fairings and soffit plates modified section in wind tunnel

Fig. 4 shows that the original section and fairing modified section lead to a single torsional flutter at high wind velocity because A_2^* change from negative values to positive values. Flutter derivatives H_2^* term, cross derivatives to a torsional aerodynamic damping, are conversely agree well with A_2^* results. Fairing modified section shows a little improvement on the unstable behavior, delaying the unstable of bridge deck from reduced velocity of 4.5 to 5. Also, it was clearly found that soffit plate modified section, and combination of soffit plate and fairings modified sections produce more stable sections, whereas the classical flutter rather than the single torsional flutter will occur because of H_2^* and A_1^*

The results was found some dispersive in A_4 * and H_4 * terms between original section and modified ones, this coefficients are considered insignificant and usually neglected in most of previous researches. Moreover, all modified sections show a little influence in A_1 * and A_3 *, which agree altogether well in trend. For H_3 * term, the fairings section agrees in trend with an original one, while soffit plates and combined sections are agree in trend to each other.

Structural Responses and Critical Wind Speeds

The data acquired from two laser displacement sensors was produced and was described via their standard deviations, both heave and pitch. The stability limit was determined roughly by increasing the wind speed and observing the behavior of the section. Subsequently, acquisition were made of the response starting below the stability limit up to wind speed where the bridge deck exhibits clear unstable behavior. The responses under smooth flow condition are described in Fig. 5 and their comparisons among four sections were also carried out.

Since IRR cable-stayed bridge was manufactured with great considerations, critical wind speed was found at very high velocity, 118 m/s in full-scale (7.45 m/s in model scale). Flutter was found under single degree-of-freedom, torsional condition. However, the tests were conducted with aimed to increase that velocity. On one hand, fairing-modified section

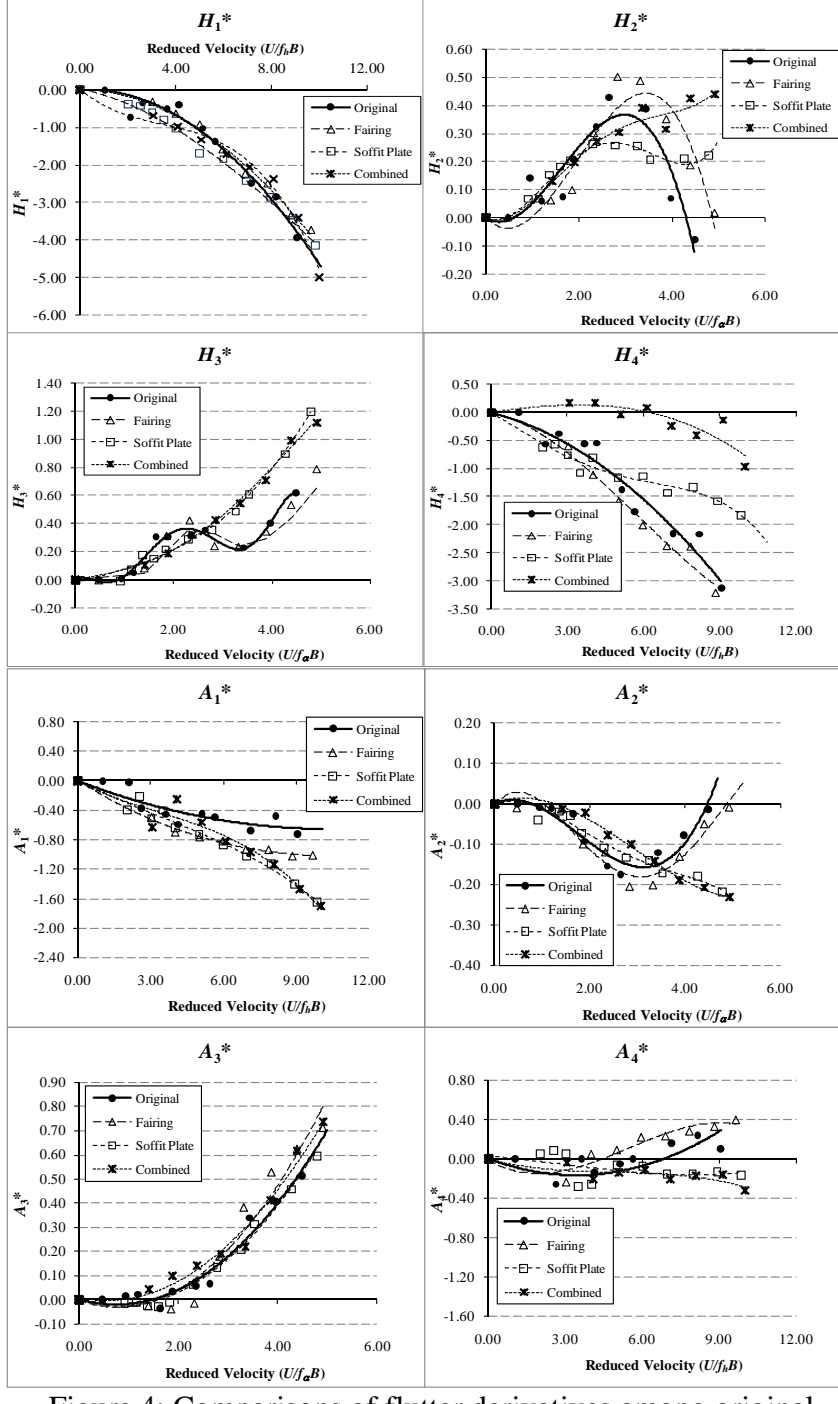


Figure 4: Comparisons of flutter derivatives among original section and modified sections

can delay the critical speed wind up velocity of 135 m/s in full scale or around 15% increased, compared with original section. On the other, for soffit plate modified section, combination and soffit plate and fairings modified sections, flutter phenomenon was found in testing velocity range.

In additional to suppression of flutter instability, the results show a reduction buffeting responses for modified sections. Moreover. vortex shedding significantly suppressed by these modifications. This concludes highly achievement of aerodynamic appendages modification to stabilize flutter phenomenon and vortex shedding responses. When comparisons of the effectivenes of three modifications suppression of buffeting response and structural instability, the results are combine > soffit plate > fairing > original.

Conclusions

The covariance-driven stochastic subspace identification technique (SSI-COV) was presented to extract the flutter derivatives from buffeting responses of bridge deck. The two-edge girder type blunt section model of Industrial Ring Road Bridge, a cable stayed bridge with a main span of 398m, Thailand, was tested in smooth flow. Applying the proposed SSI-COV technique to the buffeting test yields a straightforward, cost effective, and reliable system identification process that can be used to identify flutter derivatives of various bridge decks.

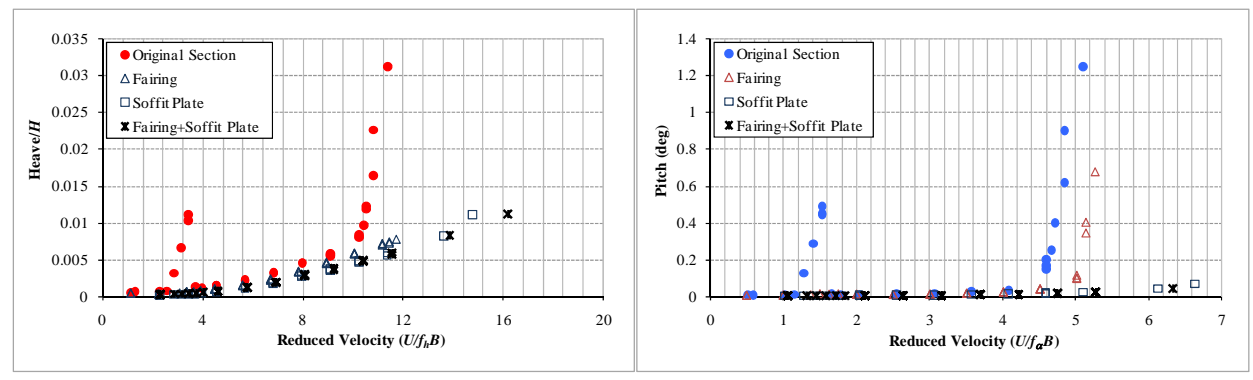


Figure 5: Comparisons of normalized heave and pitch responses among original section and three modified sections

The results found that the original section result in high vortex-shedding response and lead to a single torsional flutter at high wind velocity. The results also indicated that the combined fairing and soffit plate modified section is the most aerodynamic shape. When compared with the original section, this modified section can: a) suppress the vortex shedding significantly, b) result in the classical flutter rather than the single torsional flutter, and c) greatly increase the flutter velocity.

Acknowledgements

The authors would like to express their appreciations to The Thailand Research Fund (TRF) under grant number RMU4980012 for financial supports of this study.

References

Bosch, R. H. (1990) "Section Model Study of the Deer Isle-Sedgewick Suspension Bridge." Journal of Wind Engineering and Industrial Aerodynamics, Elsevier, 36, 601-610.

Gu, M., and Qin X. R. (2004) "Direct Identification of Flutter Derivatives and Aerodynamic Admittances of Bridge Decks." Journal of Wind Engineering and Industrial Aerodynamics, 26, 2161-2172.

Gu, M., Zhang R. X., and Xiang H. (2000) "Identification of Flutter Derivatives of Bridge Decks." Journal of Wind Engineering and Industrial Aerodynamics, 84, 151-162.

Houston R. D.., Bosch H. R., and Scanlan R. H. (1988) "Effects of Fairings and of Turbulence on the Flutter Derivatives of a Notably Unstable Bridge Deck." Journal of Wind Engineering and Industrial Aerodynamics, Elsevier, 29, 339-349.

Overschee, P. V. (1991) "Subspace Algorithms for the Stochastic Identification Problem." Proceedings of 30th Conference on Decision and Control. Brighton, 1321-1326.

Peeters, B. (1999) "Reference-based Stochastic Subspace Identification for Out-put only Modal Analysis." Mechanical Systems and Signal Processing 13, no. 6, 885-878.

Sakai, Y., Ogawa K., Shimodoi H., and Saitoh T. (1993) "An Experimental Study on Aerodynamic Improvements for Edge Girder Bridges." Journal of Wind Engineering and Industrial Aerodynamics, Elsevier, 49, 459-466.

Sarkar, P. P., Jones N., and Scanlan R. H. (1994) "Identification of Aeroelastic Parameters of Flexible Bridges." Journal of Engineering Mechanics, ASCE, 120 (8), 1718-1714.

Scanlan, R. H. (1971) "Airfoil and Bridges Deck Flutter Derivatives." Journal of Engineering Mechanics, ASCE, 97 (6), 1717-1733.

Simiu E. and Scanlan R.H. (1996) "Wind effects on structures." 3rd Ed., John Wiley & Sons, New Jersey.

Proceeding in 5th International Workshop on Regional Harmonization of Wind Loading and Wind Environmental Specifications in Asia-Pacific Economies

Taipei, Taiwan, 2009

Wind Loading Standard for Building Design in Thailand and Country Report

Virote Boonyapinyo

Associate Professor, Department of Civil Engineering, Thammasat University Rangsit Campus, Pathumthani 12120, Thailand

ABSTRACT: The new development of DPT Standard 1311-50 for wind loading calculation and response of buildings in Thailand is financially supported by Department of Public Works and Town & Country Planning. The new standard is more accurate than the building code No.6 because it considers the wind speed zoning, surrounding terrain, building shapes, and dynamic properties. The new standard format is widely used in the international codes. The new standard consists of 3 parts, namely, 1. Wind loading standard for building design, 2. Commentaries to the standard and 3. Numerical examples. Three different approaches for determining design wind loads on buildings are given in the standard, namely, the simple procedure for low- and mid-rise buildings, the detailed procedure for high-rise buildings, and wind-tunnel test procedure. Examples of wind load studies of buildings and bridges by TU-AIT wind tunnel test are also presented. Finally, losses due to wind storms in Thailand are shown.

1. INTRODUCTION

The wind load specified in the existing building code under the Building Control Act (BCA) 1979 is obsolete because it does not consider the terrain conditions and the typhoon influence. In addition, the code value is too low for very tall building, and for building in open exposure, as well as buildings in the Southern part of Thailand which is prone to typhoon attack [1, 2]. Therefore, the subcommittee on wind and earthquake effects on structures of the Engineering Institute of Thailand published the wind loading standard for building design in 2003 [3]. It considers the wind speed zoning, surrounding terrain, dynamic properties, and building shapes. The standard is mainly based on the National Building Code of Canada 1995 [4].

However, the wind loading standard for building design in 2003 has been revised again for up-to-date wind loading standard. At present, DPT standard 1311-50 for wind loading calculation and response of buildings in Thailand is newly published by Department of Public Works and Town & Country Planning [5]. To develop the new wind loading standard for building design, an evaluation and comparison of wind load and responses for building among several codes/standards were studied by Boonyapinyo et al. [5-7], among others. The comparisons include National Building Code of Canada [8], International Standard [9], ASCE Standard [10], AIJ Recommendation [11], Australian Standard [12] and European Standard [13]. The new development of DPT standard 1311-50 for wind loading calculation and response of buildings over 2003 version includes the specified wind load and response, reference wind speed map, natural frequency and damping of building, table for design wind loads for main structures, secondary members and claddings for low-rise buildings, wind tunnel test procedure, commentary, numerical examples, computer program for calculation of wind load and response, and wind load on miscellaneous structures such as,

large billboards, cylinders, poles, structural member, two- and three-dimensional trusses. The reference wind speed is based on the study of the wind climate in Thailand [1, 5, 14]. The wind speed for the Southern Thailand reflects the influence of the rare event of the typhoons in the region. The natural frequency and damping for building in Thailand are based on the measurements of 50 buildings in Bangkok [15].

2. WIND LOADING CALCULATION PROCEDURE

Three different approaches for determining design wind loads on buildings and structures are given in the standard as follows.

2.1 Simple procedure

The simple procedure is appropriate for use with the majority of wind loading applications, including the structure and cladding of low and medium rise building and the cladding design of high rise buildings. These are situations where the structure is relatively rigid. Thus, dynamic actions of the wind do not require detailed knowledge of the dynamic properties of the buildings and can be dealt with by equivalent static loads.

2.2 Detailed procedure

The detailed procedure is appropriated for buildings whose height is greater than 4 times their minimum effective width or greater than 80 m and other buildings whose light weight, low frequency and low damping properties make them susceptible to vibration





Figure 1. Boundary-layer long-wind tunnel of TU-AIT.

2.3 Wind tunnel test procedure

Wind tunnel testing is appropriate when more exact definition of dynamic response is needed and for determining exterior pressure coefficients for cladding design on buildings whose geometry deviates markedly from more common shapes for which information is already available. Detail of wind tunnel test procedure is given in [5].

Figure 1 shows the boundary-layer long-wind tunnel that was jointly built by Thammasat university (TU) and Asian Institute of Technology (AIT) at Thammasat

University. The test section is 2.5x2.5 m with 25.5 m in length. Wind speed is in the range of 0.5 to 20 m/s.

3. SPECIFIED WIND LOADING

The specified external pressure or suction due to wind on part or all of a surface of a building shall be calculated from

$$p = I_w q C_e C_g C_p \tag{1}$$

where

p = the specified external pressure acting statically and in a direction normal to the surface either as a pressure directed to wards the surface or as a suction directed away from the surface,

 I_w =importance factor for wind load, as provided in Table 1,

q = the reference velocity pressure,

 C_e = the exposure factor,

 C_g = the gust effect factor,

 C_P = the external pressure coefficient, averaged over the area of the surface considered

The net wind load for the building as a whole shall be the algebraic difference of the loads on the windward and the leeward surfaces, and in some cases may be calculated as the sum of the products of the external pressures or suctions and the areas of the surfaces over which they are averaged

The net specified pressure due to wind on part or all of a surface of a building shall be the algebraic difference of the external pressure or suction as given in Equation (1) and the specified internal pressure or suction due to wind calculated from

$$p_i = I_w q C_e C_g C_{pi} (2)$$

where

 p_i = the specified internal pressure, acting statically and in a direction normal to the surface either as a pressure (directed outwards) or as a suction (directed in wards),

q = the reference velocity pressure,

 C_e = the exposure factor, evaluated at the building mid-height instead of the height of the element considered,

 C_g = the gust effect factor,

 C_{pi} = the internal pressure coefficient

Table 1. Importance factor

Importance Category	Importance factor, I_w		
	Ultimate limit states	Serviceability limit states	
Low	0.8	0.75	
Normal	1	0.75	
High	1.15	0.75	
Post-disaster	1.15	0.75	

5th International Workshop on Regional Harmonization of Wind Loading and Wind Environmental Specifications in Asia-Pacific Economies, Taipei, Taiwan, 2009

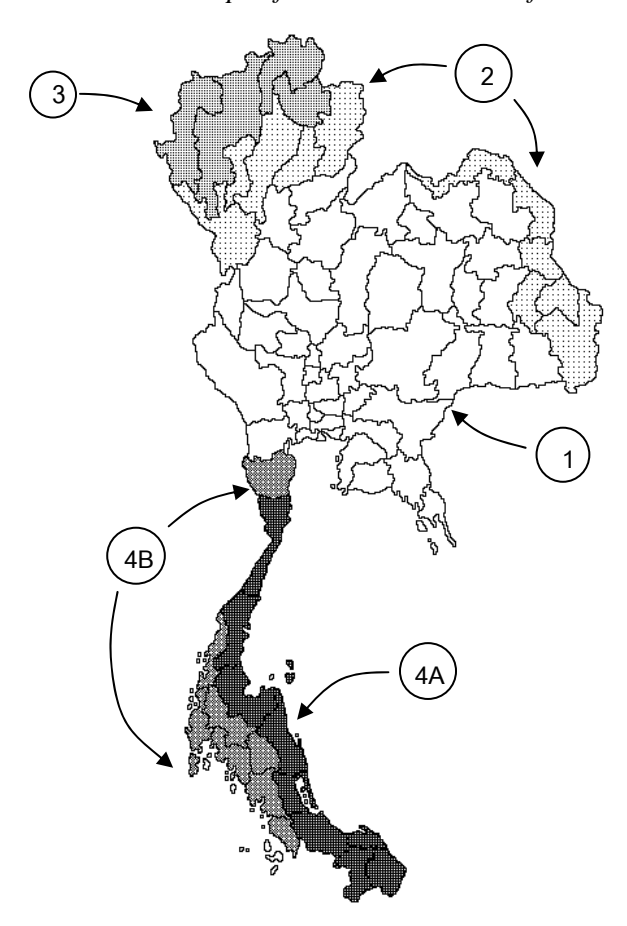


Figure 2. Reference (or design) wind speed for Thailand.

4. REFERENCE VELOCITY PRESSURE

The reference wind pressure, q, is determined from reference (or design) wind speed, \overline{V} by the following equation:

$$q(\ln kg/m^2) = \frac{1}{2} \left(\frac{\rho}{g}\right) \overline{V}^2$$
 (3)

where

 $P = \text{air density} = 1.25 \text{ kg/m}^3$ $g = \text{acceleration due to gravity} = 9.81 \text{ m/s}^2$ $\overline{V} = V_{50}$ for serviceability limit state $\overline{V} = T_F \cdot V_{50}$ for ultimate (strength) limit state

 $V_{\rm 50}$ and typhoon factor ($T_{\rm F}$) are shown in Table 2.

In this study, the annual maximum wind speeds from 73 stations were used in extreme wind analysis [5]. The data were converted to one-hour average speed at 10 m. in open terrain according to an emometer height and terrain of each station, and were fitted to a Type I extreme-value distribution using probability weighted moment method. The analysis of dispersion map and the 30-years return period speeds indicate that the area can be divided in

to four zones. The 50-year return period speed for each zone was then estimated by the representative values of dispersion and location parameters of that zone. The higher wind speeds for Zone 2 and 3 are due to the mixed effect of the weakening tropical storm entering the region from the east and the severe thunder storm happening in summer (from March to May) of every year.

Table 2. Reference wind speeds and typhoon factor

Zone	Area	V_{50}	T_F
Zone 1	Central region	25	1.0
Zone 2	Lower part of Northern region and East west border region	27	1.0
Zone 3	Upper part of Northern region	29	1.0
Zone 4 A	East coast of Southern peninsula	25	1.2
Zone 4 B	Petchaburi and West coast of Southern peninsula	25	1.08

The design wind speed of Zone 4 is governed by the South-west and the North-east Monsoons which give a design wind speed as low as 25 m/s. However, the historical records indicate that tropical cyclone may affect this region especially in November and December. In 1989, Typhoon Gay which developed in the Gulf of Thailand had crashed into Chumporn. It is reported that Typhoon Gay has a one-minute sustained surface wind speed of 100 knots (51.4 m/s.) [16], which corresponding to a one-hour average speed of 41.1 m/s. At least 600 people were killed, and more than 46,000 houses were either totally or partially destroyed by this typhoon. The design wind speed of this zone must take into account the effect of tropical cyclone to ensure that the post-disaster buildings must not collapse if a typhoon with the same intensification as Typhoon Gay would happen again. As a result, it is considered that the post-disaster buildings in this zone must be able to sustain the wind pressure developed by a wind speed of 41.1 m/s. at ultimate state. With the load factor of 1.6 and importance factor for post-disaster of 1.15, the corresponding design wind speed for zone 4 is thus $41.1/\sqrt{1.6*1.15} = 30.3 \approx 30 \text{ m/s}$. Therefore, the typhoon factor for east coast of southern peninsula = 30/25 = 1.2. However, the typhoon factor in Table 2 should be applied for buildings and structures that have importance category as post-disaster. For others, it is subjected to designer judgment.

5. EXPOSURE FACTOR

The exposure factor, C_e , reflects changes in wind speed and height, and also the effects of variations in the surrounding terrain and topography. The exposure factors for use with either the simple or detailed procedure are given as follows.

5.1 Simple procedure

Exposure A: (open or standard exposure): open level terrain with only scattered buildings, trees or other obstructions, open water or shorelines thereof.

$$C_e = \left(\frac{Z}{10}\right)^{0.2}, \quad C_e \ge 0.9$$
 (4)

Exposure B: suburban and urban areas, wooded terrain or center of large towns.

$$C_e = 0.7 \left(\frac{Z}{12}\right)^{0.30}, C_e \ge 0.7$$
 (5)

In Equations (4) to (5), Z is the height above ground in metre.

5.2 Detailed procedure

For the detailed procedure, the exposure factor, C_e , is based on the mean wind speed profile, which varies considerable depending on the general roughness of the terrain over which the wind has been blowing before it reaches the building. To determine the exposure factor, three categories have been established as follows:

Exposure A: (open or standard exposure): open level terrain with only scattered buildings, trees or other obstructions, open water or shorelines thereof. This is the exposure on which the reference wind speeds are based.

$$C_e = \left(\frac{Z}{10}\right)^{0.28} \text{ for } 1.0 \le C_e \le 2.5$$
 (6)

Exposure B: suburban and urban areas, wooded terrain or center of large towns.

$$C_e = 0.5 \left(\frac{Z}{12.7}\right)^{0.50} \text{ for } 0.5 \le C_e \le 2.5$$
 (7)

Exposure C: center of large cities with heavy concentrations of tall buildings. At least 50% of the buildings should exceed 4 stories. This exposure is only applicable to the heavily built-up center of large cities and should be used with caution because of local channeling and wake buffeting effects that can occur near tall buildings.

$$C_e = 0.4 \left(\frac{Z}{30}\right)^{0.72} \text{ for } 0.4 \le C_e \le 2.5$$
 (8)

In Equations (6) to (8), Z is the height above ground in metre.

Exposure B or C should not be used unless the appropriate terrain roughness persists in the upwind direction for at least 1 km or 10 times the height of the building, whichever is larger, and the exposure factor should be recalculated if the roughness of terrain differs from one direction to another.

6 GUST EFFECT FACTOR

The gust effect factor, C_g , is defined as the ratio of the maximum effect of the loading to the mean effect of the loading. The dynamic response includes the action of

- a) random wind gusts action for short durations over all or part of the structure.
- b) fluctuating pressures induced by the wake of the structure, including "vortex shedding forces," and
- c) fluctuating forces induced by the motion of the structure itself through the wind.

The gust effect factor for use with either the simple or detailed procedure are given as follows.

6.1 Simple procedure

The gust effect factor C_g is one of the following values:

- a) 2.0 for the building as a whole and main structural member,
- b) 2.5 for external pressures and suctions on small elements including cladding
- c) 2.0 or a value determined by detailed calculation for internal pressures (see standard [5])

6.2 Detailed procedure

The gust effect factor is calculated as

$$C_g = 1 + g_p(\sigma/\mu) \tag{9}$$

where

 μ = the mean loading effect,

 σ = the "root-mean square" loading effect, and

 g_p = a statistical peak factor for the loading effect obtained from figure in the standard.

The value of σ/μ can be expressed as

$$\sigma/\mu = \sqrt{\frac{K}{C_{oH}} \left(B + \frac{sF}{\beta}\right)}$$
 (10)

where

K = a factor related to the surface roughness coefficient of the terrain,

= 0.08 for Exposure A,

= 0.10 for Exposure B,

= 0.14 for Exposure C,

 C_{eH} = exposure factor at the top of the building, H,

B = background turbulence factor obtained from figure in the standard as a function of W/H,

W = width of windward face of the building,

H = height of windward face of the building,

s = size reduction factor obtained from figure in the standard as a function of W/H and the reduced frequency n_oH/V_H ,

 n_o = natural frequency of vibration, Hz. Values recommended in the design of concrete building = 44/H [5, 15],

 V_H = mean wind speed (m/s) at the top of structure, H,

F = gust energy ratio at the natural frequency of the structure obtained from Figure in the standard as a function of the wave number, n_o/V_H , and

 β = damping ratio. Suggested values for β must be based mainly on experiments on real structures. Values commonly used in the design of building with steel frames and concrete frames are in the range of 0.005 and 0.015 [5, 15].

7 PRESSURE COEFFICIENTS

Pressure coefficients are the non-dimensional ratios of wind-induced pressures on a building to the dynamic pressure (velocity pressure) of the wind speed at the reference height.

Pressures on the surfaces of structures vary considerably with the shape. Wind direction and profile of the wind velocity.

The information on external and internal pressure coefficients given in the standard covers requirements for the design of the cladding and the structure as a whole for a variety of simple building geometries.

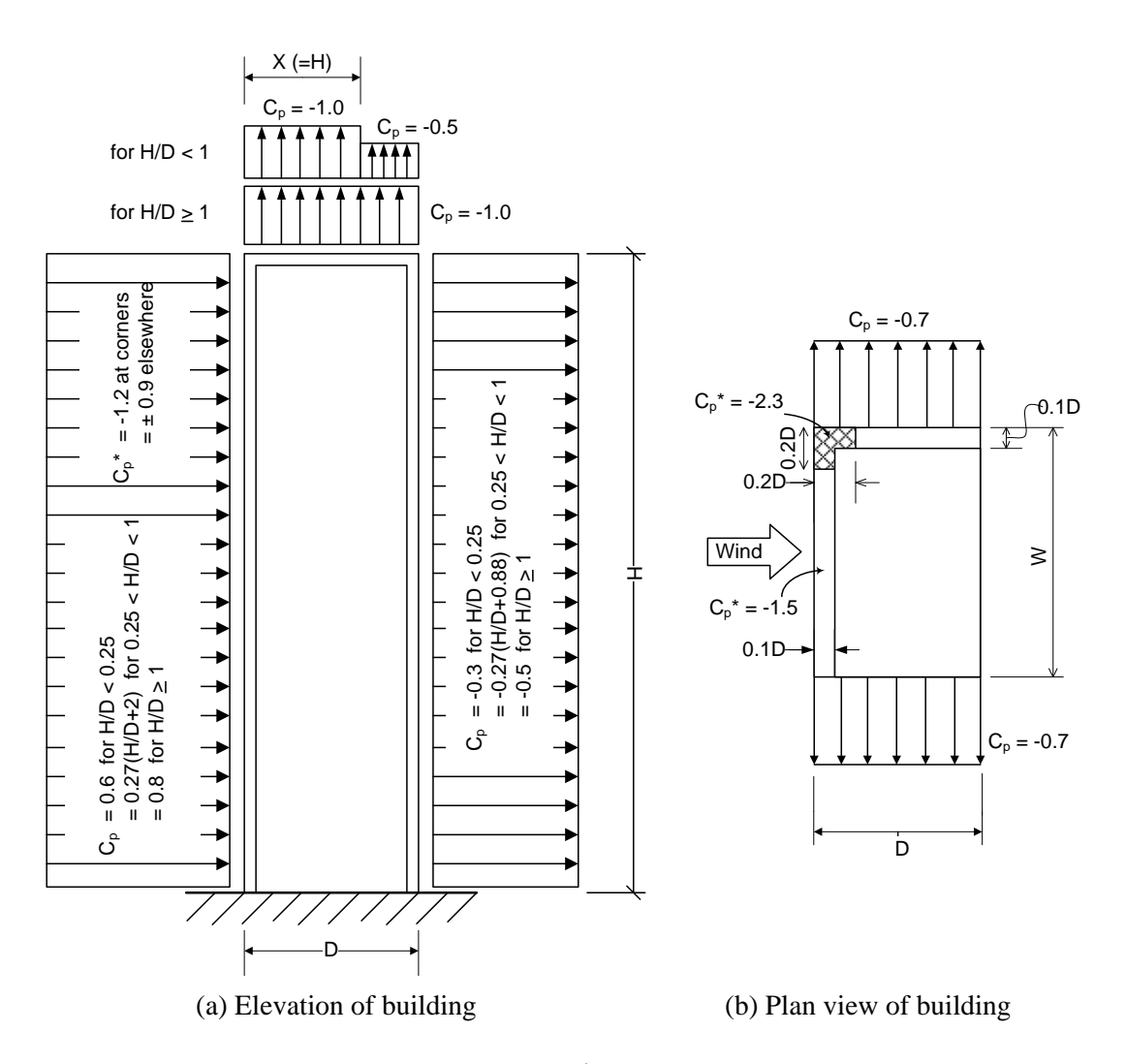


Figure 3. External pressure coefficients, C_p and C_p^* , for flat-roofed buildings greater in height than in width

For rectangular shape building, the external pressure coefficients for windward and leeward walls are 0.8 and -0.5, respectively, as shown in figure 3. Reference heights for exposure factor for the calculation of both spatially-averaged and local pressures are as follows. Leeward walls use at 0.5 H, roof and side walls use at H, any area at height Z above ground on the windward wall use at Z.

A local pressure coefficient, $C_p^* = \pm 0.9$, applicable to the design of small cladding areas (about the size of a window), can occur almost anywhere at any elevation. However, the local $C_p^* = -1.2$ given for corners apply to an edge zone of 0.1D wide.

8. LATERAL DEFECTION

Lateral deflection of tall buildings under wind loading may require consideration from the standpoints of serviceability or comfort. A maximum lateral deflection limitation of 1/500 of the building height with importance factor of 0.75 for serviceability limit states is specified.

9. BUILDING MOTION

While the maximum lateral wind-loading and deflection are generally in the direction parallel with the wind (along-wind direction), the maximum acceleration of a building leading to possible human perception of motion or even discomfort may occur in the direction perpendicular to the wind (across-wind direction) if \sqrt{WD}/H is less than one-third, where W and D are the across-wind and along-wind building dimensions and H is the height of the building.

The maximum acceleration in the along-wind direction can be found from the expression

$$a_D = 4\pi^2 n_D^2 g_p \sqrt{\frac{KsF}{C_{eH}\beta}} \cdot \frac{\Delta}{C_g}$$
 (11)

where

 a_D = peak acceleration in along wind direction, m/s²,

 $\rho_{\rm\scriptscriptstyle B}$ = average density of the building, kg/m³,

 β = damping ratio in along-wind direction,

 n_D = fundamental natural frequencies in along-wind direction, Hz.

 Δ = maximum wind-induced lateral deflection at the top of the building in along-wind direction, m.

An acceleration limitation of 1.5 to 2 % of gravity is specified for use in conjunction with Equation (11) and in the across-wind direction with importance factor of 0.75 for serviceability limit states. The lower value is considered appropriate for apartment buildings, the higher value for office buildings.

10. ACROSS-WIND AND TORSIONAL LOAD AND RESPONSE

Across-wind and torsional load and response in DPT standard 1311-50 are based on the AIJ Recommendation [17]. Details are given in Reference 5.

11. EXAMPLES OF WIND LOAD STUDY BY TU-AIT WIND TUNNEL TEST

11.1 Wind load study for cladding design

a. MahaNakhon Building in Bangkok

Wind load study for cladding design of MahaNakhon Building was performed by TU-AIT wind tunnel test as shown in Figures 1 and 4 [18]. The MahaNakhon Building is located in the embassy/financial district in the centre of Bangkok between the Sathon and Silom roads. The area surrounding the studied building generally consists of urban development in all directions from the site. The studied building has 39 m square in plan, 309.9 m in roof

height, and has surface "pixellations". The studied building was specially constructed by an acrylic rigid model. The 1:400 scale models of studied building and its surrounding buildings within 400 m radius from the studied building were mounted on a 2-m diameter turntable, allowing any wind direction to be simulated by rotating the model to the appropriate angle in the wind tunnel. The studied building model and its surroundings were tested in a boundary layer wind tunnel where the mean wind velocity profile, turbulence intensity profile, and turbulence spectrum density function of the winds approaching the study site are simulated for urban exposure based on the ASCE7 Standard [10] and ASCE Manual and Reports on Engineering Practice No. 67. In this study, overall wind load obtained from a wind tunnel test were measured on a direction-by-direction basis for 36 directions at 10-degree intervals, on the 1:400 scale model of the building exposed to an approaching wind.

According to the DPT Standard 1311-50 [5], the reference velocity pressure, q, for the design of main structure and cladding shall be based on a probability of being exceeded in any one year of 1 in 50 (50-year return period) corresponding to reference wind speed of 25 m/s at the height of 10 m in open terrain. Because the proposed building is located in the Central Bangkok with heavy concentrations of tall buildings, the exposure C (center of large cities) was applied in this study, and the typhoon factor = 1.0. Then design wind speed is 25 m/s, and corresponding to design wind speed of 36.65 m/s at the 309.9 m roof height in the exposure C.

The results of recommended peak maximum pressures and peak minimum pressures (negative or suctions) in kPa (1 kPa = 1,000 N/m²) for cladding design of walls of studied building are presented graphically (figure 4). The recommended peak maximum pressures are generally in the range of 1,000 to 1,750 N/m². The recommended peak minimum pressures (negative or suctions) are in the range of 2,250 to 3,500 N/m² in most part of the tower, in the range of 3,500 to 4,000 N/m² in some areas, and in the range of 4,000 to 5,750 N/m² in some areas of edge zones of building walls. The largest peak maximum pressure and peak minimum pressures (negative or suctions) are 2,490 and 6,910 N/m², respectively.

Finally, it was found that: 1) the local peak maximum pressures in most part of the tower obtained from wind tunnel test for studied building agree well in general with those based on the ASCE7 standard [10]; 2) the local peak minimum pressures (suctions) in most part of the tower obtained from wind tunnel test agree well in general with those based on the ASCE7 standard; 3) the local peak minimum pressures (suctions) in some areas of edge zone obtained from wind tunnel test are slightly to moderately higher than those based on the ASCE7 standard.

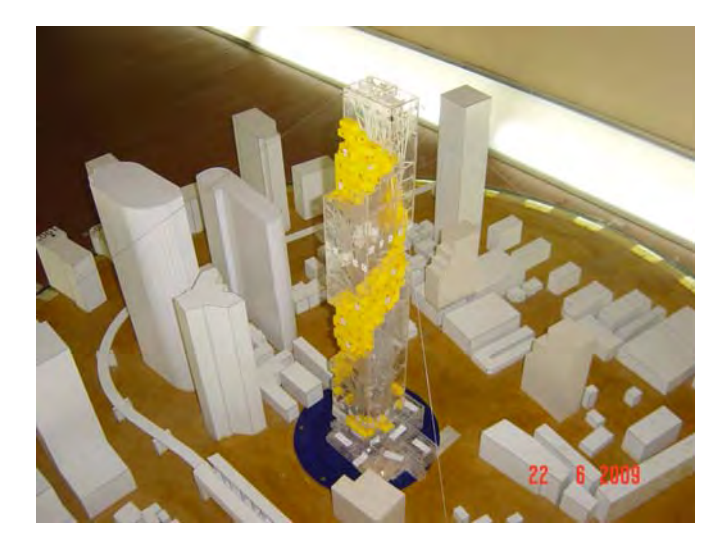
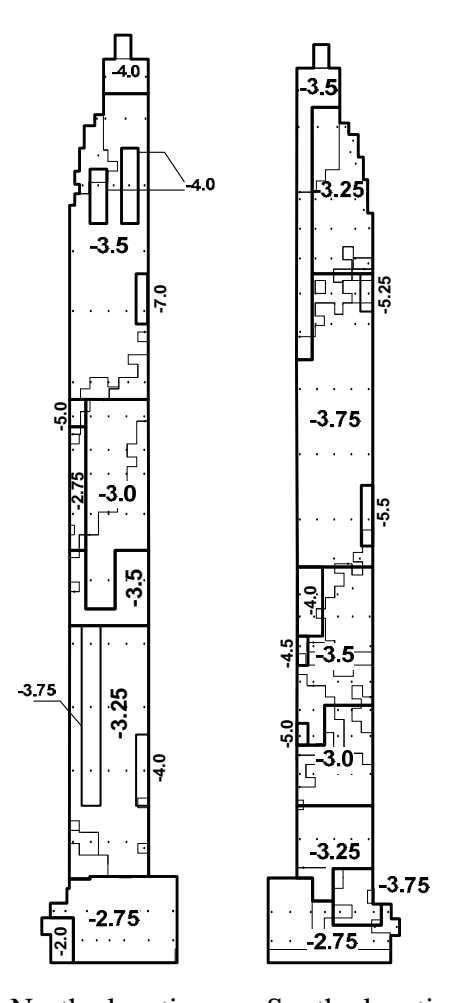


Figure 4. Rigid model of MahaNakhon building in Bangkok



North elevation South elevation

Figure 5. Recommended peak minimum pressures (negative or suctions) for cladding design (kPa)



Figure 6. Rigid model of Gramercy building in Manila



Figure 7. Rigid model of Knightbridge building in Manila

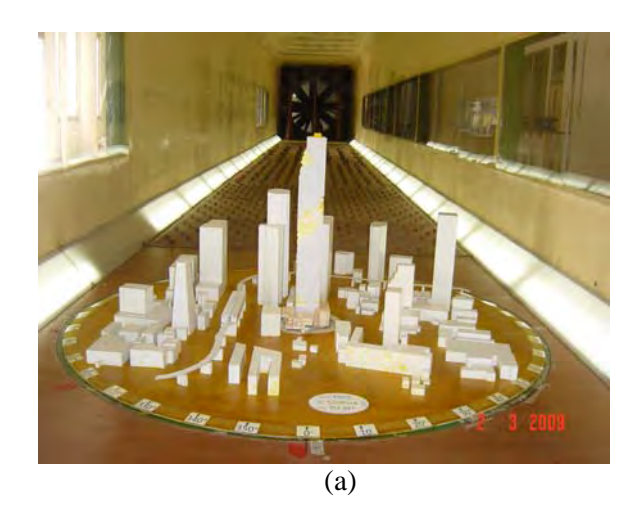
b. Gramercy building and Knighrbridge building

In addition, wind load studies for cladding design of Gramercy building and Knighrbridge building in Manila were performed by TU-AIT wind tunnel test as shown in Figures 6 and 7 [19].

11.2 Wind load study for overall fluctuating loads and dynamic response

a. MahaNakhon Building in Bangkok

Wind load study for overall fluctuating loads and dynamic response of MahaNakhon Building was performed by TU-AIT wind tunnel test as shown in Figure 8 [18]. The studied building has 39 m square in plan, 309.9 m in roof height, and has surface "pixellations". The studied building was specially constructed by a light-weight rigid model, such as balsa wood model, and the studied model was mounted on a high-frequency base balance. The 1:400 scale models of studied building and its surrounding buildings within 400 m radius from the studied building were mounted on a 2-m diameter turntable, allowing any wind direction to be simulated by rotating the model to the appropriate angle in the wind tunnel. The studied building model and its surroundings were tested in a boundary layer wind tunnel where the mean wind velocity profile, turbulence intensity profile, and turbulence spectrum density function of the winds approaching the study site are simulated. In this study, overall wind load obtained from a wind tunnel test were measured on a direction-by-direction basis for 36 directions at 10-degree intervals, on the 1:400 scale model of the building exposed to an approaching wind.



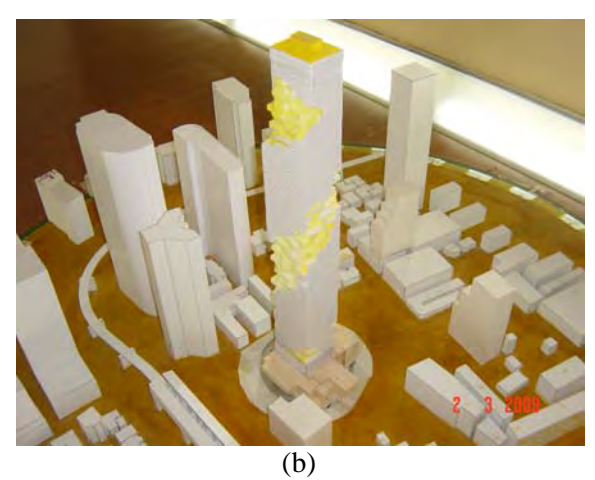


Figure 8. (a) Overall wind load study of MahaNakhon building in Bangkok by wind tunnel test, and (b) high-frequency force balance model

According to the DPT Standard 1311-50 [5], the reference velocity pressure, q, for the design of main structure and cladding shall be based on a probability of being exceeded in any one year of 1 in 50 (50-year return period) corresponding to reference wind speed of 25 m/s at the height of 10 m in open terrain. Because the proposed building is located in the Central Bangkok with heavy concentrations of tall buildings, the exposure C (center of large cities) was applied in this study, and the typhoon factor = 1.0. Then design wind speed is 25 m/s, and corresponding to design wind speed of 36.65 m/s at the 309.9 m roof height in the exposure C. For the serviceability design, the reference velocity pressure, q, shall be based on 10-year return period corresponding to reference wind speed of 20.25 m/s at the height of 10 m in open terrain. Therefore, corresponding design wind speed is 29.69 m/s at the 309.9 m roof height in the exposure C.

Table 3. Comparison of the expected peak base moments and torques for three values of natural frequencies f_o and two values of damping ratios ξ

Absolute Peak Base Moments	Damping ratio ξ			Damping ratio ξ		
or Torques	= 0.01			= 0.02		
(MN-m)	$0.8 f_o$	f_o	$1.25 f_o$	$0.8 f_o$	f_o	$1.25 f_o$
My	9,223	5,601	3,701	6,580	4,047	2,741
Mx	7,066	4,508	3,278	5,051	3,271	2,852
Mz	82	77	72	71	68	64

For damping ratio $\xi = 0.02$ for strength consideration, the results found that the absolute peak base moments M_x of 3,271 MN-m, M_y of 4,047 MN-m and torque M_z of 68 MN-m occur at wind direction 0, 90, and 290 degree, respectively. The peak base moments M_x and M_y are strongly caused by the acrosswind load.

For serviceability consideration with V_5 and V_{10} (i.e. low return periods of wind velocity and low stress levels), three natural frequencies $(0.8\,f_o\,f_o\,f_o\,f_o\,f_o\,f_o)$ of studied building in each direction of motion, four damping ratios ($\xi=0.005,\,0.0075,\,0.01$, and 0.03 (with additional damping)), are considered. Therefore, they are 24 cases of results. The predicted peak acceleration responses for two values of return periods of V_5 and V_{10} , and four values of damping ratios ξ are shown and compared in the Figure 9 for natural frequencies f_o . The results show that the predicted peak acceleration responses are strongly dependent on the building natural frequencies, damping ratio, and return periods of wind velocity. This is because the peak acceleration responses are mainly caused by the acrosswind load, in which the acrosswind spectra exhibit an evident peak around the reduced frequency (Strouhal number) of 0.1.

According to the DPT Standard 1311-50 [5], the recommended serviceability design for human comfort criteria for the studied building is that the peak acceleration under a 10 year return period should be less than 15 mg and 25 mg for residential buildings and commercial buildings, respectively. For natural frequencies of building = $0.8\,f_o$, f_o , and 1.25 f_o , the predicted peak accelerations are found below the recommended criteria of 15 mg for the residential studied building when damping ratios are greater than about 0.015, 0.0075, and 0.005, respectively.

The ISO recommended serviceability design for human comfort criteria [20] depending on the building's lowest natural frequency is that the peak acceleration under a 5 year return period should not exceed $0.928 f^{-0.412}$ (in % of g) where f is the lowest natural frequency in Hz, and corresponding to 22 mg, 20 mg, and 18 mg when natural frequencies of studied building = $0.8 f_o$, f_o , and $1.25 f_o$, respectively. The predicted peak accelerations for three values of natural frequencies are found below the recommended criteria when damping

ratio is greater than 0.005. The criteria of DPT Standard are more conservative than the ISO criteria especially for the residential studied building.

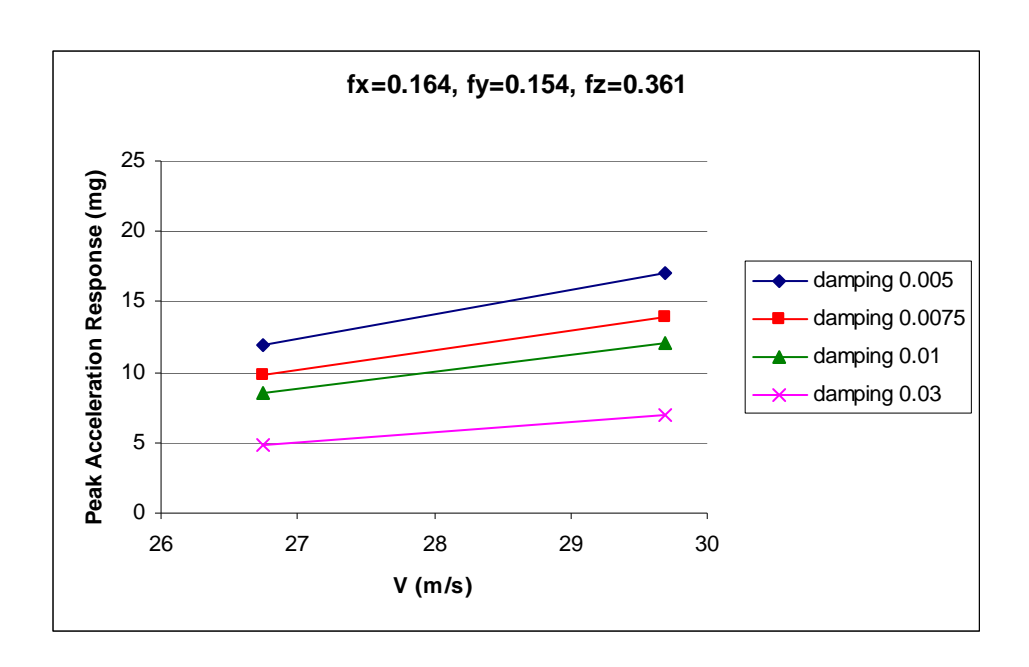


Figure 9. Comparison of predicted peak acceleration responses for two values of return periods of V_5 and V_{10} , and four values of damping ratios ξ (natural frequencies f_o)

b. Plot C42 building and Central Man-U building

In addition, wind load studies for overall fluctuating loads and dynamic response of plot C42 building in Abu Dhabi, UAE [20], and Central Man-U building in Bangkok [21] were performed by TU-AIT wind tunnel test as shown in Figures 10 and 11, respectively.



28-10

Figure 10. High-frequency force balance model of plot C42 building in Abu Dhabi

Figure 11. High-frequency force balance model of Central Man-U building in Bangkok

11.3 Wind load study for aerodynamic response of cable-supported bridges

Flutter derivatives are the essential parameters in the estimations of the critical wind velocity for flutter-instability and the responses of long-span cable supported bridges. These

derivatives can be experimentally estimated from wind tunnel tests results. Most of previous studies have used deterministic system identification techniques, in which buffeting forces and responses are considered as noises. In this research [23], the covariance-driven stochastic subspace identification technique (SSI-COV) was presented to extract the flutter derivatives of bridge decks from the buffeting test results. An advantage of this method is that it considers the buffeting forces and responses as inputs rather than as noises. The Industrial Ring Road (IRR) cable-stayed bridge crossed Chao Phraya River with main span of 398 m (Figure 12) was applied for 1:90 scale sectional model test in TU-AIT wind tunnel test as the study case. Wind tunnel tests were performed for four section bridge models, i.e. original section (Figure 13), fairing-modified section, soffit plate modified section, and combination of those two modified section (Figure 14).



Figure 12. Three-dimensional view of IRR cable-stayed bridge



Figure 13. Original section of IRR bridge in wind tunnel





Figure 14. Fairings and soffit plates modified section in wind tunnel

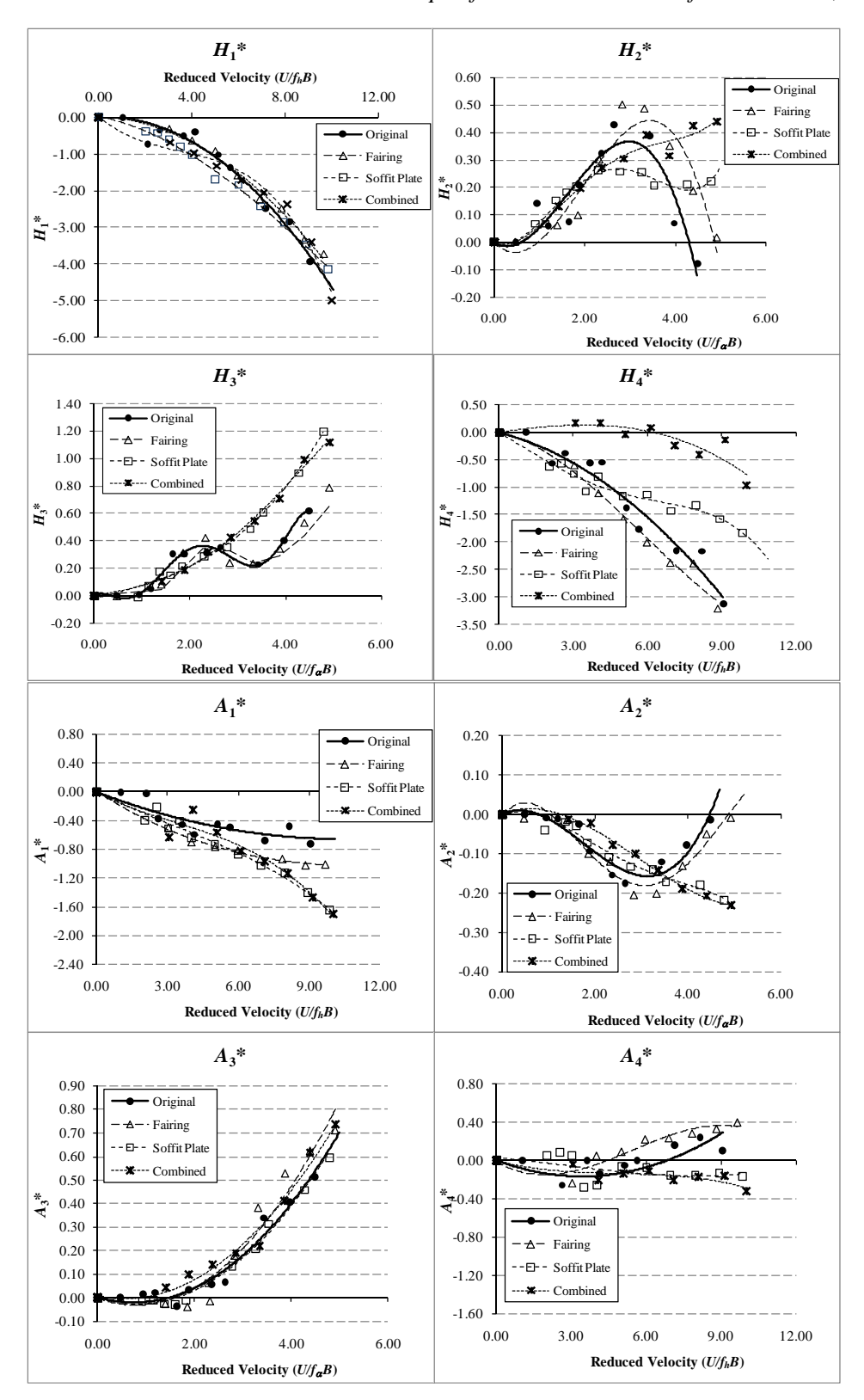


Figure 15. Comparisons of flutter derivatives among original section and modified sections

a. Flutter derivatives

The most important terms are H_1^* and A_2^* which refer respectively on vertical and torsional damping of the section. Their positive values indicate unstable conditions. For vertical aerodynamic damping coefficient, H_1^* , the modification effects considered to be negligible,

which all sections show in negative region. However, the section are influenced by the modifications in A_2^* which is most considerable in long-span bridges. The original section and fairing modified section lead to a single torsional flutter at high wind velocity because A_2^* change from negative values to positive values (Figure 15). Flutter derivatives H_2^* term, cross derivatives to a torsional aerodynamic damping, are conversely agree well with A_2^* results. Fairing modified section shows a little improvement on the unstable behavior, delaying the unstable of bridge deck from reduced velocity of 4.5 to 5. Also, it was clearly found that soffit plate modified section, and combination of soffit plate and fairings modified sections produce more stable sections, whereas the classical flutter rather than the single torsional flutter will occur because of H_2^* and A_1^* Moreover, all modified sections show a little influence in A_1^* and A_3^* , which agree altogether well in trend. For H_3^* term, the fairings section agrees in trend with an original one, while soffit plates and combined sections are agree in trend to each other.

b. Structural responses and critical wind speeds

Critical wind speed of original section was found at reduced wind velocity of 4.5 (Figure 16), corresponding to 118 m/s in full-scale (7.45 m/s in model scale). Flutter was found under single degree-of-freedom, torsional condition. On one hand, fairing-modified section can delay the critical wind speed up to velocity of 135 m/s in full scale or around 15% increased, compared with original section. On the other, for soffit plate modified section, and combination of soffit plate and fairings modified sections, flutter phenomenon was not found in testing velocity range.

The results found that the original section result in high vortex-shedding response and lead to a single torsional flutter at high wind velocity. The results also indicated that the combined fairing and soffit plate modified section is the most aerodynamic shape. When compared with the original section, this modified section can: a) suppress the vortex shedding significantly, b) result in the classical flutter rather than the single torsional flutter, and c) greatly increase the flutter velocity.

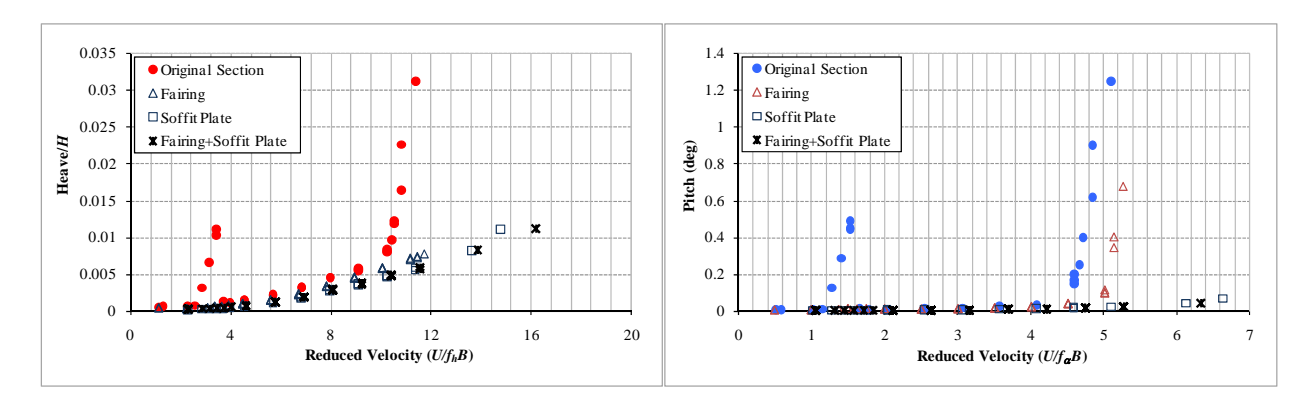


Figure 16. Comparisons of normalized heave and pitch responses among original section and three modified sections

12. LOSSES DUE TO WIND STORMS

Losses due to strong winds in Thailand are associated with two types of storms, tropical cyclone and non-tropical cyclone.

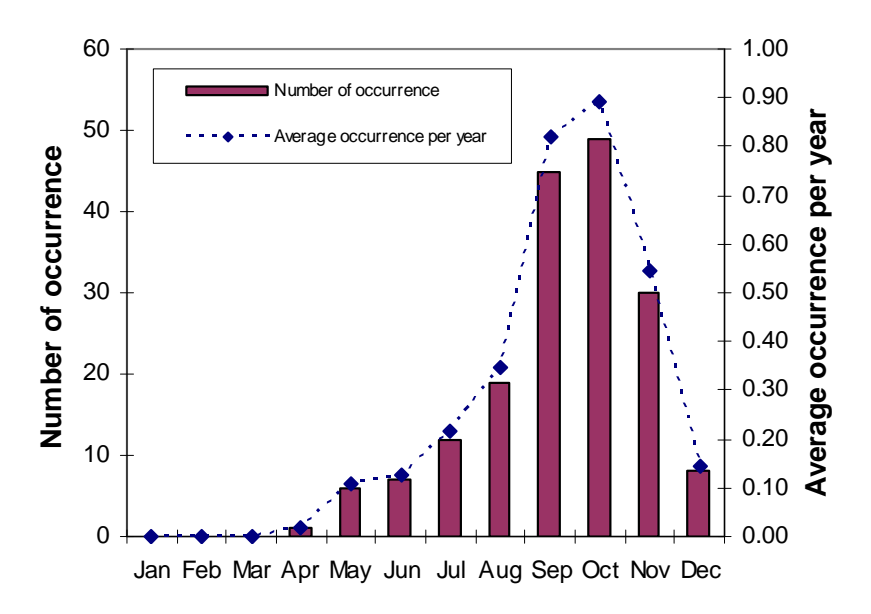


Figure 17. Occurrence rate of tropical cyclone in Thailand (1951-2006) (Source: Thai Meteorological Department)

Table 4. Significant storms in Thailand during 1951-2009

Date	Name	Type	Origin	Entrance	Effects
22 /10/1952	Vae	Tropical	Pacific	Trad (East)	Several dead, some damage in
	(5218)	storm	Ocean		Bangkok
25/10/1962	Harriet	Tropical	South	Nakhon Sri Thamarat	Wind speed of 93 Km/hr, storm surge,
	(6225)	storm	China Sea	(South)	12 provinces were affected, 935
					deaths, 50,000 houses were damaged,
					loss about 1320 M. Baht
23/09/1964	Tilda	Tropical	Pacific	Nakhon Panom	9
	(6419)	storm	Ocean	(North-East)	
03/09/1969	Doris	Tropical	South	Nakhon Panom	
	(6910)	storm	China Sea	(North-East)	
30/11/1970	Ruth	Tropical	South	Surat Thani (South)	
	(7026)	storm	China Sea		
05/12/1972	Sally	Tropical	South	Surat Thani (South)	
	(7299)	storm	China Sea		
04/11/1989	Gay	Typhoon	Thai Gulf	Chumporn (South)	602 deaths, 46,000 houses were
	(8929)				damaged, loss 11,739 M. Baht
30/08/1990	Becky	Tropical	Pacific	Nong Kai (North-	
	(9016)	storm	Ocean	East)	
1990	Ira & Loa	Tropical			38 Deaths, loss 7,326 M. Baht
		depression			
17/08/1991	Fred	Tropical	Pacific	Nakhon Panom	27 Deaths, loss 1,745 M. Baht
	(9111)	storm	Ocean	(North-East)	
15/11/1992	Forrest	Tropical	Pacific	Nakhon Sri Thamarat	Loss 3,000 M. Baht
	(9229)	storm	Ocean	(South)	
04/11/1997	Linda	Tropical	South	Prachuab Kirikhan	58 Deaths, loss 211 M. Baht
	(9728)	storm	China Sea	(South)	
13/06/2004	Chanthu	Tropical	Pacific	Ubon Ratchatani	2 deaths, loss 74 M. Baht
	(0405)	storm	Ocean	(North-East)	
02/10/2006	Xangsane	Tropical	Pacific	Ubon Ratchatani	
	(0615)	storm	Ocean	(North-East)	
30/09/2009	Ketsana	Tropical	Pacific	Ubon Ratchatani	
		storm	Ocean	(North-East)	

(Source: Thai Meteorological Department and Department of Disaster Prevention and Mitigation)

Although typhoon represents rare incident, Thailand experienced a number of wind disasters from several tropical storms and one typhoon in the past 56 year's history (1951-2006). From the record of Thai Meteorological Department (TMD), 177 tropical cyclones have affected the country, among them there were one typhoon, 12 tropical storms and 164 tropical depressions. Figure 17 shows the distribution of rate of occurrence by month of a year and average rate of occurrence per year. Table 4 lists the significant storms. Some of the devastated events are detailed as follows.

The tropical cyclone Harriet was originate in the South China Sea as a topical depression and became tropical storms on October 25, 1962, just off the east coast of Thailand. It moved inland that night as a 93 km/hr tropical storm, and crossed into the Indian Ocean. During landfall its storm surge flooded the Laem Talumphuk peninsula in Nakhon Si Thammarat Province and cause more than 900 fatalities with the loss about 1320 million baht.

Typhoon Gay developed from a tropical depression in the Gulf of Thailand and intensified into a typhoon on November 3, 1989, and then it crossed the peninsular into the Bay of Bengal with peak sustain winds of 140 kt (about 70 m/s) when it reached India. It is unique because of its small size, intensity and point of origin. Generally, an occasional tropical cyclone may move into the Gulf of Thailand from the South China Sea, but it is rare for genesis and intensification to occur in the Gulf, a relatively small body of water surrounded by land on three sides. At least 600 people were killed, more than 46,000 houses were either totally or partially destroyed, many public buildings were damage, and a large number of transmission line tower under construction were damaged.

Although the devastated tropical cyclones have caused considerable disasters, it was found that, however, almost all extreme winds in the country are caused by thunderstorms [1]. In general, thunderstorms are frequently occurred in the tropics than in higher latitudes. In Thailand, the mean annual number of thunderstorm days is over 100 in most parts, where a thunderstorm day is defined as an observation day during which thunder is heard at a station. Thunderstorms may produce a strong downdraft from air mass reaching the ground, known as microburst or macroburst depending on their size. Damages from the downdrafts are limited in relatively small area due to its size, therefore, most of the time the losses are small compared to the large-scale winds. However, due to more frequent occurrence, the cumulative losses are significant. From the report of TMD, thunderstorms, sometime associated with hails, damaged more than 3000 houses and killed 1 person during February to April of 2005 [24], and damaged more than 4000 houses and killed 3 people during February to April of 2006 [25]. Additionally, strong downdraft has been investigating as a cause of collapse of large billboard in Bangkok and other urbanized areas. A typical structure of billboard is quite vulnerable to wind loads because it has large windward area and it always be placed at several ten meters above ground. Recently, several cases of collapse of large billboards due to strong wind have been reported with a number of injuries and deaths.

13. CONCLUSIONS

The new development of DPT standard 1311-50 for wind loading calculation and response of buildings in Thailand is newly published by Department of Public Works and Town & Country Planning. Three different approaches for determining design wind loads on building are given in the standard, namely, the simple procedure for low-rise building, the detailed procedure for high-rise building, and wind-tunnel test procedure. The standard includes the calculation of: (1) wind load of the main wind resistant system and cladding; (2) lateral deflection; and (3) building motion in the along-wind and across-wind directions.

The new development of wind loading standard for building design in Thailand includes the specified wind load and response, reference wind speed map, natural frequency and damping of building, table for design wind loads for main structures, secondary members and claddings for low-rise buildings, wind tunnel test procedure, commentary, numerical examples, computer program for calculation of wind load and response, and wind load on miscellaneous structures such as, large billboards, cylinders, poles, structural member, two-and three-dimensional trusses.

Since the new development of DPT standard 1311-50, wind load standard and wind load studies of buildings and bridges by TU-AIT wind tunnel test have been increasingly interesting to Thai engineers.

14. ACKNOWLEDGEMENTS

The new development of wind loading standard for building design in Thailand is financially supported by Department of Public Works and Town & Country Planning. The author is the project head. The author would like to thank the following persons for their supports in information for writing this paper: Assoc. Prof. Dr. Nakhorn Poovarodom of Thammasat University; Asst. Prof. Dr. Naret Limsamphancharoen of Thammasat University; Assoc. Prof. Dr. Pennung Warnitchai of Asian Institute of Technology, and Prof. Dr. Panitan Lukkunaprasit of Chulalongkorn University.

15. REFERENCES

- 1. Lukkunaprasit, P., Pheinsusom, P., and Euasiriwam, N., (1995), Wind Loading for Tall Building Design in Thailand, Proc. of 2nd National Convension on Civil Engineering, Chiangmai, Thailand, pp. 51-61(in Thai).
- 2. Boonyapinyo, V., (1998), Comparison between Wind and Earthquake Loads for High-Rise Building Design in Thailand, Proc. of International Seminar on Earthquake Resistant Design of Structures, Chiangmai, Thailand., pp. 416-432 (in Thai).
- 3. Engineering Institute of Thailand (2003), E.I.T. Standard 1018-46, Wind Loading Code for Building Design (in Thai).
- 4. National Building Code of Canada (1995) issued by the Canadian Commission on Building and Fire Codes, National Research Council of Canada, Ottawa, Canada.
- 5. Boonyapinyo, V., Lukkunaprasit, P., Chucheepsakul, S., Warnitchai, P., Poovarodom, N., Thepmongkorn, S., Limsamphancharoen, N., and Leelataviwat, S. (2007), Wind Loading for Building Design in Thailand, Final Report, Submitted to Department of Public Works and Town & Country Planning (in Thai); and DPT Standard (2007), DPT 1311-50: Wind Loading Calculation and Response of Buildings, Department of Public Works and Town & Country Planning (in Thai).
- 6. Boonyapinyo, V., Kritrachatanunt, A., and Janesupasaeree, K. (2005), Wind Load Comparisons among Several Codes with Wind Tunnel Experiment Data: Part 1 Comparisons of Calculation Method, Research and Development Journal of the Engineering Institute of Thailand, Vol.16, No.1, pp.1-14 (in Thai).
- 7. Boonyapinyo, V., Kritrachatanunt, A., and Janesupasaeree, K. (2005), Wind Load comparisons among several codes with Wind Tunnel Experiment Data: Part 2 Comparisons of Numerical Examples, Research and Development Journal of the Engineering Institute of Thailand, Vol.16, No.2, pp.15-24 (in Thai).
- 8. National Building Code of Canada (2005) issued by the Canadian Commission on Building and Fire Codes, National Research Council of Canada, Ottawa, Canada.

- 5th International Workshop on Regional Harmonization of Wind Loading and Wind Environmental Specifications in Asia-Pacific Economies, Taipei, Taiwan, 2009
- 9. International Standard, ISO 4354 (1997) Wind Actions on Structures, International Organization for Standardization, Switzerland.
- 10. ASCE Standard (2005), ASCE7-05: Minimum Design Loads for Buildings and Other Structures, American Society of Civil Engineers, New York.
- 11. AIJ (1996), Recommendation for Loads on Buildings, Architectural Institute of Japan.
- 12. Australian Standard, Minimum Design Loads on Structures (1989): Part 2 Wind Loads, Standards Australia, Sydney.
- 13. European Prestandard (1995), Ratified European Text, Eurocode 1: Basis of Design and actions on structures-Part2-4: Actions on Structures-Wind Actions. European Committee for standardization.
- 14. Mikitiuk, M., Surry, D., Lukkunaprasit, P., and Euasiriwan, N. (1995), Probability Based Wind Loadings for the Design of Transmission Structures, Part A-A Study of The Wind Climate for Thailand, Joint Research Report by Boundary Layer Wind Tunnel Laboratory, University of West Ontario and Chulalongkorn University, Thailand, CU/CE/EVR 1995.001.
- 15. Poovarodom, N., Warnitchai, P., Petcharoen, C., Yinghan, P. and Jantasod, M. (2004), Dynamic Characteristics of Non-Seismically Designed Reinforced Concrete Buildings with Soft Soil Condition in Bangkok, Proc. of the 13th World Conference on Earthquake Engineering, Vancouver BC, Canada. Paper No. 1264, Oxford: Pergamon.
- 16. Plante, R.J. and Guard, C.P.(1990), 1989 Annual Tropical Cyclone Report, U.S. Naval Oceanography Command Center, Joint Typhoon Warning Center.
- 17. AIJ (2004), Recommendation for Loads on Buildings, Architectural Institute of Japan.
- 18. Boonyapinyo, V., Taleongpong, S., Sharma S. B., and Thientim N. (2009), Wind Loads Study for MahaNakhon Building by Wind Tunnel Test: Part 1 Overall Wind Load Study and Part 2 Pressure Measurement Study, Final Report, Department of Civil Engineering, Thammasat University, Submitted to Pace Development Co. Ltd.
- 19. Boonyapinyo, V., Warnitchai, P., Anwar, N., and Thientim N. (2009), Wind Tunnel Testing Study of Gramercy Building and Knighrbridge Building: Part 1 Pressure Measurement Study of Gramercy Building and Part 2 Pressure Measurement Study of Knighrbridge Building, Final Report, Department of Civil Engineering, Thammasat University, Submitted to Century Properties, Inc.
- 20. ISO 10137 (1992), International Organization for Standardization, Bases for Design of Structures Serviceability of Building against Vibration, Geneva.
- 21. Boonyapinyo, V., Periroek A, and Thamasungkeeti, W., (2008), Wind Load Study for Plot C42 Building by Wind Tunnel Test, Final Report, Department of Civil Engineering, Thammasat University, Submitted to Architects 49 International Limited.
- 22. Boonyapinyo, V., and Periroek A, (2008), Wind Load Study for Central Man-U Building by Wind Tunnel Test, Final Report, Department of Civil Engineering, Thammasat University, Submitted to Tiang Chirathivat Real Estate Co., Ltd.
- 23. Boonyapinyo, V., Janesupasaeree, T., and Thamasungkeeti, W. (2009), Identification of Flutter Derivatives of Bridge Decks by Stochastic Subspace Method, Proc. of 7th Asia-Pacific Conference on Wind Engineering, Taipei, Taiwan.
- 24. Thai Meteorological Department (2006), Meteorological Magazine, January-April 2006 issue
- 25. Thai Meteorological Department (2007), Meteorological Magazine, January-April 2007 issue